Exploring the evolution and hidden large-scale structures of galaxies with MeerKAT H I surveys

by

Sambatriniaina Hagiriche Aycha Rajohnson

born on 23 November 1996
in Antananarivo, Madagascar

Dissertation submitted in fulfillment of the requirements for the degree of
Doctor of Philosophy

in the
Faculty of Science
Department of Astronomy
University of Cape Town

February 2024

University of Cape Town

The copyright of this thesis vests in the author. No quotation from it or information derived from it is to be published without full acknowledgement of the source. The thesis is to be used for private study or non-commercial research purposes only.

Published by the University of Cape Town (UCT) in terms of the non-exclusive license granted to UCT by the author.

University of Cape Town

Supervisors

Em. Prof. Renée C. Kraan-Korteweg

Dr. Bradley Frank

“A little progress each day adds up to big results.”

– Satya Nani

Plagiarism Declaration

I, Sambatriniaina Rajohnson, hereby declare that the work on which this thesis is based is my original work (except where acknowledgements indicate otherwise) and that neither the whole work nor any part of it has been, is being, or is to be submitted for another degree in this or any other university. I authorize the University to reproduce for the purpose of research either the whole or any portion of the contents in any manner whatsoever.

Signature:..... Date: 11/02/2024

I confirm that I have been granted permission by the University of Cape Town's Doctoral Degrees Board to include the following publications in my PhD thesis, and where co-authorships are involved, my co-authors have agreed that I may include the publications:

- MIGHTEE-H I: The H I size-mass relation over the last billion years (Chapter 2, accepted for publication in Monthly Notices of the Royal Astronomical Society, Volume 512, Issue 2, pp. 2697-2706.)

- H I Galaxy Signatures in the SARAO MeerKAT Galactic Plane Survey - III. Unveiling the obscured part of the Vela Supercluster (Chapter 3, submitted to Monthly Notices of the Royal Astronomical Society).

Signature:.....

Abstract

Building upon previous high-resolution and high-sensitivity H I surveys conducted over narrow angles of the sky, such as the COSMOS H I Large Extragalactic Survey (CHILES), a new era has begun with the emergence of SKA Pathfinders such as MeerKAT and ASKAP. Deep systematic *interferometric* H I surveys of unprecedented sensitivity and resolution over very wide angles of the sky are now possible. In this thesis, I use the capabilities of MeerKAT to explore H I galaxy scaling relations and investigate concealed large-scale structures (LSS) linked to dynamically significant structures in the Southern Zone of Avoidance (ZOA). To achieve these objectives, I worked on three blind systematic H I surveys conducted with the 4k L-band data from the complete MeerKAT64 array: the MIGHTEE-H I Early Science data, the Vela SARAO MeerKAT Galactic Plane Survey (Vela– SMGPS), and the MeerKAT Vela Supercluster survey (Vela–H I).

As a first step, I validated the MIGHTEE-H I Early Science data covering a total of $\sim 5\,\mathrm{deg}^2$, distributed across three XMMLSS fields ($\sim 3.5\,\mathrm{deg}^2$) and one COSMOS field ($\sim 1.5\,\mathrm{deg}^2$). The spectral line data achieved $12''\times10''$ and $14.5''\times11''$ angular resolutions, with an rms sensitivity of 81 and 44 $\mu\mathrm{Jy\,beam}^{-1}$ per 44.1 $\mathrm{km\,s}^{-1}$ channel, for a total observing time of 13 and 17 hours per XMMLSS and COSMOS field, respectively. Following visual source identification and morphological classification, the sample comprised 276 galaxies – 176 spirals, 72 irregulars, 19 mergers, and 9 early-type galaxies. To independently verify the derived H I properties, I cross-referenced fluxes from COSMOS detections with ALFALFA galaxies, revealing agreement for high-signal-to-noise ratio sources. As an application of the data verification process, I constructed the H I size-mass relation, investigating potential systematic effects present in the early data. This relation was derived for the first time from a uniform interferometric sample, reaching an unprecedented redshift range of $z \sim 0.084$. Based on a subsample of 204 galaxies, the relation was found to be consistent with the literature at $z \sim 0$ and indicated that in the absence of significant environmental influences, gas distribution and mean surface mass density within galaxy discs have remained relatively stable over the past one billion years. A 10% intrinsic variation (0.054 ± 0.003 dex) in the H I size at a given H I mass was observed, but no evidence for evolution over the explored redshift range.

I performed a detailed census to blindly map signatures of hidden LSS in the Vela region, aiming to narrow down the ZOA in redshift space. This unexplored area hosts the enigmatic

Vela Supercluster (VSCL), with its potential merging walls and an inner core obscured in the innermost ZOA. The location of the VSCL is also essential for addressing persistent bulk flow discrepancies.

I pursued a two-phase mapping of the VSCL, with a focus on identifying its gas-rich spirals. Firstly, using data from Vela–SMGPS, which surveyed a narrow strip covering 90 deg^2 ($260^\circ \leq \ell \leq 290^\circ, -2^\circ \leq b \leq 1^\circ$). I imaged 157 individual pointings with a total observing time of $\sim$211 hours. This produced 10 contiguous mosaics with an average rms of 0.39 mJy beam^{-1} per 44 km s^{-1} channel and an angular resolution of $30''\times27''$ ($\pm1''$). Secondly, the MeerKAT Vela–H I survey was designed to explicitly fill the gaps above and below the Galactic Plane (GP) between Vela–SMGPS and prior Vela spectroscopic survey regions ($263^\circ \leq \ell \leq 284^\circ, -6.7^\circ \leq b \leq -2^\circ, 1^\circ \leq b \leq 6.2^\circ$). I processed the 667 Nyquist-sampled fields and generated 32 mosaics. With 67 hours of observations over a 242 deg^2 area, the survey reached an average rms of 0.74 mJy beam^{-1} per 44 km s^{-1} channel for the beam size of $38''\times31''$ ($\pm3''$).

By focusing on the mostly RFI-free band of $250 < V_{\rm hel} < 25000$ km s^{-1}, I identified 843 and 719 heavily obscured galaxy candidates in Vela–SMGPS and Vela–H I, respectively, most of which were previously unknown. When comparing the distribution to simulations based on the SKA H I-science method which assumes a homogeneous distribution, and examining on-sky distributions, a total of six overdensities were observed. With regard to VSCL, the new detections hint at the presence of two wall-like overdensities at $16000 - 19000$ km s^{-1} (W1) and $19000 - 23000$ km s^{-1}(W2). These may well intersect within the longitude range $270^\circ \leq \ell \leq 279^\circ$ at the lowest latitudes. Other major overdensities include the confirmation of the presence of the Hydra/Antlia wall traversing the GP at $\ell \sim 280^\circ \pm 2^\circ$ at $V_{\rm hel} \sim 2500 - 4000$ km s^{-1} and the discovery of a 30° long, narrow filament in the GP at $\sim$12000 km s^{-1}. By only considering the complete sample from Vela–SMGPS and Vela–H I, I calculated the H I mass function (HIMF) of the two surveys in an attempt to quantify these VSCL overdensities. The overall pattern of the HIMF closely aligns with the ALFALFA HIMF. Additionally, I estimated upper limit overdensity values of 3.5 ± 1.6 and 1.8 ± 2.4 in the inner ZOA for W1 and W2, respectively.

The accomplishments of the MIGHTEE-H I Early Science survey, Vela–SMGPS, and Vela–H I offer a promising glimpse into the immense capabilities that await H I science with the forthcoming SKA.

Acknowledgements

A dissertation does not come to fruition solely through the efforts of one individual, and this work is no different. I wish to extend my gratitude to everyone who played a vital role in making this work possible. Throughout these past years, these individuals have stood by me, offering their unwavering support, inspiration, and invaluable guidance. It is thanks to their contributions that my doctoral journey has been such a remarkable adventure.

Renée, I find it impossible to adequately express my gratitude in this brief paragraph. No matter how many words I use, they cannot fully convey the depth of my sincere appreciation for having you as a supervisor throughout this journey. Under your guidance, I became a better scientist and gained profound insights into the workings of our Universe. Your remarkable attention to every detail is a source of inspiration that will undoubtedly influence me for years to come. You have consistently provided teaching, guidance, and support to me, even during moments when you have not been feeling your best. For this, hats off to you.

Brad, I deeply value the contributions you have made to my work over the years. I want to express my gratitude for your patience in explaining the technical aspects of my research, for providing programming tips, and for introducing me to high-performance computing. Additionally, I must extend my thanks to the Ilifu team for patiently addressing my numerous technical inquiries and for preparing me to work exclusively on the cloud.

This journey would have been impossible without you, Claude. Thank you for accepting me as one of your students after the DARA program in Madagascar and providing me with the opportunity to come to UCT. Thank you for introducing me to Renee and Brad.

DJ, despite only meeting you since the end of 2022, your contributions have been immensely valuable over the past year and a half. I sincerely appreciate the insightful discussions during the Mega-HI group meetings and your thoughtful comments throughout my thesis and publications. Your approachability and willingness to assist with any inquiries made it effortless for me to engage with you.

A very special thanks to our collaborators Tom Jarrett, Paolo Serra, Lister Staveley-Smith, Anastasia Ponomareva, Natasha Maddox, Thijs van der Hulst, and Khaled Said, for their useful inputs, and particularly for their prompt responses to my emails.

A massive thank you to Nikki, Nadia, Sushma, and Notahiana for helping me proofread

some parts of this thesis. I also cannot forget the invaluable feedback from the writing circle on the pieces of writing I submitted at various stages, which are now included in this thesis.

Throughout the years, I am truly grateful for being in the same research groups as these awesome people: Hao, Wanga, Nadia, Sushma, Vineshree, Narges, Nikki, Martin, Henco, Mikhail, Notahiana, Austun, and Kyra. All the best in everything you do!

To my UCT friends and the 4.32 officemates, including those who have left, the diverse interactions, social activities, and enjoyable moments we shared made UCT a delightful place to work. Special mention goes to Brenda and Miriam; I will always remember our fun adventures at international conferences, with me being the guide.

I am thankful to my parents for enabling me to pursue higher education and for their confidence in my aspiration to attain a doctoral degree in Astronomy. Although I could not go home since the pandemic, their continuous support from afar has been a constant source of strength and motivation.

Last but not least, I am deeply grateful for my husband, Tolotra, whose constant encouragement has been my rock throughout this academic journey. His warm presence and infectious humor have lightened even the darkest moments, making this journey all the more enjoyable. His ability to inspire and motivate me, especially during challenging times, has been a true blessing. I am profoundly thankful to have such a loving and supportive partner beside me.

Contents

1 Introduction **1**

1.1 Galaxy evolution: Nature vs. Nurture 2
1.2 Galaxy distributions 5
1.3 Galaxy superclusters 6
1.3.1 Formation 6
1.3.2 Properties 7
1.3.3 Tracing large-scale structures 8
1.4 The Zone of Avoidance (ZOA) 10
1.4.1 Why observing the ZOA? 12
1.4.2 The Vela Supercluster 15
1.4.3 Mapping the ZOA in H I 19
1.5 The MeerKAT telescope 20
1.6 A motivation for deep blind H I systematic surveys with MeerKAT 22
1.6.1 Thesis structure 23

2 MIGHTEE -H I: the H I Size – Mass relation over the last billion years **24**

2.1 Introduction 25
2.2 MeerKAT observations and data reduction 27
2.2.1 Observation details 27
2.2.2 Data reduction and imaging 28
2.2.3 Primary beam correction and noise properties 29
2.3 Data products & H I candidate verification 32
2.3.1 H I source finding 33
2.3.2 Source subcubes 33
2.3.3 Global H I profiles 34
2.3.4 Moment maps 38
2.3.5 Morphological classification 39
2.4 Sample selection 41

2.5 H I catalogue . . . 42
2.6 H I properties . . . 45
2.6.1 H I size . . . 45
2.6.2 H I mass . . . 48
2.6.3 H I properties distribution . . . 49
2.6.4 Comparison with ALFALFA . . . 51
2.7 Constructing the $D_{\rm HI} - M_{\rm HI}$ relation for the survey . . . 53
2.7.1 $D_{\rm HI} - M_{\rm HI}$ relation . . . 53
2.7.2 $D_{\rm HI} - M_{\rm HI}$ relation and galaxy type . . . 55
2.7.3 $D_{\rm HI} - M_{\rm HI}$ relation and environment . . . 58
2.7.4 Evolution of the $D_{\rm HI} - M_{\rm HI}$ relation as a function of z . . . 58
2.8 Summary and conclusions . . . 60

3 H I Galaxy Signatures in the SARAO MeerKAT Galactic Plane Survey – Unveiling the obscured part of the Vela Supercluster 62
3.1 Introduction . . . 63
3.2 MeerKAT observations and data processing . . . 67
3.2.1 The SARAO MeerKAT Galactic Plane Survey . . . 67
3.2.2 Observations and data reduction . . . 67
3.2.3 H I imaging . . . 69
3.2.4 Mosaicking strategy . . . 70
3.3 Source finding and verification . . . 72
3.3.1 H I source finding . . . 73
3.3.2 Source verification . . . 76
3.3.3 Parameterization . . . 78
3.3.4 Quality assessment . . . 80
3.4 Vela–SMGPS catalog . . . 86
3.5 Vela–SMGPS H I properties distribution . . . 87
3.5.1 Completeness . . . 87
3.5.2 Simulations . . . 90
3.5.3 Comparison of H I properties . . . 91
3.6 Large Scale Structures Analysis . . . 94
3.6.1 LSS in velocity space . . . 95
3.6.2 LSS crossing the ZOA . . . 95
3.7 Conclusions . . . 102

4 Revealing hidden structures in the Zone of Avoidance – a blind MeerKAT H I Survey of the Vela Supercluster 105
4.1 Introduction . . . 106

4.2 Survey design and observation strategy . . . 107
4.3 H I data processing . . . 109
4.3.1 Data reduction . . . 109
4.3.2 Imaging and mosaicking . . . 109
4.3.3 H I detections . . . 112
4.4 Results . . . 114
4.4.1 The Vela–H I catalog . . . 114
4.4.2 General wedge distribution . . . 117
4.4.3 Internal quality assessment . . . 117
4.4.4 Comparison with other H I surveys . . . 118
4.4.5 Multi-wavelength counterparts . . . 120
4.4.6 H I properties distributions . . . 124
4.5 Large-scale structures discussion . . . 125
4.5.1 Observational data in the Vela region . . . 125
4.5.2 Sensitivity curve and comparison with simulations . . . 127
4.5.3 Discussion of overdensities in the Vela region . . . 128
4.6 Conclusions . . . 134

5 The H I mass functions of galaxies from MeerKAT blind systematic surveys of the Zone of Avoidance: Vela–SMGPS and Vela–H I 137
5.1 Introduction . . . 137
5.2 Sample selection and completeness . . . 139
5.2.1 Homogeneous completeness . . . 141
5.2.2 Modified $V/V_{\rm max}$ test . . . 142
5.3 Derivation of the H I mass function . . . 145
5.3.1 The $1/V_{\rm max}$ method . . . 145
5.3.2 The 2DSWML method . . . 146
5.4 Results and Discussion . . . 148
5.4.1 Overdensity estimation of the walls of VSCL . . . 154
5.5 Summary . . . 157

6 Summary and future work 159
6.1 Thesis highlights . . . 159
6.2 Future work . . . 161

Bibliography 165

A The MIGHTEE H I Size – Mass relation: sample galaxy catalog 185

B The Vela–SMGPS appendices **191**
B.1 Sofia-2 parameter file . . . 191
B.2 HIZOA detections in Vela–SMGPS . . . 193
B.3 Vela–SMGPS full catalog . . . 195
B.4 Vela–SMGPS H I atlas . . . 223
B.4.1 Solid detections . . . 224
B.4.2 Possible detections . . . 260

C The Vela–H I appendices **272**
C.1 Residual RFI . . . 272
C.1.1 Short track bugs . . . 272
C.1.2 Solar RFI and 1380 MHz spike . . . 273
C.2 Vela–H I full catalog . . . 278
C.3 Vela–H I atlas . . . 303
C.3.1 Solid detections . . . 303
C.3.2 Possible detections . . . 335

List of Figures

1.1 A map of the distribution of galaxies within 100 million Light Years, also known as the 'Virgo Supercluster' . . . 7
1.2 An Aitoff projection of the all-sky distributions of 2MRS galaxies in Galactic coordinates . . . 11
1.3 The Cosmic Microwave Background dipole anisotropy . . . 13
1.4 An Aitoff projection of the all-sky distributions of nearly 50000 galaxies from 2MASS in Galactic coordinates . . . 15
1.5 The Vela Supercluster velocity distribution out to 32000 km s^{-1} within the Vela region $(\ell, b) = (285°–255°, \pm 10°)$ . . . 17
1.6 The Vela spectroscopic survey region, along with the envisioned MeerKAT survey area . . . 18
1.7 An overview of the MeerKAT radio telescope . . . 21

2.1 Flow chart for the calibration, continuum subtraction and imaging of MIGHTEE-H I raw dataset . . . 29
2.2 Examples of various continuum residual and imaging artefacts depending on the polynomial fit order for continuum subtraction (from N=2 to N=4), and an additional median filtering to the cube. . . . 30
2.3 Effect of median filtering and primary beam correction on the noise distribution of XMMLSS12 . . . 32
2.4 Sky distributions of the 276 detections found in the MIGHTEE-H I Early Science fields . . . 34
2.5 Consecutive H I channel maps of MGTH_J021836.3 – 043236 . . . 35
2.6 Measured quantities from a baseline corrected spectrum . . . 37
2.7 Mom-0 and mom-1 maps of MGTH_J021815.4 – 041558 . . . 40
2.8 Examples of galaxies of different morphological types detected within MIGHTEE-H I . . . 41
2.9 Example illustrating the 2D Gaussian fitting procedure . . . 47

2.10 Histograms of the H I parameters distribution for the sample of 204 galaxies selected in the MIGHTEE-H I early survey 49
2.11 H I sensitivity curve of the 204 galaxies selected in the MIGHTEE-H I sample . 51
2.12 H I detections in MIGHTEE-H I (grey dots) and ALFALFA (red squares) in the COSMOS survey region 52
2.13 H I mass comparison between MIGHTEE-H I and ALFALFA 53
2.14 H I global profiles of MIGHTEE (black line) and ALFALFA (blue dashed line) in the COSMOS survey region 54
2.15 The posterior distributions of the slope, zero point and the intrinsic scatter of the $D_{\rm HI} - M_{\rm HI}$ relation 55
2.16 $D_{\rm HI} - M_{\rm HI}$ relation for 204 inclination-corrected galaxies 56
2.17 $D_{\rm HI} - M_{\rm HI}$ relation of galaxies in the MIGHTEE-H I survey for two redshift bins 59

3.1 A 2D slice of the dirty PSF along the x and y axes in a Vela–SMGPS field. The black solid line shows the PSF without taper, the red dashed line indicates the PSF after a $15''$ taper has been applied. 70
3.2 An example of the H I distribution without a taper (left) and a $15''$ taper (right). PSFs with respective sizes of $12'' \times 11''$ and $30'' \times 27''$ are shown in the lower left corner of each image, while a 10 kpc scalebar is illustrated in the lower right corner. 70
3.3 Pointing configuration of Vela–SMGPS ($260^\circ \leq \ell \leq 290^\circ$). *Top panel:* distribution of the 10 mosaics (T24-T33) of 22 fields each in the VSCL region, overlayed on the SUMSS continuum map (grayscale). *Bottom panel:* the corresponding rms levels of each field. 71
3.4 Continuum (top) and channel map (bottom) of mosaics T28 (left) and T31 (right). The color bar represents flux variation. The bottom right panel illustrates the impact of bright continuum sources in the per-channel image of a spectral line cube. 71
3.5 Top panel: A random example showing spatial noise variation for a central channel map (rms = 0.29 mJy beam^{-1}) in a Vela–SMGPS mosaic. The black rectangle outlines the SoFiA source-finding region. Bottom panel: Noise variation as a function of velocity within the central search area of the same mosaic. The mean rms is indicated by the dashed horizontal line. 73
3.6 A consecutive H I channel map showing a low-redshift source with low signal-to-noise ratio. The black contour level begins from the 4σ rms noise of the detection. A 10 kpc scale bar is displayed in the top right corner, the corresponding velocity in the top left, and the beam size is depicted by the white hatched ellipse in the bottom left corner. 74

3.7 A consecutive H I channel map, similar to Fig. 3.6, but depicting a high signal-to-noise ratio detection at the VSCL distance. Note that the color scaling is the same as in Fig. 3.6. 74
3.8 The three visual classifications of SoFiA detected sources: "Solid", "Possible", and "Reject" (from top to bottom) 77
3.9 Histogram depicting the local rms noise measured around each solid detection (shaded in grey) and possible detection (shaded in red). 79
3.10 Internal coordinate offsets for detections found on overlapping regions of adjacent mosaics. Grey dots illustrate solid detections while red ones designate possible detections. The inner (dashed) and outer (solid) circles delimit the one and two sigmas standard deviations of $2.77''$ and $5.54''$, respectively. 81
3.11 Vela–SMGPS internal coordinate offsets as a function of integrated signal-to-noise ratio (SNR). Red and grey dots represent possible and solid detections. Horizontal and vertical dashed lines mark the coordinate precision 1σ standard deviation, and an SNR of 25, respectively. 82
3.12 Moment-0 H I emission maps for two HIZOA sources (J0913-48, and J0917-49) reveal them to consist of several counterparts in Vela–SMGPS. A 10 kpc scale bar and the beam size are shown in the right and left bottom corners of each image. 84
3.13 Comparison of H I linewidth w_{50} among the 31 HIZOA detections within the Vela–SMGPS survey. The cyan lines represent the best-fit linear regressions. . 84
3.14 Comparison of heliocentric velocities from Vela–SMGPS and the difference $V_{\text{Vela–SMGPS}} - V_{\text{HIZOA}}$. 85
3.15 Comparison of the integrated fluxes of 31 galaxies in common with HIZOA. The cyan line illustrates the best-fit linear regression, closely following the one-to-one relation indicated by the grey dashed line. 85
3.16 Redshift wedge diagrams illustrating the distribution of H I-detected galaxies up to $V_{\text{hel}} < 25000$ km s^{-1} in Vela–SMGPS (blue dots) and HIZOA (red dots). The left panel depicts a longitude wedge plot covering the latitude range $-2^\circ \leq b \leq 1^\circ$, while the right panel displays a latitude wedge plot spanning the longitude range $260^\circ \leq \ell \leq 290^\circ$. 87
3.17 Completeness assessment using a log-log plot of the mean H I flux density $S_{\text{mean}} = (S_{\text{int}}/w_{50})$ for all 843 Vela–SMGPS detections in black and 646 solid detections exclusively in red. The black dashed and red dotted lines correspond to the expected $-3/2$ slope for a homogeneous distribution in both samples. 90
3.18 Velocity distribution for the full survey range ($260^\circ \leq \ell \leq 290^\circ$) of Vela–SMGPS detections (light-red histograms). The cyan lines correspond to the S45 simulations (rms $\sim$ 0.45 mJy beam^{-1}). 92

3.19 Distribution of global H I parameters in Vela–SMGPS (light-red filled histogram) and S45 simulation (cyan histogram). The four panels display, from left to right, the linewidth (w_{50}) measured at the 50% level of peak flux, the logarithm of integrated flux density ($S_{\rm int}$), the logarithm of H I mass ($M_{\rm HI}$), and the integrated signal-to-noise ratio (SNR). 92
3.20 Dependence of H I linewidth w_{50} as a function of H I mass (top panel) and H I mass versus velocity (bottom panel) 93
3.21 Velocity distribution histograms similar to Fig. 3.18, where the three different panels subsample distinct longitude ranges: $280° \leq \ell \leq 290°$, $270° \leq \ell \leq 280°$, and $260° \leq \ell \leq 270°$. 96
3.22a On-sky distributions of galaxies in the Vela–SMGPS survey, divided into three redshift intervals within the nearby velocity range $2000 < V_{\rm hel} < 15500$ km s^{-1}. An accompanying wedge diagram limited to $V_{\rm hel} < 15500$ km s^{-1} is displayed in the bottom right panel 100
3.22b Continuing from Fig. 3.22a, this figure presents two velocity bins with $\Delta v = 4500$ km s^{-1} in the left panels, covering the higher redshift range ($V_{\rm hel} > 15500$ km s^{-1}). The right panel features a wedge diagram within $15500 < V_{\rm hel} < 24500$ km s^{-1}. 101

4.1 The 242 deg^2 area covered by the MeerKAT Vela Supercluster survey, overlayed on a grayscale map from the Sydney University Molonglo Sky Survey (SUMSS; Bock et al. 1999) continuum map 108
4.2 Mosaicking configuration of Vela–H I. Each block is indicated alternatively by black or grey dashed rectangles and subdivided into four partially overlapping tiles labeled A to D. 110
4.3 Rms versus velocity in km s^{-1} as measured through the centers of the 32 mosaics. Interference from Global Positioning Satellites can be seen in the frequency band 1375 – 1387 MHz (~8500 km s^{-1}). The average rms noise of 0.74 mJy beam^{-1} is shown by the horizontal dashed lines when excluding the high noise from the mosaic A2B (brown line), which is nearly a factor of two higher than other mosaics and shows stronger fluctuations as well. 111
4.4 Example of source finding regions for the different mosaic configurations . . . 113
4.5 Longitude and latitude redshift wedge plots of detected galaxies in Vela–H I represented by dark blue dots for those above the GP and light blue dots for those below. 117
4.6 Galactic coordinates separations between Vela–H I detections found in the overlapping regions of the mosaics. The black dashed and solid circles mark the 1σ and 2σ of the coordinate separations. 118

4.7 Left panel: integrated fluxes of Vela–H I detections with known counterparts from HIZOA are compared. The one-to-one relation is represented by the black dashed line, and the best linear fit is indicated by the cyan solid line. In the right panels, the differences in systemic velocities (top panel) and H I linewidth (bottom panel) between Vela–H I and HIZOA are illustrated. The cyan lines in both panels depict the outcomes of the best-fit linear regressions, with the dashed black zero-difference line serving as a reference for comparison. 120
4.8 On-sky distribution of Vela–H I detections (light blue dots). Superimposed are associated multi-wavelength counterparts where those with spectroscopic redshift data are represented by red open squares and the blue open squares mark counterparts without available redshift information. Black contour lines delimit the Galactic foreground extinction at $A_B \simeq 3\overset{\mathrm{m}}{.}0$. 122
4.9 Histogram comparing Vela–H I detections (light-blue) and likely counterparts as a function of velocity (left panel) and H I mass (right panel) 122
4.10 Heliocentric optical velocity comparison between Vela–H I galaxies and counterparts with spectroscopic redshifts ($\Delta v = v_{\text{Vela–HI}} - v_{\text{opt}}$). The dark-shaded regions delineate the 1σ and 3σ standard deviations, respectively. 123
4.11 Barred histograms showing the heliocentric velocity distributions of the galaxies from Vela–H I that lie above the Plane (blue), Vela–SMGPS in the inner ZOA (orange), and Vela–H I galaxies below the GP (cyan), respectively. 124
4.12 Histograms of the H I parameters from the systematic blind H I surveys Vela–H I (719 galaxies, blue) and Vela–SMGPS (843 galaxies, orange). The left panel (a) displays the linewidths (w_{50}), the right panel (b) the H I mass distribution. . 125
4.13 Spatial distributions in Galactic coordinates of galaxies surveyed across the wider VSCL region ($256° < \ell < 294°, |b| < 15°$) with velocities reaching out to 25000 km s^{-1} from prior optical and H I redshift surveys, combined with the systematic MeerKAT H I surveys Vela–H I and Vela–SMGPS 126
4.14 Sensitivity curve illustrating the correlation between H I masses and heliocentric velocities for Vela–H I detections (depicted as red dots), accompanied by simulated galaxies for the full SMGPS (528 deg^2) with an rms of 0.75 mJy beam^{-1} (S75, cyan dots) 128
4.15 Annotated 2D on-sky distributions of galaxies in the surroundings of the Vela region ($244° < \ell < 306°, |b| < 25°$). The figure displays three nearby panels, each representing a redshift interval with a Δv = 4500 km s^{-1} from 2000 km s^{-1} to 15500 km s^{-1} 130
4.16 Similar to Fig. 4.15, but featuring two panels for the high-redshift velocity range. 132
4.17 Annotated redshift wedge diagrams illustrating galaxies located above the Plane (blue), below (orange), and their combination, covering the Galactic latitude range of –20° < b < +20° and Galactic longitude range $260° \leq \ell \leq 290°$ 133

5.1 The sky positions of H I detections (blue dots) detected in the Vela–SMGPS (top panel) and Vela–H I (bottom panel) surveys. 140
5.2 log $S_{\rm mean}$ vs. log N for Vela–SMGPS (left panel) and Vela–H I (right panel). . . 142
5.3 The variation of the Rauzy completeness statistic T_c for the integrated flux (top panel) and the mean flux density (bottom panel). Cyan, magenta, and dark brown lines correspond, respectively, to the statistics for Vela–SMGPS, Vela–H I, and the combined sample. 144
5.4 The H I mass function constructed for the Vela–SMGPS sample (blue) and the scaled S45 simulation (cyan), each accompanied by their respective best-fitting lines. 149
5.5 The HIMF for Vela–H I sample (in blue) and the scaled S75 simulation (in cyan), see Fig. 5.4 for details. 151
5.6 H I mass function of the samples combining Vela–SMGPS and Vela–H I detections (top panel). The distribution of H I masses per bin of 0.3 dex is displayed in the bottom panel. The blue solid line represents the best Schechter fit for the data. The black dashed line corresponds to the best fit from ALFALFA 100. . . 152
5.7 Histograms illustrating linewidth (left panel) and H I mass distributions (right panel) for the selected Vela–H I detections in the 193 deg^2 subset region (depicted in the grey-filled histograms) and the scaled S75 simulation (shown in the red histograms). 152
5.8 Similar to Fig. 4.14 in Chapter 4 but featuring the H I sensitivity curves (H I mass vs. velocity) of the selected Vela–H I detections in the 193 deg^2 subset region (red dots) and the simulation S75 (cyan dots). The solid and dashed black lines correspond to the sensitivity curves for the 5σ H I mass detection level. These curves are based on assumed w_{50} values of 150 and 300 km s^{-1}, respectively, with σ = 0.75 mJy beam^{-1}. 153
5.9 The Schechter parameters for various datasets, including Vela–SMGPS (depicted in purple), Vela–H I (green), S45 (magenta), S75 (cyan), ALFALFA 100 (black), and the combined samples (orange), are projected onto the $\alpha - \log M^*_{\rm HI}$ plane. 154
5.10 HIMFs accompanied by histograms of the mass bin counts for the velocity range of the two VSCL walls: $16000-19000$ km s^{-1}(W1, top panel) and $19000-23000$ km s^{-1}(W2, bottom panel). 156
5.11 Density fraction as a function of H I mass in the region of lowest latitudes ($270^\circ \leq \ell \leq 279^\circ, -1.7^\circ \leq b \leq 0.7^\circ$)) where galaxies from two intersecting walls (W1 in blue and W2 in red) are suspected. The estimated median H I density fractions for the two walls are represented by the blue and red horizontal dashed lines. 157

B.1 Moment-0 maps of HIZOA galaxies detected in Vela–SMGPS. The HIZOA identification name, the beam size, and a 10 kpc scale are shown in the upper right, bottom left, and bottom right corners of each image, respectively. 193
B.1 Moment-0 maps of HIZOA galaxies detected in Vela–SMGPS (Continued) . . 194
B.2 List of HIZOA galaxies resolved into several galaxies in Vela–SMGPS. 194

C.1 An example of a `CASA` 'listobs' file summarizing the observation information for the measurement set of block C2. Short-track bugs, which require flagging, have been highlighted in yellow. 272
C.2 Example of diagnostic plots for the phase calibrator J0825-5010 prior cross-calibration. The left panel displays the amplitude variation over time during the observations, with the sunrise (03:46 UTC) indicated by a red arrow. Scans impacted by solar RFI are marked by red boxes. The middle and right panels showcase the amplitude variation with UV distance, both pre and post-sunrise, respectively. In the right panel, the maximum UV distance for flagging (UVdist < 1.5 kλ or 315m) after sunrise, specifically for the affected baselines, is denoted by the red vertical line. 274
C.3 Example of PV-slices of H I cubes from two target fields. The left panel demonstrates the presence of ripple artifacts, which are effectively removed in the right panel following the solar RFI flagging process. 275
C.4 RMS variations and improvements per field before and after RFI flagging and mosaicking 276
C.5 Histogram displaying the transition of fields from showing strong stripes affected by solar and 1380 MHz RFI to a state of no RFI in each Vela–H I block, both before (dark purple) and after (light purple) data reduction 277

List of Tables

2.1 A summary of the MeerKAT observing parameters and imaging of the MIGHTEE-H I Early Science data. 31
2.2 A catalogue of H I properties of the sample of 204 galaxies in the MIGHTEE-H I Early survey. 44
2.3 Median values of the posterior distributions of the MCMC-based linear fit. Median H I mass and H I sizes for the $D_{\rm HI} - M_{\rm HI}$ relation at different redshift bins, and the corresponding log $D_{\rm HI}$ for a fixed log $M_{\rm HI}$. 57

3.1 Overview of Vela–SMGPS observational parameters 68
3.2 Mosaicking parameters of Vela–SMGPS. 75
3.3 Number of detected sources per mosaic after the two SoFiA runs, including cross-matching, elimination of duplicates between mosaics, and visual verification. The last column presents the measured global and local rms values determined around detections. 79
3.4 Vela-SMGPS catalog: H I properties (first page). 89

4.1 Vela–H I observing blocks overview 108
4.2 Survey parameters' comparison of Vela–H I and Vela–SMGPS 112
4.3 Vela–H I full galaxy catalog: H I properties (first page). 116

5.1 Rauzy completeness limits for the mean flux density at the 97.7% (T_c = –2) and 99.4% (T_c = –3) confidence bounds for Vela–SMGPS, Vela–H I, and the combined samples. The variable f represents the fraction of galaxies surpassing the completeness limit within each sample. 144
5.2 The best-fitting Schechter parameters for the Vela–SMGPS, Vela–H I, and the combined samples used in this work. For reference, HIMF parameters from the simulations S45, S75, and the literature are included for comparison, specifically from ALFALFA 100 (Jones et al., 2018) and the H I Parkes All Sky Survey (HIPASS; Zwaan et al. 2005). To facilitate a straightforward comparison, the parameters of the HIPASS HIMF have been scaled to $H_0 = 70$ km s^{-1} Mpc^{-1}. . 149

5.3 Comparison of the derived Schechter normalization parameter Φ_* for the two velocity ranges of the VSCL walls, at the suspected crossing location and the remaining surveyed area of Vela–SMGPS. 155
5.4 Summary of the best-fitting Schechter parameters for the Vela–SMGPS, Vela–H I, and the combined samples. 158

6.1 Best-fitting Schechter parameters for the Vela–SMGPS, Vela–H I, and the combined samples. 161

A.1 A catalogue of H I properties of the sample of 204 galaxies in the MIGHTEE-H I early survey. 186

B.1 Vela-SMGPS full galaxy catalog: H I properties 196

C.1 Overview of flagged Solar RFI in Vela–H I data, including the percentage of daytime data and the affected baseline length that requires flagging 274
C.2 Vela–H I full galaxy catalog: H I properties. 279

chapter 1

Introduction

A golden era has begun with the Square Kilometre Array (SKA) Pathfinders now operational, offering new opportunities to learn more about the neutral hydrogen gas (H I) content within galaxies. This is made possible through unprecedented depth and resolution, never before attained for wide-field surveys. However, sensitive and high-resolution H I surveys over narrow angles of the sky with interferometers have been conducted before. For instance, the COSMOS H I Large Extragalactic Survey (CHILES, Fernández et al. 2013), a deep 1000-hour survey conducted with the Very Large Array (VLA) over a single pointing of the COSMOS field, attained a typical beam size of $\sim 5'' \times 6''$ and sensitivities of $150 - 50\,\mu$Jy beam^{-1} per channel out to a redshift of 0.5.

In this thesis, I use data from one of the SKA Pathfinders, MeerKAT – the most powerful telescope currently available in the L-band until the SKA's completion – to harness these capabilities.

By working on a relatively RFI-free region in the MeerKAT L-band which was largely inaccessible in previous H I surveys ($\sim 1310 - 1420$ MHz, i.e., a probed volume out to $z \sim 0.08$), the data holds the potential to explore questions related to understanding the evolution of galaxy scaling relations within these surveyed volumes. This exploration is conducted using the H I Early Science data from the MeerKAT International GHz Tiered Extragalactic Exploration (MIGHTEE), presented in Chapter 2. By utilizing this new telescope, the data will also be instrumental in the initial steps of science verification and quality assurance. Tracing H I in galaxies is particularly important as the ongoing process of star formation relies on fresh supplies of gas, and the availability of hydrogen gas in a galaxy's reservoir directly impacts its star formation. Given that H I disks extend further than stellar disks, H I uniquely provides insights into local environmental interactions, such as gas distribution, removal, and accretion.

Additionally, unlike tracers at various wavelengths, H I offers the only efficient method to systematically map the large-scale structures (LSS) of galaxies behind the most obscured part of the

sky by tracing the gas-rich galaxy population. However, a complete whole-sky map of galaxies is indispensable for a comprehensive understanding of our current model of the Universe. Our surveys of the Southern Milky Way Plane, presented in Chapters 3 and 4, will contribute to unveiling previously hidden, dynamically important LSS, including the challenging exploration of structures like the Vela Supercluster (VSCL), which are relevant for flow field studies. The uncovered H I galaxies will allow at the same time the study of the H I mass function and the measurement of structure overdensities as a function of environment.

Before I present the research pursued in this thesis, I will provide essential background information necessary for comprehending the scope of this thesis in the next section. This includes an overview of galaxies with their different scaling relations (Section 1.1), the distribution of galaxies in the cosmic web (Sections 1.2 and 1.3), and the significance of mapping the galaxy distribution hidden behind the Milky Way and the relevance of VSCL in this quest (Section 1.4). Finally, I will provide in Section 1.6 the motivations for conducting this research.

1.1 Galaxy evolution: Nature vs. Nurture

Any vast collection of stars, dust, interstellar gas, and dark matter bonded together by gravity is referred to as a galaxy. It was not until the early twentieth century when Edwin Hubble was able to determine the distance to Andromeda (M31) and the Triangulum Galaxy (M33), that their presence was recognized and led to the beginning of Extragalactic Astronomy (Hubble 1925, 1926a). At present, the further we look into space, the more galaxies are visible to us. According to a study led by Conselice et al. (2016), there exist two trillion galaxies out to $z = 8$ in the observable Universe. They are seen to vary in shapes, sizes, colors, masses, and chemical compositions which are representative of their stage of evolution (Buta, 2013).

It was also Edwin Hubble who introduced in 1926 the first classification system known as the "tuning fork diagram" (Hubble, 1926b). This scheme, still in use to this day, arranged galaxies according to their optical morphology in three categories: ellipticals (or early types), spirals (additionally known as late types), and irregulars. These 'early' and 'late' terminologies were used in such a way because it was initially thought that galaxies evolve from early to late types through progressively developing spiral arms and flatter disks. This interpretation was in fact erroneous (Pfenniger, 1999; Bell et al., 2004).

Nature refers to the internal physical processes that shape the initial intrinsic properties leading to the formation of a galaxy. Galaxies exhibit clear correlations between their properties, which are thought to reflect the underlying physical processes operating within the galaxy and driving its evolution. It has been demonstrated, for example, that the galaxy's morphology is strongly related to its color, gas content, star formation rate, and luminosity (e.g., Holmberg,

1958; Roberts, 1963; Roberts & Haynes, 1994; Allen et al., 2006; Conselice, 2006). Correspondingly, early-type galaxies have no ongoing star formation. They are made up of older stars which makes them appear red. They are typically massive, with little gas, and dominate most of the high-luminosity population of the galaxy luminosity function. Nevertheless, some early-type galaxies show surprisingly large quantities of H I despite a visible lack of star formation (e.g., Morganti et al., 2006). On the other hand, late-type galaxies have relatively large reservoirs of gas, are less massive, and appear bluer with clear evidence of star formation. They are ideal objects to study with radio telescopes. It is therefore important to understand how these different galaxy types have formed and evolved throughout time.

Other scaling relations include the Tully-Fisher relation for late-type galaxies which strongly links the galaxy's luminosity and its maximum rotation velocity (Tully & Fisher, 1977). This relation has been refined in recent years to account for the stellar mass or the baryonic mass (e.g., McGaugh et al. 2000; Kassin et al. 2007; Covington et al. 2010; Torres-Flores et al. 2011; Lelli et al. 2016, 2019; Ponomareva et al. 2018, 2021) instead of luminosity. In addition, the growth of a galaxy's size in relation to its mass is an important subject of concern in the field of galaxy evolution research. Both early- and late-type galaxies are seen to follow a size-mass relation, although early types present a steeper slope than late types (e.g., Shen et al., 2003; Hyde & Bernardi, 2009; van der Wel et al., 2014). It is highly remarkable that this relation does not only hold for optical sizes but is also observed in the neutral hydrogen (H I) component relating the H I mass and the size of its H I disk, known as the H I size-mass relation (see Broeils & Rhee 1997; Verheijen & Sancisi 2001 and references therein). There also exists a relationship between the H I mass and stellar mass of a galaxy, indicating the link between star-forming activity and the available raw fuel (the $M_{\rm HI} - M_*$ relation, Huang et al. 2012; Maddox et al. 2015). Therefore, one of the primary objectives of galaxy formation theories is to accurately reproduce the scaling relations observed in both early- and late-type galaxies. The investigation of these scaling relations also emphasizes the importance of a dual focus on sensitivity, required to identify low-mass galaxies, and survey coverage extending over a large area, facilitating the exploration of a broader search volume. The combination of good sensitivity and resolution provided by MeerKAT allows for a wealth of new systematic interferometric surveys, such as MIGHTEE-H I (Maddox et al., 2021), MHONGOOSE (de Blok et al., 2016), and LADUMA (Blyth et al., 2016; Baker et al., 2019), promising a revolutionary advancement in our understanding of galaxy scaling relations across diverse galaxy populations and a cosmologically significant redshift range. In Chapter 2, I will use mostly RFI-free regions out to $z \sim 0.08$ in Early Science data from the medium-deep H I survey MIGHTEE-H I to investigate the H I size-mass relation of galaxies over one billion years in cosmic time.

Nurture, in contrast, represents the external environmental factors that modify these galaxies' properties after their formation. These external effects consist of gas accretion, tidal stripping

of gas and stars, harassment by gravitational interactions with other galaxies, and hydrodynamical effects from the intra-cluster medium such as ram pressure stripping of gas (see Kennicutt, 1998; Vollmer, 2013, for a review), which particularly affect the gas content of galaxies. The 'morphology-density' relation (Dressler, 1980) has established a widely accepted link between a galaxy's morphology and its local surface density, highlighting the significant influence of the local environment on a galaxy's characteristics and evolutionary trajectory. This relationship is supported by numerous studies (e.g., Butcher & Oemler, 1978; Coziol et al., 1998; Bassett et al., 2013; Pranger et al., 2017; Sun et al., 2018; Bianconi et al., 2020; Aoyama et al., 2022). Galaxies in high-density environments, like galaxy clusters (see Section 1.2 for more details), experience an early suppression of star formation. The majority of galaxies in these environments are early-type galaxies, including elliptical and lenticular (S0) galaxies. On the other hand, galaxies in low-density regions, like the field, can sustain their star-forming activity for longer periods. As a result, late-type galaxies, including spiral and irregular galaxies, are more prevalent in these regions (Dressler, 1980; Peng et al., 2010).

But how do the galaxies acquire and replenish their gas? It was observed by Binney et al. (2000) that the star formation rates (SFRs) have remained relatively consistent since the early stages of the Universe. The predicted gas accretion rate for the Milky Way is, for example, a few $M_\odot\ yr^{-1}$ (De Lucia & Helmi, 2008). However, the gas reservoir of a galaxy is diminished by star formation (Schmidt, 1959, 1963). From the observation of gas in and around galaxies, Sancisi et al. (2008) estimated a "visible" accretion rate of only about $\sim 0.2\,M_\odot\ yr^{-1}$. This estimate suggests that if star formation were sustained solely by the main gas reservoir within the galaxy and replenishment from minor mergers (Bigiel et al. 2008; Sancisi et al. 2008; Kauffmann et al. 2010), the observed gas supply would be depleted within a few Gyr. To maintain the observed SFRs, galaxies must therefore continuously acquire additional gas for instance from filaments in the Intergalactic medium (IGM; e.g., Kereš et al. 2005; Kauffmann et al. 2010), respectively the cosmic web (see Section 1.2).

Hydrogen, in its various states, – neutral (H I), ionized (H II) and molecular (H_2) – is the major component of the IGM and interstellar medium (ISM). The ionized gas is typically found in the halo, while neutral hydrogen is more abundant in the outer regions of the disk. Molecular hydrogen is the major element composing interstellar clouds, which can collapse into stars due to their extremely cold temperatures (~10–20 K, Giovanelli & Haynes 1988). Neutral hydrogen – detectable by the 21 cm hyperfine transition line – can give us an insight into the overall matter distribution in galaxies (Schneider, 1996). It illuminates structures not traced by stars, but a high abundance of H I suggests a potentially active ongoing star formation (Giovanelli & Haynes, 1988). In a normal, isolated environment, the H I disk is the most extended gaseous component in a galaxy, with a size typically twice as large as the optical stellar disk (Cayatte et al., 1994; Broeils & Rhee, 1997). This also makes the study of scaling relations such as the H I

size - mass and the H I mass - stellar mass relations particularly important as they offer valuable insights into the impact of the external environment on the galaxy reservoir and disk. Because of its extent, the H I gas is weakly held together by the galaxy's gravitational potential, and the gas at the outermost region is especially susceptible to being stripped away by environmental effects from the intergalactic medium (IGM) and the intra-cluster medium (ICM) (e.g., Haynes et al., 1984; Verdes-Montenegro et al., 2001; Boselli & Gavazzi, 2006; Chung et al., 2009). Chapter 2 will additionally explore the evolution of the H I size-mass relation in different environments in the MIGHTEE-H I Early Science sample.

1.2 Galaxy distributions

According to the cosmological principle, the Universe is considered to be homogeneous and isotropic on the largest scales. However, studying the matter and galaxy distribution on Mega-parsec scales has revealed that the Universe is not uniform but highly structured, forming a filament-dominated web-like structure named the "cosmic web" (Bond, Kofman & Pogosyan, 1996). The inter-connected network consists of elongated filaments connecting small and large galaxy-rich concentrations — galaxy groups, clusters, superclusters — and sheetlike walls with large empty voids between them (Colless et al. 2001; Proust et al. 2006; Jones et al. 2009). Such structure distribution is also referred to as the "Large-scale structures of the Universe" (hereafter LSS), a term which was put forth by Longair & Einasto (1978).

Galaxy groups represent the smallest and most common type of gravitationally bound aggregates of galaxies. They can be classified into low-mass poor and loose groups, compact groups, and massive, rich fossil groups (Lovisari et al., 2021). The Milky Way, for example, is part of the Local Group (LG) which is a poor group of galaxies (Grebel, 2007), with Andromeda being the most massive galaxy in the LG. Galaxy groups can merge into galaxy clusters. The latter are the largest virialized objects in the Universe, consisting of hundreds up to thousands of galaxies. They are continuously expanding by incorporating individual galaxies and galaxy groups of galaxies from surrounding filaments and the field (e.g., Bravo-Alfaro et al., 2000; Ebeling et al., 2004; Coppin et al., 2012; Gouin et al., 2020). One of the earliest galaxy cluster catalogs was created by George Abell in 1958 through the visual inspection of Palomar photographic plates. Today, this catalog is still being used and contains 4073 galaxy clusters at $z \leq 0.2$ (Abell et al., 1989). Given our focus on the southern sky, Abell clusters labeled from A2713 to A4076, extracted from the complete catalog in 1983 along with the supplementary southern clusters labeled AS0001 to AS1174 in the 1989 catalog, cover this specific sky area.

This thesis has a particular focus on exploring LSS to identify galaxies bisected by the Milky Way Plane, with a focus on the southern hemisphere to subsequently provide a 3D cartography of LSS. The goal is to fill existing gaps, as various dynamically important structures in this

region remain incompletely mapped. These structures are also integral parts of larger cosmic structures, such as superclusters, where knowledge of their mass distributions could significantly impact our understanding of the overall bulk flow of the Universe. These points will be elaborated upon in the following sections.

1.3 Galaxy superclusters

1.3.1 Formation

Structures of varying sizes merge to form larger structures, resulting in the hierarchical structure formation (e.g., White & Frenk, 1991; Navarro & White, 1994). Clusters of galaxies, for example, combine to form larger structures, which are connected by filaments spanning a few to tens of Mpc and are referred to as *superclusters*. This hierarchical clustering system also applies to the LG, which lies at the outer boundaries of the so-called Virgo Supercluster. The Virgo Supercluster, also known as the Local Supercluster, was the first identified supercluster (de Vaucouleurs, 1953, 1958). It is a smaller supercluster of about 30 Mpc in diameter with the Virgo cluster at its core, containing various groups and smaller clusters in its vicinity (de Vaucouleurs, 1953, 1958; Tully, 1982; Giuricin et al., 1988; Peebles, 2022). Their spatial distribution is illustrated in Fig. 1.1.

With dimensions as large as 100 h^{-1} Mpc[1], superclusters consist of a collection of gravitationally assembling galaxy groups and clusters that surpasses a certain spatial overdensity threshold, meaning they are more densely packed with galaxies than the average density of the Universe (Bahcall, 1988). Oort (1983b) pointed out that clusters and superclusters can be distinguished based on their level of relaxation or virialization, where clusters are typically more relaxed than superclusters. Additionally, dynamical evolution proceeds at a slower rate at larger scales. This means that the superclusters we observe today are the largest non-virialized[2] systems in the Universe. They serve as cosmic fossils that reflect the conditions of the early Universe and conserve the information during their formation (Oort 1983a; Kofman et al. 1987; Bahcall 1988). Several studies have suggested that superclusters cores should currently be experiencing gravitational collapse. This will lead to the superclusters' growth and eventual isolation as "island universes" in the future without significantly changing their internal properties (e.g., Reisenegger et al., 2000; Chiueh & He, 2002; Busha et al., 2003; Nagamine & Loeb, 2003; Dünner et al., 2006; Proust et al., 2006; Araya-Melo et al., 2009; Pearson et al., 2014; Einasto et al., 2016, 2022). Observations of supercluster cores and internal structures are important to understanding the effects of LSS on shaping the properties of galaxies, groups, and clusters

[1] Hubble constant $H_0 = 100\ h$ km s^{-1} Mpc^{-1}

[2] 'Virialization' refers to the process by which a gravitationally bound system reaches a stable state of equilibrium i.e., the processes of merging and matter collapse have ceased, indicating the completion of its formation process.

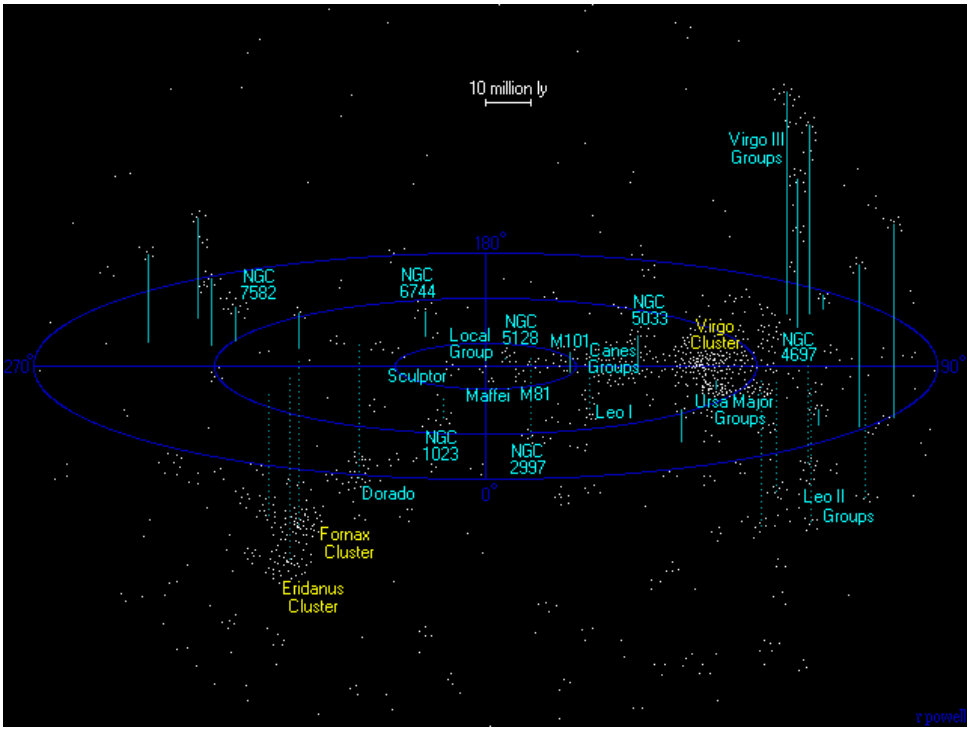

Figure 1.1: A map of the distribution of galaxies within 100 million Light Years, also known as the 'Virgo Supercluster'. Clusters and galaxy groups that make up the supercluster are written in yellow and cyan, respectively. Image credit: Richard Powell, `http://www.atlasoftheuniverse.com/virgocls.gif` (accessed February 10, 2024)

within the supercluster. In Chapter 3 and 4, my objective is to unveil the structure of the hidden core of the Vela Supercluster (further detailed in Section 1.4.2) and determine its morphology.

1.3.2 Properties

Superclusters can be characterized by their size, shape, multiplicity, and inner structure. The richness or multiplicity of a supercluster refers to the number of density field (DF) galaxy clusters or Abell class clusters it contains (Einasto et al., 2007a). Using the multiplicity parameter, Einasto et al. (2007a) have categorized superclusters into four richness classes: poor (< 3 DF-clusters), medium ($3 - 9$), rich ($10 - 19$), and extremely rich (> 20 DF-clusters), with total luminosities ranging from 10^{11} to 10^{14} $L_{\odot}$. Their overall structure from poorest to richest can also be classified into four morphological types as described by Einasto et al. (2011a): spiders, multispiders, filaments, and multibranching filaments.

Spider and multispider superclusters are identified by the presence of one or more high-density clumps, which are typically rich clusters, connected by numerous galaxy chains that extend outward from the clumps. Filament and multibranching filament superclusters are, instead, distinguished by a main body resembling a filament that links clusters. Most poor superclusters exhibit a spider-like morphology (Einasto et al., 2011a, 2012) and have a relatively symmetrical

shape (Einasto et al., 1997). In contrast, rich and luminous superclusters tend to be asymmetric (Einasto et al., 2007a), with filament-type morphologies (Einasto et al., 2011a; Costa-Duarte et al., 2011). These rich superclusters are reported to have a higher concentration of rich and X-ray clusters (Einasto et al., 2001; Luparello et al., 2011), which according to studies such as Bardelli et al. (2000); Rose et al. (2002), may be in the process of merging. The Local supercluster, which is composed of only one rich cluster (the Virgo cluster) at its center and surrounded by several galaxy filaments, is an example of a typical poor spider supercluster (see Fig. 1.1). The Shapley supercluster stands out as the richest nearby supercluster, characterized by a massive concentration of 9 Abell clusters and 2 poor clusters displaying a quite symmetric morphology (Proust et al., 2006, and references therein).

As previous studies have shown, the most dominant type of superclusters is asymmetrical, elongated, and have a filament-like shape (e.g., Jaaniste et al., 1998; Kolokotronis et al., 2002; Basilakos, 2003; Einasto et al., 2007a; Costa-Duarte et al., 2011; Einasto et al., 2011a; Luparello et al., 2011). Larger and more elongated superclusters tend to be richer and more luminous (Wray et al., 2006; Einasto et al., 2007a, 2011a). A large-scale morphology-density relation also exists within superclusters based on the spatial distribution of galaxies according to Einasto et al. (2008). Intra-clusters and supercluster outskirts typically contain late-type, star-forming galaxies, while early-type, red galaxies, and richer groups are found in core regions. Early-type, red, and quiescent galaxies are more common in filament-type and rich superclusters, particularly in their high-density cores, compared to spider-type and poor superclusters (Einasto et al., 2007b, 2014). Nonetheless, these patterns can vary between superclusters, suggesting differences in their evolutionary histories (Einasto et al., 2011a). Some superclusters show an intermediate morphology that falls in between the main types observed. It is proposed that multispiders and multibranching filaments may eventually transform into simpler spider and filament structures as their constituent clusters merge into a single entity in the future. (Einasto et al., 2011a). This will be a specific focus of investigation in this thesis, particularly for the VSCL, as it is suspected to consist of two merging walls in its obscured region. These findings, therefore, suggest that the local (group/cluster) and global (supercluster) environments of a given supercluster both have an impact on the galaxy populations, orientations of individual galaxy members, star formation rates, and properties of groups and clusters within that supercluster (e.g., Fuller et al., 1999; Einasto et al., 2003, 2007b, 2012, 2014).

1.3.3 Tracing large-scale structures

The impact of superclusters extends beyond their constituent galaxies, affecting not only their surrounding structures but also the motions of the Local Universe. According to recent topological studies (Dekel, 1994; Park et al., 2005; Hoffman et al., 2015), there is evidence indicating that superclusters, due to their overdensities, influence the linear gravitational evolution relative

to the Hubble expansion through gravitational perturbations. To comprehend this effect, the first step is to have information on the three-dimensional arrangement of galaxies across the entire sky, including their spatial coordinates and distances.

The Hubble-Lemaître law (Hubble, 1929) establishes that a galaxy's recessional velocity (cz) is directly proportional to its distance (d) in a smoothly expanding Universe, known as the Hubble flow. The recessional velocity can be determined by measuring the shift in a galaxy's spectrum caused by the stretching of photons as they travel through expanding space, commonly referred to as redshift (z). Consequently, a preliminary estimate of distance can be obtained using the formula $d = cz/H_0$, where H_0 represents the Hubble constant. Redshift surveys, assuming the dominance of the Hubble flow in the Universe, serve as a first proxy for mapping the three-dimensional distribution of galaxies in the nearby Universe.

However, determining accurate distances to a large number of galaxies, independent of redshift, is necessary for understanding large-scale dynamics (Dekel, 1994), as a galaxy's motion is not solely governed by the Hubble flow. Galaxies, galaxy groups, and galaxy clusters are influenced by the gravitational pull of nearby high-density regions, causing them to deviate from the smooth Hubble expansion (e.g., Strauss & Willick, 1995). This deviation is known as the 'peculiar' motion or 'cosmic flow field', which serves as an indicator of the mass density in the Universe. Redshift surveys do not provide a clear distinction between a galaxy's peculiar velocity and its overall observed velocity. Additionally, they need correction for velocity dispersions caused by the gravitational potential within which galaxies are bound. This concerns all galaxies in the sense that the motion of the Milky Way with respect to the LG, as well as the motion of group or cluster members relative to their mean velocity, are reflected in the observed systematic velocity. Therefore, the true measured recessional velocity of a galaxy encompasses both its peculiar velocity (V_{pec}) and its cosmological velocity ($H_0 d$). To determine the peculiar velocity, an independent method of measuring distance is required. The most commonly employed distance indicators include (i) Cepheid variable stars (Fernie, 1969), (ii) the Tully-Fisher (TF) relation (Tully & Fisher, 1977), and (iii) the Fundamental Plane (FP) relation (Djorgovski & Davis, 1987).

Redshift and peculiar velocity surveys examples

The first systematic redshift surveys began in the early 1980s with the Revised Shapley-Ames Catalog of Bright Galaxies (Sandage & Tammann, 1981) and the Center of Astrophysics redshift surveys (Davis et al. 1982; CfA1, Huchra et al. 1983; CfA2, Huchra et al. 1995). Over the years, significant progress has been made in detector technology and the development of multi-object spectrographs, enabling larger surveyed volumes and deeper systematic surveys. A few examples include the Sloan Digital Sky Survey (SDSS, York et al. 2000; Aihara et al. 2011),

the 2MASS Redshift Survey (2MRS, Huchra et al. 2012; Macri et al. 2019), and more recently the Galaxy And Mass Assembly survey (GAMA, Driver et al. 2009, 2022). These surveys have successfully measured redshifts of the whole sky to study LSS that are not bisected by the Milky Way.

Peculiar velocity surveys, such as the Six-degree Field (6dF) Galaxy Survey peculiar velocity subsample (6dFGSv, Springob et al. 2014), the 2MASS Tully-Fisher survey (2MTF, Masters et al. 2008; Springob et al. 2016), and large data compilations like Cosmicflows-3 or CF3, (Tully et al., 2016) and Cosmicflows-4 or CF4 (Kourkchi et al., 2020; Tully et al., 2023), were particularly efficient in constructing 3D velocity fields and measuring the overall bulk flows of the Local Universe (see Section 1.4 for more details).

However, both redshift and peculiar velocity surveys have multiple limitations. While restrictions on galaxy brightness are a factor to consider, the most significant challenge lies in the obstructed view caused by the Milky Way at low Galactic latitudes region, known as the "Zone of Avoidance" (ZOA). Optical redshift surveys, including advanced ones like 6dFGS, typically avoid observing galaxies near the ZOA, confining their survey area to Galactic latitudes above $|b| > 10°$. As a result, our understanding of the entire LSS of the Universe remains incomplete at the lowest latitudes. This underscores the significance of the ZOA as a region of interest in this thesis.

1.4 The Zone of Avoidance (ZOA)

In 1878, Richard Proctor identified it as the "Zone of a few Nebulae", while examining the distribution of nebulae in Herschel's General Catalogue (Herschel, 1864). Astronomers during that time were puzzled by the scarcity of objects in that particular area, which coincided with the Milky Way Plane. It was not until 1930 that Trumpler established that the absence of objects around the GP was due to dust obscuration caused by interstellar dust grains within the Milky Way (Cardelli et al., 1989). This phenomenon leads to the absorption of light from background galaxies, causing them to appear dimmer, smaller, redder in color, or even completely hidden.

This region is furthermore characterized by dense stellar populations as well as an increased sky-background brightness, and significant levels of extinction from the Milky Way. Although extensive optical surveys have notably reduced the obscuration zone (Kraan-Korteweg & Lahav, 2000; Kraan-Korteweg, 2005), there remains a persistent gap at $|b| \leq 5°$ at optical wavelength (this gap is larger for areas near the Galactic Bulge).

As the wavelength increases, the degree of obscuration decreases, making longer wavelengths more suitable for studying the ZOA. For example, the Near Infrared (NIR) wavelength, rang-

ing from 1.2 to 2.2 μm, allows improved penetration through a reduced effect of dust extinction, making it valuable for tracing LSS when compared to optical wavelengths (Cardelli et al., 1989). However, NIR observations were limited until larger CCDs became available, and stellar confusion caused by the high density of stars in the Milky Way persisted, particularly around the Galactic Bulge, affecting approximately 10% of the sky (Kraan-Korteweg & Lahav, 2000). The advent of large CCDs enabled NIR surveys over large areas such as the Two Micron All-Sky Survey (2MASS, Skrutskie et al. 2006) to become possible. Examining the distribution of extragalactic extended sources extracted from the entire NIR-sky, referred to as the 2MASS Extended Source Catalog (2MASS XSC, Jarrett et al. 2000), reveals a reduction in the NIR-ZOA across the J, H, and K_s bands thanks to 2MASS XSC's coverage. Nevertheless, acquiring redshifts for these partially obscured red galaxies proves to be a daunting task, if not impossible, since spectra are captured in the optical wavelength. For instance, the 2MASS Redshift Survey (2MRS) undertook a systematic effort to acquire follow-up redshifts for the brightest galaxies identified in 2MASS XSC. Despite achieving a 97.4% completeness down to $K_s \leq 11.75$ mag and $|b| \geq 5^\circ$ (with $|b| \geq 8^\circ$ around the Galactic bulge), approximately 10% of the sky remains unexplored in a systematic manner. This is illustrated in Fig. 1.2 as a gap between the "whole-sky" distribution of galaxies with redshifts from the 2MRS survey. Recent dedicated efforts led by Macri et al. (2019) completed the missing 2.6%, which lie in or close to the ZOA, and resulted in the addition of 1041 redshift measurements for galaxies near the ZOA (red dots in Fig. 1.2).

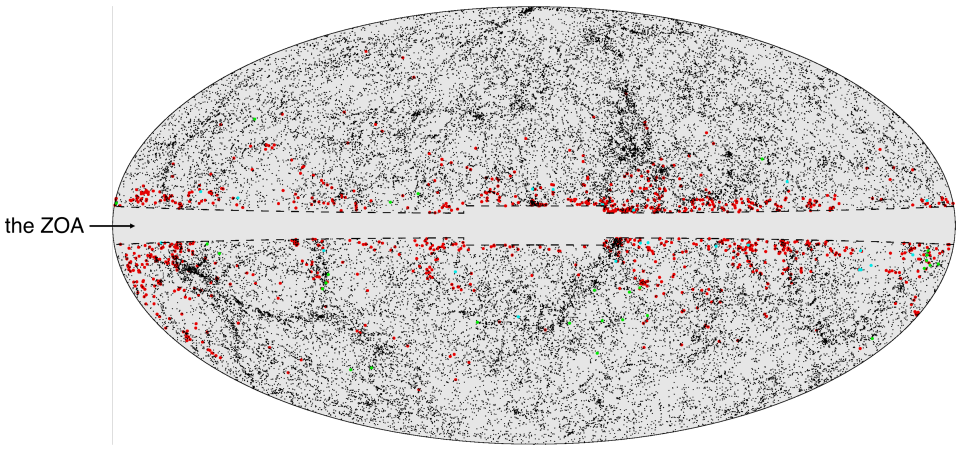

Figure 1.2: An Aitoff projection of the all-sky distributions of 2MRS galaxies in Galactic coordinates. Galaxies with known redshifts are indicated by the black dots (Huchra et al., 2012). Recently added redshifts by Macri et al. (2019) are shown by red dots. The region delimited by dashed lines represents the survey boundary ($|b| < 5^\circ$ but $|b| < 8^\circ$ near the Galactic bulge) which is devoid of galaxies due to high stellar confusion in the ZOA. (Figure from Macri et al. 2019)

On the other hand, the 21 cm line emission from H I at radio frequencies provides a clear and unobstructed view of the ZOA. This method, pioneered first by Kerr & Henning (1987), remains unaffected by dust extinction and stellar confusion (Kraan-Korteweg & Lahav, 2000). However, it can only trace gas-rich galaxy populations and cannot account for ellipticals and the core of

galaxy clusters, which predominantly contain early-type galaxies. X-ray data from surveys such as the ROSAT All-Sky Survey (RASS; Voges et al. 1999; Boller et al. 2016) and the Clusters In the Zone of Avoidance survey (CIZA; Ebeling et al. 2002; Kocevski et al. 2004, 2007) have successfully enhanced our knowledge of galaxy clusters hidden in the ZOA. However, it is important to note that these surveys still do not fully penetrate the ZOA, where the foreground gas from the Milky Way is high at $|b| \leq 5°$, thus absorbing the soft X-ray band of ROSAT. Here, the CIZA survey serves as the equivalent of the ROSAT survey (Ebeling et al., 1996) conducted in the ZOA. Section 1.4.3 will further explore the observations of the ZOA using H I.

Indeed, the ZOA is far from being devoid of galaxies. On the contrary, it hides various enigmatic dynamically relevant LSS from our view, highlighting the importance of exploring this region. Although their detection poses inherent challenges, different wavelengths offer distinct benefits as well as distinct selection biases when it comes to exploring the ZOA.

1.4.1 Why observing the ZOA?

In Section 1.3.3, we discussed how galaxy overdensities within the Local Universe influence the smooth expansion of the Universe and give rise to peculiar velocities or cosmic flow fields. The CMB dipole anisotropy, as observed by Henry (1971); Corey & Wilkinson (1976) and Smoot et al. (1977), provides the first indication of these large-scale motions. Figure 1.3 displays the dipole pattern from the Wilkinson Microwave Anisotropy Probe (WMAP; Bennett et al. 2003), revealing a slight brightness asymmetry between opposite sides of the sky. The CMB serves as a natural reference frame for studying peculiar motions and its dipole is interpreted as a Doppler effect resulting from the peculiar motion of the Local Group relative to the CMB. According to the most recent measurements from the Planck Collaboration et al. (2020), the Local Group exhibits a motion amplitude of 620 ± 15 km s^{-1} in the direction[3] $\ell = 271.9° \pm 2.0°$, $b = 29.6° \pm 1.4°$. The existence of such large-scale motion implies the presence of nearby overdensities that exert gravitational effects on the Local Group's surroundings.

As a result, analyzing the motion patterns in the Local Universe became a useful cosmological test to determine the sources of mass that contribute to the CMB and give rise to the 'bulk flow'. The approach involves reconstructing the CMB dipole independently of CMB observations by directly measuring the distribution of local mass density and velocity fields (Strauss & Willick, 1995). Extensive research has therefore been conducted to map the 3D velocity field in our Local Universe and compare the local bulk velocity's characteristics (amplitude, convergence, direction) with the dipole pattern over the years. Early studies in this field can be found in reviews by Kaiser (1988) and Strauss & Willick (1995).

[3] ℓ and b represent Galactic longitude and latitude, respectively, which are Galactic coordinates.

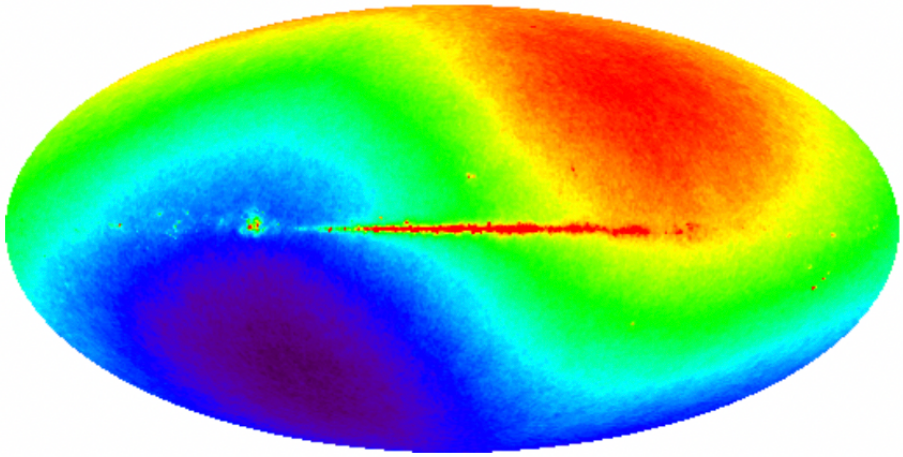

Figure 1.3: The Cosmic Microwave Background dipole anisotropy map from the Wilkinson Microwave Anisotropy Probe (WMAP) showing a temperature variation of $\Delta T = 3.346 \pm 0.017$ mK towards $(\ell, b) = 263.85° \pm 0.1°, 48.25° \pm 0.04°$. The top pattern in red corresponds to hotter regions with blue-shifted radiation, while the bottom pattern in blue corresponds to cooler regions with red-shifted radiation. The horizontal red emission indicates the emission from the Milky Way (Bennett et al., 2003). Image credit: `https://map.gsfc.nasa.gov/universe/bb_cosmo_fluct.html` (accessed February 10, 2024)

The Virgo cluster, being the closest overdensity to the Local Group, has been the subject of early measurements on peculiar velocity (e.g., Yahil et al., 1980; Davis & Huchra, 1982). Specifically, researchers aimed to detect the 'Virgo infall', representing galaxies' general inward motion toward the central region of the Virgo Supercluster (Aaronson et al., 1982). However, it became evident that relying solely on the infall towards the Virgo cluster was insufficient to explain the complete motion of the CMB dipole (e.g., Davis & Peebles, 1983; de Vaucouleurs & Peters, 1984; Sandage & Tammann, 1984; Tammann & Sandage, 1985), which was seen to account for only approximately 35% of the overall motion of the Local Group (Shaya & Tully, 2013). Other mass overdensities beyond the Virgo Supercluster must therefore contribute to the missing component. One of these missing mass concentrations, independently discovered through a survey aiming to measure precise distances of clusters, has led to the identification of the Great Attractor (GA) at $\sim 50\, h^{-1}$ Mpc, partially obscured by the Milky Way (Dressler, 1987; Lynden-Bell et al., 1988; Aaronson et al., 1989; Kraan-Korteweg et al., 1996; Woudt et al., 1999). The GA was found to be lying at the gravitational centre of a vast assembly called *Laniakea*, a significant supercluster that encompasses our own Local supercluster (Tully et al., 2014). Later the Shapley supercluster (SSC) at $\sim 150\, h^{-1}$ Mpc (Quintana et al., 1995; Proust et al., 2006; Lavaux & Hudson, 2011), was also postulated to contribute to the bulk flow. SSC is a massive and extremely rich supercluster in the local Universe. More recently, Hoffman et al. (2017) proposed that an underdensity previously unrecognized plays the role of a 'dipole' repeller, contributing to the overall bulk flow. The CMB dipole, GA, SSC, as well as some of the more prominent galaxy clusters and superclusters in the nearby Universe are pointed out in Fig. 1.4.

Despite significant advancements in both the quantity and quality of peculiar velocity data, the

reconstruction of the CMB dipole continues to face inconsistencies. The ability to determine the convergence radius contributing to the bulk flow remains limited to surveyed volumes, typically less than $\sim 150\,h^{-1}$ Mpc. This limitation occurs because the peculiar velocity error increases linearly with distance, and it is also challenging to gather sufficient samples needed for accurate error reduction (Lavaux et al., 2013). For instance, the work by Erdoğdu et al. (2006a,b) proposed a smaller convergence radius, suggesting that a mere 30% of the motion comes from structures beyond $\sim 50\,h^{-1}$ Mpc. In contrast, other surveys consistently argue for a larger convergence radius, reaching at least the Shapley concentration at $\sim 150\,h^{-1}$ Mpc (e.g., Branchini & Plionis, 1996; Plionis & Kolokotronis, 1998; Kocevski & Ebeling, 2006; Lavaux et al., 2010), and even extending beyond $300\,h^{-1}$ Mpc (e.g., Kashlinsky et al., 2008, 2010, 2011; Colin et al., 2011; Abate & Feldman, 2012). These wider radii would offer a more comprehensive explanation for the observed dipole motion and suggest a tendency to converge towards lower Galactic latitudes in the Southern ZOA as the possible location of the missing attractor(s).

Furthermore, a consensus has yet to be reached regarding the amplitude of the bulk flow. Larger bulk flow amplitudes that surpass the Λ cold dark matter (ΛCDM) predictions have been reported (e.g., Rubin et al., 1976; Lynden-Bell et al., 1988; Kashlinsky et al., 2008; Watkins et al., 2009; Feldman et al., 2010; Lavaux et al., 2010; Abate & Feldman, 2012; Howlett et al., 2022). However, lower values that align with the ΛCDM predictions have also been measured (e.g., Hart & Davies, 1982; de Vaucouleurs & Peters, 1984; Aaronson et al., 1986; Dai et al., 2011; Nusser & Davis, 2011; Turnbull et al., 2012; Hong et al., 2014; Ma & Pan, 2014; Planck Collaboration et al., 2014; Carrick et al., 2015; Scrimgeour et al., 2016; Qin et al., 2018, 2019, 2021).

Despite our knowledge of these underlying structures, there remains a 'residual' bulk flow of approximately $200 - 300$ km s^{-1} representing the unaccounted peculiar velocity of the Local Group (Springob et al., 2016). The source responsible for this residual bulk flow is still a subject of debate. However, the lack of available data in the ZOA presents a significant challenge in this regard. In their work, Scrimgeour et al. (2016) and Springob et al. (2016) have compiled various measurements of the bulk flow from different studies. Subsequent findings from these works (e.g., Hudson et al., 2004; Magoulas, 2012; Nusser et al., 2014; Boruah et al., 2020) point to the presence of a significant mass excess beyond the southern ZOA, specifically in the range of $270°$ to $330°$ in longitudes, which falls outside the scope of recent whole-sky redshift surveys i.e., beyond $200\,h^{-1}$ Mpc. Discovered in this general region, Kraan-Korteweg et al. 2017 (hereafter KK2017) identified at a velocity of around 18000 km s^{-1} ($\sim 257\,h^{-1}$ Mpc), the henceforth called Vela Supercluster (VSCL). VSCL is estimated to contribute approximately 50 km s^{-1} to the residual bulk flow based on a preliminary estimation using linear perturbation theory (KK2017). This influence is of a similar order to that of SSC with $v_{\rm LG} \sim 55$ km s^{-1} (Loeb & Narayan, 2008). Its location within the ZOA had inhibited its discovery as a major overdensity which forms part of the goals of this thesis (see Section 1.4.2).

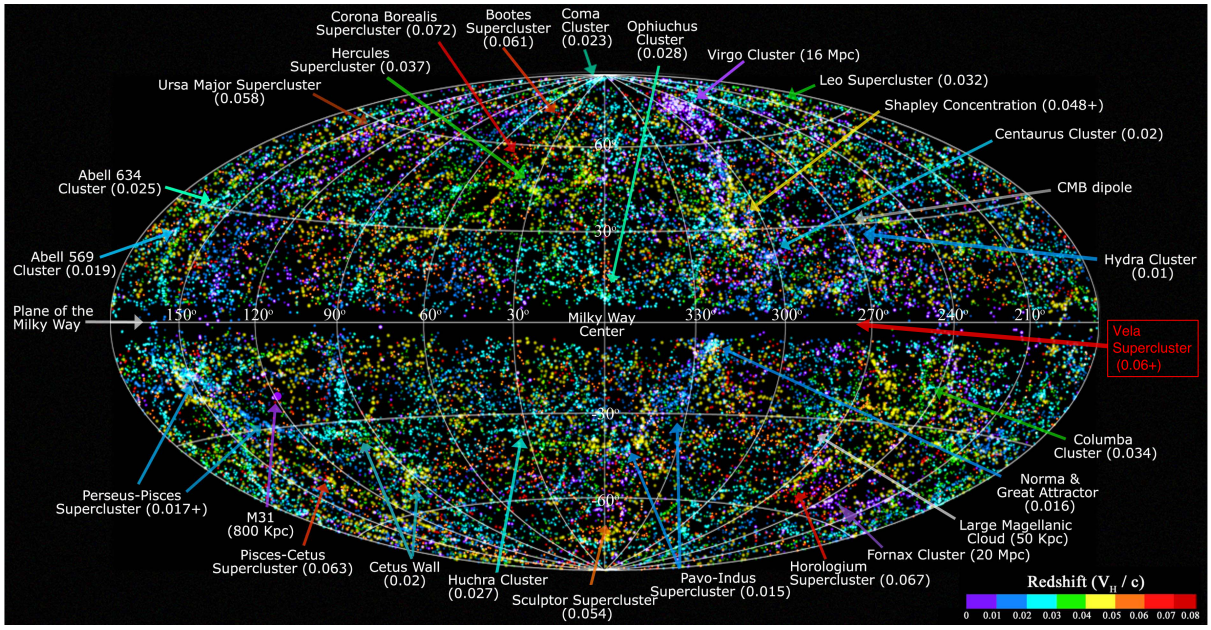

Figure 1.4: An Aitoff projection of the all-sky distributions of nearly 50000 galaxies from 2MASS in Galactic coordinates. Each dot is color-coded according to its 2MRS redshift (Huchra et al., 2012). Familiar galaxy clusters and superclusters in the Local Universe are pointed by arrows. We have added the recently discovered Vela Supercluster (highlighted in red) in the image. Image credit: T. H. Jarrett.

To gain a better understanding of the motion of the LG and address ongoing controversies, the creation of a comprehensive 3D map of the ZOA is of utmost importance. This region of the sky intersects and conceals significant mass concentrations and dynamically essential structures. As illustrated in Fig. 1.4, this includes, for example, the GA core, the Pisces-Perseus Supercluster (PPS, Einasto et al. 1980; Giovanelli et al. 1986; Haynes et al. 1988; Wegner et al. 1993; Ramatsoku et al. 2016), and the Local Void (LV, Tully et al. 2008) hidden behind the GP. The ZOA may still hold surprises, potentially including undiscovered structures like the recently found VSCL. That is why we are going to explore the Vela region within the velocity range $0 < V_{\rm hel} < 25000$ km s^{-1} in Chapters 3 and 4.

1.4.2 The Vela Supercluster

A long-term initiative aimed at revealing the hidden LSS of galaxies obscured behind our own Milky Way, in the general area of the VSCL. Nearly 4500 new spectroscopic redshifts were acquired using the multi-object spectrometer (MOS) on the 11-m Southern African Large Telescope (SALT), and the AAOmega+Two Degree Field (2dF) spectrographs on the 4-m Australian Telescope (Kraan-Korteweg et al., 2015, 2016). Analysis of this spectroscopic survey has provided evidence of a vast and dense concentration of galaxies spanning supercluster scales, centered on the Vela region ($\ell = 272.5° \pm 20°, b = 0° \pm 10°$). This concentration, now known as the Vela Supercluster, remained unnoticed for a long time due to its position just outside the volumes covered by comprehensive sky surveys for redshift and peculiar velocity (e.g., Colless

et al., 2001; Jones et al., 2009; Huchra et al., 2012) and the obscuring effect of the Milky Way. As shown in Fig. 1.4, VSCL is prominently situated in the region $(\ell, b) = (285°–255°, \pm 10°)$ at about 18000 $\mathrm{km\,s^{-1}}$, but its visibility is hindered by the obscuration caused by the Milky Way (Kraan-Korteweg et al., 2017).

Structure & Morphology

The VSCL exhibits two well-defined wall-like structures, accompanied by clusters and groups distributed throughout the region (Kraan-Korteweg et al., 2017). This prominent feature is strongly supported by the radial velocity histogram and redshift wedge diagram shown in Fig. 1.5, revealing the presence of two notable peaks. The main peak, centered at $\sim$18000 $\mathrm{km\,s^{-1}}$, corresponds to the primary broad wall (W1) extending both above and below the GP. A smaller secondary peak, observed below the plane at $\sim$22000 $\mathrm{km\,s^{-1}}$, represents the second wall (W2). Interestingly, investigations based on photometric redshift data from Bilicki et al. (2014) suggest a merger of the two walls below the GP, forming a unified structure that emerges above it. The merger point, i.e., the core, is believed to be situated behind the densest dust layers of the Milky Way. The remarkable similarity between the shapes of the red and grey-shaded histograms in Fig. 1.5, along with the spatial distribution of galaxies in the Vela region above and below the GP in Fig. 1.6, further reinforces this conclusion. Although the spectroscopic survey is highly incomplete at $|b| < 7°$ and even non-existent for $|b| < 5°$, both the spatial and redshift distribution provide compelling hints for the continuity of structures in VSCL across the ZOA. The Vela overdensity is estimated to span a minimum area of $25° \times 20°$ on the sky, corresponding to a physical scale of roughly $\sim 115 \times 90\, h_{70}^{-1}$ Mpc at the supercluster's distance.

Furthermore, various components have been discovered within the broad walls of VSCL. These include several groups, twenty potential clusters with velocity dispersions exceeding 400 $\mathrm{km\,s^{-1}}$, as well as two X-ray clusters embedded in the walls. Notably, the Clusters In the Zone of Avoidance (CIZA) survey (Ebeling et al., 2002; Kocevski et al., 2007) has identified two additional X-ray clusters, specifically CIZA J0812.5-5714 and CIZA J0820.9-5704. Despite being situated just beyond the limits of the Vela survey region, these clusters are still regarded as integral components of the VSCL walls. Surprisingly, Kocevski et al. (2007) did not list any further CIZA clusters within the Vela region because CIZA remains incomplete at lower latitudes. Noteworthy examples include two newly identified potential clusters with X-ray counterparts in ROSAT that were not detected in the CIZA survey and there might be more at lowest latitudes. Therefore, when considering the CIZA clusters and the 20 potential clusters, the VSCL can be classified as a rich (Einasto et al., 2007a), featuring an elongated, wall-like structure and multibranching filaments (Einasto et al., 2011b).

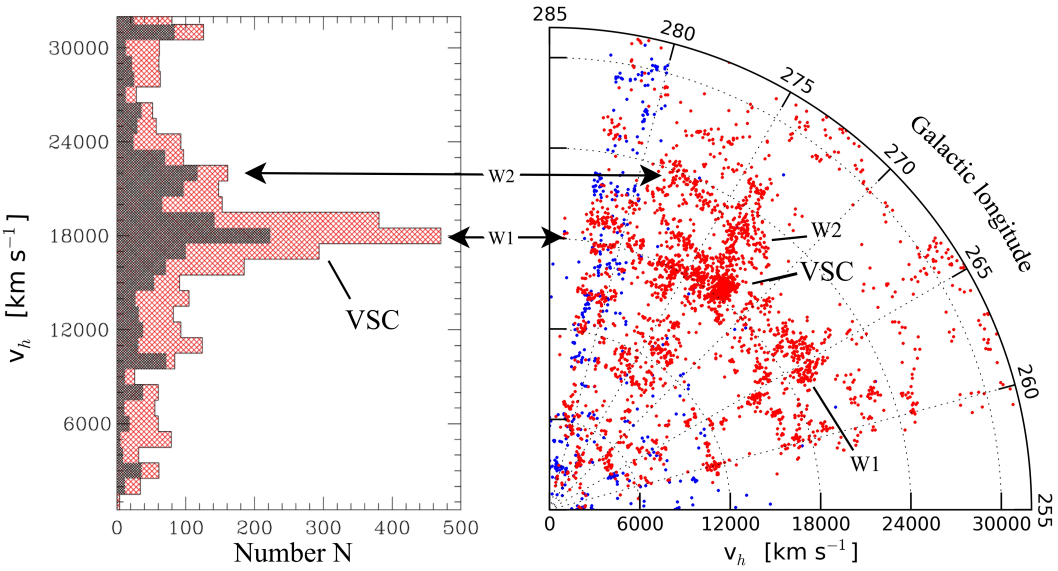

Figure 1.5: The Vela Supercluster velocity distribution out to 32000 km s^{-1} within the Vela region (ℓ, b) = (285°–255°, ±10°). The left panel displays red and grey-shaded histograms representing the velocity distribution of all galaxies in the survey region and galaxies below the Plane, respectively. The right panel shows a redshift slice of the full survey area, with red dots indicating galaxies observed in the Vela region and blue dots representing redshifts from the literature. Both panels feature the two main walls (W1, W2) of the supercluster. (Image source: Kraan-Korteweg et al. 2016)

Overdensity estimation

What remains particularly intriguing is how VSCL will influence the motion of the Local Group and whether it can provide insights into the observed residual bulk flow. VSCL is positioned in proximity to the apex, where residual bulk flows indicate a substantial surplus of mass Scrimgeour et al. (2016); Springob et al. (2016). Moreover, the unexpectedly prominent peak at around 18000 km s^{-1} obtained from two 6dF fields is approximately five times higher than the expected number based on 6dFGs (Jones et al., 2009). This finding indicates a notable overdensity at a relatively high redshift (see Von Maltitz 2012).

Despite the limitations posed by the uncharted core of VSCL and the ineffectiveness of optical spectroscopy in the highly obscured ZoA region, an initial attempt was made to estimate the density enhancement. This analysis was conducted in a region where the 2MASX catalog (Jarrett et al., 2000) provided complete coverage ($6° < |b| < 10°$), and revealed a significant increase in galaxy counts, ~1.2 times more galaxies per square degree and magnitude bin. Additionally, based on photometric redshifts, there was evidence of a higher mass density with $\delta \sim 0.5-0.77$ within the volume surrounding VSCL. This density is similar to that of the SSC, which has been measured to be $\delta \sim 0.6$, particularly when considering the possibility of a central core hidden behind thick dust layers. In Chapter 5, we aim to quantify the overdensity of this obscured inner core of the Vela Supercluster using H I mass functions.

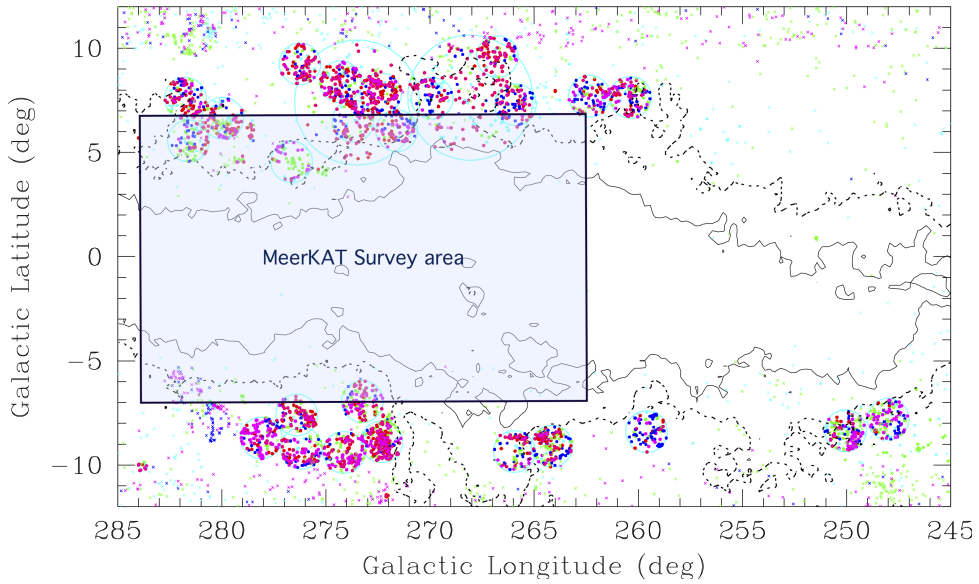

Figure 1.6: The redshift distribution of galaxies within the Vela spectroscopic survey region, sourced from Kraan-Korteweg et al. (2017). Each galaxy in the figure is color-coded according to its redshift: cyan represents $v < 8000$ km s^{-1}, green corresponds to $8000 < v < 16000$ km s^{-1}, red signifies $16000 < v < 20000$ km s^{-1}, magenta represents $20000 < v < 24000$ km s^{-1}, and blue indicates $24000 < v < 32000$ km s^{-1}. The presence of two large 6dF fields and 25 small 2°-AAOmega fields is highlighted by cyan circles. Contour lines are used to represent two levels of extinction: solid lines indicate $A_K = 0\overset{m}{.}3$, beyond which the galaxy sample becomes incomplete and obtaining spectroscopy becomes challenging, while dotted lines represent $A_K = 0\overset{m}{.}18$. The designated area for the planned MeerKAT survey in this thesis is superimposed on the Vela spectroscopic survey region.

Surprisingly, two independent assessments were conducted to provide further evidence for the existence of VSCL, separate from Kraan-Korteweg et al. (2017) redshift sample. Sorce et al. (2017) and Courtois et al. (2019) employed different approaches, namely the constrained realization techniques (CLUES) on the Cosmicflows-2 data (Tully et al., 2013) and the hierarchical Bayesian method by Graziani et al. (2019) applied to Cosmicflows-3 data (Tully et al., 2016), respectively. Both investigations unveiled a suggestive presence of massive overdensities, situated deep within the ZoA, centered at $(\ell; b; v) \simeq (269°, -9°, 19900$ km s$^{-1})$. These indirect measurements provide independent evidence for the existence of the significant and massive VSCL.

VSCL therefore represents a vast uncharted territory in the nearby Universe, akin to an undiscovered continent whose contours are only beginning to emerge. Fortunately, H I radiation serves as the sole tool capable of penetrating the deepest regions of the ZOA, providing a unique opportunity to gain fresh insights into the motion of the Local Group. The following section will provide a concise summary of the H I surveys conducted thus far to uncover obscured structures within the ZOA.

1.4.3 Mapping the ZOA in H I

The small size of Galactic dust grains ($\sim$0.1 μm, Weingartner & Draine 2001) allows the 21 cm emission line from H I to pass through unobstructed through the Milky Way without scattering or absorption. Radio observations exploit this advantageous characteristic, enabling the straightforward mapping of LSS within the ZOA, free from the constraints imposed by dust or foreground extinction (see review by Kraan-Korteweg 2005). Moreover, we can immediately obtain the redshift and rotational velocity information (though we need the inclination to derive rotational velocity) of galaxies directly from their H I detection, eliminating the need for follow-up redshift surveys.

Notable early examples of systematic blind H I surveys in the (Northern) ZOA include the pioneering work of Kerr & Henning (1987), who achieved significant advancements in blind survey techniques. Their survey, conducted using the 91-m Green Bank radio telescope, led to the discovery of 16 previously unknown galaxies spanning velocities up to 7500 km s^{-1} with a channel resolution of 22 km s^{-1} and a beam size of $10.80'$. Another one, known as the Dwingeloo Obscured Galaxies Survey (DOGS), detected a total of 36 galaxies, out of which 23 were previously unknown, within the range of $30° \leq l \leq 220°$ and $|b| \leq 5°$, reaching velocities up to 4000 km s^{-1} and exhibiting an rms sensitivity of 40 mJy (Henning et al., 1998; Rivers et al., 1999).

Since then, multi-feed array receivers on telescopes like Parkes, Arecibo, and Effelsberg have revolutionized blind systematic surveys, enabling large sky coverage and faster survey speeds. Noteworthy surveys such as the H I Parkes Zone of Avoidance Survey in the Southern ZOA (HIZOA-S, Staveley-Smith et al. 2016), its extension to Northern ZOA (HIZOA-N, Donley et al. 2005), and the Galactic Bulge (HIZOA-GB, Kraan-Korteweg et al. 2008b) covered a total nominal area of $\sim$3440 deg^2 with an rms sensitivity of $\sigma \sim 6$ mJy per beam per 27 km s^{-1} channel. HIZOA not only revealed valuable information of about a thousand individual galaxies out to 12700 km s^{-1} but also provided unprecedented insights into the connections between prominent features in the ZOA. These connections include the GA wall linking the Centaurus supercluster above the GP, the Pavo-Indus supercluster beneath the plane (Juraszek et al., 2000), the Puppis region, and enhanced our understanding of voids such as the Orion, Gemini, Canis Major, and the Local Void.

Furthermore, other comprehensive surveys include the Arecibo L-band Feed Array Zone of Avoidance (ALFAZOA, Henning et al. 2010) survey and the EZOA catalogue (Schröder et al., 2019) derived from the Effelsberg-Bonn H I survey (EBHIS, Winkel et al. 2010; Kerp et al. 2011). The ALFAZOA survey consists of two phases: the shallow phase, which has been completed, and the ongoing deep phase. In the shallow phase ($\sigma \sim 5 - 7$ mJy), covering an area of 1200 deg^2, 403 galaxies were detected out to 12000 km s^{-1}, including 259 new redshift mea-

surements. The ongoing deep phase ($\sigma \sim 1$ mJy) has already identified 61 galaxies within the initial 15 sq. deg^2 out of the total 300 deg^2, reaching velocities of nearly 19000 km s^{-1}. Its preliminary results further support the extent of clusters such as Orion and Abell 539 (McIntyre et al., 2015; Sanchez-Barrantes et al., 2019). With a remarkable sensitivity of 1 mJy beam^{-1} at a channel resolution of 9 km s^{-1}, unfortunately, the deep ALFAZOA survey is limited to a relatively small portion of the sky within the Northern ZOA.

The EBHIS survey, on the other hand, achieves homogeneous coverage of the northern sky for regions with declinations $\delta > -5°$ and extending up to a distance of 18000 km s^{-1}. To explore the ZOA, the EZOA catalogue was created from the shallow version of EBHIS. With a velocity resolution of 10.24 km s^{-1}, a beam size of $10.80'$, and a sensitivity of $\sigma \sim 23$ mJy, the catalogue contains 170 detections within $\delta > -5°$ and $|b| < 6°$ out to 12500 km s^{-1}. Notably, 67 of these findings are new H I detections (Schröder et al., 2019). Significant features such as the Supergalactic plane ($\ell \sim 140°$) and the tail-end of the Perseus-Pisces filament crossing the ZOA at $\ell \sim 90°$ (Ramatsoku et al., 2016; Kraan-Korteweg et al., 2018) have been reinforced.

While targeted H I observations from various surveys have also contributed to our understanding of structures behind the Milky Way (e.g., Kraan-Korteweg et al., 2002; Schröder et al., 2009; van Driel et al., 2009; Kraan-Korteweg et al., 2018), neither of these targeted nor blind H I surveys with single dish telescopes have uncovered the VSCL so far. Therefore, a necessity arises for systematic H I surveys employing interferometers. The initial attempt involved a blind H I survey utilizing the Westerbork Radio Synthesis Telescope (WSRT). This survey focused on the Perseus-Pisces filament crossing, covered an area of approximately ~9.6 deg^2 and disclosed 211 galaxies at distances of up to 16600 km s^{-1} (Ramatsoku et al., 2016).

It was also only recently that the MeerKAT16 Early Science Project (Kraan-Korteweg et al., 2016) probed an area along a prospective wall of the VSCL Steyn (2023). This pilot project aimed to evaluate the feasibility of conducting a larger survey using the MeerKAT telescope (Jonas & MeerKAT Team, 2016) within a reasonable timeframe. Additionally, it served as an opportunity to optimize the galaxy identification process through automated pipelines. The initial analysis of the early science data revealed the presence of 119 reliable galaxy detections, indicating an H I deficiency at the core of the recently identified VC04 cluster. VC04 is situated within the primary wall of the VSCL (Kraan-Korteweg et al., 2017).

1.5 The MeerKAT telescope

Situated near Carnarvon in the Northern Cape of South Africa, the MeerKAT radio telescope (Jonas & MeerKAT Team, 2016) serves as a precursor to the Square Kilometre Array (SKA, Driessen 2020; Weltman et al. 2020) mid-array, which is set to become the world's largest radio

Figure 1.7: An overview of the MeerKAT radio telescope. Image credit: `https://www.sarao.ac.za/gallery/meerkat/` (accessed February 10, 2024)

telescope. Until the completion of the SKA, MeerKAT currently holds the distinction of being the most sensitive radio interferometer in the Southern Hemisphere for decimetre-wavelength observations. Originally referred to as the Karoo Array Telescope (KAT), its name was changed to "MeerKAT" which symbolizes "more of KAT", to reflect the increase in its number of receptors. MeerkAT also pays tribute to the cherished *Suricata suricatta*, a small mammal native to the Karoo region.

MeerKAT is equipped with 64 interconnected receptors that consist of 13.5 m offset Gregorian dishes, as shown in Fig. 1.7. The receptors are spread across a maximum distance of 8 km, with a notable concentration of 70% (48 receptors) within a compact 1 km diameter core area and a minimum baseline of 29 m. The dense central arrangement allows for excellent sensitivity, making MeerKAT well-suited for capturing extended emissions, while the longer baselines contribute to achieving high-resolution images. Moreover, MeerKAT operates across three distinct frequency bands, namely the UHF band (580 – 1015 MHz), L-band (900 – 1670 MHz), and S-band (1750 – 3500 MHz). Its correlator offers two channelization modes (4K, 32K) and supports full polarisation recording, encompassing XX, XY, YX, and YY correlations. For a comprehensive understanding of MeerKAT's technical specifications, detailed documentation can be found in Jonas & MeerKAT Team (2016).

The preliminary MeerKAT science case, outlined in Booth et al. (2009), has laid the foundation for several ongoing Large Survey Projects (LSPs). Notable examples include the MeerKAT International GHz Tiered Extragalactic Exploration Survey (MIGHTEE; Jarvis et al. 2016), Looking At the Distant Universe with the MeerKAT Array (LADUMA; Blyth et al. 2016), the MHONGOOSE survey (de Blok et al., 2016), and the MeerKAT Fornax survey (Serra et al., 2016, 2023). MIGHTEE-H I (see Chapter 2) here is not a dedicated H I survey as the other ones but was initially conceptualized as a medium deep continuum survey, from which H I data could be extracted to investigate the H I content in galaxies.

These initiatives are not only advancing our understanding of the Universe but also showcasing the immense potential of MeerKAT, which has surpassed the sensitivity of previous interferometers by an order of magnitude. When combined with the SKA1-mid array, operating in the frequency range of 350 MHz to 15.3 GHz, the network will comprise 197 dishes distributed throughout South Africa, offering impressive baselines that extend up to 150 km. The full completion of the SKA project will push the boundaries even further, as it is expected to increase sensitivity levels by 50 times compared to existing radio facilities (Weltman et al., 2020).

1.6 A motivation for deep blind H I systematic surveys with MeerKAT

This introduction chapter has established the significance of considering both internal processes and external factors to comprehend galaxy evolution. Galaxies are subject not only to scaling relations reflecting their internal properties but also to the influence of the larger structures they inhabit. However, our comprehension of the LSS of the Universe remains constrained, particularly in obscured regions concealed by the Milky Way. Over the last decades, numerous indications revealed that these obscured areas harbor dynamically important structures that remain unexplored due to the substantial obscuration caused by the Milky Way's deepest layers. Achieving a comprehensive understanding of galaxy evolution thus necessitates (i) investigating the relationship between galaxy properties and (ii) employing suitable observational techniques to explore the ZOA.

To address the first point, H I surveys have successfully traced galaxies rich in H I gas across various environmental conditions, particularly in regions where optical and infrared observations face limitations. However, these surveys are also susceptible to systematic issues. Previous H I surveys encountered difficulties due to the intrinsic faintness of H I photons, leading to high noise levels and limited spatial resolution. These challenges impeded detailed imaging and the identification of Optical Counterparts (OCs) for closely located sources due to source confusion. Consequently, our knowledge regarding the resolved H I content of galaxies located beyond the local Universe remains limited. The range of frequencies covered by the majority of previous H I observations has primarily constrained the study to nearby galaxies within the Local Universe ($z < 0.1$). Therefore, the use of higher-sensitivity instruments is paramount in overcoming these limitations. This can now be achieved with new SKA Pathfinders, such as MeerKAT, offering enhanced spatial resolution, deeper sensitivity observations, and wider instantaneous bandwidth for probing larger distances. Of particular interest is the MIGHTEE survey, expected to explore gas-rich galaxies out to $z \sim 0.5$. With the Early Science data, this study serves as a preliminary step to obtain reliable measurements of H I parameters as a precursor before conducting the full

survey.

To address the second point, single-dish telescopes, primarily constrained by resolution, are significantly impacted by the strong continuum emission from the Milky Way, especially at lower latitudes for observations in the ZOA. Although ongoing surveys of the ZOA using H I have yielded valuable insights, their depth remains relatively limited. As discussed in Section 1.4.2, we possess a comprehensive understanding of the general galaxy distribution in the outer region of the Vela Supercluster (VSCL), except for the highly obscured and densely populated potentially merging walls region ($|b| < 5°$). This thesis, therefore, focuses on leveraging MeerKAT data to conduct blind H I surveys in well-known extragalactic regions of the Southern Hemisphere, with a specific emphasis on the Vela region across the ZOA. The objective is to thoroughly explore the multibranching morphology of VSCL, reveal its central core, and investigate its potential influence on the overall bulk flow. The intended survey region using MeerKAT is indicated by the blue box outlined in Fig. 1.6.

This thesis aims to explore the following research questions: *How does the H I size-mass relation of galaxies evolve as a function of redshift and environment? Can we contribute to the understanding of the residual bulk flow of the Universe?* By addressing these research questions, this thesis endeavors to advance our comprehension of galaxy evolution and the role played by LSS in shaping the cosmic landscape.

1.6.1 Thesis structure

This thesis is structured as follows: In Chapter 2, I discuss the Early Science verification of MeerKAT MIGHTEE-H I data, emphasizing the use of the H I size-mass relation as a diagnostic tool to validate the early survey. I also use the result to test for the evolution of this relation over the past one billion years. Chapter 3 is focused on a comprehensive blind systematic H I observation in the innermost ZOA, extracted from the SARAO MeerKAT Galactic Plane Survey (SMGPS) data. I exploit H I data from the survey to explore the distribution of gas-rich galaxies in the ZOA, providing insights into the elusive Vela Supercluster (Vela–SMGPS, $260° \leq \ell \leq 290°, -2° \leq b \leq 1°$). Chapter 4 presents results from the MeerKAT Vela Supercluster survey (Vela–H I, $263° \leq \ell \leq 284°, -6.7° \leq b \leq -2°, 1° \leq b \leq 6.2$). This survey was specifically designed to fully map the VSCL both above and below the GP, bridging the gap between Vela–SMGPS and the Vela spectroscopic observation results. I compiled a catalog list from the combined Vela–SMGPS and Vela–H I data sets. Chapter 5 delves into the completeness assessment and derivation of the H I mass function (HIMF) for highly obscured galaxies in Vela–SMGPS and Vela–H I, with a particular focus on capturing the overdensity of the VSCL. A summary of the key findings of the study is given in Chapter 6, including an outline of potential avenues for future research.

chapter 2

MIGHTEE -H I: the H I Size – Mass relation over the last billion years

S H. A. Rajohnson[1], B. S. Frank[2,3,1], A. A. Ponomareva[4], N. Maddox[5], R. C. Kraan-Korteweg[1], M. J. Jarvis[4,6], E. A. K. Adams[7,8], T. Oosterloo[7,8], M. Baes[9], K. Spekkens[10], N. J. Adams[11], M. Glowacki[12,13], S. Kurapati[1], I. Prandoni[14], I. Heywood[4,15,16], J. D. Collier[3,17], S. Sekhar[3,18,19] and Russ Taylor[3,19]

This chapter is adapted from the paper accepted for publication on 9 March 2022, Monthly Notices of the Royal Astronomical Society, Volume 512, pages 2697–2706.

[1] Department of Astronomy, University of Cape Town, Private Bag X3, Rondebosch 7701, South Africa
[2] South African Radio Astronomy Observatory, 2 Fir Street, Observatory, 7925, South Africa
[3] The Inter-University Institute for Data Intensive Astronomy (IDIA), and University of Cape Town, Private Bag X3, Rondebosch, 7701, South Africa
[4] Astrophysics, Department of Physics, University of Oxford, Keble Road, Oxford OX1 3RH, UK
[5] Faculty of Physics, Ludwig-Maximilians-Universität, Scheinerstr. 1, 81679 Munich, Germany
[6] Department of Physics and Astronomy, University of the Western Cape, Robert Sobukwe Road, 7535 Bellville, Cape Town, South Africa
[7] ASTRON, the Netherlands Institute for Radio Astronomy, Oude Hoogeveesedijk 4, 7991 PD Dwingeloo, The Netherlands
[8] Kapteyn Astronomical Institute, PO Box 800, 9700 AV Groningen, The Netherlands
[9] Sterrenkundig Observatorium Universiteit Gent, Krijgslaan 281 S9, B-9000 Gent, Belgium
[10] Department of Physics and Space Science, Royal Military College of Canada, PO Box 17000, Station Forces, Kingston, K7K 7B4, Canada
[11] Jodrell Bank Centre for Astrophysics, University of Manchester, Oxford Road, Manchester, UK
[12] International Centre for Radio Astronomy Research, Curtin University, Bentley, WA 6102, Australia
[13] Inter-University Institute for Data Intensive Astronomy, Bellville 7535, South Africa
[14] INAF-IRA, Via P. Gobetti 101, 40129, Italy
[15] Centre for Radio Astronomy Techniques and Technologies, Department of Physics and Electronics, Rhodes University, PO Box 94, Makhanda, 6140, South Africa
[16] South African Radio Astronomy Observatory, 2 Fir Street, Black River Park, Observatory, Cape Town, 7925, South Africa
[17] School of Science, Western Sydney University, Locked Bag 1797, Penrith, NSW 2751, Australia
[18] National Radio Astronomy Observatory, 1003 Lopezville Road, Socorro, NM 87801, USA
[19] Inter-University Institute for Data Intensive Astronomy, and Department of Astronomy, University of the Western Cape, Bellville, South Africa

Abstract

I present the observed H I size–mass relation of 204 galaxies from the MIGHTEE Survey Early Science data. The high sensitivity of MeerKAT allows us to detect galaxies spanning more than 4 orders of magnitude in H I mass, ranging from dwarf galaxies to massive spirals, and including all morphological types. This is the first time the relation has been explored on a blind homogeneous data set that extends over a previously unexplored redshift range of $0 < z < 0.084$, i.e., a period of around one billion years in cosmic time. The sample follows the same tight logarithmic relation derived from previous work, between the diameter ($D_{\rm HI}$) and the mass ($M_{\rm HI}$) of H I discs. I measure a slope of 0.501 ± 0.008, an intercept of $-3.252^{+0.073}_{-0.074}$, and an observed scatter of 0.057 dex. For the first time, we quantify the intrinsic scatter of 0.054 ± 0.003 dex ($\sim$10%), which provides a constraint for cosmological simulations of galaxy formation and evolution. We derive the relation as a function of galaxy type and find that their intrinsic scatters and slopes are consistent within the errors. I also calculate the $D_{\rm HI} - M_{\rm HI}$ relation for two redshift bins and do not find any evidence for evolution with redshift. These results suggest that over a period of one billion years in lookback time, galaxy discs have not undergone significant evolution in their gas distribution and mean surface mass density, indicating a lack of dependence on both morphological type and redshift.

Keywords: surveys – galaxies: evolution – galaxies: kinematics and dynamics – radio lines: galaxies

2.1 Introduction

Galaxies are gravitationally bound systems of stars, gas and dark matter. The processes governing their full gas cycle remain an area of active research. Theories of galaxy formation and evolution predict the gas infall onto galaxies to be the main mechanism supporting star formation and galaxy growth (Giovanelli & Haynes, 1988). Galaxies must continuously accrete gas from an external environment to maintain their observed levels of star formation (e.g., Kereš et al., 2005; Sancisi et al., 2008; Kauffmann et al., 2010). Consequently, the environment in which a galaxy resides affects its evolution and thus its stellar mass and morphology (see Baldry et al., 2006; Peng et al., 2010). Dense environments, for example, not only prevent further accretion of gas and ongoing star formation, but also play the crucial role in active gas stripping and subsequent loss of gas from galaxies. This can be observed through the morphology-density relation described in Dressler et al. (1997), where high-density environments are populated by early-type galaxies (E, S0) whereas low-density environments are more dominated by late-type galaxies (S, Irr).

In addition to the morphology-density relation, other relations that provide insights into galaxy

evolution include the baryonic Tully-Fisher relation (baryonic mass vs. rotational velocity; e.g., McGaugh et al. 2000; Lelli et al. 2019; Ponomareva et al. 2018, 2021); the relation between optical and H I diameters (Broeils & Rhee, 1997; Leroy et al., 2008); star formation histories, stellar masses and structural parameters (Kauffmann et al., 2003); and the mass-metallicity relation (Tremonti et al., 2004).

Another fundamental scaling relation for disc galaxies is the H I size-mass relation. First discovered by Broeils & Rhee (1997), it shows a tight correlation between the diameter of an H I disc ($D_{\rm HI}$), measured at a surface mass density level of 1 $M_\odot\,pc^{-2}$, and its total enclosed H I mass ($M_{\rm HI}$). Recent studies have demonstrated that this relation also holds true over a wide range of galaxy types, such as large spirals (Verheijen & Sancisi, 2001; Swaters et al., 2002; Wang et al., 2013; Lelli et al., 2016; Ponomareva et al., 2016), late-type dwarf galaxies (Swaters et al., 2002; Begum et al., 2008; Lelli et al., 2016), early-type spirals (Noordermeer et al., 2005), irregulars (Lelli et al., 2016) and even for the ultra-diffuse galaxies (UDGs) discovered in the Arecibo Legacy Fast ALFA (ALFALFA) survey (Leisman et al., 2017; Gault et al., 2021). Moreover, even though the intergalactic medium (IGM) of groups and clusters can affect the sizes of H I discs due to ram-pressure and tidal interactions (Verdes-Montenegro et al., 2001), it was shown that galaxies which reside in groups and clusters still follow the observed H I size-mass relation as long as their discs are not too disrupted and the diameter can be traced out to 1 $M_\odot\,pc^{-2}$ (Verheijen & Sancisi, 2001; Chung et al., 2009).

The galaxies in hydrodynamical simulations and semi-analytical models also follow the observed scaling relation between the H I mass and size, with an analytically derived limit on its scatter of ≤ 0.1 dex (e.g., Wang et al. 2014; Marinacci et al. 2017; El-Badry et al. 2018; Lutz et al. 2018). While environmental processes such as ram-pressure stripping may cause galaxy discs to truncate or have holes, this does not strongly affect the relation unless the disc is completely disturbed (Stevens et al., 2019). Moreover, Stevens et al. (2019) have shown that the robustness of the H I size-mass relation makes it a valuable tool for theories of galaxy formation and evolution: the success of any model or simulation should be based on its ability to reproduce its scatter, slope and zero point with only a few percent uncertainty.

The largest observational work-to-date was undertaken by Wang et al. (2016), who collected H I sizes for more than 500 galaxies from 14 various surveys, ranging over five decades in $M_{\rm HI}$. They obtained a remarkably tight relation with a scatter of 0.06 dex (14%). Although low-mass galaxies were found to have denser H I discs than higher-mass galaxies due to their low angular momentum (Lelli et al., 2016), the tight power law correlation indicates a nearly constant characteristic H I surface density within $D_{\rm HI}$ for most galaxies (Wang et al., 2016) – regardless of their type, mass, or environment. This relation therefore suggests that all galaxies, from small dwarfs to large spirals, experience a similar process of evolution as long as they remain gas-rich.

Little is known about the resolved H I content of galaxies located beyond the local Universe, mostly due to technical limitations such as lack of sensitivity and narrow frequency coverage of radio interferometers. To date, only a few surveys observed H I in galaxies at $z > 0.01$ (e.g., the Blind Ultra-Deep H I Environmental Survey (BUDHIES; Gogate et al. 2020) and HIGHz; Catinella & Cortese 2015). Therefore, the size-mass relation has only been studied for various nearby H I-selected samples, and remains unexplored for large, homogeneous samples, which extend to higher redshifts. With the advent of deep H I surveys with the Square Kilometre Array (SKA) pathfinders (and eventually the SKA itself), a new window is opening for studying the H I content of galaxies beyond the local volume.

This work is based on the Early Science data from the MeerKAT International GHz Tiered Extragalactic Exploration (MIGHTEE) survey (Jarvis et al., 2016). Our sample comprises 276 galaxies detected as part of the spectral line component of this project, named MIGHTEE-H I. The sample spans more than four orders of magnitude in H I mass and one billion years in look-back time ($z \leq 0.084$). Therefore, we are able to study the H I size-mass relation for the first time beyond the local Universe using a homogeneous data set and explore its possible evolution with redshift.

This chapter is organized as follows: I summarize the MeerKAT observations and data reduction strategy in Section 2.2, as well as the different tests used to assess the H I cube qualities. Section 2.3 provides details of the H I source finding and the generation of Early Science data products such as moment maps, spectra, and 2D optical cutouts which are used to select and morphologically classify the sample for the $D_{\rm HI} - M_{\rm HI}$ relation. The resulting H I catalogue of the selected sample is described in Section 2.5 and fully presented in Appendix A. To continue, I describe in Section 2.6, the methods used to derive the H I global properties, discuss their distributions, and compare them with known measurements from ALFALFA. I construct the $D_{\rm HI} - M_{\rm HI}$ relation of the MIGHTEE-H I early survey and discuss its possible evolution with redshift in Section 2.7. Finally, Section 2.8 summarizes our findings.

Throughout this chapter, I assume ΛCDM cosmology parameters of $\Omega_{\rm m} = 0.3$, $\Omega_{\Lambda} = 0.7$ and $H_0 = 70$ km s^{-1} Mpc^{-1}, for ease of comparison with previous results.

2.2 MeerKAT observations and data reduction

2.2.1 Observation details

MIGHTEE is one of the eight Large Survey Projects (LSP) of MeerKAT (Jonas & MeerKAT Team, 2016). MIGHTEE science cases include studies of the radio continuum (see Heywood

et al. 2022 for the early science data release), H I in emission (MIGHTEE-H I), H I absorption and polarisation in galaxies. This study focuses on the MIGHTEE-H I part of the survey and uses the Early Science data, details of which can be found in Maddox et al. (2021).

The observations were carried out with the full MeerKAT array between mid-2018 and mid-2019 in the L-band. The data were collected using the 4k spectral line correlator mode, with a channel width of 209 kHz, which corresponds to a velocity resolution of 44.11 $\mathrm{km\,s^{-1}}$ at $z = 0$. The observations were carried out over two of four MIGHTEE fields described in Jarvis et al. (2016), covering an effective area of approximately 3.5 $\mathrm{deg^2}$ of the sky in XMMLSS and 1.5 $\mathrm{deg^2}$ in COSMOS, resulting in a total effective area of ~ 5 $\mathrm{deg^2}$. XMMLSS fields were observed for a total integration time of $\sim 3 \times 16$ hours, with $\sim 3 \times 13$ hours of on-source time. On the other hand, COSMOS was observed during 25 hours for 17.45 hours of on-source time. Bandpass and flux calibrators were observed for $\sim 5 - 10$ minutes every 2 hours, and gain and phase calibrators were visited for ~ 3 minutes every $20 - 30$ minutes on-target scan (see also Heywood et al. 2022 for more details).

2.2.2 Data reduction and imaging

This section describes the calibration steps performed to the raw dataset: from flagging the Radio Frequency Interference (RFI) to the Fourier transform imaging of the H I cubes.

The raw visibility data was firstly obtained in a Measurement Set (MS) format from the SARAO/ MeerKAT archive[1]. Once stored on the `Ilifu` cluster[2] facility, only a limited subset of the total bandwidth of $856 - 1712$ MHz was processed. The measurement set was then split into multiple spectral windows (SPWs) of ~30 – 50 Mhz (1310 – 1330, 1330 – 1380 and 1380 – 1420 MHz). This was done to (i) optimize the compute resource for faster calibration times, (ii) enable processing multiple SPWs at a given time and, (iii) obtain a more accurate broadband response in Stokes I polarization, including the intrinsic spectrum of the phase calibrator.

Data calibration tasks such as flagging, delay, bandpass, gain and self-calibration were done with the PROCESSMEERKAT[3] pipeline (Collier et al., 2021). This is a `CASA`[4]-based pipeline developed at the Inter-University Institute for Data Intensive Astronomy (IDIA)[5]. Four frequency ranges – about 40% of the total bandwidth – with persistent Radio Frequency Interference (RFI) affecting the calibrators were flagged in the UV-data. Once satisfied with the *priori* calibration, the gain and phase solutions were applied to the target visibility data which was in turn split out

[1] https://archive.sarao.ac.za
[2] http://www.ilifu.ac.za
[3] https://idia-pipelines.github.io
[4] http://casa.nrao.edu, McMullin et al. 2007
[5] https://idia.ac.za

from the calibrator visibilities. Three rounds of self-calibration were performed and applied to the target visibilities averaged down to 1024 channels, solving for phase-only gain calibration. The gain solutions derived on the averaged data were then applied to the full resolution 4096 channel cross-calibrated data, with linear interpolation in time and frequency.

As illustrated in the flow chart in Fig. 2.1, visibility-based continuum subtraction was done in two steps. An initial subtraction of the best clean component continuum model (UVSUB) and the subtraction of a 4th-order polynomial fit to the per-baseline/per-integration spectrum (UVCONTSUB) after initial calibrations. The residual visibilities were imaged using CASA's TCLEAN task with Briggs (1995) weighting (ROBUST = 0.5) and converted into FITS files format using CASA's EXPORTFITS task. A final step of median-filtering (MF) was done on the cubes to reduce the impact of continuum-subtraction errors. The polynomial order fitting choice is demonstrated in Fig. 2.2, showing the mitigation of strong continuum sources and the variability of their sidelobes with increasing fitting order and when median-filtering is introduced. Full details of the data processing can be found in Frank et al. (in prep).

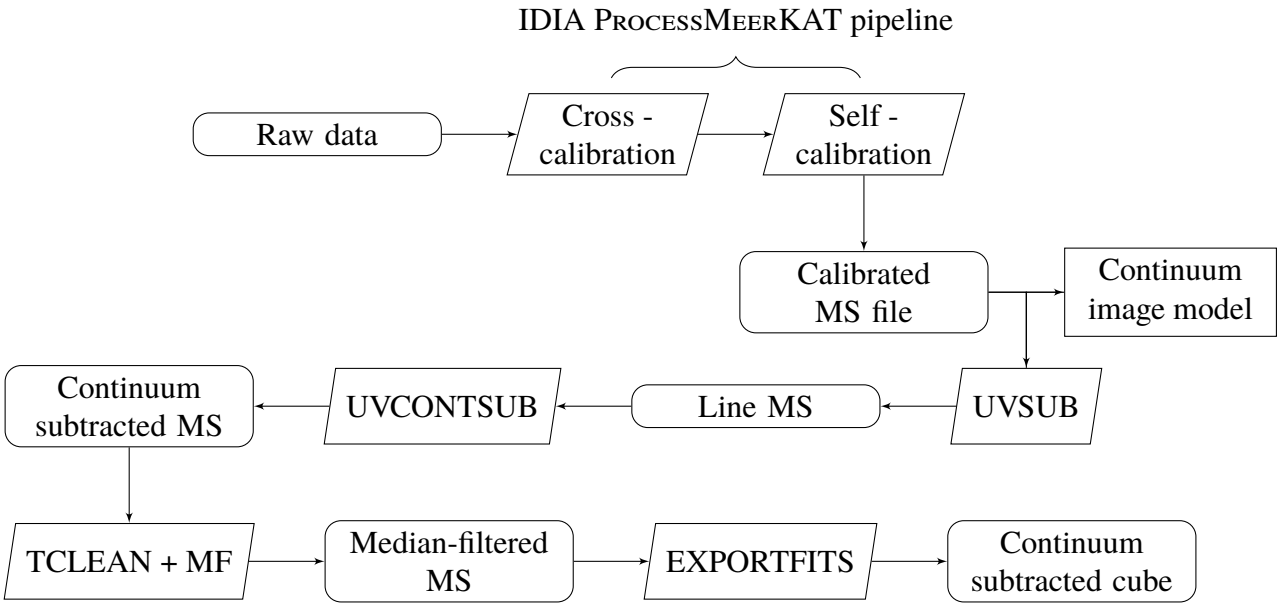

Figure 2.1: Flow chart for the calibration, continuum subtraction and imaging of MIGHTEE-H I raw dataset

2.2.3 Primary beam correction and noise properties

The image size was 4096×4096 pixel^2 with a pixel size of $2'' \times 2''$, resulting in a $\sim 2.3^\circ \times 2.3^\circ$ H I cube per pointing. This H I cube spans a redshift range of $0 < z < 0.084$, corresponding to a velocity range of 86 to 24205 km s^{-1}. While the primary beam Full Width Half Maximum (FWHM) size of MeerKAT is approximately 1 degree at 1.4 GHz, the dirty beam FWHMs are

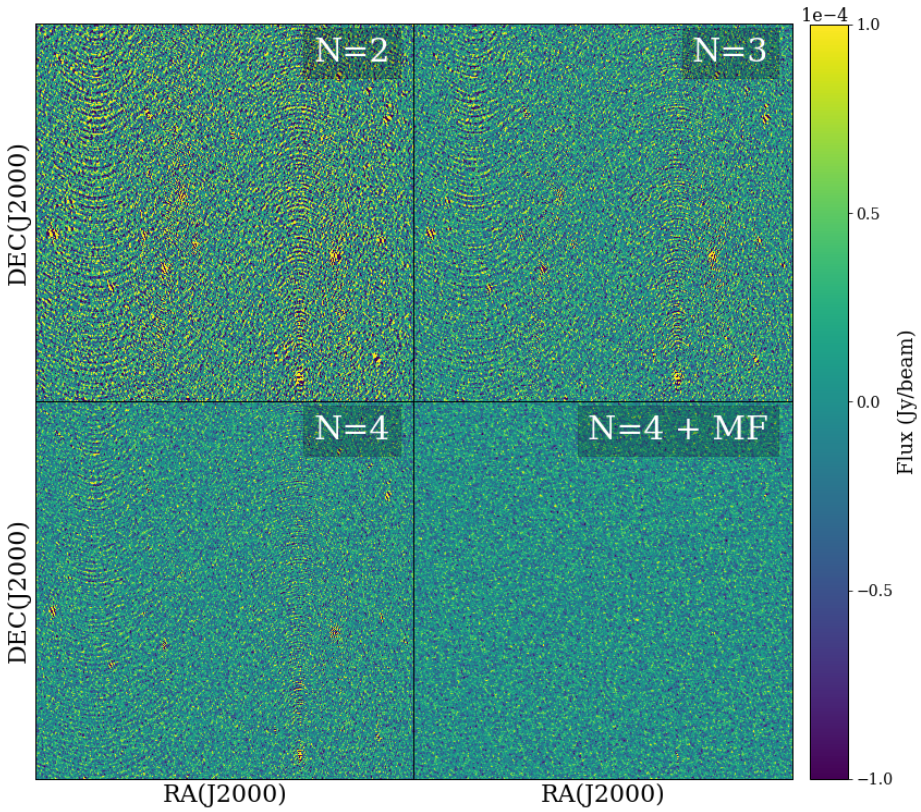

Figure 2.2: Examples of various continuum residual and imaging artefacts depending on the polynomial fit order for continuum subtraction (from N=2 to N=4), and an additional median filtering to the cube.

$14.5'' \times 11''$ and $12'' \times 10''$ for the COSMOS and XMMLSS fields, respectively. The observational and imaging parameters of the Early Science data are summarized in Table 2.1.

Flux densities are attenuated according to the finite primary beam response, which is maximal at the pointing centre, and falls off with increasing distance in the sky. This is demonstrated in Mauch et al. (2020), where the MeerKAT Stokes I beam at 1.5 GHz seems to have an attenuation pattern similar to the attenuation pattern resulting from cosine-tapered field (or cosine-squared power) illumination from Condon & Ransom (2016) out to 2.5 deg from the pointing center. This attenuation pattern is expressed as follow:

$$a_{\rm b}(\rho/\theta_{\rm b}) = \left[\frac{\cos\left(1.189\pi\rho/\theta_{\rm b}\right)}{1-4(1.189\rho/\theta_{\rm b})^2}\right]^2 . \tag{2.1}$$

The model of the primary beam corresponding to the cube size for each channel was obtained using the Eidos package from Asad et al. (2021).

Once continuum subtraction and median filtering were applied to the images, I corrected the cube for the primary beam (PB). This PB-corrected cube was obtained by dividing each pixel value in the median filtered cube by its PB model. This process corrects the attenuation of flux

Table 2.1: A summary of the MeerKAT observing parameters and imaging of the MIGHTEE-H I Early Science data.

Observing parameters	Value
Survey effective area	1.5 deg^2 (COSMOS field)
	3×1.2 deg^2 (XMMLSS field)
Total integration time	$\sim$ 17 hrs (COSMOS)
	3×13 hrs (XMMLSS)
Total frequency range (L-band)	856 – 1712 MHz
Processed frequency range	1310 – 1420 MHz
Field centre (J2000)	$10^{\mathrm{h}}00^{\mathrm{m}}28^{\mathrm{s}}$, $+02°12'21''$ (COSMOS)
	$02^{\mathrm{h}}17^{\mathrm{m}}51^{\mathrm{s}}$, $-04°49'59''$ (XMMLSS12)
	$02^{\mathrm{h}}20^{\mathrm{m}}42^{\mathrm{s}}$, $-04°49'59''$ (XMMLSS13)
	$02^{\mathrm{h}}23^{\mathrm{m}}22^{\mathrm{s}}$, $-04°49'59''$ (XMMLSS14)
Spectral resolution	209 kHz
Velocity resolution	44.11 $\mathrm{km\,s^{-1}}$ at $z = 0$
Velocity range	86 – 24205 $\mathrm{km\,s^{-1}}$
PSF (FWHM)	$14.5'' \times 11''$ (COSMOS)
	$12'' \times 10''$ (XMMLSS)
Pixel / Image size	$2''$ / 4096×4096
3σ H I column density sensitivity	4.05×10^{19} atoms $\mathrm{cm^{-2}}$ (COSMOS)
	9.83×10^{19} atoms $\mathrm{cm^{-2}}$ (XMMLSS)

at the edge of the PB pointing center but also increases the noise levels. A demonstration of the effect of median filtering and PB correction on the spatial noise variation of the continuum subtracted cube in XMMLSS12 is illustrated in Fig. 2.3. To obtain the spatial noise, I have measured the standard deviation of flux for each pixel in a 1024×1024 pixel^2 region located at the cube centre over a range of 50 channels. It is observed that the spatial noise can vary largely from 50 μJy beam^{-1} and can go above 100 μJy beam^{-1} in the initial cube, when only continuum subtraction was applied. However, once PB correction and median filtering were applied, the spatial noise distribution became narrower, and the maximum spatial rms noise in the cube does not go above 97 μJy beam^{-1}.

To confirm the results, I have also measured the averaged rms at the cube centre using the Cube Analysis and Rendering Tool for Astronomy (CARTA[6], Comrie et al. 2021) for a PB corrected cube and that shows good agreement. Consequently, I measured a mean global root mean square (rms) noise of $\sim$44 μJy beam^{-1} and $\sim$81 μJy beam^{-1} per channel in the respective cube centres of COSMOS and XMMLSS. With these characteristics, a 3σ column density sensitivity of 4.05×10^{19} atoms $\mathrm{cm^{-2}}$ and 9.83×10^{19} atoms $\mathrm{cm^{-2}}$ are achieved in COSMOS and XMMLSS, respectively (see also Table 2.1).

These noise measurements are in good agreement with the theoretical noise of MIGHTEE, which can be estimated by using the radiometer equation from Crane & Napier (1989) to cal-

[6]https://carta.idia.ac.za/

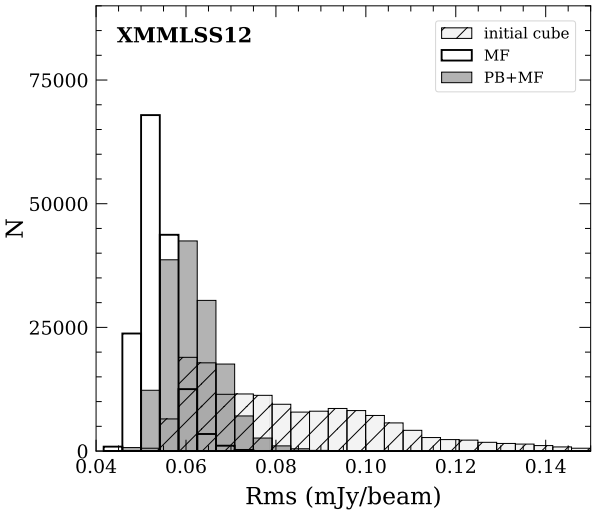

Figure 2.3: Histogram showing the effect of median filtering and primary beam correction on the spatial noise distribution of XMMLSS12. This panel illustrates the spatial noise variation for the initial continuum subtracted cube (light grey), its rms variation after median filtering (white) and the primary beam corrected final cube (dark grey).

culate the theoretical sensitivity per frequency channel and per synthesized beam for a natural weighting at 1.4 GHz:

$$\Delta S = \frac{\sqrt{2} K_B T_{sys}}{A\eta\sqrt{N(N-1)\Delta t \Delta\nu}}, \tag{2.2}$$

where T_{sys}/η = 22 K for MeerKAT at 1.4 GHz, $\eta = 0.83$, N = 64 antennae on target, A = 143.1 m^2, K_B = 1380 Jy m^{-2} K^{-1}, $\Delta\nu \sim 209 \times 10^3$ Hz and Δt is the total on source time.

For ∼13 hours on source time for XMMLSS and ∼17 hours on source time for COSMOS, the expected rms are 48 and 42 μJy beam^{-1}. However, with the expectation that the predicted limit will increase by 40% with a robust weighting of 0.5, the expected rms for MIGHTEE-H I are 68 and 59 μJy beam^{-1}, respectively for XMMLSS and COSMOS.

2.3 Data products & H I candidate verification

I performed an in-depth analysis of the reduced H I cubes using Jupyter notebooks on the IDIA cloud facility. This section outlines the process of inspecting each cube to generate a list of detected H I sources. Additionally, it explains the methods employed to produce the necessary Early Science spectral line data products for our primary objective: constructing the $D_{\rm HI} - M_{\rm HI}$ relation (refer to Section 2.7).

For this purpose, Global H I profiles, moment maps, and morphological classifications of each detected H I source are crucial. Initially, a Global H I profile is required to obtain information about the width of the H I emission line, its systemic velocity, and integrated fluxes necessary for calculating the total H I mass. The moment-0 map is then utilized to estimate the size of

the H I disk and can also measure the total H I mass. Although not specifically utilized in this work, the moment-1 map can be employed to derive the rotation curve and assess the dynamical information of the galaxy from its velocity field. Finally, the morphological classification from optical images is essential to aid in the sample selection for the relation construction.

2.3.1 H I source finding

Identifying H I detections is crucial for a systematic blind H I survey as their distributions and locations are not known in advance. As a first step to commission the early-science cubes, we conducted visual source finding on the Early Science data cubes covering 1310 – 1420 MHz, as described in Maddox et al. (2021). We used CARTA to examine non-primary beam corrected cubes. This was done to identify signals from potential galaxies and to avoid imaging artefacts or noise peaks to be considered as H I detections. No priori selection criteria have been set out in this work for source finding. With a 44 km s^{-1} resolution, candidate detections were added to the sample, and source lists were compared between the source finding team. This resulted in 276 unique H I detections, forming the basis for our analysis, in which 196 of them were from XMMLSS while 80 detections were from COSMOS.

Figure 2.4 illustrates the on-sky distributions of the H I sources in MIGHTEE-H I color-coded with their respective radio velocities. At a glance, the H I detected galaxies in the field appear to be uniformly distributed in terms of position in the sky. With MeerKAT excellent sensitivity, we were able to detect many sources beyond the primary beam FWHM.

2.3.2 Source subcubes

Once the source list details – RA, DEC, observed frequency – of all prospective detections have been listed, I extracted subcubes or a three-dimensional subset for each detection from the PB-corrected and median-filtered cubes using the python module `spectralcube`[7]. The subcube is centered on the approximate centre of the detection (at roughly its systemic velocity), and the spatial extent is chosen to span the galaxy's width. On average, a width of $2'$ in both RA and DEC was sufficient for most detections but the general range was within $0.75'$ to $12'$. The subcubes' spectral units were converted into radial velocities using the relativistic convention. This relativistic or true line-of-sight velocity is defined as:

$$v_{\rm rad} = c\left(\frac{\nu_0^2 - \nu^2}{\nu_0^2 + \nu^2}\right), \tag{2.3}$$

where ν_0 is the rest-frame frequency of the H I line with a value of 1.42040575 GHz and ν the observed sky frequency. These took part as the first data products from the early survey.

[7]https://spectral-cube.readthedocs.io/en/latest/

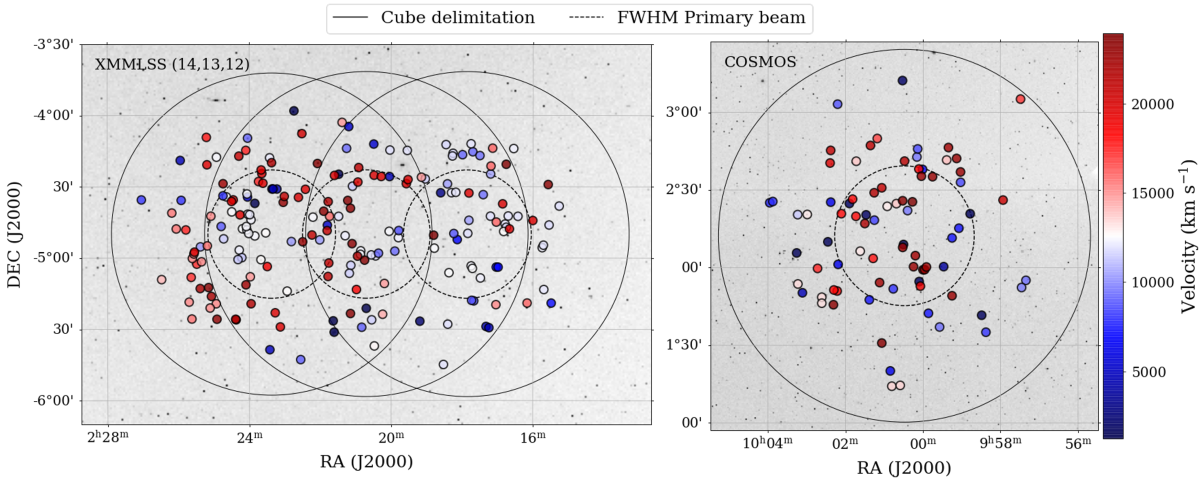

Figure 2.4: Sky distributions of the 276 detections found in the MIGHTEE-H I Early Science fields in equatorial coordinates overlaid on their DSS2 blue band image. The colorbar indicates their observed radio velocities. The small dashed circle shows the ~1 degree FWHM primary beam pointing while the bigger dashed circle represents the region of observation using the full primary beam of MeerKAT, i.e., ~2 deg. *Left panel:* Sky distributions of 196 detections in the XMMLSS fields after removing duplicates in XMMLSS14, 13 and 12. *Right panel:* Sky distributions of 80 detections in the COSMOS field.

The H I emission of a galaxy is distributed along the spectral axis due to the relativistic Doppler shift. By examining the consecutive channel maps of each subcube, we can assess the imaging quality, the neutral gas distribution, and check if any emission had been left out during extraction. This has also allowed a follow-up in the confirmation of the legitimacy of the signal as a potential detection. Fig. 2.5 shows an example of channel maps for one of the sources detected in XMMLSS12. Once satisfied, I exported them into FITS files to get ready for analysis.

2.3.3 Global H I profiles

I derived the Global H I profiles of each detection by plotting the primary-beam corrected flux density of each channel map against the velocity axis of the signal cubes. However, deriving this correct H I flux was not straightforward. The following subsections explain the steps needed to derive global H I profiles of the detections.

Baseline fitting

To find out the flux densities in Jy, I first determined the flux I per channel – expressed in Jy beam^{-1} – by summing the flux values of all the pixels contained per image plane. This will help in establishing a raw spectrum (flux vs. velocity) which will indicate the H I emission location. Some residual continuum remains in the subcubes and may affect the spectrum baseline behavior. By observing the raw spectrum, I identified clear line and line-free channels. To measure the appropriate flux values, three low-order polynomial fits (n=1,2 and 3) were fitted to the line-free channels of the signal cubes and I selected the fit with a reduced chi-square value closest to

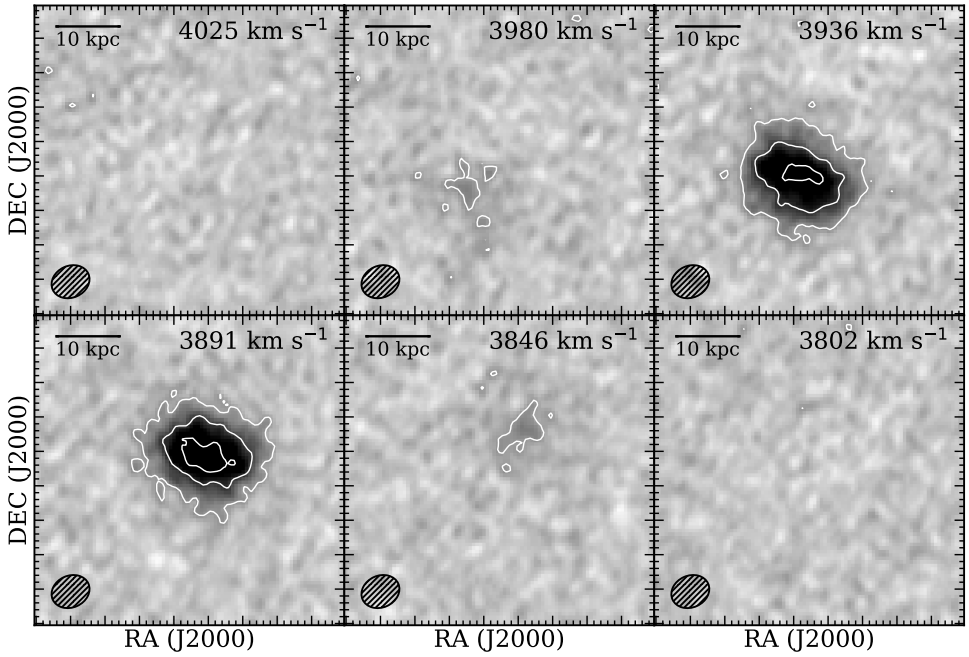

Figure 2.5: Consecutive H I channel maps of MGTH_J021836.3−043236 found in XMMLSS12. The figure displays six channel maps selected from a 3′ size signal cube. Relativistic velocity is given in the top-right corner of each panel. The white contour levels are plotted at 0.2 mJy beam^{-1} (3σ) with an incrementation of 0.5 mJy beam^{-1} until reaching 5 mJy beam^{-1}. The scale at each top left corner corresponds to 10 kpc, i.e., ∼36″ at a distance of ∼57 Mpc. The synthesized beam has an FWHM of 11.3″ × 9.2″, a position angle of −24° and is represented by the hatched ellipse in the lower-left corner of each channel map.

1. The reduced chi-square χ^2_ν or the reduced sum of square residuals between the fitted model and the line-free emission was derived from:

$$\chi^2_\nu = \sum_{i=1}^{l} \frac{(M_i - I_i)^2}{(l-m)\sigma^2_{I_i}}, \tag{2.4}$$

where M_i is the fitted model value, I_i is the sum of pixel fluxes but at a line-free channel i, σ_{I_i} is the standard deviation of I_i, l is the number of line-free channels and m is the number of fitted parameters for the polynomial. The best-fitting polynomial represents the residual continuum in the cube and can be subtracted from the spectrum to fit the baseline, remove continuum errors, and correct the flux values. As a result, the leftover continuum residuals corresponded to a variable component (fitted by n = 2 or 3) resulting in an offset quantity per detection. We applied this offset when calculating integrated flux densities to derive H I masses (see Section 2.6.2).

Jy beam^{-1} to Jy conversion

Once the baseline was corrected, I followed the method described in Meyer et al. (2017) to recover the correct flux. The flux density $S_i(v)$ expressed in Jansky at a specific channel i was derived by multiplying the flux I_i [Jy beam^{-1}] with a scaling beam factor. This factor is actually the pixel area divided by the area of the telescope beam (see Eq. 2.8) and is used to correct the

flux density by the beam. The pixel size and the PSF values were obtained from the subcube header. For a squared pixel of $2''$ length, the pixel area is just its squared value. For the telescope beam area Ω_B, most interferometers images are made with a 2D Gaussian beam. Its beam area can then be derived from its solid angle:

$$\Omega_B = 2 \times \pi \times \sigma^2 \ [\text{arcsec}], \tag{2.5}$$

where σ can be calculated from the major and minor axes of the ellipse equal to the FWHM values of the Gaussian beam. By using the axis length at FWHM of the beam, we get:

$$\sigma = \frac{\theta_{\text{FWHM}}}{2\sqrt{2\ln 2}} = \frac{\theta_{\text{FWHM}}}{\sqrt{8\ln 2}}. \tag{2.6}$$

By combining Eqs. (2.5) and (2.6), the beam solid angle or beam area Ω_B has a relation with its major and minor axes at its FWHM given by:

$$\Omega_B = \frac{\pi b_{\text{maj}} b_{\text{min}}}{4\ln 2}. \tag{2.7}$$

Consequently, we determined the flux density of the detections with:

$$\boxed{S_i(\text{Jy}) = \frac{(\text{Pixel size})^2}{\Omega_B} \times I_i(\text{Jy beam}^{-1})}. \tag{2.8}$$

The pixel size and beam values are expressed in arcseconds and let's define $(\text{Pixel size})^2/\Omega_B$ as the *scaling factor*.

Systemic velocities and linewidths

Figure 2.6 illustrates the steps from baseline fitting to linewidth estimation used to generate the H I global profile of a detection, and demonstrates the various measured quantities in a spectrum. Various parameters can be measured directly from the fitted spectrum, e.g., the peak flux density S_p expressed in Jy, the minimum and maximum velocities delimiting the profile region (v_{low} and v_{high}), the systemic velocity v_{sys}, and the velocity widths w_{50} and w_{20} in km s^{-1} of the H I line. Depending on the spectral line shape, the systemic velocity v_{sys} – the average velocity of the center of mass of the H I source (indicated by a black vertical arrow in Fig. 2.6) – is determined from the centroid of the H I emission. It is obtained from the flux-weighted velocity-average between v_{low} and v_{high} at the two percentage levels:

$$v_{\text{sys}} = 0.25(v_{\text{low,50}} + v_{\text{low,20}} + v_{\text{high,50}} + v_{\text{high,20}}). \tag{2.9}$$

From a gaussian filtered fitted spectrum, the profile linewidths at 50% and 20% levels of the

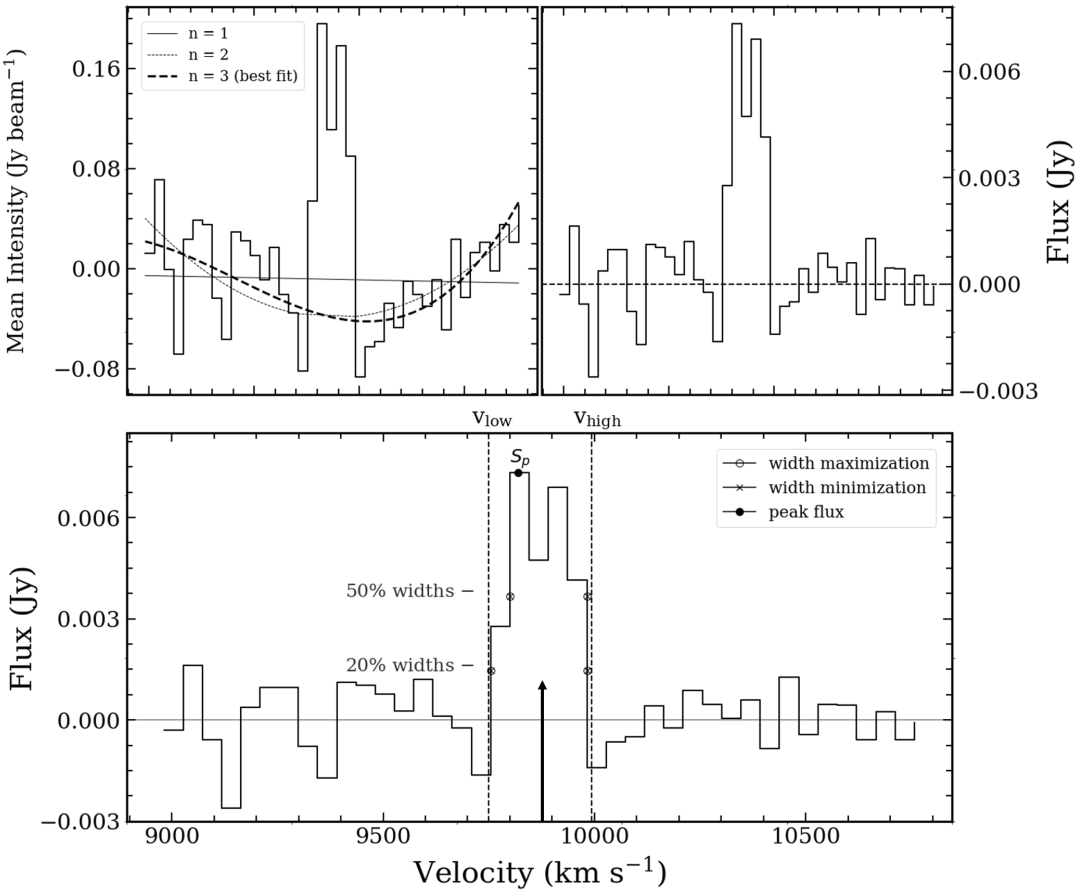

Figure 2.6: *Top panel:* Left: example of raw spectrum of MGTH_J021742.0−041520 with three order baseline polynomial fits choice where n=3 is the best fit. Right: the resulting spectrum after baseline subtraction and flux scaling from Jy beam^{-1} to Jy. *Bottom panel:* Measured quantities from a baseline corrected spectrum. The dot-dashed vertical lines indicate the velocity limits $v_{\rm low}$ and $v_{\rm high}$ of the H I line. The peak flux density $S_{\rm p}$ is illustrated by a black filled circle and the 20% and 50% profile markers are visible in the plot. Black open circles indicate linewidth maximization while (×) markers indicate linewidth minimization.

peak flux can be measured from the following equations:

$$w_{50} = v_{\rm high,50} - v_{\rm low,50}, \tag{2.10}$$

$$w_{20} = v_{\rm high,20} - v_{\rm low,20}. \tag{2.11}$$

The maximum widths ($w_{50}^{\rm max}$ or $w_{20}^{\rm max}$), marked by a black circle, are obtained by using the width maximization procedure. This consists of taking the two edge velocity values between $v_{\rm low}$ and $v_{\rm high}$ that satisfies the desired flux level. The minimum widths ($w_{50}^{\rm min}$ or $w_{20}^{\rm min}$), illustrated by a cross (×) marker in the figure, are obtained by the minimization procedure. This starts at the velocity of the peak flux $S_{\rm p}$, and searches outward. The first intersection at 20 or 50% is then considered as the minimum width (see Meyer et al. 2004 for a similar method). For the majority of the spectra, the minimum widths are similar to the maximum ones. The difference usually appears for double-horn spectra, with a characteristically deep central dip.

The width of an H I spectral line indicates the observed Doppler broadening due to the galaxy rotation. In our case, I only had an interest in the profile linewidths at 50% level of the peak flux due to the noise quality of the data. We were also not able to measure linewidths below the velocity resolution of 44.11 km s^{-1}. The FWHM of each galaxy's integrated H I line profile (w_{50}) was determined by fitting Busy Functions (BF; Westmeier et al. 2014) using PyMultiNest, which is a PYTHON interface for MULTINEST (Buchner et al., 2014), a Monte Carlo library employing Bayesian analysis to estimate parameters. A bootstrap technique was applied to iteratively refine and constrain the BF parameters across multiple PyMultiNest runs due to the coarse channel width of the Early Science data. The best fit was selected based on the line flux closest to the observed data (see Mulaudzi 2021; Ponomareva et al. 2021 for details).

The global H I profiles are seen to show typical features of H I emission such as two-horned, flat-topped, or Gaussian profiles. Double-horned profiles are indicative of rotating disks with flat rotation curves, seen at an inclination larger than ~20 deg. This rotation manifests as a strong emission at two frequencies with a broad and bright line emission. The gas on each side of the disk gets Doppler shifted to higher or lower frequencies with respect to the systemic redshift of the galaxy. Face-on disk galaxies, dwarfs, and irregulars, on the other hand, tend to show narrow, faint, and roughly Gaussian-shaped emissions known as single-horn profiles (e.g., Shostak, 1977; Roberts, 1978; Skillman, 1996).

2.3.4 Moment maps

An alternative way to represent the H I emission of a detected source in a subcube is by computing its spectral moments. The zero$^{\text{th}}$ moment map (mom-0), also known as the total intensity map, represents the overall gas distribution in the cube. It is used to determine the integrated flux over the emission line S. Mom-0 maps were made by integrating the flux density over the velocity axis, i.e., taking the sum of the plane in the channel maps that contain line emission. Obtained by:

$$M_0 = S_{\text{int}} = \int_i S_i \times dv = \sum_i S_i \times \Delta v, \tag{2.12}$$

where i represents the specific channel number, S_i is the H I emission flux density at the i-th channel and Δv the channel width.

The first-moment map (mom-1), also known as H I velocity field or mom-1 map, shows the intensity-weighted average of the velocities in each pixel of the cube. Mom-1 maps were made to give the first indication of the gas motion with respect to the systemic velocity (approaching or receding), and measure the mean velocity of the gas. It can be derived by:

$$M_1 =< \text{V} >= \frac{\int_i v_i S_i \times dv}{\int_i S_i \times dv} = \frac{\sum_i S_i \times v_i}{\sum_i S_i}, \tag{2.13}$$

where v_i is the corresponding velocity at the i-th channel.

Spatial smoothing is one way to boost faint emission, but the size of the smoothing kernel must be balanced against the resolution needed to measure distinct features for higher-redshift detections, thus allowing us to measure $D_{\rm HI}$. Therefore, I made a copy of each subcube and smoothed them into a circular $20'' \times 20''$ beam. This is the smallest common beam that matches the native resolution of all the MIGHTEE-H I Early Science data cubes. We used a 3σ threshold to clip the smoothed cube, where σ is the rms noise from the smoothed noise cubes. To get an estimation of the local rms in a subcube, I measured the standard deviation of the pixel fluxes within four emission-free regions around the detection, then took their mean values (e.g., Ramatsoku et al. 2016; Ponomareva et al. 2021). The resulting spatial mask was applied to the non-smoothed subcube to produce a *masked subcube*. Pixels outside the spatial mask were considered as noise, their values were set to zero. On the other hand, unmasked pixels were added up to make mom-0 maps and calculate the integrated flux of the emission.

In summary, I generated the mom-0 and mom-1 maps of each of the MIGHTEE-H I detections by integrating the channel maps containing the H I emissions after a $20''$ smoothing and a 3σ clipping. Figure 2.7 illustrates an example of how the moment maps will look with and without the smoothed mask for a 3σ clipping threshold. With a 3σ clipping only (no smoothing), more fine structures are observed but pixels of noise cannot be avoided. However, with a smoothed mask, it is observed that residual noises around the emission are avoided and we detect lower column density emissions.

2.3.5 Morphological classification

One of the approaches for confirming the legitimacy of an H I detection and providing data products for a survey is to cross-match them with optical or multi-wavelength counterparts. This is also needed to study the $D_{\rm HI} - M_{\rm HI}$ relation for different morphologies (see Section 2.7.2).

By design, the region of the sky covered by the MIGHTEE-H I early survey (XMMLSS and COSMOS) are a few of the foremost best studied extragalactic fields visible from the Southern Hemisphere. A few examples of photometric and spectroscopic surveys covering XMMLSS and COSMOS are XMM-SERVS[8] (X-ray), the Hyper Suprime-Cam Deep Survey (HSC, Optical; Aihara et al. 2018, 2019), UltraVISTA (NIR, McCracken et al. 2012), VISTA Deep Extragalactic Observations (VIDEO, NIR; Jarvis et al. 2013), Z-COSMOS (Lilly et al., 2009) and PRIsm MUlti-object Survey (PRIMUS; Coil et al. 2011). A more detailed list covering the full range of wavelengths, from X-ray to radio, can be seen in Table 1 of Chen et al. (2018).

[8] http://personal.psu.edu/wnb3/xmmservs/xmmservs.html

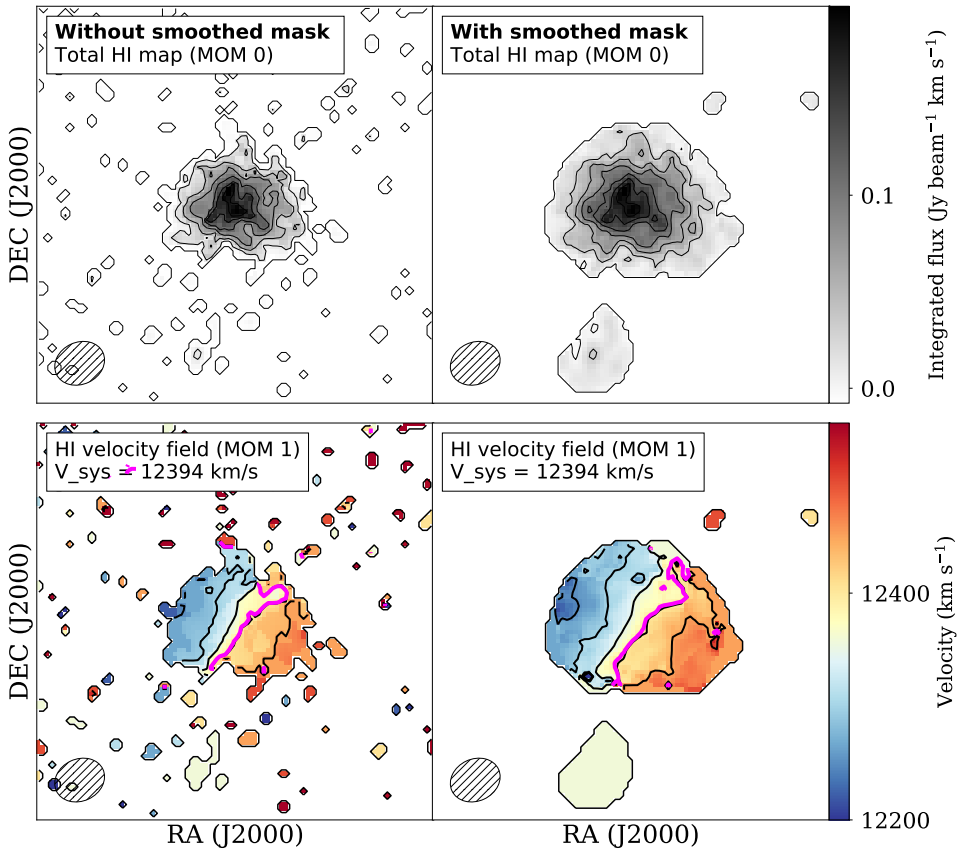

Figure 2.7: Mom-0 and mom-1 maps of MGTH_J021815.4 – 041558. Left panel: mom-0 and mom-1 maps with a 3σ non-smoothed mask. Right panel: mom-0 and mom-1 maps with a 3σ, $20''$ smoothed mask. The total intensity maps (mom-0) are shown in the top panels with black contour levels of 0, 0.03, 0.06, 0.09, 0.12 0.15, 0.18, and 0.21 Jy beam^{-1} km s^{-1} overlaid on their grayscale images. The bottom panels represent the H I velocity fields (mom-1) where the measured systemic velocity of 12363 km s^{-1} is indicated by the thick magenta line. Approaching or blue-shifted gas emission is illustrated by blue color whereas receding or redshifted gas emission is indicated by red color. Black contours describe the velocity contours for a fixed velocity interval of 50 km s^{-1}: 12250, 12300, 12350, 12400, 12450, and 12500 km s^{-1}. The synthesized beam with an FWHM of $11.6'' \times 9.5''$ is indicated in the lower-left corner of each image.

The galaxies in our sample were visually classified based on their optical morphology. Three classifiers inspected three-colour images created from Subaru HyperSuprimeCam g, r, and i-band images (HSC; Aihara et al. 2018, 2019). For the few objects lying outside the HSC imaging footprint, the three-colour images from the Sloan Digital Sky Survey Data Release 16 (SDSS DR16; Ahumada et al. 2020) were used. The SDSS imaging is substantially shallower than that from HSC, but the number of objects is small, and the different imaging does not affect our results. All the H I detections were seen to have an optical counterpart and the majority vote of the three classifiers was taken as the adopted morphology. The three-colour images are then shown into the atlas as optical 2D cutout images. While automated morphological classification algorithms are used for large datasets (e.g., the Zurich Estimator of Structural Type, Scarlata et al. 2007), visual classification is still in use (e.g., Hashemizadeh et al., 2021). The H I morphology was not used for the classification.

Online databases such as the NASA/IPAC Extragalactic Database[9] (NED), within a $0.1'$ radius search, were also used. This was done to conduct a cross-match with previous H I surveys and verify the detected H I galaxies (see Section 2.6.4 for more details).

The galaxies were divided into four morphological categories: spirals (SP), early-types (ET), irregular (IR), and mergers (ME). No distinction was made between irregular and dwarf irregular as no stellar mass information was used in the classification. ET galaxies have smooth, centrally concentrated morphology, whereas SP galaxies show clear spiral arms originating from either a central bulge or bulge/bar. IR objects show no regular patterns, and ME systems show signs of interaction between two or more galaxies, including disturbed morphology or tidal streams. Due to the quality of the HSC imaging, faint and subtle features are often visible, complicating the morphological classification. Therefore, the final classification is based on the dominant morphology, i.e., a spiral galaxy with faint tidal streams is classified as SP, not ME. Of the 276 galaxies in the original sample, there are 176 SP, 72 IR, 19 ME and 9 ET. Examples of the four classes are given in Fig. 2.8.

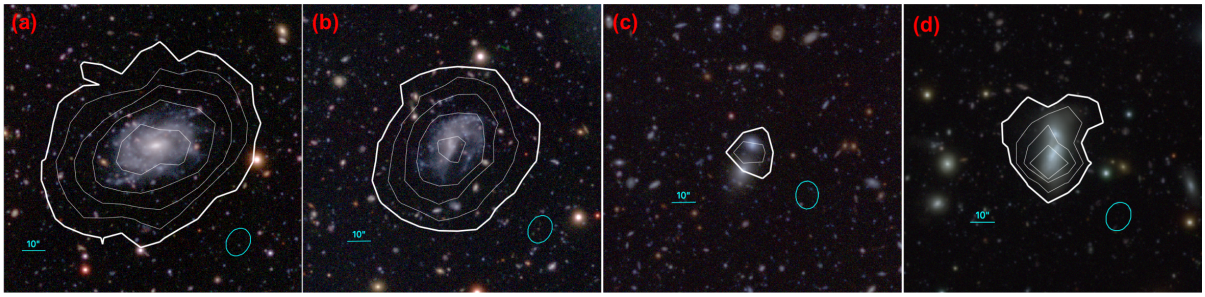

Figure 2.8: Examples of galaxies of different morphological types detected within MIGHTEE-H I. Panel (a): an undisturbed spiral galaxy at $z = 0.033$; panel (b): an irregular galaxy at $z = 0.044$; panel (c): an early type galaxy (the northern counterpart) at $z = 0.037$; panel (d): a merging system at $z = 0.032$. The optical cutouts are from the HSC *gri* images, with the H I column density contours overlaid in white. The 1.25×10^{20} atoms cm^{-2} ($1\ M_{\odot}$ pc^{-2}) contour is shown in bold. Thin contours correspond to $3, 6, 10, 15{\times}10^{20}$ atoms cm^{-2} for panels (a) and (b), $2{\times}10^{20}$ atoms cm^{-2} for panel (c), and $2, 3, 4 \times 10^{20}$ atoms cm^{-2} for panel (d). A $10''$ scale bar and the synthesized beam size are displayed in each panel, in which panel (c) has a slightly different angle due to it being from a different field than the other panels.

2.4 Sample selection

After the cross-matching with optical images and morphological classifications, the next phase is to remove galaxies that are unsuitable for this analysis. For example, after an in-depth examination of the sources, four galaxies were removed from the sample because they were classified as intermediate-stage mergers, i.e., when a system comprises two distinct stellar discs, but a single H I structure encompassing both galaxies. Early-stage mergers, where H I discs are still

[9] http://ned.ipac.caltech.edu/

associated with the individual galaxies were kept in the sample. Late-stage mergers, where the H I and the stars have both merged into a single structure were also retained. After removing these four galaxies, our sample was reduced to 272 objects.

We further imposed that galaxies must be resolved with at least one and a half resolution elements across the major axis, and that the radial extent of the inclination corrected surface mass density ($\Sigma_{\rm HI}$, see Section 2.6.1) must reach 1 $M_\odot$ pc^{-2} (1.249×10^{20} atoms cm^{-2}). Wang et al. (2016) has shown that a diameter $D_{\rm HI}$ defined at 1 $M_\odot$ pc^{-2} encloses most of the H I mass of a galaxy and is measurable for most of the galaxies, even for small H I discs that are close to being unresolved.

Additionally, the $\Sigma_{\rm HI}$ contour at 1 $M_\odot$ pc^{-2} should not be strongly disrupted due to ongoing mergers or tidal interactions (for details, see Section 2.6.1). A total of 204 out of 272 galaxies satisfy our selection criteria, and form the final sample for our study of the $D_{\rm HI} - M_{\rm HI}$ relation. The median resolution of our resulting sample is three beams across the major axis, with only 6 galaxies being resolved with more than 10 beams. Of the 204 galaxies in the original sample, there are 148 SP, 40 IR, 12 ME and 4 ET.

2.5 H I catalogue

This section describes the structure of the H I catalogue of the H I sources selected within the MIGHTEE-H I early survey. The full catalogue of the 204 detections is appended at the end of this thesis in Appendix A.
As previously observed in Sections 2.3 and 2.6, I derived various H I properties for the selected sample of galaxies in the MIGHTEE-H I early observations. I compiled the H I catalogue that forms the $D_{\rm HI} - M_{\rm HI}$ relation by presenting the results into Table A.1. This table summarizes the observational parameters after source finding, enumerates the derived H I parameters and displays their morphological classifications. The contents of Table A.1 are as follows:

1. **Column (1)**: Galaxy designated name based on the MIGHTEE-H I detections nomenclature. Names are of the form MGTH_JHHMMSS.S+DDMMSS. This identification is based on the unrounded values of the Right Ascension in hh mm ss and Declination (J2000) in dd mm ss format of the H I centroid.

2. **Column (2):** Field name in which the detection belongs to. The letter "X" indicates a detection found in XMMLSS while "C" represents a source in the COSMOS field.

3. **Column (3)**: Morphological type based on the visual classification of the optical counterpart. (SP) for Spirals, (IR) for Dwarf Irregulars and Irregular galaxies, (ET) for Early-types and (ME) for Mergers.

4. **Column (4)**: Peak flux density ($S_{\rm p}$) in mJy of the H I line profile with its uncertainty.

5. **Column (5)**: Integrated H I flux density ($S_{\rm int}$) of each MIGHTEE-H I source, expressed in Jy km s^{-1}. This value corresponds to the total H I line flux measured within the mom-0 map of a detection.

6. **Column (6)**: Local rms noise of the detection noise cubes in mJy beam^{-1}.

7. **Column (7)**: Systemic H I velocity ($v_{\rm sys}$) of the emission measured from the heliocentric central velocities of the Global H I profile in km s^{-1} (the relativistic convention is assumed for the Doppler shift). The typical uncertainty for the systemic velocity and linewidths corresponds to the width of one channel at the observed velocity frame which is $\epsilon(v_{\rm sys}) \sim 44$ km s^{-1} at $z = 0$ and $\epsilon(v_{\rm sys}) \sim 52$ km s^{-1} at $z \sim 0.084$.

8. **Column (8)**: Velocity widths of the H I line profile at 50% of the peak flux density (w_{50}) measured at the width maximization procedure and with the use of PyMultinest.

9. **Column (9)**: Luminosity distance D_L in Mpc with an uncertainty $\epsilon(D_L) \sim 0.5$ Mpc at $z = 0$ and $\epsilon(D_L) \sim 3.5$ Mpc at $z \sim 0.084$, measured from the H I emission redshift.

10. **Column (10)**: Logarithm of the total H I mass log(M$_{\rm HI}$/M$_\odot$) and its uncertainty (see Eq. 2.21).

11. **Column (11)**: Inclination and beam-smearing corrected H I diameter in kpc, measured at a surface density level of 1 M$_\odot$ pc^{-2}.

12. **Column (12)**: Measured inclinations ($i_{\rm HI}$) in degrees.

As an illustration, the first page of the catalogue table is presented in Table 2.2.

Table 2.2: A catalogue of H I properties of the sample of 204 galaxies in the MIGHTEE-H I Early survey.

MGTH	Field	Morpho	S_p (mJy)	$S_{\rm int}$ (Jy km s^{-1})	rms (mJy beam^{-1})	$v_{\rm sys}$ (km s^{-1})	w_{50} (km s^{-1})	D_L (Mpc)	log $M_{\rm HI}$ (dex)	$D_{\rm HI}$ (dex)	$i_{\rm HI}$ (deg)
(1)	(2)	(3)	(4)	(5)	(6)	(7)	(8)	(9)	(10)	(11)	(12)
J021529.1-051859	X	SP	6.14±0.24	0.738±0.037	0.240	7780	157	115	9.34	28.18	59
J021532.8-044607	X	SP	8.14±0.11	1.927±0.096	0.109	12383	291	186	10.16	67.61	50
J021534.4-042904	X	SP	1.84±0.15	0.129±0.006	0.149	23582	69	373	9.56	35.56	32
J021541.6-051317	X	IR	10.62±0.16	0.724±0.036	0.161	12635	90	190	9.75	46.03	41
J021542.4-045436	X	SP	3.76±0.11	0.497±0.025	0.108	12589	456	189	9.59	39.36	43
J021544.5-045540	X	SP	8.17±0.1	1.742±0.087	0.099	12784	226	193	10.01	64.42	56
J021600.4-044414	X	SP	8.35±0.08	0.576±0.029	0.080	20101	275	313	10.06	52.48	47
J021609.9-051858	X	SP	16.95±0.14	3.093±0.155	0.141	16423	185	252	10.62	121.06	25
J021632.8-041357	X	SP	3.45±0.17	0.216±0.011	0.175	12830	95	193	9.24	20.65	29
J021639.9-044747	X	SP	9.68±0.06	1.06±0.053	0.063	20136	137	313	10.33	98.86	33
J021642.0-044221	X	SP	8.16±0.06	0.597±0.03	0.064	12578	65	189	9.67	31.92	64
J021645.4-042035	X	IR	3.02±0.1	0.281±0.014	0.104	24009	113	381	9.91	50.70	46
J021659.0-050352	X	ET	2.72±0.08	0.194±0.019	0.081	7667	96	112	8.74	14.32	41
J021702.2-050351	X	ME	8.3±0.06	1.029±0.051	0.063	7701	130	114	9.39	29.99	42
J021702.2-044454	X	SP	2.16±0.06	0.286±0.014	0.058	16411	254	251	9.58	32.96	56
J021702.7-051940	X	SP	8.83±0.13	1.185±0.059	0.125	15657	141	239	10.16	54.45	45
J021708.4-041349	X	SP	11.05±0.14	1.778±0.089	0.138	16423	161	252	10.38	88.31	27
J021711.2-042120	X	SP	3.54±0.1	0.7±0.035	0.096	16469	385	252	9.97	54.83	67
J021711.8-042441	X	IR	2.92±0.08	0.27±0.013	0.083	11191	136	167	9.22	26.61	40
J021714.5-052922	X	SP	8.46±0.23	0.636±0.064	0.233	5190	242	76	8.92	18.45	43
J021719.4-052851	X	SP	73.0±0.18	14.931±0.747	0.179	5325	240	77	10.29	74.99	62
J021729.0-050827	X	SP	6.93±0.07	0.79±0.04	0.069	12819	102	193	9.80	48.64	29
J021729.9-041656	X	SP	1.97±0.11	0.15±0.015	0.112	10016	88	149	8.87	13.71	61
J021742.0-041520	X	SP	7.33±0.12	0.966±0.048	0.122	9880	200	147	9.67	46.67	33
J021742.5-050425	X	SP	3.82±0.06	0.457±0.023	0.059	13095	132	196	9.58	37.15	32
J021743.8-051752	X	ME	5.02±0.1	0.488±0.024	0.095	9493	131	140	9.33	24.43	45
J021744.6-050322	X	SP	3.37±0.06	0.27±0.013	0.058	12865	87	194	9.34	30.20	44
J021744.9-041158	X	SP	7.01±0.15	1.409±0.07	0.147	12497	199	188	10.03	53.95	57
J021748.5-043241	X	SP	6.3±0.06	0.875±0.044	0.062	19995	231	311	10.24	76.91	42
J021750.4-044940	X	ME	1.47±0.05	0.175±0.009	0.052	12474	142	188	9.12	24.72	40
J021759.3-041634	X	SP	8.04±0.11	0.901±0.045	0.114	9834	99	147	9.63	38.64	18
J021814.0-044944	X	SP	3.71±0.06	0.488±0.024	0.055	9413	163	140	9.32	27.80	46
J021815.4-041558	X	SP	11.98±0.13	2.232±0.112	0.129	12394	261	186	10.20	67.45	36
J021818.0-043234	X	IR	5.77±0.23	0.33±0.017	0.233	12589	86	190	9.41	26.30	62
J021822.2-050614	X	SP	2.65±0.07	0.262±0.013	0.069	13049	179	196	9.34	28.44	33
J021824.1-052754	X	SP	6.94±0.18	1.048±0.052	0.178	12474	222	188	9.90	50.47	57
J021827.2-041219	X	IR	8.32±0.16	1.148±0.057	0.160	12233	197	184	9.93	49.66	36
J021836.3-043236	X	SP	21.37±0.07	2.287±0.114	0.073	3936	93	57	9.23	25.18	32
J021847.0-045555	X	SP	1.33±0.06	0.101±0.01	0.064	13003	61	196	8.93	15.31	45
J021848.1-045028	X	SP	2.36±0.06	0.179±0.009	0.063	24092	67	382	9.72	41.78	49
J021902.3-042646	X	SP	5.65±0.17	0.523±0.026	0.167	12141	178	183	9.58	36.31	47
J021931.5-042703	X	SP	2.7±0.13	0.132±0.007	0.126	20030	64	312	9.42	28.91	50
J021932.7-041447	X	ME	5.65±0.25	0.761±0.038	0.251	12566	241	188	9.77	44.06	66
J021934.4-042846	X	IR	2.92±0.14	0.236±0.012	0.137	20124	94	313	9.68	26.30	69
J021947.7-045130	X	SP	4.39±0.09	0.818±0.041	0.093	12818	234	193	9.82	48.42	52
J021953.8-045710	X	SP	1.41±0.09	0.151±0.015	0.087	9959	155	148	8.86	11.75	33
J022002.1-041438	X	IR	3.54±0.18	0.128±0.006	0.184	12428	69	187	8.99	14.96	45
J022002.8-042547	X	SP	4.65±0.2	0.448±0.045	0.205	5325	133	78	8.79	14.69	42
J022014.4-052345	X	SP	5.34±0.23	0.531±0.027	0.229	14812	103	225	9.76	50.35	29
J022016.8-042546	X	SP	10.03±0.22	0.508±0.025	0.225	19984	88	310	10.00	66.83	60
J022021.4-045803	X	SP	2.97±0.08	0.702±0.035	0.085	9970	358	147	9.52	30.90	68
J022026.3-045912	X	IR	1.67±0.1	0.124±0.012	0.096	12531	87	188	8.98	15.35	66
J022028.5-053705	X	SP	7.27±0.55	0.243±0.012	0.548	13244	213	200	9.32	26.73	20

2.6 H I properties

One of the MIGHTEE-H I key science goals is to extend the coverage of the latest H I mass function (HIMF) from the full ALFALFA survey (Jones et al., 2018) out to $0.1 < z < 0.5$. The full MIGHTEE-H I survey will probe more galaxies at the high-mass end of the HIMF (Jarvis et al., 2016; Maddox et al., 2021). It is essential to determine reliable measurements of H I parameters from this Early Science data to complete the full survey. The $D_{\rm HI} - M_{\rm HI}$ relation is then used in this case as a powerful diagnostic tool to validate our measurements.

In this section, I describe the different methods used to determine H I properties that are needed for the construction of the $D_{\rm HI} - M_{\rm HI}$ relation of the MIGHTEE-H I early survey. The global H I properties distributions, as well as H I masses comparison with ALFALFA are also described.

2.6.1 H I size

In order to measure the size of the H I discs, we use the mom-0 maps, produced for each detection as described in detail in Section 2.3.4 (see also Ponomareva et al. 2021 and Ranchod et al. 2021).

I convert mom-0 maps from the units of flux density to surface mass density following the prescription from Meyer et al. (2017):

$$\left(\frac{\Sigma_{\rm HI}}{\rm M_\odot\,pc^{-2}}\right) = 1.00\times10^4(1+z)^3\left(\frac{S_{\rm int}}{\rm Jy\,km\,s^{-1}}\right)\left(\frac{\Omega_{\rm bm}}{\rm arcsec^2}\right)^{-1}, \tag{2.14}$$

where z is redshift, $S_{\rm int}$ is the integrated flux density and $\Omega_{\rm bm} = \frac{\pi b_{\rm maj} b_{\rm min}}{4\ln(2)}$ is the solid angle of the synthesized beam with major axis $b_{\rm maj}$ and minor axis $b_{\rm min}$.

Once the surface mass density maps are obtained, I use the following approach to determine $D_{\rm HI}$:

1. I use a 2D elliptical Gaussian function to fit the surface mass density map and measure its diameter at the 1 $\rm M_\odot\,pc^{-2}$ contour level (see left panel of Fig. 2.9). While the H I radial distribution is not Gaussian, and H I radial profiles often reveal a depletion at the center (e.g., Wang et al., 2014; Martinsson et al., 2016), we are only interested in H I distribution at the outer part of the H I disk where the H I diameter is measured. In addition, the majority of our sample galaxies are only marginally resolved with a median resolution of 3 beams. Therefore, a 2D elliptical Gaussian function works similarly to a simple ellipse fitting. The function is expressed as:

$$f(x,y) = A\exp\left(-(a(x-x_0)^2 + 2b(x-x_0)(y-y_0) + c(y-y_0)^2)\right), \tag{2.15}$$

where A is the amplitude of the Gaussian peak in $M_\odot\,pc^{-2}$, (x_0, y_0) its centre position in pixels, and a, b, and c are defined as:

$$a = \frac{\cos^2\theta}{2\sigma_X^2} + \frac{\sin^2\theta}{2\sigma_Y^2}, \tag{2.16}$$

$$b = -\frac{\sin 2\theta}{4\sigma_X^2} + \frac{\sin 2\theta}{4\sigma_Y^2}, \tag{2.17}$$

$$c = \frac{\sin^2\theta}{2\sigma_X^2} + \frac{\cos^2\theta}{2\sigma_Y^2}. \tag{2.18}$$

In the above equations, θ is the position angle in radians, σ_X and σ_Y are the semi-major and semi-minor axes of the disk. I assume the following initial values for the parameters $A, x_0, y_0, \sigma_X, \sigma_Y$ and θ to optimize the fitting process:

- the amplitude A is set to the maximum pixel value in the map in units of $M_\odot\,pc^{-2}$,
- the estimated H I emission centre x_0, y_0 is assumed to be at the centre of the map i.e., half the number of pixels contained in the x and y axis of the map,
- σ_X and σ_Y are set to 10 pixels as 20 pixels ($40''$) is the typical extent of a source in the MIGHTEE-H I early science data,
- the position angle θ was assumed to be 0.

2. With these estimates, I perform a non-linear least square fitting and obtain optimal values for the 2D Gaussian parameters listed in step (i). I use the 1 $M_\odot\,pc^{-2}$ ellipse to obtain the corresponding best-fitting central position of the H I emission (x_0, y_0), the major and minor axis values, and the position angle of the ellipse.

As an example of the 2D Gaussian fitting, Fig. 2.9 displays the fitting outcome for a galaxy with $V_{sys} \sim 1\,805$ km s^{-1} ($z = 0.006$), where ellipses, resulted from the fit are over-plotted on top of the surface mass density map (left panel). The velocity field (right panel), though not being used in the fitting process, is shown to demonstrate that the fitted centre and major axis coincide with the kinematic centre and major axis.

To derive the inclination angle of the plane of the galaxy in degrees, I use:

$$\cos^2(i_{HI}) = \frac{(2.355\,\sigma_Y)^2 - b_{min}^2}{(2.355\,\sigma_X)^2 - b_{maj}^2}, \tag{2.19}$$

where b_{maj} and b_{min} are the major and minor axes of the synthesized beam (Verheijen & Sancisi, 2001). Galaxies with low spatial resolution might appear rounder due to the beam smearing. The inclusion of the synthesized beam in Eq. 2.19 will account for the beam-smearing effect. However, it is important to note that this correction assumes that the axes of the beam are aligned

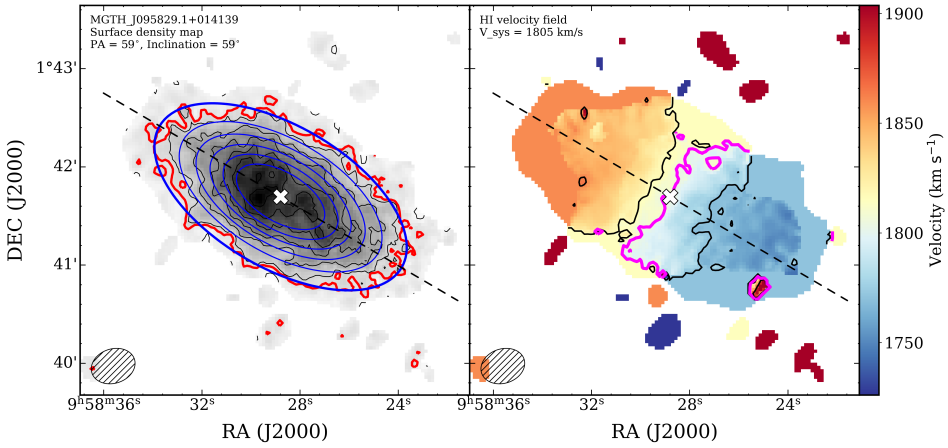

Figure 2.9: Example illustrating the 2D Gaussian fitting procedure (source MGTH_J095829.1+014139). Left panel: Surface mass density map (greyscale and black thin contours). The contour levels are 10.5, 9, 7.5, 6, 4.5, 3, 1.5 $M_\odot$ pc^{-2} and the 1 $M_\odot$ pc^{-2} contour is highlighted in red. The fitted 2D Gaussian function is shown by the thin blue ellipses; the fitted $D_{\rm HI}$ is highlighted by the thick blue outermost ellipse. Right panel: velocity field (mom-1). Iso-velocity contours are shown in black and separated by 45 km s^{-1}. The measured systemic velocity is indicated by the thick magenta line. In both panels, the white cross marks the fitted ellipse centre, and the dashed line represents the fitted major axis of the ellipse from the 2D Gaussian fitting. The beam size is indicated in the lower-left corner of each panel.

with the major axis of the galaxy, which is not necessarily the case for our data. I ran the tests to evaluate the additional error on the inclination caused by possible misalignment of the beam and the source axes. I found that for marginally resolved galaxies ($<$ 3 beams) the error on inclination is $\sim$7 degrees, for galaxies resolved with 3 - 5 beams the error is $\sim$3 degrees, while it is negligible for galaxies resolved over more than 5 beams. I add these errors in quadrature to the inclination measurement error of $\sim$5 degrees (Ponomareva et al., 2021). This results in the total error on inclination for marginally resolved galaxies: $\sim$8.5 degrees, for galaxies resolved with 3 - 5 beams: 5.8 degrees, and 5 degrees for galaxies resolved with more than 5 beams. I also note that our inclinations, measured from the HI maps are in excellent agreement with inclinations measured from the optical photometry and with inclinations derived with the 3D kinematic modeling for a sub-sample of 67 galaxies from Ponomareva et al. (2021).

3. I correct each surface mass density map for the measured inclination by multiplying each unmasked pixel value of the map by the cosine of the inclination angle. Then, we repeat steps (i) and (ii).

4. $D_{\rm HI}$ ($2\sigma_X$) is then measured from the inclination corrected maps along the major axis of the best-fitting ellipse corresponding to the surface mass density contour of 1 $M_\odot$ pc^{-2}.

5. To complete the HI size measurements, I correct $D_{\rm HI}$ for beam smearing effect using the following prescription from Wang et al. (2016):

$$D_{\rm HI,corr} = \sqrt{D_{\rm HI}^2 - b_{\rm maj} \times b_{\rm min}}, \tag{2.20}$$

where $D_{\rm HI,corr}$ is the corrected H I size which we use to construct the $D_{\rm HI} - M_{\rm HI}$ relation. This correction removes a systematic bias which induces an over-estimation of $D_{\rm HI}$ for marginally resolved galaxies.

The conservative uncertainty on $D_{\rm HI,corr}$ is assigned as half of the synthesized beam major axis $b_{\rm maj}$, expressed in kpc, and includes the uncertainty on the inclination angle. The error on the cosmological luminosity distance (D_L) is also propagated during the conversion. The latter was derived by adopting the channel width as the error on the systemic velocity and 2.2 km s^{-1} Mpc^{-1} as the error on the Hubble constant (Hinshaw et al., 2013). The resulting error on D_L is ~3.5 Mpc. The uncertainty on log $D_{\rm HI}$ slightly increases with distance and is ~0.02 kpc at $z = 0$ and ~0.11 kpc at $z \simeq 0.084$.

2.6.2 H I mass

To construct the $D_{\rm HI} - M_{\rm HI}$ relation, I measure the total H I mass enclosed within the mom-0 map of a galaxy, since the amount of H I beyond the diameter at 1 M$_\odot$ pc^{-2} is negligible for our sample. By assuming an optically thin gas ($\tau \ll 1$) with no significant self-absorption, I use the following equation from Meyer et al. (2017) which uses the cosmological luminosity distance D_L to the galaxy to determine the H I mass:

$$\left(\frac{M_{\rm HI}}{M_\odot}\right) \simeq \frac{2.356 \times 10^5}{(1+z)} \left(\frac{D_L}{\rm Mpc}\right)^2 \left(\frac{S_{\rm int}}{\rm Jy\,km\,s^{-1}}\right), \tag{2.21}$$

where z is the redshift of the source with frequency ν, defined by:

$$z = \frac{\nu_0 - \nu}{\nu}. \tag{2.22}$$

$D_L = (1+z)D_C$ is the luminosity distance in Mpc where D_C is the comoving distance which can be determined straightforwardly with `cosmo.comoving_distance` in `astropy`[10]. $S_{\rm int} = \int S_v\, dv$ is the integrated flux density derived from the mom-0 map.

The uncertainty on the integrated flux $S_{\rm int}$ was estimated from the mean rms noise within four emission-free regions around the detection (Ramatsoku et al., 2016; Ponomareva et al., 2021). As a result, an H I mass uncertainty of ~5% is measured for large mass galaxies ($M_{\rm HI} > 10^9$ M$_\odot$), ~10% for $10^8 < M_{\rm HI} < 10^9$ M$_\odot$ while the error can reach up to 20% for galaxies below $M_{\rm HI} < 10^8$ M$_\odot$ (see Maddox et al. 2021 for details).

[10] https://github.com/astropy/astropy/

2.6.3 H I properties distribution

I present an overview of the 204 selected galaxies in the MIGHTEE-H I early survey in Fig. 2.10. These histograms show the different distribution of the measured global H I parameters of the early survey and give us a hint about the characteristics of the sample. This include their recessional velocities, linewidths, integrated fluxes, and H I masses.

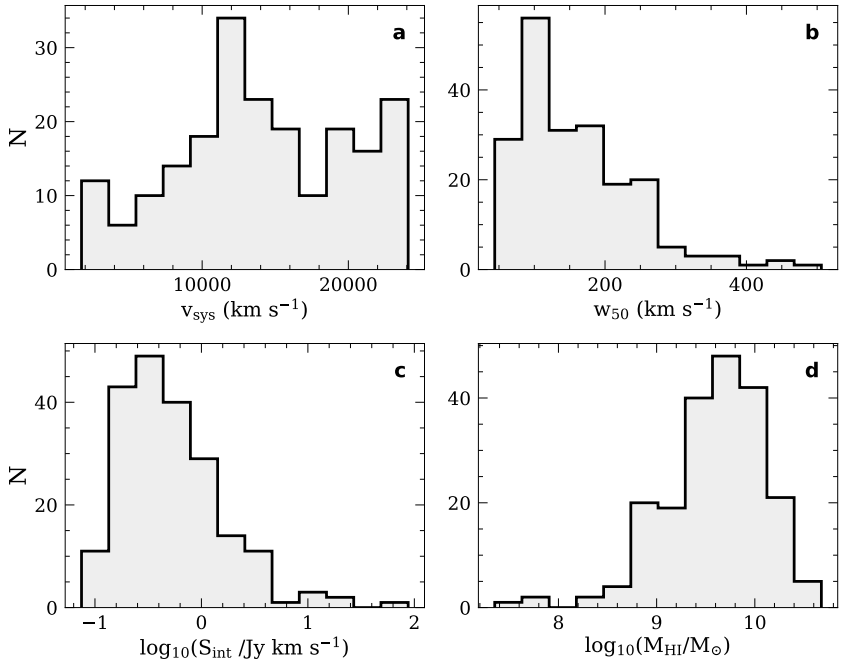

Figure 2.10: Histograms of the H I parameters distribution for the sample of 204 galaxies selected in the MIGHTEE-H I early survey. Panel (a) displays the systemic velocity in the relativistic convention. Panel (b) shows the profile linewidth at the 50% flux level w_{50}. The logarithm of the integrated flux density is presented in the bottom left panel (c) and the H I-mass distribution is shown in the bottom right panel (d).

The sources were found within a systemic velocity range of 1748 – 24 092 km s^{-1}. By assessing their velocity distributions, an overdensity of groups of galaxies indicating significant structure at $0.04 < z < 0.045$ is revealed with a peak at approximately $z \sim 0.044$ (12 500 km s^{-1}) in the XMMLSS fields. A recent detailed study by Ranchod et al. (2021) reported ~20 galaxies in the H I-rich group.

The top right panel of Fig. 2.10 displays the w_{50} linewidth histogram of the sample. Despite the coarse channel resolutions of MeerKAT 4K data, the sources cover linewidths ranging from 44 – 506 km s^{-1}. Two detections – J021542.4 – 045436 and J022154.1 – 044023 – have $w_{50} > 450\ km\ s^{-1}$, they were the largest inclined double-horn spirals in the survey. While the majority of the sources were found to have linewidths below 250 km s^{-1}, the mean and median linewidths at 50% of the peak flux density are 157 and 137 km s^{-1} respectively. This average value is lower than for the Arecibo Legacy Fast ALFA survey (ALFALFA) α.40 catalogue measuring an average w_{50} value of 186 km s^{-1} (Haynes et al., 2011). ALFALFA detects more

H I-massive than low-mass galaxies due to its lower flux limit of 2.2 mJy with a survey coverage almost ∼140 times larger than MIGHTEE. Thus, this confirms that MIGHTEE is a more sensitive survey which allows it to detect galaxies at lower H I masses and thus with narrow linewidths.

The bottom left panel shows the distribution of the integrated line fluxes' logarithm in the survey. With a mean value of $\log(S_{\rm int}/{\rm Jy\,km\,s^{-1}}) = -0.29$ ($S_{\rm int} = 0.51$ Jy km s^{-1}), our results have the same upper limit value of $\log(S_{\rm int}/{\rm Jy\,km\,s^{-1}}) \simeq 2$ ($S_{\rm int} \simeq 100$ Jy km s^{-1}) as for ALFALFA. However, its lower limit can go as low as $\log(S_{\rm int}/{\rm Jy\,km\,s^{-1}}) \simeq -1.6$ ($S_{\rm int} \simeq 0.024$ Jy km s^{-1}). This again demonstrates that the Early survey is already capable of detecting low column density or low mass sources despite its small coverage of $\sim 20\,{\rm deg}^2$.

The H I mass distribution of the survey is displayed at the bottom right panel of Fig. 2.10. The visually detected H I sources cover 4 orders of magnitude in H I masses. Ranging from $\log(M_{\rm HI}/{\rm M}_\odot) = 7.35$ to 10.68, the majority of the sample, however, spans over a tighter range of $\log(M_{\rm HI}/{\rm M}_\odot) = 8.7$ to 10.4. I measure an average logarithm of the H I mass of $\log(M_{\rm HI}/{\rm M}_\odot) = 9.58$. This mass distribution is very similar to ALFALFA with a mean of 9.5. Despite the smaller area covered by the early science survey data (in comparison to ALFALFA), MIGHTEE is already sensitive enough to detect low-mass galaxies. Moreover, due to its depth reaching up to $z \sim 0.084$, the survey is finding more high-mass galaxy populations at larger distances than ALFALFA.

Sensitivity curve

To evaluate the H I mass distribution of visually detected galaxies as a function of velocity in the survey, I show its corresponding sensitivity plot in Fig. 2.11. The black solid lines indicate the 5σ flux limit for a 150 km s^{-1} linewidth galaxy for an rms noise value equal to the median local rms from the detections i.e., $\sim$ 122 μJy beam^{-1}. The early survey detections have also been overlayed with the ALFALFA $\alpha.100$ sample (Haynes et al., 2018) to quantify their distribution compared to other large surveys. As such, MIGHTEE is clearly detecting more low H I mass galaxies at all redshifts, but ALFALFA has uncovered a larger number of detections altogether. Moreover, the H I Parkes All Sky Survey (HIPASS, Meyer et al. 2004) and ALFALFA are limited to the local Universe. Their bandpass edges prevent them from detecting galaxies at higher redshift. With a 5σ flux limit, a 150 km s^{-1} linewidth detection, and a respective sensitivity of 13 and 2.2 mJy beam^{-1}, HIPASS and ALFALFA have a respective outer limit in redshift of $z \sim 0.043$ (blue dashed line) and $z \sim 0.06$ (red dashed line). While the MIGHTEE-H I early survey extends up to $z \sim 0.084$, these results attest its higher sensitivity and depth over HIPASS and ALFALFA despite its small coverage area.

The right panel of Fig. 2.11 illustrates the early survey sensitivity curve as a function of the

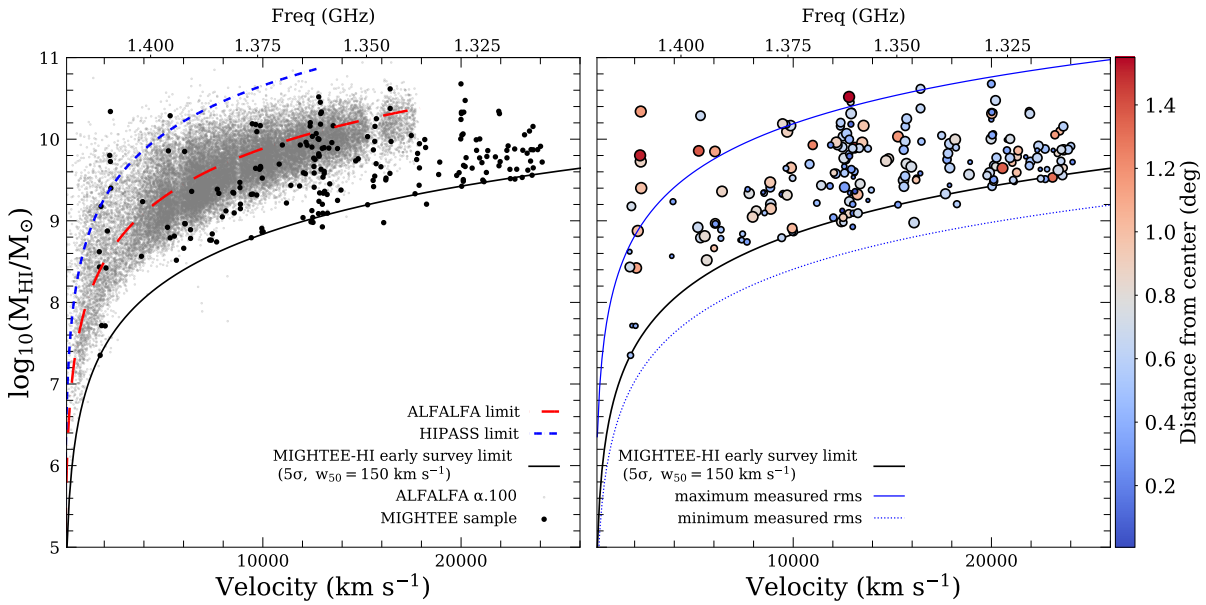

Figure 2.11: HI sensitivity curve of the 204 galaxies selected in the MIGHTEE-HI sample. The figures display the logarithm of the total HI mass as a function of the systemic radial velocity of the detections from the selected bandwitdth 1310 - 1420 Mhz. The black solid lines on both panels mark the 5σ - HI mass detection limit of the MIGHTEE-HI early survey from the mean local rms of all detections, for a galaxy with 150 km s^{-1} linewidth. *Left panel:* M_{HI} vs. radial velocity of the MIGHTEE-HI early survey (black dots) and the ALFALFA α.100 survey (grey dots). The HI mass limit of ALFALFA and HIPASS are respectively shown by the red and blue dashed curves which stop at their respective upper redshift limit of $v \sim 17\,500$ km s^{-1} ($z \sim 0.06$) and $v \sim 12\,700$ km s^{-1} ($z \sim 0.043$). *Right panel:* M_{HI} vs. radial velocity of the early survey individual detections. Each dot size varies according to the local rms noise value. The colorbar reveals their distance from the field centre. The blue curves from top to bottom indicate respectively the resulting HI mass limits for a 5σ detection using the maximum and the minimum local rms of each detections.

galaxy distance from the cube centre. A notable indication of clustering is observed at $\sim$ 12500 km s^{-1} ($z \sim 0.042$), with $\log(M_{HI}/M_\odot)$ ranging from 8.4 to 10.6 (see also Ranchod et al. 2021). The blue lines from top to bottom indicate the measured sensitivity limit from the maximum and the minimum local rms noises throughout the cubes. We can see that the detections are well distributed between the maximum and the minimum limits. Detection sizes in the figure also depend on their rms values. The marker sizes indicate the local rms.

2.6.4 Comparison with ALFALFA

Our HI mass results are compared with other HI surveys such as the latest catalogue of ALFALFA (Haynes et al., 2018), which has also covered the COSMOS field. The goal is to validate our integrated flux density and mass measurements. In total, 29 ALFALFA detections are present in the COSMOS region, as illustrated by the on-sky distributions of ALFALFA and MIGHTEE-HI detections in Fig. 2.12. After a cross-matching of the galaxies, only 17 overlapping sources were detected in MIGHTEE, although one ALFALFA source (AGC 201251) is blended and corresponds to two distinct MIGHTEE-HI detections due to the much larger PSF of ALFALFA. All undetected ALFALFA sources were located toward the cube edges (> 0.75 deg

radius from the cube centre) and with low SNR (SNR ≤ 6.5) as presented in Haynes et al. (2018).

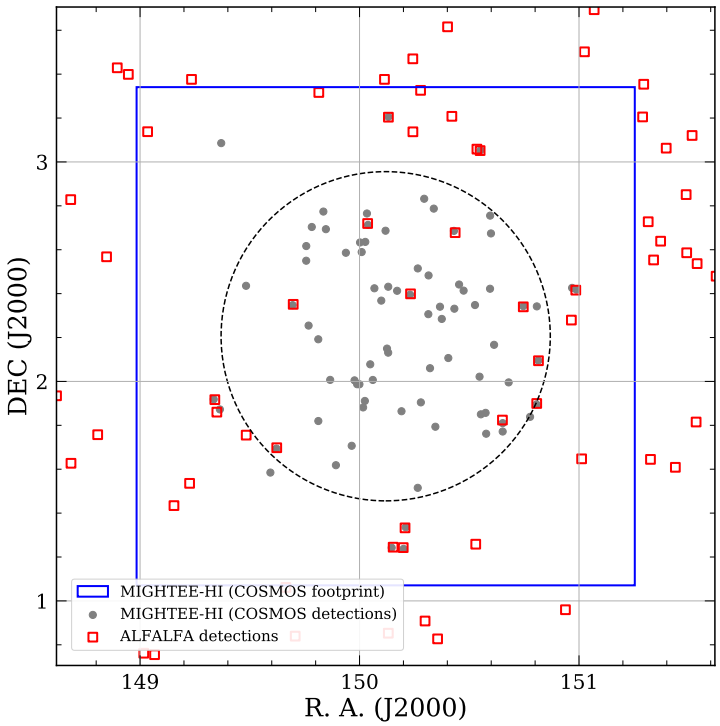

Figure 2.12: HI detections in MIGHTEE-HI (grey dots) and ALFALFA (red squares) in the COSMOS survey region. The blue square delimits the MIGHTEE-COSMOS cube search region, while the black dashed circle indicates detections that lie within 0.°75 radius of the pointing centre.

Figure 2.13 illustrates the HI mass comparison between ALFALFA and MIGHTEE-HI. Overall, our measurements are in good agreement, especially for the brighter galaxies with high SNR and which are located near the centre (< 0.75 deg, blue markers). We observe that a larger difference between the surveys is mostly driven when the sources are located near the edge (> 0.75 deg, red markers) and with low-SNR. By only considering detections near the cube centre, we obtain the mean value of the ratio of the HI masses of the two surveys to be $\sim 1.20 \pm 0.38$, and the mean ratio for the integrated flux densities to be $\sim 1.16 \pm 0.41$. Interestingly, a similar mean ratio of 1.1 was measured by Haynes et al. (2011) when computing the flux densities measured by ALFALFA and HIPASS surveys. ALFALFA measures slightly higher HI masses for some detections since large dishes are more sensitive to extended structures, but that difference only applies to some detections.

Consequently, high SNR detections are in good agreement between the two surveys. As detailed by Haynes et al. (2018), high-quality detections are assigned with code 1 in the catalogue, while code 2 detections are low-SNR sources that are not considered reliable but are likely to be real. Those detected by MIGHTEE are therefore indeed legitimate but the fluxes are much harder to compare due to the difference in spatial and velocity resolution, especially if they are not located near the cube centre. To illustrate these differences, we show a comparison of the HI

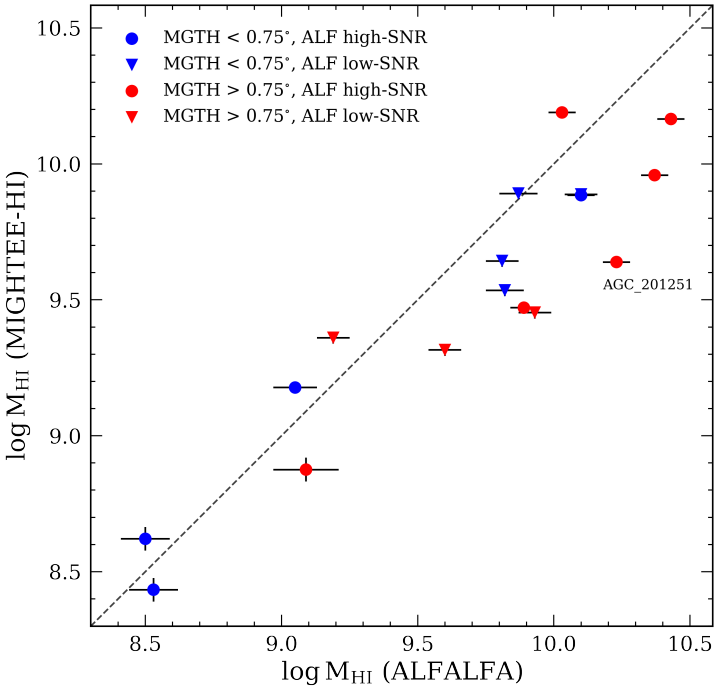

Figure 2.13: H I mass comparison between MIGHTEE-H I and ALFALFA. Blue symbols indicate MIGHTEE-H I detections which are lying within 0.75 degree radius of the Primary Beam centre, while red symbols mark detections lying toward the edge of the cube. Circles and triangles designate ALFALFA high-SNR and low-SNR sources, respectively. AGC 201251 is the blended source from ALFALFA which has at least two MIGHTEE-H I overlapping sources. The black dashed line indicates the one-to-one relation of the two surveys.

line profiles for high (code 1) and low (code 2) SNR sources located near the centre and toward the edge in Fig 2.14.

2.7 Constructing the $D_{\rm HI} - M_{\rm HI}$ relation for the survey

This section presents the correlation between the H I mass and the H I size of a selected sample of 204 galaxies from the MIGHTEE-H I Early Science data. I also show the comparison between the resulting $D_{\rm HI} - M_{\rm HI}$ relation and previous studies at $z = 0$, as well as its evolution as a function of redshift.

2.7.1 $D_{\rm HI} - M_{\rm HI}$ relation

I construct the $D_{\rm HI} - M_{\rm HI}$ relation and study its statistical properties, such as slope, zero point, and scatter, by performing a power-law fit to the relation with a maximum likelihood function that takes measurement errors of both parameters into account, and assuming a Gaussian intrinsic scatter along the vertical direction to the best-fitting line (see Eq. A4 in Lelli et al. 2019). We can therefore investigate, for the first time, whether the previously reported small scatter of the relation ($\sigma = 0.06$ dex, Wang et al. 2016) is due to measurement errors or is an intrinsic property.

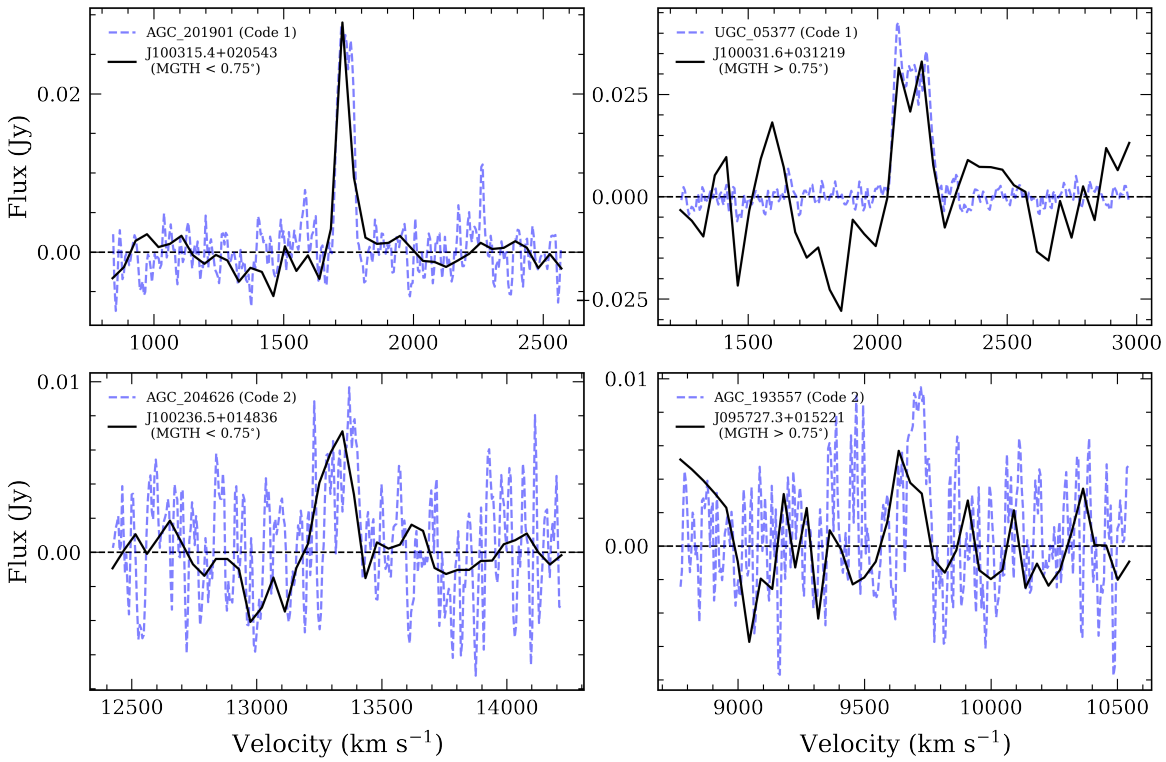

Figure 2.14: HI global profiles of MIGHTEE (black line) and ALFALFA (blue dashed line) in the COSMOS survey region. Two high-SNR sources (code 1) are shown in the first row while two low-SNR sources (code 2) are shown in the second row. Left columns indicate sources lying within 0.75 degree radius of the cube and right columns indicate sources located toward the edges.

I use the standard affine-invariant ensemble sampler for Markov chain Monte Carlo (MCMC) *emcee*[11] (Foreman-Mackey et al., 2013) to map the posterior distributions of the main statistical properties: slope, zero point and intrinsic scatter of the relation, following the prescriptions described in Lelli et al. (2019).

For the fit, I initialize the chains with 50 random walkers, run 1000 iterations, and re-run the simulation with 1000 steps. The starting position of the walkers is set randomly within realistic prior ranges: slope [0.1, 1], zero point [-6, 0], and intrinsic vertical scatter ($\sigma_{\rm int}$) [0.01, 0.1]. The convergence of the chains is then checked visually.

The posterior distributions of the parameters are shown in Fig. 2.15 and their median values are listed in Table 2.3. The resulting $D_{\rm HI} - M_{\rm HI}$ relation for our data and the associated 1σ uncertainty from the MCMC posterior distribution is presented in Fig. 2.16. I find the relation to be:

$$\boxed{\log D_{\rm HI} = 0.501^{+0.008}_{-0.008}\ \log M_{\rm HI} - 3.252^{+0.073}_{-0.074}}. \quad (2.23)$$

[11] https://emcee.readthedocs.io/en/stable/

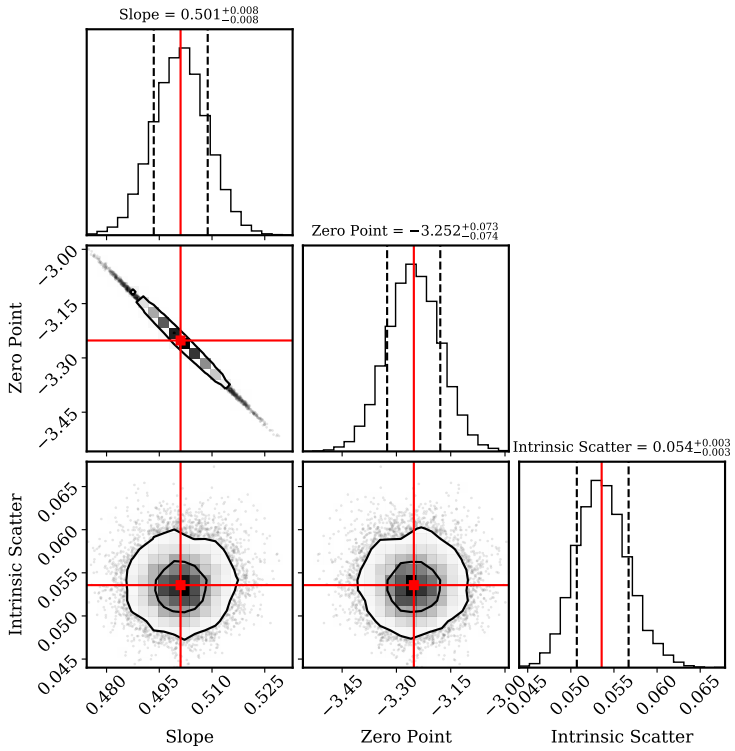

Figure 2.15: The posterior distributions of the slope, zero point and the intrinsic scatter of the $D_{\rm HI} - M_{\rm HI}$ relation. The best-fitting median values are indicated with the red squares and solid lines. Black contours are 68 (1σ) and 95 (2σ) percent confidence regions.

The non-zero intrinsic scatter (σ_{int} = 0.054 ± 0.003 dex) is comparable to the observed scatter (σ = 0.057 dex) and suggests that the scatter of the relation cannot be explained just with the measurement errors, but rather is an intrinsic property of the relation allowing for a ∼10% variation of the $D_{\rm HI}$ at a fixed H I mass. To assess whether the intrinsic scatter is introduced by an underestimation of the measurement errors, we have repeated the fit using measurement errors which are 2, 3, and 4 times larger than the original values in both directions. Consequently, all resulting intrinsic scatters were non-zero.

Furthermore, our relation is in excellent agreement with Wang et al. (2016), who found a slope of 0.506 ± 0.003, an intercept –3.293 ± 0.009, and an observed scatter of σ = 0.06 dex. Fig. 2.16 shows the distribution of the detections in the relation with respect to the 1σ confidence region of the MCMC fit and the 3σ scatter of the Wang et al. (2016) relation. It is observed that all detections lie within the black dotted lines which are the 3σ scatter of the Wang et al. (2016) relation.

2.7.2 $D_{\rm HI} - M_{\rm HI}$ relation and galaxy type

Previous studies have focused on targeted morphologies of galaxies (e.g., Begum et al. 2008 with dwarf galaxies, Noordermeer et al. 2005 with early-type galaxies). The absence of a homogeneous large sample containing various types of galaxies has led to the study of the relation

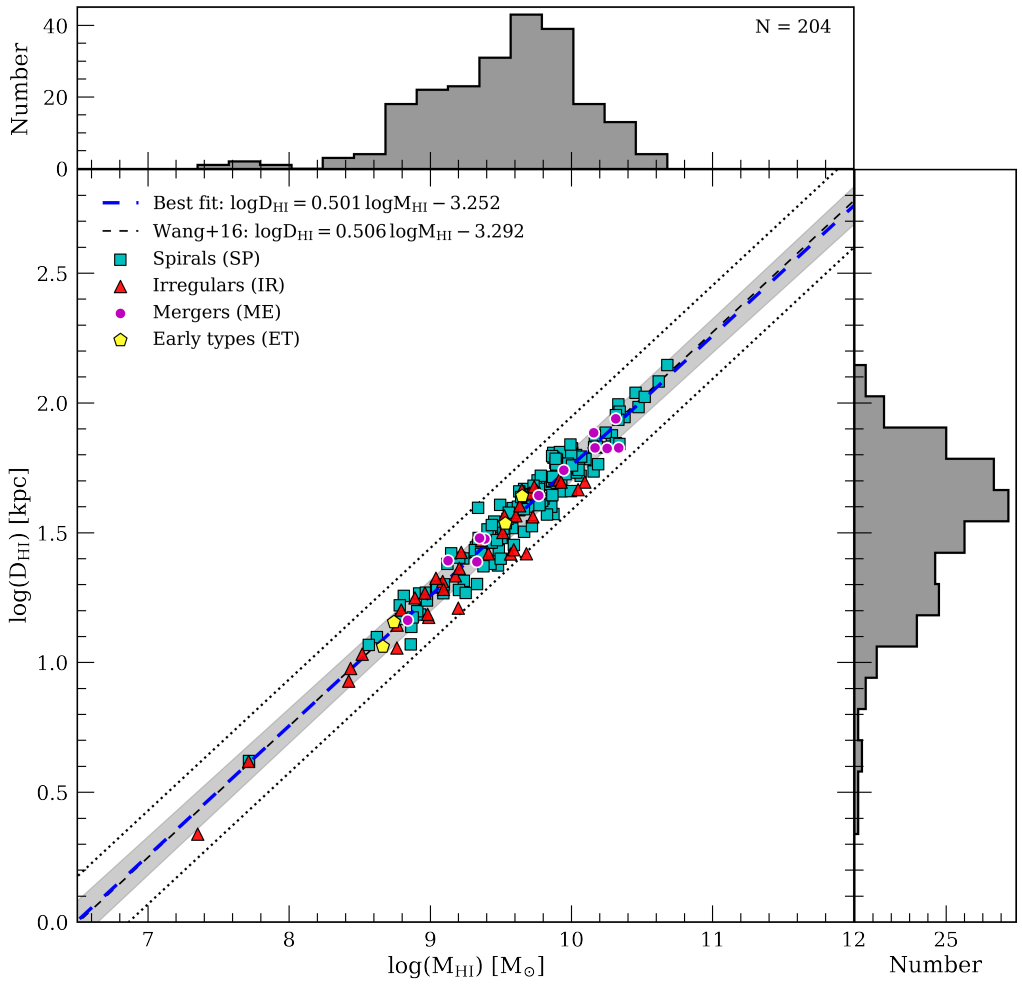

Figure 2.16: $D_{\rm HI} - M_{\rm HI}$ relation for 204 inclination-corrected galaxies. Each symbol corresponds to one of the four morphological classifications: 148 spiral galaxies (SP: cyan squares), 40 irregular galaxies (IR: red triangles), 4 early-type galaxies (ET: yellow pentagons), and 12 merging systems (ME: magenta circles). The best-fitting relation is shown with the thick dashed blue line, while the best fit from Wang et al. (2016) is shown with a dotted black line. The shaded region indicates the 1σ uncertainty from the MCMC posteriors (see Fig. 2.15) and the black dotted lines delimit the 3σ scatter from Wang et al. (2016) relation. The histograms on the sides display the H I mass and H I size distributions of the galaxies in the sample, respectively.

Table 2.3: Median values of the posterior distributions of the MCMC-based linear fit. Median H I mass and H I sizes for the $D_{\rm HI} - M_{\rm HI}$ relation at different redshift bins, and the corresponding log $D_{\rm HI}$ for a fixed log $M_{\rm HI}$.

	$0 \leq z \leq 0.084$	$z \leq 0.04$	$z > 0.04$
Sample	N = 204	N = 63	N = 141
Slope	$0.501^{+0.008}_{-0.008}$	$0.485^{+0.012}_{-0.011}$	$0.526^{+0.013}_{-0.013}$
Intercept	$-3.252^{+0.073}_{-0.074}$	$-3.104^{+0.105}_{-0.107}$	$-3.494^{+0.125}_{-0.128}$
Scatter (σ)	0.057	0.054	0.058
Intrinsic scatter ($\sigma_{\rm int}$)	$0.054^{+0.003}_{-0.003}$	$0.052^{+0.006}_{-0.005}$	$0.053^{+0.004}_{-0.004}$
Median $\log(M_{\rm HI}/{\rm M}_\odot)$	9.64	9.22	9.75
Median $\log(D_{\rm HI}/{\rm kpc})$	1.59	1.40	1.65
log $D_{\rm HI}$ (at $\log(M_{\rm HI}/{\rm M}_\odot) = 9.64$)	$1.579^{+0.015}_{-0.017}$	$1.573^{+0.021}_{-0.028}$	$1.579^{+0.029}_{-0.024}$

from compilations of data from various surveys (Lelli et al., 2016; Wang et al., 2016). This work is based on a "blind" survey, and as such, is not morphologically selected. To obtain further insight into the $D_{\rm HI} - M_{\rm HI}$ relation, we explore the morphological properties of our sources, as classified in Section 2.3.5. The dominant morphological type in our sample is very similar to Wang et al. (2016) (SP and IR, with a few ET). Figure 2.16 shows the $D_{\rm HI} - M_{\rm HI}$ for our sample galaxies, grouped by morphological type, revealing that each subset of morphological types all lie on the relation and exhibits a low intrinsic scatter. The majority of SP/IR lie within the $1-2\sigma$ confidence region of the relation. It is important to note that our sample is H I-selected, and thus is sensitive towards relatively H I-rich galaxies. This is in contrast to the H I survey of early-type galaxies ATLAS$^{\rm 3D}$ (Serra et al., 2012) which detected H I-poor ET galaxies below our column density limit and found that the typical H I column density of ETs is lower than of spiral galaxies (see Fig. 10 in Serra et al. 2012). Consequently, as far as ETs are concerned in this relation, we could not detect the faintest and H I-poorest ones due to a selection effect.

I assess the intrinsic scatter and slope of the relation as a function of morphology. The 148 spiral galaxies show a tight intrinsic scatter of $0.053^{+0.004}_{-0.003}$ with a slope of 0.491 ± 0.010, representing galaxies with large and well-defined discs. For the 40 irregulars, we find an intrinsic scatter of $0.061^{+0.009}_{-0.007}$ and a slope of $0.492^{+0.017}_{-0.016}$. This result indicates that the slopes of the $D_{\rm HI} - M_{\rm HI}$ relations for SP and IR are statistically similar, and their intrinsic scatters are consistent within 2σ error.

As highlighted in Section 2.4, only early and late-stage mergers, where the H I disc belongs to a single galaxy, were included in the ME sample. This would explain why the MEs in our sample lie in the relation. Due to the small sample sizes, we could not investigate the intrinsic scatter of MEs and ETs separately.

2.7.3 $D_{HI} - M_{HI}$ relation and environment

The H I content of galaxies is known to be sensitive to the environment (Haynes et al., 1984). Verdes-Montenegro et al. (2001) have shown that the sizes of the H I discs of galaxies in group environments are influenced by tidal interactions. Continuous tidal stripping due to the IGM in groups can lead to perturbed H I discs and H I deficiencies in galaxies. This was also investigated for simulated galaxies by Stevens et al. (2019), who showed that environmental processes, such as ram-pressure stripping, may cause disc truncation.

As mentioned in Section 2.4, I did not impose any environment-based constraint on our sample. There are indeed a variety of large-scale structures detected within the Early Science volume – the most prominent of which is the large galaxy group at $z \sim 0.044$, recently presented by Ranchod et al. (2021). This galaxy group consists of 20 galaxies distributed in a $\sim$1 deg^2 region and are all within a structure $\sim$400 km s^{-1}wide. Its unusually high gas richness and non-Gaussian velocity dispersion distribution suggests a dynamically young group, still in its early stages of assembly. Mostly dominated by disk galaxies and few irregulars, it is an intermediate mass group, with dynamical mass of $\log_{10}(M_{\rm dyn}/{\rm M}_\odot) = 12.32$. I identified all galaxies within that overdensity, and found that all lie along the relation, suggesting that this group environment has not significantly affected the H I content of these galaxies. I measured a slope of 0.515 ± 0.019 and an intercept of $-3.393^{+0.184}_{-0.185}$ for the structure, which is still consistent with the full sample. A more complete insight of the variation of the $D_{\rm HI} - M_{\rm HI}$ relation with large scale environments will be achieved with the full MIGHTEE-H I survey area and redshift range.

2.7.4 Evolution of the $D_{HI} - M_{HI}$ relation as a function of z

Whereas previous studies were restricted to the very nearby Universe, our sample and the relation derived from it extends over a previously unexplored redshift range. To investigate the evolution of the $D_{\rm HI} - M_{\rm HI}$ as a function of redshift, we use our sample to test for any redshift dependence using a similar approach as in Ponomareva et al. (2021). I divided the sample into two redshift bins with $z \leq 0.04$ and $z > 0.04$ and performed the linear fit as described in Section 2.7.1 to each bin. The low-redshift subsample consists of 63 galaxies and spans four decades in H I mass ranging from $7.4 \leq \log(M_{\rm HI}/{\rm M}_\odot) \leq 10.4$, with a median mass of $1.65 \times 10^9\,{\rm M}_\odot$. The high-redshift subsample contains 141 galaxies covering 3 orders of magnitude in mass ($8.9 \leq \log(M_{\rm HI}/{\rm M}_\odot) \leq 10.7$) and a median H I mass of $5.65 \times 10^9\,{\rm M}_\odot$. Fig. 2.17 shows the best-fitting relation for each redshift bin.

I observe a marginal difference between the slope and intercept of the two subsamples, but the findings are consistent within the errors with the best-fitting relation of the full sample. The low-redshift bin has an intrinsic scatter of $0.052^{+0.006}_{-0.005}$ and observed scatter of 0.054 dex, which is consistent with Wang et al. (2016), whose sample only reaches out to redshifts of $z \sim 0.03$.

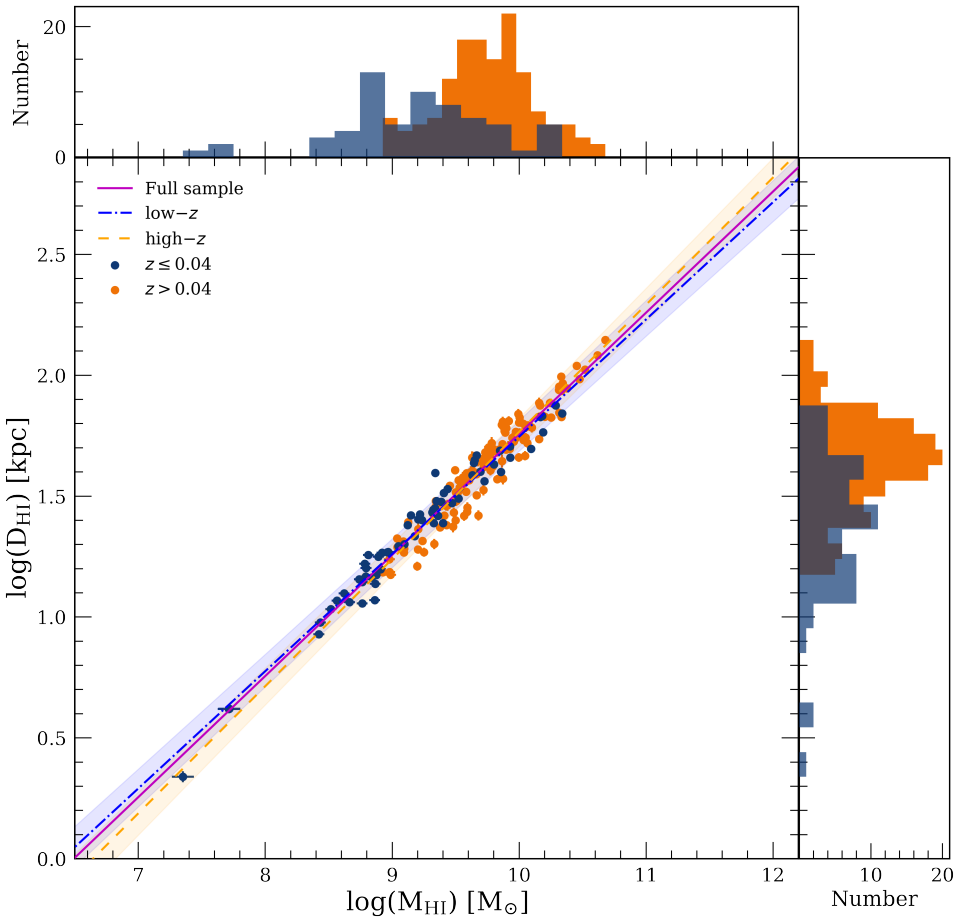

Figure 2.17: $D_{\rm HI} - M_{\rm HI}$ relation of galaxies in the MIGHTEE-H I survey for two redshift bins. The errorbars on the points are approximately the same size as the points themselves. The high-redshift subsample ($z > 0.04$) is presented in orange circles, the low-redshift subsample ($z \leq 0.04$) in blue. The magenta solid line indicates the best fit from the maximum-likelihood method of the full sample, while the orange dashed and the blue dashed-dotted lines represent the best fits from the high-redshit and the low-redshift subsamples respectively. Their respective 1σ scatter is indicated by the shaded orange and blue regions. The H I mass and H I size distributions for the two redshift bins are displayed on the upper and right sides of the main frame.

The high-redshift bin has a slightly larger scatter, both intrinsic ($\sigma_{\rm int} = 0.053^{+0.004}_{-0.003}$) and observed ($\sigma = 0.058$), but is consistent within the errors (see Table 2.3).

To investigate the effect of a possible mass bias, I performed the fit once again for each subsample, for a common H I mass range of $8.9 \leq \log(M_{\rm HI}/{\rm M}_\odot) \leq 10.4$. We observe a similar trend in the values of intrinsic scatter, slope, and only marginal difference is present between the low and high-z subsamples with the fits being consistent within the errors. This supports the conclusion that the relation features no obvious evolution with redshift, which is consistent with predictions from hydrodynamical cosmological simulations of galaxy formation and evolution, e.g., NEWHORIZON (Dubois et al., 2021). However, this cannot be fully explored due to the still considerably small redshift range of our sample and will be further investigated with the full MIGHTEE-H I survey.

2.8 Summary and conclusions

I have conducted a blind H I survey with the early observations and 4K mode from MIGHTEE. The survey was pointed towards XMMLSS and COSMOS fields, covering approximately 5 deg^2 of the sky. We detected in total 276 H I sources. In order to assess the reliability of our measurements, I have presented the $D_{\rm HI} - M_{\rm HI}$ relation and measured the statistical properties of the homogeneous MIGHTEE-H I Early Science data sample which contains 204 galaxies, spans 4 decades in H I mass and extends to a redshift of $z \sim 0.084$.

I measured galaxy H I masses and used a novel 2D Gaussian fitting method to obtain the size of galaxy H I discs. We have also classified the galaxies based on their optical morphology. An H I catalogue of the data products has therefore been produced. The main results of our study are as follows:

- For the first time, we are able to measure the intrinsic scatter of the $D_{\rm HI} - M_{\rm HI}$ relation and find that it is non-zero. Therefore, we conclude that the relation allows for an intrinsic variation of $\sim$10% in $D_{\rm HI}$ at a given $M_{\rm HI}$.
- All of the galaxies in our sample are found to lie on the $D_{\rm HI} - M_{\rm HI}$ relation, independent of morphological type. We also do not find any strong evidence for the environmental dependence when restricting our sample to the large group at $z \sim 0.044$.
- For the first time, we studied the $D_{\rm HI} - M_{\rm HI}$ relation beyond $z > 0.03$. We find no evidence that the relation has evolved over the last one billion years similarly to the baryonic Tully-Fisher relation (Ponomareva et al., 2021), suggesting that the galaxy discs have not undergone significant changes in their gas distribution and mean surface mass density over this period of time. This result is consistent with simulations of galaxy formation and evolution. For example, the latest results from the NEWHORIZON simulations show little-to-zero evolution over a Hubble time (Dubois et al., 2021).
- The measured statistical properties of the relation (slope, observed scatter and zero point) are entirely consistent with the largest $z = 0$ study by Wang et al. (2016).

In conclusion, the successful study of the $D_{\rm HI} - M_{\rm HI}$ relation using Early Science data from the MIGHTEE survey already substantiates MeerKAT's potential for transformational H I science. The full MIGHTEE survey, covering 20 square degrees, will increase the explored volume out to $z \sim 0.5$, and will be crucial to study the evolution of the $D_{\rm HI} - M_{\rm HI}$ relation as a function of redshift and large scale environments i.e., field vs groups, filaments and overdensities.

Acknowledgements

We thank the anonymous referee for their quick and helpful comments. Their careful reading of the manuscript significantly improved the quality of this paper. The authors gratefully acknowledge Prof. Dr. J.M. van der Hulst and Francesco Sinigaglia for their useful comments and suggestions to improve the early drafts of this paper.

The MeerKAT telescope is operated by the South African Radio Astronomy Observatory, which is a facility of the National Research Foundation, an agency of the Department of Science and Innovation. We acknowledge the use of the ilifu cloud computing facility,[12] a partnership between the University of Cape Town, the University of the Western Cape, the University of Stellenbosch, Sol Plaatje University, the Cape Peninsula University of Technology and the South African Radio Astronomy Observatory. The ilifu facility is supported by contributions from the Inter-University Institute for Data Intensive Astronomy (IDIA – a partnership between the University of Cape Town, the University of Pretoria, the University of the Western Cape and the South African Radio astronomy Observatory), the Computational Biology division at UCT and the Data Intensive Research Initiative of South Africa (DIRISA). The authors acknowledge the Centre for High Performance Computing (CHPC), South Africa, for providing computational resources to this research project.

The Hyper Suprime-Cam (HSC) collaboration includes the astronomical communities of Japan and Taiwan, and Princeton University. The HSC instrumentation and software were developed by the National Astronomical Observatory of Japan (NAOJ), the Kavli Institute for the Physics and Mathematics of the Universe (Kavli IPMU), the University of Tokyo, the High Energy Accelerator Research Organization (KEK), the Academia Sinica Institute for Astronomy and Astrophysics in Taiwan (ASIAA), and Princeton University. Funding was contributed by the FIRST program from Japanese Cabinet Office, the Ministry of Education, Culture, Sports, Science and Technology (MEXT), the Japan Society for the Promotion of Science (JSPS), Japan Science and Technology Agency (JST), the Toray Science Foundation, NAOJ, Kavli IPMU, KEK, ASIAA, and Princeton University.

SHAR, RKK and SK are supported by the South African Research Chairs Initiative of the Department of Science and Technology and National Research Foundation. AAP acknowledges the support of the STFC consolidated grant ST/S000488/1. MJJ and AAP acknowledge support from the Oxford Hintze Centre for Astrophysical Surveys which is funded through generous support from the Hintze Family Charitable Foundation. IH, MJJ and AAP acknowledge support from the UK Science and Technology Facilities Council [ST/N000919/1]. BSF and MJJ would like to acknowledge support from the Africa-Oxford Visiting Fellows Programme. NM acknowledges support from the Bundesministerium für Bildung und Forschung (BMBF) award 05A20WM4. EAKA is supported by the WISE research programme, which is financed by the Dutch Research Council (NWO). MG was partially supported by the Australian Government through the Australian Research Council's Discovery Projects funding scheme (DP210102103). IP acknowledges financial support from the Italian Ministry of Foreign Affairs and International Cooperation (MAECI Grant Number ZA18GR02) and the South African Department of Science and Technology's National Research Foundation (DST-NRF Grant Number 113121) as part of the ISARP RADIOSKY2020 Joint Research Scheme. IH acknowledges support from the South African Radio Astronomy Observatory which is a facility of the National Research Foundation (NRF), an agency of the Department of Science and Innovation. KS acknowledges support from the Natural Sciences and Engineering Research Council of Canada (NSERC).

This research has made use of NASA's Astrophysics Data System Bibliographic Services. This research made use of Astropy,[13] a community-developed core Python package for Astronomy (Astropy Collaboration et al., 2013, 2018).

[12] www.ilifu.ac.za
[13] http://www.astropy.org

chapter 3

H I Galaxy Signatures in the SARAO MeerKAT Galactic Plane Survey – Unveiling the obscured part of the Vela Supercluster

S. H. A. Rajohnson[1], R. C. Kraan-Korteweg[1], H. Chen[1,2], B. S. Frank[3,4,5,1], N. Steyn[1,6], S. Kurapati[1], D. J. Pisano[1], L. Staveley-Smith[6], P. Serra[7], S. Goedhart[3,8], F. Camilo[3]

Submitted to Monthly Notices of the Royal Astronomical Society, 03 February 2024.

[1] Department of Astronomy, University of Cape Town, Private Bag X3, Rondebosch 7701, South Africa
[2] Research Center for Intelligent Computing Platforms, Zhejiang Laboratory, Hangzhou 311100, China
[3] South African Radio Astronomy Observatory (SARAO), 2 Fir Street, Observatory, 7925, South Africa
[4] UK Astronomy Technology Centre, Royal Observatory Edinburgh, Blackford Hill, Edinburgh EH9 3HJ, UK
[5] The Inter-University Institute for Data Intensive Astronomy (IDIA), and University of Cape Town, Private Bag X3, Rondebosch, 7701, South Africa
[6] International Centre for Radio Astronomy Research (ICRAR), University of Western Australia, Crawley, WA 6009, Australia
[7] INAF – Osservatorio Astronomico di Cagliari, Via della Scienza 5, 09047, Selargius (CA), Italy
[8] SKAO, 2 Fir Street, Black River Park, Second Floor, Block A, Cape Town, 7925

Abstract

Using the deep SARAO MeerKAT Galactic Plane Survey (SMGPS), we searched for H I emission of the gas-rich galaxy population in the Vela region (Vela–SMGPS). Our primary objective is the investigation of the Vela Supercluster (VSCL) at $V_{\rm hel} \sim 18000$ km s^{-1}, which is largely obscured by the Zone of Avoidance (ZOA). The analysis focuses on 157 hexagonally distributed MeerKAT pointings which were combined into 10 contiguous mosaics, covering ~90 deg^2 area within $260° \leq \ell \leq 290°, -2° \leq b \leq 1°$. We restrict our search to the mostly RFI-free band of $250 < V_{\rm hel} < 25000$ km s^{-1} and identified 843 H I detections. Among these, 39 were previously discovered in the Parkes HIZOA survey ($V_{\rm hel} < 12000$ km s^{-1}; rms ~ 6 mJy beam^{-1}). With the improved rms level of the Vela–SMGPS, i.e., $0.29 - 0.56$ mJy beam^{-1}, our study unveils nearly 12 times more detections (471 candidates) in that same velocity range. We furthermore could identify 187 galaxy candidates with an H I mass limit reaching $\log(M_{\rm HI}/{\rm M}_\odot) = 9.44$ in the VSCL velocity range $V_{\rm hel} \sim 19500 \pm 3500$ km s^{-1}. We find indications of two wall-like overdensities that confirm the original suspicion that these walls intersect at low latitudes around longitudes of $\ell \sim 272° - 278°$. We also find a strong signature that is most likely associated with the Hydra/Antlia extension and find evidence for a previously unknown narrow filament at $V_{\rm hel} \sim 12000$ km s^{-1}. This chapter demonstrates the efficiency of systematic H I surveys with the SKA precursor MeerKAT even in the most obscured part of the ZOA.

Keywords: catalogs – surveys – galaxies: distances and redshifts – galaxies: general – radio lines: galaxies – cosmology: large-scale structure of Universe.

3.1 Introduction

On large scales, galaxies are arranged in a web-like pattern comprising groups, filamentary structures with high-density clusters at their nodes, surrounding low-density voids – known as the 'cosmic web' (Bond et al., 1996). Due to the gravitational instability exerted by these mass variations on their surrounding medium, these overdense – and underdense – regions induce a peculiar velocity or cosmic flow field that deviates from a pure Hubble expansion (e.g., Peebles, 1976; Lauer & Postman, 1994; Strauss & Willick, 1995). The Cosmic Microwave Background (CMB) dipole, for example, is explained by the peculiar motion of the Local Group (LG) with respect to the CMB with a velocity of around 620 ± 15 km s^{-1} and an apex at $(\ell, b) = 271.9° \pm 2.0°, 29.6° \pm 1.4°$ (Planck Collaboration et al., 2020).

Numerous efforts have been made to delineate large-scale structures (LSS) and study cosmic flow fields in the nearby Universe thanks to research using data from (i) all-sky systematic redshift (e.g., CfA/CfA2, Huchra et al. 1983; Falco et al. 1999; SSRS2, da Costa et al. 1998; 2dFGRS, Colless et al. 2001, 2003; 6dFGRS Jones et al. 2009; 2MRS, Huchra et al. 2012;

Macri et al. 2019; SDSS, Tempel et al. 2014; Ahumada et al. 2020) and (ii) peculiar velocity surveys (e.g., SFI++, Masters et al. 2006; Springob et al. 2007; 2MTF, Masters et al. 2007; Springob et al. 2016; Hong et al. 2019; 6dFGSv, Springob et al. 2014; Scrimgeour et al. 2016; Cosmicflows-3 or CF3, Tully et al. 2016; SDSS PV, Howlett et al. 2022; and Cosmicflows-4 or CF4 Kourkchi et al. 2020; Tully et al. 2023).

In spite of these advancements, neither the local bulk flow direction nor the volume as determined independently from these large data sets are fully coherent with the CMB dipole measurements (e.g., Erdoğdu et al., 2006a,b; Lavaux et al., 2010; Hoffman et al., 2017; Howlett et al., 2022). Discrepancies persist in the literature (see e.g., Table 5 in Scrimgeour et al. 2016). On scales less than $150\,h^{-1}$ Mpc, some studies show unusually large bulk flow amplitudes with respect to ΛCDM predictions (Hudson et al., 2004; Erdoğdu et al., 2006a,b; Watkins et al., 2009; Feldman et al., 2010; Lavaux et al., 2010; Howlett et al., 2022), while others present lower or consistent values (Colin et al., 2011; Branchini et al., 2012; Turnbull et al., 2012; Hoffman et al., 2015; Scrimgeour et al., 2016; Qin et al., 2018, 2019; Qin, 2021).

The so-called "Zone of Avoidance" (ZOA; Proctor 1878; Shapley 1961; Kraan-Korteweg & Lahav 2000), is considered to be a major contributor to these controversies (Loeb & Narayan, 2008) due to the incomplete mapping of the sky behind the Milky Way. Deep optical surveys in the ZOA (mostly photometric, see Kraan-Korteweg & Lahav 2000; Kraan-Korteweg 2005 for reviews) have significantly reduced its extent by covering lower latitudes (out to $|b| \leq 5°$) and higher levels of extinction ($A_B \leq 3\overset{\mathrm{m}}{.}0$). These surveys unveiled nearby dynamically significant structures such as the Norma cluster (Woudt, 1998) the Puppis cluster (Lahav et al., 1993), and the Ophiuchus cluster (Hasegawa et al., 2000; Wakamatsu et al., 2005) out to $V_{\rm hel} < 9000$ km s^{-1}. Despite these efforts, the ZOA gap persists, affecting about 20% of the sky in optical wavelengths.

This degree of obstruction diminishes, but not entirely, as we move towards longer wavelengths, e.g., Infrared (IR) wavelengths are less affected by extinction. For instance, the 2MASS Redshift Survey (2MRS), provided systematic follow-up redshifts across the entire sky for all the brightest galaxies from the near-IR (NIR) 2MASS Extended Source Catalog (2MASS XSC; Jarrett et al. 2000). This survey NIR redshift is 97.4% complete down to $K_s \leq 11.75$ mag and $|b| \geq 5°$, i.e., leaving 10% of the sky uncharted in a systematic way. Obtaining redshifts for these partly obscured red galaxies is very hard, if not impossible. It was only recently that Macri et al. (2019) have added 1041 new redshift measurements to the 2MRS NIR catalog to complete it, reducing the previous lack of redshift information for galaxies located near the ZOA.

A new avenue now exists with data from the Wide-field Infrared Survey Explorer catalog (WISE, Wright et al. 2010; Cutri et al. 2021) in the mid-IR band. The most recent efforts in addressing

the ZOA gap have been undertaken by Daza-Perilla et al. (2023), who introduced an automated classification system to distinguish galaxies from non-galaxies in low Galactic latitude regions using data from the VVV NIR Galaxy Catalogue (Baravalle et al., 2021).

In addition to the incomplete mapping of galaxies behind the ZOA, bulk flow measurements conducted so far face constraints due to the volumes they have surveyed. Bulk flows derived from the Infrared Astronomical Satellite (IRAS) Point Source catalog redshift survey (PSCz; Hudson et al. 2004), the 6dF Galaxy Survey (6dFGS; Springob et al. 2014), and the 2MASS Tully-Fisher survey (2MTF; Hong et al. 2014, 2019) have only considered structures below 10000, 12000, and 16000 km s^{-1}, respectively. The more recent surveys hint at a 'residual bulk flow' originating from a hidden mass overdensity behind the ZOA (cf. Hudson et al., 2004; Loeb & Narayan, 2008; Boruah et al., 2020). For example, the 6dFGS and 2MTF surveys implied a residual bulk flow of ~273 km s^{-1} towards the constellation of Vela ($\ell \sim 270°-330°$) in the ZOA and induced beyond $V_{\rm hel} > 16000$ km s^{-1} (Springob et al., 2014, 2016; Scrimgeour et al., 2016).

Based on multi-object spectroscopic observations, Kraan-Korteweg et al. (2017), hereafter KK2017, recently uncovered the Vela Supercluster (VSCL). VSCL, centered at $\ell = 272.5° \pm 20°$ and $b = 0° \pm 10°$, hence in close proximity to the volume range and the direction over which this residual bulk flow motion is expected to arise. Using data from the Southern African Large Telescope (SALT), followed by data from AAOmega+2dF, KK2017 have uncovered a massive concentration of galaxies at a redshift of $V_{\rm hel} \sim 18000$ km s^{-1}. This concentration extends over $115 \times 90\ h_{70}$ Mpc at this distance, with an estimated overdensity of $\delta \sim 0.50-0.77$. The inspection of VSCL's distribution in redshift space revealed a multibranching morphology consisting of two wall-like structures. A main wall that is visible on both sides of the Galactic Plane (GP) at 18000 km s^{-1}, and a second smaller one below the GP at 22000 km s^{-1}. They seem to cross in the inner ZOA, which is unfortunately obscured. Although VSCL's inner part could not be traced because of the high extinction and high stellar crowding in the optical and NIR at the lowest latitudes ($|b| \leq 5°$), a contribution to the motion of the LG based on a complete set of 2MASS galaxies on either side of the GP between $6° \leq |b| \leq 10°$ is estimated to be $V_{\rm LG} \simeq 50$ km s^{-1} (KK2017). VSCL could therefore play a crucial role in explaining the residual bulk flow and refining our understanding of the Universe's dynamics. Further kinematic evidence based on reconstructed density and velocity field data reinforces the presence of VSCL with the two merging walls hiding a dense core (see Sorce et al. 2017; Courtois et al. 2019).

As a result, it is essential to trace VSCL across the ZOA, including areas of high obscuration, to gain a better understanding of its extent and mass overdensity. The most effective method to overcome this challenge is systematic H I surveys, given that the 21-cm H I emission passes unhindered through the ZOA. Previous single-dish surveys such as the Dwingeloo Obscured Galaxy Survey (DOGS, Rivers et al. 1999), the H I Parkes Zone of Avoidance survey

(HIZOA, Staveley-Smith et al. 2016), the deep Arecibo L-band Feed Array Zone of Avoidance survey (ALFAZOA, McIntyre et al. 2015), or interferometric surveys such as the Westerbork Radio Synthesis Telescope survey of the Perseus-Pisces filament (WSRT PP, Ramatsoku et al. 2016) have demonstrated their capabilities in mapping structures bisected by the ZOA. Yet, none of these surveys had the required sensitivity, velocity coverage, and field of view to effectively map the VSCL. This makes MeerKAT ideal for observing the VSCL. A pilot project using MeerKAT16 data has already successfully mapped the galaxy cluster VC04 ($\ell \sim 272.25°,\ b \sim -9°,\ V_{\rm hel} \sim 18000$ km s^{-1}) embedded in the main VSCL wall (Steyn, 2023). With a mean rms noise of 1.2 mJy beam^{-1}, the 6 pointings have led to the detection of 119 galaxies.

In this chapter, we use *interferometric* H I data obtained as part of the SARAO MeerKAT Galactic Plane survey (referred to as SMGPS, Goedhart et al. 2024) to investigate the H I emission from the gas-rich galaxy population within the densest layer of the Milky Way Plane and focus on learning more about the crossing of the VSCL walls. Firstly, the better spatial resolution and sensitivity compared to the previously undertaken surveys in the ZOA, the L-band frequency coverage, and the field of view of SMGPS will enable us to extend the depth of our study to 25000 km s^{-1}. Secondly, the SMGPS footprint encompasses the VSCL region. This chapter presents the first result of an extensive exploration with a particular emphasis on mapping the uncharted inner core of the VSCL and uncovering possible intersections between its two walls through systematic H I surveys with MeerKAT. A dedicated survey, linking this finding to known structures beyond the ZOA will be detailed in the upcoming chapter. By detecting a significant portion of the star-forming, gas-rich population within the VSCL, we aim to derive a qualitative estimation of the supercluster's mass overdensity and gain insights into its contribution to the local bulk flow.

This chapter is structured as follows: in Section 3.2, we describe the observation details, data reduction processes and mosaicking strategies of Vela–SMGPS. We explain the methods used to detect sources and verify the measured fluxes in Section 3.3. Section 3.4 presents the new catalog and data products of highly-obscured galaxies. This is followed by a completeness estimation, a comparison of the H I properties with predictions based on simulations in Section 3.5, and a detailed discussion of the newly discovered LSS crossing the ZOA in Section 3.6. Finally, we summarize and conclude our findings in Section 3.7.

Throughout this chapter, I use the heliocentric velocity in optical convention $V_{\rm hel}$, $H_0 = 70$ km s^{-1} Mpc^{-1}, $\Omega_{\rm m} = 0.3$ and $\Omega_\Lambda = 0.7$ (Hinshaw et al., 2013).

3.2 MeerKAT observations and data processing

3.2.1 The SARAO MeerKAT Galactic Plane Survey

SMGPS is an L-band (856-1712 MHz) continuum survey centered at 1.3 GHz, covering the longitude range $251^\circ \leq \ell \leq 61^\circ$ within a narrow strip with a width of $\Delta b = 3^\circ$ centered along the GP. With approximately 900 pointings, the latitude range was slightly adjusted to approximate the warp in the Milky Way disc. Within the longitude range $298^\circ \leq \ell \leq 61^\circ$, the corresponding latitude range covered is $-1.5^\circ \leq b \leq 1.5^\circ$. In contrast, within the longitude range of $251^\circ \leq \ell \leq 298^\circ$, the survey encompasses the latitude range $-2^\circ \leq b \leq 1^\circ$.

The primary objective of SMGPS is to study the continuum emission of the Galactic populations, e.g., Supernovae remnants, Planetary Nebulae, H II regions, etc. (for more details, see Goedhart et al. 2024). However, its technical capabilities also enable the exploration of the hidden extragalactic LSS located behind the innermost Milky Way, such as the Great Attractor ($302^\circ \leq \ell \leq 332^\circ$, GA–SMGPS, Steyn et al. 2024), and the Local Void ($328^\circ \leq \ell \leq 55^\circ$, LV–SMGPS, Kurapati et al. 2024), using its H I data. Our region of interest in this work is centered on the proposed crossing of the VSCL at $\ell \sim 275^\circ$, Vela–SMGPS. It spans 30° in longitude, extending from $260^\circ \leq \ell \leq 290^\circ$, with $-2^\circ \leq b \leq 1^\circ$, covering a $30^\circ \times 3^\circ$ (90 deg^2) area.

3.2.2 Observations and data reduction

The deep observations (~1hr per pointing) were performed between July 2018 and March 2020, using the full MeerKAT array, in full polarization. Each observing block of Vela–SMGPS, i.e., the set of data collected during one observation session, comprises 9 MeerKAT pointings arranged in a hexagonal pattern. The pointing centers were offset by 0.494° to reach uniform sensitivity. Table 3.1 provides details of the analyzed region. It contains 157 individual fields observed during 19 blocks of observations, with a minimum of 58 antennas up to a maximum of 63 per observation. Due to scheduling constraints, two of these blocks were identical but split over multiple nights of observations. The observations were obtained with the 4k correlator mode and 8-second integration (Goedhart et al., 2024), where the 4k mode denotes the wideband "coarse" mode in which the L-band (856 – 1712 MHz) is channelized into 4096 channels of 208.984 kHz width. With approximately 1 hour of on-source time per pointing, a session could last from 8.54 to 12.25 hours of on-track time. Typically, the complex phase calibrator (secondary calibrator) was visited for 65 seconds every 30 minutes after a cycle between the targets (~3 min per field), and the bandpass and flux calibrators (primary calibrators) were scanned for 5 minutes every 3 hours.

Table 3.1: Overview of Vela–SMGPS observational parameters

Date (UT start)	Block ID	Block centre (ℓ, b)	Track (h)	N_{ant}	Primary calibrator	Secondary calibrators
2018-12-30	1546207810	(291.8, 0.0)	12.02	62	1215-457	J1331+3030, J1939-6342
2018-12-31	1546293818	(291.3, -1.5)	12.25	62	1215-457	J1331+3030, J1939-6342
2019-01-01	1546380746	(288.4, -0.5)	11.99	62	1215-457	J1331+3030, J1939-6342
2019-01-04	1546641291	(285.4, 0.5)	10.51	61	J0906-6829	J0408-6545, J1331+3030, J1939-6342
2019-01-05	1546727810	(285.9, -1.0)	10.39	60	J0906-6829	J0408-6545, J1331+3030, J1939-6342
2019-01-06	1546811642	(282.9, 0.0)	10.00	60	J0906-6829	J0408-6545, J1331+3030, J1939-6342
2019-01-07	1546900349	(282.4, -1.5)	8.54	62	J0906-6829	J0408-6545, J1331+3030, J1939-6342
2019-01-08	1546984998	(279.5, -0.5)	9.97	62	1215-457	J1331+3030, J1939-6342
2019-01-09	1547071945	(276.5, 0.5)	9.32	62	1215-457	J1331+3030, J1939-6342
2019-01-12	1547330621	(277.0, -1.0)	9.31	62	J0825-5010	J0408-6545, J1331+3030, J1939-6342
2019-01-13	1547413577	(274.0, 0.0)	9.31	62	J0825-5010	J0408-6545, J1331+3030, J1939-6342
2019-01-14	1547499081	(273.6, -1.5)	9.72	62	J0825-5010	J0408-6545, J1331+3030, J1939-6342
2019-01-15	1547585175	(270.6, -0.5)	9.75	63	J0825-5010	J0408-6545, J1331+3030, J1939-6342
2019-01-17	1547758692	(267.6, 0.5)	9.31	58	J0825-5010	J0408-6545, J1331+3030, J1939-6342
2019-01-18	1547839876	(268.1, -1.0)	10.01	63	J0825-5010	J0408-6545, J1331+3030, J1939-6342
2019-11-16	1573939357	(265.2, 0.0)	12.03	61	J0825-5010	J0408-6545, J0521+1638, J1331+3030, J1939-6342
2019-11-15	1573852860	(264.7, -1.5)	12.02	61	J0825-5010	J0408-6545, J0521+1638, J1331+3030, J1939-6342
2019-11-22	1574456164	(261.7, -0.5)	11.67	60	J0825-5010	J0408-6545, J0521+1638, J1331+3030, J1939-6342
2019-11-23	1574542866	(259.7, 0.5)	10.89	60	J0825-5010	J0408-6545, J0521+1638, J1331+3030
2019-11-26	1574801265	(259.2, -1.0)	9.63	63	J0825-5010	J0408-6545, J0521+1638, J1331+3030
2019-11-28	1574911560	(259.2, -1.0)	2.39	61	J0825-5010	J0408-6545, J1331+3030

We transferred each relevant block (see Table 3.1) from the SARAO archive[1] into `Ilifu`[2], consisting of approximately 211 hours of total observing time. Throughout this process, autocorrelation data were excluded, and flags generated by the monitoring system of the Telescope were automatically applied. Using orthogonal polarization components (HH/VV) only, we processed the frequency range 1308 to 1430 MHz ($-2000 \leq V_{\rm hel} \leq 26000$ km s^{-1}), which is mostly free from Radio Frequency Interference (RFI), and omitted the frequency range associated with Milky Way H I emission, spanning from 1419.4 to 1421.4 MHz. This approach allows us to explore our volume of interest which is just at the border above which RFI becomes prominent. It covers the LSS out to $V_{\rm hel} < 25000$ km s^{-1}, encompassing the entire redshift range for the study of gas-rich spirals at the supercluster distance (approximately $V_{\rm hel} \sim 16000$ km s^{-1} to about 23000 km s^{-1}), and constitutes a scientifically relevant volume for bulk flow studies (e.g., Scrimgeour et al. 2016).

We used the `CARACal` pipeline (Józsa et al., 2020) which is specifically designed for continuum and spectral line radio interferometry data reduction. `CARACal` operates a collection of `Stimela`[3] scripts (Makhathini, 2018) – a framework based on PYTHON and container technologies – which allows various radio interferometry software to make the calibration and imaging workflow running sequentially. RFI flagging was performed through `Tricolour`[4] for the gain calibrator flagging because its flux is low and its observing time was short, so it did not need

[1] https://archive.sarao.ac.za/
[2] www.ilifu.ac.za
[3] https://github.com/SpheMakh/Stimela
[4] https://github.com/ratt-ru/tricolour

much flagging. On the other hand, `Tfcrop` (a `CASA`[5] task) was used for the bandpass and flux calibrators, as thorough flagging is necessary to ensure adequate per-channel sensitivity for effective calibration. Basic cross-calibration procedures such as delay, bandpass, and gain calibrations were undertaken with `CASA`. Before self-calibration, we flagged target fields for RFI using `AOflagger` (Offringa, 2010) with a strategy to only inspect the Stokes-Q amplitudes of the visibilities. This resulted in an average of 21% of the data being flagged. The solution intervals obtained from calibration were then used to perform two iterations of self-calibration with `Cubical` (Kenyon et al., 2018).

3.2.3 H I imaging

To obtain emission-only visibilities, we initially subtracted the continuum sky model generated after self-calibration. We then applied a third-order polynomial subtraction to the visibilities using `Uvcontsub`. Additionally, each data cube has been Doppler-corrected to the barycentric reference frame and regridded with a channel resolution of 210 kHz and the same start frequency of 1309 MHz to ensure they have the same number of channels, enabling their combination into mosaics (see Section 3.2.4).

We produced 157 dirty H I cubes of 570 channels each ($-1696 < V_{\rm hel} < 25515$ km s^{-1}) with a Briggs robust weighting parameter of $r = 0$, a pixel size of $3''$, and a taper of $15''$ using `WSClean` (Offringa et al., 2014). We introduced a taper of $15''$ to reduce the non-Gaussian pattern of the dirty Point Spread Function (PSF), i.e., smoothing the wings visible by the black solid lines in Fig. 3.1, and improving the filling factor of extended low H I-column densities sources to increase the image fidelity (e.g., see Fig. 3.2). The tapered dirty beams are on average $30'' \times 27''$ with a variation of about $\pm 2''$ over the whole SMGPS survey, and around $\pm 1''$ in Vela–SMGPS. We can therefore spatially resolve galaxies with H I sizes larger than 39×35 (± 1.25) kpc or H I masses $\log(M_{\rm HI}/{\rm M}_\odot) \gtrsim 9.62 \pm 0.03$ at the VSCL distance ($\sim$18000 km s^{-1}), based on the H I size-mass relation (Rajohnson et al., 2022).

Figure 3.3 provides a visual representation of the pointing configuration for the 157 MeerKAT pointings in Vela–SMGPS. In the bottom panel, the color gradient, from yellow to dark red, illustrates the measured global rms noise values at the central region of each individual pointing. These values range from 0.28 to 1.09 mJy beam^{-1}. The fields with high rms noise (bottom panel) are closely related to the regions of extended continuum sources, e.g., $\ell \sim 283°$–$289°$ and $267.5°$ (see top panel). Fortunately, only a few fields are affected by these large and bright continuum sources. Non-contaminated areas, on average, exhibit an rms noise value of 0.42 mJy beam^{-1}. The necessary data quality for our science goals can be achieved by mosaicking the MeerKAT pointings in hexagonal patterns, as detailed in the next section. This is also observed in Fig. 3.4,

[5] http://casa.nrao.edu

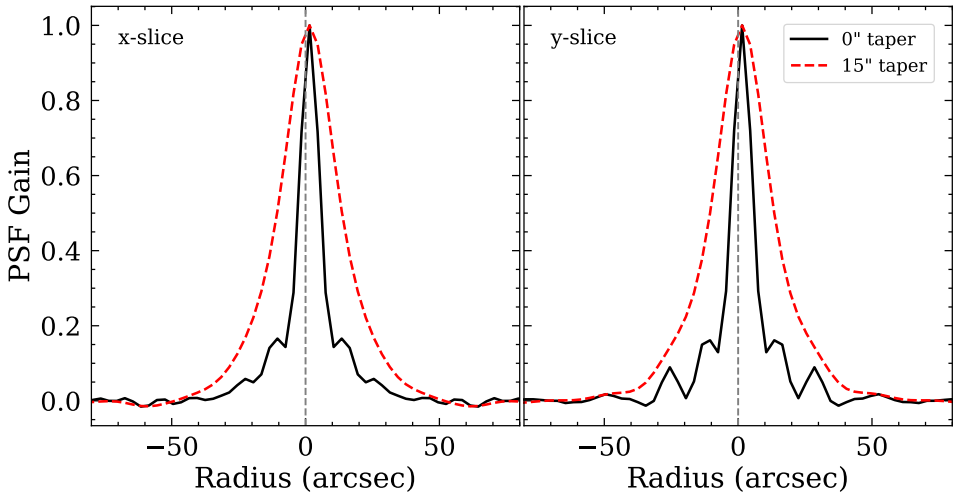

Figure 3.1: A 2D slice of the dirty PSF along the x and y axes in a Vela–SMGPS field. The black solid line shows the PSF without taper, the red dashed line indicates the PSF after a 15″ taper has been applied.

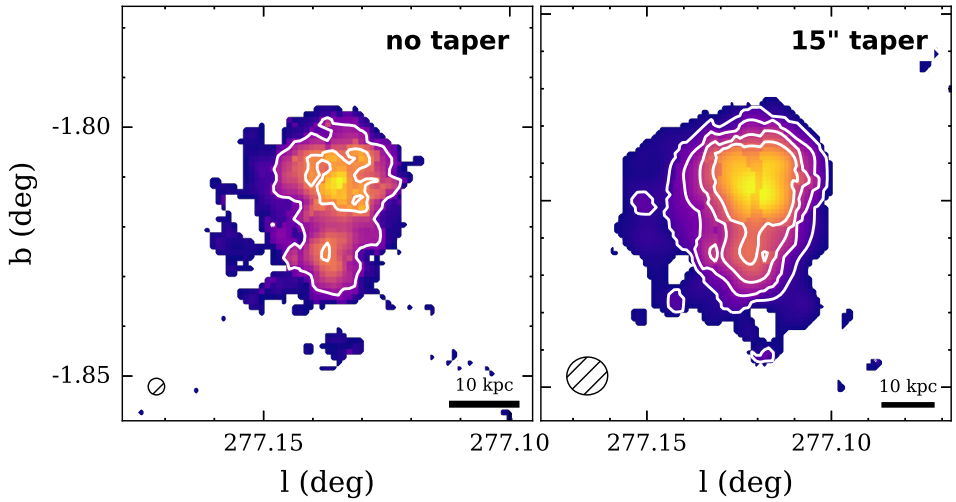

Figure 3.2: An example of the H I distribution without a taper (left) and a 15″ taper (right). PSFs with respective sizes of 12″ × 11″ and 30″ × 27″ are shown in the lower left corner of each image, while a 10 kpc scalebar is illustrated in the lower right corner.

which illustrates the continuum maps and H I channel map of mosaics T28 (left) and T31 (right) from MeerKAT. In general, the regions with higher rms noise and image artifacts (continuum residuals) correspond to the locations of the bright continuum sources in the continuum map. The presence of bright continuum sources (both compact and diffuse) presents challenges in continuum subtraction, which naturally translates to higher uncertainty in the H I mass.

3.2.4 Mosaicking strategy

We utilize the `Montage`[6] software within `CARACal` with the `mosaic`[7] worker parameter set to 'spectral' type for the generation of the mosaics. To perform the assembling and re-gridding,

[6]http://montage.ipac.caltech.edu/
[7]https://github.com/caracal-pipeline/MosaicQueen

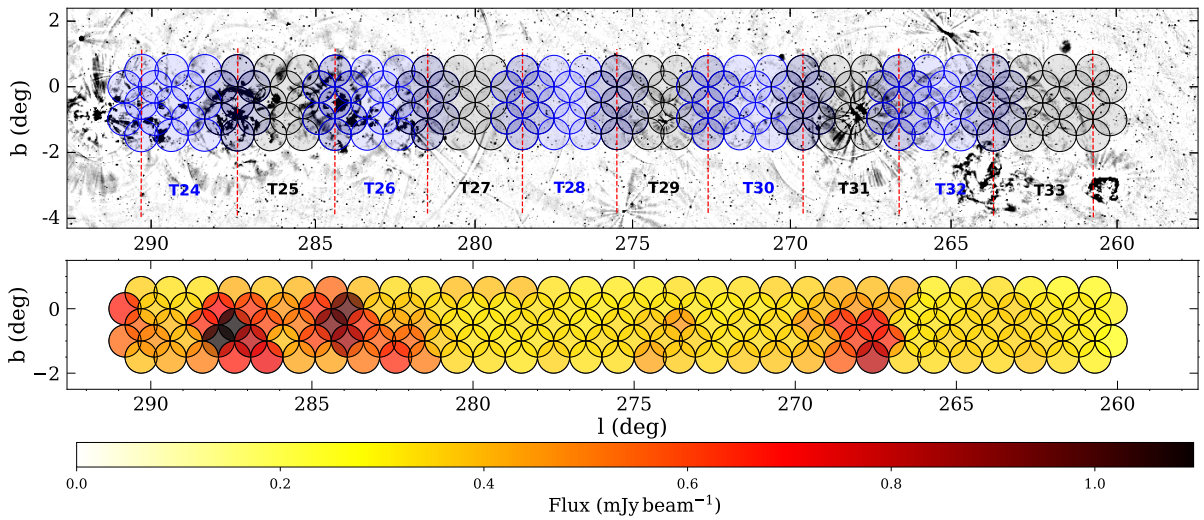

Figure 3.3: Pointing configuration of Vela–SMGPS ($260° \leq \ell \leq 290°$). *Top panel:* distribution of the 10 mosaics (T24-T33) of 22 fields each in the VSCL region, overlayed on the SUMSS continuum map (grayscale). *Bottom panel:* the corresponding rms levels of each field.

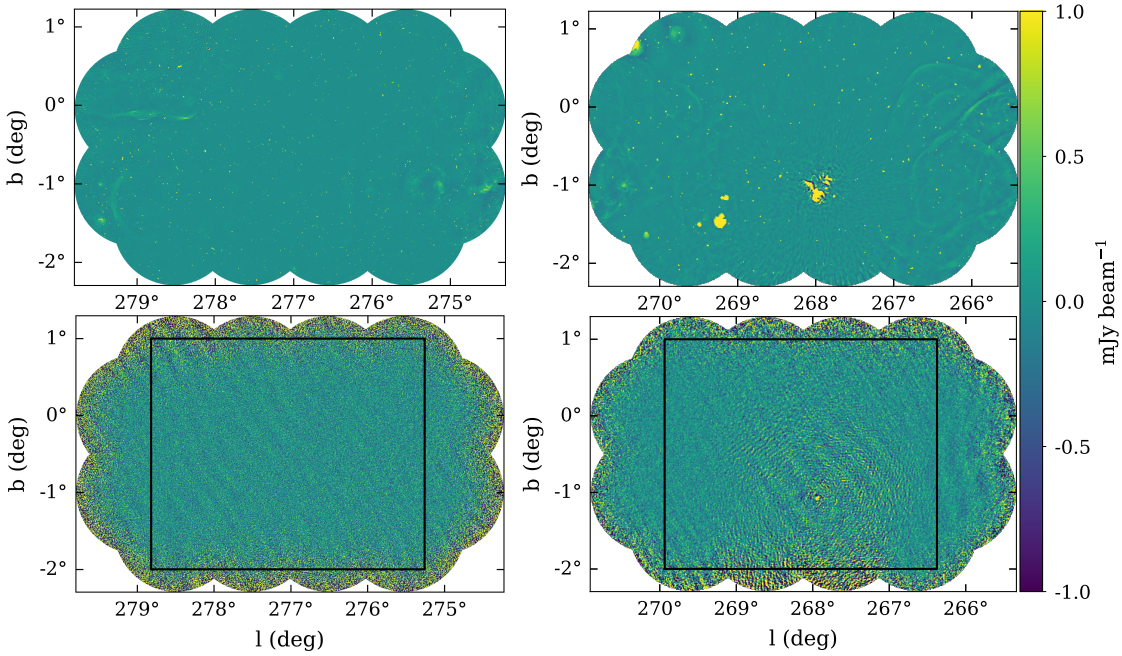

Figure 3.4: Continuum (top) and channel map (bottom) of mosaics T28 (left) and T31 (right). The color bar represents flux variation. The bottom right panel illustrates the impact of bright continuum sources in the per-channel image of a spectral line cube.

we input the dirty cubes along with their "Mauchian" Primary Beam (PB) models (i.e., a cosine-squared power illumination as seen in Mauch et al. 2020) in a common folder. Fields of $0.8°$ radius, corresponding to a normalized PB gain of 0.2, are used for mosaicking the PB-corrected dirty beams. This enhances the sensitivity and uniformity of the survey area.

As the variation of the PSF size is only $\sim 2\%$ within the redshift range of our survey, the mosaic PSF can be determined as the median value from the PSFs of each input cube. We divide the

Vela–SMGPS survey into 10 overlapping mosaics, named T24 to T33, each containing 22 fields. One mosaic covers an area of the sky slightly over 5×3.5 deg^2, producing a nearly uniform data cube of approximately 3.5×3 deg^2. Each mosaic centre is offset by $\Delta\ell = 3°$, This configuration ensures that we do not miss possible extended sources at the edges of the mosaic. It allows an independent data quality assessment of the source finding algorithm and their derived H I parameters from the overlapping area of $\Delta\ell \sim 1°$ (see Section 3.3.4).

The `CARACal` run outputs three types of mosaics: the main mosaic containing the data and its corresponding weight and noise mosaics, all in fits format and projected in equatorial coordinates. To facilitate the analysis along the GP, we transformed the coordinates in Galactic coordinates using the `CASA` task `imregrid`, applied to the three mosaic files.

The 10 final H I mosaics are indicated in the top panel of Fig. 3.3 (red dashed lines), superimposed on the Sydney University Molonglo Sky Survey (SUMSS) Galactic continuum map (Bock et al., 1999) in the top panel. The alternating blue and black MeerKAT pointings indicate the 22 pointings that conform one individual mosaic.

Due to the hexagonal configuration of the MeerKAT pointings, the rms after mosaicking is consistently lower. The 10 H I mosaics have rms values ranging from 0.29 to 0.56 mJy beam^{-1}, with a mean rms noise of 0.39 mJy beam^{-1}. Figure 3.5 displays a sample mosaic with an rms of 0.29 mJy beam^{-1}. The noise variation as a function of velocity in the bottom panel illustrates that the spatial and spectral noise variation remains fairly uniform within the central area of the mosaic outlined by the black box. To provide a more detailed assessment of the mosaic's noise within a reasonable velocity range, Fig. 3.6 and 3.7 show the consecutive H I channel maps of two detections. One was found at low redshift ($cz \sim 4467$ km s^{-1}) but with a low signal-to-noise ratio (SNR), and the second one with a high SNR but detected at the VSCL distance ($cz \sim 17151$ km s^{-1}). The method to obtain these galaxies is explained in the next section. Assuming a 200 km s^{-1} linewidth galaxy and a mean global rms of 0.39 mJy beam^{-1}, we can achieve a 5σ H I mass detection limit of $2.75{\times}10^9$ M$_\odot$ at the VSCL distance ($V_{\rm hel} \sim 18000$ km s^{-1}, $D \sim 257$ Mpc). Table 3.2 lists the properties of the 10 Vela–SMGPS mosaics.

3.3 Source finding and verification

The following section details the algorithms used to arrive at a reliable list of H I detections. As a first step, we apply the automated source finder SoFiA-2 (Westmeier et al., 2021) for source identification after optimizing its parameters, as discussed in Section 3.3.1. We discuss a visual verification and classification method in Section 3.3.2 to differentiate between solid detections and possible ones. In Section 3.3.4, a search for duplicates in the overlapping regions of the mosaics is performed to check for internal consistency, and a comparison with HIZOA is conducted

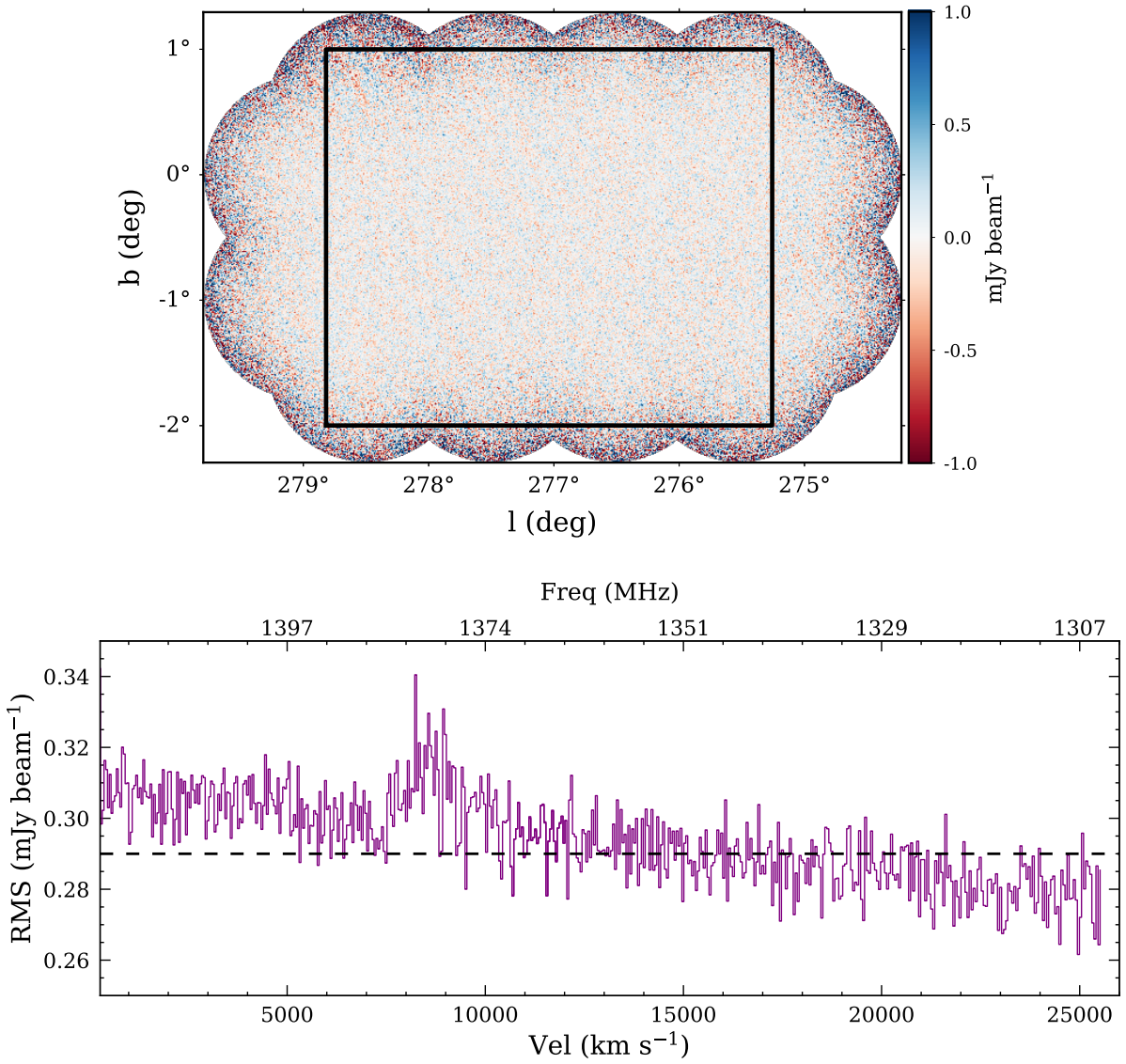

Figure 3.5: Top panel: A random example showing spatial noise variation for a central channel map (rms = 0.29 mJy beam^{-1}) in a Vela–SMGPS mosaic. The black rectangle outlines the SoFiA source-finding region. Bottom panel: Noise variation as a function of velocity within the central search area of the same mosaic. The mean rms is indicated by the dashed horizontal line.

to assess the quality of the measured fluxes.

3.3.1 H I source finding

It is not realistic to perform source finding by eye for such large surveys. Hence, we used the second version of the H I Source Finding Application SoFiA-2[8] (Westmeier et al., 2021), an automated source finding and parameterization algorithm to identify galaxy candidates based on their H I emission. Due to continuum residuals, the rms noise level from pointing to pointing is not uniform (see bottom panel of Fig. 3.3). It is therefore crucial to optimize the parameter

[8]https://github.com/SoFiA-Admin/SoFiA-2

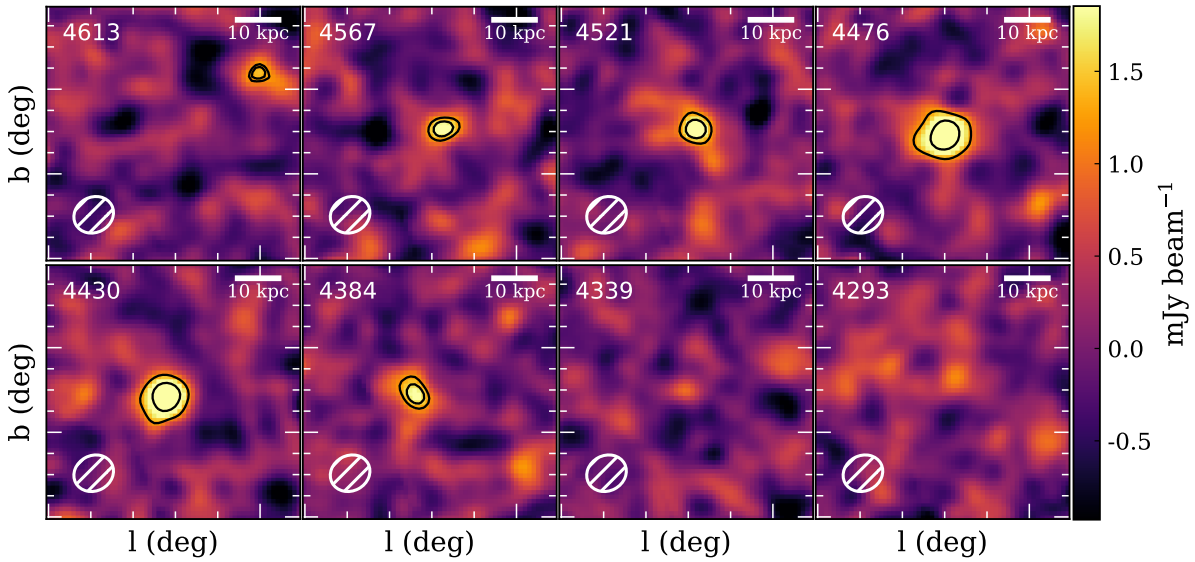

Figure 3.6: A consecutive H I channel map showing a low-redshift source with low signal-to-noise ratio. The black contour level begins from the 4σ rms noise of the detection. A 10 kpc scale bar is displayed in the top right corner, the corresponding velocity in the top left, and the beam size is depicted by the white hatched ellipse in the bottom left corner.

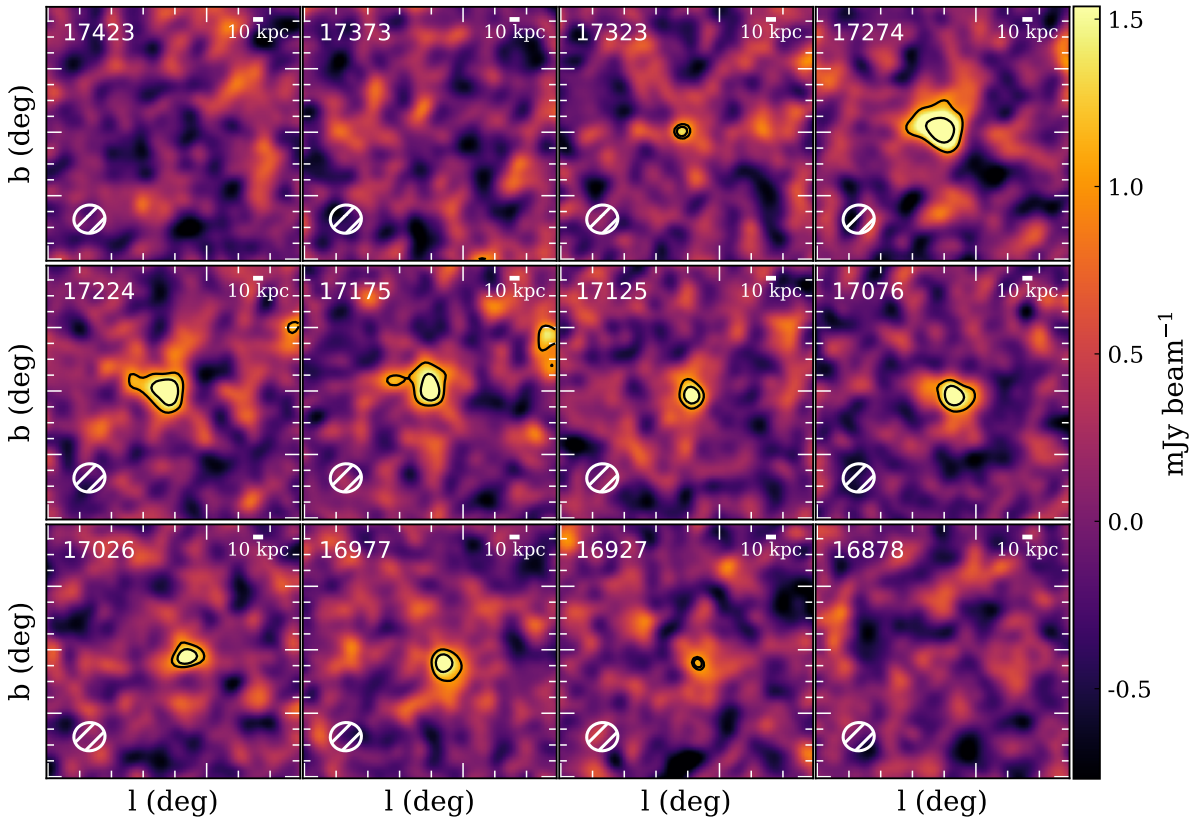

Figure 3.7: A consecutive H I channel map, similar to Fig. 3.6, but depicting a high signal-to-noise ratio detection at the VSCL distance. Note that the color scaling is the same as in Fig. 3.6.

settings for SoFiA that performs reliably on all mosaics in finding the galaxy candidates, without resulting in a high number of false detections.

Table 3.2: Mosaicking parameters of Vela–SMGPS.

Mosaicking property	Value
Number of fields per mosaic	22
Number of mosaics	10 (T24 to T33)
Galactic longitude	$260^\circ \leq \ell \leq 290^\circ$
Galactic latitude	$-2^\circ \leq b \leq 1^\circ$
Total sky coverage	90 deg^2
Sky coverage per mosaic	$\sim 5 \times 3.5$ deg^2
– with uniform sensitivity	3.5×3 deg^2
Velocity resolution	44.11 km s^{-1} at $z = 0$
Mosaic velocity range	$-1696 < cz < 25515$ km s^{-1}
H I cube weighting	Briggs *robust* = 0
Pixel size	$3'' \times 3''$
H I cube size	2200×2200 pixels
Beam size ($15''$ tapering)	$30'' \times 27''$ ($\pm 1''$)
Mean global rms noise per channel	0.39 mJy beam^{-1}
Mosaics rms range	0.29 – 0.56 mJy beam^{-1}

Our final source finding strategy is summarized below:

(i) We first defined the search window for the input mosaic cube. Our three-dimensional search window was set to the central area of 3.5×3 deg^2 ($\sim 4200 \times 3600 \times 517$ pixels) where the rms is mostly uniform. This search area is outlined by the black box in Fig. 3.5. The source finding velocity range was from channel 9 to 525, i.e., $250 \leq V_{\rm hel} \leq 25000$ km s^{-1}.

(ii) We normalized the noise level across the mosaic by adding the noise mosaic as an additional input to the pipeline. We used the 'local' scaling noise mode of SoFiA to correct for local noise variations within both the spectral and spatial domains of the data. This approach differs slightly from the one employed by Steyn et al. (2024), who used the 'spectral' scaling noise mode, relying solely on spectral domain correction. We chose a grid size of 301 pixels on the xy-axis and 15 channels on the spectral axis for this noise scaling step.

(iii) The source finding step itself is performed with the 'Smooth and Clip' (S+C) finder algorithm, specifically designed for blind source detection. It smoothes the mosaic with a set of spatial Gaussian filters and spectral boxcar kernels. We set these to (0, 7, 15) pixels, and (0, 135, 225, and 315) km s^{-1}, respectively. After each iteration of the smoothing process, the local rms noise is measured. SoFiA then clips all pixels below the source finding threshold of 4σ. The remaining pixels are stored in a source mask and, if connected pixels satisfy the specified linking radius set in the parameter file, they are merged into individual sources.

(iv) Each detected source undergoes a reliability assessment using the method outlined in Serra et al. (2012). To be considered a valid detection and included in the SoFiA output catalog, a minimum SoFiA source-finding reliability threshold of 90% is set.

(v) To ensure that sources near the detection threshold of the survey were not overlooked due to stochastic noise, we conducted a second run of SoFiA with a source finding threshold of 3.5σ. Both resulting SoFiA catalogs were cross-matched using `Cross_matching`[9], duplicates were removed, and unique detections from each run were retained. After a verification process discussed in the next section, we obtained a final list of detections which also allowed us to reject false positives.

The final parameter settings, which encompass all these procedures, can be found in the SoFiA parameter file provided in Appendix B.1. The outlined approach was applied to all 10 mosaics.

3.3.2 Source verification

For the verification process, a PYTHON script was created to automatically generate total flux density (mom-0), velocity field (mom-1) maps, and the global H I profiles for each detection listed in the SoFiA catalog, following the format shown in Fig. 3.8.

To generate moment maps and global H I profiles, we extracted cubelets with a spectral length of 10 MHz and dimensions defined by the bounding box results obtained from the SoFiA catalog around each H I detection. Additionally, we added extra padding of $30''$ to $1'$ in both longitude and latitude depending on the redshift of the detection to account for the noise outside the source. To compute mom-0 and mom-1 maps, we selected the cubelet channels both before and after the systemic velocity provided by SoFiA, each with widths equal to half of the linewidth at the 20% peak flux (w_{20}) and an additional channel on both sides. A 3σ clipping threshold was therefore applied, where σ is the local rms derived from four emission-free areas around each detected H I signal, used to mask the moment maps.

After the production of these data products, visual verification was performed on unmasked mom-0 maps and on masked mom-1 maps to assess noise levels surrounding the source. Each potential detection was classified as 'solid', 'possible', or 'reject'.

To be considered a solid detection, specific criteria must be met. Firstly, we require that the detection's 3σ contour level exceeds 1.5 times the beam size along the major axis during visual inspection ($\gtrsim 55$ kpc of H I diameter at $cz \sim 18000$ km s^{-1}). This is to avoid sources that are difficult to quantify as real or not. Secondly, the global H I profile should exhibit a clear peak, with a signal well above the noise level. Additionally, the source should have a well-defined

[9]https://github.com/TrystanScottLambert/Cross_Matching

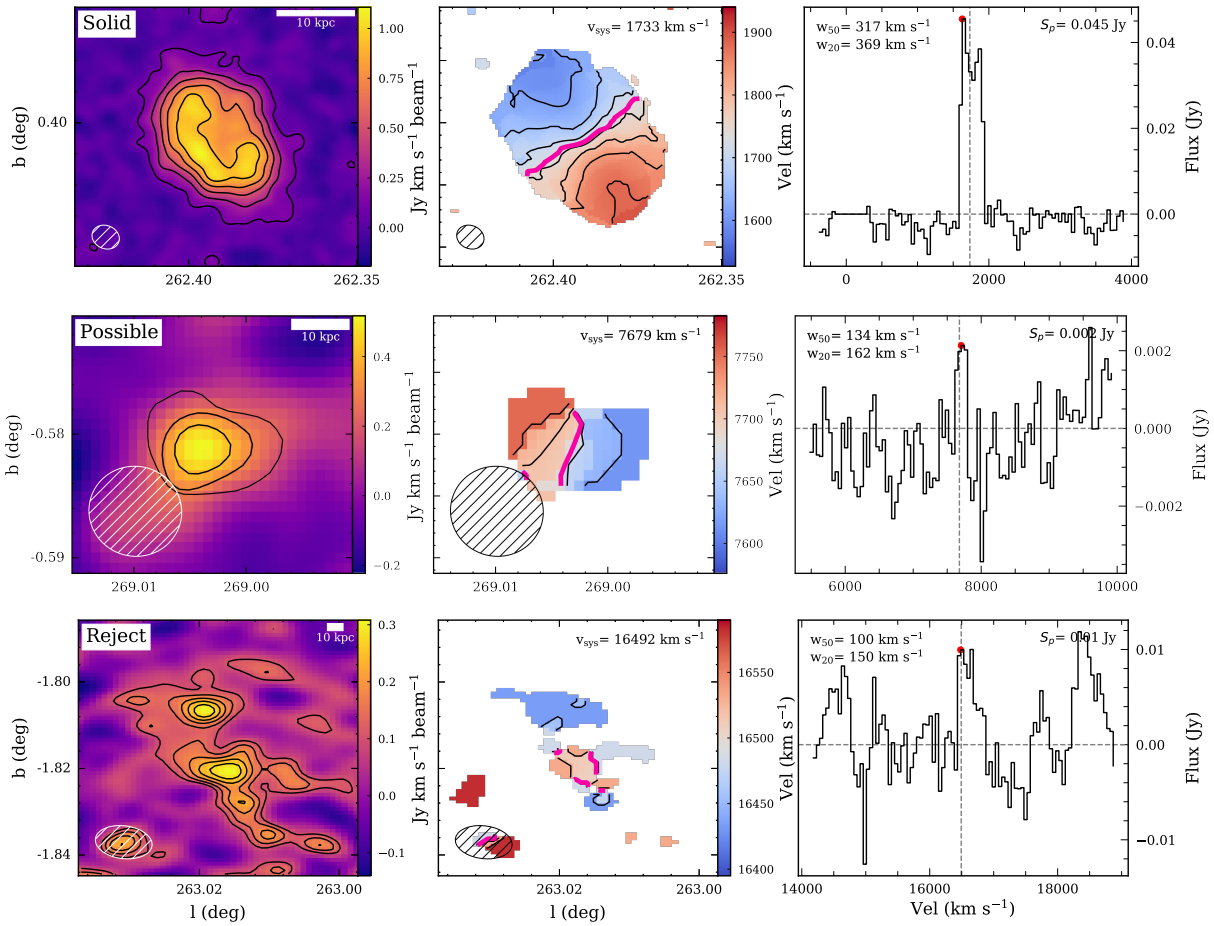

Figure 3.8: The three visual classifications of SoFiA detected sources: "Solid", "Possible", and "Reject" (from top to bottom). *Left panel:* Total flux (mom-0) map in Galactic coordinates with a color bar, a 10 kpc scale bar at the top, and the synthesized beam (white hatched ellipse) at the bottom corner. *Middle panel:* Masked mom-1 map in Galactic coordinates with a color bar revealing velocity fields. The heliocentric velocity is given in the top right corner and indicated as a magenta contour. *Right panel:* Global H I profile with a dashed vertical line indicating the heliocentric velocity of the galaxy; measured linewidths at 50% and 20% of the peak flux density are presented in the top left corner, with the peak flux value denoted by the red point shown in the top right corner.

disc in the mom-0 map and a distinct velocity field with evident rotation over multiple channels in the mom-1 map. Assessing this last criterion can be challenging for narrow-width sources. For instance, the existence of an extremely large source compared to its beam size (see bottom panel of Fig. 3.8) or a small dwarf is not likely to be detectable in this survey at high redshift.

In cases where one of these criteria is not met, but the detection is still deemed to be real, it is classified as a possible detection. An example is shown in the second panel of Fig. 3.8, where despite an evident rotation spanning four channels, its extent is only about the size of the beam. The highest point in its spectrum is also not very clear due to the varying noise in the detection area.

A detection is otherwise labeled as a reject. This could arise from a small noise peak (few pixels) that SoFiA misinterpreted as a detection, a source detected in more than 20 channels, or the identification of an imaging artifact caused by a residual continuum. The latter assessment was facilitated by an additional visual verification of each detection using CARTA[10] – an interactive Astronomy Visualization tool. The adjudication process involved multiple team members to ensure the robustness of the source verification. 5-30% of outputs from each SoFiA run per mosaic were rejected as false positives. Figure 3.8 displays typical examples of these three categories.

We then cataloged a total of 843 detections, comprising 646 solids and 197 possible detections based on this classification scheme. These detections were compiled into a Galaxy Atlas, which showcases their masked moment maps and H I global profiles. The Galaxy Atlas is available in Appendix B.4. Table 3.3 provides the number of detected sources per SoFiA run and per mosaic, their final classifications, as well as the average global and local rms variations per mosaic. The per-channel local rms noise of the 843 detections ranges from 0.22 to 0.94 mJy beam^{-1}, with an average of 0.33 mJy beam^{-1}. This is lower than the average global rms value of the mosaics and is consistent for solid and possible detections (see peak in Fig. 3.9). The solid and possible detections from each mosaic are combined into a final catalog (see Section 3.4 for details) with flags according to their classifications.

3.3.3 Parameterization

The SoFiA output list provides source parameters in native pixels and flux units. To convert them into physical parameters, such as centroid positions (in pixels) into Galactic coordinates (ℓ and b in degrees), and to enable SoFiA to adjust the integrated fluxes (S_{int}) by the beam solid angle, we set SoFiA `parameter.wcs` and `parameter.physical` to `True`.

[10] https://cartavis.github.io

Table 3.3: Number of detected sources per mosaic after the two SoFiA runs, including cross-matching, elimination of duplicates between mosaics, and visual verification. The last column presents the measured global and local rms values determined around detections.

Mosaic	Thresholds		Total retained	Solid	Possible	Mean rms (mJy beam^{-1})	
	3.5σ	4σ	(w/o dupl.)			Global	Local
T24	51	65	54	42	12	0.47	0.39 ± 0.12
T25	56	58	32	25	7	0.49	0.50 ± 0.12
T26	60	72	53	48	5	0.50	0.41 ± 0.11
T27	137	155	116	97	19	0.30	0.32 ± 0.09
T28	108	116	102	65	37	0.29	0.28 ± 0.04
T29	98	111	91	70	21	0.31	0.29 ± 0.06
T30	120	134	114	92	22	0.30	0.31 ± 0.08
T31	119	107	75	52	23	0.56	0.38 ± 0.09
T32	131	125	103	72	31	0.31	0.31 ± 0.08
T33	138	139	103	83	20	0.33	0.30 ± 0.07
Total			**843**	**646**	**197**		

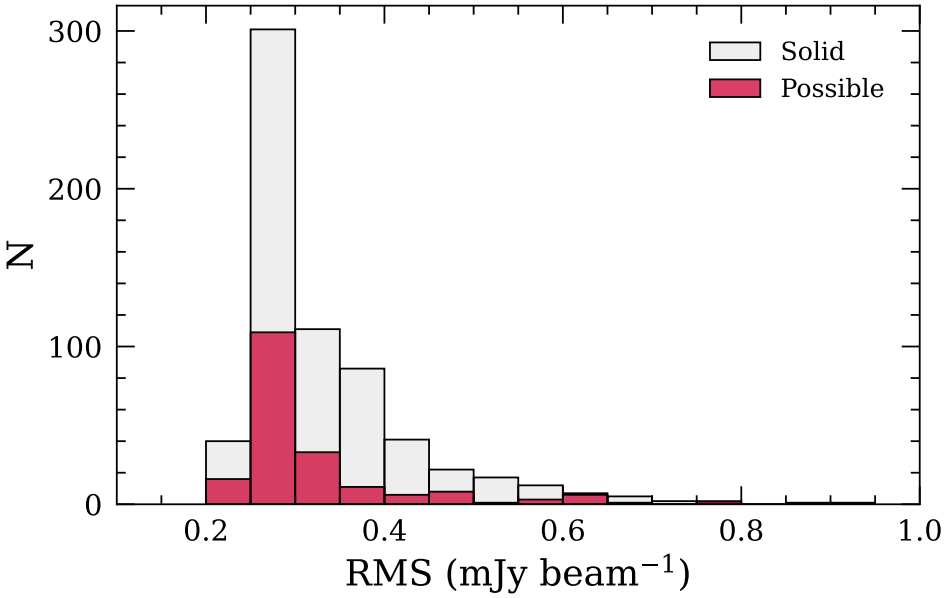

Figure 3.9: Histogram depicting the local rms noise measured around each solid detection (shaded in grey) and possible detection (shaded in red).

We first convert the SoFiA output parameters. The heliocentric systemic velocity $V_{\rm hel}$ is determined from the central frequency of the H I profile to the optical definition using the equation:

$$V_{\rm hel} = c\left(\frac{\nu_0}{\nu} - 1\right), \tag{3.1}$$

where c is the speed of light and ν_0 is the rest-frequency of the 21 cm line. No corrections have been applied to $V_{\rm hel}$ for the barycentre of the Local Group ($V_{\rm LG}$).

In a few isolated cases, where the detection was composed of one or more companions, the SoFiA central frequency has been found slightly off-center. We then determined the systemic

velocity as follows:

$$V_{\rm hel} = 0.25(\mathrm{v}_{20}^{\rm A} + \mathrm{v}_{50}^{\rm A} + \mathrm{v}_{20}^{\rm R} + \mathrm{v}_{50}^{\rm R}), \tag{3.2}$$

where v_{20} and v_{50} are the corresponding velocities measured at the 20% and 50% levels of the peak flux densities (see Ramatsoku et al. 2016). A and R indicate the approaching and receding sides of the profile respectively. To convert (w_{20}, w_{50}) from Hz to km s^{-1}, we use the equation:

$$w\ [\mathrm{km\ s^{-1}}] = \frac{\mathrm{c}}{\nu_0} \times \left(1 + \frac{V_{\rm hel}}{\mathrm{c}}\right)^2 \times w\ [\mathrm{Hz}]. \tag{3.3}$$

When the signal-to-noise ratio is low, SoFiA could output an under- or overestimate, where the values of w_{20} and w_{50} are erroneously identical, contrary to what is expected in the spectrum. In such cases, we re-calculated the linewidths as:

$$w_{20} = \mathrm{v}_{20}^{\rm R} - \mathrm{v}_{20}^{\rm A} \text{ and } w_{50} = \mathrm{v}_{50}^{\rm R} - \mathrm{v}_{50}^{\rm A}. \tag{3.4}$$

The 20% and 50% levels are measured from the first crossings of the peak flux density. The differences between the SoFiA linewidths and the re-calculated ones are on the order of half to one channel width.

We convert the integrated flux $\mathrm{S_{int}}$ from Jy Hz to Jy km s^{-1}as follows:

$$S_{\rm int}\ [\mathrm{Jy\ km\ s^{-1}}] = \mathrm{S_{int}}\ [\mathrm{Jy\ Hz}] \times \frac{\Delta \mathrm{z}[\mathrm{km\ s^{-1}}]}{\Delta\nu[\mathrm{Hz}]}. \tag{3.5}$$

Here, $\Delta z = 44.11$ km s^{-1}(at $z = 0$) is the channel width resolution in velocity and $\Delta\nu = 210$ kHz is the corresponding spectral resolution in frequency.

We can then determine the H I mass in $\mathrm{M_\odot}$ from $\mathrm{S_{int}}$ and the distance D in Mpc, where D was based on $V_{\rm hel}$. The H I mass is calculated using the following equation:

$$M_{\rm HI} = 2.356 \times 10^5\ (1/1 + z)\ D^2\ S_{\rm int}. \tag{3.6}$$

3.3.4 Quality assessment

Internal quality assessment

We first conducted an internal consistency check for sources located within the overlapping regions of the mosaics to ensure consistency in source finding, and to assess internal data quality. A source from an overlapping region was identified in adjacent mosaics consisting of a slightly different configuration of pointings. We first investigated the positional agreement as demonstrated in Fig. 3.10. A mean coordinate precision of $2.16''$ with a 1σ standard deviation of $2.77''$ was achieved – less than one pixel size. No difference in positional offset between possi-

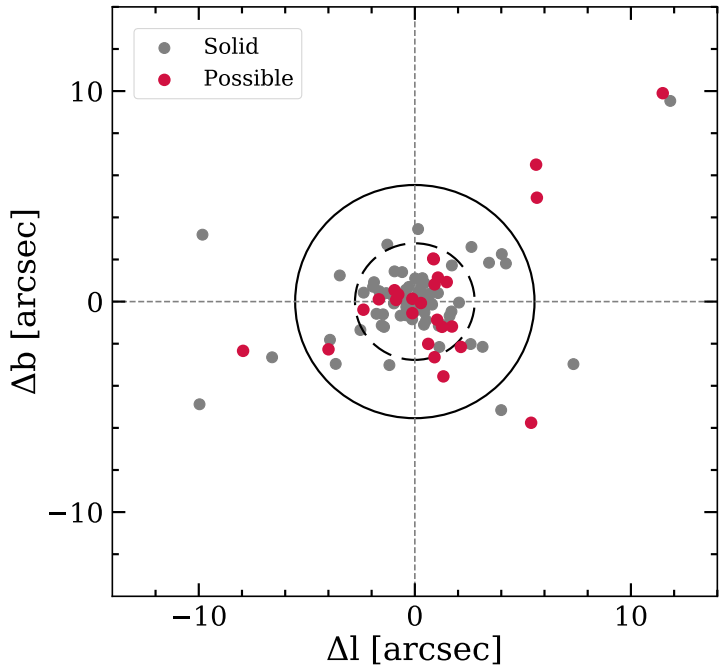

Figure 3.10: Internal coordinate offsets for detections found on overlapping regions of adjacent mosaics. Grey dots illustrate solid detections while red ones designate possible detections. The inner (dashed) and outer (solid) circles delimit the one and two sigmas standard deviations of $2.77''$ and $5.54''$, respectively.

ble and solid detections was observed. We then examined the positional offsets as a function of the integrated signal-to-noise ratio (SNR; see Fig. 3.11). The integrated signal-to-noise ratio is defined as:

$$\mathrm{SNR} = \mathrm{S_{int}}/(\mathrm{w_{50}} \times \sigma), \tag{3.7}$$

where S_{int} is the integrated flux in Jy km s^{-1}, w_{50} is the 50% peak flux linewidth and σ is the local rms of the detection.

Possible detections have on average a lower SNR compared to solid ones, while the 2σ-outliers (outside black solid circle in Fig. 3.10) all have SNR < 25. The separation is seen to decrease with increasing SNR as shown in Fig. 3.11.

The absolute differences in integrated fluxes, linewidths, and systemic velocities of the overlapping sources (i.e., the same object detected in two different mosaics) exhibit mean absolute errors and standard deviations in the range of 0.17 ± 0.12 Jy km s^{-1}, 22 ± 27 km s^{-1}, and 10 ± 12 km s^{-1}, respectively. These values are consistent with their errors, and uncertainties in linewidths and velocities are well below the coarse channel resolution. However, for sources with very low SNR and detections situated close to the mosaic edges, the masking threshold may vary if the rms values differ in the two mosaics, potentially leading to larger flux uncertainties.

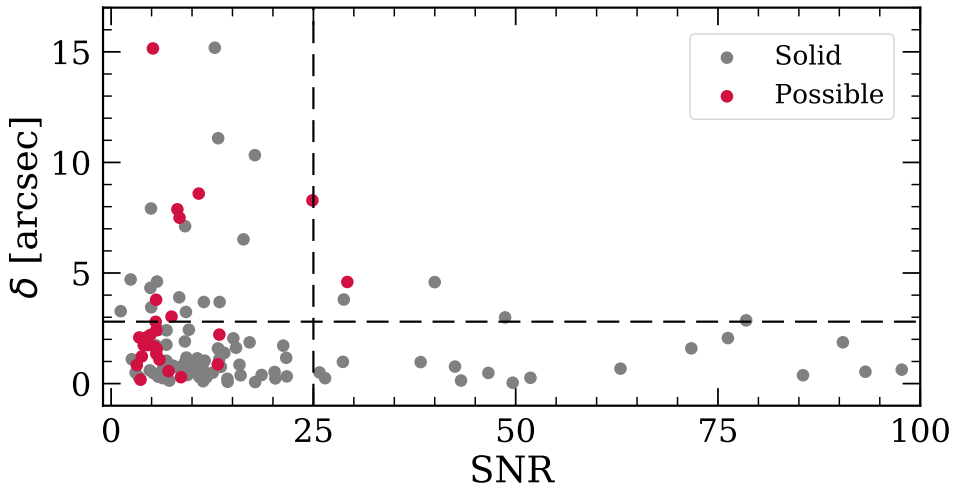

Figure 3.11: Vela–SMGPS internal coordinate offsets as a function of integrated signal-to-noise ratio (SNR). Red and grey dots represent possible and solid detections. Horizontal and vertical dashed lines mark the coordinate precision 1σ standard deviation, and an SNR of 25, respectively.

Ancillary data comparison

In the next step, we quantify the accuracy of Vela–SMGPS H I parameters. Despite the high extinction in the inner ZOA, we utilized the NASA/IPAC Extragalactic Database (NED)[11], and the Vizier[12] Catalogue access tool to search for Optical, IR, and H I counterparts within our survey region. The search radius was determined in quadrature to the positional uncertainty of Vela–SMGPS (as discussed in Section 3.3.4) and the typical coordinate precision of the catalog used for comparison. For instance, we conducted searches within a radius of $10''$ from each galaxy's position for OPT/IR counterparts, and $\sim 4'$ for H I counterparts, considering that HIZOA galaxies (Staveley-Smith et al., 2016) are with few exceptions the only H I counterparts available at these latitudes.

Out of 843 detections, 57 detections (~7%) have likely IR and/or H I counterparts in the existing literature. Among these 57, the distribution of IR counterparts is as follows: 7 (12%) have IRAS counterparts, 40 (70%) are associated with 2MASS/2MASX counterparts, 50 (88%) are identified with WISE counterparts, and 17 (30%) have InfraRed Survey Facility (IRSF) counterparts. The median coordinate separation between the H I position and the potential IR counterpart is approximately $3.3''$.

In terms of H I counterparts, our survey area encompasses 39 HIZOA detections (68% of 57), with 6 of them also detected in the H I Parkes All Sky Survey (HIPASS, Meyer et al. 2004). Vela–SMGPS successfully retrieved all HIZOA detections. Interestingly, we recovered the most H I-massive spiral galaxy hidden behind the Milky Way, identified as HIZOA J0836-43 (see

[11] http://ned.ipac.caltech.edu
[12] https://vizier.cds.unistra.fr/viz-bin/VizieR

Kraan-Korteweg et al., 2005), named SMGPS-HI J083650-433738 in Vela–SMGPS (displayed in the top left panel of Fig. B.1). This galaxy is the most H I-massive object within the entire HIPASS volume, and underwent subsequent follow-up observations with the Australian Telescope Compact Array (ATCA; Donley et al. 2006). This optically obscured galaxy was found to be a Luminous Infrared Galaxy (LIRG) with an actively star-forming disk spanning over 50 kpc (Cluver et al., 2010).

I used the ATCA data for this H I massive galaxy to examine the consistency in our positions, fluxes, velocities, and linewidths. I observe a positional difference of $9''$ and $23''$, respectively. While the ATCA and HIZOA measurements report integrated H I flux densities of 14.5 ± 0.7 Jy km s^{-1} and 14.38 ± 1.69 Jy km s^{-1}, our analysis using Vela–SMGPS yields a slightly higher value of 14.63 ± 1.54 Jy km s^{-1}. These values remain within the range of expected errors, indicating excellent agreement with each other. The slightly higher flux value of J083650 in Vela–SMGPS may be attributed to its position near the mosaic edge. We observed higher noise levels and baseline irregularities in this area, which could have influenced the flux measurement in this case. Nevertheless, the systemic velocities and linewidths exhibit exceptional agreement with the ATCA results, both showing differences of less than 10 km s^{-1}. When compared to HIZOA, there is an 8 km s^{-1} difference in velocities, and larger offsets of 20 km s^{-1} and 30 km s^{-1} in the w_{50} and w_{20} values, respectively.

The comparison with the sole interferometric dataset within our survey region provides consistent measurements. However, the statistical analysis is limited to only one galaxy. Hence, I utilize the HIZOA dataset for an independent comparison of H I parameters, given its unique status as the only source with redshift information in our multi-wavelength counterpart search.

The 39 HIZOA galaxies are identified out to 12000 km s^{-1}. The Vela–SMGPS dataset comprises 471 detections within this velocity range, marking a noteworthy twelve-fold increase in the galaxy count. The mean positional offset is $\sim 2'$, a reasonable value given the pixel size of HIZOA. This is also consistent with findings between HIZOA/HIPASS and other data sets (e.g., Staveley-Smith et al., 2016). Six of the HIZOA detections were resolved into several distinct H I sources due to the higher resolution of the MeerKAT interferometric data. Figure 3.12 presents an illustration of two examples, showcasing HIZOA J0913-48 blended into two distinct sources, and HIZOA J0917-49 with a satellite companion as seen in their H I distributions. Moment maps of the 39 HIZOA detections as observed by Vela–SMGPS are shown in Appendix B.2. Furthermore, 19 of these HIZOA detections have likely WISE counterparts.

Figures 3.13, 3.14, and 3.15 display the comparison between the linewidths, systemic velocities, and integrated fluxes of the Vela–SMGPS detections and their corresponding HIZOA counterparts. Out of the 39 detections, I excluded detections that conformed of multiple counterparts

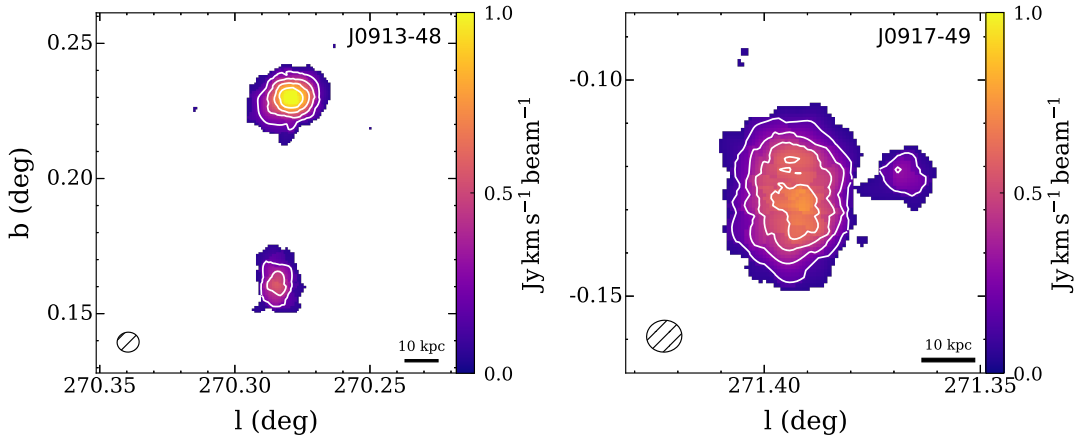

Figure 3.12: Moment-0 H I emission maps for two HIZOA sources (J0913-48, and J0917-49) reveal them to consist of several counterparts in Vela–SMGPS. A 10 kpc scale bar and the beam size are shown in the right and left bottom corners of each image.

or close to a continuum residual artifact, leaving 31 detections for comparison.

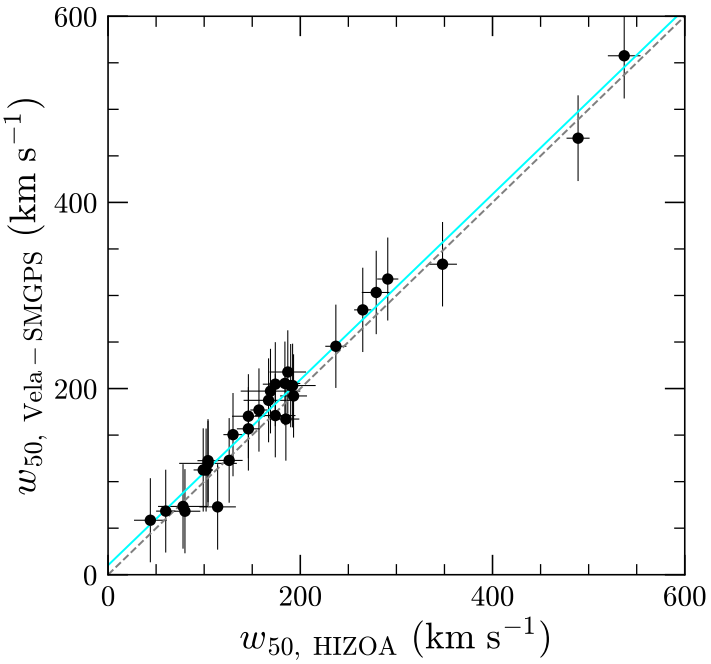

Figure 3.13: Comparison of H I linewidth w_{50} among the 31 HIZOA detections within the Vela–SMGPS survey. The cyan lines represent the best-fit linear regressions.

The 50% peak flux linewidths show a nearly indistinguishable deviation from a one-to-one relation (black dashed line), with a mean error of approximately 17 km s^{-1} and a standard deviation of 10 km s^{-1}. A formal fit yields a regression with a slope of 0.997 ± 0.058 (cyan line) reaching an R^2 value of 0.98 at a 95% confidence interval. Similarly, the one-to-one linear fit for Vela–SMGPS and HIZOA heliocentric velocities also exhibits a slope of almost unity (1.002 ± 0.002). I chose to plot their differences, $\Delta v = V_{\mathrm{Vela–SMGPS}} - V_{\mathrm{HIZOA}}$, for a more comprehensive comparison. The results show a mean error of 15 ± 10 km s^{-1}. Given the coarse

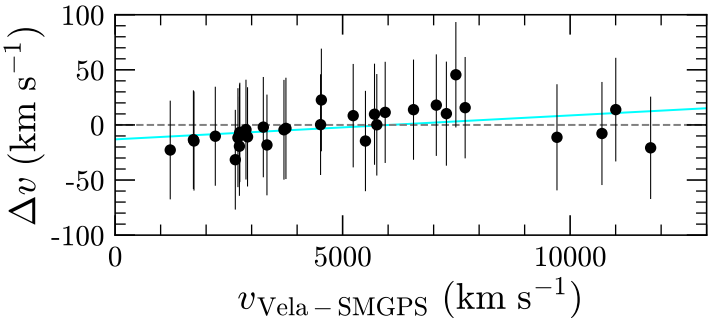

Figure 3.14: Comparison of heliocentric velocities from Vela–SMGPS and the difference $V_{\rm Vela-SMGPS} - V_{\rm HIZOA}$.

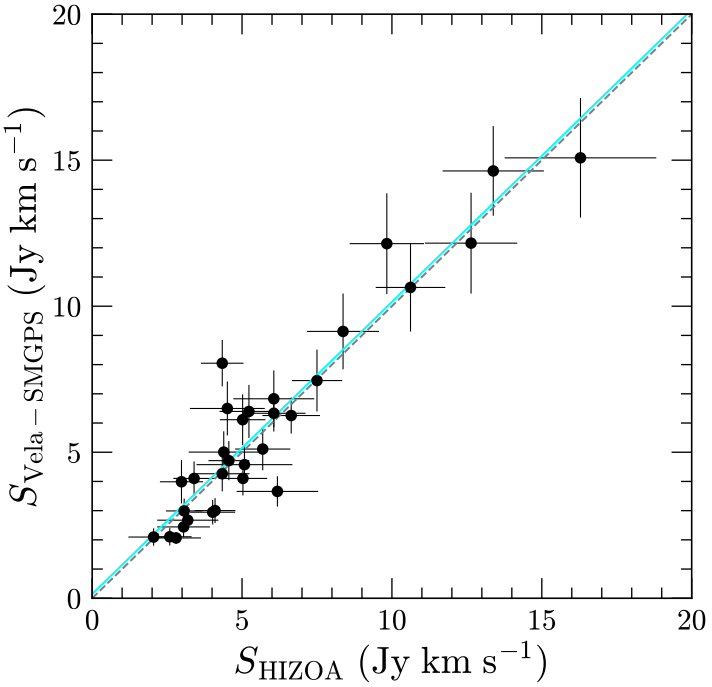

Figure 3.15: Comparison of the integrated fluxes of 31 galaxies in common with HIZOA. The cyan line illustrates the best-fit linear regression, closely following the one-to-one relation indicated by the grey dashed line.

SMGPS channel width (44 km s^{-1}) and the (smoothed) HIZOA spectral resolution (27 km s^{-1}), this achievement is remarkable, affirming the high quality of the SMGPS calibration and H I parameters.

I furthermore verified the agreement in integrated fluxes, as illustrated in Fig. 3.15. To derive the integrated flux error err$_{(S_{\rm int})}$, I adopt the method used by Ramatsoku et al. (2016). I selected four emission-free regions located at the corners of the cubelet by dividing each cubelet into a 3×3 grid of the same size as the source mask. err$_{(S_{\rm int})}$ is then computed as the mean of the standard deviations of the measured integrated fluxes within these boxes. I observe typical flux uncertainties of ~32%, 19%, 14%, and 10% for H I masses below 10^8, 10^9, 10^{10} and above 10^{10} M$_\odot$, respectively. The measured slope, nearly equal to unity (1.0003 ± 0.1332), along with R^2 = 0.89 at a 95% confidence interval, underlines the consistency between SMGPS and

HIZOA flux measurements with less than 0.5% offset to unity. Overall, the parameters of the comparison sample show excellent agreement with our measurements.

3.4 Vela–SMGPS catalog

The resulting Vela–SMGPS catalog contains 843 H I detections. Across the full velocity range ($V_{\rm hel} < 25000$ km s^{-1}), this corresponds to an average of ~9.37 galaxies per deg^2. Around 93% of the galaxies have no optical or IR counterpart. Apart from the 39 HIZOA galaxies +1 ATCA (massive galaxy), no other redshift measurements exist. Of the 843 detections, 187 galaxies have velocities within 19500 ± 3500 km s^{-1} and might be associated with the Vela overdensity. Of these, 76 galaxies lie within the velocity range of $16000 - 19000$ km s^{-1}, and 111 galaxies within the $19000 - 23000$ km s^{-1} range, which conform to the two walls of the VSCL. The H I parameters of the 843 H I detections are compiled into a catalog. The first 10 rows of the catalog are listed as an example in Table 3.4. The complete catalog is presented in Appendix B.3 as Table B.1.

The Vela–SMGPS galaxy catalog lists the following:

Column 1: Galaxy identifier (ID): prefixed with SMGPS-HI followed by its coordinates in the form JHHMMSS-DDMMSS. The latter corresponds to the rounded values of the right ascension and declination of the flux-weighted centroid of the source in J2000 equatorial coordinates.

Column 2: The Vela–SMGPS Mosaic (Txx) in which the source has been detected (see e.g., top panel of Fig. 3.3).

Columns 3 and 4: Galactic coordinates ℓ and b in units of degrees.

Column 5: Peak flux $S_{\rm peak}$ as derived from the Global H I profile in Jy.

Columns 6 and 7: Integrated flux density $S_{\rm int}$ with its corresponding error in Jy km s^{-1}(see Eq. 3.5 in Section 3.3.3).

Column 8: Mean local rms in mJy beam^{-1}.

Column 9: Optical heliocentric systemic velocity $V_{\rm hel}$ in km s^{-1}.

Columns 10 and 11: Linewidths (w_{20}, w_{50}) in km s^{-1}. These represent the measured linewidths at which the profile reaches 20% and 50% of its peak flux density (see Eq. 3.3).

Column 12: Logarithm of the H I mass determined from Eq. 3.6 [$\log(M_{\rm HI}/{\rm M}_\odot)$].

Column 13: Flags 1 or 2, where 1 signifies that the detection was classified as solid, 2 for a possible detection according to the visual verification process of each source (see Section 3.3.2). An asterisk (*) next to the flag code means that the detection has also been found in the area with the adjacent mosaic.

Column 14: Notes describing whether a galaxy is interacting (i), presents one or multiple companions (w.comp), exhibits a wiggly baseline in its profile (BL) or if the measurement of w_{20} is uncertain due to the baseline behaviour (w_{20} unc.). Additionally, galaxies detected in major H I and IR catalogs are marked. For galaxies found in HIZOA (Staveley-Smith et al., 2016),

their object names (e.g., J0831-42) are provided. 'H' denotes H I counterparts for galaxies also detected in HIPASS (Meyer et al., 2004). 'I' refers to the IRAS Point Source Catalog (Helou & Walker, 1988), 'M' stands for 2MASX (Jarrett et al., 2000), 'W' represents matches from the Wide-field Infrared Survey Explorer catalog (WISE, Cutri et al. 2021), and 'Z' signifies Deep NIR follow-up observations of HIZOA galaxies obtained with the IRSF Telescope (Williams et al., 2014; Said et al., 2016).

Figure 3.16 illustrates the wedge diagrams in Galactic longitude and latitude of the Vela–SMGPS detections which demonstrate the impressive sensitivity of this survey. The newly detected H I galaxies are indicated by the light blue dots, and the previously known HIZOA galaxies by red dots. The majority of the galaxies below 4000 km s^{-1} were also found by HIZOA with its sensitivity of 6 mJy beam^{-1}. At higher velocities, the HIZOA dataset predominantly captures the more massive spiral galaxies, but the uncovered structure closely aligns with the general shape (filaments) delineated by Vela–SMGPS. A detailed discussion of the LSS uncovered by Vela–SMGPS will be presented in Section 3.6.

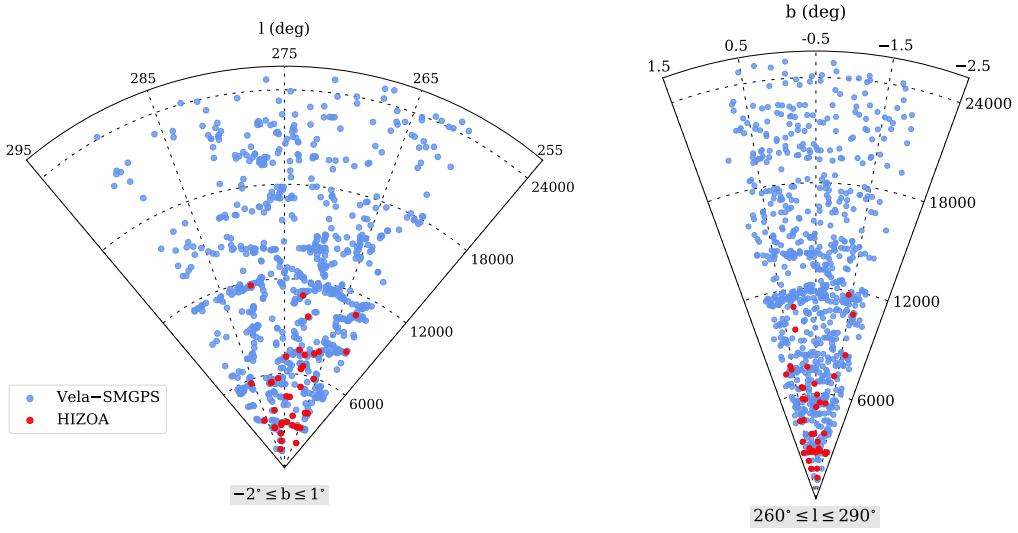

Figure 3.16: Redshift wedge diagrams illustrating the distribution of H I-detected galaxies up to $V_{\rm hel} < 25000$ km s^{-1} in Vela–SMGPS (blue dots) and HIZOA (red dots). The left panel depicts a longitude wedge plot covering the latitude range $-2^\circ \leq b \leq 1^\circ$, while the right panel displays a latitude wedge plot spanning the longitude range $260^\circ \leq \ell \leq 290^\circ$.

3.5 Vela–SMGPS H I properties distribution

3.5.1 Completeness

One way to determine the completeness of a survey involves fitting a power law to the histogram of mean flux density, calculated as the integrated flux divided by the linewidth (cf. Donley et al.

2005; McIntyre et al. 2015; Staveley-Smith et al. 2016). The distribution is expected to follow an Euclidean power law, $N(S) \sim S_{\rm mean}^{-2.5}$, corresponding to a linear power law with a slope $-3/2$ in log-log space. The completeness threshold becomes apparent when the histogram distribution starts to deviate from this projected line. In Fig. 3.17, I illustrate solid detections (red), as well as the sample including both solid and possible detections (black). I use w_{50} rather than w_{20} because w_{20} is more influenced by noise variations.

Table 3.4: Vela-SMGPS catalog: H I properties (first page).

Name	Mosaic	l	b	$S_{\rm peak}$	$S_{\rm int}$	err$_{(S_{\rm int})}$	RMS	$V_{\rm hel}$	w_{20}	w_{50}	$M_{\rm HI}$	Flag	Note
J2000	TXX	deg	deg	Jy	Jy km s^{-1}	Jy km s^{-1}	mJy beam^{-1}	km s^{-1}	km s^{-1}	km s^{-1}	log($M_{\rm HI}$/M$_\odot$)	1/2	
(1)	(2)	(3)	(4)	(5)	(6)	(7)	(8)	(9)	(10)	(11)	(12)	(13)	(14)
J082930-421453	T33	260.566	-1.903	0.010	1.24	0.23	0.46	2710	215	97	8.64	1	
J083133-422815	T33	260.970	-1.726	0.018	6.28	0.62	0.40	8242	481	429	10.32	1	J0831-42? w.comp (J083154-422631), M, W, Z
J083154-422631	T33	260.983	-1.659	0.018	2.91	0.41	0.36	8346	245	182	10.00	1	J0831-42, i, w.comp (J083133-422815)
J083217-415102	T33	260.548	-1.251	0.005	0.59	0.06	0.23	21824	342	301	10.15	1	
J083223-421453	T33	260.881	-1.471	0.003	0.25	0.05	0.27	8427	262	210	8.94	2	
J083236-423939	T33	261.237	-1.683	0.008	1.21	0.17	0.40	10767	466	345	9.84	1	
J083253-425142	T33	261.429	-1.762	0.006	1.19	0.17	0.43	8250	409	376	9.60	1	M, W
J083312-425407	T33	261.497	-1.737	0.011	2.19	0.22	0.39	11612	353	298	10.16	1	
J083406-414353	T33	260.655	-0.907	0.007	0.59	0.11	0.25	5427	136	77	8.92	1	
J083418-413412	T33	260.548	-0.780	0.003	0.18	0.03	0.24	10672	135	84	9.00	1	
J083440-413902	T33	260.653	-0.775	0.006	0.39	0.04	0.24	24375	197	108	10.06	1	
J083442-430649	T33	261.830	-1.644	0.007	1.11	0.16	0.32	8239	248	193	9.56	1	
J083446-422256	T33	261.251	-1.197	0.008	0.58	0.06	0.26	19549	140	104	10.04	1	
J083513-431435	T33	261.989	-1.647	0.004	0.29	0.04	0.35	11227	132	92	9.25	1	
J083523-413320	T33	260.657	-0.610	0.002	0.33	0.05	0.24	18204	398	295	9.74	2	
J083545-411907	T33	260.508	-0.414	0.015	4.43	0.63	0.26	4976	533	502	9.73	1	M, W
J083547-415531	T33	260.999	-0.771	0.006	0.42	0.06	0.25	13350	112	61	9.56	2	
J083550-430530	T33	261.937	-1.465	0.018	1.61	0.23	0.30	11223	137	102	10.00	1	
J083603-431104	T33	262.033	-1.491	0.010	2.17	0.31	0.33	5273	293	248	9.47	1	
J083611-411912	T33	260.560	-0.348	0.004	0.58	0.08	0.25	18221	438	423	9.98	1	
J083632-430608	T33	262.021	-1.371	0.017	1.91	0.27	0.30	5291	170	134	9.41	1	I, M, W
J083650-433738	T33	262.474	-1.642	0.054	14.63	1.54	0.39	10699	617	557	10.91	1	J0836-43, BL, e, w.comp, I, H, M, W
J083703-425113	T33	261.881	-1.144	0.005	0.25	0.04	0.27	22008	110	84	9.79	2	
J083730-430654	T33	262.138	-1.237	0.005	0.59	0.06	0.28	24035	502	462	10.23	2	
J083732-431307	T33	262.225	-1.294	0.013	1.06	0.15	0.30	5278	117	86	9.16	1	
J083742-413835	T33	260.989	-0.316	0.011	0.81	0.11	0.26	9389	118	77	9.54	1	
J083746-435546	T33	262.817	-1.690	0.005	0.49	0.05	0.37	24183	297	276	10.16	1	
J083751-421432	T33	261.482	-0.658	0.004	0.29	0.04	0.26	11416	212	172	9.26	1	
J083815-435953	T33	262.924	-1.663	0.015	2.05	0.29	0.39	3898	160	130	9.18	1	
J083818-420056	T33	261.352	-0.454	0.002	0.31	0.04	0.25	10807	190	168	9.25	1	
J083824-413039	T33	260.963	-0.132	0.003	0.37	0.07	0.26	7061	207	153	8.95	1	
J083826-441859	T33	263.196	-1.831	0.009	0.53	0.07	0.56	10188	206	94	9.43	1	

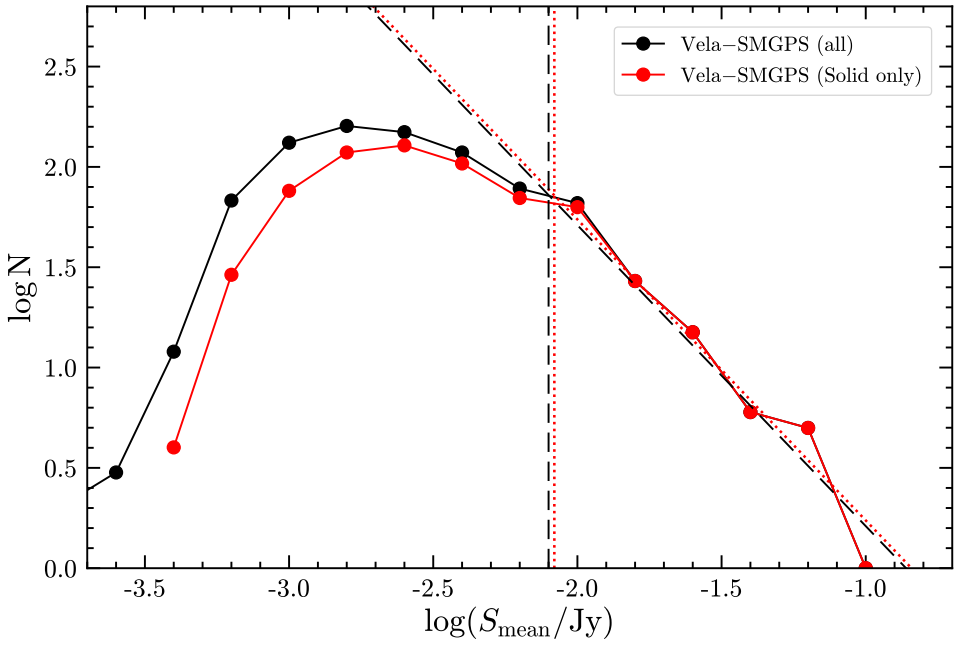

Figure 3.17: Completeness assessment using a log-log plot of the mean H I flux density $S_{\rm mean} = (S_{\rm int}/w_{50})$ for all 843 Vela–SMGPS detections in black and 646 solid detections exclusively in red. The black dashed and red dotted lines correspond to the expected $-3/2$ slope for a homogeneous distribution in both samples.

The difference in completeness is a mere 0.02 dex in the last bin, indicating that galaxies with $S_{\rm mean}$ exceeding 7.9 and 8.3 mJy are detected with high completeness in the full and solid samples, respectively.

The similarity implies that possible detections are also quite reliable galaxy candidates. I therefore include both solid and possible detections in the further analysis. However, it is important to note that this method works best under the assumption of survey homogeneity and isotropy. A more rigorous completeness test (Rauzy, 2001) will be conducted in the forthcoming Chapter 5. This first assessment indicates that we can include the possible detections together with the solid ones for analysis.

3.5.2 Simulations

For a better interpretation of our results, especially in discerning the presence of overdensity peaks relative to a homogeneous distribution, we compare our H I data with a simulation. The latter, referred to as S45, utilizes a similar framework as the one discussed in Staveley-Smith & Oosterloo (2015) for the SKA-H I science case. In this approach, constant H I mass and velocity width functions are assumed across redshifts, using the bivariate stepwise maximum likelihood method outlined in Zwaan et al. (2005). The simulation randomly distributes galaxies up to the observations sensitivity threshold (see also Steyn et al. 2024), providing output H I parameters such as peak flux density, integrated fluxes, H I masses, linewidths, and redshifts, without any spatial structure. Here, S45 is tailored to the specifications of the SMGPS, i.e., a sensitivity

of 0.45 mJy beam^{-1} to account for the average noise variation, the coarse channel widths of 44.3 km s^{-1}, and a survey area of 528 deg^2 similar to the full SMGPS survey. As a result, S45 does not simulate LSS. Instead, it represents a close proxy for a homogeneous distribution. S45 predicts the number of galaxies (with SNR > 5) as a function of redshift, distributed over an area equivalent to the full SMGPS. For the specification of the full SMGPS, it predicts 5591 galaxies in the volume delimited by $V_{\rm hel} < 25000$ km s^{-1}, respectively 953 galaxies for the Vela survey region (528 deg^2/90 deg^2). By comparing it to our observations, we can identify and quantify peaks and gaps indicative of overdensities and underdensities. While LSS in the data can be discerned visually, some structures may result from observational effects. Thus, using S45 enables a clear distinction between real structures and those influenced by selection effects, facilitating a more robust characterization of LSS through its comparison with a homogeneous galaxy distribution (see Section 3.6.1).

3.5.3 Comparison of H I properties

I display the distribution of H I properties for our detections with light-red filled histograms in Figs. 3.18 and 3.19. The light blue lines overlaid on the detections represent the S45 simulations and reflect a more uniform distribution. I appropriately scaled the S45 counts per bin to match the surveyed area. The properties under comparison include velocities (Fig. 3.18), linewidths, integrated fluxes, H I masses, and SNR (Fig. 3.19).

Velocity distribution. Fig. 3.18 visually presents an initial view of the overall velocity distribution in the survey area of Vela–SMGPS. The survey counts exhibit a shape quite similar to the simulations, with comparable median velocities: 11592 km s^{-1} (Vela–SMGPS) and 11209 km s^{-1} (S45). However, some peaks stand out. A prominent narrow peak around ~12000 km s^{-1} with roughly 1.85 times higher than the predicted counts, and a hint of broader overdensity at the high-velocity end, i.e., $V_{\rm hel} > 18500 - 23000$ km s^{-1}.

w_{50} linewidth distribution. The linewidth histogram for Vela–SMGPS ranges from $50 - 645$ km s^{-1}. As expected from a systematic blind H I survey (e.g., Haynes et al. 2011; Staveley-Smith et al. 2016), a strong prevalence at low-linewidth galaxies ($w_{50} \sim 50 - 200$ km s^{-1}) is observed. This trend is also confirmed by S45. Both distributions exhibit maximum peaks in the 100–150 km s^{-1} bin range. I measure mean values of 173±99 km s^{-1} and 147±68 km s^{-1} for Vela–SMGPS and S45, respectively. The lower value of $\langle w_{50} \rangle$ for S45 reflects its higher proportion of low linewidth galaxies. On the other hand, the distribution in Vela–SMGPS shows more high-w_{50} galaxies. The deviations at the low and high linewidth distributions can be attributed to the inclusion of sources captured with their satellites, which were not spatially resolved separately in our catalog. In contrast, S45 exclusively simulated unique galaxies.

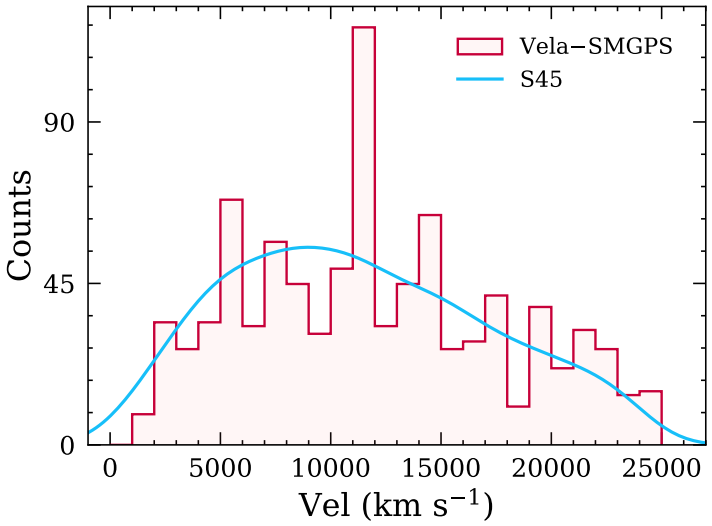

Figure 3.18: Velocity distribution for the full survey range ($260° \leq \ell \leq 290°$) of Vela–SMGPS detections (light-red histograms). The cyan lines correspond to the S45 simulations (rms $\sim$ 0.45 mJy beam^{-1}).

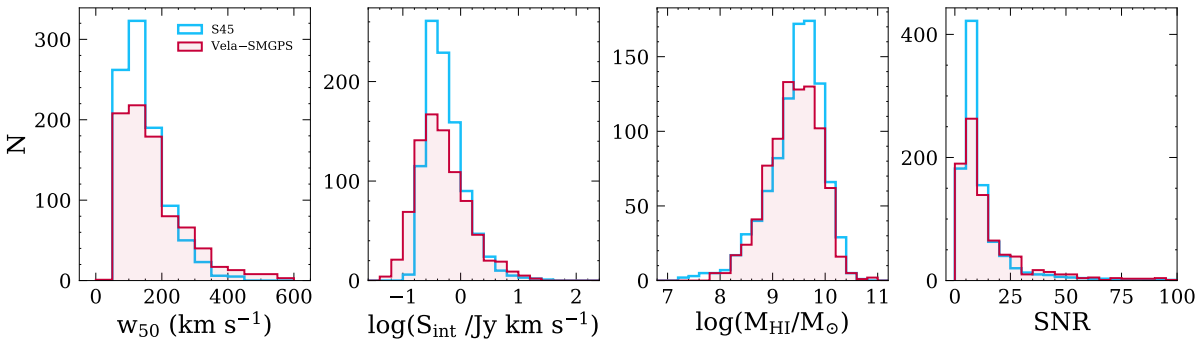

Figure 3.19: Distribution of global H I parameters in Vela–SMGPS (light-red filled histogram) and S45 simulation (cyan histogram). The four panels display, from left to right, the linewidth (w_{50}) measured at the 50% level of peak flux, the logarithm of integrated flux density ($S_{\rm int}$), the logarithm of H I mass ($M_{\rm HI}$), and the integrated signal-to-noise ratio (SNR).

Integrated H I flux densities. The second panel illustrates the distribution of the logarithm of the integrated flux density. It ranges from a minimal value of $\log(S_{\rm int}/{\rm Jy\,km\,s^{-1}}) = -1.21$ ($S_{\rm int} = 0.06$ Jy km s^{-1}) to a maximum of $\log(S_{\rm int}/{\rm Jy\,km\,s^{-1}}) = 1.28$ ($S_{\rm int} = 19.26$ Jy km s^{-1}). Vela–SMGPS and S45 both peak at $\log(S_{\rm int}/{\rm Jy\,km\,s^{-1}}) \sim -0.5$. However, S45 presents a slightly higher mean value ($S_{\rm int} = 0.55$ Jy km s^{-1}) compared to Vela–SMGPS with a mean value of $S_{\rm int} = 0.48$ Jy km s^{-1}. This difference may be attributed to some of our mosaics having slightly lower rms than the simulation, making Vela–SMGPS detect more faint sources.

H I mass distribution. In both Vela–SMGPS and S45, the galaxies span three orders of magnitude in the logarithm of the H I mass, ranging from $10^{7.8}$ M$_\odot$ to $10^{10.9}$ M$_\odot$ and $10^{7.1}$ M$_\odot$ to $10^{10.8}$ M$_\odot$ respectively. Apart from the more pronounced peaks at $\log(M_{\rm HI}/{\rm M_\odot}) \sim 9.3$ in Vela–SMGPS and 9.7 in S45, the overall distributions are very similar. Their mean H I masses only differ by at most $\log(M_{\rm HI}/{\rm M_\odot}) = 0.03$, with S45 being slightly higher. I find an average

H I mass of $10^{9.41}$ $M_\odot$ and $10^{9.44}$ $M_\odot$ for Vela–SMGPS and S45, respectively. These values are comparable to the H I mass of the Milky Way.

Integrated signal-to-noise ratio. In the rightmost panel, I compare the integrated signal-to-noise ratio between the simulation and the H I detections from our survey, calculated using Eq. 3.7. Both distributions exhibit striking similarity, with a peak occurring at $\sim 7\sigma$. As the SNR decreases, the number of detections increases steeply.

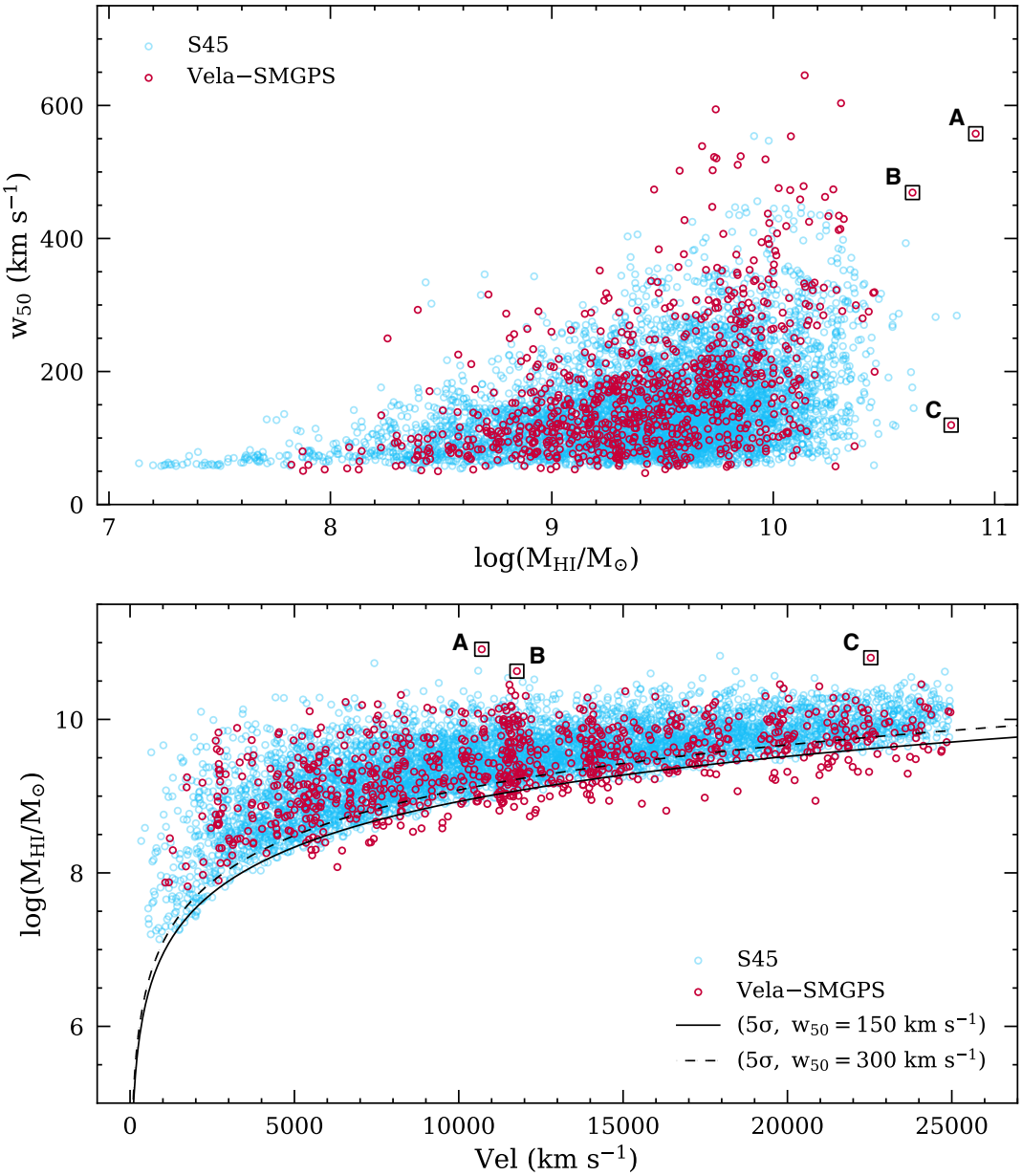

Figure 3.20: Dependence of H I linewidth w_{50} as a function of H I mass (top panel) and H I mass versus velocity (bottom panel). Vela–SMGPS detections (red dots) are overlaid on simulated S45 galaxies (cyan dots). The solid and dashed black lines represent sensitivity curves for the 5σ H I mass detection level, assuming w_{50} values of 150 and 300 km s^{-1}, with $\sigma = 0.45$ mJy beam^{-1}. SMGPS-HI J083650-433738 (A), J095513-561846 (B), and J084731-432134 (C) are marked inside black squares.

In Fig. 3.20, I compare the distribution of the individual detections in Vela–SMGPS (red dots) in w_{50} – log $M_{\rm HI}$ and log $M_{\rm HI}$ – $V_{\rm hel}$ plots. We again add simulations to provide an idea about the expected distribution. The resulting distributions suggest that both the simulations and Vela–SMGPS sample the same population. Vela–SMGPS detects a slightly larger fraction of galaxies toward the high-mass end. I mark three galaxies with broad linewidths exceeding 450 km s^{-1}. The first one, SMGPS-HI J083650-433738 (marked as galaxy A), with w_{50} = 557 km s^{-1} and $M_{\rm HI}$ = $10^{10.91}$ M$_\odot$), is the most H I-massive spiral recovered in HIPASS/HIZOA J0836-43, discussed earlier in Section 3.3.4. J095513-561846 (B) or HIZOA J0955-56, another broad linewidth galaxy with w_{50} = 468 km s^{-1} and $M_{\rm HI}$ = $10^{10.63}$ M$_\odot$. Another massive spiral galaxy, with a lower linewidth, J084731-432134 (C, w_{50} = 119 km s^{-1}, $M_{\rm HI}$ = $10^{10.8}$ M$_\odot$), was also detected as an outlier in Fig. 3.20 at $V_{\rm hel}$ $\sim$ 22500 km s^{-1}. It resembles a large face-on galaxy when examined in the galaxy atlas.

The bottom panel of Fig. 3.20 shows the so-called sensitivity curve displaying log $M_{\rm HI}$ vs. velocity. The black solid and dashed lines represent the 5σ detection limit for galaxies with 150 km s^{-1}and 300 km s^{-1} linewidth as a function of redshift, respectively. First, Vela–SMGPS only found galaxies with masses log($M_{\rm HI}$/M$_\odot$) > 7.8, whereas the simulation identifies galaxies below that threshold. This discrepancy may be attributed to the lower number of low linewidth galaxies (50 to 150 km s^{-1}) detected in Vela–SMGPS compared to S45 (see the left panel in Fig. 3.19). It could also be due to the coarse channel width or even LSS because we did not detect galaxies in the volume below cz $\leq$ 800 km s^{-1}. Second, the distributions of detections and simulations both show that we are sensitive to normal spirals (w_{50} $\sim$ 200 km s^{-1}) with 5σ log($M_{\rm HI}$/M$_\odot$) $\geq$ 9.5 at the VSCL distance of $V_{\rm hel}$ = 18000 km s^{-1}, and 5σ log($M_{\rm HI}$/M$_\odot$) $\geq$ 9.7 out to the surveyed redshift limit of $V_{\rm hel}$ = 25000 km s^{-1}. This demonstrates that we are sensitive to galaxies below $M^*_{\rm HI}$ at the VSCL distance.

The figure also highlights various signatures of LSS in its distribution. These high degrees of clustering seem to occur at various scales and are closely aligned to the hint of peak overdensities observed in the velocity distribution presented earlier in Fig 3.18. Four prominent clumps around 3000 km s^{-1}, 5000–6000 km s^{-1}, 11000–12000 km s^{-1}, and ~14000 km s^{-1} are observed. Notably, the clump at 11000–12000 km s^{-1} exhibits an elongated distribution along the H I mass. To examine this more closely, I will, in the next sections, divide the survey into different longitude ranges, and wedge diagrams, for a further analysis of the uncovered LSS.

3.6 Large Scale Structures Analysis

In this section, I will first inspect the velocity distribution of the survey detections in comparison to the simulation to assess peak overdensities, giving particular emphasis to areas where the VSCL walls are predicted to intersect. Subsequently, I examine the distribution of Vela–SMGPS

galaxies in the inner ZOA to pinpoint these overdensities and assess their significance on on-sky plots and redshift slice diagrams.

3.6.1 LSS in velocity space

In Section 3.5.3, I showed the overall velocity distribution of Vela–SMGPS (see Fig. 3.18) with potential peak overdensities. To localize these peaks and set a better understanding of these potential filaments and/or walls, I divide the survey area into different subregions with a longitude interval of $\Delta\ell = 10°$ (see Fig. 3.21).

The first panel of Fig. 3.21 spans the range $280° \leq \ell \leq 290°$. I observe a subtle enhancement at $2000 - 4000$ km s^{-1} and a more pronounced peak at $5000 - 6000$ km s^{-1}, also notable in Fig. 3.20. These hints are suggestive of links with the Hydra/Antlia wall (Kraan-Korteweg et al., 1995) and AS639 cluster (Stein, 1996), respectively (see Section 3.6.2 for further details). Most prominent is the significant peak at ∼12000 km s^{-1} which is also present in the other subregions. Its visibility is particularly pronounced in this first panel, with a factor of ∼2 higher than predicted counts. It is also quite conspicuous in the sensitivity curve (see bottom panel of Fig. 3.20). The peak appears to be due to a narrow but very extended filament aligned along the survey's length in both longitude and latitude (see also Section 3.5.3).

The second panel covers the longitude range of $270° \leq \ell \leq 280°$. I see distinct features corresponding to higher redshift structures in Vela–SMGPS. This includes the significant clump observed at velocities of $14000 - 16000$ km s^{-1} in Fig. 3.20, which is also visible in the other panels at velocities of $14000 - 15000$ km s^{-1}. Furthermore, two additional prominent peaks related to the VSCL ($V_{\rm hel} > 16000$ km s^{-1}) stand out over the predicted counts from S45. The counts are roughly 2.8 times higher than expected for the velocity range of $17000–18000$ km s^{-1}, and nearly 3.6 times higher for the range of $19000 - 20000$ km s^{-1}. This closely matches the longitude range ($270° - 280°$) of the first Wall (W1) in VSCL, found from optical spectroscopy at latitudes $|b| \gtrsim 7°$ (KK2017). There is a hint of the second higher redshift Wall (W2) visible around $21000 - 22000$ km s^{-1}. The second Wall is, however, quite prominent in the last panel, $260° \leq \ell \leq 270°$, with counts that are roughly 2.5 times higher than those in the simulations.

3.6.2 LSS crossing the ZOA

I now look at the on-sky distributions of the newly discovered galaxies in a sequence of velocity intervals and discuss the unveiled LSS in connection to known LSS above and below the ZOA. Figures 3.22a and 3.22b present a total of five on-sky (2D) distributions, each spanning a velocity range of $\Delta v = 4500$ km s^{-1}. The recently identified H I galaxies are located within black dashed boxes that demarcate the survey area of Vela–SMGPS. Symbolized by cyan, green, and

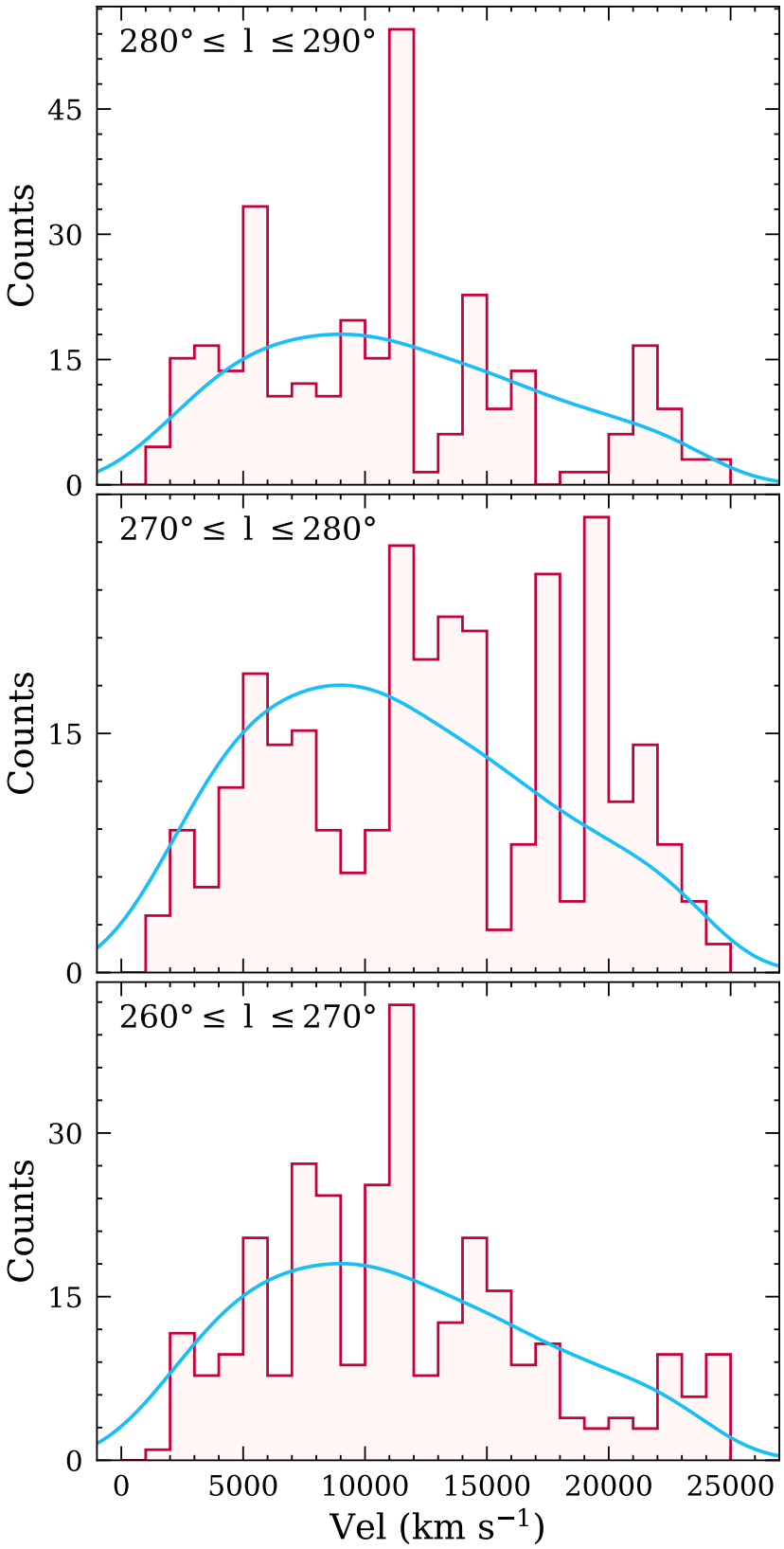

Figure 3.21: Velocity distribution histograms similar to Fig. 3.18, where the three different panels subsample distinct longitude ranges: $280° \leq \ell \leq 290°$, $270° \leq \ell \leq 280°$, and $260° \leq \ell \leq 270°$.

blue, each 1500 $\mathrm{km\,s^{-1}}$ bin represents the closest to the highest velocity bin within the respective panel. Grey contour lines, representing DIRBE/IRAS extinction contours (Schlegel et al., 1998; Schlafly & Finkbeiner, 2011) at $A_{\mathrm{B}} = 3\overset{\mathrm{m}}{.}0$, highlight regions where the ZOA is opaque to optical galaxies (e.g., Woudt & Kraan-Korteweg, 2001). I display redshift wedges alongside the on-sky plots since galaxies that appear spatially aligned in the sky might not share the same alignment in redshift space. An investigation of both displays simultaneously allows a comprehensive examination of the galaxy clustering and density peaks which will be assessed as well with the peaks seen in Figs. 3.20 and 3.21.

I will start from the nearest velocity bin in Fig. 3.22a:

(*2000 < V_{hel} < 6500 km s^{-1}*): a noticeable concentration of cyan dots ($2000 - 3500$ $\mathrm{km\,s^{-1}}$) is centered around $\ell \sim 280° \pm 4°, b \sim 0°$ (see red circle). This spatial arrangement hints at a potential overdensity which is subtly reflected in the second panel of Fig. 3.21 (as well as the 2000–4000 $\mathrm{km\,s^{-1}}$ range). An alignment of blue points at ~3000 $\mathrm{km\,s^{-1}}$ in the wedge diagram provides further support. This could be the signature associated with the filamentary structure known as the Hydra/Antlia extension (Kraan-Korteweg et al., 1995; Kraan-Korteweg, 2000), which crosses the ZOA at these coordinates.

A second prominent peak is observed in all panels of the histograms in Fig. 3.21 at $5000 - 6000$ $\mathrm{km\,s^{-1}}$. In the on-sky plot, I observe green and blue dots dispersed across almost the entire 90 $\mathrm{deg^2}$ region. However, the structure is not yet clear enough in the accompanying wedge diagram to draw any definitive conclusions.

The upper right panel of the on-sky plot (*6500 < V_{hel} < 11000 km s^{-1}*) exhibits fewer pronounced features. Nevertheless, I observe a peak overdensity at $7000 - 9000$ $\mathrm{km\,s^{-1}}$ in the last panel of Fig. 3.21, specifically within the $260° \leq \ell \leq 270°$ longitude range. If we extend the region to $\ell < 275°$ and compare it to the wedge diagram, I note a filament from $260° \leq \ell \leq 277°$, followed by an underdense region up to $\ell \sim 282°$. The concentration around $285° \leq \ell \leq 290°$ at $6000 - 8000$ $\mathrm{km\,s^{-1}}$ may well be linked to the cluster AS639 ($280°, +6°, 6000$ $\mathrm{km\,s^{-1}}$; Stein 1996).

In the bottom left panel (*11000 < V_{hel} < 15500 km s^{-1}*), the distribution of galaxies in the velocity range of $11000 - 12500$ $\mathrm{km\,s^{-1}}$ (cyan dots) is most remarkable. It spans the entire longitude range of $\Delta\ell = 30°$ within the survey area. This filament is evident as a highly significant peak present in all the panels of Fig. 3.21. The on-sky plot and wedge unveil a narrow filament at constant velocity lying behind the inner ZOA. The filament is estimated to have a width of ~500 $\mathrm{km\,s^{-1}}$ (~7 Mpc) and an approximate length of 90 Mpc at ~12000 $\mathrm{km\,s^{-1}}$.

Upon closer examination of the wedge slice, it looks like this structure could potentially consist of two intersecting filaments, possibly crossing between $270° \leq \ell \leq 280°$. One filament from $\ell \sim 275° - 290°$ with another one extending in the entire longitude range of the survey.

To gain a more in-depth understanding of the intricate distribution of these potential narrow filaments, I analyzed the new Vela–SMGPS in context to known LSS data from the literature in the surrounding area ($245° < \ell < 305°$, $|b| < 25°$). These include data from HyperLEDA (Paturel et al., 2003), 2MRS (Huchra et al., 2012; Macri et al., 2019), combined with unpublished redshift data from AAOmega+2dF, SALT, OPTOPUS, and 6dF in the Hydra/Antlia region (Kraan-Korteweg, priv. comm), as displayed in the bottom left panel of Fig. 3.22a. The clustering of green dots ($12500 - 14000$ km s^{-1}) appears to traverse through Abell clusters AS601 ($259.90°, -18.89°, 13221$ km s^{-1}) and AS606 ($267.01°, -12.33°, 11692$ km s^{-1}), also known as CIZA J0757.7–5315 (Ebeling et al., 2002). Its trajectory suggests a ZOA crossing around $275° \leq \ell \leq 280°$ (indicated by the red circle), continuing toward positive latitudes above the GP and slightly higher redshifts (blue dots). Another less prominent filamentary structure seems to lie just below that wall – its potential extent indicated by the thin dashed line in the on-sky plot. Two further galaxy concentrations situated at $\ell \sim 265°$ and $270°$ (blue points in magenta box) show no obvious links with known structures. The follow-up MeerKAT survey designed to fill the gap in the inner ZOA at $|b| \lesssim 7°$, namely the Vela–H I (see Chapter 4) should provide further insight into how these overdensities are linked to LSS.

We now turn our attention to the structures at the highest velocity intervals (*15500 < V_{hel} < 24500 km s^{-1}*), illustrated in Fig. 3.22b. This specific redshift incorporates the volume of the Vela Supercluster ($\ell = 272.5° \pm 20°$, $b = 0° \pm 10°$, 19500 ± 3500 km s^{-1}, KK2017). As before, I will take into account the on-sky distributions of the galaxies and a zoomed-in wedge plot (Fig. 3.22b), as well as the velocity histograms in Fig. 3.21.

In the upper left panel (*15500 < V_{hel} < 20000 km s^{-1}*), a distinct clustering of green dots ($17000 - 18500$ km s^{-1}) is observed, concentrated primarily around $\ell \sim 270° - 277°$ (light green rectangle). This marks the identified main VSCL Wall (W1). Figure 3.21 already reveals a density enhancement with its higher-than-predicted number of detections within this specific velocity and longitude range. Additionally, a segment of the second Wall (W2) at higher velocities (blue dots at $18500 - 20000$ km s^{-1}) is noted in a similar region ($\ell \sim 272° - 280°$, indicated by the blue rectangle), with a higher density peak towards $\ell \sim 277°$. The latter is the highest density peak enhancement when compared to simulations in the third panel of Fig. 3.21. These data supports the significant prominence of the two VSCL walls within the inner ZOA.

As we transition to the lower left panel (*20000 < V_{hel} < 24500 km s^{-1}*) to investigate W2, around 22000 km s^{-1}, a consistent pattern emerges. The clustering of points, although more

diffuse, indicates the presence of a broader and less compact wall. With the cyan and green dots converging around $\ell \sim 272° - 278°$, and $V_{hel} \sim 20000 - 23000$ km s^{-1} (marked by the intersection of the cyan and green rectangles). This coincides with the low peak in the last two panels of Fig. 3.21. It is less notable compared to W1. Interestingly, the representation of the walls in the wedge plot (see red arrows) strikingly mirrors the structures identified on both sides of the ZOA as seen in Fig. 3 of the VSCL discovery paper (KK2017).

Consequently, our findings are in support of the existence of clear overdensities associated with the surmised walls of the VSCL, W1 at ∼18500 km s^{-1} and W2 at ∼21500 km s^{-1}, and point in the approximate direction of the core of a substantial overdensity as derived from independent reconstructions (Sorce et al., 2017; Courtois et al., 2019). These structures might cross in the inner ZOA around $272° \leq \ell \leq 278°$ (see orange circle in the wedge), thus reinforcing the findings presented by KK2017.

Even with the addition of new SMGPS data, notable in the on-sky plots is the paucity of data at intermediate latitudes ($1.5° \leq |b| \leq 7°$), which makes it difficult to comprehend the dynamics of the inner VSCL, estimate its overdensity, and visualize the morphology of the walls and any potential merging process in detail. The forthcoming MeerKAT Vela–H I survey, discussed in the following chapter, will present newly obtained H I data similar to the SMGPS, but bridging the gap between the SMGPS and the optical spectroscopic data ($1.5° \leq |b| \leq 7°$) in the VSCL region. These will allow an in-depth discussion into how these overdensity peaks in the inner ZOA from Vela–SMGPS connect with known LSS at much higher latitudes above $|b| \gtrsim 7°$.

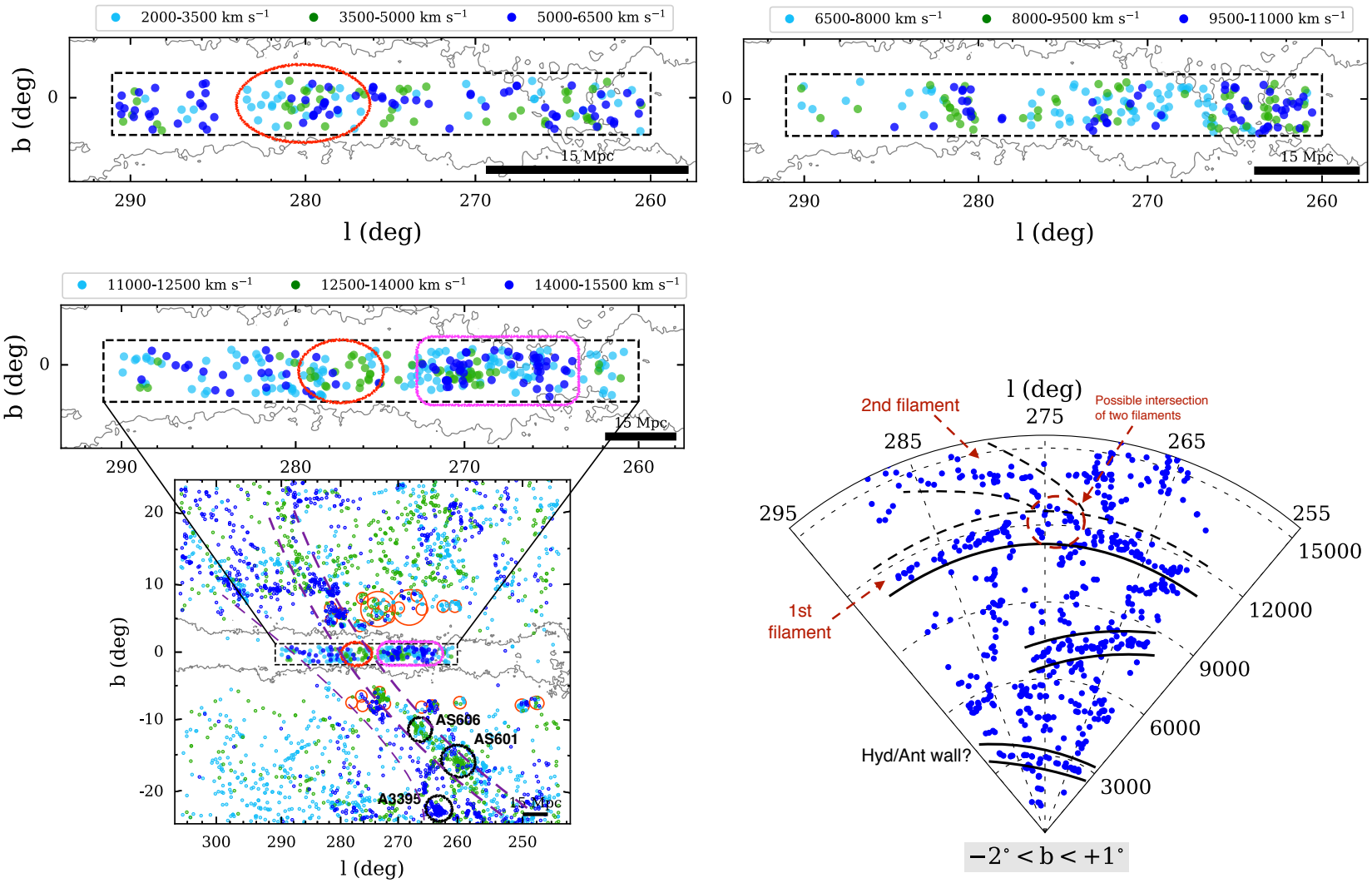

Figure 3.22a: On-sky distributions of galaxies in the Vela–SMGPS survey, divided into three redshift intervals within the nearby velocity range $2000 < V_{\rm hel} < 15500$ km s^{-1}. Each panel spans $\Delta v = 4500$ km s^{-1}, with cyan, green, and blue indicating velocity bins increasing in steps of 1500 km s^{-1}. The black dashed box highlights the newly detected H I galaxies. The bottom left panel (velocity interval $11000 - 15500$ km s^{-1}) is accompanied by the on-sky plot of its surrounding area ($245° < \ell < 305°$, $|b| < 25°$), and includes ancillary data with known redshifts from HyperLEDA, 2MRS, and KK2017. The latter is shown inside the orange open circles. Grey contour outlines dust extinction based on DIRBE maps (Schlegel et al., 1998; Schlafly & Finkbeiner, 2011) at $A_{\rm B} = 3\overset{\rm m}{.}0$. Each on-sky plot has a 15 Mpc scale bar at its bottom right corner. An accompanying wedge diagram limited to $V_{\rm hel} < 15500$ km s^{-1} is displayed in the bottom right panel.

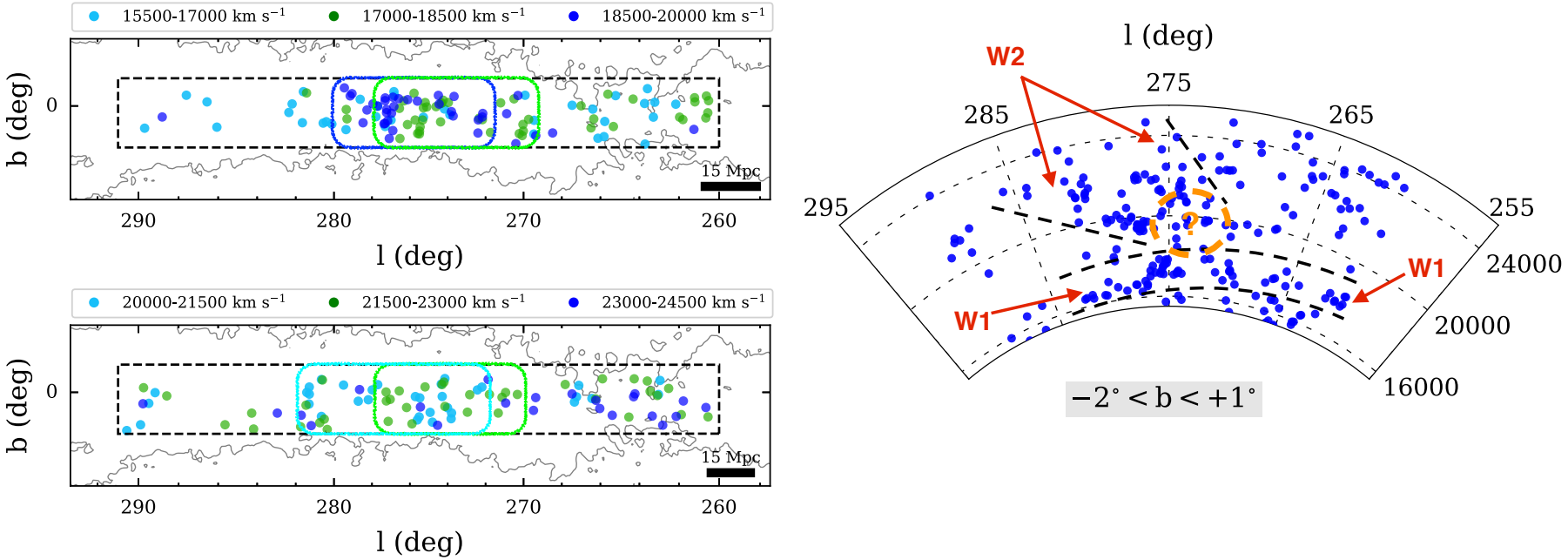

Figure 3.22b: Continuing from Fig. 3.22a, this figure presents two velocity bins with $\Delta v = 4500$ km s^{-1} in the left panels, covering the higher redshift range ($V_{\rm hel} > 15500$ km s^{-1}). The right panel features a wedge diagram within $15500 < V_{\rm hel} < 24500$ km s^{-1}.

3.7 Conclusions

This chapter presents the H I data extracted from the SARAO MeerKAT Galactic Plane Survey, centered on the Vela region (Vela–SMGPS; $260^\circ \leq \ell \leq 290^\circ, -2^\circ \leq b \leq 1^\circ$). With a velocity coverage reaching out to $V_{\rm hel} \sim 25000$ km s^{-1}, and a sensitivity of $\sim$0.39 mJy beam^{-1}, I have successfully cataloged galaxies along a narrow 3° strip covering the most opaque part of the ZOA. Using SoFiA in conjunction with a visual verification process, I identified 843 H I galaxies across the 10 contiguous mosaics covering the survey area. Among them, only 39 possessed ancillary redshift information for independent comparison, having previously been detected by the HIZOA survey. Six of these sources were found to consist of two or more counterparts (illustrated in Fig. B.2). Notably, Vela–SMGPS successfully recovered the most H I-massive spiral, HIZOA J0836-43, exhibiting consistent measurements with ATCA and HIZOA. The H I properties of the galaxies in common are also in excellent agreement and exhibit a linear relation, consistent – within the errors – with a one-to-one relation over the entire range of the parameters. Following our expectations, we detect H I sources well below the characteristic $M^*_{\rm HI}$ out to the edge of Vela–SMGPS.

A non-homogeneous distribution has been revealed from the comparison of the velocity distribution of Vela–SMGPS to the expectations of a homogeneously filled volume at a sensitivity threshold of 0.45 mJy beam^{-1} (S45). Our analysis pinpointed a high degree of clustering showing galaxy counts with a factor $\sim 2-4$ times higher compared to S45 in the velocity ranges of $5000-6000$ km s^{-1} ($\ell \sim 280^\circ - 290^\circ$), $11000-12000$ km s^{-1} (full $\Delta\ell \sim 30^\circ$), $17000-20000$ km s^{-1} and $21000-22000$ km s^{-1} ($\ell \sim 270^\circ - 280^\circ$), and $22000-25000$ km s^{-1} ($\ell \sim 260^\circ - 270^\circ$). The last two peaks of overdensity align with the position and redshift space of the previously identified two walls of the VSCL, providing strong evidence for the existence of their continuity within the surveyed volume. A thorough 3D distribution analysis of the notable density enhancements observed in the velocity distribution has resulted in several key observations of both various new structures, as well as confirmation of suspected links to known structures beyond the ZOA, such as:

- A distinct signature at 3500 km s^{-1}, substantiating the surmised Hydra/Antlia wall crossing into the ZOA at approximately $\ell \sim 280^\circ$.
- The identification of one or more intersecting filaments connecting structures both above and below the GP within $270^\circ \leq \ell \leq 280^\circ$, $V_{\rm hel} \sim 12000$ km s^{-1}.
- A glimpse of two wall-like overdensities in VSCL, with both W1 ($16000-19000$ km s^{-1}) and W2 ($19000-23000$ km s^{-1}) potentially crossing the GP at $\sim$20000 km s^{-1} within the longitude range of $272^\circ \leq \ell \leq 278^\circ$.

I found a previously uncharted population of highly obscured galaxies, particularly at the lowest latitudes and within an unprecedented redshift range for blind systematic H I surveys in the ZOA. These results clearly demonstrate the power of MeerKAT in providing a new window using systematic H I surveys to explore the innermost ZOA despite extreme obscuration as well as continuum source contamination.

In view of the success of this endeavor, we have launched a similar survey using MeerKAT for a wider systematic H I survey to bridge the gap between Vela–SMGPS and previous research extending to higher latitudes. This survey has meanwhile been concluded. Its analysis together with the results presented here is expected to enable us to connect structures above and below the GP, fully trace the extent and morphology of the hidden part of VSCL, and measure its effect on the cosmic flow fields.

Acknowledgements

We would like to extend our gratitude to Gyula Józsa for his support in running CARACal, and Sarah White for her contributions to the development of the mosaicking module in CARACal.

The MeerKAT telescope is operated by the South African Radio Astronomy Observatory, which is a facility of the National Research Foundation, an agency of the Department of Science and Innovation. We acknowledge the use of the Ilifu cloud computing facility, a partnership between the University of Cape Town, the University of the Western Cape, the University of Stellenbosch, Sol Plaatje University, the Cape Peninsula University of Technology and the South African Radio Astronomy Observatory. The Ilifu facility is supported by contributions from the Inter-University Institute for Data Intensive Astronomy (IDIA a partnership between the University of Cape Town, the University of Pretoria, the University of the Western Cape and the South African Radio Astronomy Observatory), the Computational Biology division at UCT and the Data Intensive Research Initiative of South Africa (DIRISA). We also applied the CARTA (Cube Analysis and Rendering Tool for Astronomy) software (DOI 10.5281/zenodo.3377984) in our analysis.

This paper makes use of the MeerKAT data with Project IDs: SSV-20180721-FC-01 and SCI-20180721-SP. The data published here have been reduced using the CARACal pipeline (`https://caracal.readthedocs.io/en/latest/`).
SHAR, RCKK, HC, NS, SK, and DJP gratefully acknowledge support by the South African Research Chairs Initiative of the Department of Science and Technology and the National Research Foundation.

We acknowledge the usage of the HyperLeda database (`http://leda.univ-lyon1.fr`). This research has made use of: the NASA/IPAC Extragalactic Database (NED), which is operated by the Jet Propulsion Laboratory, California Institute of Technology, under contract with the National Aeronautics and Space Administration; the NASA's Astrophysics Data System Bibliographic Services; the VizieR catalogue access tool, CDS, Strasbourg, France (DOI:10.26093/cds/vizier). The original description of the VizieR service was published in 2000, A&AS 143, 23. This publication utilizes data products from: the Two Micron All Sky Survey, which is a joint project of the University of Massachusetts and the Infrared Processing and Analysis Center/California Institute of Technology, funded by the National Aeronautics and Space Administration and the National Science Foundation; the Wide-field Infrared Survey Explorer, which is a joint project of the University of California, Los Angeles, and the Jet Propulsion Laboratory/California Institute of Technology, funded by the National Aeronautics and Space Administration. We also used Astropy, a community-developed core Python package for Astronomy (Astropy Collaboration et al., 2013, 2018).

chapter 4

Revealing hidden structures in the Zone of Avoidance – a blind MeerKAT H I Survey of the Vela Supercluster

Abstract

I conducted the MeerKAT Vela Supercluster survey, named Vela–H I, with the aim of bridging the gap between the Vela SARAO MeerKAT Galactic Plane Survey (Vela–SMGPS, $-2^\circ \leq b \leq 1^\circ$), and optical and near-infrared spectroscopic observations of the Vela Supercluster (hereafter Vela–OPT/NIR) at $|b| \gtrsim 7^\circ$. Covering coordinates from $263^\circ \leq \ell \leq 284^\circ$ and $1^\circ \leq b \leq 6.2^\circ$ above, while $-6.7^\circ \leq b \leq -2^\circ$ below the Galactic Plane (GP), I sampled 667 Nyquist fields spread across a total area of ~242 deg^2. With a beam size of $38'' \times 31''$, Vela–H I achieved a sensitivity of $\langle \text{rms} \rangle = 0.74$ mJy beam^{-1} at 44.1 km s^{-1} velocity resolution over ~67 hours of observations. I catalogued 719 galaxies, with only 211 (29%) previously documented in the literature, primarily through the HIZOA, 2MASX, and WISE databases. Among these known galaxies, only 66 provided optical spectroscopic redshift information. I found marginal differences of less than one channel resolution for all galaxies in common between HIZOA and Vela–SMGPS. I obtained a mean difference of 70 ± 15 km s^{-1} between optical and H I velocities, in agreement with the optical velocities error margins. Combining data from Vela–SMGPS, Vela–H I, and Vela–OPT/NIR confirmed the connection of the Hydra/Antlia filament across the GP and revealed a previously unknown diagonal wall at $6500-8000$ km s^{-1}. Vela–H I reinforces the connection between W1 at $18500-20000$ km s^{-1} and the inner ZOA. Similarly, W2 seems to traverse the GP at lower latitudes within $270^\circ \leq \ell \leq 279^\circ$, where it appears that both walls seem to intersect, jointly covering the velocity range $18500-21500$ km s^{-1}.

4.1 Introduction

The recently discovered Vela Supercluster (hereafter VSCL) is of particular interest among the large-scale structures (LSS) bisected by the ZOA because of its close alignment with the apex of the residual bulk flow ($\ell \sim 272.5° \pm 20°, |b| < 10°$), expected to originate from distances beyond $cz \geq 16000$ km s^{-1}. As part of a wide-area campaign aiming to explore LSS along the entire 360° circle of the ZOA and learn more about the overall bulk flow, spectroscopic observations from Kraan-Korteweg et al. 2017 (or KK2017) encompassing the region that contains the VSCL, have revealed it as an extended massive overdensity with multibranching filaments (Einasto et al., 2011a). Its mass excess was estimated to contribute to at least 50 km s^{-1} to the motion of the Local Group (LG). However, optical and near-infrared (NIR) data do not provide sufficient information to chart the overdensity and its surmised walls due to its incompleteness at $|b| < 5°$. Nonetheless, independent analyses using kinematic models have hinted at the presence of the dense core of VSCL deep within the ZOA (Sorce et al., 2017; Courtois et al., 2019).

As presented in Chapter 3, the results of the first extensive exploration to map the VSCL in H I using data from the Vela-SARAO MeerKAT Galactic Plane survey (Vela–SMGPS) has proven to be highly successful. This survey spans a region of 90 deg^2 along a 3° narrow strip centered on $\ell \sim 275°$, and identified a total of 843 heavily obscured galaxies. Most importantly in context to the VSCL, signatures of the obscured walls at $16000-19000$ km s^{-1} (W1) and $19000-23000$ km s^{-1}(W2) were identified at the lowest latitudes.

I therefore conduct a blind systematic interferometric survey referred to as the MeerKAT Vela Supercluster survey or Vela–H I in this study. With its 667 pointings distributed both above and below the GP, covering the Galactic coordinates $263° \leq \ell \leq 284°, |b| \lesssim 6.7°$, the large survey area ∼242 deg^2 aims to achieve the following three main objectives:

(i) The Vela–H I survey, with its sensitivity and depth out to 260 h^{-1} Mpc, covers the area that bridges the gap between Vela–SMGPS (Chapter 3), and ancillary data in the more transparent surroundings at latitudes $|b| \gtrsim 7°$, where data availability is scarce. These OPT/NIR data include published data from KK2017 (AAOmega+2dF+SALT), along with additional redshift data provided by OPTOPUS and 6dF in the Hydra/Antlia region that remain unpublished (Kraan-Korteweg, priv. comm). I will collectively refer to the published and unpublished datasets as Vela–OPT/NIR for convenient reference in future analyses.

(ii) To combine the results obtained from Vela–H I with those from Vela–SMGPS, encompassing various structures up to 25000 km s^{-1} and filling in the gaps in the missing part of the VSCL walls at much higher latitudes. The objective is to obtain a complete view of the full extent of the VSCL and its morphology at $V_{\rm hel} \sim 19500 \pm 3500$ km s^{-1}.

(iii) Apart from higher redshift VSCL, its sensitivity will provide insight into many nearby structures that were either incompletely mapped or previously unknown.

This chapter is organized as follows. I present the observing strategy of Vela–H I in Section 4.2. Section 4.3 delves into the techniques and steps employed for H I data processing, including data reduction, mosaic generation, and strategies for source identification. The resulting catalog is presented in Section 4.4, accompanied by a thorough internal assessment of sample reliability and survey performance. Additionally, I compare properties with cross-matched data from other surveys, in H I, or multi-wavelength. In Section 4.5, I explore the alignment of the newly discovered galaxies with LSS and analyze the identified structures in the local Universe, particularly when combined with Vela–SMGPS. A comprehensive summary of our findings is then provided in Section 4.6.
Throughout this work, all velocities are in the heliocentric optical convention ($V_{\rm hel} = cz$). I adopt a standard cosmological model with $H_0 = 70$ km s^{-1} Mpc^{-1}, $\Omega_{\rm m} = 0.3$, and $\Omega_\Lambda = 0.7$.

4.2 Survey design and observation strategy

Vela–H I was observed using the full MeerKAT array (Jonas & MeerKAT Team, 2016) in 8 sessions between August 15 and October 30, 2021 (MeerKAT Open-Time Proposal ID: SCI-20210212-SR-01). The observations were carried out with an array of 60 to 63 antennas using the 4K spectral line correlator mode in L-band ($856 - 1712$ MHz bandwidth), with visibilities recorded every 8 seconds. I used the coarse channel spacing of 209 KHz, corresponding to a velocity resolution of 44.1 km s^{-1} at $z = 0$ and 46.8 km s^{-1} at the VSCL distance ($V_{\rm hel} \sim 18000$ km s^{-1}). This setup has been found to be sufficient for detecting and extracting H I-signatures of normal spiral galaxies with typical linewidths of $w_{50} > 150$ km s^{-1} as per our results from the Vela–SMGPS (see Chapter 3).

Vela–H I covers two strips, each spanning approximately $\Delta l \times \Delta b \sim 21^\circ \times 6^\circ$ on either side of the GP. With a MeerKAT Primary Beam Full Width Half Maximum (FWHM) of $\sim 1.02^\circ$, the survey consists of 352 and 315 fields for the strips above and below the GP, respectively, as illustrated in Fig. 4.1. The area between $-2^\circ \leq b \leq 1^\circ$ was already surveyed by Vela–SMGPS. To ensure uniform sensitivity across the survey area, I used a Nyquist sampling configuration with a spacing of $r = 0.671^\circ$.

The observations were divided into 8 sessions, referred to as 'blocks', each having been observed between 7.6 to 9 hours. While the majority of the data collection occurred at night, some data in each block were observed during the day. The data captured during daylight hours were susceptible to solar radio-frequency interference (RFI) and required special flagging strategies (see Appendix C.1.2).

The strip above the GP was observed in four blocks, denoted by suffix 1, with field prefixes

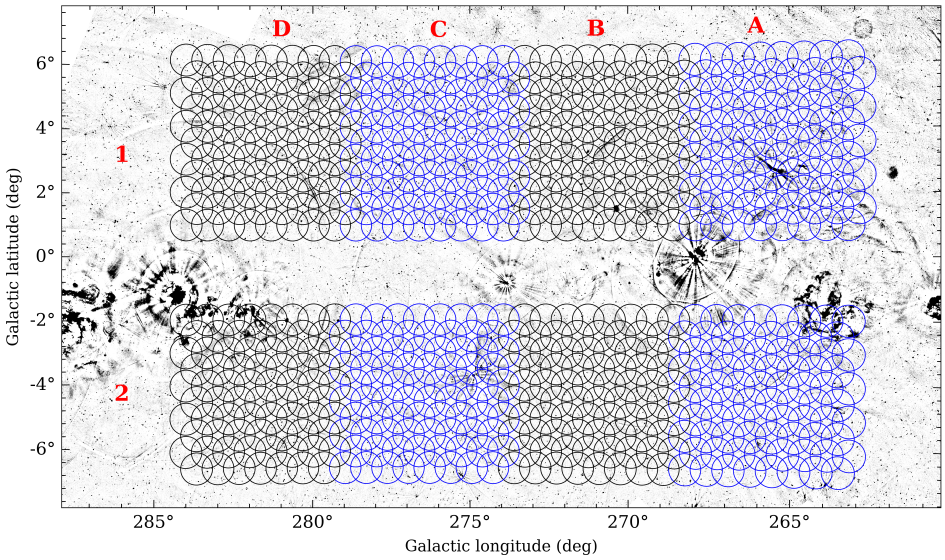

Figure 4.1: The 242 deg^2 area covered by the MeerKAT Vela Supercluster survey, overlayed on a grayscale map from the Sydney University Molonglo Sky Survey (SUMSS; Bock et al. 1999) continuum map. The 667 individual pointings are distributed into 8 observing blocks (A1, A2, B1, B2, C1, C2, D1, and D2) above and below the GP. The gap between the two sets of pointings is the surveyed area of Vela–SMGPS in Chapter 3.

ranging from A to D in increasing longitudes. Each block consists of 88 fields. The strip below the GP was observed in another set of four blocks, labelled with suffix 2, which contained 80 fields each, except for block D2 (lower left), conformed of 75 fields. Within a block, each target field was visited twice during a cycle of observation, with each scan lasting 150 seconds. Bandpass and flux calibrators were observed for 3 minutes at the beginning, after the first cycle, and at the end of each run. Phase calibrators were observed for 2 minutes every 25 minutes, repeated in general after 10 fields had been observed. The complete survey was performed in approximately 56 hours of on-source time, respectively 67.44 hours in total, including overhead. Details of the observations for each block, in ascending order of the observed area, are provided in Table 4.1.

Table 4.1: Vela–H I observing blocks overview

Obs Date (UT start)	Block ID	ℓ (deg)	b (deg)	Fields	Track (h)	N_{ant}	Primary calibrators (gaincal)	Secondary calibrators (fluxcal, bpcal, delaycal)	Notes
2021-08-22	1629602495 (A1)	$263° \leq \ell \leq 269°$	$1° \leq b \leq 6.2°$	88	8.88	61	J0828-3731	J0408-6545	*a*
2021-10-01	1633050310 (B1)	$269° \leq \ell \leq 274°$	$1° \leq b \leq 6.2°$	88	8.84	61	J0825-5010	J0408-6545	*a*
2021-10-30	1635552081 (C1)	$274° \leq \ell \leq 279°$	$1° \leq b \leq 6.2°$	88	8.93	61	J0825-5010	J0408-6545, J1939-6342	*a*
2021-09-04	1630723298 (D1)	$279° \leq \ell \leq 284°$	$1° \leq b \leq 6.2°$	88	8.94	61	J0825-5010, J0906-6829	J0408-6545, J1939-6342	*a*, *b*
2021-08-15	1628997934 (A2)	$263° \leq \ell \leq 269°$	$-6.7° \leq b \leq -2°$	80	8.11	60	J0828-3731	J0408-6545	*a*
2021-10-24	1635037887 (B2)	$269° \leq \ell \leq 274°$	$-6.7° \leq b \leq -2°$	80	8.06	63	J0825-5010	J0408-6545, J1939-6342	*a*
2021-10-02	1633134084 (C2)	$274° \leq \ell \leq 279°$	$-6.7° \leq b \leq -2°$	80	8.09	61	J0825-5010	J0408-6545	*a*
2021-09-12	1631417493 (D2)	$279° \leq \ell \leq 284°$	$-6.7° \leq b \leq -2°$	75	7.59	61	J0906-6829	J0408-6545	*a*, *c*

[a] This data is affected by the short track bug (see Appendix C.1.1).
[b] M039 (V-pol) shows dips in its power spectrum and will likely need to be flagged.
During the last scan, M058's data were flagged since it did not lock on target.
[c] There was a wind stow event at the end of the observation.

4.3 H I data processing

I closely followed the strategy to Vela–SMGPS for data transfer, reduction procedures, software usage, imaging and H I source finding. Modifications were tailored to suit the specific requirements of the Vela–H I dataset, as detailed in the upcoming sections.

4.3.1 Data reduction

As in Vela–SMGPS, I only retrieved the frequency range of $1308-1430$ MHz with their parallel-hand visibilities (HH-VV) for each observation from the SARAO archive[1] for transfer to the `Ilifu` cloud computing facility[2]. This frequency range was selected for its flat, mostly RFI-free band, excluding bandpass roll-offs, and its high-redshift end corresponding to $z \simeq 0.08$ ($cz \sim 25000$ km s^{-1}) over the full extent of VSCL. The Containerised Automated Radio Astronomical Calibration `CARACal`[3] (Józsa et al., 2020) was used for reducing the Vela–H I observations. The pipeline that was executed on each dataset, involved several steps such as automatic flagging, cross-calibration, self-calibration, Doppler-tracking correction, continuum subtraction, imaging, and mosaicking. Unlike Vela–SMGPS, where a single `Ilifu` node processed a block, handling an entire block of 88 fields in Vela–H I is computationally expensive, and could take several weeks to complete. To enhance efficiency, I adopted parallel processing with ten nodes, each managing eight fields, reducing the processing time to around three to four days per block.

Following cross-calibration, the pipeline generated diagnostic plots of the calibrators and target using `shadeMS`[4]. This enabled a swift assessment of the quality of calibrated visibilities and helped identify any remaining RFI for flagging. I encountered two distinct issues during the inspection of cross-calibrated visibilities' diagnostic plots: short-track bugs and solar interference. Despite setting `Sunblocker`[5] to `True` during the imaging step, the latter issue persisted. This led us to incorporate an additional manual flagging step (see residual RFI flagging procedures in Appendix C.1) prior to the automatic flagging procedure in the pipeline, which however required a complete re-run of the reduction process.

4.3.2 Imaging and mosaicking

I employed `WSClean` (Offringa et al., 2014) for imaging, with a pixel size of $3''$, Briggs $r = 0$, and a UV-taper of $15''$. This produced a total of 667 H I cubes, each composed of 570 channels with a width of 210 kHz after Doppler correction. After some adjustments, including primary

[1] https://archive.sarao.ac.za/
[2] www.ilifu.ac.za
[3] https://caracal.readthedocs.io/
[4] https://github.com/ratt-ru/shadeMS
[5] https://github.com/gigjozsa/sunblocker

beam (PB) correction and resizing the radii of the H I cubes to a normalized PB sensitivity cut-off of 0.2 (equivalent to $0.8°$), the partially overlapping H I cubes were prepared for mosaicking.

The H I cubes were extracted per pointing. Each of the eight observing blocks, consisting of 80 to 88 cubes, was divided into four mosaics labeled A to D. Above the GP, mosaics were constructed based on 27 contiguous H I cubes. For the blocks below the GP, the initial two mosaics (with suffixes A and B) were composed of 22 cubes, while the remaining two (C and D) contained 27 cubes each. This arrangement resulted in an on-sky coverage of approximately $3.5° \times 4°$ or $3.5° \times 3.5°$ per mosaic, with an overlap of $\Delta\ell = \Delta b \sim 1.5°$ (except $\Delta\ell \sim 2°$ for D2) for mosaics within the same block, and $\Delta\ell \sim 0.75°$ overlap between two mosaics from two adjacent blocks. These overlapping regions were essential for capturing extended sources that might be detected at the edge of the mosaic and was used at the same time for conducting an internal data quality assessment based on the properties of detected galaxies in these regions (see Section 4.4.3). The overall mosaic layout is illustrated in Fig. 4.2.

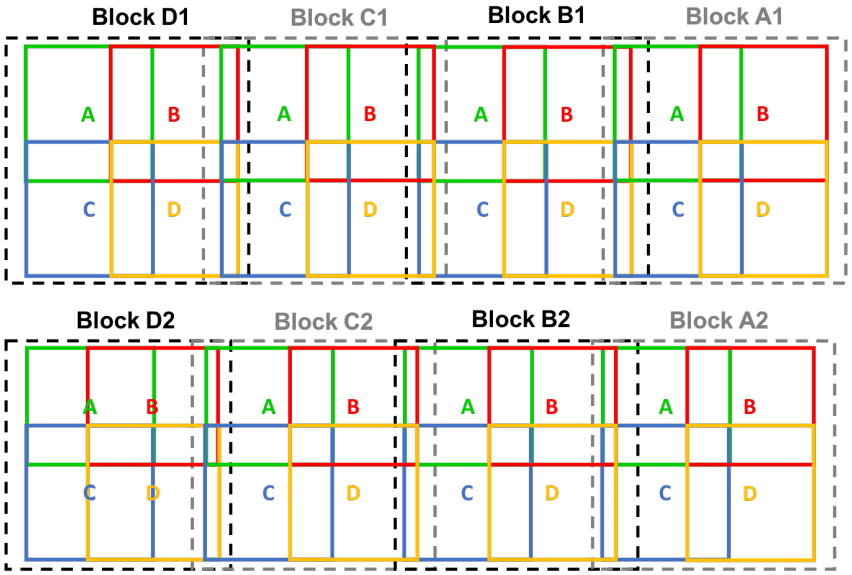

Figure 4.2: Mosaicking configuration of Vela–H I. Each block is indicated alternatively by black or grey dashed rectangles and subdivided into four partially overlapping tiles labeled A to D.

In total, 32 mosaics were produced, comprising 16 consecutive ones above and below the GP, respectively. These mosaics were generated from individual fields with rms values ranging from 0.88 to 2.57 mJy beam^{-1}. The Nyquist sampling setup of the survey has provided us with a nearly uniform central region covering approximately $3° \times 3.5°$ and $3° \times 3°$ (utilized for source finding regions). Additionally, it also facilitated a twofold increase in sensitivity after mosaicking compared to an individual field, as illustrated in Fig. C.4 of Appendix C.2. The figure showcases three subfigures presenting the RMS variations per field before solar RFI removal, after solar RFI removal, and after mosaicking, respectively. The spectral baselines of the mosaic central regions, as a function of velocity, now generally maintain a relatively flat profile with minimal

noise level fluctuations ranging from 0.68 to 1.24 mJy beam^{-1}, as displayed in Fig. 4.3. Only for a few cases do we observe increased noise levels towards the edge of the mosaic's spectral axis ($V_{\rm hel} > 24000$ km s^{-1}), or residual RFI spikes from Global Positioning Satellites (GPS), i.e., around 1375–1387 MHz (~ 8500 km s^{-1}). I excluded the high-noise region from mosaic A2B from the subsequent assessment and analysis of the survey. This region shows nearly double the noise compared to other mosaics, as indicated by the brown line in Fig. 4.3, which is possibly due to the presence of the Vela Supernova remnant ($\ell \sim 263.93°$, $b \sim -3.36°$, Green 2009) at the mosaic location. I therefore measure an average noise value of 0.74 mJy beam^{-1}.This average rms translates to an H I mass of $5{\times}10^9$ M$_\odot$ and $7.1{\times}10^9$ M$_\odot$ for a source detected at 5σ and with 200 km s^{-1} linewidth at $V_{\rm hel} \sim 17500$ km s^{-1} (Wall 1) and ~ 21000 km s^{-1} (Wall 2), respectively.

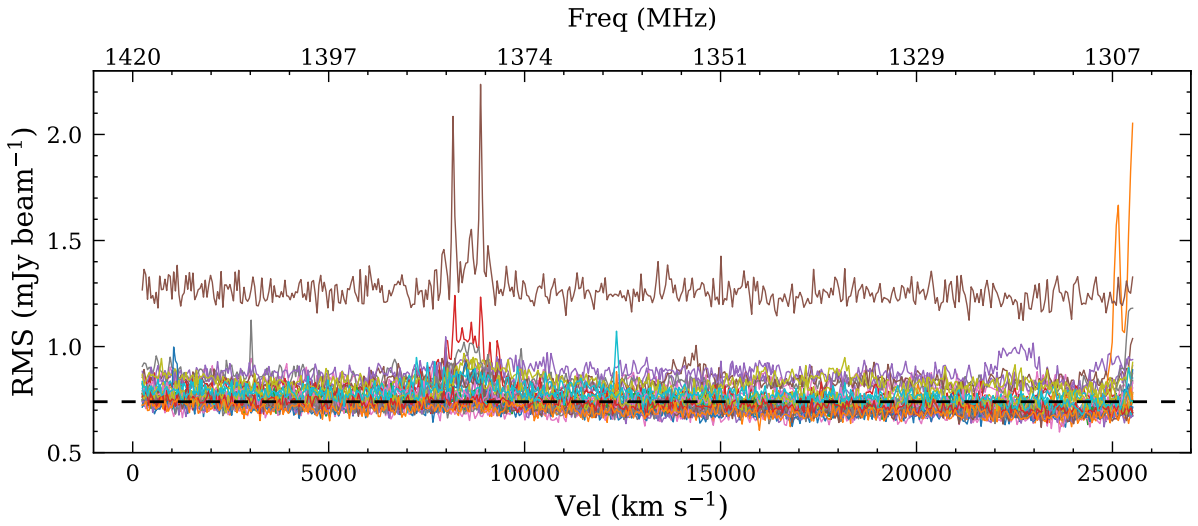

Figure 4.3: Rms versus velocity in km s^{-1} as measured through the centers of the 32 mosaics. Interference from Global Positioning Satellites can be seen in the frequency band 1375 – 1387 MHz (~8500 km s^{-1}). The average rms noise of 0.74 mJy beam^{-1} is shown by the horizontal dashed lines when excluding the high noise from the mosaic A2B (brown line), which is nearly a factor of two higher than other mosaics and shows stronger fluctuations as well.

The mosaic beam size is derived as the median value obtained from the individual beams of each input cube. The beam size information in the individual H I cubes shows only 9% minor variation across the full survey area and less than 3% across channels. An average beam size of $38''{\times}31''(\pm 3'')$ has been derived for Vela–H I (slightly larger than for SMGPS). This corresponds to a spatial resolution of about 47×39 (± 3.7) kpc at the VSCL distance ($V_{\rm hel} \sim 18000$ km s^{-1}), adequate for our scientific objectives. For comparison, the mosaicking parameters for the two systematic H I surveys, Vela–SMGPS and Vela–H I, are provided in Table 4.2.

Table 4.2: Survey parameters' comparison of Vela–H I and Vela–SMGPS

Parameter	Vela–H I	Vela–SMGPS
Date of observations	2021	2018–2020
Sky coverage	~242 deg^2	~90 deg^2
Effective area (ℓ)	$263^\circ \leq \ell \leq 284^\circ$	$260^\circ \leq \ell \leq 290^\circ$
Effective area (b)	$1^\circ \leq b \leq 6.2^\circ$, $-6.7^\circ \leq b \leq -2^\circ$	$-2^\circ \leq b \leq 1^\circ$
Integration time per pointing	~300 s	~3600 s
Velocity resolution[a]	44.11 km s^{-1}	44.11 km s^{-1}
Velocity range[b]	< 25000 km s^{-1}	< 25000 km s^{-1}
Beam size	$38'' \times 31''(\pm 3'')$	$30'' \times 27''(\pm 1'')$
Mosaic numbers	32	10
Mosaic rms	0.68–1.24 mJy beam^{-1}	0.29–0.56 mJy beam^{-1}
Mosaic mean rms	0.74 mJy beam^{-1}	0.39 mJy beam^{-1}

Note: [a] at $z = 0$. [b] H I source finding velocity range.

4.3.3 H I detections

In extensive surveys like Vela–H I, visually identifying sources becomes impractical due to the size of each mosaic, approximately 55 GB with ~5150 pix × 5000 pix × 526 chans voxels. Applying automated source-finding methods is therefore crucial. Following the approach used in Vela–SMGPS, I employed the SoFiA-2 algorithm[6] (Westmeier et al., 2021) to search for H I sources. This process was applied to all mosaics in the velocity range $250 < V_{\rm hel} < 25000$ km s^{-1}. Two different source-finding regions were defined. The first box encompasses 3600 pix × 4200 pix × 517 chans (~3.5° × 3°) for the mosaics above the GP and half of the mosaics below the GP. For the remaining half below the GP, I defined mosaics of 3600 pix × 3600 pix × 517 chans (~3° × 3°). These distinct source-finding regions, outlined by white rectangles in Fig. 4.4, have boundaries selected to maximize sensitivity in the central part while avoiding lower sensitivity at the edges of the mosaics. Additionally, some overlap between adjacent mosaics is ensured.

Apart from noise normalization through the weighting by noise cubes, I performed an additional continuum subtraction step using a polynomial of order $n = 1$ with a threshold of 2σ to eliminate residual low-level continuum emission. Subsequently, I applied SoFiA's default source-finding algorithm, Smooth and Clip (S+C) finder. In comparison to Vela–SMGPS, I introduced two additional spatial smoothing kernels of 20 and 30 pixels, equivalent to $60''$ and $90''$ angular resolution smoothing, to account for the larger beam size in our survey. However, the spectral kernels and the two-run thresholds of 3.5σ and 4σ remain consistent with Vela–SMGPS. I then merged all detected pixels with a minimum linking size of 14 pixels (slightly larger than one beam) to obtain coherent sources.

[6] https://github.com/SoFiA-Admin/SoFiA-2

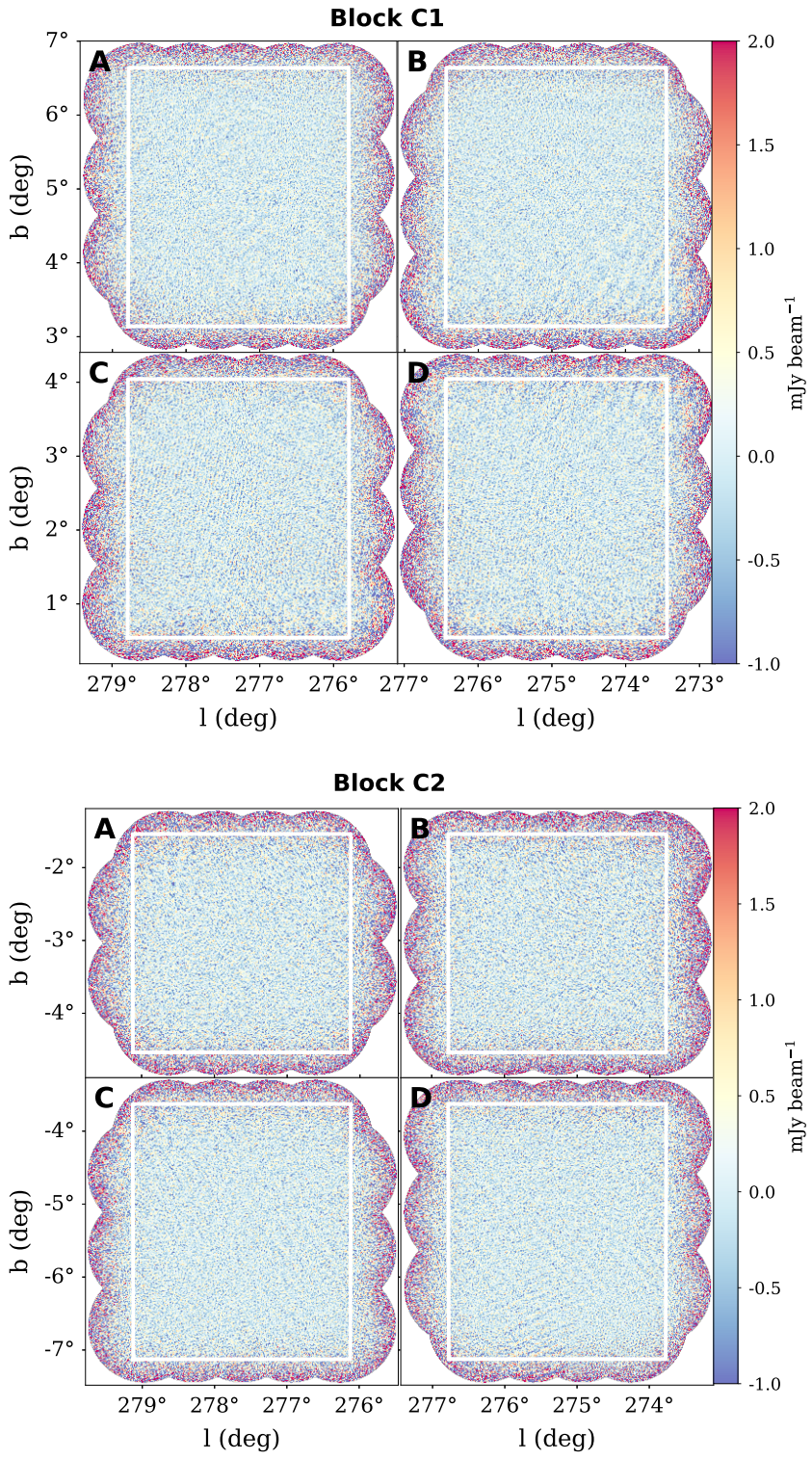

Figure 4.4: Example of source finding regions for the different mosaic configurations. The top panel illustrates regions of $\sim 3.5^\circ \times 3^\circ$ for a block of four mosaics located above the GP (e.g., block C1). The bottom panel shows two mosaics with $\sim 3^\circ \times 3^\circ$ regions (top), and the other two with $\sim 3.5^\circ \times 3^\circ$ (bottom) for a block located below the GP (e.g., block C2). The white rectangles outline the source finding regions.

For source validation, each SoFiA run produced a catalog of detected sources, including both genuine detections and false positives. To ensure accuracy, three team members independently adjudicated the sources. They meticulously assessed the catalog to eliminate false positives and categorized the remaining list as either solid or possible detections. The evaluation involved a thorough examination of various attributes, such as mom-0 and mom-1 maps (looking at the H I extent of the source and its rotation), and the global H I profile of each potential source (considering signal-to-noise ratio and baseline behavior). The assessment utilized a PYTHON script prepared by myself. Additional details on this adjudication process can be found in Chapter 3. The final results of the panels describing the source (i.e., mom-0, mom-1, global H I profile) are presented in a galaxy atlas available in Appendix C.3.

4.4 Results

In this section, I present the findings and validations of H I sources in the Vela–H I survey. This includes an overview of the catalog of detected galaxies and their derived H I parameters, an evaluation of the quality of H I data, and a comparative analysis of parameters with prior H I surveys in the ZOA. I conclude with a search for multi-wavelength counterparts and an examination of the H I properties distribution in Vela–H I.

4.4.1 The Vela–H I catalog

I identified a total of 719 H I sources. All detections with their derived H I parameters are presented in the full catalog in Table C.2 of Appendix C.2. The first page of the catalog is available in Table 4.3. Unless specified otherwise, the parameters described in the column description below are derived from the SoFiA output:

Column (1): Source identifier (VSCL–H I Jhhmmss-ddmmss) representing rounded right ascension and declination in equatorial coordinates (J2000) of the centroid position.

Column (2): Indicates the name of the mosaic to which the source belongs. It is presented in the format of the block name along with the mosaic configuration (A-D), e.g., B1C.

Columns (3) and (4): Galactic coordinates (ℓ and b) of the centroid position in degrees.

Column (5): Peak flux measured from the global H I profile in Jy.

Columns (6) and (7): Integrated flux along with its corresponding error in a unit of Jy km s^{-1}. This error value is the average standard deviation of the integrated fluxes, which are measured from four emission-free regions around the source.

Column (8): Mean local rms in mJy beam^{-1}, averaged from four emission-free regions around the detection.

Column (9): Optical heliocentric systemic velocity (V_{hel}) in km s^{-1}.

Columns (10) and (11): Linewidths (w_{20}, w_{50}) in km s^{-1}, representing the widths at which the profile achieves 20% and 50% of its peak flux density.

Column (12): Logarithm of H I Mass [$\log(M_{\rm HI}/{\rm M}_\odot)$]. No corrections to the Local Group barycenter nor for instrumental resolution were applied.

Column (13): Flags denoting the classification of detections. A flag of 1 indicates a solid detection, while 2 signifies a possible detection. Additional notations include an asterisk (*) alongside the flag, indicating that the detection was also identified in the overlapping mosaic. A double asterisk (**) denotes that the detection was found in more than two adjacent mosaics, and an exclamation mark (!) indicates a common detection with Vela–SMGPS.

Column (14): Additional notes and multi-wavelength counterparts (if available).

The notes cover various attributes:

- whether the detection's moment maps have been smoothed to a specific angular resolution (e.g., $B = 40''$),
- if its global profile shows a wiggly baseline (BL),
- its proximity to the mosaic edge (e),
- any indications of interactions or mergers (i),
- if it is located in a particularly noisy area due to the ripple caused by residual solar RFI (r),
- if it presents one or multiple companions (w.comp),
- if the measurement of w_{20} is uncertain due to baseline behavior (w_{20} unc.).

Additionally, galaxies detected in major H I, OPT, and NIR catalogs are also indicated. The methodology for identifying multi-wavelength counterparts is explained in Section 4.4.5. For galaxies found in the Parkes H I Zone of Avoidance survey (HIZOA; Staveley-Smith et al. 2016) and/or Vela–OPT/NIR (KK2017, Kraan-Korteweg priv. comm), their object names (e.g., J0847-46, HyA0009, Vel0617) are provided. 'H' signifies H I counterparts found in the H I Parkes All Sky Survey (HIPASS; Meyer et al. 2004). The notation 'I' corresponds to entries from the Infrared Astronomical Satellite (IRAS) Point Source Catalog (Helou & Walker, 1988). 'M' designates matches with the Two Micron All-Sky Survey (2MASS) Extended Source Catalog (2MASX; Jarrett et al. 2000) and other 2MASS detections (Skrutskie et al. 2006, in the absence of 2MASX). 'W' signifies associations with sources from the Wide-field Infrared Survey Explorer catalog (WISE; Wright et al. 2010; Cutri et al. 2021), and 'Z' indicates sources identified through deep NIR follow-up observations conducted using the InfraRed Survey Facility (IRSF; Williams et al. 2014; Said et al. 2016).

Table 4.3: Vela–H I full galaxy catalog: H I properties (first page).

Name	Mosaic	l	b	$S_{\rm peak}$	$S_{\rm int}$	err$_{(S_{\rm int})}$	RMS	$V_{\rm hel}$	w_{20}	w_{50}	$M_{\rm HI}$	Flag	Note
J2000	–	deg	deg	Jy	Jy km s^{-1}	Jy km s^{-1}	mJy beam^{-1}	km s^{-1}	km s^{-1}	km s^{-1}	log($M_{\rm HI}$/M$_\odot$)	1/2	
(1)	(2)	(3)	(4)	(5)	(6)	(7)	(8)	(9)	(10)	(11)	(12)	(13)	(14)
J081815-465710	A2D	263.291	-6.232	0.013	2.78	0.28	0.77	7803	261	221	9.92	1	w. comp (J081828-471025)
J081828-471025	A2D	263.497	-6.324	0.011	0.65	0.14	0.71	7821	163	117	9.29	1	B=40″, i, w.comp (J081815-465710)
J081845-473700	A2D	263.893	-6.531	0.017	4.38	0.25	0.71	7510	349	311	10.08	1	
J081859-483716	A2D	264.757	-7.055	0.013	0.60	0.11	0.98	18637	141	99	10.01	2	e
J082034-464906	A2D	263.401	-5.829	0.002	0.89	0.13	0.70	2148	81	67	8.30	1	
J082116-474921	A2D	264.305	-6.293	0.010	2.33	0.32	0.66	11823	423	380	10.20	1	i
J082148-463756	A2D	263.366	-5.549	0.011	1.23	0.20	0.72	9704	208	166	9.75	1	
J082210-473533	A2D	264.198	-6.040	0.011	1.81	0.19	0.67	7657	232	209	9.71	1	i, w.comp
J082259-493012	A2C	265.864	-7.005	0.024	1.41	0.30	1.14	7182	152	99	9.55	1*	e, i, M, W
J082307-484243	A2D	265.217	-6.542	0.010	0.39	0.08	0.64	10256	214	179	9.30	1	
J082323-483719	A2D	265.168	-6.454	0.006	0.34	0.09	0.58	19440	235	137	9.80	2	
J082328-474526	A2D	264.460	-5.951	0.011	0.87	0.15	0.65	7561	215	98	9.38	1	M, W
J082339-461117	A2D	263.180	-5.036	0.011	0.92	0.16	0.70	9605	269	127	9.62	1	BL
J082403-484045	A2D	265.279	-6.395	0.020	3.13	0.25	0.77	7950	170	118	9.98	1	w.comp, M, W
J082415-490116	A2D	265.581	-6.562	0.019	1.26	0.10	0.67	2229	113	75	8.48	1*	M, W
J082511-494217	A2C	266.234	-6.825	0.034	7.27	0.48	1.10	2218	267	225	9.24	1	e
J082525-465223	A2D	263.918	-5.177	0.010	1.70	0.24	0.65	11762	329	277	10.06	1	i?
J082600-495546	A2C	266.495	-6.845	0.016	1.09	0.18	1.27	8088	228	211	9.54	1	e, w.comp, M, W
J082640-481845	A2D	265.226	-5.831	0.012	0.80	0.23	0.66	4384	240	143	8.87	1	i
J082720-504023	A2C	267.233	-7.095	0.021	2.02	0.10	1.40	3942	124	87	9.18	1	B=40″, e
J082740-490308	A2C	265.929	-6.120	0.012	1.22	0.21	0.74	10744	224	187	9.84	1*	
J082833-475415	A2D	265.071	-5.338	0.010	0.57	0.12	0.64	8639	176	105	9.32	2	
J083055-464513	A2D	264.369	-4.341	0.011	0.33	0.07	0.75	10785	338	83	9.28	2	
J083154-485210	A2C	266.178	-5.448	0.009	0.28	0.06	0.66	18038	261	217	9.66	2	
J083216-481004	A2D	265.652	-4.986	0.011	1.21	0.22	0.64	14775	205	157	10.12	1*	i, w.comp
J083336-503002	A2C	267.674	-6.185	0.013	2.26	0.32	0.61	11486	459	430	10.17	1	M, W
J083428-445041	A2B	263.194	-2.712	0.014	1.29	0.17	1.39	18949	126	88	10.36	2	r
J083453-492218	A2C	266.885	-5.352	0.010	0.70	0.20	0.66	7745	175	104	9.31	1	
J083531-472125	A2D	265.321	-4.067	0.002	0.49	0.10	0.82	9317	256	189	9.32	2	BL
J083612-453957	A2B	264.034	-2.984	0.014	0.65	0.13	1.57	10989	193	163	9.58	2	r
J083649-521526	B2D	269.397	-6.823	0.011	1.09	0.24	0.73	7757	251	191	9.50	1	e

4.4.2 General wedge distribution

Among the 719 detections, 432 galaxies are detected above the GP, while 287 are situated below. Their distribution in longitude and latitude redshift slice diagrams is illustrated in Fig. 4.5 where blue points indicate those above GP and cyan for those below the GP. In the latitude wedge diagram (right panel), the sources exhibit a uniform distribution across full velocity range of the Vela–H I ($V_{\rm hel} < 24000$ km s^{-1}), irrespective of their spatial position relative to the GP. However, in the longitude wedge diagram (left panel), distinct structures begin to be apparent. Some structures are exclusively present below the GP (e.g., cyan dots at ~10000 km s^{-1}), while others overlap, suggesting potential connections across the ZOA (e.g., at ~8000 km s^{-1}). Further details regarding the LSS observed in the wedges will be discussed in Section 4.5.3.

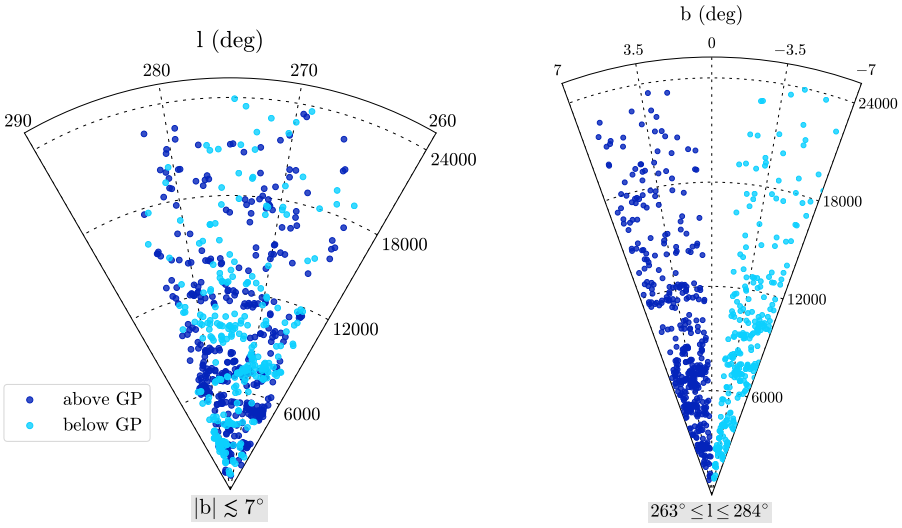

Figure 4.5: Longitude and latitude redshift wedge plots of detected galaxies in Vela–H I represented by dark blue dots for those above the GP and light blue dots for those below.

4.4.3 Internal quality assessment

Thanks to the presence of overlapping regions within the mosaics described in Section 4.3.2, I conducted an independent assessment of the H I data quality. A total of 163 detections were found in one or more adjacent mosaics. The heliocentric velocities and 50% linewidths of these sources exhibited only small median differences of 6.5 ± 10 km s^{-1} and 11.8 ± 30 km s^{-1}, respectively, measuring less than half a channel width ($\Delta v = 44.1$ km s^{-1} at $z = 0$). The median integrated flux difference was found to be 0.3 ± 0.8 Jy km s^{-1}, lower in most cases than the integrated flux errors of the individual detections. The high level of consistency in the H I parameters from overlapping regions confirms the robustness of the derivation of these properties.

I also used the duplicates to assess the positional accuracy of the survey. In Fig. 4.6, the respective offsets are displayed. By measuring the differences in galactic coordinates of each dupli-

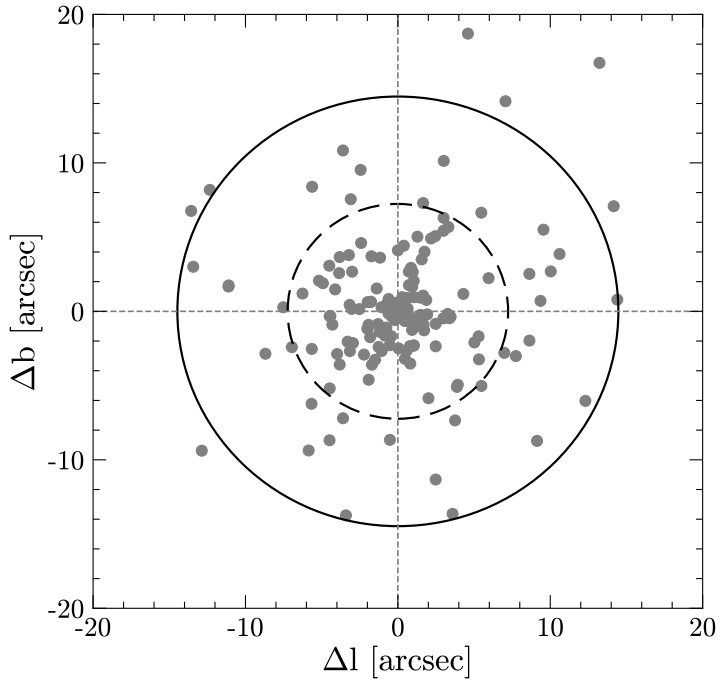

Figure 4.6: Galactic coordinates separations between Vela–H I detections found in the overlapping regions of the mosaics. The black dashed and solid circles mark the 1σ and 2σ of the coordinate separations.

cate, I achieved an average coordinate precision of $6.03''$, with a 1σ standard deviation of $7.23''$. This value is close to three times larger than that of Vela–SMGPS, which can be attributed to the larger beam size of Vela–H I, however, still less than two pixels. I did not distinguish between solid and possible detections, because only two of the duplicates are possibles. The estimate of positional accuracy is an important parameter in our search for multi-wavelength counterparts (see Section 4.4.5).

4.4.4 Comparison with other H I surveys

We now explore any potential systematics in the measured H I parameters of our survey by comparing them with other H I surveys that have some overlapping footprint with Vela–H I, such as HIZOA and the Vela–SMGPS.

Comparison with Vela–SMGPS

In comparing Vela–H I with Vela–SMGPS, I identified 15 galaxies in common that have separations below $10''$ and velocity offsets limited to 100 $\mathrm{km\,s^{-1}}$. The mean separation of these counterparts was $5.4'' \pm 2.7''$, well within the coordinate precisions of both surveys. However, 3 of these detections were situated in strong continuum regions at the edge of Vela–H I, and 6 others had very low SNR (SNR < 6) in Vela–H I, making their fluxes unreliable for comparison. We therefore limited our comparison to the remaining 6 galaxies with SNR > 9.

Upon examining differences in $V_{\rm hel}$ and w_{50}, we noted that Vela–H I galaxies exhibit slightly higher velocities compared to those in Vela–SMGPS, showing an offset of 9.6 ± 5.1 km s^{-1}. This disparity appears to slightly increase with redshift, irrespective of SNR. Similarly, we observed an average difference of 9.3 ± 5.2 km s^{-1} in linewidth. Unlike the velocity trend, the linewidth difference is smaller for larger linewidths, except for cases with low SNR and large w_{50}, where the emission peaks are easily hidden by noise. Despite these variations, all values fall within the one channel resolution of both surveys and lie within the expected error margin.

In terms of fluxes, the linear regression fit found for the 6 galaxies in common follows a near one-to-one relation with a slope of 0.981 ± 0.294, an intercept of -0.867 ± 1.892, and an R^2 value of 0.94. No statistically significant (3σ) systematic effects are noticeable for this small sample of galaxies with high SNR.

To further assess the reliability and completeness of our survey, we investigated the Vela–H I detections not found in Vela–SMGPS, and vice versa. The three Vela–H I galaxies not catalogued in Vela–SMGPS had a low SNR < 5 with a Flag of 2. They were all positioned at the high edge of the Vela–SMGPS mosaics which could have led to them being missed by SoFiA.

Conversely, 49 Vela–SMGPS galaxies (28 above and 21 below the GP) were not detected by Vela–H I. This is not surprising given the higher sensitivity of Vela–SMGPS, with a mean rms of 0.39 mJy beam^{-1} compared to 0.74 mJy beam^{-1}. Undetected galaxies in Vela–H I revealed a median SNR of 8, median integrated fluxes of 0.45 Jy km s^{-1}, median velocities around 11500 km s^{-1}, and a median w_{50} of 150 km s^{-1} in Vela–SMGPS. Those with SNR > 8 but undetected in Vela–H I typically had local rms values below the average noise, indicating they were close to the detection limit threshold and located in low-rms areas of Vela–SMGPS, hence too faint for our survey. Only galaxies with high SNR and relatively nearby were therefore likely to be detected in common by both surveys.

Comparison with HIZOA

We successfully identified 87 HIZOA detections out of the 90 present within our surveyed area. Three sources – J0932-44, J0916-55, and J0933-58 – remained undetected. The absence of J0932-44 and J0916-55 in our Vela–H I data can be attributed to their narrow w_{50} linewidths in HIZOA. Also no w_{20} information is available in the HIZOA catalog, making them easily overlooked by our coarse resolution. As for J0933-58, it was not recovered by SoFiA, likely due to (a) its location in an area that is strongly affected by residual solar RFI and (b) its proximity to the edge of the source-finding region. Among the 87 HIZOA detections, 5 were resolved into multiple counterparts in the Vela–H I survey. These sources resolved into several counterparts were excluded from the comparison. To ensure a robust comparison, we also excluded sources

with a low integrated signal-to-noise ratio (SNR < 10) in Vela–H I, and those affected by residual solar RFI, leading to poor baselines. This filtering process led to 59 galaxies for comparison.

The remaining detections displayed a mean coordinate precision of $1.9' \pm 1.5'$. The flux fit regression, illustrated in Fig. 4.7, reveals a slope close to unity (1.017 ± 0.041), an intercept of -0.303 ± 0.399, with $R^2 = 0.98$. The right panels of Fig. 4.7 display the differences in systemic velocities and linewidths. The systemic velocity plot (top right panel) yields a mean absolute difference of $\Delta v \sim 12.5$ km s^{-1} with a standard deviation of 9.4 km s^{-1}. A regression that is indistinguishable from zero, given the errors. The linewidth difference (bottom right panel) presents a slight offset of 12.3 ± 11.1 km s^{-1}, where Vela–H I values are slightly larger than HIZOA's linewidths. In view of the coarse resolution ($\sim$44 km s^{-1}), neither this offset nor the trend (cyan line) are significant.

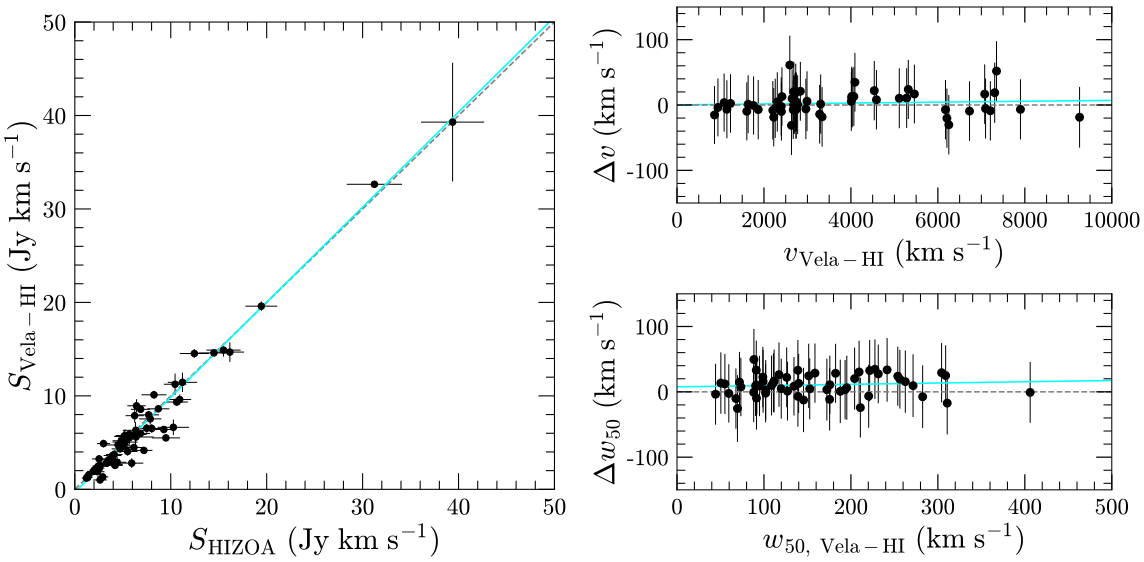

Figure 4.7: Left panel: integrated fluxes of Vela–H I detections with known counterparts from HIZOA are compared. The one-to-one relation is represented by the black dashed line, and the best linear fit is indicated by the cyan solid line. In the right panels, the differences in systemic velocities (top panel) and H I linewidth (bottom panel) between Vela–H I and HIZOA are illustrated. The cyan lines in both panels depict the outcomes of the best-fit linear regressions, with the dashed black zero-difference line serving as a reference for comparison.

4.4.5 Multi-wavelength counterparts

The Vela–H I survey uniquely connects the Vela–SMGPS to the higher latitudes where deep optical and NIR surveys like Vela–OPT/NIR, 2MRS, etc., become successful in unveiling LSS. Moreover, at the latitudes of Vela–H I, the likelihood to find multi-wavelength counterparts increases.

We therefore initiated a comprehensive search for multi-wavelength counterparts for our Vela–H I

detections using online databases such as the NASA/IPAC Extragalactic Database (NED)[7] and the Vizier[8] Catalogue access tool, accessed through their respective websites. Data retrieval (e.g., tables) employed remote web querying forms facilitated by the Python module `Astroquery`[9]. The search radii were determined by the quadrature of the positional accuracy of the two cross-matched surveys. For instance, the search radius for H I surveys like HIPASS (Meyer et al., 2004) and HIZOA (Staveley-Smith et al., 2016) typically spans a few arcminutes, while OPT and NIR catalogs have accuracies of a few arcseconds (e.g., 2MASX, has positional accuracy less than $1''$, as detailed in Jarrett et al. 2000). Additionally, it is necessary to consider potential offsets between a galaxy's stellar and neutral hydrogen structures. We therefore applied a search radius of $15''$ to be appropriate when taking into account the positional accuracy of Vela–H I of $\Delta\delta \simeq 6''$. This approach resulted in a list of potential counterparts with names, separations – and redshifts if available. To assist in identifying the most likely counterpart, an examination of a $2' \times 2'$ image stamp from the Digitized Sky Survey (DSS), 2MASS-K band, and WISE-1 band ($3.4\,\mu$m) was conducted using `Skyview`, a package in `Astroquery`.

Figure 4.8 illustrates the distribution of Vela–H I detections and their potential multi-wavelength counterparts. Those with available optical spectroscopic redshifts are marked in red, while those lacking redshift data are marked in blue. Below $|b| \leq 5°$, the availability of redshift information rapidly diminishes due to increasing foreground extinction (see contours). Out of the 719 H I detections, we identified 211 probable counterparts, constituting approximately 29% of all sources in our sample. Their mean separation is minimal, measuring only $5.6'' \pm 3.4''$, which is even smaller than the positional accuracy of Vela–H I. Among these, 110 galaxies have redshift information, 66 (~31% of 211) of which originating from optical spectroscopy and 27 based on H I redshifts (HIZOA and HIPASS). Another 16 are based on photometric redshifts (Bilicki et al., 2014), too large uncertainties for a comparison. For Vela–H I galaxies with velocities exceeding 16000 km s^{-1}, i.e., at the VSCL distance, 19 of them have likely counterparts, but only 5 have available spectroscopic redshift information.

The histograms in Fig. 4.9 compare the distribution in velocity and H I mass for the Vela–H I detections (light-blue) with their likely counterparts (blue). Counterparts with spectroscopic redshift information are depicted in red. In the left panels, we observe a decrease in the number of counterparts as velocities increase. The peaks in counterpart distributions align with overdensities in Vela–H I (see Section 4.5.2). In the right panel, galaxies with low H I masses $\log(M_{\rm HI}/{\rm M}_\odot) < 8.4$ have few matches. There is a slight increase in the number of cross-identified H I detections with increasing H I masses, which are generally large spirals that are prominent in optical as well. They peak at the same point as the H I mass distributions of Vela–H I. The results

[7] http://ned.ipac.caltech.edu
[8] https://vizier.cds.unistra.fr/viz-bin/VizieR
[9] https://astroquery.readthedocs.io/en/latest/

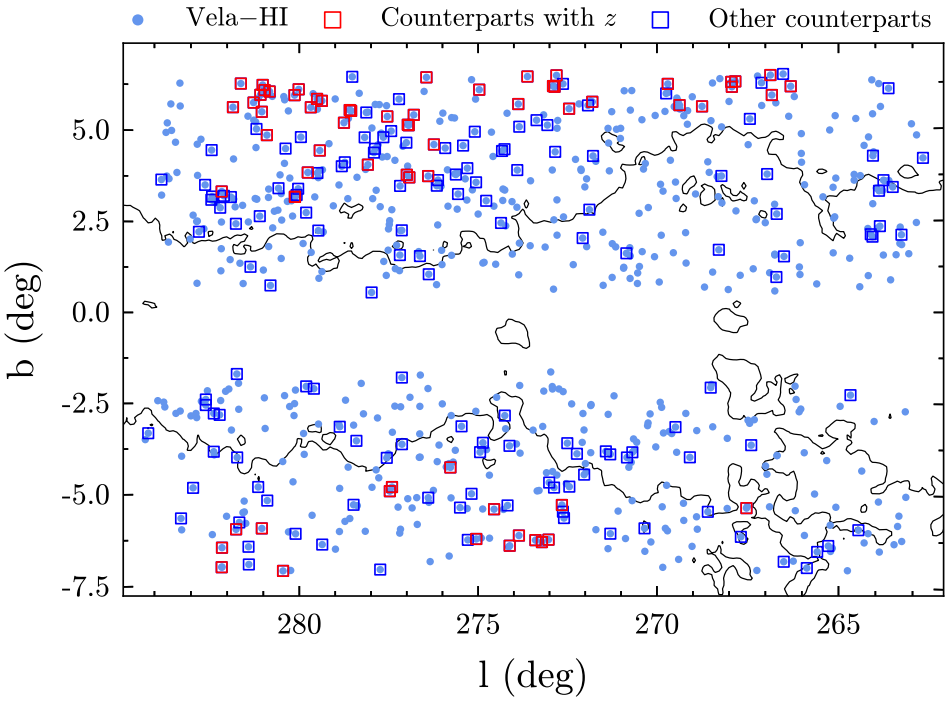

Figure 4.8: On-sky distribution of Vela–H I detections (light blue dots). Superimposed are associated multi-wavelength counterparts where those with spectroscopic redshift data are represented by red open squares and the blue open squares mark counterparts without available redshift information. Black contour lines delimit the Galactic foreground extinction at $A_B \simeq 3.^{\rm m}0$.

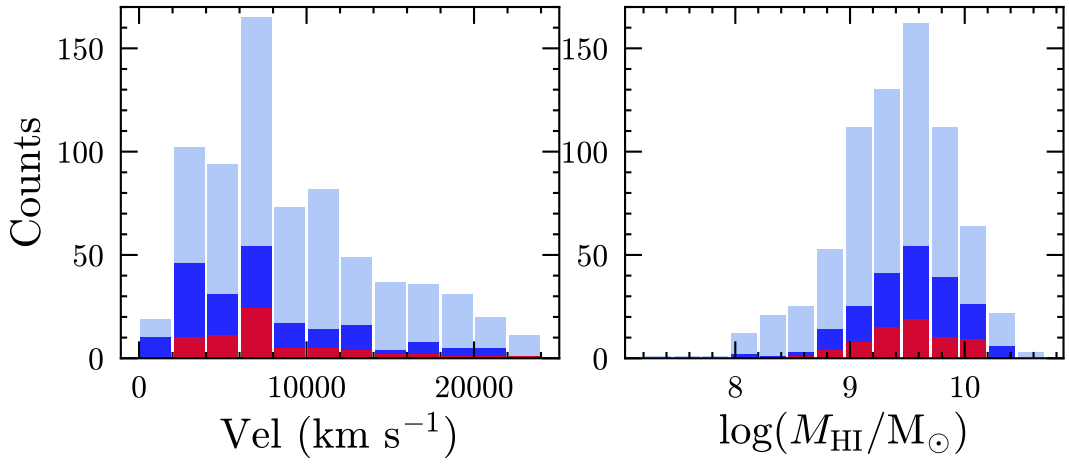

Figure 4.9: Histogram comparing Vela–H I detections (light-blue) and likely counterparts as a function of velocity (left panel) and H I mass (right panel). Galaxies with counterparts are depicted by the blue-shaded histograms. Counterparts with spectroscopic redshifts are represented by the red-shaded histograms.

from Figs. 4.8 and 4.9 suggest that the likelihood of an H I source having a potential counterpart increases with H I mass but decreases as foreground extinction rises at lower latitudes. This is because there are no deep systematic surveys in the GP at high redshift. The only systematic survey is 2MASS, but it is also incomplete with increasing redshift, brightness-limited, and affected by extinctions at lower latitudes, making massive and nearby galaxies likely to have more counterparts than dwarfs and high-z galaxies.

I will now investigate the correspondence between spectroscopic and H I redshifts. A one-to-one comparison results in a slope close to unity (0.997 ± 0.004) with an $R^2 = 0.999$ and an intercept of 17.7 ± 36.2. These findings demonstrate a high level of consistency. A more detailed analysis, examining the difference between H I and optical velocities ($\Delta v = v_{\rm Vela–HI} - v_{\rm opt}$) as illustrated in Fig. 4.10 reveals an average difference of 70 ± 51 km s^{-1}. The best-fitting parameters of the velocity differences have a slope and intercept of -0.003 ± 0.004 and 15.6 ± 36.4, respectively, showing no significant difference with increasing velocities. Based on the comparison with HIZOA, the Vela–H I velocity uncertainties are found to be of the order of 12.5 ± 9.4 km s^{-1}. Errors compared to the optical velocities, generated from multi-object spectroscopy such as AAOmega, have uncertainties on the order of $\sim$100 km s^{-1} (Baldry et al., 2014). The determined offsets between optical and Vela–H I velocities range from 0.14 km s^{-1} to 234 km s^{-1}.

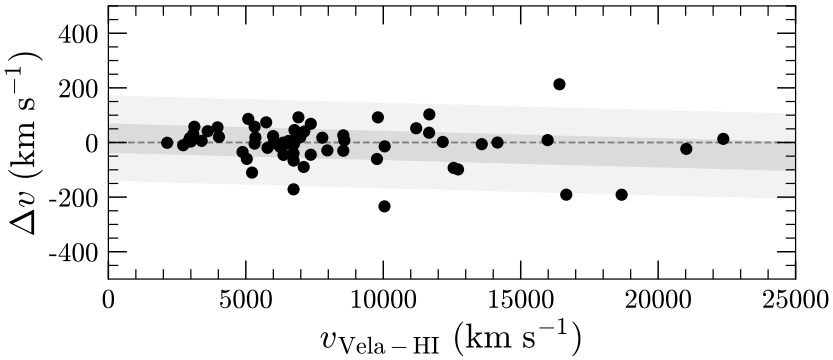

Figure 4.10: Heliocentric optical velocity comparison between Vela–H I galaxies and counterparts with spectroscopic redshifts ($\Delta v = v_{\rm Vela–HI} - v_{\rm opt}$). The dark-shaded regions delineate the 1σ and 3σ standard deviations, respectively.

In summary, of the 211 identified galaxies, 38 (18%) have IRAS counterparts, 146 (70%) are associated with 2MASS/2MASX counterparts, 140 (66%) have WISE counterparts, 35 (17%) are linked to HIPASS counterparts, and 49 (23%) have IRSF counterparts. Of the 92 Vela–H I detections with likely HIZOA counterparts, 27 have probable WISE counterparts. A noteworthy aspect of Vela–H I is its partial overlap with the Vela–OPT/NIR survey. More than half (121 out of 211) of the identified counterparts originate from the overlap between Vela–H I and Vela–OPT/NIR. These are labeled with prefixes 'HyA' and 'Vel' in the last column of the galaxy catalog (Table C.2 in Appendix C.2).

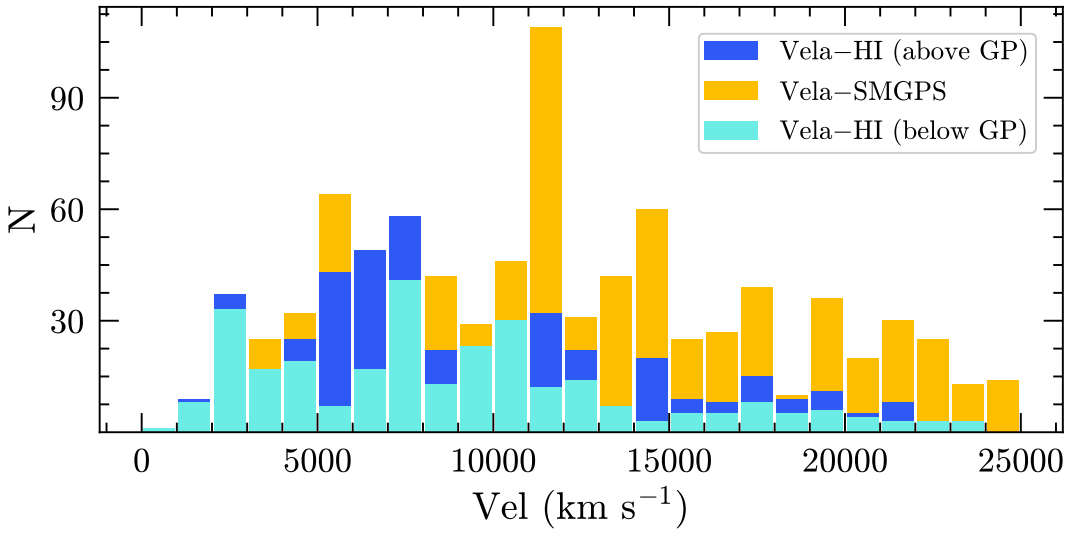

Figure 4.11: Barred histograms showing the heliocentric velocity distributions of the galaxies from Vela–H I that lie above the Plane (blue), Vela–SMGPS in the inner ZOA (orange), and Vela–H I galaxies below the GP (cyan), respectively.

4.4.6 H I properties distributions

As a next step, we explore the overall distribution of the global H I properties between Vela–H I and Vela–SMGPS such as the recessional velocities (Fig. 4.11), and the linewidths (w_{50}) and H I masses (Fig. 4.12).

The heliocentric velocity distributions of Vela–H I and Vela–SMGPS are shown in Fig. 4.11. The blue histogram indicates galaxies above the GP, the orange galaxies in Vela–SMGPS, and the light blue galaxies below the GP. Because of the lower sensitivity of Vela–H I, the median velocity is lower (7700 km s^{-1}) compared to that of Vela–SMGPS (~11600 km s^{-1}). However, both surveys uncover galaxies out to the redshift limit of the surveys (24000 km s^{-1}). Several prominent peaks are discernible across regions above, within, and below the GP, suggesting a continuity of LSS. While the significance of these peaks will be discussed in detail in Section 4.5, we identify and highlight some of them here.
Four peaks stand out in Fig. 4.11 at 2000−3000 km s^{-1}, 5000−6000 km s^{-1}, 7000−8000 km s^{-1} (or possibly 5000 − 8000 km s^{-1}), and 11000 − 12000 km s^{-1}. The first peak is observed in both surveys. The second peak is mostly present above the GP while the third peak is present both above and below the GP in Vela–H I. They seem to be conformed of various condensations and galaxy clumps. The fourth peak has its origin entirely from the narrow filament unexpectedly discovered at 11000 − 12000 km s^{-1} in Vela–SMGPS.

Despite Vela–H I covering a larger area with an rms nearly twice that of Vela–SMGPS, the distributions of linewidth and H I mass in both surveys (Fig. 4.12) exhibit similar patterns. The average linewidths of 176 and 173 km s^{-1} are practically the same. However, the increase in the

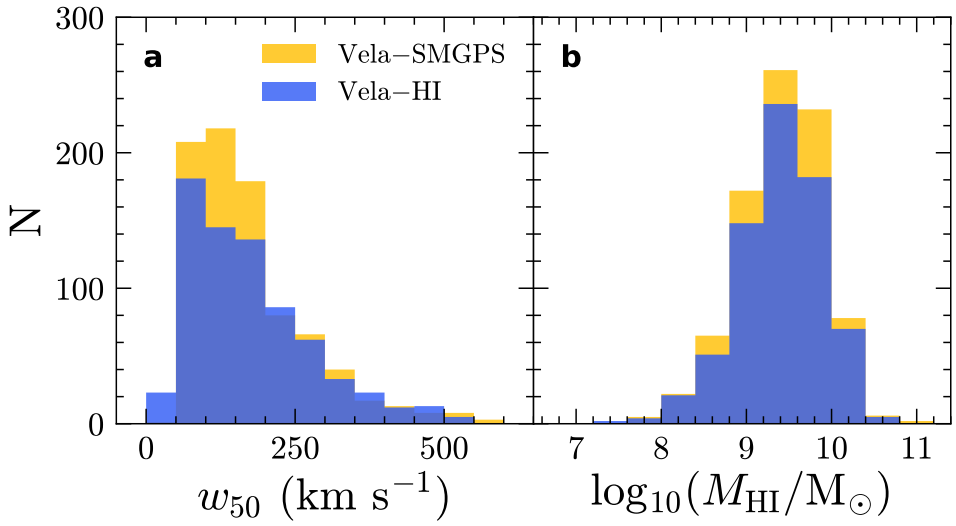

Figure 4.12: Histograms of the H I parameters from the systematic blind H I surveys Vela–H I (719 galaxies, blue) and Vela–SMGPS (843 galaxies, orange). The left panel (a) displays the linewidths (w_{50}), the right panel (b) the H I mass distribution.

number of galaxies towards lower linewidths (50 km s^{-1}) is more gradual for Vela–H I, while Vela–SMGPS displays a broad peak between 50 – 200 km s^{-1}. But both surveys follow the skewed pattern typical of blind systematic H I surveys (cf. HIZOA, Staveley-Smith et al. 2016; the EBHIS Zone of Avoidance survey or EZOA, Schröder et al. 2019). This contrasts to optically or NIR-selected H I surveys, which follow a more Gaussian distribution with an upswing towards larger linewidths ($w_{50} > 200$ km s^{-1}) because these tend to miss the bluer, low surface brightness dwarf population, as exemplified by Kraan-Korteweg et al. (2018).

The distribution of H I masses (panel b) reveals about three orders of magnitudes in $\log(M_{\rm HI}/{\rm M}_\odot)$, 7.3 to 10.6 in Vela–H I and 7.8 to 10.9 in Vela–SMGPS. They both peak between 9.2 – 9.6, and have the same mean at $\log(M_{\rm HI}/{\rm M}_\odot) = 9.4$, despite Vela–SMGPS having slightly higher number of galaxies per bin.

4.5 Large-scale structures discussion

4.5.1 Observational data in the Vela region

In this section, I discuss connections between previously identified and newly revealed LSS. As a starting point, I present Fig. 4.13 to visually guide the interpretation of these structures. Figure 4.13 is based on a combination of MeerKAT data from heavily obscured galaxies acquired through Vela–SMGPS and Vela–H I (purple and green boxes), along with additional redshift information obtained from optical and single dish spectroscopic measurements of galaxies identified in deep optical and/or the NIR 2MASX survey at higher latitudes.

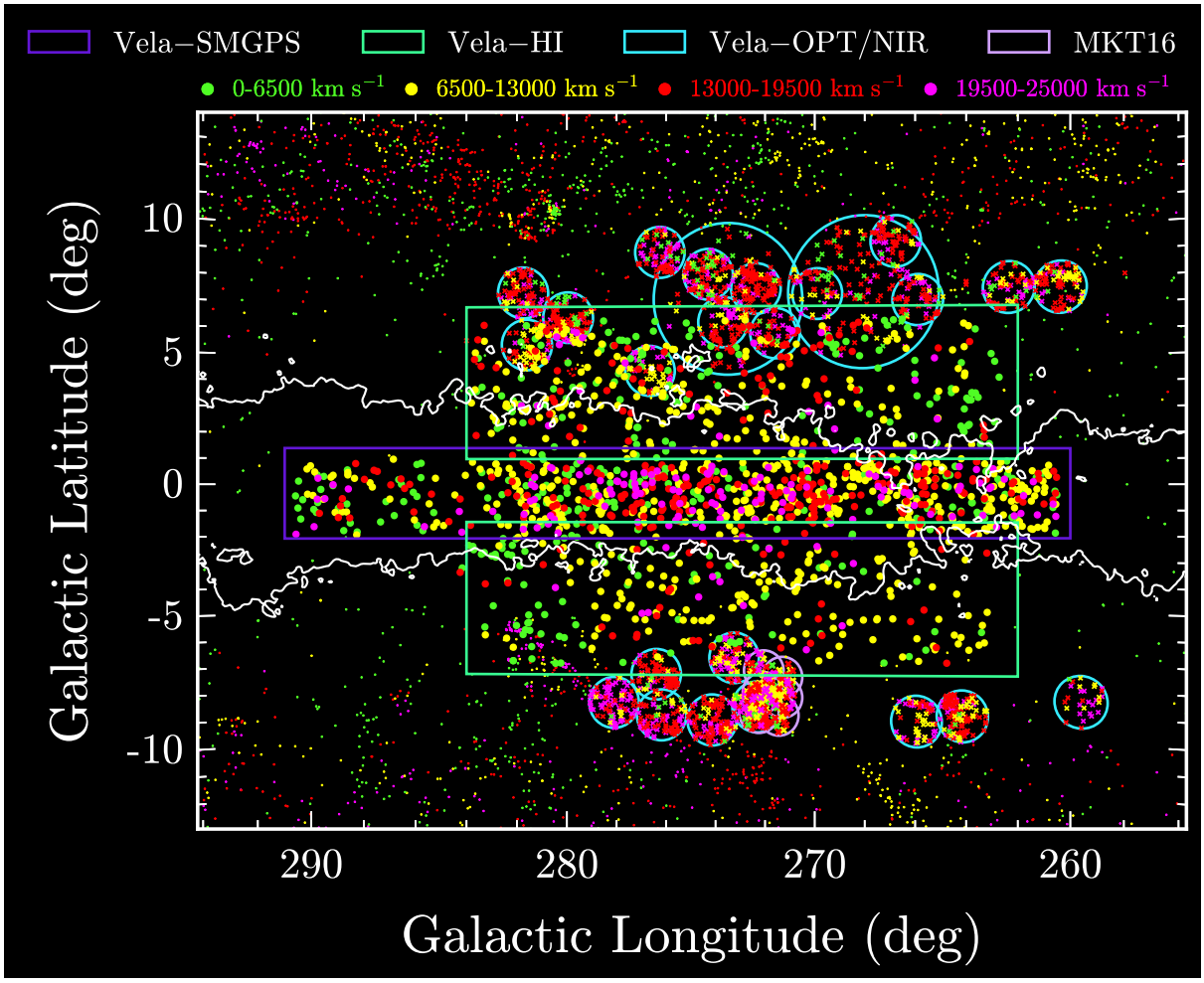

Figure 4.13: Spatial distributions in Galactic coordinates of galaxies surveyed across the wider VSCL region ($256° < \ell < 294°, |b| < 15°$) with velocities reaching out to 25000 km s^{-1} from prior optical and H I redshift surveys, combined with the systematic MeerKAT H I surveys Vela–H I and Vela–SMGPS. Color codes indicate different velocity intervals (light green: < 6500 km s^{-1}, yellow: $6500-13000$ km s^{-1}, red: $13000-19500$ km s^{-1}, and magenta: $19500-25000$ km s^{-1}). Large dots, enclosed by green and purple rectangles, respectively represent newly identified H I-detected galaxies from Vela–H I ($N = 719$), and previously detected H I galaxies from Vela–SMGPS ($N = 843$) in the inner ZOA. Small crosses within cyan circles mark galaxies with redshifts obtained from Vela–OPT/NIR ($N = 2803$), while small dots encompass all other compiled redshifts from various surveys (HyperLEDA and 2MRS). MeerKAT16 survey detections ($N = 156$) are marked by crossed symbols located within the six light purple circles around $b = -7°$ (Hatamkhani et al., 2023; Steyn, 2023). The white contour outlines corrected dust extinction at $A_B \simeq 3\overset{\text{m}}{.}0$ based on the DIRBE maps (Schlegel et al., 1998; Schlafly & Finkbeiner, 2011).

The ancillary dataset, represented by cyan and light purple circles, includes galaxies with known redshifts from Vela–OPT/NIR and recent H I data from the MeerKAT16 observations of the surrounding of the galaxy cluster VC04 ($272.25°, –9°, 18000$ km s^{-1}, Hatamkhani et al. 2023), which is embedded in Wall 1 of the VSCL (Steyn, 2023). We incorporate galaxies with redshifts at higher latitudes ($5° \leq |b| \leq 15°$) from the 2MASS Redshift Survey (Huchra et al., 2012; Macri et al., 2019) and the HyperLEDA database (Makarov et al., 2014), denoted by small dots in the figure. The prominence of red and magenta dots is already noticeable, with red containing the distance range of W1 and magenta for W2.

The region of high extinction, where optical and NIR galaxy counts become highly incomplete, is delineated by the white contour representing the dust extinction limit in the optical of $A_B \simeq 3\overset{\text{m}}{.}0$, derived from the Diffuse Infrared Background Experiment (DIRBE) maps (Schlegel et al., 1998; Schlafly & Finkbeiner, 2011; Schröder et al., 2021). There is a bias in the spatial distribution of observed fields in redshift space below this contour. Caution is therefore advised when interpreting this on-sky plot, and later LSS plots as the presence of gaps does not necessarily indicate an area of underdensity.
The ZOA has now been quite thoroughly surveyed, particularly for the longitudinal range of $263° < \ell < 284°$. With the new Vela–H I detections with a sensitivity of 0.74 mJy beam^{-1}, we now have a systematic survey of galaxies extending up to 24000 km s^{-1}. Due to the difference in rms, the coverage in Vela–H I is approximately 3 galaxies per square degree compared to Vela–SMGPS with 9 galaxies per square degree. Both surveys highlight the effectiveness of systematic interferometric H I surveys in mapping LSS across the most obscured part of the ZOA, representing a significant step toward understanding the continuity of LSS.

4.5.2 Sensitivity curve and comparison with simulations

As an initial step in understanding how the overdensities within the inner ZOA align with known LSS situated beyond $|b| > 7°$, we analyze the velocity distribution and sensitivity curve of Vela–H I detections across the survey volume (see Fig. 4.14). Similar to the simulation S45 in Section 3.5.2 of Chapter 3, we overlaid our H I detections on simulations, but adjusted the simulations to match the area where Vela–H I is complete (i.e., 528 deg^2/193 deg^2 after removing the high-noise regions toward the outermost edges and the mosaic A2B region) and sensitivity (0.75 mJy beam^{-1}) – hereafter referred to as S75 – which predicts 769 galaxies. The prediction from the S75 velocity distribution, representative of a more uniform distribution, is shown by the cyan solid line. Upon initial inspection, the Vela–H I distribution deviates significantly from uniformity. The distribution reveals three pronounced peaks, clustering around ~2500 km s^{-1}, 7000 km s^{-1}, and 17000 – 20000 km s^{-1}. The latter peak coincides with the redshift range of W1 and shows an elongated distribution with H I mass, along with a hint of a more marginal broad overdensity at 21000 – 24000 km s^{-1}. An underdensity from 13000 – 17000 km s^{-1} is

observed to be present in front of the VSCL.

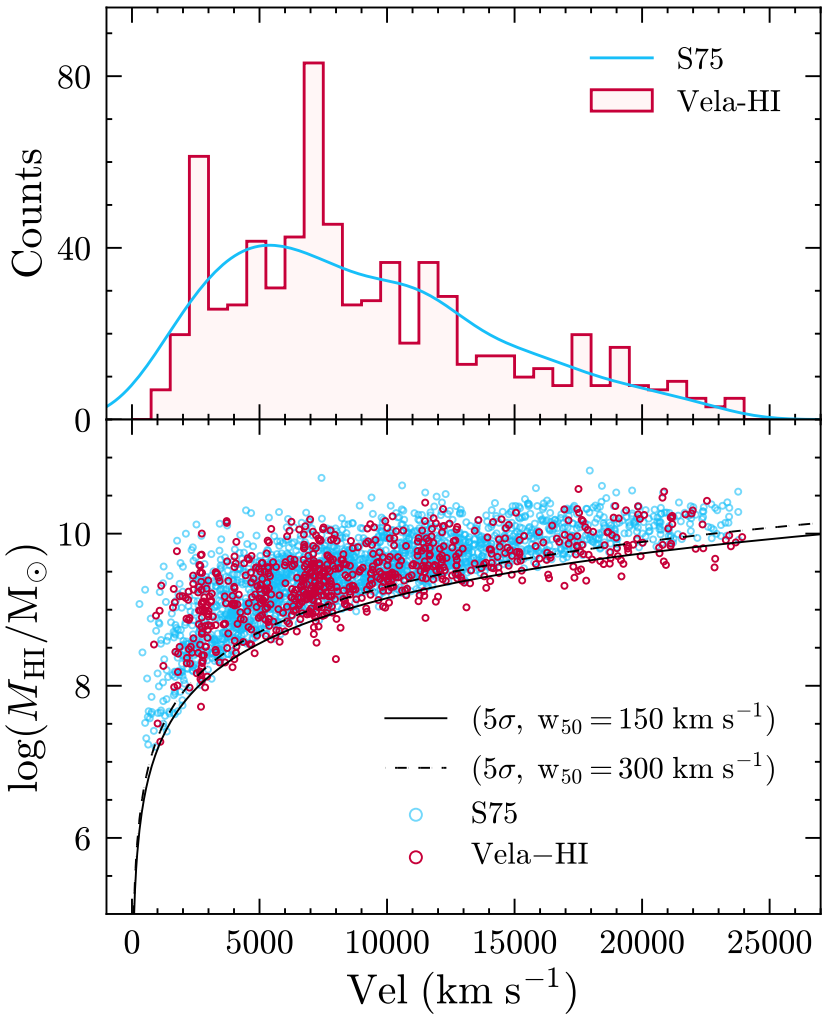

Figure 4.14: Sensitivity curve illustrating the correlation between H I masses and heliocentric velocities for Vela–H I detections (depicted as red dots), accompanied by simulated galaxies for the full SMGPS (528 deg^2) with an rms of 0.75 mJy beam^{-1} (S75, cyan dots). The solid and dashed lines represent the 5σ detection limits for w_{50} values of 150 and 300 km s^{-1}, respectively. The top panel presents the histogram distribution of heliocentric velocities in light red. The cyan solid line corresponds to simulations with rms values of 0.75 mJy beam^{-1} (S75) when scaled to the Vela–H I survey area.

4.5.3 Discussion of overdensities in the Vela region

I will now look in more detail at the on-sky distributions across varied redshift intervals, each with a $\Delta v = 4500$ km s^{-1} increment range, aiming to locate and identify the distinct peaks. Our study is divided into two main parts: one focusing on nearby structures within the velocity range $2000 < V_{\rm hel} \leq 15500$ km s^{-1} (see Fig. 4.15), and another one on the high redshift LSS for galaxies at the high distance range ($V_{\rm hel} > 15500$ km s^{-1}; Fig. 4.16) that encloses VSCL. To discern further LSS, the redshifts in each 4500 km s^{-1} panel are subdivided into three increasing intervals of $\Delta v = 1500$ km s^{-1}, from cyan, green, to blue color symbols, respectively. A zoomed-in panel of each on-sky plot within the longitude and latitude ranges $256^\circ \leq \ell \leq 294^\circ, |b| < 15^\circ$

is presented to the right panels of Figs. 4.15 and 4.16, allowing a more detailed insight into the new Vela–H I data.

In Fig. 4.17, I additionally present redshift wedges for the near and high redshift intervals that include galaxies with redshifts lying beyond the ZOA. This improves our insight into the LSS and illustrates the ZOA results above and below the Plane. These data are represented by blue and orange dots, respectively.

Nearby structures: $V_{hel} \leq$ 15500 km s^{-1}

$2000 \leq V_{hel} \leq 6500$ *km s*$^{-1}$: A substantial filament extends from the Hydra (270°, +27°, 3400 km s^{-1}) and Antlia (273°, +19°, 2600 km s^{-1}) clusters, often referred to as the Hydra Wall across the GP (Kraan-Korteweg et al., 1994, 1995; Fairall et al., 1998; Kraan-Korteweg, 2000; Kraan-Korteweg et al., 2002). Cyan and green points from the Vela–H I together with our findings in Chapter 3 can now trace the Hydra wall as a continuous structure across the ZOA to about $b \sim -10°$. The alignment of blue and orange points in the wedge slices (first-row panels of Fig. 4.17) further confirms these results. Also recognized as the Hydra-Antlia extension (Kraan-Korteweg et al., 1995; Kraan-Korteweg, 2000), the zoomed plot in the right panel reveals two branching structures crossing the GP at $\ell \sim 278°$ and 282° at 2000 – 3500 km s^{-1} and $\ell \sim 280°$ at 3500 – 5000 km s^{-1}, concluding with a group of galaxies at (281°, –7°). This feature is also evident as a prominent peak at 2000 – 3000 km s^{-1} in the sensitivity curve plot in Fig. 4.14.

In the higher velocity range of 3500 – 6500 km s^{-1} (dark blue dots), the Vela cluster AS639 (280°, +6°, ~6000 km s^{-1}; Stein 1996) seems to be linked to an overdensity at lower latitudes (blue dots) and into the inner GP but not further. This is also reflected as a peak in the velocity histogram in Fig. 4.14 at 5000 – 6000 km s^{-1}. The alignment of blue dots in the wedge suggests the presence of a significant structure above the GP connecting to AS639, possibly originating from $\ell \sim 265°$, $V_{\rm hel} \sim 5500$ km s^{-1}.

$6500 \leq V_{hel} \leq 11000$ *km s*$^{-1}$: The inclusion of new Vela–H I data clearly manifests previously completely unknown wall-like interconnecting structures (cyan dots) that cross the ZOA. Examining on-sky plots, a discernible diagonal structure of cyan dots (6500 – 8000 km s^{-1}) becomes apparent, crossing the inner GP within the extensive longitudinal range of $266° \leq \ell \leq 274°$. This structure not only extends spatially below the GP but also seems to be connected to AS639 and further linked to higher velocity structures when below the Plane. It then reaches the blue dots within 9500 – 11000 km s^{-1} at $276° \leq \ell \leq 280°$, $b \sim -6°$ which also appear to originate from the alignment of blue dots that cross the GP at $\ell \sim 281°$. This crossing results in a distinctive void of approximately 10 Mpc in size at $\ell \sim 279°$, $b \sim 0°$ (see magenta circle), which was seen as an underdensity in Vela–SMGPS.

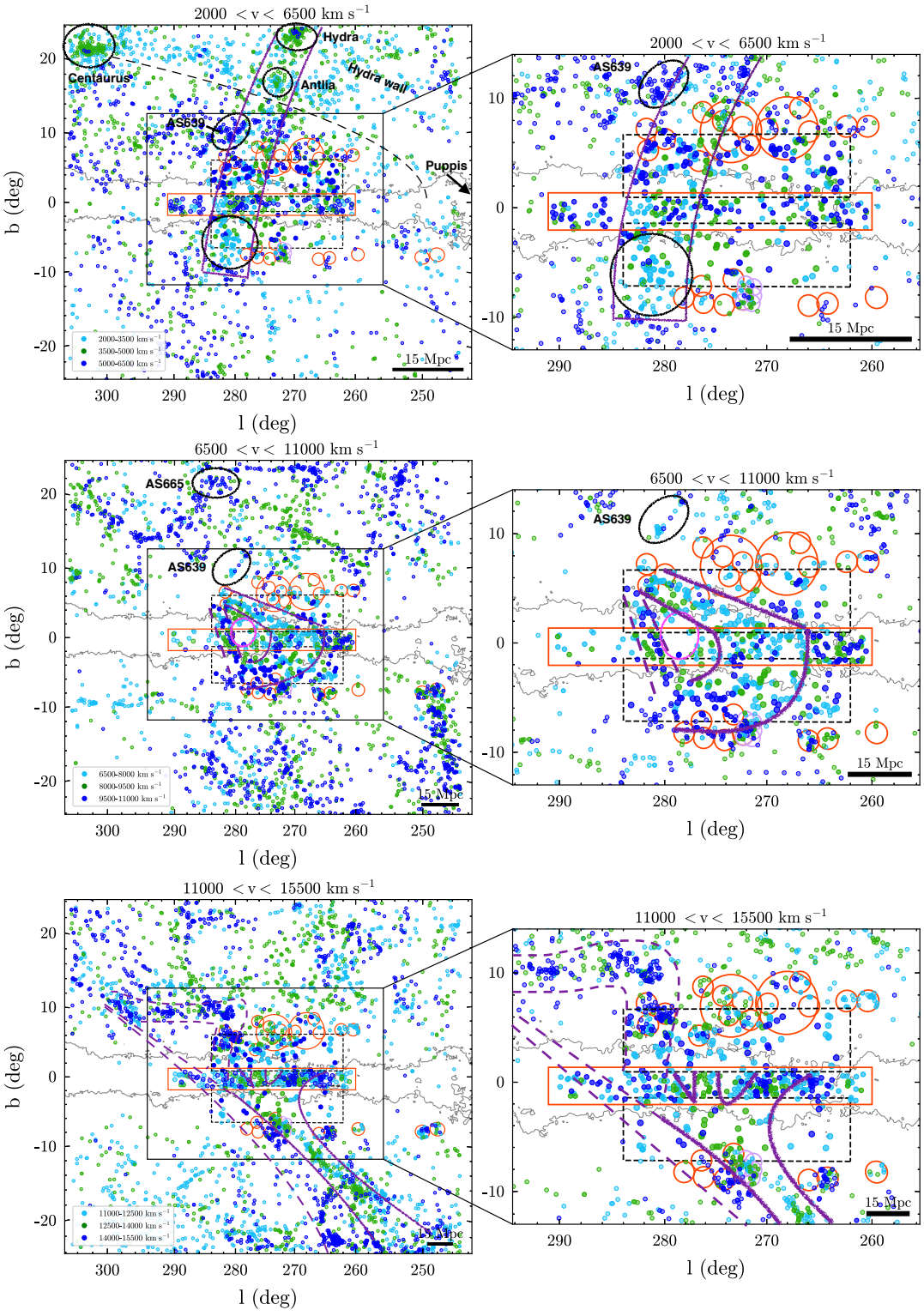

Figure 4.15: Annotated 2D on-sky distributions of galaxies in the surroundings of Vela region ($244° < \ell < 306°, |b| < 25°$). The figure displays three nearby panels, each representing a redshift interval with a $\Delta v = 4500$ km s^{-1} from 2000 km s^{-1} to 15500 km s^{-1}. The color codes within each panel signify increasing velocity intervals of 1500 km s^{-1}, in cyan, green, and blue. Vela–H I's survey region is outlined by black dashed boxes, and Vela–SMGPS detections an orange rectangle. Vela–OPT/NIR and MKT16 observations are denoted by orange and light purple open circles, respectively. The dust extinction contour at $A_B \simeq 3.^{\rm m}0$ from DIRBE maps is represented by a solid grey line. Each panel includes a zoomed-in section ($256° \leq \ell \leq 294°, |b| < 15°$) with a 15 Mpc scale bar positioned at its lower right side, representing the mean redshift range of that panel.

11000 $\leq V_{\rm hel} \leq$ *15500* km s^{-1}: Despite some missing data points beyond our surveyed areas, the continuation of green dots (12500 – 14000 km s^{-1}) indicates a branching of three structures, crossing the GP at three distinct locations ($\ell \sim 270°, 276°$, and 279°). However, the limited number of Vela–H I detections makes it unlikely that the filament extends above the GP (see thinner dashed purple lines). With regard to the two clumps of blue dots in Section 3.6.2 of Chapter 3 at 14000 – 15500 km s^{-1}, we see no obvious links to Vela–H I and how they link with other structures in the cosmic web.

Higher-z structures: $V_{\rm hel}$> 15500 km s^{-1}

Figure 4.16 presents the higher redshift ranges, which are directly relevant to our investigation of VSCL. The panels are divided into two segments (15500 – 20000 km s^{-1} and 20000 – 24500 km s^{-1}) that should provide insights into both VSCL walls. Due to the lower sensitivity, the links are not as clearly depicted compared to the lower redshift ranges.

15500 $\leq V_{hel} \leq$ *20000 km s*$^{-1}$: the continuation of green points (17000 – 18500 km s^{-1}) implies the presence of Wall 1 (W1). This structure appears to originate from a clustering point at (∼272.5°, 6°), intersecting the ZOA at least at around $\ell \sim 275° \pm 1°$, and reaching another clustering below the GP at (∼276.5°, –7°). The alignment of blue dots at 18500 – 20000 km s^{-1}, on the other hand, seems to cross at least two locations in the GP (see purple-shaded circle). One branch likely merges in the inner GP at $\ell \sim 277°$, while another filament of blue dots, originating from above the GP, crosses at $\ell \sim 272.5°$, reaching the clustering below the Plane at (∼272.5°, –8°). The velocity distribution of Vela–H I shown in Fig. 4.14 further supports these findings, displaying two peaks indicating overdensities at 17000 – 18000 and 19000 – 20000 km s^{-1}, although with lower significance than in Vela–SMGPS distribution (see Fig. 4.11).

A notable observation in this panel is the connection from the cluster A3391 (262.37°, –25.16°, 15919 km s^{-1}), where cyan and green dots (15500 – 18500 km s^{-1}) extend to the clustering of blue dots (18500 – 20000) below the GP. This connection aligns with two X-ray clusters (CIZA J0812.5-5714 and CIZA J0820.9-5704; Ebeling et al. 2002), at approximately the same redshift (18587 and 18287 km s^{-1}, respectively). The structure then continues as a dense filamentary structure containing clusters and groups above the GP. This might explain why the two peaks at 17000 – 18000 km s^{-1} and 19000 – 20000 km s^{-1} are predominantly prominent above the Plane for Vela-H I, as shown in Fig. 4.11. I think that the underdensity visible above the GP at $\ell \sim 273°$, $b \sim 15°$, around 15500 km s^{-1}, just before the redshift of the first wall, is a genuine void (designated as V1) due to the low number of galaxies shown by the sensitivity curve in Fig. 4.14. Moreover, the wedge diagrams in Fig. 4.17 have hardly any galaxies in that region for the combined sample out to $0° < b < 20°$. The overall arrangement of the two walls in this velocity

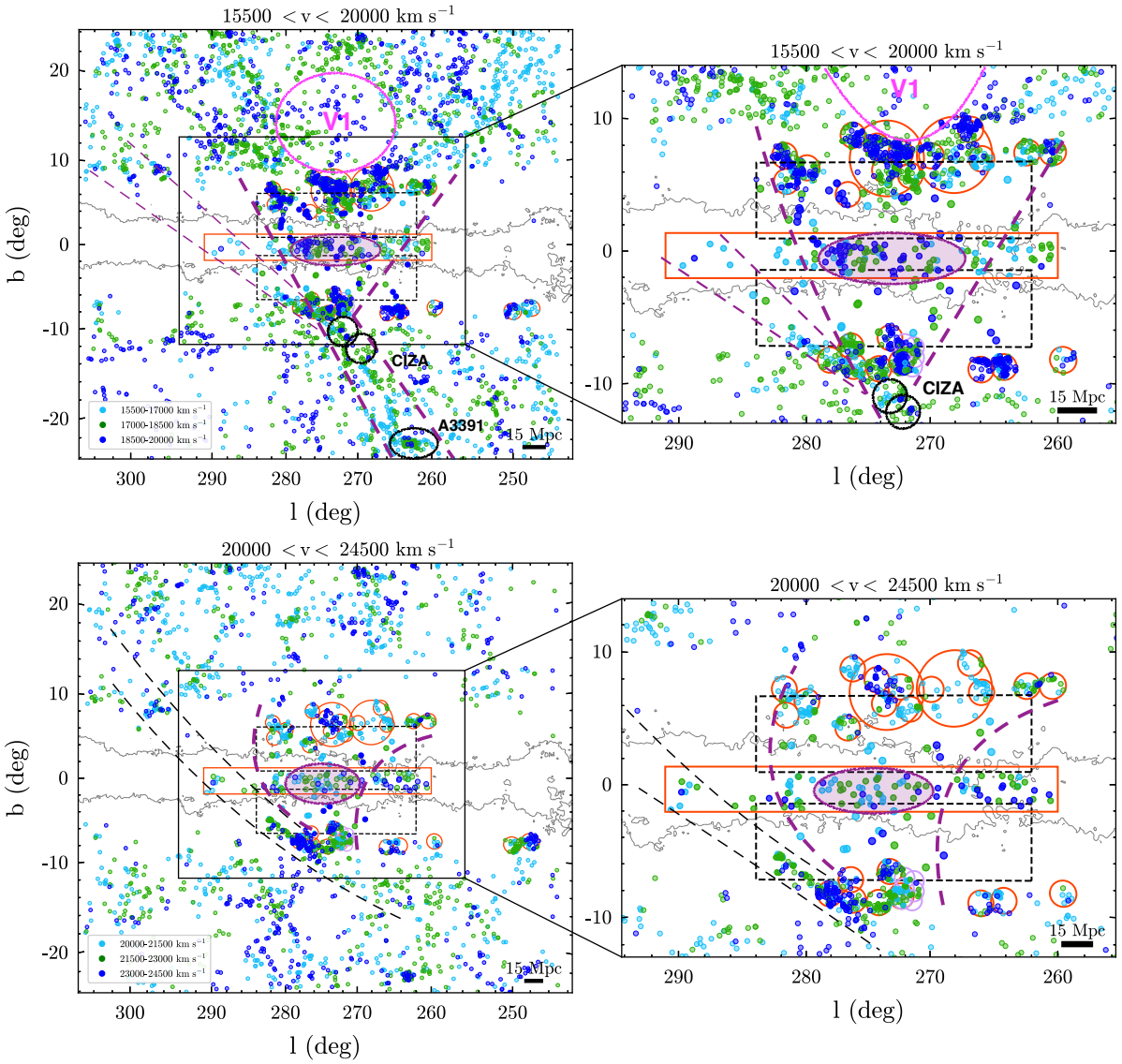

Figure 4.16: Similar to Fig. 4.15, but featuring two panels for the high-redshift velocity range.

range appears to be part of a multi-branching structure that coincidentally intersects within the longitude range of $270° \leq \ell \leq 279°$ and around $b \sim 0°$.

20000 ≤ V_{hel} ≤ 24500 km s^{-1}: Despite the low number of detections due to sensitivity drop, a hint of a broad crossing is observed around $20000 - 21500$ km s^{-1} (cyan dots) and $21500 - 23000$ km s^{-1} (green dots) within the range $270° \leq \ell \leq 279°$ – slightly broader than suspected by Vela–SMGPS. The structure seems to align with the X-ray cluster CIZA J0745.1-5404/ESO 163-IG015 ($266.84°, -14.36°, 22185$ km s^{-1}; Kocevski et al. 2007). It reinforces the findings from Vela–SMGPS that the crossing seems to occur in the inner GP around velocities of $18500 - 21500$ km s^{-1}. This potential intersection corresponds with the rough estimate that places the center of mass overdensity of the VSCL at approximately ~272° in the lowest latitudes (also see the cyan circle in the wedge diagram). This estimation was derived by interpolating spectroscopic and photometric redshifts in the region near Vela–OPT/NIR in KK2017.

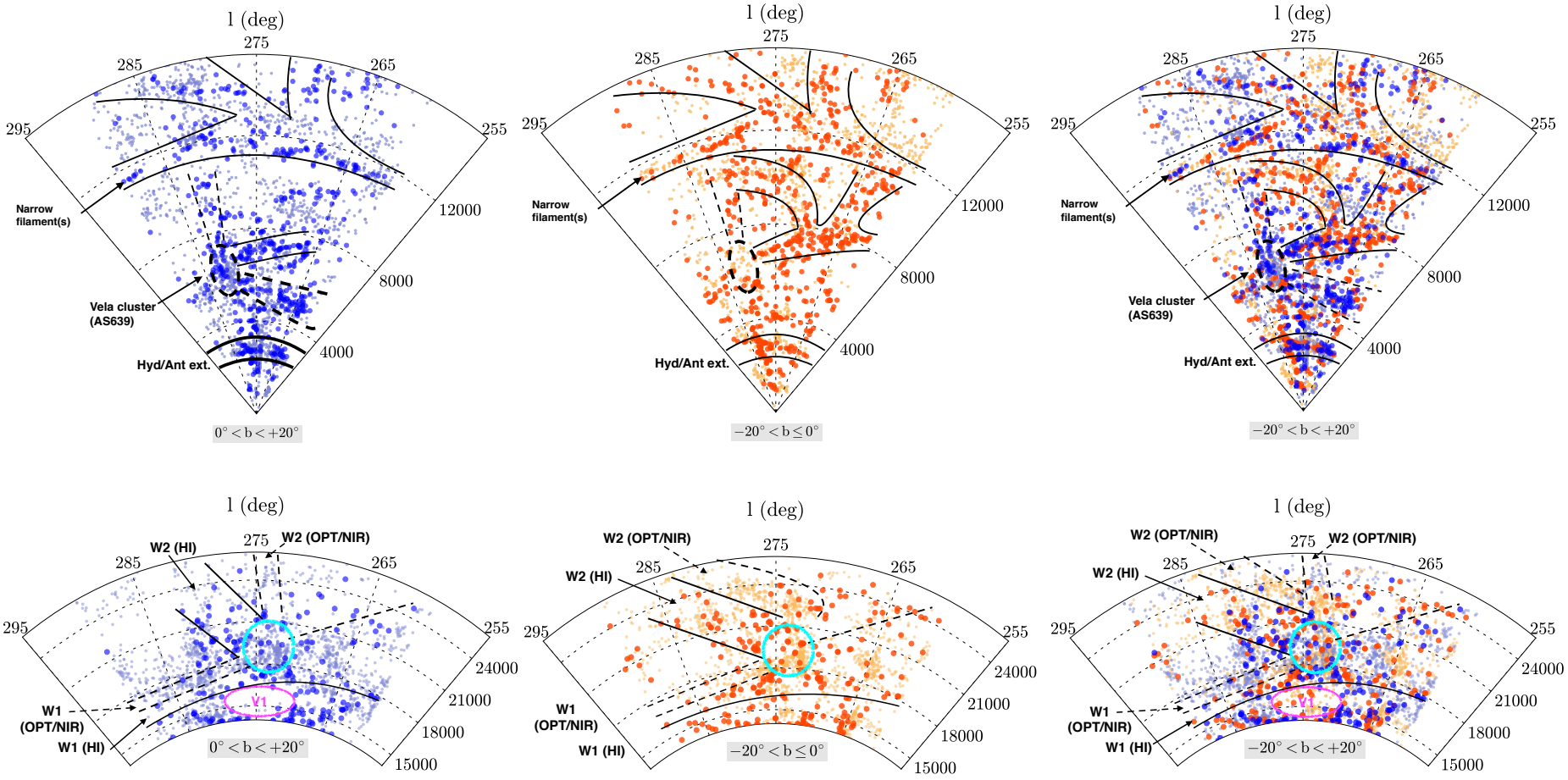

Figure 4.17: Annotated redshift wedge diagrams illustrating galaxies located above the Plane (blue), below (orange), and their combination, covering the Galactic latitude range of $-20° < b < +20°$ and Galactic longitude range $260° \leq \ell \leq 290°$. The smaller and lighter points represent ancillary data from OPT and NIR surveys surrounding the surveyed area, while the larger dots exclusively denote H I detections from Vela–SMGPS and Vela–H I. The top panels highlight the velocity range below $V_{\rm hel} \leq 15500$ km s^{-1}, and the bottom panels the high velocity range $V_{\rm hel} > 15500$ km s^{-1} within which the VSCL resides. The cyan circles in the bottom panels represent the possible crossing location of W1 and W2.

This result also aligns with the general direction of the core of a significant overdensity, as suggested from independent density and velocity field reconstructions by Sorce et al. (2017) and Courtois et al. (2019).
The wedge diagrams (bottom panels of Fig. 4.17) reveal distinguishable features between the walls traced by H I detections and those observed in OPT/NIR detections, suggesting possible offsets between them. This observation points to an ongoing collapse process within the VSCL, with H I detections exhibiting a shift toward or parallel alignment with OPT/NIR walls. The gravitational pull of these walls may attract galaxies from the surrounding cosmic web and potentially making galaxies at the periphery more H I-rich. Alternatively, the gas in the OPT/NIR wall might have been stripped due to interactions and pre-processing in the filaments (e.g., Sarron et al., 2019). Further investigations, particularly through deeper surveys are needed to substantiate this scenario.

The less pronounced supercluster signature in Vela–H I compared to Vela–SMGPS may not only be due to its lower sensitivity. It is plausible that the relatively high number of detections concentrated in Vela–SMGPS is caused by the signature of the walls crossing at these lowest latitudes, raising – nearly doubling – the galaxy counts. In contrast, Vela–H I, with its 0.75 mJy beam^{-1} sensitivity, is 'only' revealing the most H I-massive galaxies in Vela. They also trace the filaments or walls, but because of the lower density, the wall also contains fewer very rich H I galaxies, while some of them might be feeding into the VSCL core. This interpretation aligns with KK2017, proposing that the VSCL is a supercluster in formation, characterized by two merging wall-like structures. This hypothesis would also bolster the expectation, as suggested by Einasto et al. (2007c) that high-density clusters are connected by lower-density filaments. In combination with the lower density, this could explain the low number of detections along the walls of VSCL. The spatial arrangement of galaxies evident in both the on-sky plot and wedge diagrams strongly suggests that the VSCL possesses the characteristic morphology of a rich supercluster. This morphology is characterized by an elongated, wall-like structure and the presence of multi-branching filaments, as proposed by (Einasto et al., 2011b).

4.6 Conclusions

In our quest to unravel the morphology and characteristics of the Vela Supercluster, concealed within the ZOA, we conducted the blind H I systematic MeerKAT Vela Supercluster survey, denoted as Vela–H I. This survey was strategically positioned to address the formerly unexplored patches at $1° \leq b \leq 6.2°$ and $-6.7° \leq b \leq -2°$ in the Vela region. The design aimed to establish connections between the Vela-SARAO MeerKAT Galactic Plane Survey (Vela–SMGPS, Chapter 3) focused on the innermost ZOA ($-2° \leq b \leq 1°$), and deep OPT/NIR observations of the outer edges of VSCL ($5° \leq |b| \leq 10°$). Over approximately 67 hours, 667 MeerKAT pointings were collected, each lasting 5 minutes, covering an extensive area ($\sim$242 deg^2) both above and

below the GP at $263° \leq \ell \leq 284°$. The dataset was analyzed and reduced, encompassing a velocity range up to $cz \sim 25000$ km s^{-1}.

The survey's Nyquist sampling configuration effectively reduced the initial rms during data acquisition, ranging from 0.88 to 9.27 mJy beam^{-1}, to a final noise level of 0.68–1.24 mJy beam^{-1} after meticulous solar RFI flagging and mosaicking.

In total, 719 H I sources in Vela–H I were detected and parameterized, revealing 508 previously unknown detections. Merely 211 of these detections were previously recorded in the literature as potential galaxies, and among them, only 66 possess available redshift information with just five surpassing $cz > 16000$ km s^{-1}. These figures underscore the efficacy of blind H I surveys in identifying obscured galaxies within the ZOA. Obtaining the redshifts of these galaxies would be arduous or nearly impossible in optical, particularly at higher redshifts (VSCL distance). The Vela–H I parameters and positions demonstrate high quality: the measured integrated fluxes, linewidths, and systemic velocities exhibit no deviation in a one-to-one relation, confirming the overall consistency of Vela-H I detections with Vela–SMGPS and HIZOA.

The majority of OPT/NIR cross-matches lie within $5.6'' \pm 3.4''$ of the H I positions. Considering that Vela–H I's internal coordinate precision is approximately $5.4'' \pm 2.7''$, this demonstrates excellent positional accuracy. The observed difference of 70 ± 15 km s^{-1} between the optical and H I velocities is also smaller than the uncertainty of the optical velocities, which is on the order of 100 km s^{-1}.

The inclusion of 719 new redshift measurements significantly solidifies our understanding of the overall picture of the LSS when linking previously known structures at much higher latitudes in the Vela region. It clearly confirms the continuation of the Hydra/Antlia extension across the GP, marked by two branching structures at $\ell \sim 278°$ and $282°$ in the velocity range of $2000 - 3500$ km s^{-1}, reaching a group of galaxies at $(281°, –7°)$. Additionally, we have uncovered previously unknown LSS, including a diagonally structured wall possibly linked to AS639, and a void with a diameter of approximately 10 Mpc at $\ell \sim 279°$, $b \sim 0°$, at 6500–8000 km s^{-1}. At the distance of the VSCL, the distribution, connected to known clusters, reinforces the multi-branching morphology of the supercluster and affirms the existence of two potentially merging walls at $270° \leq \ell \leq 279°$, $18500 - 21500$ km s^{-1}. We also observe the presence of underdense structures just before W1, ranging from 13000 to 17000 km s^{-1}, as indicated by the sensitivity curve. When looking at the wedge diagrams, apparent offsets between the H I and OPT/NIR walls are observed, which seems to support the notion that VSCL is a supercluster in formation.

Our ultimate goal is to estimate the mass-overdensity of VSCL and construct cosmic flow fields in the Vela region. The forthcoming chapter will analyze H I Mass Functions (HIMFs), com-

bining data from Vela–SMGPS and Vela–H I to derive the VSCL overdensity. To get further insight into the crossing, a deeper H I survey targeting the suggested core location of the VSCL is deemed essential for further validation. Alternatively, running the DisPerSE filament finder (Sousbie, 2011) might also help identify persistent structures quantitatively. Future endeavors involve deriving apparent magnitudes from WISE-detected galaxies to obtain distance indicators, facilitating the measurement of peculiar velocities and their influence on cosmic flow fields, as discussed in future work (Section 6.2).

chapter 5

The H I mass functions of galaxies from MeerKAT blind systematic surveys of the Zone of Avoidance: Vela–SMGPS and Vela–H I

Abstract

This study estimates the H I mass function (HIMF) of galaxies of the two systematic H I surveys presented in the previous chapters. To mitigate any selection bias due to the varying distances of these LSS, I employed the two-dimensional stepwise maximum likelihood (2DSWML) to determine the number of space densities used for the HIMF. Overall, the results of the best-fitting Schechter parameters of Vela–SMGPS and Vela–H I are consistent with an ALFALFA HIMF within 2σ errors, while parameters from the combined sample are consistent within 3σ errors. However, they suggest a slightly flatter slope and a lower knee mass $M^*_{\rm HI}$ than ALFALFA. The Vela–H I HIMF exhibits a lower normalization parameter Φ_*, possibly due to underdensities preceding the VSCL, lacking galaxies with $M_{\rm HI} > 10^{9.3}\ h_{70}^{-2}\,{\rm M}_\odot$. Estimating the overdensity factors at the walls yields a value of 3.5 ± 1.6 for W1 ($16000 - 19000$ km s^{-1}) and 1.8 ± 2.4 for W2 ($19000 - 23000$ km s^{-1}). These findings provide additional evidence for the existence of the VSCL walls, with the second wall being broader and less dense.

5.1 Introduction

The influence of the environment on the neutral gas content of galaxies has long been recognized as a significant driver of galaxy evolution (Haynes et al., 1984; Cortese et al., 2021). One can assess the number of galaxies with a specific H I mass that is present per cubic Mpc within a designated volume. This quantification is referred to as the neutral atomic hydrogen mass function (HIMF), generally well-described by the 'Schechter function' (Schechter, 1976), which has also been widely used to describe luminosity functions in the optical and various other wavebands (e.g., Marzke et al., 1998; Loveday, 2000). This specific functional form is expressed

as:

$$\Phi(M_{\rm HI}) = \ln 10 \Phi_* \left(\frac{M_{\rm HI}}{M^*_{\rm HI}}\right)^{(\alpha+1)} e^{-\frac{M_{\rm HI}}{M^*_{\rm HI}}}, \tag{5.1}$$

defined by three key parameters: α, $M^*_{\rm HI}$, and, Φ_*. α represents the slope at the low-mass, end where ($M_{\rm HI} \ll M^*_{\rm HI}$). The 'knee' or characteristic H I mass, $M^*_{\rm HI}$, marks the point where the function undergoes an exponential drop-off toward the high-mass end. Finally, Φ_* denotes the normalization constant of the HIMF. We use the ordinary non-linear least squares minimization method[1] to determine the best-fitting Schechter parameters.

The HIMF can serve as an indicator of the galaxy's environment, i.e., local density such as in clusters vs. field, as well as the evolution of neutral hydrogen content as a function of redshift. The shape of the HIMF has been extensively investigated, primarily in the Local Universe (at $z = 0$), using targeted 21-cm observations (e.g., Springob et al. 2005; Catinella et al. 2008), various blind H I surveys conducted with single-dish telescopes (e.g., Zwaan et al. 2003; Martin et al. 2010; Jones et al. 2016, 2018; Said et al. 2019; Xi et al. 2021), and interferometers (e.g., Gogate 2022; Ponomareva et al. 2023). To date, the only surveys that have uniquely achieved *direct* measurements of the HIMF beyond the Local Universe include the MeerKAT MIGHTEE HIMF (Ponomareva et al., 2023), which extends up to $z \sim 0.084$, the Arecibo Ultra-Deep Survey (AUDS, Xi et al. 2021), probing the HIMF up to $z \sim 0.16$, and the Blind Ultra-Deep H I Environmental Survey (BUDHIES, Gogate 2022) conducted with the Westerbork Synthesis Radio Telescope (WSRT), reaching out to $z \sim 0.2$.

These studies have revealed that the HIMF exhibits variations based on morphological type, as well as the local and global environment (Jones et al., 2020). Despite these insights, a consensus on the faint-end slope of the HIMF has yet to be achieved. Additionally, it remains less well-known how the HIMF varies as a function of redshift; however, this knowledge is crucial for understanding the evolution of the HIMF relative to the H I content of the Universe as a function of z. For instance, Zwaan et al. (2005) observed an increased proportion of galaxies with low H I masses (i.e., a steeper faint-end slope) in more densely populated environments, whereas Springob et al. (2005) noted the opposite trend (i.e., a flatter faint-end slope). More recently, Said et al. (2019) identified a flatter slope in the dense regions of the ZOA, yet observed no distinct trend in the knee or characteristic mass $M^*_{\rm HI}$. Notably, Jones et al. (2016) found no apparent trend of the low-mass slope among galaxies in different density environments. Instead, they observed an increased knee mass with higher density. Xi et al. (2021) observed similar outcomes, although not in relation to density but in association with redshift.

In this chapter, I examine two blind extragalactic H I surveys of the ZOA carried out with MeerKAT, as detailed in Chapters 3 and 4. These surveys revealed previously unknown struc-

[1] `scipy.optimize.curve_fit` routine in PYTHON

tures within the most obscured regions of the sky and, most significantly, provided insights into the previously obscured segment of the VSCL. An examination of the HIMF in the Vela region can be used as a tracer to quantify the overdensity in VSCL and understand the galaxy population present in that region.

By using the samples obtained from the Vela SARAO MeerKAT Galactic Plane survey (Chapter 3) and the MeerKAT Vela Supercluster survey (Chapter 4), I aim to calculate the HIMF of the Vela region which extends to larger distances ($V_{\rm hel} \sim 25000$ km s^{-1}), with deeper sensitivities compared to most previous systematic H I surveys in the ZOA. In the subsequent sections, I will describe how we select our sample with different completeness estimations and outline the different methods used to calculate the HIMFs. I will conclude by presenting the measured HIMFs in the Vela region compared to simulations and estimate the overdensity of the walls within the velocity range 19500 ± 3500 km s^{-1}.

5.2 Sample selection and completeness

Prior to conducting a statistical analysis for HIMF construction on any sample, it is crucial to ascertain its completeness. The survey's ability to detect a galaxy is contingent on both its integrated flux density and velocity linewidth. Detection is, for example, more straightforward for galaxies with high integrated fluxes and small to moderate linewidths. Reducing a galaxy's integrated flux or increasing its linewidth typically reduces its likelihood of standing out over the rms noise. The completeness could be defined by a mean flux-limit (e.g., Donley et al., 2005), which is the minimum mean flux density required for the detection of each galaxy.

Numerous factors, including non-uniform noise distribution, the presence of RFI, and residual continuum, can influence the detection of galaxies in the data. The likelihood of detecting a galaxy with identical integrated flux and linewidth across different survey regions can vary due to local noise variations. Therefore, we need to ensure the selection of a complete sample from regions with relatively consistent local noise, minimizing the impact of high rms patches which is particularly important to H I surveys that have a high prevalence of continuum sources.

In the initial step, illustrated in Fig. 5.1, I exclude part of the survey where noise reaches values above 2σ of the global rms noise measured in Vela–SMGPS (i.e., rms > 0.6 mJy beam^{-1}) and Vela–H I (rms > 1.35 mJy beam^{-1}); these are represented by magenta circles in the pointing

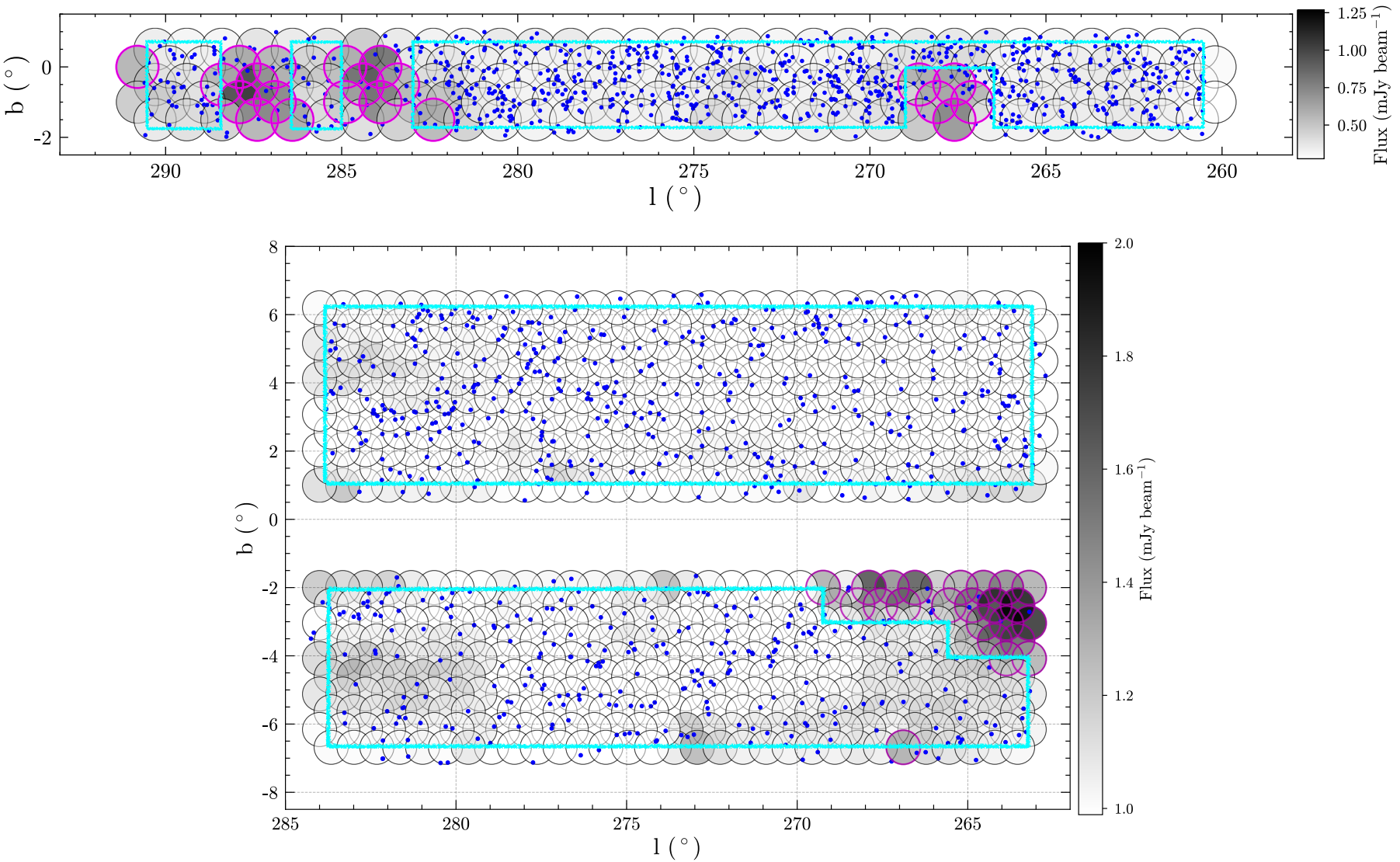

Figure 5.1: The sky positions of H I detections (blue dots) detected in the Vela–SMGPS (top panel) and Vela–H I (bottom panel) surveys. The pointing configurations of both surveys are shown by partly overlapping circles, with grayscale color indicating the rms value of each respective field. Magenta-bordered fields highlight regions with rms values exceeding 0.6 mJy beam^{-1} (top) and 1.35 mJy beam^{-1} (bottom), the areas with high noise. The cyan solid lines represent the applied cuts, ensuring the inclusion of regions with predominantly uniform rms values.

configurations. Additionally, regions near the outermost edges of the survey borders were excluded, where the survey did not reach the same level of uniformity. These are still valuable for investigations of LSS as shown in Chapters 3 and 4, but not for deriving the HIMF. Only a few galaxies are observed in the magenta regions. We therefore restrict our further analysis to the region with minor rms fluctuations delimited by the cyan lines, resulting in 691 detections spread across 58.2 deg^2 in Vela–SMGPS and 631 detections in a 192.8 deg^2 area in Vela–H I. This yields a total of 1322 galaxies when combined, suitable for a completeness estimate as well as a more robust HIMF determination.

5.2.1 Homogeneous completeness

The most dependable method for assessing a survey's completeness involves injecting synthetic galaxies into the H I cubes and recovering them using the same methodology applied to identify real sources (e.g., Zwaan et al. 2004; Hoppmann et al. 2015). However, the result would still be uncertain due to local noise variations inherent to surveys at such low latitudes. Alternatively, an approach can be taken by restricting our sample to a mean flux threshold, ensuring that we achieve a sample that is nearly complete.

To establish the mean flux limit, I apply the method described in Section 3.5.1 of Chapter 3, which assumes the sample's homogeneity and isotropy, expected to follow a Euclidean power law. I perform a power-law fit with a slope of $-3/2$ on the right-hand side of the histogram of mean flux density in log-log space. The completeness limit is identified where the histogram starts to deviate notably from the slope (e.g., Donley et al., 2005; McIntyre et al., 2015; Staveley-Smith et al., 2016; Schröder et al., 2019).

I illustrate in Fig. 5.2 the approximate mean flux density completeness limits for two blind systematic surveys in the ZOA and their respective simulations. In the plots, I included simulations tailored for the SKA science case with characteristics corresponding to each survey, as a representation of expectations that reflect a more uniform distribution in space. These include the simulation S45 with an rms of 0.45 mJy beam^{-1} (hereafter S45) for Vela–SMGPS, as presented in Section 3.5.2 of Chapter 3, and S75 with an rms of 0.75 mJy beam^{-1} for Vela–H I as presented in Section 4.5 of Chapter 4. For the entire SMGPS area of 528 deg^2, S45, and S75 predict 5510 and 2105 galaxies out to $V_{\rm hel} < 24000$ km s^{-1} respectively. To facilitate comparison, we scaled the S45 and S75 counts per bin to match the respective surveyed area. These are reduced to 607 and 769 galaxies to match the $\sim$58 deg^2 and $\sim$193 deg^2 selected survey areas in Vela–SMGPS and Vela–H I, for use in the rest of the analysis. Both simulations are shown in cyan in Fig. 5.2. After measuring their completeness, our samples are observed to deviate earlier than the simulations, confirming that they become incomplete at lower mean flux levels most likely due to continuum residuals and patches of higher rms in the surveys, and are likely dominated by

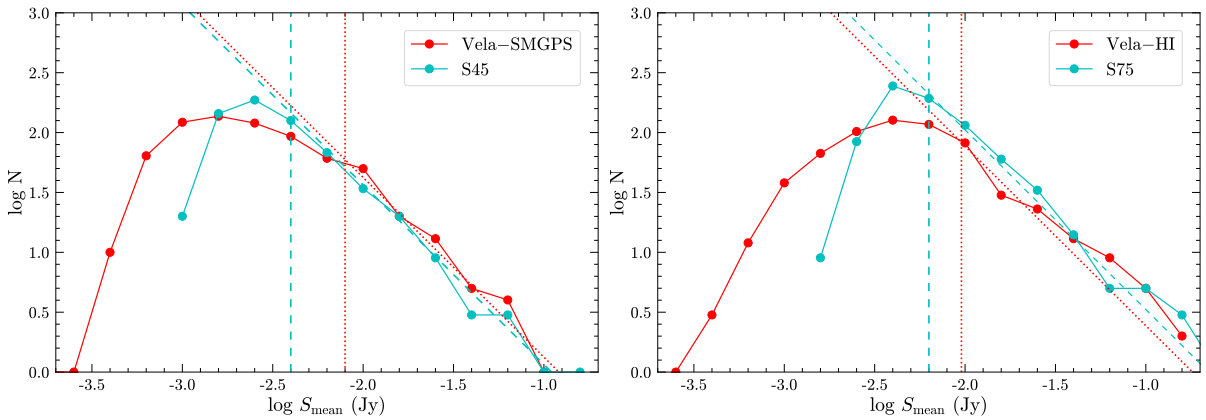

Figure 5.2: log $S_{\rm mean}$ vs. log N for Vela–SMGPS (left panel) and Vela–H I (right panel). The distributions of the respective surveys are represented by the red dotted lines, and the simulation distribution is illustrated by the cyan dashed line for S45 and S75, respectively. Diagonal lines with slopes of $-3/2$ correspond to the expected homogeneous distribution of each sample. Vertical lines are indicative of where completeness is reached.

LSS.

5.2.2 Modified V/V$_{\rm max}$ test

A robust alternative for evaluating survey completeness involves using the Test for Completeness (T_c), a statistical technique developed by Rauzy (2001) to originally assess magnitude-limited optical catalogs. The test shares similarities to the V/V_{max} test by Schmidt (1968), although it relies on the assumption of a uniform shape of the HIMF with position. This characteristic makes it less sensitive to LSS, which is considerable in the southern ZOA (see previous two chapters). The Rauzy test has also been used to assess the completeness of H I catalogs (e.g., Zwaan et al., 2004; Toribio et al., 2011; Staveley-Smith et al., 2016; Xi et al., 2021), thereby providing an independent, more robust completeness limit to our H I surveys, independent of LSS.

In essence, the process is as follows: a sample of galaxies exceeding a specific flux threshold within a defined volume is selected. The flux is varied iteratively in ascending order during this selection. Following that, the completeness assessment involves comparing the number of galaxies brighter or fainter than each galaxy in the chosen sample (see Zwaan et al. 2004 for more details). For each flux limit, this comparison is translated into the completeness variable:

$$T_c = \frac{\sum_{i=1}^{N_{\rm gal}} (\zeta_i - 0.5)}{\left(\sum_{i=1}^{N_{\rm gal}} V_i\right)^{1/2}}, \tag{5.2}$$

where for an object i:

$$\begin{cases} \zeta_i = \frac{r_i}{n_i+1}, \text{ and,} \\ V_i = \frac{n_i-1}{12(n_i+1)}. \end{cases} \tag{5.3}$$

ζ_i is a uniformly distributed random variable with values ranging from 0 to 1 for each galaxy in the sample, while V_i represents its variance. When gradually increasing the flux limits, we have the option to use either the integrated flux density or the mean flux density. For a given integrated flux limit $F_{\rm bin}$, for example, the procedure involves counting the number of objects with $S_{\rm int} \geq F_{\rm bin}$ within the volume. For each bright galaxy i meeting this criterion, r_i represents the count of objects with $M_{\rm HI} \geq M_{{\rm HI},i}$ and $D \leq D_i$. In turn, n_i corresponds to the count of objects with $M_{\rm HI} \geq M_{{\rm lim},i}$ and $M_{\rm HI} \geq M_{{\rm HI},i}$ and $D \leq D_i$. Here, D_i denotes the distance at which the galaxy i was detected in the survey and $M_{{\rm lim},i}$ refers to the most massive galaxy at a specific distance D_i that remains visible or detectable at a flux limit $F_{\rm bin}$.

I computed the logarithms of the equivalent H I mass ($\log M_{{\rm HI},i}$) and the H I mass limit ($\log M_{{\rm lim},i}$) using the following equations:

$$\log M_{{\rm HI},i} = \log(D_i^2 \times S_{{\rm int},i}), \text{ and,} \tag{5.4}$$

$$\log M_{{\rm lim},i} = \log(D_i^2 \times F_{\rm bin}). \tag{5.5}$$

The Rauzy statistics can then be expressed as a function of integrated flux and/or mean flux density. When examining the distribution of integrated flux and mean flux density with linewidth, it is observed that galaxies with narrow linewidths are more easily detectable given a specific integrated flux, while galaxies with broad linewidths require greater baseline stability to be detected. Opting for completeness values derived from integrated flux may introduce more instabilities and uncertainties toward broad linewidth galaxies. However, in this study, our focus is not on dwarfs but rather on massive galaxies that populate the VSCL walls. Therefore, selecting completeness based on the mean flux density is more appropriate to account for baseline instabilities without excluding narrow linewidth galaxies from the sample.

The outcomes obtained from the T_c statistics for the Vela–SMGPS sample (in cyan), the Vela–H I sample (in magenta), and the combined sample (in dark brown) are presented in Fig. 5.3. While the top panel illustrates the variation of the Rauzy completeness statistic as a function of integrated flux, we opt for the results in the bottom panel for the subsequent analysis, demonstrating the variation as a function of mean flux density. T_c is expected to conform to a Gaussian distribution with an average value of 0 and unit variance for statistically complete galaxy samples, shifting systematically towards negative values for incomplete samples. The shaded area represents errors linked to the variance unity of T_c associated with counting statistics.

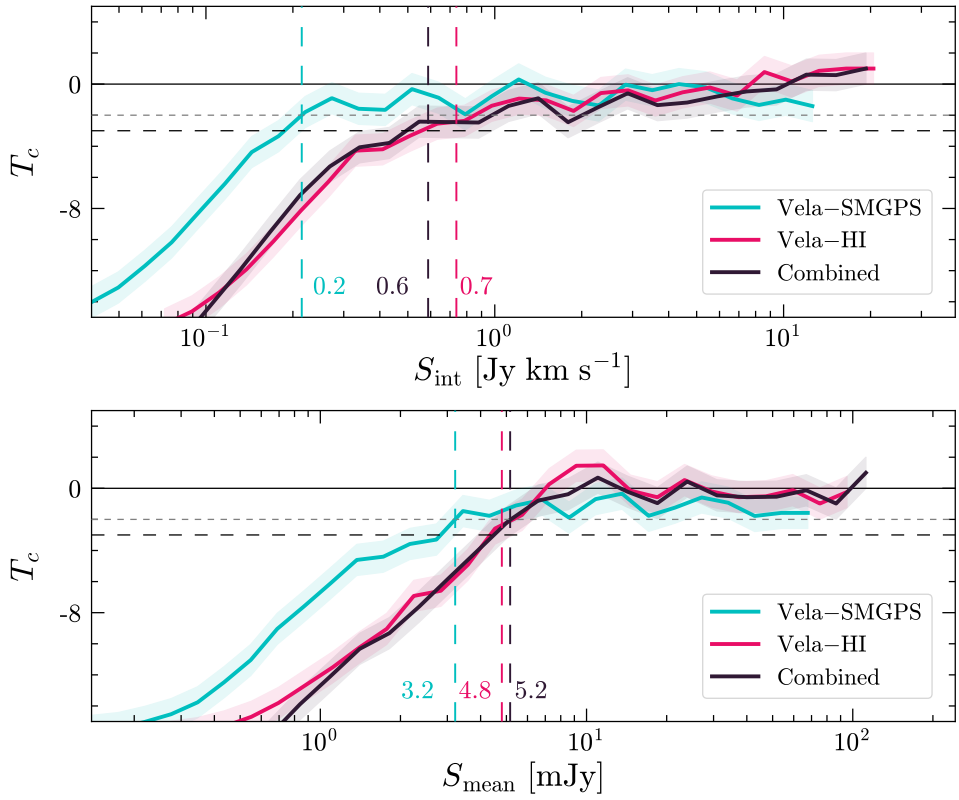

Figure 5.3: The variation of the Rauzy completeness statistic T_c for the integrated flux (top panel) and the mean flux density (bottom panel). Cyan, magenta, and dark brown lines correspond, respectively, to the statistics for Vela–SMGPS, Vela–H I, and the combined sample. The horizontal lines reflect the lower limits of the completeness, where the 97.7% (T_c = –2) and 99.4% (T_c = –3) confidence bounds are represented by the closely spaced grey and widely spaced black dashed lines, respectively. The best characterization of completeness, set at T_c = –2 for each sample, is shown by vertical lines. The shaded area highlights errors attributed to counting statistics.

The completeness limit is determined when T_c consistently decreases to negative values, usually with T_c = –2(–3), representing a 97.7% (99.4%) confidence level, as illustrated by closely spaced grey (widely spaced black) dashed lines in Fig. 5.3. Summarized Rauzy test results for the two T_c levels and the proportion of galaxies in the sample above the completeness limits are detailed in Table 5.1. At T_c = –2, which we use for the rest of the analysis, we measured mean flux density limits ($S_{\rm lim}$) of 3.2, 4.8, and 5.2 mJy for Vela–SMGPS, Vela–H I, and the combined samples, respectively. These limits are met by 44%, 58%, and 40% of the respective subsets which decreases our samples to 314, 361, and 535 galaxies for Vela–SMGPS, Vela–H I, and the combined samples, forming the basis for constructing the HIMF.

Table 5.1: Rauzy completeness limits for the mean flux density at the 97.7% (T_c = –2) and 99.4% (T_c = –3) confidence bounds for Vela–SMGPS, Vela–H I, and the combined samples. The variable f represents the fraction of galaxies surpassing the completeness limit within each sample.

Dataset	T_c = –2		T_c = –3	
	$S_{\rm lim}$ [mJy]	f	$S_{\rm lim}$ [mJy]	f
Vela–SMGPS (691)	3.2	0.44	2.8	0.48
Vela–H I (631)	4.8	0.58	4.3	0.62
Combined (1322)	5.2	0.40	4.5	0.45

5.3 Derivation of the H I mass function

We use the above derived completeness limits to derive the H I mass function (HIMF) for all galaxies meeting our selection criteria in both surveys. The HIMF is a measure of the average number density of galaxies in the Universe based on their H I masses, denoted as $\Phi(M_{\rm HI})$ in units of h_{70}^3 Mpc^{-3}. Given the wide range of H I masses among galaxies, it is common practice to calculate this number density per decade of H I mass on a logarithmic scale, defined by:

$$\Phi(M_{\rm HI}) = \frac{{\rm d}N_{\rm gal}}{{\rm d}V\,{\rm d}\log_{10}(M_{\rm HI})}. \tag{5.6}$$

${\rm d}N_{\rm gal}$ represents the mean count of galaxies within the volume ${\rm d}V$, each having H I masses within an infinitesimally small range around $M_{\rm HI}$.

It is important to note that the H I mass distribution of galaxies is significantly influenced by a selection bias arising from survey sensitivity limits. For instance, the detection range for massive galaxies extends much farther than that for lower-mass galaxies. This makes the conversion of the average number count into the intrinsic space density of galaxies a complex process. One can compensate for the bias by weighting each source, taking into account the maximum detectable volume determined by the survey's sensitivity limits, as calculated in Section 5.2.2. Two widely employed techniques for measuring these detectable volumes and correcting the survey selection bias include using the V_{max} (Schmidt, 1968) and the $V_{\it eff}$ (Efstathiou et al., 1988; Zwaan et al., 2003, 2005) volume definitions, also referred to as the $1/V_{max}$ and the two-dimensional stepwise maximum likelihood (2DSWML) estimators.

5.3.1 The 1/V$_{\rm max}$ method

In this approach, the objective is to count the number of galaxies within each mass bin of the flux-limited sample, normalized by the survey-detectable volume $V_{max,j}$ for galaxies within the specific logarithmic mass bin ΔM. The HIMF is then computed by aggregating $1/V_{max}$ over the mass bins using the formula:

$$\Phi(M_{\rm HI}) = n_j = \frac{1}{\Delta M}\sum_i \frac{1}{V_{max,i}}, \tag{5.7}$$

where the summation includes all galaxies i with the specified mass bin j. $V_{max,i}$ is defined as the maximum volume within which a galaxy i can be reliably detected, and is expressed as:

$$V_{max,i} = \frac{1}{3}\Omega_{\rm survey}(D_{max,i}\times h_{70})^3, \tag{5.8}$$

see Appendix A of Papastergis (2013). $\Omega_{\rm survey}$ is the area of the survey footprint expressed in square radians:

$$\Omega_{\rm survey} = survey\ area \times \left(\frac{\pi}{180}\right)^2. \tag{5.9}$$

To determine the value of D_{max}, representing the maximum distance at which each galaxy remains detectable and leading to the value of V_{max}, we use the survey completeness limit. This involves iteratively assessing the distance of each detection across the redshift range of the entire sample. Although we have initial knowledge of the distance at which each galaxy was detected, denoted as D_i, we calculate the maximum distance, $D_{\rm lim}$, using the formula:

$$D_{\rm lim} = D_i \times \left(\frac{S_i}{S_{\rm lim}}\right)^{1/2}, \tag{5.10}$$

where S_i represents the mean flux density of object i, and $S_{\rm lim}$ the limiting mean flux density derived from the Rauzy statistic in Section 5.2.2. If the iterated distance value exceeds $D_{\rm lim}$, then D_{max} is set to $D_{\rm lim}$. On the other hand, if the iterated distance consistently remain below $D_{\rm lim}$, it suggests the potential for V_{max} to surpass the volume associated with the redshift boundary of the survey. In such cases, we designate D_{max} as the maximum distance at $z = 0.08$, representing our survey limit. Once V_{max} is computed using Eq. 5.8, the Poisson counting error of the bin values' $1/V_{max}$ estimates is determined by the simple expression:

$$\sigma_j^2 = \frac{1}{\Delta M^2} \sum_i \frac{1}{V_{max,i}^2}. \tag{5.11}$$

While the $1/V_{max}$ method is commonly employed for its simplicity and efficiency, it comes with a notable limitation. The method assumes a uniform distribution of the galaxies within the survey volume. This condition is not met in our surveys and can therefore lead to biases in space density estimates, given the LSS uncovered in our surveys. This sensitivity to cosmic variance can result in biases affecting the shape and amplitude of the HIMF, particularly in small samples. To address this issue, density-independent estimators like the 2DSWML method have been developed (cf. Efstathiou et al., 1988; Zwaan et al., 2003, 2005; Martin et al., 2010; Jones et al., 2018), aiming to mitigate biases introduced by density fluctuations. This alternative approach is discussed in the following section.

5.3.2 The 2DSWML method

The difference between the two methods lies in the manner in which the volumes V_{max} and V_{eff} are calculated. The 2DSWML method, alternatively referred to as the $1/V_{eff}$ method, involves binning the two-dimensional distribution of H I mass and H I linewidth. The goal is to iteratively determine the maximum likelihood solution for the number density of galaxies (Φ_{jk}), starting from an initial guess (see Eq. B6 in Martin et al. 2010). The derivation of the maximum

likelihood solution follows these iterative steps:

$$\Phi_{jk} = \frac{n_{jk}}{\sum_i \frac{H_{ijk}}{\sum_m \sum_n H_{imn}\Phi_{mn}}}, \tag{5.12}$$

where, in mass bins j and width bins k, n_{jk} represents the count of galaxies per bin. By defining $M = \log M_{\rm HI}$ and $W = \log w_{50}$, we employed a configuration with approximately three and a half mass bins per dex ($\Delta M = 0.3$ dex) and five width bins per dex ($\Delta W = 0.2$ dex) for our surveys. H_{ijk} serves as a function that ensures the summation encompasses only galaxies within the volume accessible to sources in bin jk, i.e., the fraction of the bin available to source i (cf. Eq. 11 in Zwaan et al. 2003):

$$H_{ijk} = \frac{1}{\Delta M \Delta W} \int_{W=W_k-\Delta W/2}^{W^+} \int_{M=M^-}^{M_j+\Delta M/2} dM dW, \tag{5.13}$$

where M_j and W_k are the central bin jk values, M_j^- is the lower mass limit value in bin j and M_j^+ the maximum mass value in bin j (same for W with W_k^-, and W_k^+). For an object i,

$$M^-_{{\rm lim},i} = M_i + \log(S_{\rm lim}/S_i) - W_i + W_k^-, \text{ and, } M^+_{{\rm lim},i} = M_i + \log(S_{\rm lim}/S_i) - W_i + W_k^+.$$

This simplifies the value of H_{ijk} to:

$$H_{ijk} = \begin{cases} 1, & \text{if } M_j^- \geq M^+_{{\rm lim},i}\ , \\ \frac{(M_j^+ - M^-_{{\rm lim},i})^2}{2\Delta M \Delta W}, & \text{if } M^-_{{\rm lim},i} < M_j^+ < M^+_{{\rm lim},i}\ , \\ \frac{2M_j^+ - M^+_{{\rm lim},i} - M^-_{{\rm lim},i}}{2\Delta M}, & \text{if } M_j^- \leq M^-_{{\rm lim},i} \text{ and } M_j^+ \geq M^+_{{\rm lim},i}\ , \\ 1 - \frac{M^+_{{\rm lim},i} - M_j^-}{2\Delta M \Delta W}, & \text{if } M^-_{{\rm lim},i} \leq M_j^- < M^+_{{\rm lim},i}\ , \\ 0, & \text{if } M_j^+ \leq M^-_{{\rm lim},i}; \text{ or } M_j^- \geq M^-_{{\rm lim},i} \text{ and } M_j^+ \leq M^+_{{\rm lim},i}\ . \end{cases}$$

The denominator in Eq. 5.12 represents the effective volume that galaxies within bin jk can utilize. It can be alternatively expressed as:

$$\Phi_{jk} = \frac{1}{\Delta M \Delta W} \sum_i \frac{1}{V_{eff,i}}, \tag{5.14}$$

for every galaxy i falling within the mass bin j and width bin k. $V_{eff,i}$ takes into account the number of galaxies l present within the detectable volume of galaxy i, and can be defined as:

$$V_{eff,i} = \sum_l \frac{1}{\sum_m \sum_n H_{lmn}\Phi_{mn}}. \tag{5.15}$$

While H_{lmn} can be computed in a manner analogous to Eq. 5.13, Φ_{mn} is represented as a 2D array with dimensions corresponding to the number of mass bins (m) and width bins (n). The values in this array are initially set to $1/mn\Delta M \Delta W$. The galaxy candidates l are those that

meet the criterion $D_{\mathrm{lim},l} > D_i$, where $D_{\mathrm{lim},l}$ is computed using the expression from Eq. 5.10.

Additionally, it is important to note that the value of $V_{eff,i}$ in Eq. 5.14 must be normalized before obtaining the average number densities. This involves dividing its value by the normalization parameter n_1 defined by Eq. A.29 in Papastergis (2013). In simpler terms, we use the minimum variance estimator proposed by Davis & Huchra (1982) to estimate the projected size of the survey, assuming spherical symmetry to calculate the volume. The latter is derived using Eq. 5.8, where D_{max} is the maximum distance reached by the survey at $z = 0.08$.

Upon normalizing $V_{eff,i}$, one has the option to obtain either the velocity width function by marginalizing over the H I mass (as demonstrated by Papastergis et al. 2011) or the H I mass function (HIMF) by marginalizing over the linewidth (as illustrated by Martin et al. 2010; Said et al. 2019). Given our objective to calculate the HIMF, we derive the H I mass distribution from the bivariate distribution by marginalizing Eq. 5.12 over the linewidth, expressed as:

$$\Phi_j = \sum_k \Phi_{jk} \Delta W. \tag{5.16}$$

The counting error associated with the HIMF can be computed using the Poisson error defined in Eq. 5.11, now expressed as:

$$\sigma^2_{jk} = \frac{1}{\Delta M^2 \Delta W^2} \sum_i \frac{1}{V^2_{eff,i}}. \tag{5.17}$$

5.4 Results and Discussion

Figures 5.4, 5.5, and 5.6 present the HIMFs obtained through the 2DSWML method, utilizing mass bins of 0.3 dex and width bins of 0.2 dex for the Vela–SMGPS, Vela–H I, and the combined samples above the completeness limits S_{lim}, respectively. The blue dots illustrate the intrinsic number density per logarithmic H I mass bins, the solid line represents the best-fit Schechter function described by Eq. 5.1, and the error bars indicate Poisson errors defined by Eq. 5.17. The histogram below each HIMF visualizes the count of H I sources above completeness in each mass bin. For each fitted Schechter function, the best-fitting parameters are detailed in Table 5.2.

For comparison, we incorporate the S45 simulation results with cyan colors in Fig. 5.4, while in Fig. 5.5, the S75 results are included. All HIMF figures, including Fig. 5.6, also showcase the HIMF from the Arecibo Legacy Fast ALFA survey 100 per cent catalogue (ALFALFA 100; Jones et al. 2018) as black dashed lines. It is worth noting that mass bins below $10^{7.8} h_{70}^{-2}\,\mathrm{M}_\odot$ and above $10^{10.5} h_{70}^{-2}\,\mathrm{M}_\odot$ tend to exhibit increased errors due to limited statistical numbers. Therefore, when comparing the Vela–SMGPS sample with S45 and the Vela–H I sample with S75, we appropriately focus on the intermediate mass bins.

Table 5.2: The best-fitting Schechter parameters for the Vela–SMGPS, Vela–H I, and the combined samples used in this work. For reference, HIMF parameters from the simulations S45, S75, and the literature are included for comparison, specifically from ALFALFA 100 (Jones et al., 2018) and the H I Parkes All Sky Survey (HIPASS; Zwaan et al. 2005). To facilitate a straightforward comparison, the parameters of the HIPASS HIMF have been scaled to $H_0 = 70$ km s^{-1} Mpc^{-1}.

Survey	Sample size	α	$\log_{10}(M^*_{\rm HI}/h_{70}^{-2}\,{\rm M}_\odot)$	$\Phi_*(10^{-3}\,h_{70}^{-3}\,{\rm Mpc}^{-3})$
Vela–SMGPS	314	-1.11 ± 0.08	9.84 ± 0.06	7.6 ± 1.4
Vela–H I	361	-1.07 ± 0.11	9.83 ± 0.07	3.5 ± 0.8
Combined	535	-1.12 ± 0.07	9.81 ± 0.05	4.6 ± 0.8
S45	331	-1.18 ± 0.09	9.84 ± 0.06	7.5 ± 1.5
S75	576	-1.18 ± 0.08	9.9 ± 0.06	4.1 ± 0.9
ALFALFA 100	23621	-1.25 ± 0.02 ± 0.1	9.94 ± 0.01 ± 0.05	4.5 ± 0.2 ± 0.8
HIPASS	4010	-1.37 ± 0.03 ± 0.05	9.86 ± 0.03	4.88 ± 0.65

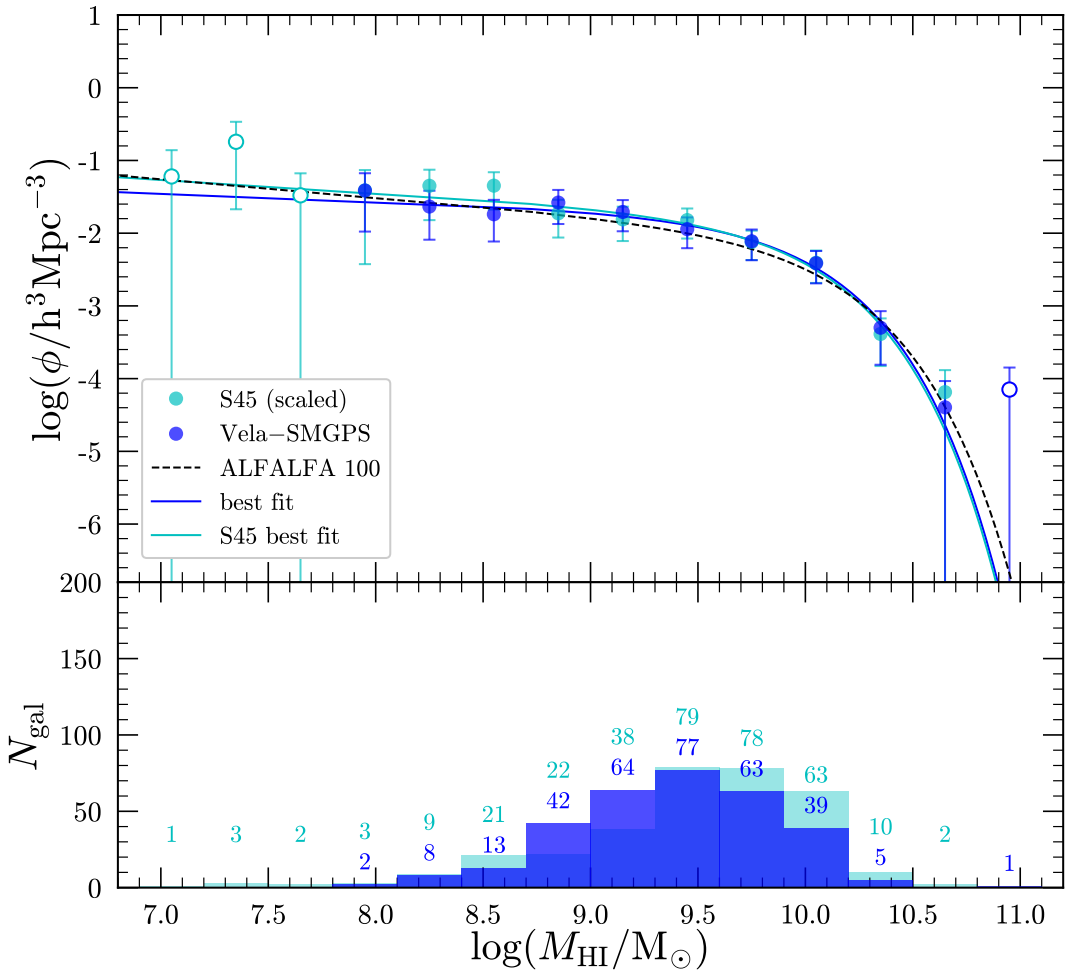

Figure 5.4: The H I mass function constructed for the Vela–SMGPS sample (blue) and the scaled S45 simulation (cyan), each accompanied by their respective best-fitting lines. The open circles have been excluded from the fits. The lower panel illustrates the number counts in logarithmic H I mass bins for both samples. The H I mass function from ALFALFA 100 (Jones et al., 2018) is represented by the black dashed line.

We will start by examining the HIMF of Vela–SMGPS. The blue dots in Fig. 5.4 represent

the number density values obtained from the 2DSWML method for the complete sample of 314 galaxies. The best-fitting Schechter parameters resulted in α = –1.11 ± 0.08, log($M^*_{\rm HI}/h^{-2}_{70}$ $M_\odot$) = 9.84 ± 0.06, and Φ_* = 7.6 ± 1.4 × 10^{-3} h^3_{70} Mpc^{-3}. The scaled simulation S45, shown in cyan, exhibits best-fitting parameters of α = –1.18 ± 0.09, log($M^*_{\rm HI}/h^{-2}_{70}$ $M_\odot$) = 9.84 ± 0.06, and Φ_* = 7.5 ± 1.5 × 10^{-3} h^3_{70} Mpc^{-3}. Except for the $10^{8.25}, 10^{8.55}, 10^{9.45}$, and $10^{10.65} h^{-2}_{70}$ $M_\odot$ bins, which show a higher number density than Vela–SMGPS, the S45 HIMF is consistent within the error. A closer look at the HIMF pattern reveals that the number space density of Vela–SMGPS closely follows the ALFALFA 100 best-fitting line. Considering the Schechter parameters, Vela–SMGPS shows a slightly flatter slope of -1.11 ± 0.08 compared to ALFALFA 100 with a slope of -1.25 ± 0.02, and a slightly lower $M^*_{\rm HI}$, but still consistent at the 2σ level. Regarding the normalization parameter Φ_*, we observe higher values of 7.6 and 7.5×10^{-3} h^3_{70} Mpc^{-3} for Vela–SMGPS and S45, while ALFALFA 100 and HIPASS measured lower values of 4.5 and 4.88×10^{-3} h^3_{70} Mpc^{-3}, respectively. It is interesting to observe the higher normalization of Vela–SMGPS, particularly with respect to S45, despite our knowledge of being less complete compared to the simulation. This discrepancy could indicate a higher density in the survey, attributed to its nature as a narrow strip, which is likely more affected by cosmic variance. Additionally, this region is known to be rich in structures, as mentioned in Section 3.6 of Chapter 3.

The results for Vela–H I are presented in Fig. 5.5. The best-fitting parameters were determined as α = –1.07 ± 0.11, log($M^*_{\rm HI}/h^{-2}_{70}$ $M_\odot$) = 9.83 ± 0.07, Φ_* = 3.5 ± 0.8 × 10^{-3} h^3_{70} Mpc^{-3}. A comparative analysis was then conducted with the HIMF derived from the scaled S75 simulation, characterized by parameters α = -1.18 ± 0.08, log($M^*_{\rm HI}/h^{-2}_{70}$ $M_\odot$) = 9.9 ± 0.06, Φ_* = $4.1 \pm 0.9 \times 10^{-3}$ h^3_{70} Mpc^{-3}, and the literature-based ALFALFA 100 results. The Vela–H I HIMF exhibits a suppression toward the low-mass end, leading to the exclusion of the low-mass bins below $10^{8.1} h^{-2}_{70}$ $M_\odot$ for fitting purposes. In addition to its flatter slope, the Vela–H I HIMF also displays a lower normalization factor, Φ_*, compared to both S75 and ALFALFA 100. These observations may be attributed to predicted galaxies having a higher count in the lowest-width bins, while observed detections are more prevalent in the largest linewidths, as discussed in Section 3.5.3 of Chapter 3. This effect arises from the coarse resolution of our surveys and a limitation in resolution due to a larger beam size. This could lead to an overestimate of linewidths and H I masses for normal spirals because they might include nearby dwarfs. This also results in an under-sampling of the low-linewidth population at the same time. This discrepancy is more pronounced in Vela–H I than in Vela–SMGPS due to the former's larger beam size. The effect of having fewer low-linewidth galaxies compared to the simulations is seen clearly in Fig. 5.7. By inspecting the right panel of the same figure, we furthermore notice that our counts are lower than predictions for massive galaxies ranging from $10^{9.3}$ to $10^{10.5}$ h^{-2}_{70} $M_\odot$ in Vela–H I. This disparity can be attributed to underdensity gaps (denoted as V1 in Chapter 4) within the redshift ranges $13000 - 14500$ km s^{-1} and $15000 - 17000$ km s^{-1}, as illustrated in the

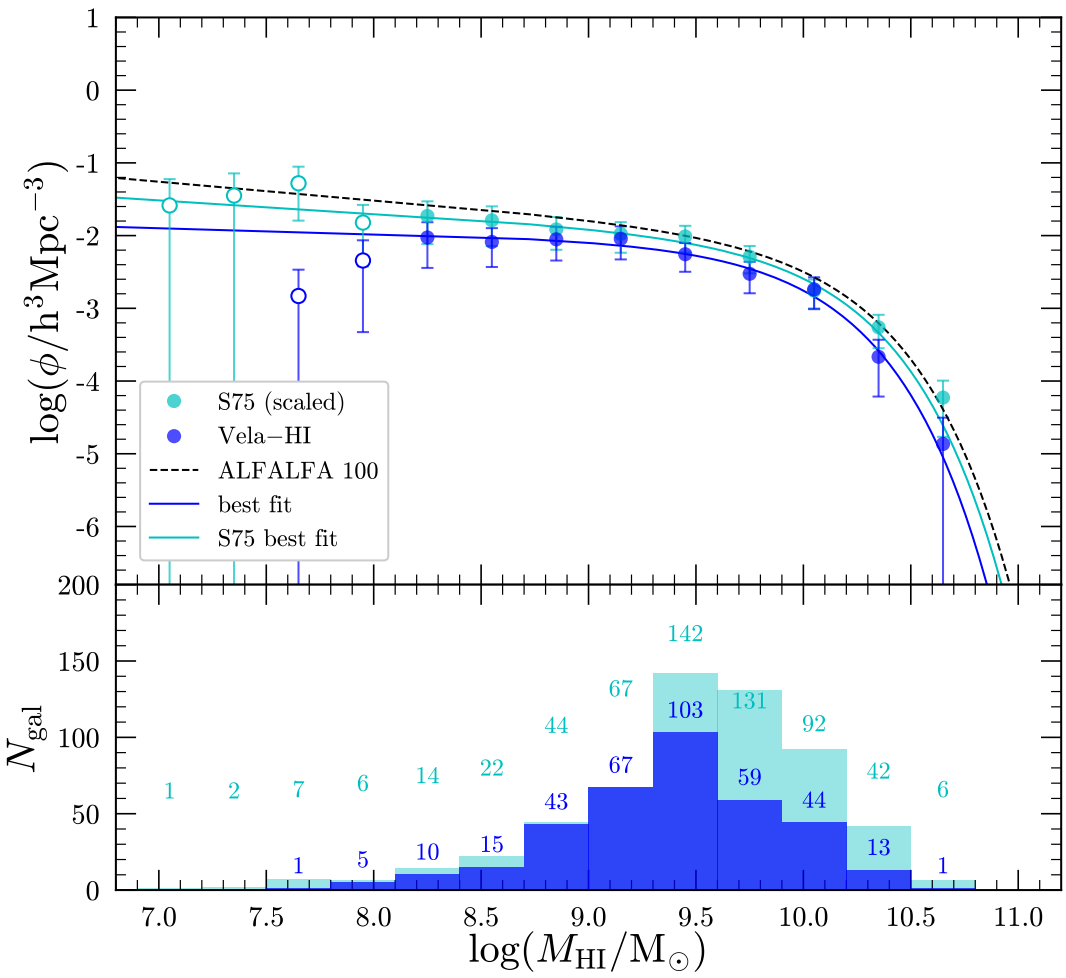

Figure 5.5: The HIMF for Vela–H I sample (in blue) and the scaled S75 simulation (in cyan), see Fig. 5.4 for details.

sensitivity curve in Fig. 5.8. This had also been noted in other surveys in the general Vela region (e.g., Jarrett 2004). These underdense regions appear to precisely lack galaxies with H I masses above $10^{9.3}$ and $10^{9.5}$ h_{70}^{-2} $M_\odot$, respectively. This underscores the non-homogeneous nature of Vela–H I, and with a large survey area of approximately 200 deg^2, these underdense regions significantly impact the counts, resulting in the observed lower normalization factor.

Combining the Vela–SMGPS and Vela–HI samples, we establish the HIMF for 535 detections surpassing a mean flux density completeness limit of 5.16 mJy within an area of 245 deg^2 in Fig. 5.6. The best-fitting Schechter parameters yield $\alpha = -1.12 \pm 0.07$, $\log(M^*_{\rm HI}/h_{70}^{-2}\ M_\odot) = 9.81 \pm 0.05$, $\Phi_* = 4.6 \pm 0.8 \times 10^{-3}\ h_{70}^3$ Mpc^{-3}. The normalization factor Φ_* is very similar to that of ALFALFA 100, however, we observe a flatter slope, attributed to the under-sampling of low linewidth galaxies in both samples. Despite this, the value remains consistent within 3σ errors with the literature, with $M^*_{\rm HI}$ value closer to HIPASS in the high-mass end.

In Fig. 5.9, we project the obtained Schechter parameters onto the α – log $M^*_{\rm HI}$ plane. The con-

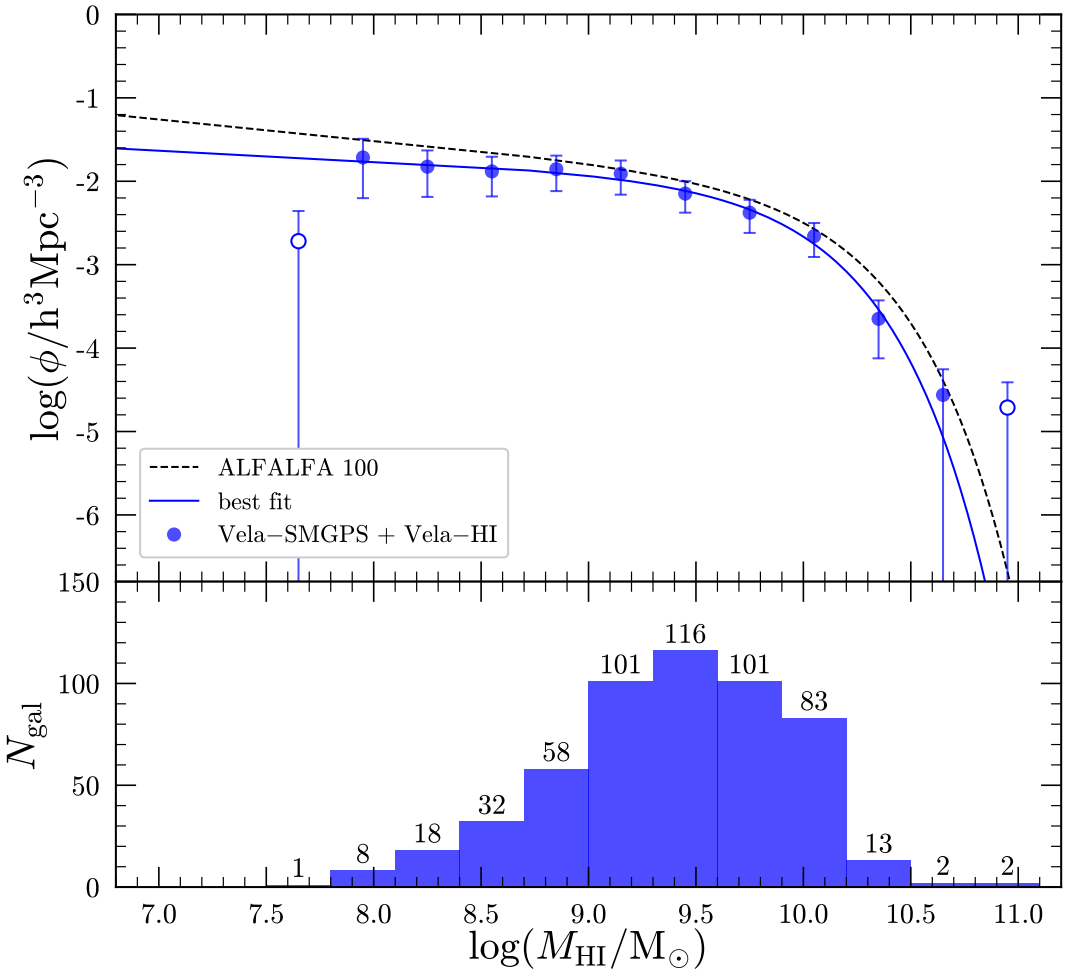

Figure 5.6: H I mass function of the samples combining Vela–SMGPS and Vela–H I detections (top panel). The distribution of H I masses per bin of 0.3 dex is displayed in the bottom panel. The blue solid line represents the best Schechter fit for the data. The black dashed line corresponds to the best fit from ALFALFA 100.

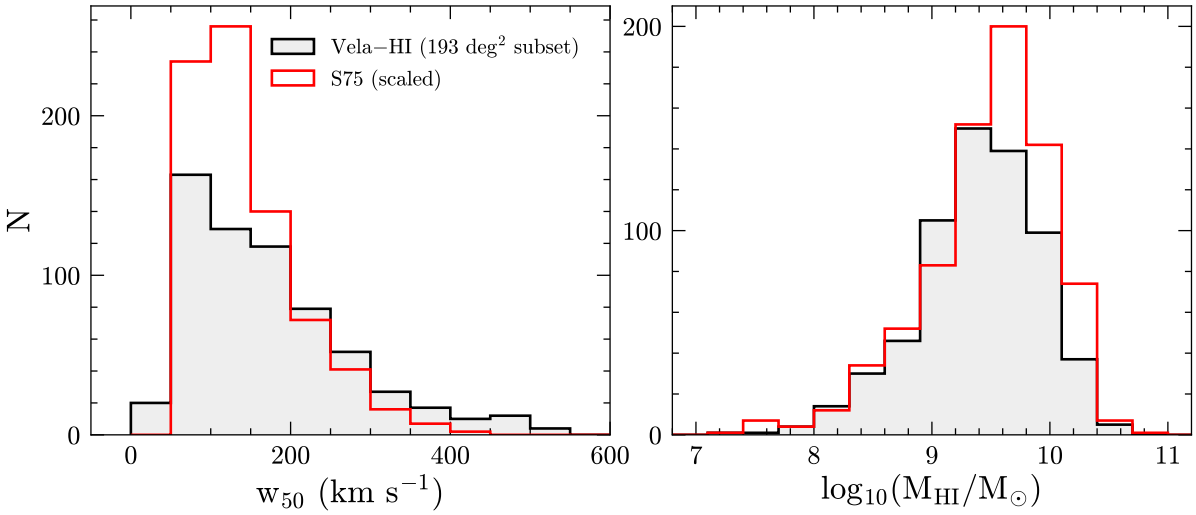

Figure 5.7: Histograms illustrating linewidth (left panel) and H I mass distributions (right panel) for the selected Vela–H I detections in the 193 deg^2 subset region (depicted in the grey-filled histograms) and the scaled S75 simulation (shown in the red histograms).

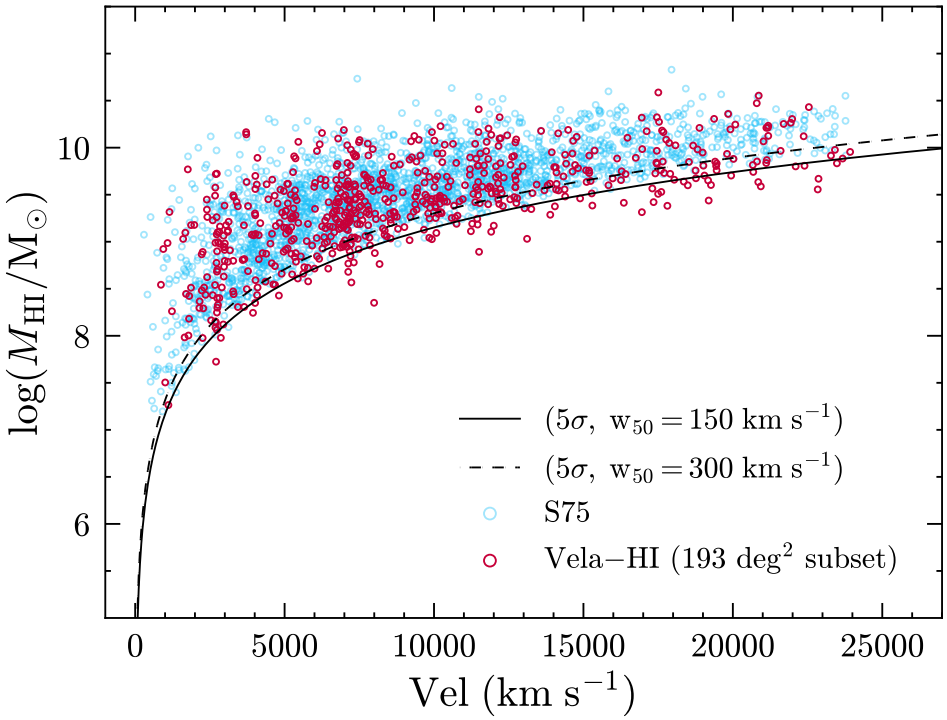

Figure 5.8: Similar to Fig. 4.14 in Chapter 4 but featuring the H I sensitivity curves (H I mass vs. velocity) of the selected Vela–H I detections in the 193 deg^2 subset region (red dots) and the simulation S75 (cyan dots). The solid and dashed black lines correspond to the sensitivity curves for the 5σ H I mass detection level. These curves are based on assumed w_{50} values of 150 and 300 km s^{-1}, respectively, with σ = 0.75 mJy beam^{-1}.

fidence ellipses are constructed based on the correlated parameters (α, log $M^*_{\rm HI}$, σ_α, $\sigma_{\log M^*_{\rm HI}}$, θ). Here, θ is determined through the covariance matrix:

$$\tan(2\theta) = 2\frac{\sigma_\alpha \log M^*_{\rm HI}}{\sigma^2_\alpha - \sigma^2_{\log M^*_{\rm HI}}}, \tag{5.18}$$

where θ represents the angle between the slope and the major axis of the ellipses. The filled ellipses delimit the 1σ contours of the various samples. The light-orange filled ellipse represents the 3σ contour of the combined sample. Overall, it is evident that the slopes and knee masses of Vela–SMGPS, Vela–HI, and simulations align within 1σ intervals. While their slopes are lower than those of ALFALFA, they generally agree within 2σ (for Vela–SMGPS and Vela–H I) to 3σ errors (for the combined sample only). $M^*_{\rm HI}$, in turn, closely resemble the value of HIPASS with $10^{9.86\pm0.03}\ h_{70}^{-2}\ {\rm M}_\odot$, rather than ALFALFA. However, in general, the α – log $M^*_{\rm HI}$ planes of our surveys are more closely aligned with the ALFALFA results within 2σ errors than HIPASS.

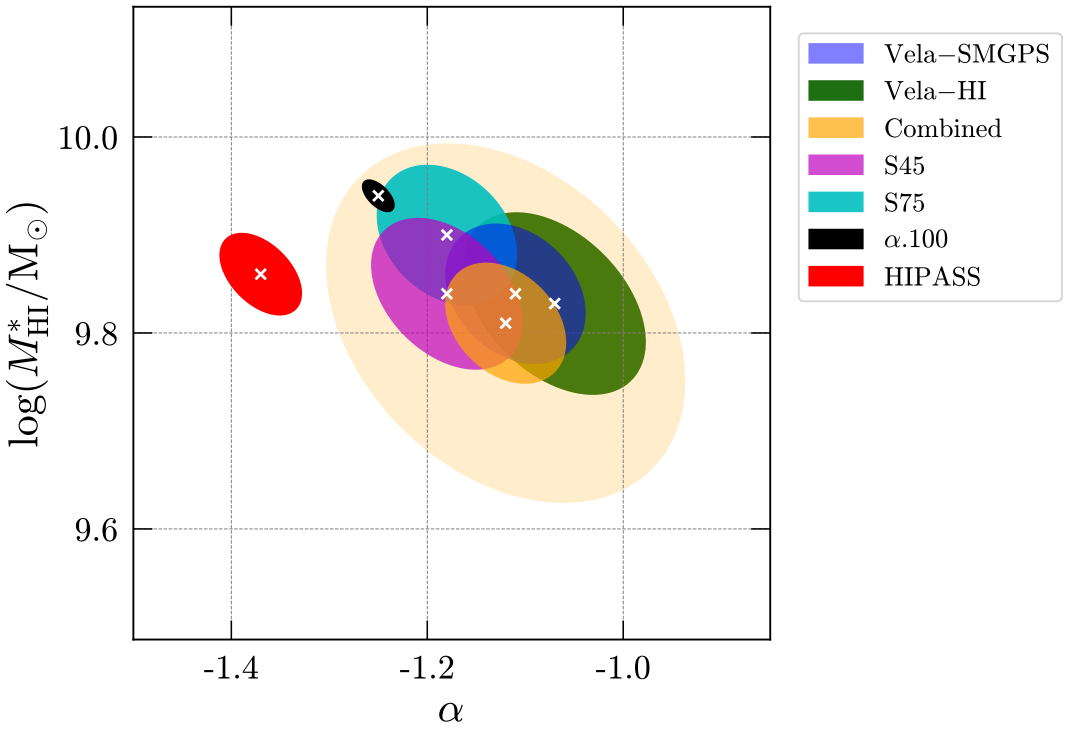

Figure 5.9: The Schechter parameters for various datasets, including Vela–SMGPS (depicted in purple), Vela–H I (green), S45 (magenta), S75 (cyan), ALFALFA 100 (black), and the combined samples (orange), are projected onto the $\alpha - \log M^*_{\rm HI}$ plane. Dark-shaded ellipses represent 1σ contours. These ellipses are characterized by parameters $\alpha, \log M^*_{\rm HI}, \sigma_\alpha, \sigma_{\log M^*_{\rm HI}}$, and θ. The light-shaded orange ellipse represents the 3σ error ellipse for the combined samples.

5.4.1 Overdensity estimation of the walls of VSCL

The two H I surveys presented in Chapters 3 and 4 encompass the suspected extent of the VSCL, across the obscured part of the ZOA ($|b| \lesssim 7°$). Various signatures of the two distinct walls detected at higher latitudes were uncovered with these H I surveys. The likelihood that these walls intersect at the lowest latitudes could be reinforced. They are particularly prominent within the range $270° \leq \ell \leq 279°$ for the velocity intervals of 16000–19000 km s^{-1} (W1) and 19000–23000 km s^{-1} (W2), i.e., in the surveyed Vela–SMGPS area. I will utilize their complete detections above the analysis presented in this section, with a completeness limit of $S_{\rm lim} = 3.2$ mJy for Vela–SMGPS (see Table 5.1).

Our first objective is to assess the mass overdensities of the presumed walls at the distance of the VSCL by comparing them to the HIMFs of the Vela–SMGPS survey region outside the suspected crossings, covering an area of ~36.5 deg^2 within $260° \leq \ell \leq 270°$ and $279° \leq \ell \leq 290°$. This approach allows us to explore two distinct environments with varying density conditions, both within the same velocity range and observed in the same manner. The region outside the suspected crossing corresponds to volumes of 27048 Mpc^3 for the first wall range and 50700 Mpc^3 for the second wall range. In contrast, the crossing region, spanning 21.6 deg^2($270° \leq \ell \leq 279°, -1.7° \leq$ b $\leq 0.7°$), corresponds to volumes of 14334 Mpc^3 and

29274 Mpc^3 for the two walls, respectively.

Figure 5.10 displays the HIMFs derived for the first wall (top panel) and the second wall velocity ranges (bottom panel). It is noticeable that only galaxies with H I masses above $10^{9.3}\ h_{70}^{-2}\,\mathrm{M}_\odot$ are present from 16000 to 19000 $\mathrm{km\,s^{-1}}$ while the lower H I mass limit for W2 was found to be $10^{9.75}\ h_{70}^{-2}\,\mathrm{M}_\odot$ are observed in the 19000 to 23000 $\mathrm{km\,s^{-1}}$ range. Smaller mass bins of $\Delta M = 0.15$ dex were utilized due to statistical limitations; only 9 and 7 galaxies were observed in the regions outside the suspected crossing for both wall distances, and only 5 and 8 galaxies were detected in the crossing regions. Due to the low number counts, low-mass galaxies are overlooked, which is essential for better constraining the HIMF Schechter parameters. To address this, we assumed that the slope and knee mass remain unchanged, fixing them to the ALFALFA100 values, and only varied the normalization factor to gain insights into the density of these regions. The results of the fits are summarized in Table 5.3. We observe that Φ_* is very similar for the velocity range of W1, with no evident overdensity observed. However, in W2, the value of Φ_* for the crossing region is nearly three times higher than in the outside region, suggesting a subtle hint of a higher-density environment.

Table 5.3: Comparison of the derived Schechter normalization parameter Φ_* for the two velocity ranges of the VSCL walls, at the suspected crossing location and the remaining surveyed area of Vela–SMGPS.

Velocity range	Region	Sample size	$\Phi_*(10^{-3}\ h_{70}^{-2}\ \mathrm{Mpc}^{-3})$
W1 (16000–19000 $\mathrm{km\,s^{-1}}$)	$260^\circ \leq \ell \leq 270^\circ, 279^\circ \leq \ell \leq 290^\circ$	9	1.1 ± 0.2
	$270^\circ \leq \ell \leq 279^\circ$	5	1.3 ± 0.4
W2 (19000–23000 $\mathrm{km\,s^{-1}}$)	$260^\circ \leq \ell \leq 270^\circ, 279^\circ \leq \ell \leq 290^\circ$	7	0.7 ± 0.2
	$270^\circ \leq \ell \leq 279^\circ$	8	2.0 ± 0.6

In an attempt to quantify mass overdensities, we perform an integration of the HIMF for the two walls within the common mass range of $10^{9.3}-10^{10.35}\ h_{70}^{-2}\,\mathrm{M}_\odot$ in W1 and $10^{9.75}-10^{10.5}\ h_{70}^{-2}\,\mathrm{M}_\odot$ in W2. Subsequently, we compare these integrated values with the HIMF within the corresponding velocity range for Vela–SMGPS. Empty mass bins are excluded, and the results are presented in Fig. 5.11. Errors are propagated from the Poisson errors in the HIMF. Due to the lower error being notably large, we can only estimate the upper limits of H I overdensities based on this study due to poor statistics. The integrated values from the suspected crossing region are divided by the full selected region of Vela–SMGPS. When taking the median value of the density ratios, the W1 overdensity is measured to be 3.5 ± 1.6, and the W2 overdensity is measured to be 1.8 ± 2.4. Despite the statistical limitations, this aligns with the findings from the previous chapters, where the second wall is observed to be more washed out than the first wall. We can also observe that W1 appears to exhibit a high-density fraction at $\log(M_{\mathrm{HI}}/h_{70}^{-2}\,\mathrm{M}_\odot) = 9.82$, indicating a decrease in H I density fraction with increasing mass. In contrast, W2 demonstrates an opposite trend, with H I density fraction increasing as mass increases. However, more robust

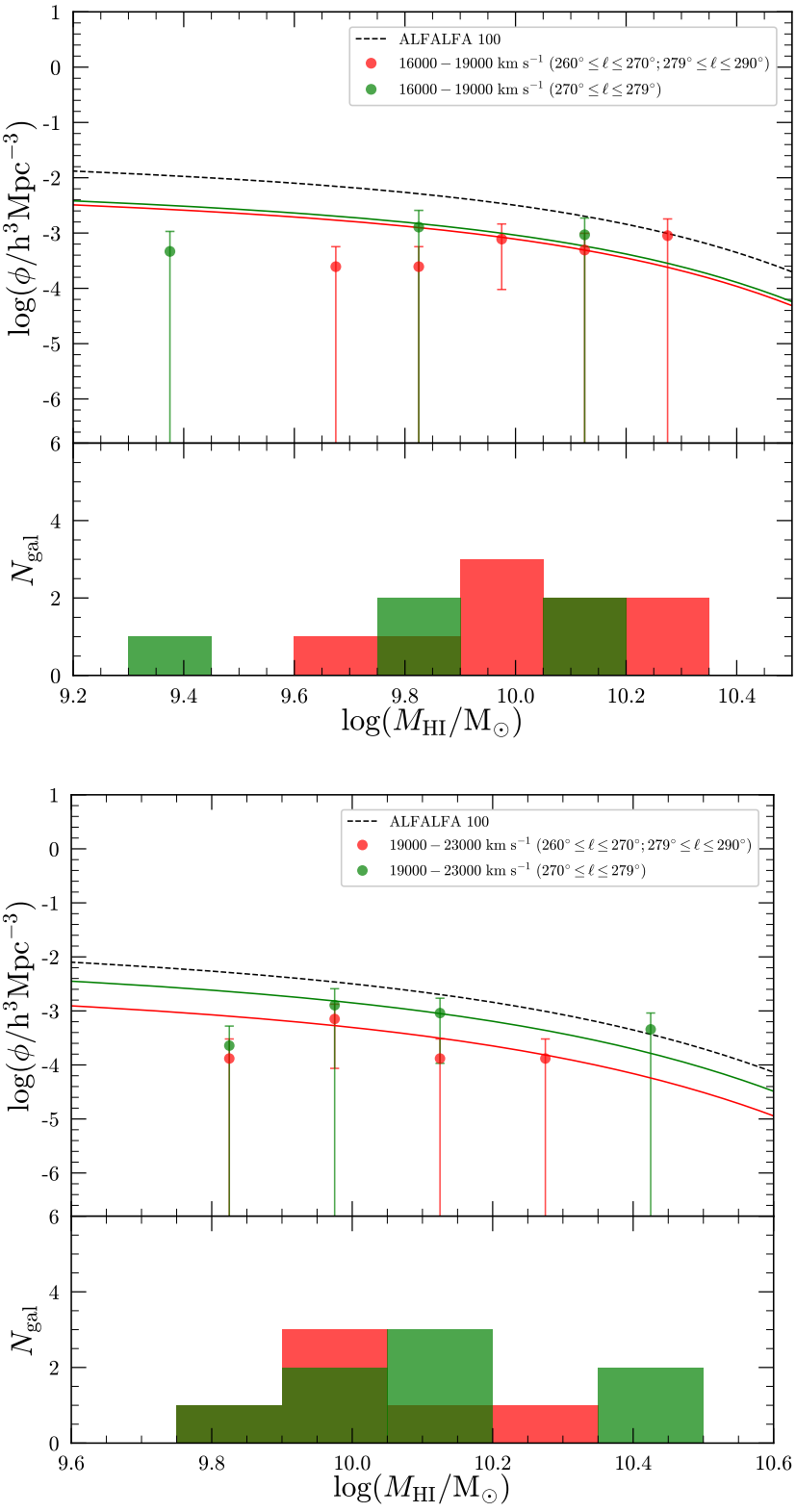

Figure 5.10: HIMFs accompanied by histograms of the mass bin counts for the velocity range of the two VSCL walls: 16000 – 19000 km s^{-1}(W1, top panel) and 19000 – 23000 km s^{-1}(W2, bottom panel). The HIMFs in the remaining survey region ($260° \leq \ell \leq 270°, 279° \leq \ell \leq 290°$) are shown in red, while the HIMFs of the suspicion of crossing walls at $260° \leq \ell \leq 290°$ are displayed in green in both panels. Their best-fitting lines, obtained by fixing M^*_{HI} and α to the ALFALFA 100 HIMF parameters, are represented by the red and green solid lines, respectively.

counts are needed for confirmation.

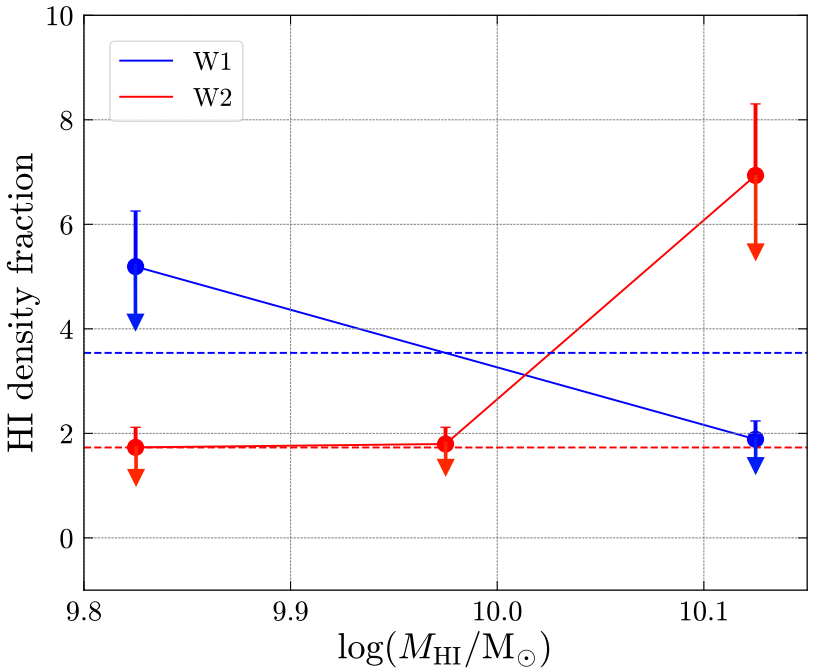

Figure 5.11: Density fraction as a function of H I mass in the region of lowest latitudes ($270° \leq \ell \leq 279°, -1.7° \leq b \leq 0.7°$)) where galaxies from two intersecting walls (W1 in blue and W2 in red) are suspected. The estimated median H I density fractions for the two walls are represented by the blue and red horizontal dashed lines.

5.5 Summary

In this Chapter, I constructed the HIMF using direct H I detections from the Vela SARAO MeerKAT Galactic Plane Survey (Vela–SMGPS) combined with the MeerKAT Vela Supercluster survey (Vela–H I) within the redshift range of $0 < z < 0.08$. As part of this analysis, I conducted completeness corrections using the Rauzy statistical test based on the completeness of the mean flux density, considering its dependence on both integrated flux and linewidth. At a confidence bound of 97.7% ($T_c = -2$), I determined completeness limits ($S_{\rm lim}$) of 3.2 mJy, 4.8 mJy, and 5.2 mJy for Vela–SMGPS, Vela–H I, and the combined samples, respectively. Approximately 44%, 58%, and 40% of the samples met these criteria.

Using the mean flux-limited samples, the HIMF was fitted as a Schechter function using non-linear least squares fitting. I applied the 2DSWML to obtain the number density for the fit. For the Vela–SMGPS, Vela–H I, and the combined samples, the best-fitting Schechter parameters are presented in Table 5.4.

The surveys HIMFs are generally consistent with the ALFALFA 100 HIMF within a 2σ error (within 3σ error for the combined sample) but closer to the HIPASS knee mass on the high-mass end of the HIMF. However, we observe a slightly flatter slope compared to the simulations

Table 5.4: Summary of the best-fitting Schechter parameters for the Vela–SMGPS, Vela–H I, and the combined samples.

Survey	α	$\log_{10}(M^*_{\rm HI}/h_{70}^{-2}\ {\rm M}_\odot)$	$\Phi_*(10^{-3}\ h_{70}^{-3}\ {\rm Mpc}^{-3})$
Vela–SMGPS	-1.11 ± 0.08	9.84 ± 0.06	7.6 ± 1.4
Vela–H I	-1.07 ± 0.11	9.83 ± 0.07	3.5 ± 0.8
Combined	-1.12 ± 0.07	9.81 ± 0.05	4.6 ± 0.8

and ALFALFA 100. This could be attributed to our incompleteness in low-linewidth due to our coarse channel resolution plus the large beam which might not be able to distinguish satellites close to a spiral galaxy. This effect lowers the counts at the faint end while leading to an overestimate of more massive galaxies (see Fig. 5.7). Vela–H I also appears to have underdense regions toward high–z between structures in its extensive survey region (see Fig. 5.8), significantly affecting the counts and resulting in a lower normalization factor (Φ_*). On the other hand, although the low-mass end is under-sampled, the Vela–SMGPS sample is prone to cosmic variance due to its smaller selected survey region compared to Vela–H I, potentially accounting for its higher normalization factor.

I have tried to quantify the overdensity of the presumed Vela crossing walls at $16000 - 19000$ km s^{-1} (W1) and $19000 - 23000$ km s^{-1} (W2) within the longitude range $270^\circ \leq \ell \leq 279^\circ$ which corresponds to an effective area of 21.6 deg^2, and a volume of 14334 Mpc^3 and 29274 Mpc^3 at both velocity ranges. I compared them to the Vela–SMGPS survey area, excluding the suspected crossing region from $260^\circ \leq \ell \leq 270^\circ$ and $279^\circ \leq \ell \leq 290^\circ$ (36.5 deg^2, 27048 Mpc^3, 50700 Mpc^3). To calculate their H I density fractions, I integrated the number densities of mass bins between $10^{9.3} - 10^{10.5}\ h_{70}^{-2}\ {\rm M}_\odot$. Due to substantial lower Poisson errors and the statistical limitation of only 5 and 8 galaxies above completeness in both walls, only the upper limit was estimated. The W1 overdensity is determined to be 3.5 ± 1.6, while the W2 overdensity is measured to be 1.8 ± 2.4. Despite the statistical limitations, this aligns with the findings from the previous chapters, where the second wall is observed to be more diffuse but still noteworthy.

The upcoming era of deep H I surveys facilitated by SKA pathfinder telescopes like the Australian SKA Pathfinder telescope (ASKAP) and MeerKAT, and later SKA-1, is poised to significantly advance our comprehension of the redshift evolution of the HIMF and H I. New frontiers are on the horizon, with forthcoming surveys such as DINGO (Meyer, 2009), expanding investigations out to $z \sim 0.4$ with ASKAP, the full MIGHTEE-H I survey which will reach $z \sim 0.5$, and LADUMA (Blyth et al., 2016; Baker et al., 2019) pushing the boundaries to explore up to $z \sim 1$ with MeerKAT.

chapter 6

Summary and future work

In this concluding chapter, I present an overview of the key scientific highlights discussed in the previous sections and summarize the findings of the overall thesis. Following this, I provide a forward-looking perspective, sharing insights into planned future studies that directly build upon the foundations laid in this thesis.

6.1 Thesis highlights

In Chapter 2, I presented a comprehensive analysis of the H I size-mass relation using Early Science data from the MIGHTEE survey (Rajohnson et al., 2022). This study, based on a uniform interferometric sample of 204 galaxies spanning four decades in H I mass and extending to $z \sim 0.084$, represents a significant milestone by measuring the non-zero intrinsic scatter of the relation ($\sim$10%). Notably, all galaxies in the sample adhere to the relation, irrespective of morphological differences, indicating its universal applicability. The research also highlights the stability of the H I size-mass relation over the past one billion years, in line with simulations of galaxy formation. These findings not only served as a diagnostic tool to validate flux measurements in the Early Science data but also underscored the critical role of the upcoming full MIGHTEE survey.

One of the other primary objectives of this thesis is to map the full extent and morphology of a major overdensity, the Vela Supercluster (VSCL), which remains largely unexplored at low latitudes. The unique approach for unveiling this overdensity, particularly its core in the innermost ZOA, relied on the identification of 21-cm line emissions from gas in galaxies obtained from interferometric data. None of the previous all-sky surveys at other wavebands could penetrate so far at the VSCL distance range. Chapters 3 and 4 collectively represent these systematic H I surveys, comprising over 800 MeerKAT pointings, spanning an extensive area of more than 300 deg^2 in the inner GP ($\ell \approx 260^\circ - 290^\circ$; $b \approx \pm 6.7^\circ$). Data reduction, imaging, and mosaicking of all pointings were executed using the `CARAcal` pipeline on the `Ilifu` cloud server.

In Chapter 3, the SARAO MeerKAT Galactic Plane Survey centered on the Vela region (Vela–SMGPS) successfully cataloged 843 heavily obscured H I galaxies within the most opaque part of the ZOA. This study emphasizes MeerKAT's effectiveness in systematically populating the ZOA, overcoming challenges posed by extreme obscuration. The analysis of on-sky and velocity distributions revealed a non-homogeneous distribution, indicating significant clustering of galaxies. It led to the identification of several key structures, including a distinct signature at 3500 $\mathrm{km\,s^{-1}}$, suggestive of the Hydra/Antlia wall crossing into the ZOA. The study unveiled a previously unknown narrow filament within the 30° strip in the GP at ∼12000 $\mathrm{km\,s^{-1}}$ i.e., extending at least 90 h^{-1} Mpc in length. Most importantly, the survey revealed two peak overdensities at the redshift range of the previously suspected walls (W1 at 16000–19000 $\mathrm{km\,s^{-1}}$and W2 at 19000–23000 $\mathrm{km\,s^{-1}}$) that seem to be the most prominent within the longitude range $272° \leq \ell \leq 278°$.

Building on this success, Chapter 4 introduces the systematic MeerKAT Vela Supercluster survey (Vela–H I), strategically designed to unravel the morphology and characteristics of the wider Vela supercluster. It aims to link the results from Vela–SMGPS to known structures in the surrounding area at higher latitudes. The survey successfully identified and characterized 719 H I sources, with 508 being previously unknown. The newly acquired redshift measurements significantly enhance our understanding of the LSS in the Vela region. For the first time, they can trace the Hydra/Antlia filament all the way across the GP to the other side. Previously undiscovered structures, such as a diagonal feature associated with AS639 and a void measuring approximately 10 Mpc in diameter at $\ell \sim 279°$, $b \sim 0°$, within the redshift range 6500–8000 $\mathrm{km\,s^{-1}}$ were also uncovered. The additional data further reinforces the outcomes presented in Vela–SMGPS, emphasizing the intricate multibranching morphology of the Vela supercluster. It also adds further evidence of two walls where W2 is likely to pass through the GP within the longitude range of $270° \leq \ell \leq 279°$, and possibly intersecting with W1 in the velocity range of 18500–21500 $\mathrm{km\,s^{-1}}$. The galaxy candidates identified in these two surveys, a majority of which are novel discoveries, undeniably contribute to the reduction of the ZOA in redshift space. Their H I properties hold potential for future analyses, including the estimation of the peculiar velocity field or for computing HIMFs (Chapter 5).

In Chapter 5, I applied the two-dimensional Stepwise Maximum Likelihood (2DSWML) method to derive number densities from completeness-corrected mass histograms of Vela–SMGPS, Vela–H I, and the combined sample. Mass bins were set at 0.3 dex, and width bins at 0.2 dex. The best non-linear least squares fitting using a Schechter function (Schechter, 1976) resulted in the following HIMF parameters:

Table 6.1: Best-fitting Schechter parameters for the Vela–SMGPS, Vela–H I, and the combined samples.

Survey	α	$\log(M^*_{\rm HI})$ $[\log(h_{70}^{-2}\ {\rm M}_\odot)]$	Φ_* $[10^{-3}\ h_{70}^{-3}\ {\rm Mpc}^{-3}]$
Vela–SMGPS	-1.11 ± 0.08	9.84 ± 0.06	7.6 ± 1.4
Vela–H I	-1.07 ± 0.11	9.83 ± 0.07	3.5 ± 0.8
Combined	-1.12 ± 0.07	9.81 ± 0.05	4.6 ± 0.8

Our overall fit closely aligns with the ALFALFA 100 best fit within a 3σ margin, but our sample exhibits flatter slopes, potentially due to our coarse channel resolution and large beam, where dwarf companions of large spiral galaxies are not resolved separately. Attempting to gauge the overdensity of the VSCL walls, we obtained upper limits due to statistical constraints. The calculated values are 3.5 ± 1.6 for W1 ($16000-19000$ km s^{-1}) and 1.8 ± 2.4 for W2 ($19000-23000$ km s^{-1}) at the suspected intersection, i.e., the longitude range $270^\circ \leq \ell \leq 279^\circ$.

The MIGHTEE-H I Early Science data (Chapter 2), Vela–SMGPS findings (Chapter 3), and insights from Vela–H I (Chapter 4) collectively showcase the impressive capacity of the SKA precursor, MeerKAT, for H I exploration. This extends to a new observational window and ensures homogeneity, even in the most obscured part of the sky. These results also indicate the potential of the eagerly awaited complete SKA array expected in the next few years.

6.2 Future work

Here I outline four areas that merit follow-up investigations. The first involves a comprehensive exploration of galaxy scaling relations, leveraging the enhanced resolution and sensitivities offered by the advent of the full MIGHTEE 32K data. The second one consists of studying the evolution of the HIMFs as a function of different environments. This can be achieved by combining and comparing the complete SMGPS dataset thanks to the various over- and underdense structures and different local densities that have been probed in the Southern Plane, e.g., the Great Attractor (GA; Steyn et al. 2024), the Local Void (LV; Kurapati et al. 2024), and the Vela supercluster (this work). The third and fourth components entail measuring cluster member deficiencies to address the richness of the VSCL and constructing cosmic flow fields for distinct overdensities in the ZOA through the Tully-Fisher (TF) relation. We will now elaborate on these points in the next paragraphs.

Our analysis of the MIGHTEE-H I Early Science data has provided compelling insights into the H I size-mass relation's evolution over the past one billion years (out to $z \sim 0.084$), showing promising agreement with existing literature. Extending this investigation by validating these findings using the forthcoming 32K data from the full MIGHTEE DR1 (Heywood et al. in prep), encompassing the COSMOS field ($\sim$4 deg^2) will be interesting. It is important to note,

however, that the previous investigation was made possible thanks to the mostly RFI-free region extending out to $z \sim 0.08$. The additional 32K data will allow an improvement in data quality, but the pervading RFI from $z = 0.08 - 0.2$ will restrict our ability to investigate the H I size-mass relation for galaxies in this redshift range. However, it will be possible to explore this at the highest redshifts ($z \sim 0.2 - 0.5$), albeit only for H I masses above 10^{10} $M_\odot$ spanning approximately two to five billion years in cosmic time.

The next phase of our research involves computing the HIMF for the entire SMGPS survey, similar to the approach taken for HIZOA (see Said et al. 2019). This task requires consolidating the 528 deg^2 datasets from different regions, such as Vela-SMGPS (Chapter 3), LV-SMGPS (Kurapati et al., 2024), GA-SMGPS (Steyn et al., 2024), and the remaining patch between Vela-SMGPS and GA-SMGPS ($290° \leq \ell \leq 302°$), into a systematic catalog. As mentioned in Chapter 3, source finding for the GA region was conducted slightly differently, necessitating a re-run of source finding and adjudication for that area only. Following this, we can estimate overall and individual completeness limits using the Rauzy method (cf. Chapter 5) and compute the HIMFs.

The HIMF is influenced by both the number of dwarfs and the gas richness of galaxies. Despite the typically universal nature of the bright end of the HIMF, conflicting findings in previous studies, particularly regarding the faint end (e.g., Zwaan et al. 2005 vs. Springob 2004; Jones et al. 2016) have been observed. This discrepancy is attributed to challenges such as low resolution, leading to under-sampling of the low-mass population of galaxies in the survey (see Kraan-Korteweg et al. 2008a and references therein), emphasizing the need for a comprehensive investigation. SMGPS's high sensitivity to low $M_{\rm HI}$ dwarfs, coupled with the observation of multiple structures in the ZOA, provides an excellent opportunity to accurately measure the slope at the low-mass end and explore the HIMF's dependence on environments. A comparative analysis, considering the nearby velocity range $cz < 8000$ km s^{-1}, would allow us to characterize the LV region as a very low-density environment, GA as highly ($cz \sim 3500 - 6500$ km s^{-1}), and Vela–SMGPS as an intermediate environment, since its overdensities are peaking at $cz \sim 12000$ km s^{-1} and at the VSCL distance ($cz \sim 18000$ km s^{-1}).

Vela–SMGPS (Chapter 3) and Vela–H I (Chapter 4) sources underwent cross-matching with existing literature. In the innermost ZOA where Vela–SMGPS is located, only 7% showed likely counterparts, all lacking redshift data. In contrast, Vela–H I, situated at higher latitudes, exhibited a higher match rate (~30%), with 31% of them having redshift information. Combining H I observations from both surveys has offered valuable insights into the two merging walls of the VSCL. Given the known tendency of rich galaxy clusters to reside at these intersections, they remain hidden in H I. Investigating the variations in H I properties across different LSS (e.g., void edges, along the filaments) and inspecting moment maps for potential signs of ram pressure stripping could provide hints for their existence. The identification of rich clusters within this

new dataset will provide further evidence for the richness of VSCL.

To identify potential cluster members, we plan to search for further counterparts using follow-up IR observations. This will involve utilizing data from the Wide-field Infrared Survey Explorer (WISE; Wright et al. 2010) and the Galactic Legacy Infrared Mid-Plane Survey Extraordinaire (GLIMPSE; Churchwell et al. 2009). Although the VVV NIR galaxy catalogue (Baravalle et al., 2021) is currently unavailable for the Vela region, we are also considering using its Southern part in the VVV eXtended survey (VVVX, Minniti et al. 2018) that will cover the area. Once the Southern NIR galaxy catalog is released, we aim to explore counterparts within this survey, extending our analysis to encompass the entire SMGPS survey. Probing the richness of the potential clusters also involves searching for X-ray counterparts, with preference from eROSITA (Merloni et al., 2012, 2024). Additionally, studies have indicated that gas stripping in galaxies has discernible effects on the radio continuum within the core of clusters, especially in regions experiencing strong ram pressure (Murphy et al., 2009; Vollmer et al., 2010, 2013). Given that we have radio continuum maps for our mosaics, these data offer a complementary diagnostic tool to investigate interactions between late-type galaxies and the cluster environment.

Aiming to obtain a significant sub-sample of IR counterparts, we could determine the peculiar velocities for selected galaxies. However, despite the existence of an independent NIR Tully-Fisher relation specifically tailored for the ZOA (Said et al., 2015), obtaining reliable NIR photometry may prove challenging, since typically only the bulges of spirals remain visible, if at all. An alternative approach is to identify galaxies detected in the WISE W1 ($3.4\ \mu$m) waveband, minimally affected by extinction. Massive galaxies with clear rotation, especially those fairly edge-on, are more likely to exhibit a strong W1 signal and reliable linewidths suitable for the W1-TF relation. As such, by selecting galaxies with an integrated SNR ≥ 6, 50% linewidths greater than three channels, and unperturbed moment maps showing the well-defined extent of the source with clear rotation, we can make predictions. We predict that around 104 (12%) and 118 (16%) galaxies in Vela–SMGPS and Vela–H I, respectively, will have a good likelihood for accurate linewidth and inclination measurements, making them good candidates for the W1-TF relation. Preliminary checks on a few promising galaxy candidates have shown W1 signals (T. Jarrett, private communication).

Utilizing the calibration of the Tully-Fisher relation based on W1 magnitudes (W1-TF relation) by Bell et al. (2023) offers a viable method. This approach has been successfully applied in the WALLABY pilot observations data (Koribalski et al., 2020), as discussed by Courtois et al. (2023). Using the W1-TF relation, we could estimate linewidths and H I masses for a 5σ detection, providing an upper limit for estimating the overall H I deficiencies of cluster members, aligning with methodologies employed in Hatamkhani's Ph.D. thesis. W1 photometry and TF distances for the selected sample would also allow us to discern the peculiar velocities of galaxies, resulting from the gravitational force induced by the non-uniform mass density distribution.

The generated peculiar velocity maps will help comprehend the significance of the overdensity associated with VSCL on the cosmic flow fields.

The success of Vela–H I, with only 5 minutes per pointing using MeerkAT, and the capability of SMGPS in revealing LSS at low latitudes demonstrate the wealth of information available despite challenges in mapping structures in the ZOA. Looking forward, SKA's enhanced sensitivity and resolution will revolutionize H I observations, allowing the identification and characterization of H I morphologies in galaxies with much lower mass than currently feasible. The influx of new data from wide-area optical spectroscopy (e.g., 4MOST, de Jong et al. 2019) and blind H I surveys with SKA Pathfinders (e.g., MIGHTEE, LADUMA, WALLABY) promises fresh insights into the dynamics of the Local Universe, offering valuable knowledge for analyzing clusters at various masses and redshifts in the future. The prospect of significant progress in this field is exciting, and I eagerly look forward to contributing to these advancements.

Bibliography

Aaronson M., Huchra J., Mould J., Schechter P. L., Tully R. B., 1982, Astrophysical Journal, 258, 64

Aaronson M., Bothun G., Mould J., Huchra J., Schommer R. A., Cornell M. E., 1986, Astrophysical Journal, 302, 536

Aaronson M., et al., 1989, Astrophysical Journal, 338, 654

Abate A., Feldman H. A., 2012, Monthly Notices of the Royal Astronomical Society, 419, 3482

Abell G. O., 1958, Astrophysical Journal, Supplement, 3, 211

Abell G. O., Corwin H. G. J., 1983, in Abell G. O., Chincarini G., eds, Proceedings of the Symposium, Kolymbari, Greece, August 30-September 2, 1982 (A84-13653 03-90) Vol. 104, Early Evolution of the Universe and its Present Structure. pp 179–184

Abell G. O., Corwin Harold G. J., Olowin R. P., 1989, Astrophysical Journal, Supplement, 70, 1

Ahumada R., et al., 2020, Astrophysical Journal, Supplement, 249, 3

Aihara H., et al., 2011, Astrophysical Journal, Supplement, 195, 26

Aihara H., et al., 2018, Publications of the Astronomical Society of Japan, 70, S4

Aihara H., et al., 2019, Publications of the Astronomical Society of Japan, 71, 114

Allen P. D., Driver S. P., Graham A. W., Cameron E., Liske J., de Propris R., 2006, Monthly Notices of the Royal Astronomical Society, 371, 2

Aoyama K., Kodama T., Suzuki T. L., Tadaki K.-i., Shimakawa R., Hayashi M., Koyama Y., Pérez-Martínez J. M., 2022, Astrophysical Journal, 924, 74

Araya-Melo P. A., Reisenegger A., Meza A., van de Weygaert R., Dünner R., Quintana H., 2009, Monthly Notices of the Royal Astronomical Society, 399, 97

Asad K. M. B., et al., 2021, Monthly Notices of the Royal Astronomical Society, 502, 2970

Astropy Collaboration et al., 2013, Astronomy and Astrophysics, 558, A33

Astropy Collaboration et al., 2018, The Astronomical Journal, 156, 123

Bahcall N. A., 1988, ARA&A, 26, 631

Baker A. J., Blyth S., Holwerda B., 2019, in American Astronomical Society Meeting Abstracts #233. p. 333.01

Baldry I. K., Balogh M. L., Bower R. G., Glazebrook K., Nichol R. C., Bamford S. P., Budavari T., 2006, Monthly Notices of the Royal Astronomical Society, 373, 469

Baldry I. K., et al., 2014, Monthly Notices of the Royal Astronomical Society, 441, 2440

Baravalle L. D., et al., 2021, Monthly Notices of the Royal Astronomical Society, 502, 601

Bardelli S., Zucca E., Zamorani G., Moscardini L., Scaramella R., 2000, Monthly Notices of the Royal Astronomical Society, 312, 540

Basilakos S., 2003, Monthly Notices of the Royal Astronomical Society, 344, 602

Bassett R., et al., 2013, Astrophysical Journal, 770, 58

Begum A., Chengalur J. N., Karachentsev I. D., Sharina M. E., Kaisin S. S., 2008, Monthly Notices of the Royal Astronomical Society, 386, 1667

Bell E. F., et al., 2004, Astrophysical Journal, 608, 752

Bell R., Said K., Davis T., Jarrett T. H., 2023, Monthly Notices of the Royal Astronomical Society, 519, 102

Bennett C. L., et al., 2003, Astrophysical Journal, Supplement, 148, 1

Bianconi M., Smith G. P., Haines C. P., McGee S. L., Finoguenov A., Egami E., 2020, Monthly Notices of the Royal Astronomical Society, 492, 4599

Bigiel F., Leroy A., Walter F., Brinks E., de Blok W. J. G., Madore B., Thornley M. D., 2008, The Astronomical Journal, 136, 2846

Bilicki M., Jarrett T. H., Peacock J. A., Cluver M. E., Steward L., 2014, Astrophysical Journal, Supplement, 210, 9

Binney J., Dehnen W., Bertelli G., 2000, Monthly Notices of the Royal Astronomical Society, 318, 658

Blyth S., et al., 2016, in MeerKAT Science: On the Pathway to the SKA. p. 4

Bock D. C. J., Large M. I., Sadler E. M., 1999, The Astronomical Journal, 117, 1578

Boller T., Freyberg M. J., Trümper J., Haberl F., Voges W., Nandra K., 2016, Astronomy and Astrophysics, 588, A103

Bond J. R., Kofman L., Pogosyan D., 1996, Nature, 380, 603

Booth R. S., de Blok W. J. G., Jonas J. L., Fanaroff B., 2009, arXiv e-prints, p. arXiv:0910.2935

Boruah S. S., Hudson M. J., Lavaux G., 2020, Monthly Notices of the Royal Astronomical Society, 498, 2703

Boselli A., Gavazzi G., 2006, Publications of the Astronomical Society of the Pacific, 118, 517

Branchini E., Plionis M., 1996, Astrophysical Letters and Communications, 33, 113

Branchini E., Davis M., Nusser A., 2012, Monthly Notices of the Royal Astronomical Society, 424, 472

Bravo-Alfaro H., Cayatte V., van Gorkom J. H., Balkowski C., 2000, The Astronomical Journal, 119, 580

Briggs D. S., 1995, in American Astronomical Society Meeting Abstracts. p. 112.02

Broeils A. H., Rhee M. H., 1997, Astronomy and Astrophysics, 324, 877

Buchner J., et al., 2014, Astronomy and Astrophysics, 564, A125

Busha M. T., Adams F. C., Wechsler R. H., Evrard A. E., 2003, Astrophysical Journal, 596, 713

Buta R. J., 2013, in Falcón-Barroso J., Knapen J. H., eds, , Secular Evolution of Galaxies. p. 155, doi:10.48550/arXiv.1304.3529

Butcher H., Oemler A. J., 1978, Astrophysical Journal, 226, 559

Cardelli J. A., Clayton G. C., Mathis J. S., 1989, Astrophysical Journal, 345, 245

Carrick J., Turnbull S. J., Lavaux G., Hudson M. J., 2015, Monthly Notices of the Royal Astronomical Society, 450, 317

Catinella B., Cortese L., 2015, Monthly Notices of the Royal Astronomical Society, 446, 3526

Catinella B., Haynes M. P., Giovanelli R., Gardner J. P., Connolly A. J., 2008, Astrophysical Journal, Letters, 685, L13

Cayatte V., Kotanyi C., Balkowski C., van Gorkom J. H., 1994, The Astronomical Journal, 107, 1003

Chen C. T. J., et al., 2018, Monthly Notices of the Royal Astronomical Society, 478, 2132

Chiueh T., He X.-G., 2002, Phys. Rev. D, 65, 123518

Chung A., van Gorkom J. H., Kenney J. D. P., Crowl H., Vollmer B., 2009, The Astronomical Journal, 138, 1741

Churchwell E., et al., 2009, Publications of the Astronomical Society of the Pacific, 121, 213

Cluver M. E., Jarrett T. H., Kraan-Korteweg R. C., Koribalski B. S., Appleton P. N., Melbourne J., Emonts B., Woudt P. A., 2010, Astrophysical Journal, 725, 1550

Coil A. L., et al., 2011, Astrophysical Journal, 741, 8

Colin J., Mohayaee R., Sarkar S., Shafieloo A., 2011, Monthly Notices of the Royal Astronomical Society, 414, 264

Colless M., et al., 2001, Monthly Notices of the Royal Astronomical Society, 328, 1039

Colless M., et al., 2003, arXiv e-prints, pp astro–ph/0306581

Collier J. D., Frank B., Sekhar S., Taylor A. R., 2021, in 2021 XXXIVth General Assembly and Scientific Symposium of the International Union of Radio Science (URSI GASS). pp 1–4, doi:10.23919/URSIGASS51995.2021.9560276

Comrie A., et al., 2021, CARTA: The Cube Analysis and Rendering Tool for Astronomy, doi:10.5281/zenodo.4905459, `https://doi.org/10.5281/zenodo.4905459`

Condon J. J., Ransom S. M., 2016, Essential Radio Astronomy

Conselice C. J., 2006, Monthly Notices of the Royal Astronomical Society, 373, 1389

Conselice C. J., Wilkinson A., Duncan K., Mortlock A., 2016, Astrophysical Journal, 830, 83

Coppin K. E. K., et al., 2012, Astrophysical Journal, Letters, 749, L43

Corey B. E., Wilkinson D. T., 1976, in Bulletin of the American Astronomical Society. p. 351

Cortese L., Catinella B., Smith R., 2021, Publ. Astron. Soc. Australia, 38, e035

Costa-Duarte M. V., Sodré L. J., Durret F., 2011, Monthly Notices of the Royal Astronomical Society, 411, 1716

Courtois H. M., Kraan-Korteweg R. C., Dupuy A., Graziani R., Libeskind N. I., 2019, Monthly Notices of the Royal Astronomical Society, 490, L57

Courtois H. M., et al., 2023, Monthly Notices of the Royal Astronomical Society, 519, 4589

Covington M. D., et al., 2010, Astrophysical Journal, 710, 279

Coziol R., Ribeiro A. L. B., de Carvalho R. R., Capelato H. V., 1998, Astrophysical Journal, 493, 563

Crane P. C., Napier P. J., 1989, in Perley R. A., Schwab F. R., Bridle A. H., eds, Astronomical Society of the Pacific Conference Series Vol. 6, Synthesis Imaging in Radio Astronomy. p. 139

Cutri R. M., et al., 2021, VizieR Online Data Catalog, p. II/328

Dai D.-C., Kinney W. H., Stojkovic D., 2011, Journal of Cosmology and Astroparticle Physics, 2011, 015

Davis M., Huchra J., 1982, Astrophysical Journal, 254, 437

Davis M., Peebles P. J. E., 1983, Annual Review of Astronomy and Astrophysics, 21, 109

Davis M., Huchra J., Latham D. W., Tonry J., 1982, Astrophysical Journal, 253, 423

Daza-Perilla I. V., et al., 2023, Monthly Notices of the Royal Astronomical Society, 524, 678

De Lucia G., Helmi A., 2008, Monthly Notices of the Royal Astronomical Society, 391, 14

Dekel A., 1994, Annual Review of Astronomy and Astrophysics, 32, 371

Djorgovski S., Davis M., 1987, Astrophysical Journal, 313, 59

Donley J. L., et al., 2005, The Astronomical Journal, 129, 220

Donley J. L., Koribalski B. S., Staveley-Smith L., Kraan-Korteweg R. C., Schröder A., Henning P. A., 2006, Monthly Notices of the Royal Astronomical Society, 369, 1741

Dressler A., 1980, Astrophysical Journal, 236, 351

Dressler A., 1987, Scientific American, 257, 46

Dressler A., et al., 1997, Astrophysical Journal, 490, 577

Driessen L., 2020, Astronomy and Geophysics, 61, 5.12

Driver S. P., et al., 2009, Astronomy and Geophysics, 50, 5.12

Driver S. P., et al., 2022, Monthly Notices of the Royal Astronomical Society, 513, 439

Dubois Y., et al., 2021, Astronomy and Astrophysics, 651, A109

Dünner R., Araya P. A., Meza A., Reisenegger A., 2006, Monthly Notices of the Royal Astronomical Society, 366, 803

Ebeling H., Voges W., Bohringer H., Edge A. C., Huchra J. P., Briel U. G., 1996, Monthly Notices of the Royal Astronomical Society, 281, 799

Ebeling H., Mullis C. R., Tully R. B., 2002, Astrophysical Journal, 580, 774

Ebeling H., Barrett E., Donovan D., 2004, Astrophysical Journal, Letters, 609, L49

Efstathiou G., Ellis R. S., Peterson B. A., 1988, Monthly Notices of the Royal Astronomical Society, 232, 431

Einasto J., Joeveer M., Saar E., 1980, Monthly Notices of the Royal Astronomical Society, 193, 353

Einasto M., Tago E., Jaaniste J., Einasto J., Andernach H., 1997, Astronomy and Astrophysics Supplement Series, 123, 119

Einasto M., Einasto J., Tago E., Müller V., Andernach H., 2001, The Astronomical Journal, 122, 2222

Einasto M., Jaaniste J., Einasto J., Heinämäki P., Müller V., Tucker D. L., 2003, Astronomy and Astrophysics, 405, 821

Einasto J., et al., 2007a, Astronomy and Astrophysics, 462, 397

Einasto M., et al., 2007b, Astronomy and Astrophysics, 464, 815

Einasto M., et al., 2007c, Astronomy and Astrophysics, 476, 697

Einasto M., et al., 2008, ApJ, 685, 83

Einasto M., Liivamägi L. J., Tago E., Saar E., Tempel E., Einasto J., Martínez V. J., Heinämäki P., 2011a, Astronomy and Astrophysics, 532, A5

Einasto M., et al., 2011b, Astrophysical Journal, 736, 51

Einasto M., et al., 2012, Astronomy and Astrophysics, 542, A36

Einasto M., Lietzen H., Tempel E., Gramann M., Liivamägi L. J., Einasto J., 2014, Astronomy and Astrophysics, 562, A87

Einasto M., et al., 2016, Astronomy and Astrophysics, 595, A70

Einasto M., et al., 2022, Astronomy and Astrophysics, 666, A52

El-Badry K., et al., 2018, Monthly Notices of the Royal Astronomical Society, 473, 1930

Erdoğdu P., et al., 2006a, Monthly Notices of the Royal Astronomical Society, 368, 1515

Erdoğdu P., et al., 2006b, Monthly Notices of the Royal Astronomical Society, 373, 45

Fairall A. P., Woudt P. A., Kraan-Korteweg R. C., 1998, Astronomy and Astrophysics Supplement Series, 127, 463

Falco E. E., et al., 1999, Publications of the Astronomical Society of the Pacific, 111, 438

Feldman H. A., Watkins R., Hudson M. J., 2010, Monthly Notices of the Royal Astronomical Society, 407, 2328

Fernández X., et al., 2013, Astrophysical Journal, Letters, 770, L29

Fernie J. D., 1969, Publications of the Astronomical Society of the Pacific, 81, 707

Foreman-Mackey D., Hogg D. W., Lang D., Goodman J., 2013, Publications of the Astronomical Society of the Pacific, 125, 306

Fuller T. M., West M. J., Bridges T. J., 1999, Astrophysical Journal, 519, 22

Gault L., et al., 2021, Astrophysical Journal, 909, 19

Giovanelli R., Haynes M. P., 1988, in Kellermann K. I., Verschuur G. L., eds, , Galactic and Extragalactic Radio Astronomy. pp 522–562

Giovanelli R., Haynes M. P., Chincarini G. L., 1986, Astrophysical Journal, 300, 77

Giuricin G., Gondolo P., Mardirossian F., Mezzetti M., Ramella M., 1988, Astronomy and Astrophysics, 199, 85

Goedhart S., et al., 2024, Monthly Notices of the Royal Astronomical Society, 531, 649

Gogate A., 2022, PhD thesis, University of Groningen, doi:10.33612/diss.206445119

Gogate A. R., Verheijen M. A. W., Deshev B. Z., van Gorkom J. H., Montero-Castaño M., van der Hulst J. M., Jaffé Y. L., Poggianti B. M., 2020, Monthly Notices of the Royal Astronomical Society, 496, 3531

Gouin C., Aghanim N., Bonjean V., Douspis M., 2020, Astronomy and Astrophysics, 635, A195

Graziani R., Courtois H. M., Lavaux G., Hoffman Y., Tully R. B., Copin Y., Pomarède D., 2019, Monthly Notices of the Royal Astronomical Society, 488, 5438

Grebel E. K., 2007, in Saviane I., Ivanov V. D., Borissova J., eds, Groups of Galaxies in the Nearby Universe. ESO Astrophysics Symposium. p. 3 (arXiv:astro-ph/0605564), doi:10.1007/978-3-540-71173-5˙1

Green D. A., 2009, Bulletin of the Astronomical Society of India, 37, 45

Hart L., Davies R. D., 1982, Nature, 297, 191

Hasegawa T., et al., 2000, Monthly Notices of the Royal Astronomical Society, 316, 326

Hashemizadeh A., et al., 2021, Monthly Notices of the Royal Astronomical Society, 505, 136

Hatamkhani N., 2022, PhD thesis, University of Cape Town, South Africa, http://hdl.handle.net/11427/37337

Hatamkhani N., Kraan-Korteweg R. C., Blyth S. L., Said K., Elagali A., 2023, Monthly Notices of the Royal Astronomical Society, 522, 2223

Haynes M. P., Giovanelli R., Chincarini G. L., 1984, Annual Review of Astronomy and Astrophysics, 22, 445

Haynes M. P., Giovanelli R., Starosta B. M., Magri C., 1988, The Astronomical Journal, 95, 607

Haynes M. P., et al., 2011, The Astronomical Journal, 142, 170

Haynes M. P., et al., 2018, Astrophysical Journal, 861, 49

Helou G., Walker D. W., 1988, in Infrared astronomical satellite (IRAS) catalogs and atlases. Volume 7.

Henning P. A., Kraan-Korteweg R. C., Rivers A. J., Loan A. J., Lahav O., Burton W. B., 1998, The Astronomical Journal, 115, 584

Henning P. A., et al., 2010, The Astronomical Journal, 139, 2130

Henry P. S., 1971, Nature, 231, 516

Herschel J. F. W., 1864, Philosophical Transactions of the Royal Society of London Series I, 154, 1

Heywood I., et al., 2022, Monthly Notices of the Royal Astronomical Society, 509, 2150

Hinshaw G., et al., 2013, Astrophysical Journal, Supplement, 208, 19

Hoffman Y., Courtois H. M., Tully R. B., 2015, Monthly Notices of the Royal Astronomical Society, 449, 4494

Hoffman Y., Pomarède D., Tully R. B., Courtois H. M., 2017, Nature Astronomy, 1, 0036

Holmberg E., 1958, Meddelanden fran Lunds Astronomiska Observatorium Serie II, 136, 1

Hong T., et al., 2014, Monthly Notices of the Royal Astronomical Society, 445, 402

Hong T., et al., 2019, Monthly Notices of the Royal Astronomical Society, 487, 2061

Hoppmann L., Staveley-Smith L., Freudling W., Zwaan M. A., Minchin R. F., Calabretta M. R., 2015, Monthly Notices of the Royal Astronomical Society, 452, 3726

Howlett C., Said K., Lucey J. R., Colless M., Qin F., Lai Y., Tully R. B., Davis T. M., 2022, Monthly Notices of the Royal Astronomical Society, 515, 953

Huang S., Haynes M. P., Giovanelli R., Brinchmann J., 2012, Astrophysical Journal, 756, 113

Hubble E. P., 1925, Popular Astronomy, 33, 252

Hubble E. P., 1926a, Astrophysical Journal, 63, 236

Hubble E. P., 1926b, Astrophysical Journal, 64, 321

Hubble E., 1929, Proceedings of the National Academy of Science, 15, 168

Huchra J., Davis M., Latham D., Tonry J., 1983, Astrophysical Journal, Supplement, 52, 89

Huchra J. P., Geller M. J., Corwin Harold G. J., 1995, Astrophysical Journal, Supplement, 99, 391

Huchra J. P., et al., 2012, Astrophysical Journal, Supplement, 199, 26

Hudson M. J., Smith R. J., Lucey J. R., Branchini E., 2004, Monthly Notices of the Royal Astronomical Society, 352, 61

Hyde J. B., Bernardi M., 2009, Monthly Notices of the Royal Astronomical Society, 394, 1978

Jaaniste J., Tago E., Einasto M., Einasto J., Andernach H., Mueller V., 1998, Astronomy and Astrophysics, 336, 35

Jarrett T., 2004, Publ. Astron. Soc. Australia, 21, 396

Jarrett T. H., Chester T., Cutri R., Schneider S., Skrutskie M., Huchra J. P., 2000, The Astronomical Journal, 119, 2498

Jarvis M. J., et al., 2013, Monthly Notices of the Royal Astronomical Society, 428, 1281

Jarvis M., et al., 2016, in MeerKAT Science: On the Pathway to the SKA. p. 6 (arXiv:1709.01901)

Jonas J., MeerKAT Team 2016, in MeerKAT Science: On the Pathway to the SKA. p. 1

Jones D. H., et al., 2009, Monthly Notices of the Royal Astronomical Society, 399, 683

Jones M. G., Papastergis E., Haynes M. P., Giovanelli R., 2016, Monthly Notices of the Royal Astronomical Society, 457, 4393

Jones M. G., Haynes M. P., Giovanelli R., Moorman C., 2018, Monthly Notices of the Royal Astronomical Society, 477, 2

Jones M. G., Hess K. M., Adams E. A. K., Verdes-Montenegro L., 2020, Monthly Notices of the Royal Astronomical Society, 494, 2090

Józsa G. I. G., et al., 2020, CARACal: Containerized Automated Radio Astronomy Calibration pipeline (ascl:2006.014)

Juraszek S. J., et al., 2000, The Astronomical Journal, 119, 1627

Kaiser N., 1988, Monthly Notices of the Royal Astronomical Society, 231, 149

Kashlinsky A., Atrio-Barandela F., Kocevski D., Ebeling H., 2008, Astrophysical Journal, Letters, 686, L49

Kashlinsky A., Atrio-Barandela F., Ebeling H., Edge A., Kocevski D., 2010, Astrophysical Journal, Letters, 712, L81

Kashlinsky A., Atrio-Barandela F., Ebeling H., 2011, Astrophysical Journal, 732, 1

Kassin S. A., et al., 2007, Astrophysical Journal, Letters, 660, L35

Kauffmann G., et al., 2003, Monthly Notices of the Royal Astronomical Society, 341, 54

Kauffmann G., Li C., Heckman T. M., 2010, Monthly Notices of the Royal Astronomical Society, 409, 491

Kennicutt Robert C. J., 1998, Annual Review of Astronomy and Astrophysics, 36, 189

Kenyon J. S., Smirnov O. M., Grobler T. L., Perkins S. J., 2018, Monthly Notices of the Royal Astronomical Society, 478, 2399

Kereš D., Katz N., Weinberg D. H., Davé R., 2005, Monthly Notices of the Royal Astronomical Society, 363, 2

Kerp J., Winkel B., Ben Bekhti N., Flöer L., Kalberla P. M. W., 2011, Astronomische Nachrichten, 332, 637

Kerr F. J., Henning P. A., 1987, Astrophysical Journal, Letters, 320, L99

Kocevski D. D., Ebeling H., 2006, Astrophysical Journal, 645, 1043

Kocevski D. D., Ebeling H., Mullis C. R., 2004, in Mulchaey J. S., Dressler A., Oemler A., eds, Clusters of Galaxies: Probes of Cosmological Structure and Galaxy Evolution. p. 26 (arXiv:astro-ph/0304453)

Kocevski D. D., Ebeling H., Mullis C. R., Tully R. B., 2007, Astrophysical Journal, 662, 224

Kofman L. A., Linde A. D., Einasto J., 1987, Nature, 326, 48

Kolokotronis V., Basilakos S., Plionis M., 2002, Monthly Notices of the Royal Astronomical Society, 331, 1020

Koribalski B. S., et al., 2020, Astrophysics and Space Science, 365, 118

Kourkchi E., et al., 2020, Astrophysical Journal, 902, 145

Kraan-Korteweg R. C., 2000, Astronomy and Astrophysics Supplement Series, 141, 123

Kraan-Korteweg R. C., 2005, Reviews in Modern Astronomy, 18, 48

Kraan-Korteweg R. C., Lahav O., 2000, The Astronomy and Astrophysics Review, 10, 211

Kraan-Korteweg R. C., Cayette V., Balkowski C., Fairall A. P., Henning P. A., 1994, in Balkowski C., Kraan-Korteweg R. C., eds, Astronomical Society of the Pacific Conference Series Vol. 67, Unveiling Large-Scale Structures Behind the Milky Way. p. 99

Kraan-Korteweg R. C., Fairall A. P., Balkowski C., 1995, Astronomy and Astrophysics, 297, 617

Kraan-Korteweg R. C., Woudt P. A., Cayatte V., Fairall A. P., Balkowski C., Henning P. A., 1996, Nature, 379, 519

Kraan-Korteweg R. C., Henning P. A., Schröder A. C., 2002, Astronomy and Astrophysics, 391, 887

Kraan-Korteweg R. C., Staveley-Smith L., Donley J., Koribalski B., Henning P. A., 2005, in Colless M., Staveley-Smith L., Stathakis R. A., eds, IAU Symposium No. 216 Vol. 216, Maps of the Cosmos. Astron. Soc. Pac., San Franciso. p. 203, doi:10.1017/S0074180900196640

Kraan-Korteweg R. C., van Derheyden K. J., Cluverand M. E., Woudt P. A., 2008a, in First Middle East-Africa Regional IAU Meeting. p. 8 (arXiv:0810.3929), doi:10.48550/arXiv.0810.3929

Kraan-Korteweg R. C., Shafi N., Koribalski B. S., Staveley-Smith L., Buckland P., Henning P. A., Fairall A. P., 2008b, in Galaxies in the Local Volume. p. 13 (arXiv:0710.1795), doi:J47-5257810.1007/978-1-4020-6933-8˙2

Kraan-Korteweg R. C., Jarrett T. H., Elagali A., Cluver M. E., Bilicki M., Colless M. M., 2015, in SALT Science Conference 2015 (SSC2015). p. 40, doi:10.22323/1.250.0040

Kraan-Korteweg R. C., et al., 2016, in MeerKAT Science: On the Pathway to the SKA. p. 21 (arXiv:1708.03587), doi:10.22323/1.277.0021

Kraan-Korteweg R. C., Cluver M. E., Bilicki M., Jarrett T. H., Colless M., Elagali A., Böhringer H., Chon G., 2017, Monthly Notices of the Royal Astronomical Society, 466, L29

Kraan-Korteweg R. C., van Driel W., Schröder A. C., Ramatsoku M., Henning P. A., 2018, Monthly Notices of the Royal Astronomical Society, 481, 1262

Kurapati S., et al., 2024, Monthly Notices of the Royal Astronomical Society, 528, 542

Lahav O., Yamada T., Scharf C., Kraan-Korteweg R. C., 1993, Monthly Notices of the Royal Astronomical Society, 262, 711

Lauer T. R., Postman M., 1994, Astrophysical Journal, 425, 418

Lavaux G., Hudson M. J., 2011, Monthly Notices of the Royal Astronomical Society, 416, 2840

Lavaux G., Tully R. B., Mohayaee R., Colombi S., 2010, Astrophysical Journal, 709, 483

Lavaux G., Afshordi N., Hudson M. J., 2013, Monthly Notices of the Royal Astronomical Society, 430, 1617

Leisman L., et al., 2017, Astrophysical Journal, 842, 133

Lelli F., McGaugh S. S., Schombert J. M., 2016, The Astronomical Journal, 152, 157

Lelli F., McGaugh S. S., Schombert J. M., Desmond H., Katz H., 2019, Monthly Notices of the Royal Astronomical Society, 484, 3267

Leroy A. K., Walter F., Brinks E., Bigiel F., de Blok W. J. G., Madore B., Thornley M. D., 2008, The Astronomical Journal, 136, 2782

Lilly S. J., et al., 2009, Astrophysical Journal, Supplement, 184, 218

Loeb A., Narayan R., 2008, Monthly Notices of the Royal Astronomical Society, 386, 2221

Longair M. S., Einasto J., eds, 1978, The large scale structure of the universe. IAU Symposium Vol. 79

Loveday J., 2000, Monthly Notices of the Royal Astronomical Society, 312, 557

Lovisari L., Ettori S., Gaspari M., Giles P. A., 2021, Universe, 7, 139

Luparello H., Lares M., Lambas D. G., Padilla N., 2011, Monthly Notices of the Royal Astronomical Society, 415, 964

Lutz K. A., et al., 2018, Monthly Notices of the Royal Astronomical Society, 476, 3744

Lynden-Bell D., Faber S. M., Burstein D., Davies R. L., Dressler A., Terlevich R. J., Wegner G., 1988, Astrophysical Journal, 326, 19

Ma Y.-Z., Pan J., 2014, Monthly Notices of the Royal Astronomical Society, 437, 1996

Macri L. M., et al., 2019, Astrophysical Journal, Supplement, 245, 6

Maddox N., Hess K. M., Obreschkow D., Jarvis M. J., Blyth S. L., 2015, Monthly Notices of the Royal Astronomical Society, 447, 1610

Maddox N., et al., 2021, Astronomy and Astrophysics, 646, A35

Magoulas C., 2012, Phd thesis, The University of Melbourne, School of Physics

Makarov D., Prugniel P., Terekhova N., Courtois H., Vauglin I., 2014, Astronomy and Astrophysics, 570, A13

Makhathini S., 2018, PhD thesis, Rhodes University, South Africa

Marinacci F., Grand R. J. J., Pakmor R., Springel V., Gómez F. A., Frenk C. S., White S. D. M., 2017, Monthly Notices of the Royal Astronomical Society, 466, 3859

Martin A. M., Papastergis E., Giovanelli R., Haynes M. P., Springob C. M., Stierwalt S., 2010, Astrophysical Journal, 723, 1359

Martinsson T. P. K., Verheijen M. A. W., Bershady M. A., Westfall K. B., Andersen D. R., Swaters R. A., 2016, Astronomy and Astrophysics, 585, A99

Marzke R. O., da Costa L. N., Pellegrini P. S., Willmer C. N. A., Geller M. J., 1998, Astrophysical Journal, 503, 617

Masters K. L., Springob C. M., Haynes M. P., Giovanelli R., 2006, Astrophysical Journal, 653, 861

Masters K. L., et al., 2007, in American Astronomical Society Meeting Abstracts #210. p. 84.03

Masters K. L., Springob C. M., Huchra J. P., 2008, The Astronomical Journal, 135, 1738

Mauch T., et al., 2020, Astrophysical Journal, 888, 61

McCracken H. J., et al., 2012, Astronomy and Astrophysics, 544, A156

McGaugh S. S., Schombert J. M., Bothun G. D., de Blok W. J. G., 2000, Astrophysical Journal, Letters, 533, L99

McIntyre T. P., Henning P. A., Minchin R. F., Momjian E., Butcher Z., 2015, The Astronomical Journal, 150, 28

McMullin J. P., Waters B., Schiebel D., Young W., Golap K., 2007, in Shaw R. A., Hill F., Bell D. J., eds, Astronomical Society of the Pacific Conference Series Vol. 376, Astronomical Data Analysis Software and Systems XVI. p. 127

Merloni A., et al., 2012, arXiv e-prints, p. arXiv:1209.3114

Merloni A., et al., 2024, Astronomy and Astrophysics, 682, A34

Meyer M., 2009, in Panoramic Radio Astronomy: Wide-field 1-2 GHz Research on Galaxy Evolution. p. 15 (arXiv:0912.2167), doi:10.22323/1.089.0015

Meyer M. J., et al., 2004, Monthly Notices of the Royal Astronomical Society, 350, 1195

Meyer M., Robotham A., Obreschkow D., Westmeier T., Duffy A. R., Staveley-Smith L., 2017, Publ. Astron. Soc. Australia, 34, 52

Minniti D., et al., 2018, Astronomy and Astrophysics, 616, A26

Morganti R., et al., 2006, Monthly Notices of the Royal Astronomical Society, 371, 157

Mulaudzi W., 2021, The Galaxy Velocity Function from MIGHTEE-H I Early Science Data., http://hdl.handle.net/11427/35959

Murphy E. J., Kenney J. D. P., Helou G., Chung A., Howell J. H., 2009, Astrophysical Journal, 694, 1435

Nagamine K., Loeb A., 2003, New Astron., 8, 439

Navarro J. F., White S. D. M., 1994, Monthly Notices of the Royal Astronomical Society, 267, 401

Noordermeer E., van der Hulst J. M., Sancisi R., Swaters R. A., van Albada T. S., 2005, Astronomy and Astrophysics, 442, 137

Nusser A., Davis M., 2011, Astrophysical Journal, 736, 93

Nusser A., Davis M., Branchini E., 2014, Astrophysical Journal, 788, 157

Offringa A. R., 2010, AOFlagger: RFI Software (ascl:1010.017)

Offringa A. R., et al., 2014, Monthly Notices of the Royal Astronomical Society, 444, 606

Oort J. H., 1983a, ARA&A, 21, 373

Oort J. H., 1983b, in Abell G. O., Chincarini G., eds, Proceedings IAU Symposium Vol. 104, Early Evolution of the Universe and its Present Structure. pp 1–6

Papastergis E., 2013, PhD thesis, Cornell University, New York

Papastergis E., Martin A. M., Giovanelli R., Haynes M. P., 2011, Astrophysical Journal, 739, 38

Park C., Kim J., Gott J. Richard I., 2005, Astrophysical Journal, 633, 1

Paturel G., Petit C., Prugniel P., Theureau G., Rousseau J., Brouty M., Dubois P., Cambrésy L., 2003, Astronomy and Astrophysics, 412, 45

Pearson D. W., Batiste M., Batuski D. J., 2014, Monthly Notices of the Royal Astronomical Society, 441, 1601

Peebles P. J. E., 1976, Astrophysical Journal, 205, 318

Peebles P. J. E., 2022, Monthly Notices of the Royal Astronomical Society, 511, 5093

Peng Y., et al., 2010, Astrophysical Journal, 721, 193

Pfenniger D., 1999, Astrophysics and Space Science, 269, 149

Planck Collaboration et al., 2014, Astronomy and Astrophysics, 561, A97

Planck Collaboration et al., 2020, Astronomy and Astrophysics, 641, A1

Plionis M., Kolokotronis V., 1998, Astrophysical Journal, 500, 1

Ponomareva A. A., Verheijen M. A. W., Bosma A., 2016, Monthly Notices of the Royal Astronomical Society, 463, 4052

Ponomareva A. A., Verheijen M. A. W., Papastergis E., Bosma A., Peletier R. F., 2018, Monthly Notices of the Royal Astronomical Society, 474, 4366

Ponomareva A. A., et al., 2021, Monthly Notices of the Royal Astronomical Society, 508, 1195

Ponomareva A. A., et al., 2023, Monthly Notices of the Royal Astronomical Society, 522, 5308

Pranger F., Trujillo I., Kelvin L. S., Cebrián M., 2017, Monthly Notices of the Royal Astronomical Society, 467, 2127

Proctor R., 1878, The Universe of Stars: Presenting Researches Into and New Views Respecting the Constitution of the Heavens. Longmans, Green, and Company

Proust D., et al., 2006, Astronomy and Astrophysics, 447, 133

Qin F., 2021, Research in Astronomy and Astrophysics, 21, 242

Qin F., Howlett C., Staveley-Smith L., Hong T., 2018, Monthly Notices of the Royal Astronomical Society, 477, 5150

Qin F., Howlett C., Staveley-Smith L., Hong T., 2019, Monthly Notices of the Royal Astronomical Society, 482, 1920

Qin F., Parkinson D., Howlett C., Said K., 2021, Astrophysical Journal, 922, 59

Quintana H., Ramirez A., Melnick J., Raychaudhury S., Slezak E., 1995, The Astronomical Journal, 110, 463

Rajohnson S. H. A., et al., 2022, Monthly Notices of the Royal Astronomical Society, 512, 2697

Ramatsoku M., et al., 2016, Monthly Notices of the Royal Astronomical Society, 460, 923

Ranchod S., et al., 2021, Monthly Notices of the Royal Astronomical Society, 506, 2753

Rauzy S., 2001, Monthly Notices of the Royal Astronomical Society, 324, 51

Reisenegger A., Quintana H., Carrasco E. R., Maze J., 2000, The Astronomical Journal, 120, 523

Rivers A. J., Henning P. A., Kraan-Korteweg R. C., 1999, Publ. Astron. Soc. Australia, 16, 48

Roberts M. S., 1963, Annual Review of Astronomy and Astrophysics, 1, 149

Roberts M. S., 1978, The Astronomical Journal, 83, 1026

Roberts M. S., Haynes M. P., 1994, Annual Review of Astronomy and Astrophysics, 32, 115

Rose J. A., Gaba A. E., Christiansen W. A., Davis D. S., Caldwell N., Hunstead R. W., Johnston-Hollitt M., 2002, The Astronomical Journal, 123, 1216

Rubin V. C., Thonnard N., Ford W. K. J., Roberts M. S., 1976, The Astronomical Journal, 81, 719

Said K., Kraan-Korteweg R. C., Jarrett T. H., 2015, Monthly Notices of the Royal Astronomical Society, 447, 1618

Said K., Kraan-Korteweg R. C., Jarrett T. H., Staveley-Smith L., Williams W. L., 2016, Monthly Notices of the Royal Astronomical Society, 462, 3386

Said K., Kraan-Korteweg R. C., Staveley-Smith L., 2019, Monthly Notices of the Royal Astronomical Society, 486, 1796

Sanchez-Barrantes M., et al., 2019, The Astronomical Journal, 158, 234

Sancisi R., Fraternali F., Oosterloo T., van der Hulst T., 2008, The Astronomy and Astrophysics Review, 15, 189

Sandage A., Tammann G. A., 1981, A Revised Shapley-Ames Catalog of Bright Galaxies

Sandage A., Tammann G. A., 1984, Nature, 307, 326

Sarron F., Adami C., Durret F., Laigle C., 2019, Astronomy and Astrophysics, 632, A49

Scarlata C., et al., 2007, Astrophysical Journal, Supplement, 172, 406

Schechter P., 1976, Astrophysical Journal, 203, 297

Schlafly E. F., Finkbeiner D. P., 2011, Astrophysical Journal, 737, 103

Schlegel D. J., Finkbeiner D. P., Davis M., 1998, Astrophysical Journal, 500, 525

Schmidt M., 1959, Astrophysical Journal, 129, 243

Schmidt M., 1963, Astrophysical Journal, 137, 758

Schmidt M., 1968, Astrophysical Journal, 151, 393

Schneider S. E., 1996, in Skillman E. D., ed., Astronomical Society of the Pacific Conference Series Vol. 106, The Minnesota Lectures on Extragalactic Neutral Hydrogen. p. 323

Schröder A. C., Kraan-Korteweg R. C., Henning P. A., 2009, Astronomy and Astrophysics, 505, 1049

Schröder A. C., Flöer L., Winkel B., Kerp J., 2019, Monthly Notices of the Royal Astronomical Society, 489, 2907

Schröder A. C., van Driel W., Kraan-Korteweg R. C., 2021, Monthly Notices of the Royal Astronomical Society, 503, 5351

Scrimgeour M. I., et al., 2016, Monthly Notices of the Royal Astronomical Society, 455, 386

Serra P., et al., 2012, Monthly Notices of the Royal Astronomical Society, 422, 1835

Serra P., et al., 2016, in MeerKAT Science: On the Pathway to the SKA. p. 8 (arXiv:1709.01289), doi:10.22323/1.277.0008

Serra P., et al., 2023, Astronomy and Astrophysics, 673, A146

Shapley H., 1961, Galaxies.

Shaya E. J., Tully R. B., 2013, Monthly Notices of the Royal Astronomical Society, 436, 2096

Shen S., Mo H. J., White S. D. M., Blanton M. R., Kauffmann G., Voges W., Brinkmann J., Csabai I., 2003, Monthly Notices of the Royal Astronomical Society, 343, 978

Shostak G. S., 1977, Astronomy and Astrophysics, 58, L31

Skillman E. D., 1996, in Skillman E. D., ed., Astronomical Society of the Pacific Conference Series Vol. 106, The Minnesota Lectures on Extragalactic Neutral Hydrogen. p. 208

Skrutskie M. F., et al., 2006, The Astronomical Journal, 131, 1163

Smoot G. F., Gorenstein M. V., Muller R. A., 1977, Phys. Rev. Lett., 39, 898

Sorce J. G., Colless M., Kraan-Korteweg R. C., Gottlöber S., 2017, Monthly Notices of the Royal Astronomical Society, 471, 3087

Sousbie T., 2011, Monthly Notices of the Royal Astronomical Society, 414, 350

Springob C. M., 2004, in American Astronomical Society Meeting Abstracts. p. 122.03

Springob C. M., Haynes M. P., Giovanelli R., 2005, Astrophysical Journal, 621, 215

Springob C. M., Masters K. L., Haynes M. P., Giovanelli R., Marinoni C., 2007, Astrophysical Journal, Supplement, 172, 599

Springob C. M., et al., 2014, Monthly Notices of the Royal Astronomical Society, 445, 2677

Springob C. M., et al., 2016, Monthly Notices of the Royal Astronomical Society, 456, 1886

Staveley-Smith L., Oosterloo T., 2015, in Advancing Astrophysics with the Square Kilometre Array (AASKA14). p. 167 (arXiv:1506.04473)

Staveley-Smith L., Kraan-Korteweg R. C., Schröder A. C., Henning P. A., Koribalski B. S., Stewart I. M., Heald G., 2016, The Astronomical Journal, 151, 52

Stein P., 1996, Astronomy and Astrophysics Supplement Series, 116, 203

Stevens A. R. H., Diemer B., Lagos C. d. P., Nelson D., Obreschkow D., Wang J., Marinacci F., 2019, Monthly Notices of the Royal Astronomical Society, 490, 96

Steyn N., 2023, First MeerKAT H I survey results mapping large scale structures hidden behind the Milky Way out to z = 0.08, http://hdl.handle.net/11427/38045

Steyn N., et al., 2024, Monthly Notices of the Royal Astronomical Society, 529, L88

Strauss M. A., Willick J. A., 1995, Phys. Rep., 261, 271

Sun S., Guo Q., Wang L., Lacey C. G., Wang J., Gao L., Pan J., 2018, Monthly Notices of the Royal Astronomical Society, 477, 3136

Swaters R. A., van Albada T. S., van der Hulst J. M., Sancisi R., 2002, Astronomy and Astrophysics, 390, 829

Tammann G. A., Sandage A., 1985, Astrophysical Journal, 294, 81

Tempel E., Stoica R. S., Martínez V. J., Liivamägi L. J., Castellan G., Saar E., 2014, Monthly Notices of the Royal Astronomical Society, 438, 3465

Toribio M. C., Solanes J. M., Giovanelli R., Haynes M. P., Martin A. M., 2011, Astrophysical Journal, 732, 93

Torres-Flores S., Epinat B., Amram P., Plana H., Mendes de Oliveira C., 2011, Monthly Notices of the Royal Astronomical Society, 416, 1936

Tremonti C. A., et al., 2004, Astrophysical Journal, 613, 898

Trumpler R. J., 1930, Publications of the Astronomical Society of the Pacific, 42, 214

Tully R. B., 1982, Astrophysical Journal, 257, 389

Tully R. B., Fisher J. R., 1977, Astronomy and Astrophysics, 500, 105

Tully R. B., Shaya E. J., Karachentsev I. D., Courtois H. M., Kocevski D. D., Rizzi L., Peel A., 2008, Astrophysical Journal, 686, 1523

Tully R. B., et al., 2013, The Astronomical Journal, 146, 86

Tully R. B., Courtois H., Hoffman Y., Pomarède D., 2014, Nature, 513, 71

Tully R. B., Courtois H. M., Sorce J. G., 2016, The Astronomical Journal, 152, 50

Tully R. B., et al., 2023, Astrophysical Journal, 944, 94

Turnbull S. J., Hudson M. J., Feldman H. A., Hicken M., Kirshner R. P., Watkins R., 2012, Monthly Notices of the Royal Astronomical Society, 420, 447

Verdes-Montenegro L., Yun M. S., Williams B. A., Huchtmeier W. K., Del Olmo A., Perea J., 2001, Astronomy and Astrophysics, 377, 812

Verheijen M. A. W., Sancisi R., 2001, Astronomy and Astrophysics, 370, 765

Voges W., et al., 1999, Astronomy and Astrophysics, 349, 389

Vollmer B., 2013, in Oswalt T. D., Keel W. C., eds, , Vol. 6, Planets, Stars and Stellar Systems. Volume 6: Extragalactic Astronomy and Cosmology. p. 207, doi:10.1007/978-94-007-5609-0˙5

Vollmer B., Soida M., Chung A., Beck R., Urbanik M., Chyży K. T., Otmianowska-Mazur K., van Gorkom J. H., 2010, Astronomy and Astrophysics, 512, A36

Vollmer B., Soida M., Beck R., Chung A., Urbanik M., Chyży K. T., Otmianowska-Mazur K., Kenney J. D. P., 2013, Astronomy and Astrophysics, 553, A116

Von Maltitz K., 2012, Master's thesis, University of Cape Town

Wakamatsu K., Malkan M. A., Nishida M. T., Parker Q. A., Saunders W., Watson F. G., 2005, in Fairall A. P., Woudt P. A., eds, Astronomical Society of the Pacific Conference Series Vol. 329, Nearby Large-Scale Structures and the Zone of Avoidance. p. 189

Wang J., et al., 2013, Monthly Notices of the Royal Astronomical Society, 433, 270

Wang J., et al., 2014, Monthly Notices of the Royal Astronomical Society, 441, 2159

Wang J., Koribalski B. S., Serra P., van der Hulst T., Roychowdhury S., Kamphuis P., Chengalur J. N., 2016, Monthly Notices of the Royal Astronomical Society, 460, 2143

Watkins R., Feldman H. A., Hudson M. J., 2009, Monthly Notices of the Royal Astronomical Society, 392, 743

Wegner G., Haynes M. P., Giovanelli R., 1993, The Astronomical Journal, 105, 1251

Weingartner J. C., Draine B. T., 2001, Astrophysical Journal, 548, 296

Weltman A., et al., 2020, Publ. Astron. Soc. Australia, 37, e002

Westmeier T., Jurek R., Obreschkow D., Koribalski B. S., Staveley-Smith L., 2014, Monthly Notices of the Royal Astronomical Society, 438, 1176

Westmeier T., et al., 2021, Monthly Notices of the Royal Astronomical Society, 506, 3962

White S. D. M., Frenk C. S., 1991, Astrophysical Journal, 379, 52

Williams W. L., Kraan-Korteweg R. C., Woudt P. A., 2014, Monthly Notices of the Royal Astronomical Society, 443, 41

Winkel B., Kalberla P. M. W., Kerp J., Flöer L., 2010, Astrophysical Journal, Supplement, 188, 488

Woudt P. A., 1998, PhD thesis, University of Cape Town, South Africa

Woudt P. A., Kraan-Korteweg R. C., 2001, Astronomy and Astrophysics, 380, 441

Woudt P. A., Kraan-Korteweg R. C., Fairall A. P., 1999, Astronomy and Astrophysics, 352, 39

Wray J. J., Bahcall N. A., Bode P., Boettiger C., Hopkins P. F., 2006, Astrophysical Journal, 652, 907

Wright E. L., et al., 2010, The Astronomical Journal, 140, 1868

Xi H., Staveley-Smith L., For B.-Q., Freudling W., Zwaan M., Hoppmann L., Liang F.-H., Peng B., 2021, Monthly Notices of the Royal Astronomical Society, 501, 4550

Yahil A., Sandage A., Tammann G. A., 1980, Astrophysical Journal, 242, 448

York D. G., et al., 2000, The Astronomical Journal, 120, 1579

Zwaan M. A., et al., 2003, The Astronomical Journal, 125, 2842

Zwaan M. A., et al., 2004, Monthly Notices of the Royal Astronomical Society, 350, 1210

Zwaan M. A., Meyer M. J., Staveley-Smith L., Webster R. L., 2005, Monthly Notices of the Royal Astronomical Society, 359, L30

da Costa L. N., et al., 1998, The Astronomical Journal, 116, 1

de Blok W. J. G., et al., 2016, in MeerKAT Science: On the Pathway to the SKA. p. 7 (arXiv:1709.08458), doi:10.22323/1.277.0007

de Jong R. S., et al., 2019, The Messenger, 175, 3

de Vaucouleurs G., 1953, The Astronomical Journal, 58, 30

de Vaucouleurs G., 1958, The Astronomical Journal, 63, 253

de Vaucouleurs G., Peters W. L., 1984, Astrophysical Journal, 287, 1

van Driel W., Schneider S. E., Kraan-Korteweg R. C., Monnier Ragaigne D., 2009, Astronomy and Astrophysics, 505, 29

van der Wel A., et al., 2014, Astrophysical Journal, 788, 28

appendix A

The MIGHTEE H I Size – Mass relation: sample galaxy catalog

This appendix presents the derived H I parameters for the sample of 204 galaxies in the MIGHTEE-H I Early survey (see Chapter 2). The column descriptions are as follows:

1. **Column (1)**: Galaxy designated name based on the MIGHTEE-H I detections nomenclature. Names are of the form MGTH_JHHMMSS.S+DDMMSS. This identification is based on the unrounded values of the Right Ascension in hh mm ss and Declination (J2000) in dd mm ss format of the H I centroid.

2. **Column (2):** Field name in which the detection belongs to. The letter "X" indicates a detection found in XMMLSS while "C" represents a source in the COSMOS field.

3. **Column (3)**: Morphological type based on the visual classification of the optical counterpart. (SP) for Spirals, (IR) for Dwarf Irregulars and Irregular galaxies, (ET) for Early-types and (ME) for Mergers.

4. **Column (4)**: Peak flux density ($S_{\rm p}$) in mJy of the H I line profile with its uncertainty.

5. **Column (5)**: Integrated H I flux density ($S_{\rm int}$) of each MIGHTEE-H I source, expressed in Jy km s^{-1}. This value corresponds to the total H I line flux measured within the mom-0 map of a detection.

6. **Column (6)**: Local rms noise of the detection noise cubes in mJy beam^{-1}.

7. **Column (7)**: Systemic H I velocity ($v_{\rm sys}$) of the emission measured from the heliocentric central velocities of the global H I profile in $\rm km\,s^{-1}$ (the relativistic convention is assumed for the Doppler shift). The typical uncertainty for the systemic velocity and linewidths corresponds to the width of one channel at the observed velocity frame which is $\epsilon(v_{\rm sys}) \sim 44\ \rm km\,s^{-1}$ at $z = 0$ and $\epsilon(v_{\rm sys}) \sim 52\ \rm km\,s^{-1}$ at $z \sim 0.084$.

8. **Column (8)**: Velocity widths of the H I line profile at 50% of the peak flux density (w_{50}) measured at the width maximization procedure and with the use of PYMULTINEST.

9. **Column (9)**: Luminosity distance D_L in Mpc with an uncertainty $\epsilon(D_L) \sim 0.5$ Mpc at $z = 0$ and $\epsilon(D_L) \sim 3.5$ Mpc at $z \sim 0.084$, measured from the H I emission redshift.

10. **Column (10)**: Logarithm of the total H I mass $\log(M_{\rm HI}/{\rm M}_\odot)$ and its uncertainty (see Eq. 2.21).

11. **Column (11)**: Inclination and beam-smearing corrected H I diameter in kpc, measured at a surface density level of 1 $M_\odot$ pc^{-2}.

12. **Column (12)**: Measured inclinations ($i_{\rm HI}$) in degrees.

Table A.1: A catalogue of H I properties of the sample of 204 galaxies in the MIGHTEE-H I early survey.

MGTH	Field	Morpho	S_p (mJy)	$S_{\rm int}$ (Jy km s^{-1})	rms (mJy beam^{-1})	$v_{\rm sys}$ (km s^{-1})	w_{50} (km s^{-1})	D_L (Mpc)	log $M_{\rm HI}$ (dex)	$D_{\rm HI}$ (dex)	$i_{\rm HI}$ (deg)
(1)	(2)	(3)	(4)	(5)	(6)	(7)	(8)	(9)	(10)	(11)	(12)
J021529.1-051859	X	SP	6.14±0.24	0.738±0.037	0.240	7780	157	115	9.34	28.18	59
J021532.8-044607	X	SP	8.14±0.11	1.927±0.096	0.109	12383	291	186	10.16	67.61	50
J021534.4-042904	X	SP	1.84±0.15	0.129±0.006	0.149	23582	69	373	9.56	35.56	32
J021541.6-051317	X	IR	10.62±0.16	0.724±0.036	0.161	12635	90	190	9.75	46.03	41
J021542.4-045436	X	SP	3.76±0.11	0.497±0.025	0.108	12589	456	189	9.59	39.36	43
J021544.5-045540	X	SP	8.17±0.1	1.742±0.087	0.099	12784	226	193	10.01	64.42	56
J021600.4-044414	X	SP	8.35±0.08	0.576±0.029	0.080	20101	275	313	10.06	52.48	47
J021609.9-051858	X	SP	16.95±0.14	3.093±0.155	0.141	16423	185	252	10.62	121.06	25
J021632.8-041357	X	SP	3.45±0.17	0.216±0.011	0.175	12830	95	193	9.24	20.65	29
J021639.9-044747	X	SP	9.68±0.06	1.06±0.053	0.063	20136	137	313	10.33	98.86	33
J021642.0-044221	X	SP	8.16±0.06	0.597±0.03	0.064	12578	65	189	9.67	31.92	64
J021645.4-042035	X	IR	3.02±0.1	0.281±0.014	0.104	24009	113	381	9.91	50.70	46
J021659.0-050352	X	ET	2.72±0.08	0.194±0.019	0.081	7667	96	112	8.74	14.32	41
J021702.2-050351	X	ME	8.3±0.06	1.029±0.051	0.063	7701	130	114	9.39	29.99	42
J021702.2-044454	X	SP	2.16±0.06	0.286±0.014	0.058	16411	254	251	9.58	32.96	56
J021702.7-051940	X	SP	8.83±0.13	1.185±0.059	0.125	15657	141	239	10.16	54.45	45
J021708.4-041349	X	SP	11.05±0.14	1.778±0.089	0.138	16423	161	252	10.38	88.31	27
J021711.2-042120	X	SP	3.54±0.1	0.7±0.035	0.096	16469	385	252	9.97	54.83	67
J021711.8-042441	X	IR	2.92±0.08	0.27±0.013	0.083	11191	136	167	9.22	26.61	40
J021714.5-052922	X	SP	8.46±0.23	0.636±0.064	0.233	5190	242	76	8.92	18.45	43
J021719.4-052851	X	SP	73.0±0.18	14.931±0.747	0.179	5325	240	77	10.29	74.99	62
J021729.0-050827	X	SP	6.93±0.07	0.79±0.04	0.069	12819	102	193	9.80	48.64	29
J021729.9-041656	X	SP	1.97±0.11	0.15±0.015	0.112	10016	88	149	8.87	13.71	61
J021742.0-041520	X	SP	7.33±0.12	0.966±0.048	0.122	9880	200	147	9.67	46.67	33
J021742.5-050425	X	SP	3.82±0.06	0.457±0.023	0.059	13095	132	196	9.58	37.15	32
J021743.8-051752	X	ME	5.02±0.1	0.488±0.024	0.095	9493	131	140	9.33	24.43	45
J021744.6-050322	X	SP	3.37±0.06	0.27±0.013	0.058	12865	87	194	9.34	30.20	44
J021744.9-041158	X	SP	7.01±0.15	1.409±0.07	0.147	12497	199	188	10.03	53.95	57
J021748.5-043241	X	SP	6.3±0.06	0.875±0.044	0.062	19995	231	311	10.24	76.91	42
J021750.4-044940	X	ME	1.47±0.05	0.175±0.009	0.052	12474	142	188	9.12	24.72	40
J021759.3-041634	X	SP	8.04±0.11	0.901±0.045	0.114	9834	99	147	9.63	38.64	18
J021814.0-044944	X	SP	3.71±0.06	0.488±0.024	0.055	9413	163	140	9.32	27.80	46
J021815.4-041558	X	SP	11.98±0.13	2.232±0.112	0.129	12394	261	186	10.20	67.45	36
J021818.0-043234	X	IR	5.77±0.23	0.33±0.017	0.233	12589	86	190	9.41	26.30	62
J021822.2-050614	X	SP	2.65±0.07	0.262±0.013	0.069	13049	179	196	9.34	28.44	33

Table A.1 continued

MGTH	Field	Morpho	S_p (mJy)	$S_{\rm int}$ (Jy km s^{-1})	rms (mJy beam^{-1})	$v_{\rm sys}$ (km s^{-1})	w_{50} (km s^{-1})	D_L (Mpc)	log $M_{\rm HI}$ (dex)	$D_{\rm HI}$ (dex)	$i_{\rm HI}$ (deg)
(1)	(2)	(3)	(4)	(5)	(6)	(7)	(8)	(9)	(10)	(11)	(12)
J021824.1-052754	X	SP	6.94±0.18	1.048±0.052	0.178	12474	222	188	9.90	50.47	57
J021827.2-041219	X	IR	8.32±0.16	1.148±0.057	0.160	12233	197	184	9.93	49.66	36
J021836.3-043236	X	SP	21.37±0.07	2.287±0.114	0.073	3936	93	57	9.23	25.18	32
J021847.0-045555	X	SP	1.33±0.06	0.101±0.01	0.064	13003	61	196	8.93	15.31	45
J021848.1-045028	X	SP	2.36±0.06	0.179±0.009	0.063	24092	67	382	9.72	41.78	49
J021902.3-042646	X	SP	5.65±0.17	0.523±0.026	0.167	12141	178	183	9.58	36.31	47
J021931.5-042703	X	SP	2.7±0.13	0.132±0.007	0.126	20030	64	312	9.42	28.91	50
J021932.7-041447	X	ME	5.65±0.25	0.761±0.038	0.251	12566	241	188	9.77	44.06	66
J021934.4-042846	X	IR	2.92±0.14	0.236±0.012	0.137	20124	94	313	9.68	26.30	69
J021947.7-045130	X	SP	4.39±0.09	0.818±0.041	0.093	12818	234	193	9.82	48.42	52
J021953.8-045710	X	SP	1.41±0.09	0.151±0.015	0.087	9959	155	148	8.86	11.75	33
J022002.1-041438	X	IR	3.54±0.18	0.128±0.006	0.184	12428	69	187	8.99	14.96	45
J022002.8-042547	X	SP	4.65±0.2	0.448±0.045	0.205	5325	133	78	8.79	14.69	42
J022014.4-052345	X	SP	5.34±0.23	0.531±0.027	0.229	14812	103	225	9.76	50.35	29
J022016.8-042546	X	SP	10.03±0.22	0.508±0.025	0.225	19984	88	310	10.00	66.83	60
J022021.4-045803	X	SP	2.97±0.08	0.702±0.035	0.085	9970	358	147	9.52	30.90	68
J022026.3-045912	X	IR	1.67±0.1	0.124±0.012	0.096	12531	87	188	8.98	15.35	66
J022028.5-053705	X	SP	7.27±0.55	0.243±0.012	0.548	13244	213	200	9.32	26.73	20
J022028.9-042514	X	SP	2.13±0.12	0.228±0.011	0.116	20206	102	314	9.67	39.36	49
J022029.4-041207	X	SP	6.19±0.18	0.523±0.052	0.184	6066	134	89	8.97	18.58	52
J022033.0-052605	X	SP	7.38±0.32	1.266±0.063	0.319	12176	245	183	9.96	55.98	46
J022049.8-052913	X	SP	9.67±0.4	0.951±0.048	0.402	9891	225	146	9.65	44.57	59
J022049.9-044928	X	IR	2.15±0.08	0.257±0.013	0.078	16213	132	248	9.52	36.81	46
J022051.5-045703	X	SP	17.7±0.09	3.479±0.174	0.090	12899	254	194	10.45	109.40	53
J022054.9-042201	X	SP	2.92±0.12	0.27±0.014	0.121	21300	146	333	9.79	50.12	16
J022056.3-042806	X	SP	1.17±0.12	0.151±0.008	0.116	20112	68	313	9.48	27.04	61
J022058.7-051320	X	IR	1.72±0.31	0.208±0.01	0.310	18870	114	292	9.57	26.24	51
J022105.4-042951	X	SP	3.61±0.09	0.544±0.027	0.093	12050	228	181	9.59	37.67	40
J022108.8-043907	X	SP	3.48±0.09	0.246±0.012	0.088	23332	330	368	9.83	48.53	38
J022108.8-052326	X	SP	3.92±0.25	0.263±0.013	0.252	23641	101	374	9.87	64.27	74
J022111.7-040445	X	SP	71.84±0.33	3.981±0.199	0.331	6054	48	89	9.85	48.75	42
J022113.4-043551	X	ET	1.91±0.1	0.159±0.008	0.098	23641	182	373	9.65	43.85	43
J022115.4-041355	X	SP	2.95±0.19	0.167±0.017	0.187	9948	92	148	8.91	15.78	52
J022117.8-045040	X	IR	2.59±0.11	0.152±0.008	0.112	12807	71	193	9.09	20.56	26
J022123.0-040259	X	SP	10.71±0.39	0.933±0.047	0.392	15286	139	233	10.03	62.95	44
J022128.8-042448	X	SP	102.91±2.48	9.586±0.479	2.480	2332	178	34	9.40	24.43	71
J022128.9-044232	X	SP	1.49±0.11	0.143±0.007	0.107	12520	102	188	9.04	19.45	34
J022135.9-042519	X	SP	6.7±0.25	1.031±0.052	0.247	20018	181	312	10.31	69.98	24
J022136.5-053117	X	SP	160.07±0.67	87.494±4.375	0.672	2309	271	33	10.34	69.50	51
J022138.1-052631	X	IR	23.83±0.3	1.284±0.128	0.302	2087	46	30	8.42	8.49	35
J022144.2-044231	X	SP	3.33±0.1	0.244±0.012	0.097	16202	67	248	9.50	32.81	27
J022145.5-050210	X	SP	2.05±0.13	0.173±0.009	0.127	21277	143	332	9.59	28.38	48
J022146.5-043621	X	SP	7.1±0.1	0.917±0.046	0.099	21902	328	343	10.34	92.68	57
J022146.8-050750	X	SP	2.31±0.13	0.319±0.016	0.134	21347	184	333	9.86	49.77	51
J022147.9-044614	X	ET	3.54±0.09	0.265±0.027	0.088	6009	89	88	8.66	11.53	61
J022148.3-044833	X	SP	1.81±0.1	0.233±0.012	0.096	21053	207	329	9.71	43.65	36
J022154.1-044023	X	SP	3.14±0.11	0.456±0.023	0.105	23451	506	370	10.10	60.81	77
J022204.6-042017	X	SP	4.42±0.14	0.261±0.013	0.144	23866	138	377	9.87	37.33	45
J022212.3-044252	X	SP	1.67±0.08	0.193±0.01	0.080	13002	161	196	9.20	19.05	56
J022214.0-045023	X	SP	1.25±0.07	0.134±0.007	0.071	21158	128	332	9.48	23.66	49
J022229.7-045314	X	SP	3.44±0.12	0.421±0.021	0.116	23202	310	365	10.05	61.09	45
J022230.9-040742	X	SP	9.2±0.56	0.21±0.01	0.561	20559	46	320	9.65	38.99	60
J022233.1-054249	X	IR	27.84±0.84	2.707±0.135	0.843	9697	44	144	10.09	49.66	39
J022236.8-043432	X	SP	1.58±0.1	0.158±0.008	0.100	20112	192	313	9.50	30.20	49

Table A.1 continued

MGTH	Field	Morpho	S_p (mJy)	$S_{\rm int}$ (Jy km s^{-1})	rms (mJy beam^{-1})	$v_{\rm sys}$ (km s^{-1})	w_{50} (km s^{-1})	D_L (Mpc)	log $M_{\rm HI}$ (dex)	$D_{\rm HI}$ (dex)	$i_{\rm HI}$ (deg)
(1)	(2)	(3)	(4)	(5)	(6)	(7)	(8)	(9)	(10)	(11)	(12)
J022244.3-035807	X	IR	184.34±1.07	21.095±1.055	1.070	2309	109	33	9.73	36.48	34
J022248.8-045308	X	SP	9.1±0.16	1.446±0.072	0.164	10985	202	164	9.93	45.60	37
J022256.0-051359	X	IR	3.21±0.09	0.477±0.024	0.094	13094	103	198	9.61	36.81	37
J022302.5-043637	X	ET	2.17±0.17	0.127±0.006	0.172	23084	67	364	9.53	34.36	39
J022307.6-052904	X	SP	10.35±0.2	1.49±0.074	0.197	20206	416	312	10.47	96.38	57
J022313.2-043102	X	SP	42.89±0.31	5.502±0.275	0.311	5234	180	76	9.86	39.81	42
J022322.2-041956	X	SP	3.53±0.15	0.22±0.011	0.146	21972	98	345	9.72	43.35	44
J022325.3-053839	X	IR	6.59±0.42	0.213±0.021	0.417	5638	71	83	8.52	10.79	49
J022325.5-041753	X	SP	7.82±0.23	1.48±0.074	0.233	12692	271	191	10.07	62.09	73
J022332.2-044928	X	IR	3.75±0.07	0.272±0.014	0.066	13117	91	198	9.36	29.51	30
J022336.8-042834	X	SP	4.73±0.1	0.561±0.028	0.101	20042	190	312	10.05	55.21	48
J022340.4-050045	X	SP	10.14±0.41	0.932±0.047	0.408	13094	126	198	9.90	49.32	48
J022344.3-042752	X	IR	3.06±0.12	0.36±0.018	0.123	17760	95	273	9.75	44.87	17
J022350.6-045045	X	IR	13.95±0.07	1.86±0.093	0.073	12910	122	195	10.18	68.23	41
J022350.6-043703	X	SP	276.92±0.83	26.101±1.305	0.833	2276	106	32	9.80	42.76	34
J022357.0-051918	X	SP	5.17±0.12	0.196±0.01	0.120	21913	45	344	9.67	44.06	51
J022357.1-044357	X	SP	5.34±0.08	0.76±0.038	0.079	12841	45	194	9.79	41.98	69
J022358.3-050756	X	IR	2.6±0.08	0.136±0.007	0.084	15286	123	233	9.20	16.22	57
J022402.8-040935	X	ME	21.16±0.3	3.091±0.155	0.296	9868	179	147	10.17	67.14	33
J022403.0-043422	X	IR	6.24±0.09	0.515±0.052	0.089	6077	86	89	8.96	18.54	48
J022403.8-043305	X	ME	10.3±0.1	2.604±0.13	0.102	12956	250	196	10.33	67.30	37
J022404.1-044812	X	SP	48.61±0.72	4.105±0.205	0.717	12818	151	193	10.52	105.68	43
J022405.7-051120	X	IR	2.37±0.09	0.125±0.006	0.090	22716	93	358	9.51	31.77	40
J022405.8-041444	X	ME	3.75±0.27	0.554±0.028	0.270	17900	205	276	9.94	55.08	36
J022411.5-044745	X	SP	1.64±0.08	0.147±0.007	0.078	13025	119	197	9.09	18.49	33
J022412.6-045953	X	SP	7.8±0.08	1.227±0.061	0.078	11889	242	178	9.93	50.82	48
J022415.6-044153	X	SP	5.21±0.09	1.075±0.054	0.086	20018	264	311	10.33	86.10	52
J022417.6-041710	X	SP	3.28±0.17	0.268±0.013	0.166	20935	190	328	9.77	46.67	45
J022419.1-050041	X	SP	3.26±0.08	0.383±0.019	0.084	11855	126	179	9.43	23.99	45
J022422.4-052604	X	ME	9.44±0.18	0.854±0.043	0.178	21937	162	344	10.31	87.10	48
J022427.1-043533	X	SP	2.77±0.09	0.341±0.017	0.094	20782	254	323	9.86	50.23	20
J022429.6-044037	X	SP	3.51±0.1	0.522±0.026	0.099	12933	208	195	9.63	38.82	42
J022430.0-043614	X	SP	10.47±0.1	2.389±0.119	0.104	19995	322	311	10.68	139.96	56
J022438.7-043418	X	SP	7.36±0.12	1.229±0.061	0.125	12830	237	193	10.00	63.83	56
J022443.4-045158	X	IR	2.19±0.1	0.153±0.008	0.097	12026	103	181	9.04	21.13	22
J022444.3-042845	X	SP	2.85±0.12	0.293±0.015	0.124	22705	167	358	9.88	50.82	42
J022444.4-043351	X	SP	3.67±0.13	0.687±0.034	0.132	8845	378	129	9.41	32.58	51
J022447.5-044645	X	SP	19.34±0.11	3.346±0.167	0.106	9640	176	143	10.18	67.92	48
J022454.9-052548	X	SP	4.4±0.24	0.152±0.008	0.239	23368	93	369	9.62	39.81	46
J022455.3-041735	X	SP	14.73±0.31	2.513±0.126	0.311	12922	313	195	10.31	89.74	56
J022456.0-051918	X	SP	8.83±0.2	0.782±0.039	0.199	15645	178	238	9.97	58.34	39
J022504.2-051611	X	SP	5.95±0.17	0.331±0.017	0.175	22374	97	351	9.92	64.71	54
J022504.9-044225	X	SP	3.99±0.15	0.618±0.031	0.147	15575	203	237	9.87	51.88	56
J022506.4-052105	X	SP	2.83±0.25	0.261±0.013	0.252	15564	218	237	9.50	40.46	53
J022509.0-051228	X	ME	3.21±0.15	0.511±0.026	0.148	23628	102	373	10.16	76.91	49
J022511.5-042047	X	IR	2.59±0.22	0.196±0.01	0.216	19901	98	310	9.59	27.23	60
J022512.4-040915	X	SP	9.68±0.54	0.604±0.03	0.544	18169	93	280	10.00	45.71	64
J022520.8-050137	X	SP	4.02±0.17	0.291±0.015	0.172	15645	93	239	9.55	35.81	47
J022522.7-045519	X	SP	5.85±0.15	0.857±0.043	0.146	10825	179	162	9.69	39.90	45
J022523.2-051252	X	IR	3.9±0.19	0.237±0.012	0.187	22314	90	350	9.77	45.19	28
J022528.9-050236	X	SP	4.84±0.18	0.431±0.022	0.175	17807	278	272	9.83	37.15	57
J022532.9-045733	X	SP	3.8±0.15	0.291±0.015	0.148	20253	163	315	9.77	40.36	38
J022533.7-045819	X	SP	3.34±0.18	0.218±0.011	0.184	15587	131	238	9.42	28.91	51
J022536.4-050012	X	ME	9.63±0.2	1.454±0.073	0.196	15726	253	240	10.25	66.83	36

Table A.1 continued

MGTH	Field	Morpho	S_p (mJy)	$S_{\rm int}$ (Jy km s^{-1})	rms (mJy beam^{-1})	$v_{\rm sys}$ (km s^{-1})	w_{50} (km s^{-1})	D_L (Mpc)	log $M_{\rm HI}$ (dex)	$D_{\rm HI}$ (dex)	$i_{\rm HI}$ (deg)
(1)	(2)	(3)	(4)	(5)	(6)	(7)	(8)	(9)	(10)	(11)	(12)
J022538.4-050810	X	SP	3.28±0.22	0.139±0.007	0.223	17679	56	272	9.33	20.04	23
J022541.9-051835	X	IR	6.43±0.35	0.414±0.021	0.345	15714	118	239	9.70	44.98	63
J022547.3-044811	X	IR	6.08±0.22	0.28±0.014	0.221	17900	51	276	9.65	46.34	48
J022555.1-043544	X	SP	4.96±0.28	0.427±0.021	0.281	8867	466	130	9.20	25.35	76
J022556.7-041857	X	SP	16.03±0.57	0.448±0.045	0.566	5537	227	80	8.81	18.07	48
J022603.6-044747	X	SP	3.39±0.28	0.075±0.004	0.285	16097	51	245	8.98	17.34	49
J022611.0-044104	X	SP	5.31±0.37	0.364±0.018	0.372	15958	138	244	9.66	38.99	48
J022628.5-050905	X	IR	15.24±0.64	0.514±0.026	0.643	14684	94	222	9.73	47.64	63
J022702.5-043531	X	SP	12.98±1.44	0.368±0.018	1.436	8867	44	131	9.15	26.36	60
J095720.6+015507	C	SP	18.52±0.23	3.534±0.177	0.227	9464	196	141	10.19	58.08	37
J095727.3+015221	C	SP	7.14±0.23	0.45±0.023	0.232	9692	97	144	9.32	27.10	52
J095822.5+013505	C	SP	3.08±0.22	0.414±0.021	0.224	8137	67	120	9.12	23.99	62
J095829.1+014139	C	IR	69.72±0.13	9.467±0.473	0.129	1837	110	26	9.18	21.63	60
J095846.8+022051	C	SP	20.43±0.05	2.907±0.291	0.053	1748	120	25	8.62	12.53	55
J095901.7+023300	C	SP	2.8±0.07	0.35±0.017	0.066	8556	156	127	9.10	20.00	47
J095904.3+021516	C	IR	3.0±0.05	0.225±0.022	0.046	7323	92	107	8.76	13.96	36
J095914.9+014911	C	IR	3.12±0.06	0.164±0.008	0.064	22807	91	359	9.63	40.18	43
J095920.5+024626	C	SP	5.32±0.09	0.132±0.007	0.091	22488	157	351	9.52	32.81	40
J095923.2+024137	C	SP	4.7±0.07	0.248±0.012	0.075	13941	228	211	9.38	23.50	54
J095927.9+020025	C	SP	5.85±0.04	0.509±0.051	0.045	3874	87	56	8.57	11.69	36
J095934.2+013706	C	IR	2.17±0.1	0.143±0.014	0.104	9419	84	140	8.79	15.96	48
J095951.4+014224	C	ME	3.13±0.07	0.258±0.026	0.072	7447	91	109	8.84	14.55	38
J095954.5+020017	C	SP	1.85±0.04	0.169±0.008	0.042	22464	137	353	9.63	45.60	37
J095959.9+015913	C	SP	4.71±0.04	0.273±0.014	0.042	23115	139	365	9.86	44.16	37
J100003.9+015253	C	SP	2.37±0.05	0.294±0.015	0.049	18924	190	293	9.72	33.57	61
J100005.8+015440	C	SP	3.5±0.05	0.312±0.062	0.045	1870	86	27	7.72	4.18	51
J100008.1+024554	C	SP	5.85±0.08	0.606±0.03	0.082	8533	272	127	9.34	39.45	34
J100009.3+024247	C	SP	5.64±0.07	0.967±0.048	0.070	9635	177	143	9.64	43.45	54
J100031.6+031219	C	SP	38.59±0.86	3.442±0.344	0.860	2159	129	31	8.88	14.93	50
J100035.1+011433	C	SP	15.81±0.61	1.007±0.05	0.609	13481	162	205	9.96	53.21	43
J100041.1+022446	C	SP	3.25±0.04	0.19±0.01	0.041	13768	66	208	9.25	18.54	51
J100048.1+011414	C	SP	31.76±0.61	1.62±0.081	0.611	13550	73	205	10.17	74.99	39
J100050.5+012008	C	SP	16.39±0.36	1.176±0.059	0.360	6409	95	93	9.36	26.24	38
J100055.2+022344	C	SP	2.98±0.04	0.413±0.021	0.042	13032	231	196	9.53	34.43	40
J100103.7+013055	C	SP	4.5±0.13	0.269±0.013	0.129	23530	97	371	9.87	61.52	44
J100103.7+023053	C	SP	2.5±0.05	0.454±0.023	0.049	20766	233	325	9.99	69.18	44
J100107.1+015416	C	SP	3.02±0.05	0.291±0.015	0.050	22311	179	351	9.86	62.37	36
J100115.2+021823	C	ME	6.18±0.04	0.646±0.032	0.044	8488	163	125	9.35	30.20	59
J100117.1+020337	C	SP	2.13±0.04	0.171±0.009	0.044	17884	182	276	9.44	28.97	41
J100121.2+024714	C	SP	2.81±0.1	0.142±0.007	0.097	21096	98	330	9.50	25.12	39
J100122.9+014737	C	IR	3.16±0.07	0.219±0.022	0.068	7402	94	109	8.76	11.38	24
J100129.9+021705	C	SP	1.92±0.04	0.254±0.013	0.044	21732	252	343	9.78	52.48	39
J100143.2+024109	C	SP	5.37±0.09	0.821±0.041	0.092	13768	184	208	9.88	58.75	44
J100153.8+022449	C	IR	4.55±0.06	0.258±0.052	0.061	2048	66	29	7.71	4.17	37
J100211.2+020118	C	SP	3.84±0.07	0.312±0.031	0.071	6353	105	93	8.78	16.60	36
J100212.1+030312	C	SP	8.81±0.58	0.778±0.039	0.581	8840	186	131	9.47	29.65	78
J100212.7+015100	C	IR	3.24±0.09	0.097±0.005	0.091	18258	124	281	9.20	23.12	36
J100217.9+015124	C	SP	3.48±0.09	0.484±0.024	0.090	18211	254	280	9.90	60.53	51
J100218.5+014542	C	SP	3.68±0.11	0.197±0.01	0.106	23506	111	369	9.73	47.97	51
J100222.7+022520	C	IR	3.6±0.08	0.399±0.04	0.082	6353	126	93	8.89	17.74	46
J100222.8+024519	C	SP	4.57±0.15	0.461±0.023	0.151	20943	247	326	10.00	57.41	61
J100223.7+024027	C	SP	4.12±0.12	0.184±0.009	0.120	19779	90	308	9.56	37.76	60
J100227.1+021000	C	IR	3.14±0.08	0.148±0.03	0.079	1793	58	25	7.35	2.18	43
J100236.5+014618	C	IR	1.23±0.14	0.143±0.007	0.139	13262	67	201	9.09	19.19	42

Table A.1 continued

MGTH	Field	Morpho	S_p (mJy)	$S_{\rm int}$ (Jy km s^{-1})	rms (mJy beam^{-1})	$v_{\rm sys}$ (km s^{-1})	w_{50} (km s^{-1})	D_L (Mpc)	log $M_{\rm HI}$ (dex)	$D_{\rm HI}$ (dex)	$i_{\rm HI}$ (deg)
(1)	(2)	(3)	(4)	(5)	(6)	(7)	(8)	(9)	(10)	(11)	(12)
J100236.5+014836	C	SP	8.08±0.14	0.886±0.044	0.137	13331	137	202	9.89	57.94	38
J100243.1+015944	C	IR	0.56±0.11	0.196±0.01	0.106	17488	104	268	10.05	46.45	41
J100259.0+022035	C	SP	7.26±0.13	0.931±0.047	0.127	12997	267	196	9.89	60.95	45
J100313.5+015343	C	SP	6.51±0.21	0.323±0.016	0.209	13377	130	202	9.45	34.91	41
J100313.9+022031	C	SP	5.9±0.17	0.422±0.021	0.166	11415	175	172	9.43	33.88	57
J100315.4+020543	C	IR	29.85±0.19	1.889±0.189	0.188	1759	65	25	8.43	9.51	38
J100352.4+022534	C	SP	7.13±0.41	0.366±0.018	0.407	7956	61	117	9.05	19.63	44

appendix B

The Vela–SMGPS appendices

B.1 Sofia-2 parameter file

The appendix below provides the parameter file employed in SoFiA 2.3.1, using the Smooth + Clip (S + C) finder with a 4σ noise threshold. The same parameter configuration is utilized for the second SoFiA run but with the adjustment `scfind.threshold = 3.5`.

```
### SoFiA 2.3.1 - Source Finding Application    ###
### Copyright (C) 2020 Tobias Westmeier        ###

# Global settings

pipeline.verbose           =  false
pipeline.pedantic          =  false

# Input

input.data                 =  Taper15_T30/to_galactic/T30_gal_taper15.fits
input.region               =  1268, 5470, 355, 3958, 9, 525
#xmin, xmax,ymin,ymax,zmin,zmax
#For Vela$-$SMGPS mosaics, we need to specify a square region of ~3.5x3 sq. deg
input.gain                 =
input.noise                =  Taper15_T30/to_galactic/T30_gal_taper15_noise.fits
input.weights              =
input.mask                 =
input.invert               =  false

# Flagging

flag.region                =
flag.auto                  =  false
flag.threshold             =  5.0
flag.log                   =  true

# Noise scaling

scaleNoise.enable          =  true
scaleNoise.mode            = local
#for Vela$-$SMGPS only, other SMGPS mosaics use spectral
scaleNoise.statistic       =  mad
scaleNoise.windowXY        =  301
```

```
scaleNoise.windowZ         =  15
scaleNoise.gridXY          =  0
scaleNoise.gridZ           =  0
scaleNoise.interpolate     =  true
scaleNoise.scfind          =  false

# S+C finder (smooth & clip)

scfind.enable              =  true
scfind.kernelsXY           =  0, 7, 15
scfind.kernelsZ            =  0, 3, 5, 7
scfind.threshold           =  4 #and 3.5
scfind.replacement         =  1.5
scfind.statistic           =  mad
scfind.fluxRange           =  negative

# Linker

linker.radiusXY            =  5
linker.radiusZ             =  3
linker.minSizeXY           =  10
linker.minSizeZ            =  3
linker.maxSizeXY           =  0
linker.maxSizeZ            =  50

# Reliability

reliability.enable         =  true
reliability.threshold      =  0.90
reliability.scaleKernel    =  0.25
reliability.minSNR         =  3
reliability.plot           =  true
reliability.debug          =  true

# Parameterisation

parameter.enable           =  true
parameter.wcs              =  true
parameter.physical         =  true
parameter.prefix           =  SoFiA
parameter.offset           =  true

# Output

output.directory           =  Taper15_T30/sofia_new/local/4_sigma
output.filename            =  T30_gal_local_4_sigma_
output.writeCatASCII       =  true
output.writeCatXML         =  false
output.writeCatSQL         =  false
output.writeNoise          =  false
output.writeFiltered       =  false
output.writeMask           =  true
output.writeMask2d         =  false
output.writeMoments        =  false
output.writeCubelets       =  false
output.marginCubelets      =  0
output.overwrite           =  true
```

B.2 HIZOA detections in Vela–SMGPS

The 39 Vela–SMGPS detections in common with HIZOA (Staveley-Smith et al., 2016) are shown in Fig. B.1 (unique) and B.2 (multiple counterparts).

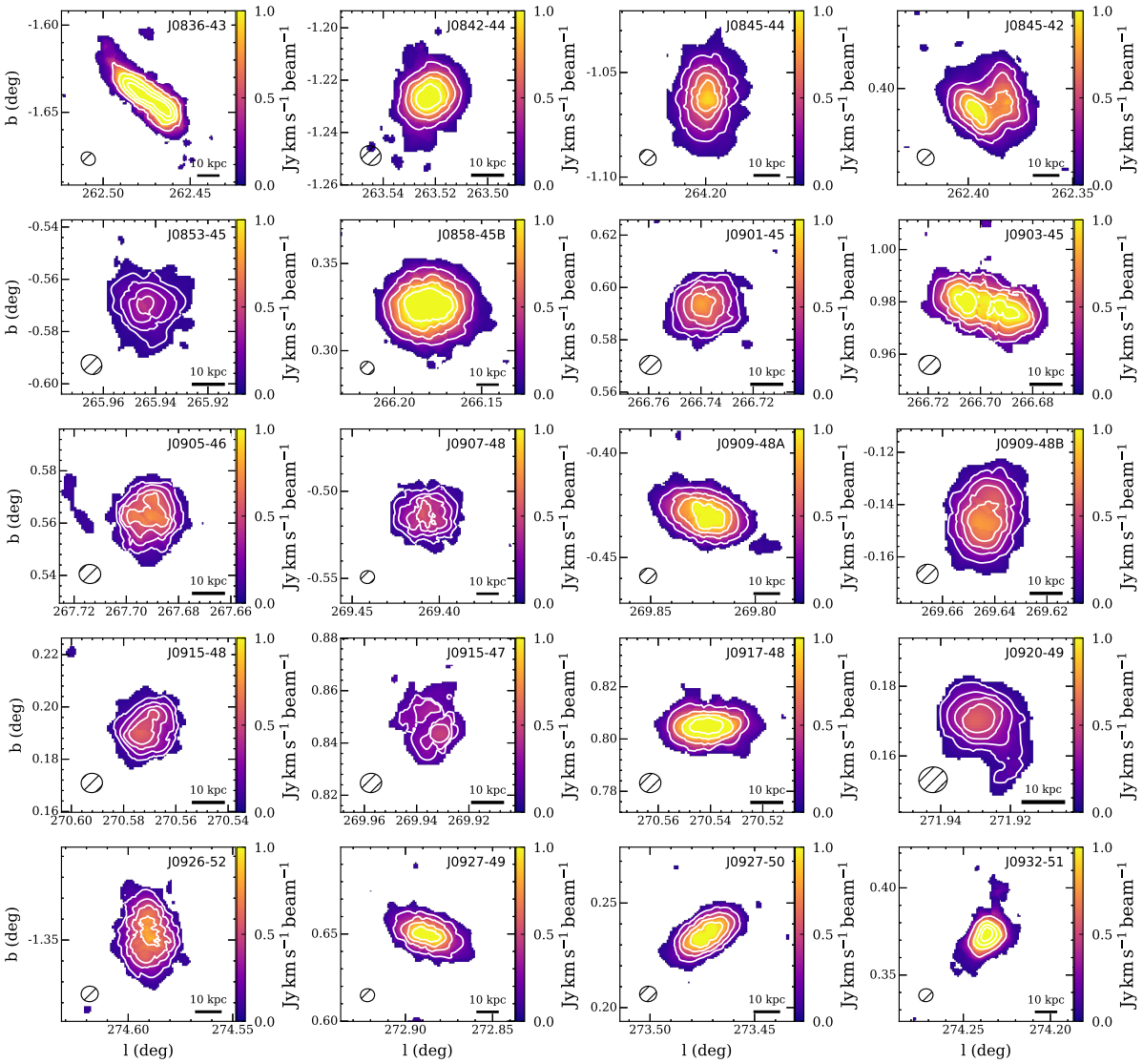

Figure B.1: Moment-0 maps of HIZOA galaxies detected in Vela–SMGPS. The HIZOA identification name, the beam size, and a 10 kpc scale are shown in the upper right, bottom left, and bottom right corners of each image, respectively.

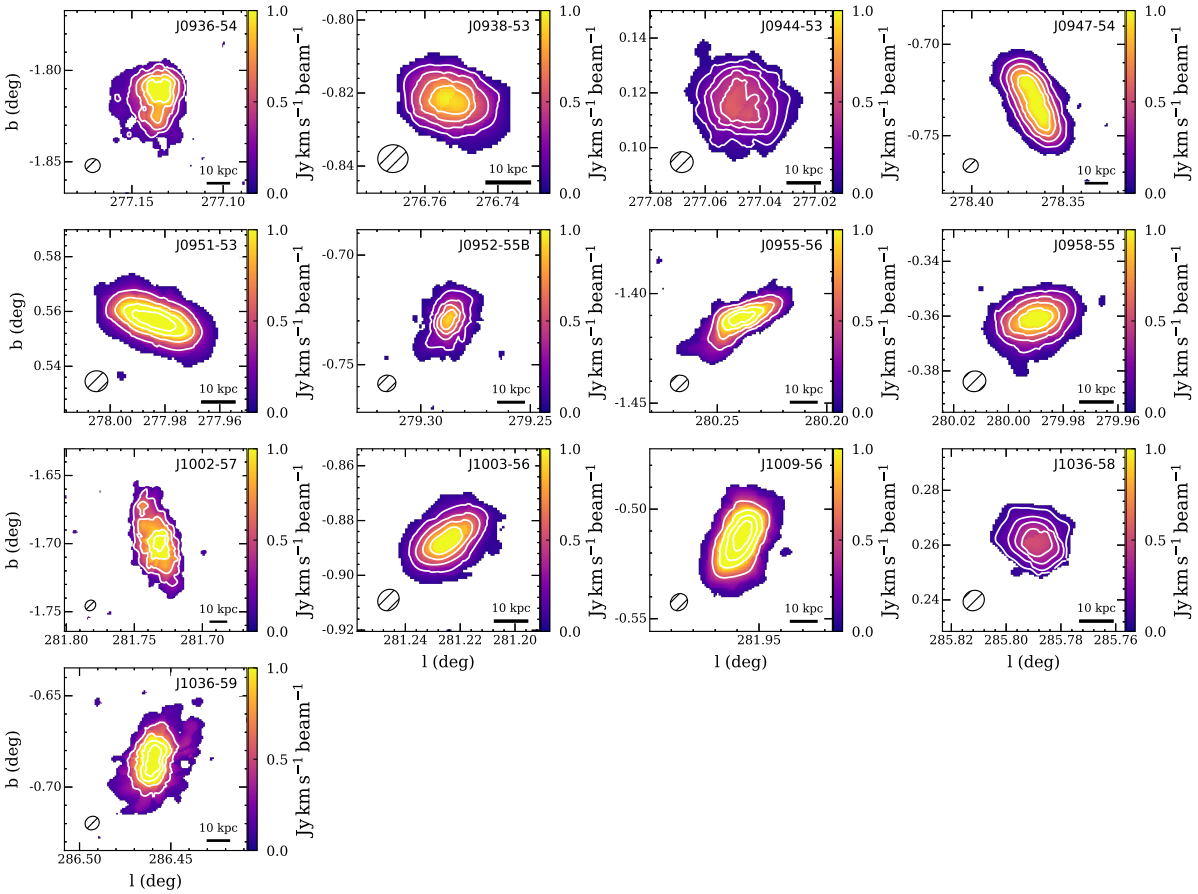

Figure B.1: Moment-0 maps of HIZOA galaxies detected in Vela–SMGPS (Continued)

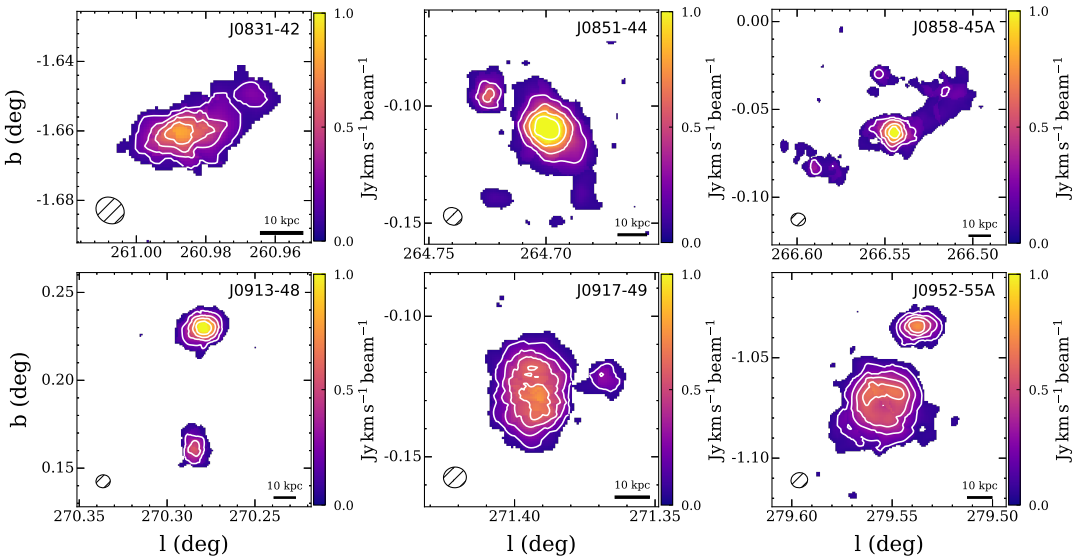

Figure B.2: List of HIZOA galaxies resolved into several galaxies in Vela–SMGPS.

B.3 Vela–SMGPS full catalog

This appendix lists the derived H I properties obtained for the 843 detected Vela–SMGPS detections ($260^\circ \leq \ell \leq 290^\circ$) in Chapter 3. A brief description of the columns of the catalog is provided below:

- (1) Galaxy identifier (SMGPS-HI) Jmmhhss±ddmmss.
- (2) Mosaic [T24–T33].
- (3,4) Galactic longitude and latitude [deg].
- (5) Peak flux density from the Global H I profile $S_{\rm peak}$ [Jy].
- (6,7) Integrated flux $S_{\rm int}$ and its uncertainty $\rm err_{(S_{int})}$ [Jy km s^{-1}].
- (8) Mean local rms noise [mJy beam^{-1}].
- (9) Optical heliocentric velocity $V_{\rm hel}$ [km s^{-1}]
- (10, 11) Linewidths at 20% (w_{20}) and 50% (w_{50}) of the peak flux density [km s^{-1}].
- (12) H I masses [log($M_{\rm HI}$/M$_\odot$)].
- (13) Flag [1 (Solid) or 2 (Possible)]. A flag code accompanied by an asterisk indicates that the detection has also been identified in the area with the adjacent mosaic.
- (14) Note.
    - BL: Wiggly baseline in the Global H I profile.
    - i: With signs of interactions.
    - w.comp(s): galaxy with one (or several) companion(s).
    - w_{20} unc.: w_{20} measurement unclear due to baseline behaviour.
    - I: counterpart from the IRAS Point Source Catalog (Helou & Walker, 1988).
    - H: counterpart from the southern region of the HIPASS catalog (Meyer et al., 2004).
    - M: counterpart from 2MASX (Jarrett et al., 2000).
    - W: counterpart from WISE (Cutri et al., 2021).
    - Z: counterpart from the IRSF catalogs (Williams et al., 2014; Said et al., 2016).

Table B.1: Vela-SMGPS full galaxy catalog: H I properties.

Name	Mosaic	l	b	$S_{\rm peak}$	$S_{\rm int}$	err$_{(S_{\rm int})}$	RMS	$V_{\rm hel}$	w_{20}	w_{50}	$M_{\rm HI}$	Flag	Note
J2000	TXX	deg	deg	Jy	Jy km s^{-1}	Jy km s^{-1}	mJy beam^{-1}	km s^{-1}	km s^{-1}	km s^{-1}	log($M_{\rm HI}$/M$_\odot$)	1/2	
(1)	(2)	(3)	(4)	(5)	(6)	(7)	(8)	(9)	(10)	(11)	(12)	(13)	(14)
J082930-421453	T33	260.566	-1.903	0.010	1.24	0.23	0.46	2710	215	97	8.64	1	
J083133-422815	T33	260.970	-1.726	0.018	6.28	0.62	0.40	8242	481	429	10.32	1	J0831-42? w.comp (J083154-422631), M, W, Z
J083154-422631	T33	260.983	-1.659	0.018	2.91	0.41	0.36	8346	245	182	10.00	1	J0831-42, i, w.comp (J083133-422815)
J083217-415102	T33	260.548	-1.251	0.005	0.59	0.06	0.23	21824	342	301	10.15	1	
J083223-421453	T33	260.881	-1.471	0.003	0.25	0.05	0.27	8427	262	210	8.94	2	
J083236-423939	T33	261.237	-1.683	0.008	1.21	0.17	0.40	10767	466	345	9.84	1	
J083253-425142	T33	261.429	-1.762	0.006	1.19	0.17	0.43	8250	409	376	9.60	1	M, W
J083312-425407	T33	261.497	-1.737	0.011	2.19	0.22	0.39	11612	353	298	10.16	1	
J083406-414353	T33	260.655	-0.907	0.007	0.59	0.11	0.25	5427	136	77	8.92	1	
J083418-413412	T33	260.548	-0.780	0.003	0.18	0.03	0.24	10672	135	84	9.00	1	
J083440-413902	T33	260.653	-0.775	0.006	0.39	0.04	0.24	24375	197	108	10.06	1	
J083442-430649	T33	261.830	-1.644	0.007	1.11	0.16	0.32	8239	248	193	9.56	1	
J083446-422256	T33	261.251	-1.197	0.008	0.58	0.06	0.26	19549	140	104	10.04	1	
J083513-431435	T33	261.989	-1.647	0.004	0.29	0.04	0.35	11227	132	92	9.25	1	
J083523-413320	T33	260.657	-0.610	0.002	0.33	0.05	0.24	18204	398	295	9.74	2	
J083545-411907	T33	260.508	-0.414	0.015	4.43	0.63	0.26	4976	533	502	9.73	1	M, W
J083547-415531	T33	260.999	-0.771	0.006	0.42	0.06	0.25	13350	112	61	9.56	2	
J083550-430530	T33	261.937	-1.465	0.018	1.61	0.23	0.30	11223	137	102	10.00	1	
J083603-431104	T33	262.033	-1.491	0.010	2.17	0.31	0.33	5273	293	248	9.47	1	
J083611-411912	T33	260.560	-0.348	0.004	0.58	0.08	0.25	18221	438	423	9.98	1	
J083632-430608	T33	262.021	-1.371	0.017	1.91	0.27	0.30	5291	170	134	9.41	1	I, M, W
J083650-433738	T33	262.474	-1.642	0.054	14.63	1.54	0.39	10699	617	557	10.91	1	J0836-43, BL, e, w.comp, I, H, M, W
J083703-425113	T33	261.881	-1.144	0.005	0.25	0.04	0.27	22008	110	84	9.79	2	
J083730-430654	T33	262.138	-1.237	0.005	0.59	0.06	0.28	24035	502	462	10.23	2	
J083732-431307	T33	262.225	-1.294	0.013	1.06	0.15	0.30	5278	117	86	9.16	1	
J083742-413835	T33	260.989	-0.316	0.011	0.81	0.11	0.26	9389	118	77	9.54	1	
J083746-435546	T33	262.817	-1.690	0.005	0.49	0.05	0.37	24183	297	276	10.16	1	
J083751-421432	T33	261.482	-0.658	0.004	0.29	0.04	0.26	11416	212	172	9.26	1	
J083815-435953	T33	262.924	-1.663	0.015	2.05	0.29	0.39	3898	160	130	9.18	1	
J083818-420056	T33	261.352	-0.454	0.002	0.31	0.04	0.25	10807	190	168	9.25	1	
J083824-413039	T33	260.963	-0.132	0.003	0.37	0.07	0.26	7061	207	153	8.95	1	
J083826-441859	T33	263.196	-1.831	0.009	0.53	0.07	0.56	10188	206	94	9.43	1	

* Detected by the overlapping region of the next mosaic as well.

Table B.1 continued

Name J2000 (1)	Mosaic TXX (2)	l deg (3)	b deg (4)	$S_{\rm peak}$ Jy (5)	$S_{\rm int}$ Jy km s^{-1} (6)	err$_{(S_{\rm int})}$ Jy km s^{-1} (7)	RMS mJy beam^{-1} (8)	$V_{\rm hel}$ km s^{-1} (9)	w_{20} km s^{-1} (10)	w_{50} km s^{-1} (11)	$M_{\rm HI}$ log($M_{\rm HI}$/M$_\odot$) (12)	Flag 1/2 (13)	Note (14)
J083831-440328	T33	263.000	-1.661	0.007	0.34	0.06	0.37	5656	210	104	8.73	1	
J083841-405454	T33	260.521	0.270	0.004	0.27	0.04	0.24	17808	185	144	9.63	1	
J083843-423114	T33	261.801	-0.699	0.003	0.22	0.03	0.25	18031	315	283	9.56	2	
J083847-444025	T32	263.519	-1.997	0.007	0.60	0.09	0.61	10138	497	383	9.48	2	BL
J083849-425455	T33	262.125	-0.924	0.010	1.32	0.19	0.29	10760	276	247	9.87	1	
J083851-440501	T33	263.057	-1.629	0.007	0.55	0.08	0.38	10380	216	128	9.46	1	w.comp (J083855-440223)
J083855-440223	T33	263.029	-1.594	0.017	2.17	0.21	0.38	10586	316	272	10.08	1	i, w.comp (J083851-440501), M, W
J083901-432543	T33	262.555	-1.207	0.006	0.34	0.05	0.29	8028	130	102	9.03	1	
J083902-441944	T33	263.272	-1.752	0.008	0.62	0.09	0.48	10210	213	153	9.50	1	
J083910-414722	T33	261.270	-0.189	0.002	0.10	0.04	0.26	9504	230	173	8.65	2	
J083935-444823	T32	263.711	-1.965	0.009	0.50	0.07	0.53	15791	309	105	9.79	1*	
J083942-412453	T33	261.034	0.119	0.003	0.18	0.03	0.25	10684	251	108	9.00	2	
J083944-422055	T33	261.778	-0.446	0.003	0.29	0.04	0.25	24072	206	196	9.92	1	
J083948-423436	T33	261.967	-0.574	0.003	0.26	0.04	0.25	17695	147	68	9.61	1	
J083951-420632	T33	261.602	-0.282	0.002	0.16	0.03	0.25	10540	112	79	8.93	2	
J083952-423922	T33	262.037	-0.614	0.003	0.20	0.03	0.26	10558	136	121	9.03	1	
J083958-410700	T33	260.829	0.341	0.004	0.26	0.05	0.24	7548	161	110	8.85	1	
J084001-405123	T33	260.629	0.508	0.003	0.20	0.03	0.24	17669	211	146	9.49	1	i
J084020-425103	T33	262.244	-0.665	0.004	0.16	0.03	0.26	10577	180	119	8.93	1	
J084025-421634	T33	261.798	-0.302	0.017	1.61	0.30	0.28	2714	145	98	8.76	1	
J084037-412924	T33	261.199	0.209	0.008	1.08	0.11	0.26	17801	342	326	10.23	1	
J084050-414324	T33	261.408	0.097	0.001	0.13	0.02	0.24	24694	287	252	9.60	1	
J084050-445537	T32	263.941	-1.864	0.007	0.59	0.08	0.53	7934	254	169	9.26	1*	
J084054-440439	T33	263.277	-1.334	0.008	0.56	0.10	0.31	3591	108	84	8.55	1	
J084057-420725	T33	261.738	-0.130	0.003	0.17	0.03	0.26	8215	168	104	8.74	1	
J084058-410610	T33	260.933	0.498	0.002	0.19	0.04	0.25	8233	139	110	8.80	1	
J084102-411337	T33	261.040	0.433	0.011	0.56	0.10	0.27	2785	141	59	8.32	1	
J084110-413150	T33	261.293	0.265	0.006	0.55	0.10	0.26	5003	207	152	8.82	1	
J084115-434114	T33	263.006	-1.046	0.008	1.22	0.17	0.31	8001	236	157	9.58	1	w.comps (one is J084129-433917)
J084121-422045	T33	261.959	-0.208	0.003	0.12	0.01	0.25	10601	169	123	9.51	2	
J084129-433917	T33	263.007	-0.992	0.013	1.81	0.26	0.31	8083	303	145	9.76	1	i, w.comp (J084115-434114), M, W
J084130-434638	T33	263.106	-1.064	0.004	0.35	0.07	0.29	5481	350	315	8.71	2	

* Detected by the overlapping region of the next mosaic as well.

Table B.1 continued

Name J2000 (1)	Mosaic TXX (2)	l deg (3)	b deg (4)	$S_{\rm peak}$ Jy (5)	$S_{\rm int}$ Jy km s^{-1} (6)	err$_{(S_{\rm int})}$ Jy km s^{-1} (7)	RMS mJy beam^{-1} (8)	$V_{\rm hel}$ km s^{-1} (9)	w_{20} km s^{-1} (10)	w_{50} km s^{-1} (11)	$M_{\rm HI}$ log($M_{\rm HI}$/M$_\odot$) (12)	Flag 1/2 (13)	Note (14)
J084134-412229	T33	261.218	0.421	0.008	0.99	0.10	0.27	17740	466	194	10.19	1	w.comp
J084137-405157	T33	260.822	0.741	0.005	0.54	0.08	0.30	11637	182	160	9.56	1	
J084137-440359	T33	263.348	-1.225	0.003	0.14	0.02	0.28	24284	207	207	9.61	2	
J084143-423941	T33	262.249	-0.348	0.009	0.82	0.12	0.28	13746	207	120	9.88	2	
J084144-420904	T33	261.849	-0.031	0.008	0.29	0.04	0.26	11375	116	73	9.26	2	
J084158-422930	T33	262.144	-0.207	0.009	1.59	0.16	0.28	11363	445	360	10.00	1	BL, i, w.comp (J084218-422946), M, W
J084159-440321	T33	263.378	-1.168	0.006	0.35	0.07	0.29	3747	316	67	8.38	2	
J084159-430044	T33	262.556	-0.526	0.004	0.31	0.04	0.28	10873	228	189	9.25	1	
J084205-434825	T33	263.195	-0.999	0.006	0.35	0.05	0.28	9402	169	106	9.18	1	
J084213-441221	T32	263.523	-1.227	0.034	5.01	0.71	0.30	3753	211	170	9.53	1*	J0842-44, W, Z
J084218-422946	T33	262.186	-0.161	0.007	2.28	0.22	0.27	11398	461	425	10.16	1	w.comp (J084158-422930), M, W
J084219-425250	T33	262.489	-0.397	0.003	0.29	0.05	0.27	5228	161	102	8.58	1	
J084227-433808	T33	263.100	-0.842	0.003	0.13	0.02	0.27	11316	86	71	8.90	2	
J084233-445800	T32	264.159	-1.649	0.011	0.65	0.09	0.40	7781	122	92	9.28	1	
J084246-412920	T33	261.445	0.526	0.007	1.21	0.17	0.27	11527	316	280	9.90	1	
J084252-450235	T32	264.254	-1.651	0.006	0.42	0.06	0.39	7728	130	96	9.09	1	
J084254-441017	T32	263.572	-1.108	0.014	1.43	0.20	0.30	4478	126	111	9.14	1*	
J084300-421251	T33	262.044	0.115	0.003	0.23	0.03	0.24	11489	269	221	9.18	1	
J084311-445941	T32	264.251	-1.578	0.008	0.72	0.10	0.36	9301	168	138	9.49	1	
J084312-422427	T33	262.218	0.024	0.004	0.22	0.03	0.25	13772	222	187	9.30	1	
J084317-421906	T33	262.158	0.091	0.007	0.77	0.08	0.25	16772	219	186	10.03	1	
J084319-432446	T33	263.021	-0.582	0.003	0.19	0.04	0.27	8268	160	94	8.80	2	
J084320-451123	T32	264.420	-1.677	0.015	2.14	0.30	0.39	7737	325	308	9.80	1	
J084358-433829	T33	263.273	-0.631	0.006	0.48	0.09	0.29	5573	329	68	8.86	1	M, W
J084400-421558	T33	262.199	0.228	0.020	1.21	0.23	0.27	2693	84	69	8.63	1	
J084416-433712	T33	263.290	-0.575	0.003	0.15	0.02	0.28	16396	141	125	9.30	1	
J084424-424448	T33	262.622	-0.012	0.004	0.24	0.04	0.28	8253	239	116	8.90	1	
J084429-433211	T33	263.249	-0.492	0.007	0.77	0.11	0.30	8155	229	171	9.40	1	
J084443-454133	T32	264.966	-1.798	0.010	0.67	0.09	0.48	8144	101	73	9.33	1	
J084444-454709	T32	265.040	-1.854	0.014	1.53	0.15	0.55	14074	364	330	10.18	1	M, W
J084457-423159	T33	262.516	0.199	0.004	0.35	0.05	0.25	22478	301	197	9.94	2	
J084458-444013	T32	264.191	-1.129	0.004	0.18	0.03	0.26	14758	172	106	9.29	1	

* Detected by the overlapping region of the next mosaic as well.

Table B.1 continued

Name J2000 (1)	Mosaic TXX (2)	l deg (3)	b deg (4)	$S_{\rm peak}$ Jy (5)	$S_{\rm int}$ Jy km s^{-1} (6)	err$_{(S_{\rm int})}$ Jy km s^{-1} (7)	RMS mJy beam^{-1} (8)	$V_{\rm hel}$ km s^{-1} (9)	w_{20} km s^{-1} (10)	w_{50} km s^{-1} (11)	$M_{\rm HI}$ log($M_{\rm HI}$/M$_\odot$) (12)	Flag 1/2 (13)	Note (14)
J084458-450543	T32	264.525	-1.392	0.008	0.56	0.08	0.30	11309	126	89	9.54	1	
J084507-430208	T33	262.928	-0.091	0.014	3.69	0.36	0.30	8132	528	472	10.08	1	M, W
J084512-440508	T32	263.760	-0.732	0.005	0.51	0.10	0.29	3356	204	170	8.45	1*	
J084513-424336	T33	262.699	0.118	0.014	1.61	0.30	0.28	2755	130	107	8.77	1	
J084517-443806	T32	264.199	-1.062	0.039	6.11	0.87	0.29	2731	206	176	9.34	1	J0845-44, W, Z
J084518-440603	T32	263.783	-0.727	0.003	0.19	0.04	0.28	5564	203	104	8.46	2	
J084520-431229	T33	263.089	-0.165	0.007	0.57	0.06	0.28	22252	267	110	10.15	1	
J084522-421848	T33	262.392	0.395	0.046	12.14	1.72	0.26	1733	369	317	9.25	1	J0845-42, I, M, W, Z
J084522-430750	T33	263.032	-0.113	0.004	0.22	0.03	0.27	20838	327	168	9.67	1	W
J084530-450210	T32	264.537	-1.282	0.005	0.25	0.04	0.28	22618	96	60	9.81	2	
J084546-450241	T32	264.573	-1.251	0.005	0.33	0.05	0.29	9535	187	123	9.17	2	
J084549-424337	T33	262.767	0.202	0.006	0.67	0.13	0.27	5107	220	206	8.93	1	M, W
J084600-421004	T33	262.352	0.579	0.003	0.18	0.03	0.30	11234	227	198	9.06	1	
J084618-460230	T32	265.412	-1.799	0.008	0.42	0.08	0.44	6260	170	138	8.91	1	
J084624-435746	T32	263.799	-0.487	0.004	0.38	0.05	0.27	11243	337	198	9.38	2*	
J084700-452834	T32	265.046	-1.351	0.002	0.26	0.04	0.29	14208	213	169	9.40	2	
J084708-444731	T32	264.527	-0.903	0.012	0.92	0.17	0.28	4117	173	141	8.88	1	
J084713-424301	T33	262.920	0.409	0.007	0.60	0.08	0.29	10402	173	138	9.50	1	
J084717-422558	T33	262.706	0.597	0.003	0.16	0.03	0.28	11248	135	71	8.99	2	
J084719-430510	T33	263.219	0.191	0.007	0.70	0.10	0.29	16431	353	302	9.97	1	
J084731-432134	T32	263.455	0.049	0.024	2.51	0.25	0.29	22535	168	119	10.80	1*	i, w.comp
J084738-420048	T33	262.422	0.912	0.017	2.14	0.30	0.54	4889	174	124	9.40	1	
J084746-423651	T33	262.903	0.552	0.004	0.36	0.05	0.29	9192	122	90	9.17	1	
J084753-451709	T32	264.995	-1.111	0.005	0.24	0.03	0.28	9515	84	70	9.02	1	
J084753-440535	T32	264.067	-0.360	0.003	0.19	0.03	0.26	14907	229	192	9.33	2	
J084755-441119	T32	264.145	-0.416	0.010	2.36	0.23	0.32	10195	645	553	10.08	1	M, W
J084758-441230	T32	264.167	-0.421	0.002	0.24	0.05	0.30	8369	196	169	8.92	2	
J084811-423659	T33	262.954	0.611	0.004	0.40	0.06	0.31	21213	304	304	9.96	1	
J084813-462001	T32	265.847	-1.724	0.005	0.31	0.04	0.38	8300	249	155	9.02	1	
J084813-421337	T33	262.656	0.862	0.009	0.71	0.10	0.40	8152	175	156	9.36	1	
J084823-464139	T32	266.145	-1.928	0.009	0.44	0.06	0.69	7612	173	139	9.09	1	
J084831-460825	T32	265.728	-1.563	0.008	0.53	0.08	0.30	6302	217	108	9.01	2	

* Detected by the overlapping region of the next mosaic as well.

Table B.1 continued

Name J2000 (1)	Mosaic TXX (2)	l deg (3)	b deg (4)	$S_{\rm peak}$ Jy (5)	$S_{\rm int}$ Jy km s^{-1} (6)	err$_{(S_{\rm int})}$ Jy km s^{-1} (7)	RMS mJy beam^{-1} (8)	$V_{\rm hel}$ km s^{-1} (9)	w_{20} km s^{-1} (10)	w_{50} km s^{-1} (11)	$M_{\rm HI}$ log($M_{\rm HI}$/M$_\odot$) (12)	Flag 1/2 (13)	Note (14)
J084833-440720	T32	264.166	-0.285	0.004	0.36	0.05	0.27	15086	185	171	9.60	1	
J084834-441019	T32	264.205	-0.316	0.006	0.73	0.10	0.31	8355	255	190	9.39	1	i
J084840-425345	T33	263.227	0.504	0.014	1.75	0.25	0.33	4841	238	179	9.30	1	
J084842-461332	T32	265.814	-1.592	0.007	0.61	0.09	0.32	16633	246	224	9.92	1	
J084847-424221	T33	263.093	0.640	0.005	0.23	0.07	0.37	2690	133	59	7.90	1	
J084850-433142	T32	263.736	0.128	0.005	0.28	0.04	0.27	15948	161	115	9.54	1*	
J084857-453839	T32	265.390	-1.192	0.003	0.25	0.04	0.26	23259	332	264	9.83	2	
J084902-452938	T32	265.284	-1.085	0.016	2.34	0.33	0.29	5952	271	256	9.61	1	w.comp (J084909-453234), M
J084909-453234	T32	265.334	-1.100	0.004	0.20	0.04	0.27	5878	117	87	8.53	1	w.comp (J084902-452938)
J084911-432810	T32	263.732	0.216	0.005	0.57	0.08	0.27	14047	383	355	9.75	1*	BL
J084913-451301	T32	265.089	-0.885	0.004	0.38	0.05	0.27	9571	181	96	9.24	2	
J084915-441112	T32	264.294	-0.230	0.006	0.23	0.03	0.27	23914	109	85	9.83	2	
J084917-453107	T32	265.330	-1.067	0.003	0.06	0.01	0.26	17484	124	77	8.98	2	
J084921-460424	T32	265.768	-1.407	0.003	0.34	0.05	0.27	14412	224	179	9.54	1	
J084927-463119	T32	266.127	-1.677	0.005	0.61	0.09	0.39	16616	391	217	9.92	1	
J084930-461726	T32	265.952	-1.526	0.007	0.48	0.09	0.31	4291	149	87	8.63	1	
J084939-440217	T32	264.225	-0.079	0.003	0.12	0.02	0.25	23730	143	53	9.51	2	
J084957-440836	T32	264.340	-0.105	0.012	1.79	0.25	0.30	10138	236	227	9.96	1	
J085007-424438	T33	263.277	0.805	0.007	0.42	0.06	0.49	10475	133	98	9.35	2	
J085013-461004	T32	265.935	-1.353	0.009	1.00	0.14	0.28	4976	91	91	9.08	1	
J085013-462501	T32	266.130	-1.509	0.005	0.52	0.07	0.33	7200	170	124	9.12	1	
J085017-463558	T32	266.277	-1.617	0.015	0.79	0.11	0.36	8364	107	61	9.43	1	
J085017-430800	T33	263.597	0.582	0.003	0.31	0.04	0.30	22055	306	218	9.88	1*	
J085025-453538	T32	265.515	-0.960	0.003	0.15	0.03	0.27	5937	92	92	8.40	2	
J085111-452112	T32	265.413	-0.705	0.004	0.69	0.10	0.28	7937	176	161	9.33	2	BL
J085113-442532	T32	264.702	-0.109	0.057	8.11	1.15	0.30	3701	210	151	9.73	1	J0851-44, i, w.comp, W, Z
J085126-453420	T32	265.610	-0.810	0.007	0.55	0.08	0.26	14042	176	126	9.73	1	
J085131-462516	T32	266.274	-1.339	0.004	0.35	0.06	0.29	7654	179	146	9.00	1	W
J085132-450447	T32	265.243	-0.481	0.004	0.29	0.04	0.27	9749	116	85	9.12	2	
J085133-425550	T32	263.589	0.891	0.007	1.57	0.15	0.45	15978	467	434	10.30	1*	M, W
J085149-442844	T32	264.811	-0.061	0.004	0.12	0.02	0.26	11990	118	79	8.94	2	
J085152-435013	T32	264.323	0.356	0.011	0.68	0.07	0.28	17742	133	101	10.02	1	

* Detected by the overlapping region of the next mosaic as well.

Table B.1 continued

Name J2000 (1)	Mosaic TXX (2)	l deg (3)	b deg (4)	$S_{\rm peak}$ Jy (5)	$S_{\rm int}$ Jy km s^{-1} (6)	err$_{(S_{\rm int})}$ Jy km s^{-1} (7)	RMS mJy beam^{-1} (8)	$V_{\rm hel}$ km s^{-1} (9)	w_{20} km s^{-1} (10)	w_{50} km s^{-1} (11)	$M_{\rm HI}$ log($M_{\rm HI}$/M$_\odot$) (12)	Flag 1/2 (13)	Note (14)
J085203-454143	T32	265.774	-0.805	0.004	0.29	0.04	0.26	15588	218	163	9.55	2	
J085206-464105	T31	266.542	-1.430	0.009	0.51	0.07	0.30	7732	91	65	9.17	1*	
J085219-461341	T32	266.214	-1.110	0.003	0.09	0.02	0.25	8607	93	81	8.54	2	
J085250-455458	T32	266.031	-0.842	0.005	0.35	0.05	0.26	23094	192	113	9.97	1	
J085256-470941	T31	267.000	-1.625	0.003	0.46	0.06	0.48	11550	175	143	9.48	1	
J085300-440408	T32	264.632	0.365	0.006	0.27	0.05	0.27	4994	207	141	8.51	1	
J085303-451624	T32	265.561	-0.401	0.006	0.37	0.05	0.25	14287	108	58	9.57	2	
J085307-433430	T32	264.265	0.696	0.006	0.27	0.04	0.37	22591	153	131	9.84	1	
J085309-454426	T32	265.933	-0.685	0.006	1.09	0.16	0.26	11530	565	523	9.85	1	M, W
J085311-462719	T31	266.484	-1.140	0.005	0.58	0.08	0.27	17633	298	283	9.95	1*	BL
J085315-444917	T32	265.237	-0.084	0.004	0.28	0.04	0.24	15399	195	195	9.52	1	
J085323-441225	T32	264.782	0.329	0.008	0.76	0.14	0.27	3732	131	108	8.71	1	
J085334-440625	T32	264.726	0.418	0.006	0.36	0.05	0.26	15114	224	185	9.61	1	
J085342-454028	T32	265.943	-0.570	0.029	2.11	0.30	0.27	5935	111	68	9.56	1	J0853-45
J085342-452233	T32	265.714	-0.378	0.002	0.18	0.02	0.25	14851	195	174	9.28	2	
J085342-434122	T32	264.423	0.706	0.016	1.67	0.24	0.37	5405	133	114	9.37	1	
J085345-462655	T31	266.542	-1.061	0.004	0.14	0.02	0.30	14870	188	156	9.19	2	
J085358-460401	T32	266.274	-0.787	0.007	0.51	0.07	0.26	12198	189	156	9.58	1	w.comp (J085406-460319)
J085406-460319	T32	266.280	-0.761	0.006	0.92	0.13	0.27	12134	359	318	9.82	1	w.comp (J085358-460401), W
J085422-443613	T32	265.198	0.208	0.025	2.02	0.29	0.28	8386	124	88	9.84	1	
J085424-443700	T32	265.213	0.205	0.003	0.25	0.04	0.24	15464	390	334	9.48	1	
J085425-462543	T31	266.600	-0.961	0.003	0.29	0.05	0.31	7368	303	264	8.89	2*	
J085435-450802	T32	265.630	-0.103	0.005	0.32	0.05	0.25	14619	93	58	9.53	2	
J085443-460254	T32	266.343	-0.676	0.003	0.53	0.07	0.26	17690	426	367	9.91	1	
J085444-460725	T31	266.402	-0.723	0.014	2.03	0.20	0.27	11445	245	189	10.12	1*	
J085457-441324	T32	264.976	0.534	0.003	0.15	0.03	0.30	8974	94	94	8.77	2	
J085459-454736	T32	266.178	-0.476	0.009	1.56	0.22	0.28	7810	235	185	9.67	1	
J085459-440524	T32	264.878	0.625	0.008	1.05	0.15	0.32	10184	268	139	9.72	1	w.comp (J085526-440611)
J085511-445242	T32	265.501	0.141	0.012	1.45	0.21	0.27	8306	266	199	9.69	1	
J085520-451121	T32	265.758	-0.037	0.004	0.16	0.02	0.24	15291	138	103	9.26	2	
J085522-445251	T32	265.525	0.165	0.017	1.34	0.19	0.26	11477	194	93	9.94	1	
J085526-440611	T32	264.939	0.677	0.006	0.36	0.05	0.34	10073	135	101	9.25	1	w.comp (J085459-440524)

* Detected by the overlapping region of the next mosaic as well.

Table B.1 continued

Name J2000 (1)	Mosaic TXX (2)	l deg (3)	b deg (4)	$S_{\rm peak}$ Jy (5)	$S_{\rm int}$ Jy km s^{-1} (6)	err$_{(S_{\rm int})}$ Jy km s^{-1} (7)	RMS mJy beam^{-1} (8)	$V_{\rm hel}$ km s^{-1} (9)	w_{20} km s^{-1} (10)	w_{50} km s^{-1} (11)	$M_{\rm HI}$ log($M_{\rm HI}$/M$_\odot$) (12)	Flag 1/2 (13)	Note (14)
J085526-454748	T32	266.232	-0.417	0.005	0.28	0.04	0.25	23759	133	84	9.90	2	
J085533-450322	T32	265.680	0.077	0.007	0.60	0.08	0.25	15030	125	90	9.82	1	
J085549-454527	T32	266.246	-0.341	0.003	0.24	0.03	0.24	22439	237	196	9.79	2	
J085550-442422	T32	265.216	0.535	0.007	0.57	0.08	0.29	16342	324	275	9.88	1	
J085637-455329	T31	266.438	-0.321	0.003	0.21	0.03	0.25	20959	195	174	9.67	2*	
J085645-444218	T32	265.551	0.467	0.003	0.17	0.02	0.25	11386	191	164	9.03	1	
J085648-443706	T32	265.489	0.528	0.007	0.66	0.09	0.28	10093	134	118	9.52	1	
J085652-444850	T32	265.647	0.412	0.005	0.41	0.06	0.24	14814	187	103	9.65	1	
J085657-440927	T32	265.158	0.850	0.006	0.13	0.02	0.49	11323	134	75	8.92	2	
J085700-450923	T32	265.921	0.206	0.004	0.13	0.02	0.25	11363	134	94	8.92	1	
J085708-454520	T32	266.393	-0.165	0.005	0.61	0.09	0.26	15978	247	199	9.89	1	
J085712-461138	T31	266.732	-0.443	0.004	0.62	0.09	0.30	11850	211	70	9.63	1*	i
J085717-455459	T31	266.531	-0.251	0.004	0.10	0.02	0.26	7415	93	84	8.44	2	
J085725-454339	T31	266.403	-0.110	0.004	0.23	0.03	0.26	11780	143	131	9.20	1*	
J085735-445640	T32	265.828	0.422	0.004	0.30	0.04	0.24	15198	177	140	9.54	1	
J085736-443930	T32	265.613	0.611	0.005	0.47	0.07	0.28	18190	247	211	9.89	1	
J085745-450353	T32	265.939	0.367	0.006	0.30	0.04	0.26	14763	154	64	9.51	2	
J085755-442607	T32	265.481	0.799	0.009	1.11	0.16	0.37	10098	344	200	9.75	1	
J085801-463229	T31	267.089	-0.561	0.010	0.77	0.11	0.53	11700	430	96	9.71	1	w.comp (J085803-463915)
J085803-463915	T31	267.177	-0.631	0.007	0.47	0.07	0.49	11468	191	178	9.48	1	w.comp (J085801-463229)
J085810-454817	T31	266.548	-0.060	0.021	6.24	0.89	0.32	2699	328	255	9.34	1*	J0858-45A, i
J085814-443142	T32	265.588	0.781	0.008	1.46	0.21	0.35	11354	586	518	9.96	1	W
J085814-455101	T31	266.590	-0.081	0.017	1.82	0.34	0.32	2828	186	137	8.85	1	One of J0858-45A's companions
J085815-465136	T31	267.356	-0.738	0.007	0.49	0.09	0.49	4876	120	85	8.75	1	
J085828-451630	T32	266.181	0.325	0.099	19.26	2.73	0.31	2690	286	240	9.83	1	J0858-45B, I, H, M, W, Z
J085832-472623	T31	267.825	-1.082	0.011	1.37	0.19	0.67	4881	199	157	9.20	1	
J085833-454015	T32	266.489	0.076	0.004	0.14	0.03	0.28	7705	123	87	8.61	2*	
J085841-445601	T32	265.947	0.577	0.002	0.14	0.02	0.29	15450	218	178	9.22	1	
J085901-444836	T32	265.892	0.702	0.006	0.45	0.04	0.34	22947	324	128	10.07	2	
J085902-461756	T31	267.020	-0.269	0.006	0.83	0.12	0.34	7492	266	244	9.36	1	
J085914-464157	T31	267.344	-0.507	0.006	0.28	0.04	0.43	20019	143	124	9.75	1	
J085918-460511	T31	266.889	-0.096	0.005	0.40	0.04	0.30	24958	260	250	10.09	1*	

* Detected by the overlapping region of the next mosaic as well.

Table B.1 continued

Name J2000 (1)	Mosaic TXX (2)	l deg (3)	b deg (4)	$S_{\rm peak}$ Jy (5)	$S_{\rm int}$ Jy km s^{-1} (6)	err$_{(S_{\rm int})}$ Jy km s^{-1} (7)	RMS mJy beam^{-1} (8)	$V_{\rm hel}$ km s^{-1} (9)	w_{20} km s^{-1} (10)	w_{50} km s^{-1} (11)	$M_{\rm HI}$ log($M_{\rm HI}$/M$_\odot$) (12)	Flag 1/2 (13)	Note (14)
J085936-480854	T31	268.479	-1.410	0.006	0.48	0.07	0.38	19660	292	84	9.97	1	
J090000-462624	T31	267.235	-0.237	0.008	0.65	0.06	0.37	20087	191	164	10.12	1	
J090010-460609	T31	267.000	0.007	0.005	0.23	0.03	0.31	17352	297	297	9.53	2	
J090034-462609	T31	267.296	-0.161	0.003	0.22	0.03	0.39	11728	157	124	9.17	1	
J090117-453901	T31	266.788	0.451	0.011	0.71	0.10	0.35	14288	178	114	9.85	1*	
J090120-461723	T31	267.273	0.034	0.007	0.73	0.10	0.35	14065	275	252	9.85	1	
J090132-464811	T31	267.682	-0.279	0.007	0.29	0.04	0.49	11423	135	91	9.27	1	
J090133-463052	T31	267.468	-0.085	0.004	0.47	0.05	0.35	24276	204	156	10.14	1	
J090139-474512	T31	268.408	-0.891	0.004	0.52	0.07	0.51	14928	325	194	9.76	1	
J090142-453108	T31	266.738	0.593	0.029	2.99	0.42	0.39	7692	139	122	9.94	1*	J0901-45
J090204-462557	T31	267.465	0.036	0.006	0.65	0.09	0.37	16584	431	262	9.94	2	i
J090209-454345	T31	266.947	0.512	0.004	0.21	0.03	0.35	14366	194	194	9.34	1*	
J090209-455723	T31	267.117	0.362	0.006	0.14	0.02	0.34	21227	189	166	9.49	2	
J090225-485443	T31	269.360	-1.558	0.006	0.25	0.11	0.37	19940	335	281	9.69	2	i
J090241-471529	T31	268.153	-0.432	0.003	0.20	0.03	0.46	13368	139	123	9.24	2	
J090259-482628	T31	269.070	-1.181	0.003	0.12	0.02	0.32	12509	192	174	8.97	1	
J090301-490306	T30	269.530	-1.583	0.004	0.24	0.03	0.36	10057	202	107	9.08	2	
J090309-484812	T31	269.359	-1.401	0.003	0.36	0.07	0.34	3753	404	292	8.39	2	
J090312-451400	T31	266.697	0.978	0.046	7.45	1.06	0.71	2699	216	203	9.42	1*	J0903-45, W, Z
J090315-485528	T31	269.461	-1.469	0.007	0.60	0.09	0.34	15500	402	299	9.86	2*	
J090322-481912	T31	269.022	-1.054	0.006	0.41	0.08	0.35	6687	208	167	8.95	1	w.comp (J090327-482346)
J090327-482346	T31	269.089	-1.093	0.009	0.71	0.10	0.32	6762	136	113	9.20	1	w.comp (J090322-481912)
J090340-482052	T31	269.077	-1.034	0.005	0.45	0.06	0.32	12404	213	155	9.54	2	
J090341-461941	T31	267.572	0.314	0.003	0.41	0.04	0.31	24899	266	219	10.11	1	
J090358-473135	T31	268.497	-0.449	0.012	0.98	0.14	0.50	13260	188	151	9.93	1	w.comp
J090407-460259	T31	267.415	0.556	0.008	0.46	0.07	0.37	11432	202	159	9.47	1	
J090411-483953	T30	269.369	-1.182	0.002	0.26	0.04	0.31	12546	186	170	9.30	1*	
J090430-482338	T31	269.204	-0.961	0.003	0.16	0.02	0.35	10073	147	97	8.90	2	
J090432-463202	T31	267.822	0.285	0.004	0.13	0.02	0.33	8233	87	72	8.62	2	
J090433-464436	T31	267.980	0.147	0.004	0.23	0.03	0.34	11592	195	167	9.18	2	
J090448-495749	T30	270.404	-1.974	0.008	0.30	0.04	0.64	19202	150	150	9.74	2	
J090453-474342	T31	268.751	-0.469	0.006	0.78	0.11	0.45	7382	291	259	9.32	2	BL, w.comp?

* Detected by the overlapping region of the next mosaic as well.

Table B.1 continued

Name J2000 (1)	Mosaic TXX (2)	l deg (3)	b deg (4)	$S_{\rm peak}$ Jy (5)	$S_{\rm int}$ Jy km s^{-1} (6)	err$_{(S_{\rm int})}$ Jy km s^{-1} (7)	RMS mJy beam^{-1} (8)	$V_{\rm hel}$ km s^{-1} (9)	w_{20} km s^{-1} (10)	w_{50} km s^{-1} (11)	$M_{\rm HI}$ log($M_{\rm HI}$/M$_\odot$) (12)	Flag 1/2 (13)	Note (14)
J090504-462707	T31	267.824	0.409	0.003	0.25	0.03	0.31	22664	375	321	9.80	2	
J090505-455504	T31	267.429	0.768	0.008	0.45	0.06	0.45	15163	195	195	9.71	1	
J090513-461504	T31	267.692	0.562	0.025	3.66	0.52	0.37	7488	229	197	10.00	1	J0905-46, M, W
J090517-460554	T31	267.585	0.672	0.010	0.74	0.11	0.38	7426	130	116	9.30	1	
J090518-471541	T31	268.452	-0.103	0.013	3.09	0.30	0.44	11720	400	290	10.31	1	w.comp (J090553-472056)
J090520-460530	T31	267.586	0.684	0.010	1.08	0.15	0.39	5136	182	105	9.14	1	w.comp (J090526-460504)
J090522-492610	T30	270.074	-1.553	0.004	0.73	0.07	0.37	17491	353	288	10.04	1	
J090524-475928	T31	269.003	-0.581	0.002	0.16	0.03	0.42	7679	162	134	8.67	2	
J090526-460504	T31	267.592	0.700	0.010	0.71	0.10	0.39	5626	155	83	9.04	1	w.comp (J090520-460530)
J090526-462127	T31	267.795	0.518	0.004	0.36	0.07	0.34	7408	147	96	8.99	1	
J090541-483526	T30	269.481	-0.948	0.003	0.24	0.03	0.27	24008	207	144	9.85	2	
J090545-465324	T31	268.226	0.201	0.004	0.17	0.02	0.32	11673	134	118	9.06	1	
J090546-463737	T31	268.033	0.379	0.003	0.06	0.01	0.34	6306	153	54	8.08	2	
J090551-482819	T30	269.411	-0.848	0.012	3.15	0.45	0.32	6696	365	348	9.84	1*	M
J090553-472056	T31	268.581	-0.091	0.017	1.64	0.16	0.40	11787	187	139	10.05	1	w.comps (one is J090518-471541)
J090554-480541	T31	269.137	-0.588	0.005	0.90	0.13	0.35	13056	291	114	9.87	1	
J090612-491359	T30	270.013	-1.317	0.003	0.33	0.05	0.30	17484	239	210	9.70	1	
J090617-481155	T31	269.257	-0.610	0.008	1.36	0.13	0.33	13057	463	418	10.06	1	i, W
J090625-482605	T30	269.447	-0.752	0.009	1.15	0.11	0.29	16899	353	297	10.21	1*	
J090628-492858	T30	270.228	-1.452	0.006	0.44	0.06	0.33	17886	262	137	9.85	1	
J090633-465354	T31	268.325	0.297	0.012	0.61	0.11	0.35	5164	130	116	8.90	1	
J090633-462039	T31	267.915	0.670	0.007	0.51	0.07	0.43	7453	275	181	9.14	1	
J090649-460729	T31	267.783	0.851	0.008	1.19	0.17	0.51	11722	252	228	9.90	1	W
J090649-462701	T31	268.024	0.633	0.011	1.64	0.23	0.45	7486	324	307	9.65	1	
J090651-464741	T31	268.282	0.404	0.010	1.28	0.18	0.39	11917	388	327	9.95	1	
J090656-491507	T30	270.107	-1.241	0.008	1.31	0.19	0.31	11389	395	337	9.92	1	
J090659-470105	T31	268.463	0.271	0.003	0.30	0.04	0.33	11630	195	172	9.30	2	
J090703-490718	T30	270.025	-1.138	0.006	0.32	0.05	0.29	14747	127	93	9.54	1	
J090707-483649	T30	269.658	-0.787	0.002	0.20	0.03	0.28	12828	190	153	9.21	1*	
J090719-481439	T30	269.406	-0.514	0.028	4.57	0.65	0.31	5232	223	187	9.78	1*	J0907-48, M, W, Z
J090725-484244	T30	269.763	-0.818	0.003	0.18	0.03	0.27	12883	173	118	9.17	2*	
J090749-483657	T30	269.736	-0.705	0.002	0.33	0.05	0.27	17300	295	214	9.69	2*	W

* Detected by the overlapping region of the next mosaic as well.

Table B.1 continued

Name J2000 (1)	Mosaic TXX (2)	l deg (3)	b deg (4)	$S_{\rm peak}$ Jy (5)	$S_{\rm int}$ Jy km s^{-1} (6)	err$_{(S_{\rm int})}$ Jy km s^{-1} (7)	RMS mJy beam^{-1} (8)	$V_{\rm hel}$ km s^{-1} (9)	w_{20} km s^{-1} (10)	w_{50} km s^{-1} (11)	$M_{\rm HI}$ log($M_{\rm HI}$/M$_\odot$) (12)	Flag 1/2 (13)	Note (14)
J090751-490047	T30	270.033	-0.969	0.003	0.46	0.06	0.27	17560	359	290	9.84	1	
J090753-465328	T31	268.473	0.470	0.002	0.16	0.02	0.33	11416	243	206	9.01	2	BL
J090754-482422	T30	269.590	-0.553	0.003	0.36	0.05	0.28	11753	167	85	9.39	1*	
J090756-482311	T30	269.580	-0.535	0.002	0.14	0.03	0.29	13320	238	152	9.08	2*	
J090812-480306	T30	269.364	-0.276	0.003	0.27	0.04	0.27	23590	346	84	9.88	2	
J090813-471517	T31	268.779	0.266	0.021	2.75	0.39	0.34	7426	186	186	9.87	1	
J090815-484027	T30	269.829	-0.690	0.002	0.18	0.03	0.27	13060	229	211	9.17	1*	
J090818-490253	T30	270.109	-0.938	0.005	0.43	0.06	0.27	14638	183	163	9.65	1	
J090831-484919	T30	269.967	-0.758	0.004	0.61	0.09	0.29	13062	331	234	9.71	1	w.comp (J090847-484916)
J090837-462740	T31	268.243	0.855	0.009	0.65	0.09	0.60	14299	209	132	9.82	2	
J090847-484916	T30	269.995	-0.726	0.005	0.63	0.11	0.28	13350	646	594	9.74	1	w.comp (J090831-484919), M, W
J090851-470752	T31	268.761	0.428	0.030	2.08	0.20	0.34	15065	179	87	10.37	1	M, W
J090852-481924	T30	269.639	-0.378	0.004	0.31	0.08	0.27	13999	208	119	9.47	1*	
J090853-474727	T31	269.251	-0.014	0.015	2.69	0.38	0.33	7204	315	289	9.83	1	M, W
J090907-492111	T30	270.424	-1.046	0.005	0.37	0.07	0.29	2751	187	52	8.13	2	
J090923-482937	T30	269.823	-0.430	0.034	8.05	0.79	0.31	6557	336	284	10.23	1*	J0909-48A
J090944-465316	T31	268.685	0.704	0.009	0.79	0.11	0.42	6524	173	157	9.21	1	
J090952-473855	T31	269.258	0.203	0.004	0.30	0.04	0.30	12943	263	134	9.39	2	
J090952-482335	T30	269.803	-0.303	0.003	0.28	0.04	0.27	11912	188	150	9.29	1*	w.comp (J090958-482533)
J090955-481005	T30	269.644	-0.145	0.029	4.26	0.61	0.30	2740	193	150	9.19	1*	J0909-48B
J090955-493550	T30	270.691	-1.117	0.006	0.86	0.12	0.31	6745	226	186	9.28	1	
J090958-482533	T30	269.838	-0.314	0.006	0.68	0.10	0.28	11878	260	208	9.67	1*	w.comp (J090952-482335)
J091001-495746	T30	270.970	-1.354	0.008	0.63	0.09	0.33	7843	239	186	9.27	1	Hole in the middle of MOM1
J091001-495256	T30	270.912	-1.298	0.005	0.51	0.07	0.30	14823	228	169	9.75	1	
J091008-484117	T30	270.049	-0.472	0.005	0.75	0.11	0.28	14840	341	335	9.91	1	
J091008-485410	T30	270.207	-0.617	0.003	0.24	0.03	0.27	11696	148	105	9.21	1	
J091017-504030	T30	271.521	-1.808	0.007	0.51	0.10	0.44	5328	125	92	8.85	1	
J091033-495915	T30	271.046	-1.308	0.005	0.35	0.05	0.30	14823	189	167	9.58	1	
J091037-492044	T30	270.585	-0.862	0.003	0.30	0.04	0.27	13421	181	161	9.43	1	
J091104-474016	T30	269.412	0.335	0.002	0.10	0.02	0.31	7328	127	100	8.40	2	
J091105-492122	T30	270.644	-0.814	0.005	1.54	0.15	0.27	13688	689	645	10.14	1	w.comp
J091117-480529	T30	269.744	0.075	0.005	0.79	0.11	0.29	14202	243	243	9.89	1*	

* Detected by the overlapping region of the next mosaic as well.

Table B.1 continued

Name J2000 (1)	Mosaic TXX (2)	l deg (3)	b deg (4)	$S_{\rm peak}$ Jy (5)	$S_{\rm int}$ Jy km s^{-1} (6)	err$_{(S_{\rm int})}$ Jy km s^{-1} (7)	RMS mJy beam^{-1} (8)	$V_{\rm hel}$ km s^{-1} (9)	w_{20} km s^{-1} (10)	w_{50} km s^{-1} (11)	$M_{\rm HI}$ log($M_{\rm HI}$/M$_\odot$) (12)	Flag 1/2 (13)	Note (14)
J091127-485110	T30	270.318	-0.426	0.004	0.37	0.05	0.27	13991	215	177	9.56	1	
J091138-484641	T30	270.284	-0.352	0.003	0.21	0.03	0.26	14000	163	104	9.32	2	
J091143-484129	T30	270.230	-0.284	0.005	1.04	0.10	0.28	14005	342	264	10.00	1	
J091153-501751	T30	271.418	-1.365	0.004	0.27	0.04	0.31	11286	173	121	9.23	1	
J091155-494040	T30	270.972	-0.935	0.003	0.70	0.10	0.27	14568	373	324	9.86	1	
J091212-494148	T30	271.017	-0.914	0.002	0.20	0.03	0.27	14253	220	169	9.29	2	w.comp (J091155-494040)
J091213-483248	T30	270.182	-0.123	0.004	0.30	0.04	0.27	13998	228	173	9.46	1	
J091218-492335	T30	270.806	-0.696	0.005	0.52	0.07	0.28	6683	163	129	9.05	1	
J091218-482237	T30	270.068	0.003	0.005	0.93	0.09	0.27	15030	430	407	10.02	1	M, W
J091226-494559	T30	271.093	-0.936	0.002	0.16	0.02	0.25	14169	166	134	9.19	2	w.comp (J091234-494502)
J091234-494502	T30	271.096	-0.909	0.006	0.46	0.07	0.27	14380	428	278	9.67	2	w.comps (J091155, J091212 and J091226)
J091234-492735	T30	270.885	-0.709	0.004	0.37	0.07	0.28	6698	207	168	8.91	1	
J091245-500241	T30	271.331	-1.089	0.005	0.40	0.04	0.27	22459	198	161	10.00	1	
J091252-483837	T30	270.325	-0.113	0.003	0.24	0.03	0.26	21824	248	205	9.76	1	
J091304-492224	T30	270.878	-0.591	0.004	0.32	0.05	0.27	13941	201	96	9.49	2	
J091309-503303	T30	271.742	-1.392	0.003	0.17	0.02	0.29	17969	143	123	9.44	1	
J091310-483138	T30	270.276	0.004	0.003	0.20	0.03	0.27	14019	187	171	9.28	2	
J091327-492401	T30	270.940	-0.564	0.005	0.35	0.05	0.26	23811	246	180	9.99	2	
J091330-473234	T30	269.601	0.722	0.006	0.60	0.08	0.36	13725	231	178	9.74	1*	
J091336-503146	T30	271.775	-1.326	0.011	1.71	0.24	0.34	8222	345	295	9.75	1	
J091344-504624	T30	271.966	-1.478	0.004	0.34	0.05	0.33	11958	156	101	9.37	1	
J091354-482529	T30	270.284	0.161	0.009	1.39	0.20	0.29	6359	254	215	9.44	1	J0913-48 (blended HIZOA detection), M, W, Z
J091356-491507	T30	270.887	-0.405	0.004	0.43	0.06	0.26	19739	228	191	9.92	1	
J091403-492707	T30	271.045	-0.530	0.005	0.32	0.06	0.29	7373	189	144	8.93	1	
J091404-485216	T30	270.626	-0.127	0.005	0.30	0.04	0.26	14135	166	96	9.46	1	
J091405-472109	T30	269.531	0.926	0.012	2.29	0.23	0.53	11586	481	322	10.18	1*	M
J091407-475312	T30	269.922	0.561	0.006	0.58	0.08	0.33	16039	286	271	9.87	1	
J091410-494602	T30	271.286	-0.734	0.004	0.16	0.02	0.27	24844	214	182	9.70	2	
J091410-482229	T30	270.280	0.229	0.016	3.13	0.44	0.30	6403	257	226	9.79	1	J0913-48 (blended HIZOA detection)
J091416-491341	T30	270.908	-0.349	0.007	1.43	0.20	0.27	11801	286	218	9.99	1	
J091429-483621	T30	270.483	0.107	0.004	0.51	0.07	0.27	14167	272	219	9.70	1	
J091439-474438	T30	269.880	0.724	0.004	0.19	0.03	0.38	14185	175	136	9.28	1*	

* Detected by the overlapping region of the next mosaic as well.

Table B.1 continued

Name J2000 (1)	Mosaic TXX (2)	l deg (3)	b deg (4)	$S_{\rm peak}$ Jy (5)	$S_{\rm int}$ Jy km s^{-1} (6)	err$_{(S_{\rm int})}$ Jy km s^{-1} (7)	RMS mJy beam^{-1} (8)	$V_{\rm hel}$ km s^{-1} (9)	w_{20} km s^{-1} (10)	w_{50} km s^{-1} (11)	$M_{\rm HI}$ log($M_{\rm HI}$/M$_\odot$) (12)	Flag 1/2 (13)	Note (14)
J091441-492511	T30	271.093	-0.432	0.005	0.44	0.06	0.28	8979	129	114	9.24	1	
J091446-501010	T30	271.643	-0.943	0.004	0.14	0.03	0.27	11263	83	54	8.95	1	
J091455-474530	T30	269.922	0.747	0.008	0.65	0.09	0.42	14993	206	141	9.86	1	
J091458-491219	T30	270.971	-0.250	0.005	0.29	0.04	0.26	11874	125	72	9.30	1	
J091500-491522	T30	271.011	-0.282	0.002	0.33	0.05	0.26	10617	358	310	9.26	1	i
J091506-500015	T30	271.561	-0.789	0.003	0.22	0.04	0.28	7561	346	287	8.79	2	
J091514-483634	T30	270.570	0.193	0.021	2.67	0.26	0.30	9710	196	119	10.09	1	J0915-48
J091520-480644	T30	270.224	0.550	0.003	0.42	0.06	0.35	11505	227	181	9.43	1	
J091525-474154	T30	269.936	0.847	0.035	2.44	0.35	0.57	7280	139	73	9.80	1	J0915-47
J091537-480949	T30	270.294	0.548	0.011	1.47	0.15	0.34	19772	339	319	10.46	1	
J091537-491950	T30	271.134	-0.262	0.007	0.53	0.05	0.26	22452	172	114	10.12	1	
J091543-482610	T30	270.502	0.372	0.006	0.29	0.04	0.28	17000	128	92	9.62	1	
J091547-510222	T29	272.383	-1.428	0.005	0.47	0.07	0.30	10905	133	117	9.43	1*	
J091554-510251	T29	272.401	-1.421	0.004	0.36	0.05	0.29	19731	534	510	9.84	1*	
J091556-490111	T30	270.946	-0.009	0.002	0.08	0.01	0.24	22483	98	80	9.32	2	
J091558-492057	T30	271.188	-0.233	0.005	0.25	0.05	0.27	7323	117	69	8.82	2	
J091605-480639	T30	270.311	0.642	0.003	0.12	0.02	0.35	9670	119	86	8.73	1	
J091609-510253	T29	272.428	-1.394	0.008	1.79	0.18	0.29	10771	412	381	10.01	1*	
J091630-493522	T30	271.420	-0.338	0.005	0.99	0.14	0.27	13952	545	399	9.98	1	i
J091641-484532	T30	270.845	0.262	0.001	0.21	0.03	0.27	14097	216	155	9.31	2	
J091641-494721	T30	271.585	-0.455	0.002	0.15	0.02	0.25	13781	178	153	9.14	1	
J091718-492515	T30	271.391	-0.126	0.027	5.69	0.56	0.29	7537	335	269	10.20	1	J0917-49, i, w.comp, I, M, W, Z
J091728-515713	T29	273.222	-1.877	0.006	0.22	0.03	0.60	10466	230	194	9.08	1	
J091745-480943	T30	270.541	0.805	0.031	5.11	0.73	0.44	3336	250	217	9.44	1	J0917-48
J091747-490507	T30	271.205	0.164	0.002	0.22	0.03	0.26	17340	277	241	9.52	1	w.comp
J091755-502411	T30	272.161	-0.744	0.003	0.40	0.06	0.27	12166	511	473	9.46	1	M, W
J091756-494530	T30	271.704	-0.289	0.003	0.45	0.06	0.27	14026	257	212	9.64	1	
J091801-505621	T29	272.556	-1.106	0.003	0.28	0.04	0.27	10787	227	178	9.21	1*	
J091803-502335	T30	272.169	-0.721	0.005	0.38	0.05	0.26	17917	142	125	9.79	1	
J091820-510310	T29	272.671	-1.152	0.009	1.30	0.18	0.29	8536	187	172	9.66	1*	
J091828-503349	T29	272.338	-0.793	0.005	0.25	0.05	0.28	8266	93	93	8.92	1*	
J091840-501737	T30	272.168	-0.580	0.002	0.17	0.02	0.25	19839	218	154	9.53	1	

* Detected by the overlapping region of the next mosaic as well.

Table B.1 continued

Name J2000 (1)	Mosaic TXX (2)	l deg (3)	b deg (4)	$S_{\rm peak}$ Jy (5)	$S_{\rm int}$ Jy km s^{-1} (6)	err$_{(S_{\rm int})}$ Jy km s^{-1} (7)	RMS mJy beam^{-1} (8)	$V_{\rm hel}$ km s^{-1} (9)	w_{20} km s^{-1} (10)	w_{50} km s^{-1} (11)	$M_{\rm HI}$ log($M_{\rm HI}$/M$_\odot$) (12)	Flag 1/2 (13)	Note (14)
J091858-503324	T29	272.388	-0.732	0.005	0.62	0.06	0.27	19859	236	172	10.09	1*	
J091900-505249	T29	272.622	-0.956	0.003	0.08	0.02	0.26	12317	240	120	8.78	1*	
J091902-484000	T30	271.051	0.604	0.006	0.48	0.07	0.38	7169	210	149	9.08	1	
J091907-494203	T30	271.796	-0.113	0.004	0.24	0.03	0.25	22393	291	242	9.78	1	
J091908-502743	T30	272.339	-0.647	0.004	0.22	0.03	0.25	18437	172	114	9.57	1	
J091917-494513	T30	271.853	-0.131	0.004	0.98	0.14	0.26	14070	370	338	9.98	1	i, M, W
J091924-515723	T29	273.431	-1.668	0.009	1.04	0.15	0.39	10477	211	179	9.75	1	M, W
J091925-500852	T30	272.148	-0.393	0.004	0.26	0.04	0.25	19856	176	113	9.70	1	
J091930-510118	T29	272.778	-0.998	0.003	0.10	0.02	0.28	7269	87	72	8.39	1*	
J091937-513048	T29	273.141	-1.331	0.003	0.17	0.03	0.29	10579	129	109	8.98	1	
J091952-511718	T29	273.008	-1.146	0.004	0.33	0.05	0.29	8686	162	132	9.09	1	
J092001-500209	T30	272.135	-0.247	0.003	0.29	0.04	0.26	12145	225	186	9.32	1	
J092006-511054	T29	272.958	-1.044	0.003	0.34	0.05	0.26	22967	447	394	9.95	2	
J092012-483336	T30	271.110	0.815	0.009	0.63	0.09	0.53	11338	156	106	9.60	1	
J092025-512218	T29	273.128	-1.143	0.004	0.28	0.04	0.28	12498	164	122	9.33	1	
J092055-493541	T30	271.927	0.169	0.027	2.06	0.20	0.26	11002	142	72	10.09	1	J0920-49, i
J092114-504633	T29	272.797	-0.631	0.007	0.53	0.07	0.29	12408	144	144	9.60	1*	w.comp
J092123-504955	T29	272.853	-0.655	0.005	0.52	0.07	0.28	7191	285	70	9.12	2	
J092127-515408	T29	273.616	-1.405	0.005	0.48	0.09	0.31	4015	168	138	8.57	1	
J092129-483248	T30	271.251	0.975	0.012	0.65	0.29	0.77	9393	501	336	9.45	2	
J092137-490410	T30	271.635	0.619	0.013	1.35	0.19	0.33	9263	182	167	9.75	1	
J092137-485233	T30	271.499	0.757	0.014	2.23	0.22	0.38	11220	367	332	10.14	1	
J092137-500628	T29	272.368	-0.115	0.003	0.17	0.02	0.25	11245	135	120	9.02	1*	
J092143-514632	T29	273.556	-1.286	0.003	0.19	0.03	0.28	11291	186	117	9.07	1	
J092146-490555	T30	271.673	0.617	0.005	0.31	0.04	0.30	11273	272	69	9.29	1	
J092154-502919	T29	272.668	-0.354	0.011	1.38	0.14	0.27	12207	209	135	10.00	1*	i
J092206-514715	T29	273.606	-1.254	0.006	0.35	0.07	0.30	6643	97	57	8.88	2	
J092213-503257	T29	272.747	-0.361	0.008	1.03	0.15	0.28	5860	184	172	9.24	1*	
J092227-520157	T29	273.818	-1.388	0.003	0.21	0.04	0.29	20720	318	284	9.65	2	
J092231-490341	T30	271.735	0.730	0.009	0.55	0.08	0.40	9396	164	99	9.37	1	
J092231-495120	T30	272.294	0.166	0.004	0.41	0.06	0.27	7377	226	160	9.03	1*	
J092233-494226	T30	272.192	0.275	0.006	1.23	0.12	0.26	20969	552	290	10.43	1	

* Detected by the overlapping region of the next mosaic as well.

Table B.1 continued

Name J2000 (1)	Mosaic TXX (2)	l deg (3)	b deg (4)	$S_{\rm peak}$ Jy (5)	$S_{\rm int}$ Jy km s^{-1} (6)	err$_{(S_{\rm int})}$ Jy km s^{-1} (7)	RMS mJy beam^{-1} (8)	$V_{\rm hel}$ km s^{-1} (9)	w_{20} km s^{-1} (10)	w_{50} km s^{-1} (11)	$M_{\rm HI}$ log($M_{\rm HI}$/M$_\odot$) (12)	Flag 1/2 (13)	Note (14)
J092236-510400	T29	273.155	-0.686	0.004	0.70	0.10	0.33	12166	324	289	9.71	1	
J092248-500445	T29	272.484	0.039	0.004	0.33	0.05	0.26	14019	240	223	9.51	1*	
J092251-491135	T30	271.865	0.674	0.004	0.35	0.05	0.34	23094	139	99	9.97	1	
J092253-495827	T29	272.419	0.123	0.020	1.42	0.20	0.27	7384	112	61	9.58	1*	
J092257-495856	T29	272.431	0.124	0.003	0.18	0.03	0.25	20607	314	87	9.57	1*	
J092320-500423	T29	272.540	0.103	0.005	0.36	0.05	0.26	13966	145	106	9.54	1*	
J092339-502642	T29	272.837	-0.126	0.004	0.12	0.02	0.24	21855	141	120	9.47	1	
J092340-494740	T29	272.382	0.339	0.006	0.58	0.08	0.27	9236	187	170	9.39	1*	
J092340-491154	T30	271.965	0.765	0.009	0.98	0.14	0.44	11288	251	153	9.79	1	
J092344-514805	T29	273.796	-1.086	0.003	0.17	0.02	0.28	20689	135	105	9.57	1	
J092413-524651	T29	274.535	-1.733	0.004	0.20	0.04	0.37	23912	510	207	9.76	1	
J092428-503201	T29	272.990	-0.100	0.014	2.21	0.31	0.28	6522	220	189	9.66	1	
J092502-503253	T29	273.065	-0.047	0.002	0.17	0.02	0.25	11175	132	73	9.02	2	
J092508-514441	T29	273.911	-0.894	0.005	0.52	0.07	0.32	12637	179	127	9.61	1	
J092513-504721	T29	273.255	-0.198	0.011	1.18	0.17	0.29	10726	190	148	9.82	1	
J092522-503238	T29	273.101	-0.006	0.002	0.13	0.02	0.25	13968	177	136	9.11	1	
J092541-495937	T29	272.755	0.424	0.003	0.09	0.02	0.26	12347	189	132	8.82	2*	
J092551-512031	T29	273.711	-0.526	0.007	0.50	0.07	0.33	19868	191	151	9.99	1	
J092557-514513	T29	274.009	-0.811	0.003	0.09	0.01	0.29	20973	101	89	9.27	1	
J092615-525114	T29	274.806	-1.571	0.006	0.58	0.06	0.36	20872	208	149	10.10	1	
J092615-523237	T29	274.591	-1.348	0.031	6.33	0.62	0.37	7058	382	333	10.19	1	J0926-52, M, W
J092627-505440	T29	273.480	-0.151	0.007	0.47	0.10	0.35	6276	204	113	8.96	1	
J092655-514801	T29	274.148	-0.742	0.003	0.20	0.03	0.28	22440	340	307	9.71	2	
J092658-512442	T29	273.884	-0.456	0.005	0.44	0.06	0.32	15838	192	151	9.73	1	
J092715-495524	T29	272.887	0.650	0.034	6.50	0.92	0.38	4515	219	205	9.81	1	J0927-49
J092717-511426	T29	273.802	-0.298	0.003	0.20	0.06	0.29	19930	276	180	9.59	2	
J092728-522455	T29	274.635	-1.127	0.007	0.88	0.12	0.33	7061	180	143	9.33	1	
J092733-520133	T29	274.375	-0.836	0.002	0.18	0.02	0.28	18454	315	184	9.47	2	
J092807-503741	T29	273.473	0.235	0.019	4.71	0.67	0.29	2910	261	245	9.29	1	J0927-50
J092816-494613	T29	272.899	0.873	0.006	0.28	0.05	0.51	8322	93	93	8.98	1	
J092829-530538	T29	275.215	-1.512	0.003	0.25	0.05	0.33	6913	177	94	8.76	1	
J092903-524320	T29	275.021	-1.183	0.014	1.97	0.28	0.31	4495	207	176	9.29	1	

* Detected by the overlapping region of the next mosaic as well.

Table B.1 continued

Name J2000 (1)	Mosaic TXX (2)	l deg (3)	b deg (4)	$S_{\rm peak}$ Jy (5)	$S_{\rm int}$ Jy km s^{-1} (6)	err$_{(S_{\rm int})}$ Jy km s^{-1} (7)	RMS mJy beam^{-1} (8)	$V_{\rm hel}$ km s^{-1} (9)	w_{20} km s^{-1} (10)	w_{50} km s^{-1} (11)	$M_{\rm HI}$ log($M_{\rm HI}$/M$_\odot$) (12)	Flag 1/2 (13)	Note (14)
J092909-523748	T29	274.969	-1.106	0.002	0.29	0.04	0.27	12504	294	269	9.35	2	i
J092911-523359	T29	274.929	-1.056	0.003	0.39	0.06	0.27	20595	243	144	9.91	2	
J092921-531251	T28	275.392	-1.509	0.010	0.95	0.18	0.31	3987	212	167	8.86	1*	
J092930-524018	T29	275.036	-1.100	0.003	0.34	0.05	0.27	12383	198	138	9.41	1	
J092937-512341	T29	274.172	-0.159	0.002	0.23	0.03	0.27	16034	184	91	9.46	2	
J092942-512211	T29	274.165	-0.131	0.011	0.54	0.10	0.26	6128	84	52	9.00	1	
J092944-515926	T29	274.594	-0.580	0.007	0.32	0.06	0.31	2951	107	65	8.13	1	
J092948-524044	T29	275.074	-1.073	0.004	0.25	0.03	0.26	14375	264	187	9.39	2	
J092949-503730	T29	273.668	0.424	0.003	0.17	0.03	0.28	7484	118	82	8.67	1	
J092954-513113	T29	274.290	-0.220	0.002	0.11	0.02	0.25	21027	219	135	9.38	2	
J093002-531530	T28	275.497	-1.472	0.003	0.13	0.02	0.26	17477	148	61	9.31	2*	
J093008-503351	T29	273.663	0.502	0.003	0.09	0.01	0.26	19549	94	77	9.23	1	
J093009-510014	T29	273.966	0.184	0.003	0.36	0.05	0.26	17137	345	238	9.72	2	
J093035-531813	T28	275.589	-1.447	0.002	0.18	0.03	0.24	17302	220	129	9.42	1*	
J093039-531910	T28	275.606	-1.452	0.003	0.51	0.05	0.26	21334	311	233	10.07	1	
J093039-530847	T28	275.488	-1.326	0.004	0.18	0.03	0.25	17489	104	76	9.43	1*	
J093041-521723	T29	274.906	-0.698	0.003	0.22	0.04	0.27	4148	328	249	8.26	2	
J093054-530808	T28	275.507	-1.293	0.002	0.27	0.04	0.25	21191	605	219	9.77	2*	
J093105-533944	T28	275.888	-1.658	0.003	0.18	0.03	0.37	21846	102	102	9.62	1	
J093113-515814	T29	274.748	-0.408	0.006	0.52	0.10	0.30	5319	137	102	8.85	1	
J093129-523512	T29	275.198	-0.831	0.002	0.29	0.05	0.26	7023	185	152	8.84	2	
J093132-525730	T28	275.456	-1.099	0.002	0.18	0.03	0.29	17106	241	47	9.42	2*	
J093140-504601	T29	273.978	0.519	0.008	0.31	0.06	0.33	4480	80	50	8.49	1	
J093140-511548	T29	274.317	0.157	0.004	0.23	0.03	0.25	17203	227	90	9.52	1	
J093146-511747	T29	274.350	0.143	0.006	0.91	0.09	0.26	17151	377	245	10.12	1	
J093147-514939	T29	274.713	-0.245	0.008	2.84	0.28	0.30	12038	642	603	10.31	1	M, W
J093156-510619	T29	274.240	0.301	0.003	0.18	0.03	0.25	17276	231	99	9.43	1	
J093203-512355	T29	274.452	0.098	0.003	0.18	0.03	0.24	18868	268	144	9.49	2	i
J093213-513627	T29	274.614	-0.037	0.004	0.32	0.05	0.26	17077	281	200	9.66	1	
J093214-510300	T29	274.237	0.373	0.037	6.83	0.97	0.29	4532	277	203	9.83	1	J0932-51, i, I, M, Z
J093216-515945	T29	274.884	-0.316	0.008	0.69	0.13	0.28	5326	122	89	8.98	1	
J093231-523634	T28	275.328	-0.741	0.007	0.91	0.09	0.24	17598	344	327	10.14	1*	

* Detected by the overlapping region of the next mosaic as well.

Table B.1 continued

Name J2000 (1)	Mosaic TXX (2)	l deg (3)	b deg (4)	$S_{\rm peak}$ Jy (5)	$S_{\rm int}$ Jy km s^{-1} (6)	err$_{(S_{\rm int})}$ Jy km s^{-1} (7)	RMS mJy beam^{-1} (8)	$V_{\rm hel}$ km s^{-1} (9)	w_{20} km s^{-1} (10)	w_{50} km s^{-1} (11)	$M_{\rm HI}$ log($M_{\rm HI}$/M$_\odot$) (12)	Flag 1/2 (13)	Note (14)
J093240-510358	T29	274.298	0.408	0.004	0.19	0.03	0.25	21557	152	92	9.65	1	
J093245-505416	T29	274.197	0.535	0.002	0.40	0.06	0.28	21754	458	437	9.98	1	
J093256-524235	T28	275.442	-0.772	0.004	0.11	0.02	0.28	23305	140	68	9.49	2	
J093258-522817	T28	275.285	-0.593	0.002	0.23	0.03	0.29	15726	313	183	9.46	2*	
J093259-510439	T29	274.341	0.432	0.002	0.12	0.02	0.25	21353	152	133	9.45	1	
J093305-524517	T28	275.490	-0.789	0.002	0.22	0.04	0.27	6877	162	116	8.70	2	
J093320-504400	T29	274.149	0.723	0.005	0.31	0.04	0.36	21445	356	274	9.85	1	
J093327-525749	T28	275.672	-0.906	0.002	0.13	0.02	0.27	13159	137	118	9.04	2*	
J093353-510516	T29	274.452	0.521	0.009	0.47	0.11	0.27	4421	86	52	8.65	1	
J093353-525541	T28	275.696	-0.836	0.003	0.12	0.02	0.25	12768	311	259	9.00	2	
J093400-540801	T28	276.523	-1.713	0.005	0.33	0.05	0.34	17295	283	149	9.69	2	
J093401-534017	T28	276.213	-1.370	0.002	0.11	0.02	0.27	13899	136	121	9.03	1	
J093414-510521	T29	274.493	0.556	0.003	0.29	0.04	0.27	19471	274	187	9.74	1	w.comp
J093419-505455	T29	274.386	0.694	0.004	0.33	0.06	0.32	7176	296	233	8.92	2	w.comp?
J093426-525227	T28	275.721	-0.740	0.003	0.38	0.05	0.29	17139	302	242	9.75	1*	
J093430-515708	T29	275.107	-0.052	0.002	0.12	0.02	0.24	17832	195	178	9.28	1	
J093438-523942	T28	275.599	-0.563	0.003	0.20	0.03	0.28	13094	180	160	9.22	1*	w.comp (J093441-523744)
J093441-523744	T28	275.584	-0.533	0.005	0.84	0.12	0.27	13138	316	271	9.85	1*	w.comp (J093438-523942)
J093443-504536	T29	274.329	0.852	0.005	0.49	0.07	0.45	6703	258	218	9.03	2	
J093451-510739	T29	274.592	0.594	0.004	0.18	0.03	0.28	12727	135	105	9.17	1	
J093509-520622	T29	275.284	-0.099	0.003	0.25	0.04	0.25	17815	406	149	9.59	1	
J093512-521335	T28	275.371	-0.182	0.008	0.39	0.05	0.28	8213	84	52	9.10	2	
J093513-522238	T28	275.474	-0.292	0.002	0.08	0.01	0.27	20219	174	57	9.21	2	
J093517-532425	T28	276.174	-1.054	0.005	0.25	0.04	0.26	13878	178	78	9.37	1	w.comp
J093522-531928	T28	276.127	-0.980	0.002	0.17	0.02	0.27	17191	245	227	9.41	1	
J093554-515009	T29	275.189	0.180	0.002	0.13	0.02	0.25	17645	198	142	9.30	2	
J093621-521128	T28	275.478	-0.038	0.006	0.46	0.09	0.28	5742	122	76	8.87	1*	
J093624-514546	T29	275.196	0.285	0.003	0.25	0.04	0.26	22442	204	181	9.79	1	
J093624-531326	T28	276.174	-0.801	0.004	0.31	0.04	0.24	21782	408	317	9.87	2	
J093626-520845	T28	275.456	0.003	0.002	0.24	0.04	0.27	8616	175	156	8.93	2*	
J093638-541538	T28	276.894	-1.548	0.007	0.40	0.06	0.33	7961	162	115	9.09	1	
J093638-543723	T28	277.137	-1.817	0.093	10.64	1.51	0.58	2733	169	112	9.58	1	J0936-54

* Detected by the overlapping region of the next mosaic as well.

Table B.1 continued

Name J2000 (1)	Mosaic TXX (2)	l deg (3)	b deg (4)	$S_{\rm peak}$ Jy (5)	$S_{\rm int}$ Jy km s^{-1} (6)	err$_{(S_{\rm int})}$ Jy km s^{-1} (7)	RMS mJy beam^{-1} (8)	$V_{\rm hel}$ km s^{-1} (9)	w_{20} km s^{-1} (10)	w_{50} km s^{-1} (11)	$M_{\rm HI}$ log($M_{\rm HI}$/M$_\odot$) (12)	Flag 1/2 (13)	Note (14)
J093640-522905	T28	275.710	-0.224	0.003	0.22	0.03	0.24	21281	203	178	9.69	1	i?
J093642-533923	T28	276.498	-1.091	0.008	0.52	0.07	0.29	8885	123	93	9.30	1	
J093643-520914	T28	275.494	0.027	0.003	0.22	0.03	0.26	11691	143	143	9.17	1*	
J093652-520737	T28	275.495	0.063	0.014	1.44	0.20	0.28	6344	159	111	9.45	1*	
J093653-543036	T28	277.087	-1.709	0.003	0.21	0.03	0.37	19394	147	93	9.59	1	
J093745-523439	T28	275.894	-0.184	0.006	0.79	0.11	0.27	13280	428	277	9.83	1	
J093750-540431	T28	276.901	-1.293	0.005	0.18	0.03	0.30	19293	210	76	9.52	1	
J093800-542441	T28	277.144	-1.527	0.004	0.73	0.07	0.30	22072	454	433	10.25	1	
J093814-520318	T28	275.603	0.256	0.003	0.31	0.04	0.29	19998	151	151	9.79	1*	
J093830-532009	T28	276.483	-0.675	0.003	0.10	0.02	0.26	8867	94	76	8.58	2	
J093835-540554	T28	276.999	-1.237	0.004	0.18	0.03	0.28	12340	177	145	9.14	2	
J093838-513506	T28	275.337	0.649	0.007	0.74	0.11	0.31	11703	191	164	9.70	1*	
J093843-522553	T28	275.908	0.024	0.009	0.77	0.11	0.26	5764	168	76	9.09	1	
J093906-512449	T29	275.278	0.825	0.004	0.27	0.03	0.42	11511	353	212	9.24	1*	
J093907-535208	T28	276.906	-1.013	0.009	1.02	0.14	0.28	7830	185	134	9.48	1	
J093912-533731	T28	276.753	-0.822	0.016	2.95	0.42	0.28	2875	236	192	9.07	1	J0938-53, W, Z
J093924-515551	T28	275.655	0.468	0.002	0.18	0.02	0.27	11794	226	186	9.08	2*	
J094035-522115	T28	276.071	0.270	0.005	0.73	0.10	0.26	13331	276	189	9.81	1	
J094047-534324	T28	276.994	-0.741	0.003	0.26	0.04	0.25	16795	204	152	9.56	1	
J094052-541056	T28	277.305	-1.079	0.002	0.18	0.03	0.26	16271	207	182	9.38	2	
J094053-515144	T28	275.780	0.670	0.005	0.26	0.04	0.34	17846	125	96	9.62	1*	
J094056-541601	T28	277.369	-1.136	0.004	0.09	0.02	0.28	9499	102	77	8.58	1	
J094104-522012	T28	276.115	0.332	0.005	0.53	0.08	0.27	19379	384	351	10.00	1	
J094113-521440	T28	276.071	0.416	0.013	1.04	0.15	0.30	6331	130	77	9.31	1	
J094115-525806	T28	276.550	-0.126	0.003	0.19	0.03	0.25	17014	285	108	9.44	1	
J094131-535218	T28	277.173	-0.782	0.003	0.33	0.05	0.30	19281	383	56	9.79	2	
J094137-540349	T28	277.311	-0.917	0.004	0.53	0.05	0.26	19461	256	205	10.00	1	
J094142-520341	T28	276.008	0.604	0.007	0.73	0.14	0.36	5297	164	132	9.00	1	w.comp (J094157-520308)
J094148-523056	T28	276.316	0.269	0.004	0.76	0.07	0.26	17534	235	201	10.06	1	
J094148-540703	T28	277.366	-0.940	0.003	0.30	0.04	0.27	19442	341	304	9.75	1	
J094157-520308	T28	276.029	0.635	0.003	0.18	0.03	0.35	5354	107	74	8.39	1	
J094200-531607	T28	276.832	-0.280	0.004	0.31	0.06	0.27	6760	139	128	8.84	1	

* Detected by the overlapping region of the next mosaic as well.

Table B.1 continued

Name J2000 (1)	Mosaic TXX (2)	l deg (3)	b deg (4)	$S_{\rm peak}$ Jy (5)	$S_{\rm int}$ Jy km s^{-1} (6)	err$_{(S_{\rm int})}$ Jy km s^{-1} (7)	RMS mJy beam^{-1} (8)	$V_{\rm hel}$ km s^{-1} (9)	w_{20} km s^{-1} (10)	w_{50} km s^{-1} (11)	$M_{\rm HI}$ log($M_{\rm HI}$/M$_\odot$) (12)	Flag 1/2 (13)	Note (14)
J094210-524930	T28	276.561	0.073	0.002	0.23	0.03	0.22	22091	314	266	9.74	2	
J094212-542646	T28	277.626	-1.150	0.003	0.36	0.05	0.23	14334	279	229	9.56	2	
J094215-532618	T28	276.971	-0.384	0.007	0.49	0.07	0.25	19434	333	79	9.97	1	
J094225-522520	T28	276.327	0.402	0.009	1.34	0.19	0.28	6849	211	182	9.49	1	
J094235-524304	T28	276.538	0.194	0.010	0.58	0.11	0.26	4508	117	82	8.76	1	
J094239-532824	T28	277.040	-0.370	0.002	0.18	0.03	0.24	21863	351	205	9.64	2	
J094308-522041	T28	276.359	0.533	0.002	0.12	0.04	0.28	24679	544	501	9.58	2	
J094310-530512	T28	276.845	-0.028	0.004	0.46	0.06	0.26	19777	274	192	9.95	1	
J094311-552945	T27	278.418	-1.853	0.007	1.52	0.22	0.41	11343	476	391	9.98	1*	
J094317-530347	T28	276.843	0.002	0.003	0.56	0.08	0.27	13852	499	447	9.72	1	M
J094319-534009	T28	277.243	-0.454	0.002	0.19	0.03	0.26	21841	264	88	9.66	2	
J094339-523637	T28	276.591	0.382	0.002	0.25	0.04	0.26	19740	265	142	9.69	2	
J094343-533456	T28	277.231	-0.350	0.004	0.21	0.03	0.30	19418	115	71	9.60	2	
J094356-552847	T27	278.487	-1.773	0.005	0.27	0.04	0.36	12118	155	100	9.30	1*	
J094359-553458	T27	278.561	-1.845	0.010	0.76	0.11	0.41	12113	325	303	9.74	1*	
J094423-522603	T28	276.562	0.588	0.003	0.29	0.04	0.28	13880	160	113	9.43	1	w.comp (J094436-523539)
J094425-532714	T28	277.227	-0.184	0.004	0.26	0.04	0.25	19590	271	183	9.70	1	
J094430-553031	T27	278.568	-1.742	0.006	0.58	0.08	0.34	12182	143	143	9.63	1*	
J094430-545453	T28	278.184	-1.289	0.002	0.15	0.02	0.27	13191	195	102	9.12	2	
J094436-523539	T28	276.690	0.488	0.005	0.43	0.06	0.29	13852	167	123	9.60	1	w.comp (J094423-522603)
J094445-524813	T28	276.843	0.343	0.007	0.62	0.12	0.28	4506	174	110	8.79	1	i
J094449-530629	T28	277.047	0.117	0.028	4.10	0.58	0.28	5700	207	170	9.81	1	J0944-53, W, Z
J094504-545459	T27	278.246	-1.237	0.003	0.16	0.02	0.26	13235	226	128	9.15	1*	
J094527-531914	T28	277.258	0.016	0.002	0.10	0.01	0.28	21984	299	140	9.38	2	
J094530-524441	T28	276.891	0.460	0.001	0.08	0.01	0.29	19633	124	78	9.21	2	
J094530-523757	T28	276.819	0.546	0.003	0.27	0.04	0.30	16621	419	357	9.57	2	
J094535-543357	T28	278.077	-0.922	0.006	0.40	0.13	0.26	2214	134	52	7.97	2	
J094541-540631	T28	277.792	-0.564	0.002	0.15	0.02	0.23	16652	181	156	9.32	1	
J094543-535448	T28	277.670	-0.411	0.003	0.11	0.02	0.25	13986	176	115	9.02	2	
J094552-532617	T28	277.380	-0.034	0.005	0.59	0.11	0.28	2716	200	88	8.32	1	
J094605-555133	T27	278.965	-1.864	0.008	0.74	0.11	0.58	11965	227	197	9.72	1	
J094609-540336	T28	277.813	-0.482	0.003	0.21	0.03	0.27	14018	194	58	9.30	2	

* Detected by the overlapping region of the next mosaic as well.

Table B.1 continued

Name J2000 (1)	Mosaic TXX (2)	l deg (3)	b deg (4)	$S_{\rm peak}$ Jy (5)	$S_{\rm int}$ Jy km s^{-1} (6)	err$_{(S_{\rm int})}$ Jy km s^{-1} (7)	RMS mJy beam^{-1} (8)	$V_{\rm hel}$ km s^{-1} (9)	w_{20} km s^{-1} (10)	w_{50} km s^{-1} (11)	$M_{\rm HI}$ log($M_{\rm HI}$/M$_\odot$) (12)	Flag 1/2 (13)	Note (14)
J094620-553842	T27	278.854	-1.679	0.011	0.68	0.13	0.38	4883	136	80	8.90	1	
J094621-531930	T28	277.363	0.099	0.010	0.87	0.16	0.25	1699	114	86	8.08	1	
J094629-522925	T28	276.842	0.752	0.005	0.32	0.05	0.37	16539	179	141	9.64	1	
J094630-542620	T28	278.097	-0.739	0.008	0.58	0.11	0.26	2229	113	80	8.14	1	
J094646-542636	T28	278.129	-0.718	0.004	0.36	0.07	0.27	5354	128	110	8.70	1	
J094650-530910	T28	277.308	0.277	0.003	0.35	0.05	0.23	19633	238	188	9.83	1	
J094706-554932	T27	279.052	-1.748	0.003	0.15	0.02	0.42	14060	177	143	9.17	2	
J094720-550816	T27	278.637	-1.198	0.003	0.29	0.04	0.25	10817	192	104	9.22	1*	
J094725-530220	T28	277.303	0.422	0.004	0.19	0.03	0.25	19626	122	73	9.55	1	
J094730-550328	T27	278.604	-1.122	0.003	0.14	0.03	0.26	10869	95	78	8.90	1*	
J094738-533707	T28	277.697	-0.004	0.001	0.20	0.03	0.25	19984	326	282	9.61	2	
J094739-533809	T28	277.711	-0.015	0.004	0.75	0.07	0.24	16642	434	374	10.01	1	
J094745-545318	T27	278.523	-0.968	0.002	0.16	0.02	0.26	11641	152	92	9.01	1*	
J094751-544722	T27	278.471	-0.883	0.005	0.23	0.03	0.26	19988	214	102	9.66	1*	i?
J094758-543619	T27	278.366	-0.731	0.070	9.14	1.30	0.27	1720	126	112	9.12	1*	J0947-54, H
J094800-545708	T27	278.592	-0.995	0.005	0.58	0.11	0.27	5389	177	139	8.92	1*	
J094816-550531	T27	278.710	-1.078	0.003	0.24	0.03	0.26	12056	324	306	9.24	1*	
J094833-541400	T28	278.194	-0.391	0.003	0.12	0.02	0.26	21237	185	81	9.42	2	
J094921-531819	T28	277.696	0.402	0.006	0.93	0.09	0.31	20036	525	473	10.27	1	w.comp
J094926-534126	T28	277.949	0.111	0.003	0.60	0.06	0.22	19815	492	310	10.07	1	i
J094927-542159	T27	278.380	-0.410	0.003	0.21	0.03	0.27	12161	95	82	9.18	1*	i
J094942-540825	T28	278.265	-0.212	0.001	0.11	0.01	0.28	19604	155	67	9.30	1*	
J094942-534215	T28	277.989	0.126	0.002	0.15	0.02	0.22	20500	151	117	9.50	1	
J094942-545225	T27	278.731	-0.778	0.003	0.18	0.03	0.26	12068	161	104	9.10	1*	
J094946-555155	T27	279.367	-1.539	0.005	0.36	0.05	0.30	14153	118	90	9.55	1	
J094947-544310	T27	278.641	-0.652	0.009	1.25	0.18	0.28	11805	263	221	9.93	1*	
J095002-541659	T27	278.394	-0.291	0.002	0.08	0.01	0.26	12164	124	85	8.74	1*	
J095047-535531	T27	278.253	0.056	0.016	2.35	0.44	0.28	2197	205	168	8.74	1*	
J095048-545426	T27	278.874	-0.704	0.005	0.77	0.11	0.27	11958	556	522	9.73	1	M, W
J095049-545250	T27	278.859	-0.682	0.004	0.35	0.05	0.27	13818	183	163	9.52	1	
J095050-560333	T27	279.606	-1.595	0.007	0.45	0.15	0.27	1752	105	59	7.82	1	
J095102-543737	T28	278.723	-0.466	0.004	0.32	0.05	0.29	20209	344	313	9.81	2	

* Detected by the overlapping region of the next mosaic as well.

Table B.1 continued

Name J2000 (1)	Mosaic TXX (2)	l deg (3)	b deg (4)	$S_{\rm peak}$ Jy (5)	$S_{\rm int}$ Jy km s^{-1} (6)	err$_{(S_{\rm int})}$ Jy km s^{-1} (7)	RMS mJy beam^{-1} (8)	$V_{\rm hel}$ km s^{-1} (9)	w_{20} km s^{-1} (10)	w_{50} km s^{-1} (11)	$M_{\rm HI}$ log($M_{\rm HI}$/M$_\odot$) (12)	Flag 1/2 (13)	Note (14)
J095142-551815	T27	279.223	-0.932	0.020	1.36	0.44	0.26	1070	112	79	7.87	1	
J095108-553804	T27	279.369	-1.240	0.002	0.17	0.02	0.26	16640	222	135	9.36	2	
J095130-532200	T28	277.984	0.557	0.055	6.40	0.91	0.37	2201	159	122	9.18	1	J0951-53, H
J095155-550644	T27	279.127	-0.764	0.009	1.41	0.14	0.27	13795	362	187	10.12	1	
J095200-543745	T27	278.833	-0.380	0.003	0.15	0.02	0.25	11819	95	95	9.00	1	
J095201-534207	T28	278.254	0.344	0.003	0.45	0.06	0.31	11054	261	216	9.43	2	
J095216-544802	T27	278.970	-0.490	0.005	0.32	0.06	0.27	5610	125	83	8.68	1	
J095233-543848	T27	278.906	-0.344	0.007	0.75	0.11	0.27	5602	198	149	9.06	1	
J095240-543556	T27	278.890	-0.295	0.015	0.89	0.13	0.26	5567	104	62	9.13	1	
J095241-543331	T27	278.866	-0.263	0.004	0.29	0.05	0.26	5542	227	211	8.64	1	
J095247-562217	T27	280.013	-1.667	0.004	0.28	0.04	0.40	11860	226	189	9.29	1	
J095254-553649	T27	279.551	-1.066	0.091	8.81	0.87	0.30	5464	142	82	10.11	1	J0952-55A, w.comps (J095258, J095307), H
J095256-551112	T27	279.287	-0.730	0.018	3.00	0.43	0.28	5501	252	204	9.64	1	J0952-55B, W, Z
J095258-553452	T27	279.537	-1.035	0.012	1.70	0.24	0.29	5597	213	184	9.41	1	w.comp (J095254-553649)
J095307-553227	T27	279.530	-0.990	0.015	1.60	0.23	0.29	5560	163	114	9.38	1	w.comp (J095254-553649)
J095317-540633	T27	278.654	0.143	0.003	0.07	0.02	0.27	23658	368	70	9.29	2	
J095320-550947	T27	279.317	-0.676	0.003	0.31	0.04	0.25	17946	245	197	9.69	1	W
J095328-564805	T27	280.354	-1.945	0.005	0.48	0.05	0.52	21744	305	238	10.06	2	
J095341-544803	T27	279.131	-0.361	0.004	0.50	0.07	0.26	13880	234	219	9.68	1	i
J095346-542745	T27	278.929	-0.090	0.005	0.82	0.12	0.25	11844	236	181	9.75	1	
J095348-534511	T27	278.492	0.469	0.005	0.48	0.09	0.33	4715	165	109	8.72	2*	
J095351-563944	T27	280.309	-1.803	0.006	0.84	0.12	0.43	8313	219	196	9.45	1	
J095400-535542	T27	278.623	0.349	0.009	0.53	0.07	0.30	16407	129	99	9.85	1*	
J095425-561750	T27	280.143	-1.469	0.007	0.74	0.10	0.32	5451	187	140	9.03	1	
J095431-562318	T27	280.210	-1.531	0.004	0.30	0.04	0.31	11742	127	88	9.31	1	
J095443-551509	T27	279.527	-0.623	0.006	0.98	0.14	0.26	11878	412	375	9.83	1	
J095452-543623	T27	279.143	-0.104	0.007	0.30	0.06	0.26	4878	108	77	8.54	1	
J095502-561603	T27	280.191	-1.393	0.004	0.51	0.07	0.29	11625	182	134	9.53	1	w.comp (J095513-561846)
J095511-555109	T27	279.951	-1.053	0.007	0.59	0.11	0.27	3028	100	74	8.42	1	
J095513-561846	T27	280.239	-1.412	0.018	6.26	0.62	0.32	11769	508	468	10.63	1	J0955-56, w.comp (J095502-561603), W, Z
J095519-535620	T28	278.781	0.461	0.003	0.09	0.02	0.31	14035	136	115	8.95	2	
J095520-534351	T27	278.655	0.627	0.007	0.44	0.08	0.37	5654	115	74	8.84	1*	

* Detected by the overlapping region of the next mosaic as well.

Table B.1 continued

Name J2000 (1)	Mosaic TXX (2)	l deg (3)	b deg (4)	$S_{\rm peak}$ Jy (5)	$S_{\rm int}$ Jy km s^{-1} (6)	err$_{(S_{\rm int})}$ Jy km s^{-1} (7)	RMS mJy beam^{-1} (8)	$V_{\rm hel}$ km s^{-1} (9)	w_{20} km s^{-1} (10)	w_{50} km s^{-1} (11)	$M_{\rm HI}$ log($M_{\rm HI}$/M$_\odot$) (12)	Flag 1/2 (13)	Note (14)
J095540-544810	T27	279.356	-0.186	0.004	0.34	0.05	0.25	18150	149	134	9.75	1	
J095546-560020	T27	280.110	-1.123	0.022	1.12	0.37	0.27	1183	81	50	7.88	1	
J095558-560854	T27	280.219	-1.219	0.004	0.29	0.04	0.28	9180	204	158	9.07	1	
J095632-555215	T27	280.111	-0.951	0.003	0.31	0.04	0.26	16974	323	260	9.65	1	
J095647-562819	T27	280.509	-1.403	0.005	0.50	0.05	0.29	22308	201	183	10.09	1	
J095701-561819	T27	280.432	-1.252	0.002	0.11	0.02	0.27	11682	229	215	8.86	1	
J095718-564556	T27	280.746	-1.591	0.005	0.25	0.05	0.36	22021	460	406	9.77	1	w.comp?
J095733-535738	T27	279.053	0.646	0.008	0.65	0.06	0.41	18520	196	158	10.04	1	
J095734-540641	T27	279.149	0.530	0.004	0.10	0.01	0.31	19995	96	74	9.32	1	
J095738-540724	T27	279.162	0.525	0.007	1.14	0.16	0.34	4872	245	188	9.12	1	
J095756-560827	T27	280.432	-1.044	0.004	0.35	0.05	0.28	10443	322	111	9.28	1	
J095800-562201	T27	280.577	-1.217	0.002	0.14	0.02	0.28	14352	158	121	9.17	1	
J095802-555940	T27	280.352	-0.920	0.010	3.19	0.31	0.30	9212	535	458	10.12	1	
J095816-562710	T27	280.659	-1.263	0.004	0.10	0.01	0.27	21251	148	131	9.37	1	
J095825-551952	T27	279.991	-0.362	0.027	4.10	0.58	0.28	3710	201	156	9.44	1	J0958-55, W, Z
J095844-555702	T27	280.404	-0.825	0.003	0.17	0.02	0.26	16325	139	124	9.34	1	
J095849-555928	T27	280.437	-0.851	0.002	0.24	0.04	0.27	9196	222	182	8.99	1	
J095850-565818	T27	281.036	-1.627	0.013	1.22	0.23	0.47	3719	178	109	8.91	1	
J095850-542635	T27	279.498	0.380	0.003	0.28	0.04	0.27	20096	379	218	9.75	2	
J095856-564038	T27	280.869	-1.384	0.004	0.15	0.05	0.34	11659	284	207	8.99	1	
J095906-553959	T27	280.273	-0.568	0.014	2.59	0.37	0.28	4269	227	227	9.36	1	I, M, W
J095907-544852	T27	279.756	0.109	0.004	0.30	0.04	0.27	11867	168	127	9.32	1	
J095914-570929	T27	281.193	-1.742	0.004	0.16	0.02	0.48	23241	263	206	9.65	2	w_{20} unc.
J095921-560625	T27	280.566	-0.898	0.004	0.28	0.04	0.29	16358	244	184	9.57	1	
J095927-550949	T27	280.007	-0.138	0.008	1.00	0.14	0.26	5402	172	143	9.15	1	
J095934-555434	T27	280.471	-0.722	0.004	0.43	0.06	0.28	10299	136	121	9.35	1	
J095944-565252	T27	281.079	-1.480	0.018	1.58	0.42	0.46	8482	193	101	9.76	2	cont. nearby
J100041-555943	T27	280.649	-0.695	0.013	1.31	0.24	0.29	2463	131	116	8.58	1	
J100048-554827	T27	280.548	-0.536	0.002	0.25	0.04	0.26	14141	291	291	9.39	1	
J100051-560501	T27	280.720	-0.752	0.003	0.33	0.05	0.30	9857	168	94	9.20	2	
J100054-545924	T27	280.066	0.125	0.015	0.83	0.12	0.27	13797	110	63	9.89	1	
J100058-535753	T27	279.456	0.949	0.011	1.29	0.13	0.55	19883	407	279	10.40	1	

* Detected by the overlapping region of the next mosaic as well.

Table B.1 continued

Name J2000 (1)	Mosaic TXX (2)	l deg (3)	b deg (4)	$S_{\rm peak}$ Jy (5)	$S_{\rm int}$ Jy km s^{-1} (6)	err$_{(S_{\rm int})}$ Jy km s^{-1} (7)	RMS mJy beam^{-1} (8)	$V_{\rm hel}$ km s^{-1} (9)	w_{20} km s^{-1} (10)	w_{50} km s^{-1} (11)	$M_{\rm HI}$ log($M_{\rm HI}$/M$_\odot$) (12)	Flag 1/2 (13)	Note (14)
J100113-544302	T27	279.937	0.370	0.008	1.17	0.22	0.33	3697	273	220	8.89	1	
J100113-540934	T27	279.603	0.816	0.007	0.44	0.08	0.46	5797	132	117	8.86	1	
J100124-542756	T27	279.809	0.588	0.010	0.64	0.12	0.37	3007	114	77	8.45	1	
J100128-560759	T27	280.819	-0.739	0.005	0.32	0.06	0.29	4820	123	85	8.55	1	
J100154-560146	T27	280.804	-0.621	0.009	1.49	0.15	0.31	11703	391	331	10.00	1	
J100200-565847	T27	281.386	-1.372	0.009	0.97	0.19	0.40	11603	318	278	9.81	1	
J100210-544426	T27	280.062	0.434	0.013	0.86	0.16	0.34	3704	103	66	8.75	1	
J100214-573213	T26	281.745	-1.799	0.005	0.33	0.05	0.60	22322	387	261	9.92	2	
J100233-563659	T26	281.227	-1.037	0.008	0.70	0.10	0.35	9129	132	91	9.45	1*	
J100238-572656	T26	281.734	-1.697	0.110	16.09	2.28	0.62	2607	282	220	9.72	1*	J1002-57
J100246-550814	T27	280.368	0.167	0.009	0.81	0.12	0.29	11835	201	143	9.75	1	
J100247-543322	T27	280.022	0.635	0.008	1.19	0.12	0.41	14095	247	109	10.07	1	
J100300-572031	T26	281.712	-1.581	0.006	0.77	0.11	0.49	11586	191	170	9.70	1*	w.comp (J100310-571755)
J100303-552755	T27	280.597	-0.071	0.012	0.79	0.11	0.29	9044	120	87	9.50	1	
J100309-553414	T27	280.670	-0.148	0.005	0.68	0.10	0.28	10199	189	189	9.54	1	
J100310-571755	T26	281.703	-1.533	0.012	4.39	0.43	0.55	11541	450	318	10.45	1*	BL, w.comps (J100300-572031)
J100311-562939	T26	281.224	-0.887	0.058	3.99	0.74	0.31	1211	82	68	8.45	1*	J1003-56
J100406-555315	T27	280.966	-0.323	0.004	0.50	0.09	0.29	4776	172	140	8.75	1	
J100414-570922	T27	281.734	-1.333	0.003	0.12	0.02	0.42	14533	146	110	9.11	2	
J100423-563012	T26	281.363	-0.796	0.011	0.80	0.11	0.35	9192	116	79	9.52	1*	
J100428-553440	T27	280.824	-0.043	0.007	0.50	0.09	0.28	5810	155	105	8.91	1	
J100431-560922	T27	281.173	-0.504	0.006	1.27	0.18	0.33	4780	228	228	9.15	1	
J100437-565616	T27	281.646	-1.126	0.007	0.57	0.08	0.38	8641	283	226	9.32	1	
J100441-570213	T27	281.714	-1.200	0.004	0.11	0.04	0.39	23902	395	318	9.48	2	
J100450-561917	T26	281.305	-0.612	0.004	0.35	0.05	0.33	21426	135	99	9.91	2*	w_{20} unc.
J100454-545308	T27	280.465	0.552	0.005	0.26	0.09	0.35	10427	339	181	9.15	1	
J100456-563115	T26	281.435	-0.765	0.007	1.58	0.16	0.40	11662	508	475	10.02	1*	
J100458-554308	T27	280.964	-0.115	0.004	0.17	0.03	0.28	10120	138	107	8.93	1	
J100529-562752	T26	281.463	-0.674	0.006	0.37	0.05	0.37	21668	338	108	9.94	1*	
J100544-564423	T26	281.653	-0.876	0.012	0.87	0.09	0.40	16497	142	107	10.07	1*	
J100604-545333	T27	280.605	0.646	0.005	0.23	0.03	0.37	21537	198	163	9.73	2	
J100628-545420	T27	280.658	0.668	0.004	0.14	0.04	0.37	21443	292	246	9.52	2	

* Detected by the overlapping region of the next mosaic as well.

Table B.1 continued

Name J2000 (1)	Mosaic TXX (2)	l deg (3)	b deg (4)	$S_{\rm peak}$ Jy (5)	$S_{\rm int}$ Jy km s^{-1} (6)	err$_{(S_{\rm int})}$ Jy km s^{-1} (7)	RMS mJy beam^{-1} (8)	$V_{\rm hel}$ km s^{-1} (9)	w_{20} km s^{-1} (10)	w_{50} km s^{-1} (11)	$M_{\rm HI}$ log($M_{\rm HI}$/M$_\odot$) (12)	Flag 1/2 (13)	Note (14)
J100633-574608	T26	282.347	-1.644	0.014	1.36	0.19	0.61	11518	276	251	9.95	1	
J100655-555346	T27	281.291	-0.096	0.017	0.84	0.08	0.29	21394	91	57	10.28	2*	
J100713-562115	T26	281.592	-0.444	0.004	0.20	0.03	0.34	14956	137	122	9.35	1*	
J100720-551405	T27	280.952	0.474	0.015	0.79	0.11	0.34	10116	109	60	9.60	1	w.comp (J100730-551027)
J100721-564409	T26	281.831	-0.742	0.009	1.55	0.15	0.42	11974	285	268	10.04	1	
J100723-551136	T27	280.934	0.512	0.005	0.25	0.04	0.34	12776	390	288	9.30	2	
J100725-562753	T27	281.679	-0.518	0.007	0.40	0.06	0.37	8804	401	288	9.18	2	w.comp
J100725-562755	T26	281.679	-0.518	0.006	0.20	0.04	0.36	8818	126	82	8.88	1	
J100730-551027	T27	280.935	0.537	0.014	2.53	0.25	0.39	10093	339	178	10.10	1	i, w.comp (J100720-551405)
J100736-545522	T27	280.801	0.750	0.022	3.56	0.35	0.53	9044	344	269	10.15	1	M, W
J100804-555400	T26	281.424	-0.006	0.005	0.30	0.04	0.29	20173	252	207	9.78	1*	
J100828-553542	T27	281.293	0.276	0.001	0.04	0.02	0.28	20853	337	290	8.94	2	
J100829-554522	T26	281.387	0.145	0.016	1.21	0.23	0.29	2671	151	97	8.62	1*	
J100829-575415	T26	282.636	-1.604	0.007	0.75	0.11	0.68	10285	222	198	9.59	1	
J100905-560355	T26	281.635	-0.059	0.006	0.36	0.07	0.32	3108	90	85	8.23	1*	
J100905-563726	T26	281.958	-0.514	0.082	12.16	1.73	0.41	2641	226	167	9.61	1	J1009-56, H
J100923-544845	T27	280.946	0.989	0.009	0.39	0.04	0.88	4454	278	225	8.58	1	
J100924-563231	T26	281.948	-0.421	0.042	5.35	0.76	0.38	2731	135	129	9.29	1	
J100932-563718	T26	282.008	-0.476	0.005	0.21	0.03	0.35	15105	143	121	9.38	1	
J100937-562248	T26	281.878	-0.272	0.005	0.51	0.06	0.32	8145	380	351	9.22	1	w.comp
J101025-553850	T26	281.547	0.391	0.004	0.35	0.05	0.28	14285	282	233	9.55	1*	i? with a hole in the centre?
J101033-574438	T26	282.768	-1.313	0.018	1.75	0.33	0.54	2607	156	110	8.76	1	w.comp
J101056-552048	T27	281.435	0.680	0.002	0.07	0.01	0.31	18482	149	149	9.06	2	
J101100-552019	T26	281.437	0.691	0.006	0.32	0.04	0.33	10143	94	67	9.20	1*	
J101131-561931	T26	282.061	-0.076	0.004	0.16	0.03	0.29	7865	140	114	8.67	1	
J101131-561056	T26	281.980	0.041	0.007	1.47	0.21	0.31	9048	372	351	9.77	1	
J101208-551909	T26	281.558	0.799	0.016	1.27	0.24	0.38	2647	128	68	8.63	1*	
J101209-560712	T26	282.017	0.143	0.004	0.37	0.05	0.30	11846	239	213	9.41	1	
J101211-552311	T27	281.602	0.748	0.003	0.05	0.03	0.36	16313	446	250	8.81	2	
J101211-564237	T26	282.357	-0.339	0.011	0.47	0.07	0.34	16372	88	59	9.80	1	
J101242-573947	T26	282.957	-1.083	0.008	0.99	0.10	0.42	24072	206	199	10.46	1	
J101258-571946	T26	282.797	-0.788	0.008	0.98	0.14	0.45	11586	298	227	9.81	1	

* Detected by the overlapping region of the next mosaic as well.

Table B.1 continued

Name J2000 (1)	Mosaic TXX (2)	l deg (3)	b deg (4)	$S_{\rm peak}$ Jy (5)	$S_{\rm int}$ Jy km s^{-1} (6)	err$_{(S_{\rm int})}$ Jy km s^{-1} (7)	RMS mJy beam^{-1} (8)	$V_{\rm hel}$ km s^{-1} (9)	w_{20} km s^{-1} (10)	w_{50} km s^{-1} (11)	$M_{\rm HI}$ log($M_{\rm HI}$/M$_\odot$) (12)	Flag 1/2 (13)	Note (14)
J101301-561450	T26	282.188	0.107	0.004	0.16	0.02	0.29	16412	240	224	9.34	1	
J101317-565425	T26	282.594	-0.415	0.007	0.49	0.09	0.36	3127	129	98	8.36	1	
J101327-552239	T26	281.747	0.859	0.007	0.44	0.06	0.49	14239	183	112	9.64	1	
J101403-561711	T26	282.329	0.156	0.006	0.52	0.10	0.29	3138	117	81	8.40	1	
J101408-560003	T26	282.177	0.398	0.004	0.28	0.04	0.29	11860	143	80	9.29	1	
J101446-574032	T26	283.192	-0.937	0.007	1.30	0.18	0.50	7081	259	200	9.50	1	
J101551-555254	T26	282.309	0.631	0.004	0.29	0.04	0.31	11796	142	70	9.30	2	
J101553-583655	T26	283.841	-1.633	0.010	0.40	0.06	0.55	14241	139	85	9.60	2	
J101611-571957	T26	283.158	-0.546	0.029	1.45	0.27	0.45	2671	96	58	8.70	1	i
J101654-590156	T25	284.183	-1.905	0.003	0.22	0.03	0.64	22527	607	520	9.74	2*	
J101745-561805	T26	282.764	0.430	0.020	4.04	0.40	0.33	7543	279	263	10.05	1	
J101804-561022	T26	282.728	0.561	0.009	0.53	0.08	0.33	7315	87	72	9.14	1	
J101836-563331	T26	283.004	0.281	0.002	0.08	0.02	0.29	14575	137	122	8.94	2	
J101935-570636	T26	283.418	-0.107	0.019	2.90	0.54	0.50	2656	173	156	9.00	1	
J101939-560134	T26	282.833	0.806	0.013	1.47	0.21	0.55	8938	281	253	9.76	1	
J101949-562439	T26	283.062	0.496	0.004	0.15	0.03	0.34	7504	90	73	8.62	1	
J101958-570507	T26	283.448	-0.058	0.011	0.84	0.12	0.54	11864	136	82	9.76	1	
J102101-582352	T25	284.281	-1.081	0.003	0.09	0.01	0.47	22142	246	230	9.32	2	
J102142-563705	T26	283.394	0.464	0.025	2.48	0.46	0.38	2671	158	107	8.93	1	
J102201-585725	T25	284.694	-1.481	0.005	0.22	0.03	0.38	14561	127	94	9.37	1*	
J102240-563220	T26	283.462	0.602	0.005	0.33	0.05	0.37	11495	184	169	9.33	1	
J102244-591200	T25	284.901	-1.637	0.011	1.02	0.14	0.51	10794	142	142	9.77	1	
J102252-575753	T25	284.251	-0.586	0.012	0.61	0.09	0.62	14350	126	96	9.79	1*	
J102449-575624	T25	284.458	-0.426	0.014	0.75	0.11	0.64	7324	91	74	9.29	1*	
J102500-591447	T25	285.171	-1.521	0.006	0.57	0.08	0.39	11605	143	143	9.57	1	
J102505-592708	T25	285.290	-1.690	0.010	0.62	0.09	0.46	11577	132	117	9.61	1	w.comp
J102518-570330	T26	284.044	0.355	0.015	0.97	0.14	0.63	7266	144	80	9.40	1	
J102534-562759	T26	283.763	0.877	0.006	0.45	0.06	0.68	11684	221	194	9.48	1	
J102719-594756	T25	285.713	-1.835	0.010	0.67	0.10	0.65	6115	276	262	9.09	1	
J102724-585810	T25	285.288	-1.123	0.006	1.26	0.18	0.39	6163	270	255	9.37	1	
J102733-593751	T25	285.650	-1.677	0.003	0.14	0.02	0.46	22735	347	303	9.55	2	
J102946-594348	T25	285.940	-1.616	0.015	1.72	0.24	0.62	5724	210	143	9.44	1	i?

* Detected by the overlapping region of the next mosaic as well.

Table B.1 continued

Name J2000 (1)	Mosaic TXX (2)	l deg (3)	b deg (4)	$S_{\rm peak}$ Jy (5)	$S_{\rm int}$ Jy km s^{-1} (6)	err$_{(S_{\rm int})}$ Jy km s^{-1} (7)	RMS mJy beam^{-1} (8)	$V_{\rm hel}$ km s^{-1} (9)	w_{20} km s^{-1} (10)	w_{50} km s^{-1} (11)	$M_{\rm HI}$ log($M_{\rm HI}$/M$_\odot$) (12)	Flag 1/2 (13)	Note (14)
J102959-584555	T25	285.467	-0.775	0.005	0.17	0.02	0.42	11434	95	95	9.04	1	
J103054-582318	T25	285.376	-0.390	0.004	0.25	0.02	0.40	14916	433	247	9.44	1	
J103118-593619	T25	286.043	-1.410	0.004	0.22	0.03	0.54	11495	286	286	9.15	1	
J103218-574611	T25	285.220	0.236	0.005	0.23	0.03	0.40	11263	143	138	9.16	1	
J103243-592040	T25	286.065	-1.094	0.005	0.58	0.08	0.45	16758	363	295	9.90	1	i?
J103418-584521	T25	285.944	-0.483	0.014	1.98	0.28	0.42	5762	184	183	9.50	1	
J103552-584106	T25	286.086	-0.319	0.013	0.73	0.10	0.41	5435	105	69	9.02	1	
J103607-580202	T25	285.790	0.261	0.039	2.10	0.30	0.38	5751	98	58	9.53	1	J1036-58
J103659-591113	T25	286.458	-0.685	0.061	15.08	2.05	0.54	3257	340	303	9.89	1	J1036-59, M, Z
J103723-595048	T25	286.826	-1.235	0.015	1.34	0.25	0.56	3276	145	98	8.84	1	
J103801-582850	T25	286.228	-0.004	0.005	0.21	0.03	0.41	15193	146	130	9.39	1	
J103809-573204	T25	285.780	0.830	0.013	0.60	0.09	0.62	5968	165	57	9.02	2	
J103844-584312	T25	286.426	-0.167	0.007	0.74	0.10	0.42	14684	390	352	9.89	1	i
J103903-573926	T25	285.945	0.781	0.010	0.49	0.09	0.58	5350	272	256	8.83	2	
J104007-601914	T24	287.356	-1.482	0.013	1.33	0.19	0.58	5689	173	160	9.32	1*	
J104010-583801	T25	286.547	-0.002	0.034	2.42	0.45	0.40	1300	102	57	8.30	1	
J104104-592140	T25	286.998	-0.584	0.011	1.43	0.20	0.70	9084	407	334	9.76	1	w.comp
J104104-582725	T25	286.566	0.210	0.003	0.07	0.01	0.36	15571	331	192	8.90	2	
J104133-583131	T25	286.653	0.180	0.013	0.99	0.14	0.44	5667	121	96	9.19	1	i
J104143-593109	T24	287.147	-0.683	0.007	0.53	0.10	0.79	3261	126	99	8.44	1*	
J104253-585109	T25	286.961	-0.025	0.007	0.79	0.11	0.49	15322	293	180	9.96	1	
J104447-611148	T24	288.273	-1.983	0.007	0.36	0.05	0.76	9530	198	91	9.20	2	
J104505-610513	T24	288.255	-1.868	0.011	1.46	0.21	0.61	4380	216	188	9.13	1	
J104549-575442	T25	286.861	0.986	0.010	0.26	0.05	0.94	6628	92	92	8.75	2	
J104729-591531	T24	287.673	-0.110	0.008	0.90	0.13	0.59	6765	151	82	9.30	1	
J104820-583730	T24	287.482	0.504	0.005	0.89	0.13	0.37	14051	240	223	9.94	1*	
J104821-605352	T24	288.519	-1.518	0.017	1.87	0.27	0.41	4460	152	120	9.26	1	
J104842-590858	T24	287.762	0.058	0.020	3.58	0.35	0.57	11593	346	299	10.37	1	
J104905-611626	T24	288.769	-1.813	0.007	0.10	0.02	0.66	6449	92	92	8.29	2	
J104915-604343	T24	288.539	-1.318	0.011	0.63	0.09	0.41	13693	118	76	9.76	1	
J104923-583835	T24	287.612	0.550	0.004	0.16	0.02	0.37	16569	94	77	9.34	1*	
J105040-590738	T24	287.977	0.192	0.010	2.02	0.20	0.49	13919	339	322	10.29	1	

* Detected by the overlapping region of the next mosaic as well.

Table B.1 continued

Name J2000 (1)	Mosaic TXX (2)	l deg (3)	b deg (4)	$S_{\rm peak}$ Jy (5)	$S_{\rm int}$ Jy km s^{-1} (6)	err$_{(S_{\rm int})}$ Jy km s^{-1} (7)	RMS mJy beam^{-1} (8)	$V_{\rm hel}$ km s^{-1} (9)	w_{20} km s^{-1} (10)	w_{50} km s^{-1} (11)	$M_{\rm HI}$ log($M_{\rm HI}$/M$_\odot$) (12)	Flag 1/2 (13)	Note (14)
J105100-603433	T24	288.663	-1.085	0.004	0.58	0.08	0.36	11505	209	161	9.58	1	
J105202-601726	T24	288.651	-0.772	0.003	0.13	0.02	0.38	5648	127	93	8.30	1	
J105211-603832	T24	288.823	-1.079	0.004	0.10	0.02	0.32	11236	143	125	8.81	1	
J105230-605431	T24	288.974	-1.302	0.003	0.15	0.02	0.33	13779	145	145	9.15	1	
J105251-604027	T24	288.909	-1.072	0.003	0.13	0.03	0.29	5512	309	103	8.30	1	
J105328-591538	T24	288.358	0.232	0.007	0.52	0.07	0.36	11568	187	170	9.53	1	
J105333-602739	T24	288.893	-0.843	0.002	0.16	0.02	0.32	14491	193	170	9.21	2	
J105342-594417	T24	288.594	-0.185	0.007	0.83	0.08	0.37	21775	441	412	10.30	1	
J105349-603457	T24	288.976	-0.938	0.013	0.89	0.13	0.31	5514	83	69	9.12	1	
J105401-601037	T24	288.821	-0.562	0.004	1.08	0.11	0.37	19334	534	414	10.30	2	
J105408-604654	T24	289.097	-1.100	0.004	1.17	0.17	0.31	9135	578	538	9.68	2	
J105506-584313	T24	288.313	0.810	0.005	0.65	0.09	0.37	15428	228	197	9.88	1	
J105543-591510	T24	288.614	0.364	0.006	0.76	0.11	0.29	11505	190	169	9.69	1	
J105601-590956	T24	288.612	0.459	0.003	0.15	0.02	0.27	11561	143	117	9.00	1	
J105629-590449	T24	288.629	0.562	0.004	0.17	0.03	0.31	5705	92	80	8.44	2	
J105809-613714	T24	289.896	-1.650	0.003	0.24	0.05	0.41	21483	216	181	9.73	2	BL
J105823-595219	T24	289.182	-0.053	0.018	3.21	0.46	0.31	3410	259	240	9.26	1	
J105827-595011	T24	289.175	-0.017	0.005	0.55	0.05	0.28	20648	251	197	10.07	1	
J105827-610353	T24	289.694	-1.131	0.002	0.13	0.02	0.43	15960	313	260	9.22	2	
J105853-602745	T24	289.487	-0.562	0.004	0.60	0.06	0.31	21462	508	478	10.14	1	
J105913-603021	T24	289.543	-0.584	0.004	0.23	0.04	0.33	6694	138	125	8.71	1	
J105928-610452	T24	289.811	-1.094	0.028	4.79	0.68	0.44	5808	244	181	9.90	1	
J105940-593005	T24	289.174	0.351	0.003	0.25	0.04	0.27	11486	296	198	9.21	2	
J110000-593619	T24	289.256	0.274	0.008	0.79	0.11	0.27	11523	262	195	9.71	1	Faint double horn? i?
J110022-604242	T24	289.757	-0.713	0.005	0.19	0.02	0.35	5442	106	65	8.43	1	
J110035-610058	T24	289.907	-0.979	0.024	5.25	0.75	0.38	3572	308	295	9.51	1	
J110057-603559	T24	289.777	-0.581	0.003	0.16	0.02	0.31	24136	362	137	9.66	1	
J110113-601148	T24	289.639	-0.201	0.004	0.33	0.06	0.31	4467	189	105	8.51	1	
J110204-594121	T24	289.528	0.306	0.002	0.12	0.02	0.27	5540	183	134	8.23	2	
J110223-620954	T24	290.576	-1.938	0.005	0.18	0.21	0.62	20903	519	427	9.60	2	
J110239-603157	T24	289.938	-0.435	0.007	0.61	0.09	0.39	11450	142	120	9.59	1	
J110302-613311	T24	290.397	-1.348	0.011	1.00	0.19	0.33	4508	152	121	8.99	1	

* Detected by the overlapping region of the next mosaic as well.

Table B.1 continued

Name	Mosaic	l	b	$S_{\rm peak}$	$S_{\rm int}$	$\mathrm{err}_{(S_{\rm int})}$	RMS	$V_{\rm hel}$	w_{20}	w_{50}	$M_{\rm HI}$	Flag	Note
J2000	TXX	deg	deg	Jy	Jy km s^{-1}	Jy km s^{-1}	mJy beam^{-1}	km s^{-1}	km s^{-1}	km s^{-1}	$\log(M_{\rm HI}/{\rm M}_\odot)$	1/2	
(1)	(2)	(3)	(4)	(5)	(6)	(7)	(8)	(9)	(10)	(11)	(12)	(13)	(14)
J110325-595036	T24	289.747	0.234	0.003	0.21	0.03	0.28	21663	392	352	9.70	1	
J110359-594426	T24	289.771	0.357	0.007	0.43	0.08	0.30	3516	94	51	8.41	2	
J110419-603412	T24	290.141	-0.386	0.008	0.65	0.09	0.40	7479	186	179	9.25	1	
J110459-605022	T24	290.324	-0.600	0.015	1.56	0.22	0.42	5440	168	135	9.35	1	
J110506-594013	T24	289.871	0.478	0.011	1.50	0.21	0.34	11530	281	263	9.99	1	
J110516-611219	T24	290.502	-0.922	0.004	0.27	0.05	0.41	5784	138	138	8.64	1	
J110700-593047	T24	290.030	0.717	0.012	0.73	0.10	0.42	6707	82	66	9.20	1	
J110730-604836	T24	290.595	-0.452	0.017	1.54	0.22	0.44	5481	201	167	9.35	1	
J110734-594045	T24	290.162	0.592	0.004	0.20	0.04	0.34	9062	140	92	8.91	1	
J110827-601412	T24	290.480	0.121	0.006	0.65	0.09	0.41	5676	174	136	9.01	1	

B.4 Vela–SMGPS H I atlas

This section presents the H I galaxy atlas comprising 843 galaxies detected in the Vela–SMGPS survey, as detailed in Chapter 3.

Left panel: Masked total flux (mom-0) map in Galactic coordinates with a color bar. A 3σ clipping threshold, where σ is the local rms of the detection, is applied to generate the mask. The unique galaxy identifier (SMGPS-HI) Jhhmmss±ddmmss is featured in the top-left corner outside the panel. If the galaxy is also detected in HIZOA, this information will be indicated beside its galaxy identifier. A 10 kpc scale bar is located at the top-right corner, and the hatched ellipse at the bottom-left corner corresponds to the FWHM of the synthesized beam.

Middle panel: Masked mom-1 map in Galactic coordinates with a color bar revealing velocity fields. The heliocentric velocity is given in the top right corner and indicated as a magenta contour. The synthesized beam is located at the bottom left corner.

Right panel: The Global H I profile, i.e., flux density as a function of velocity, includes a dashed vertical line indicating the heliocentric velocity of the galaxy. In the top left corner, measured linewidths at 50% and 20% of the peak flux density are displayed. Furthermore, the red point in the spectrum corresponds to the peak flux value, explicitly shown in the top right corner.

The images are arranged in ascending order of Right Ascension (RA), moving from left to right across the columns and then from top to bottom within the rows from solid (see B.4.1) to possible detections (see B.4.2).

B.4.1 Solid detections

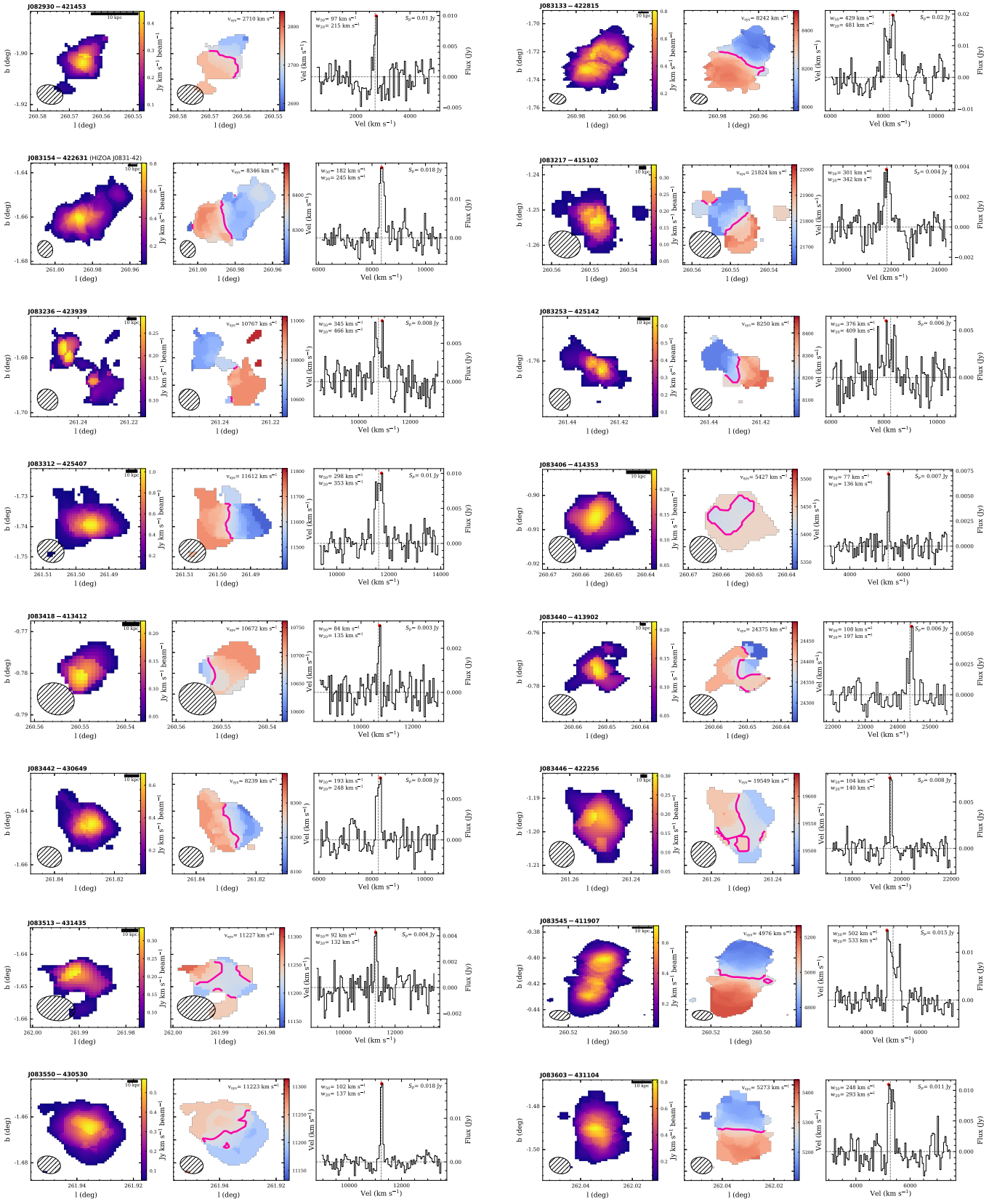

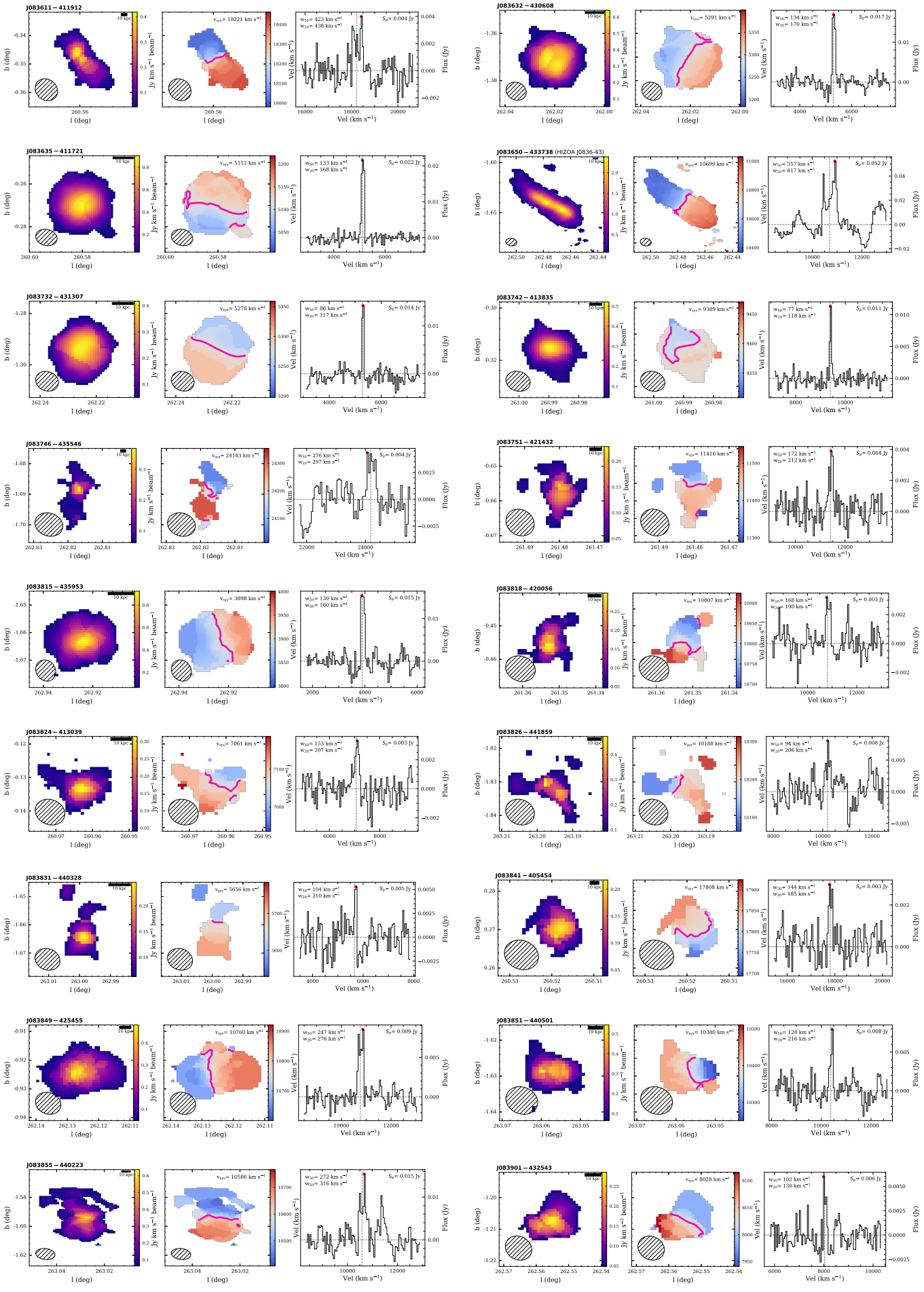
J083611 − 411912
J083632 − 430608
J083635 − 411721
J083650 − 433738 (HIZOA J0836-43)
J083732 − 431307
J083742 − 413835
J083746 − 435546
J083751 − 421432
J083815 − 435953
J083818 − 420056
J083824 − 413039
J083826 − 441859
J083831 − 440328
J083841 − 405454
J083849 − 425455
J083851 − 440501
J083855 − 440223
J083901 − 432543
b (deg)
l (deg)
Jy km s⁻¹ beam⁻¹
Vel (km s⁻¹)
Vel (km s⁻¹)
Flux (Jy)

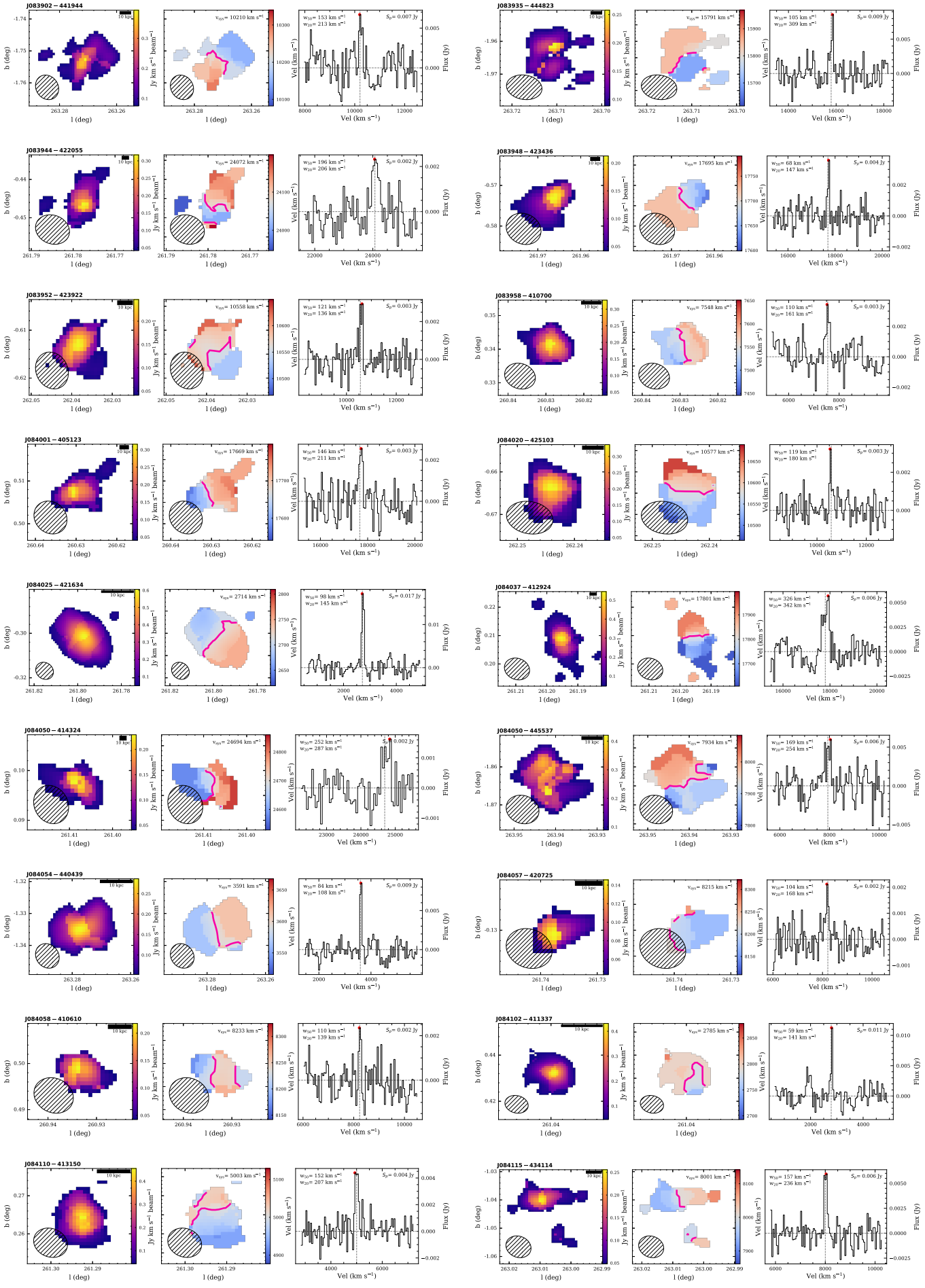
J083902 – 441944
J083935 – 444823
J083944 – 422055
J083948 – 423436
J083952 – 423922
J083958 – 410700
J084001 – 405123
J084020 – 425103
J084025 – 421634
J084037 – 412924
J084050 – 414324
J084050 – 445537
J084054 – 440439
J084057 – 420725
J084058 – 410610
J084102 – 411337
J084110 – 413150
J084115 – 434114
l (deg)
b (deg)
Vel (km s−1)
Flux (Jy)
Jy km s−1 beam−1
10 kpc

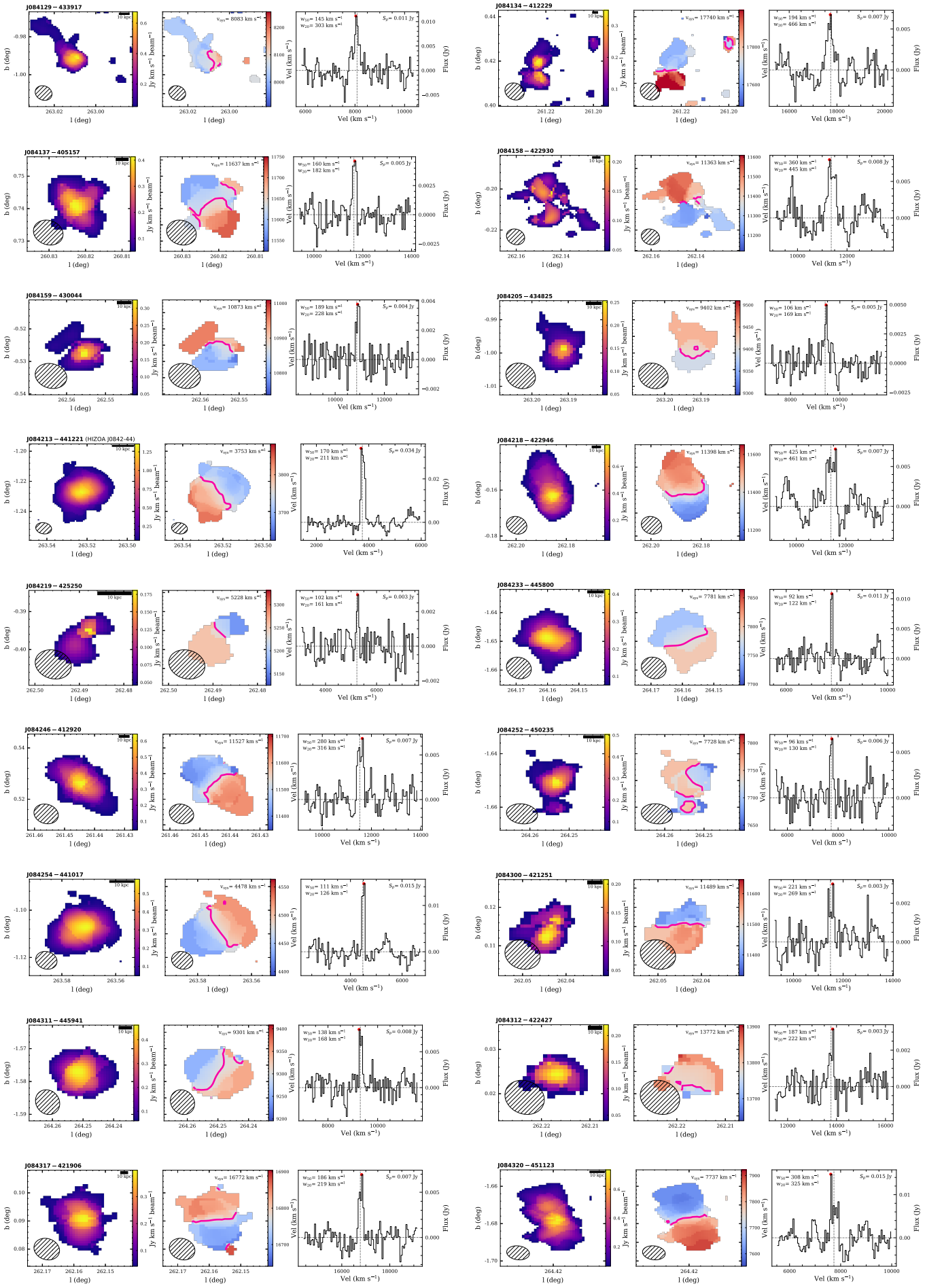
J084129 – 433917
J084134 – 412229
J084137 – 405157
J084158 – 422930
J084159 – 430044
J084205 – 434825
J084213 – 441221 (HIZOA J0842-44)
J084218 – 422946
J084219 – 425250
J084233 – 445800
J084246 – 412920
J084252 – 450235
J084254 – 441017
J084300 – 421251
J084311 – 445941
J084312 – 422427
J084317 – 421906
J084320 – 451123
l (deg)
b (deg)
Vel (km s^{-1})
Flux (Jy)
Jy km s^{-1} beam^{-1}

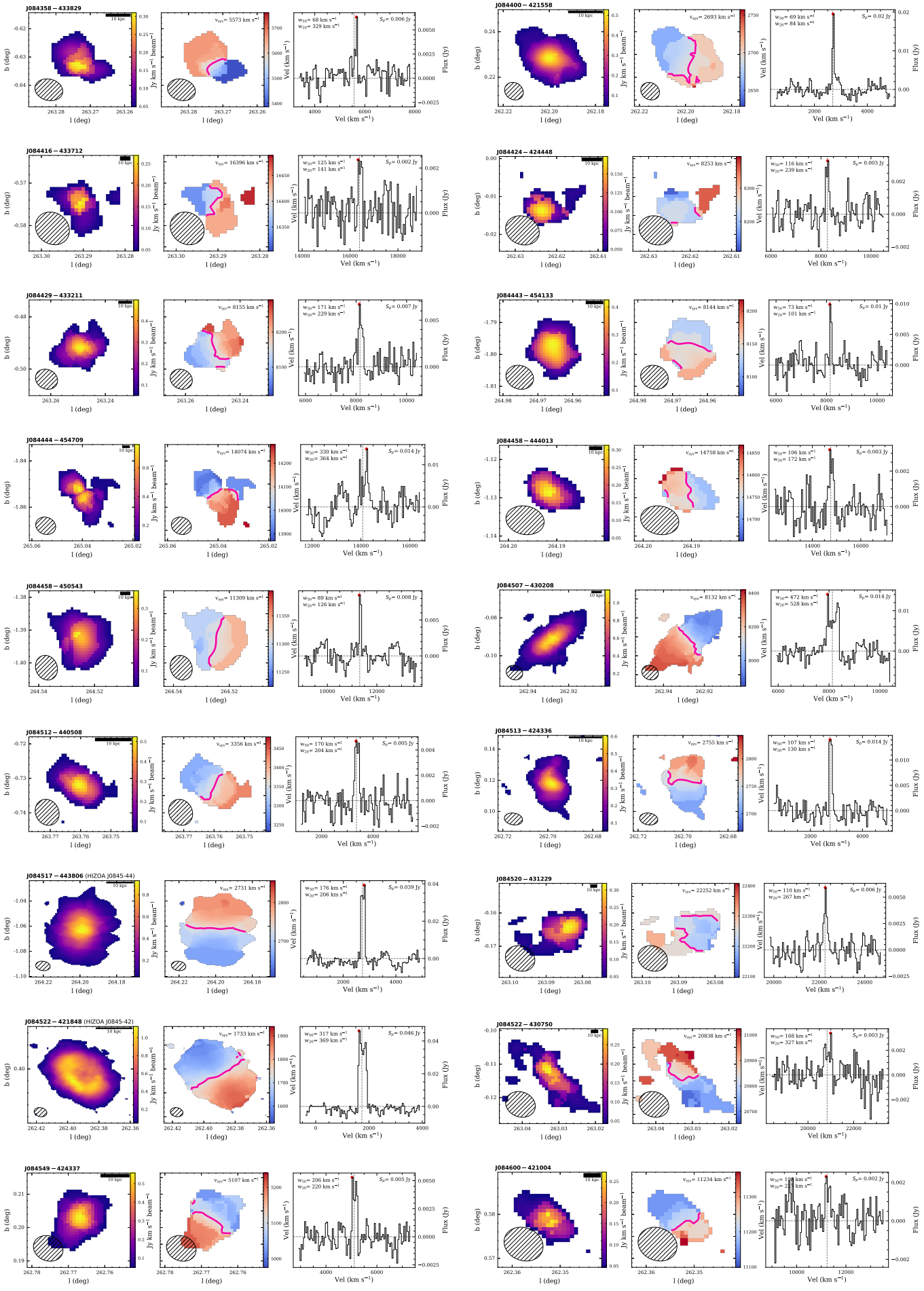
J084358 − 433829
J084400 − 421558
J084416 − 433712
J084424 − 424448
J084429 − 433211
J084443 − 454133
J084444 − 454709
J084458 − 444013
J084458 − 450543
J084507 − 430208
J084512 − 440508
J084513 − 424336
J084517 − 443806 (HIZOA J0845-44)
J084520 − 431229
J084522 − 421848 (HIZOA J0845-42)
J084522 − 430750
J084549 − 424337
J084600 − 421004
b (deg)
l (deg)
Jy km s−1 beam−1
Vel (km s−1)
Flux (Jy)

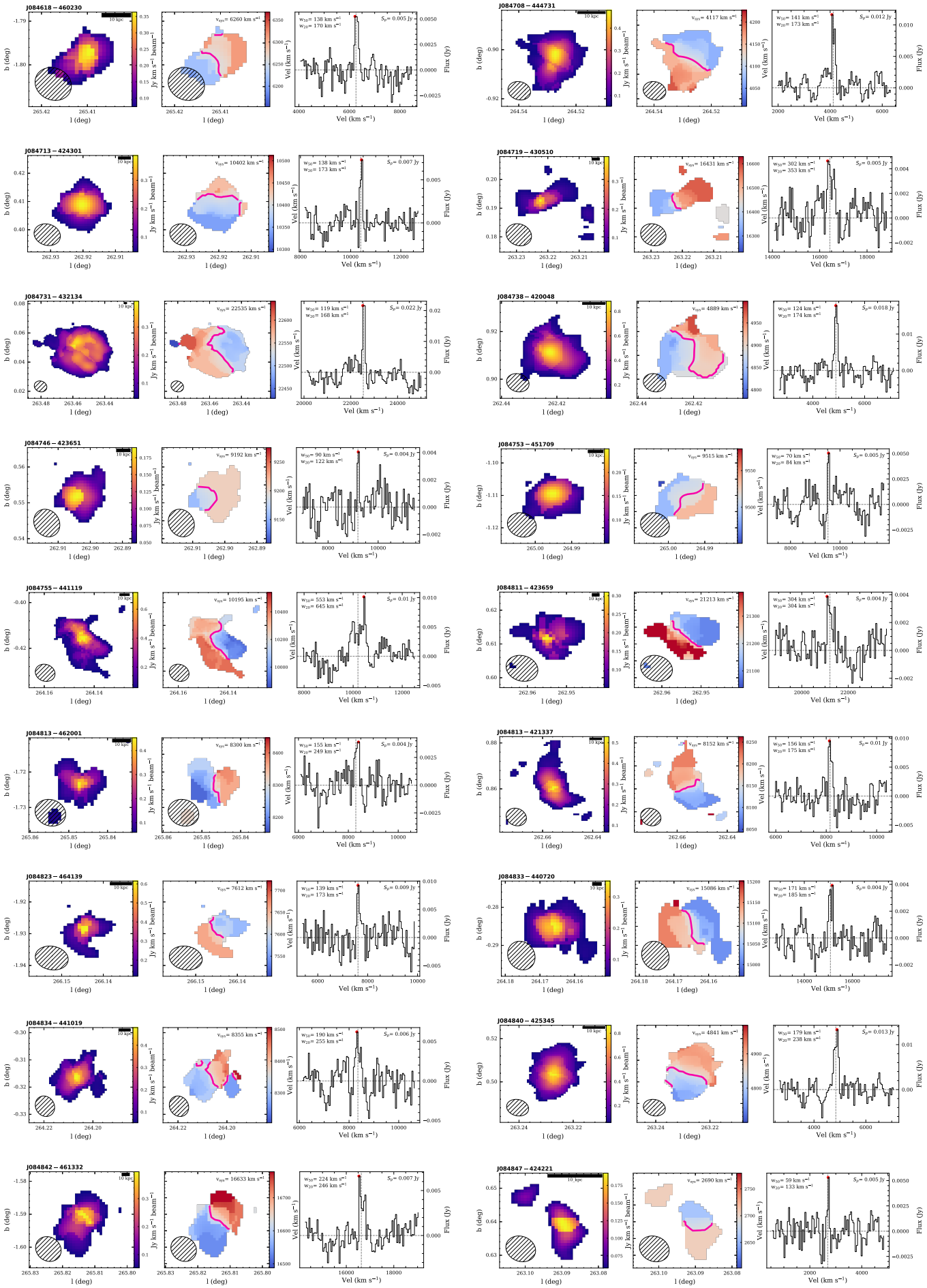
J084618 − 460230
J084708 − 444731
J084713 − 424301
J084719 − 430510
J084731 − 432134
J084738 − 420048
J084746 − 423651
J084753 − 451709
J084755 − 441119
J084811 − 423659
J084813 − 462001
J084813 − 421337
J084823 − 464139
J084833 − 440720
J084834 − 441019
J084840 − 425345
J084842 − 461332
J084847 − 424221
l (deg)
b (deg)
Vel (km s−1)
Flux (Jy)
Jy km s−1 beam−1

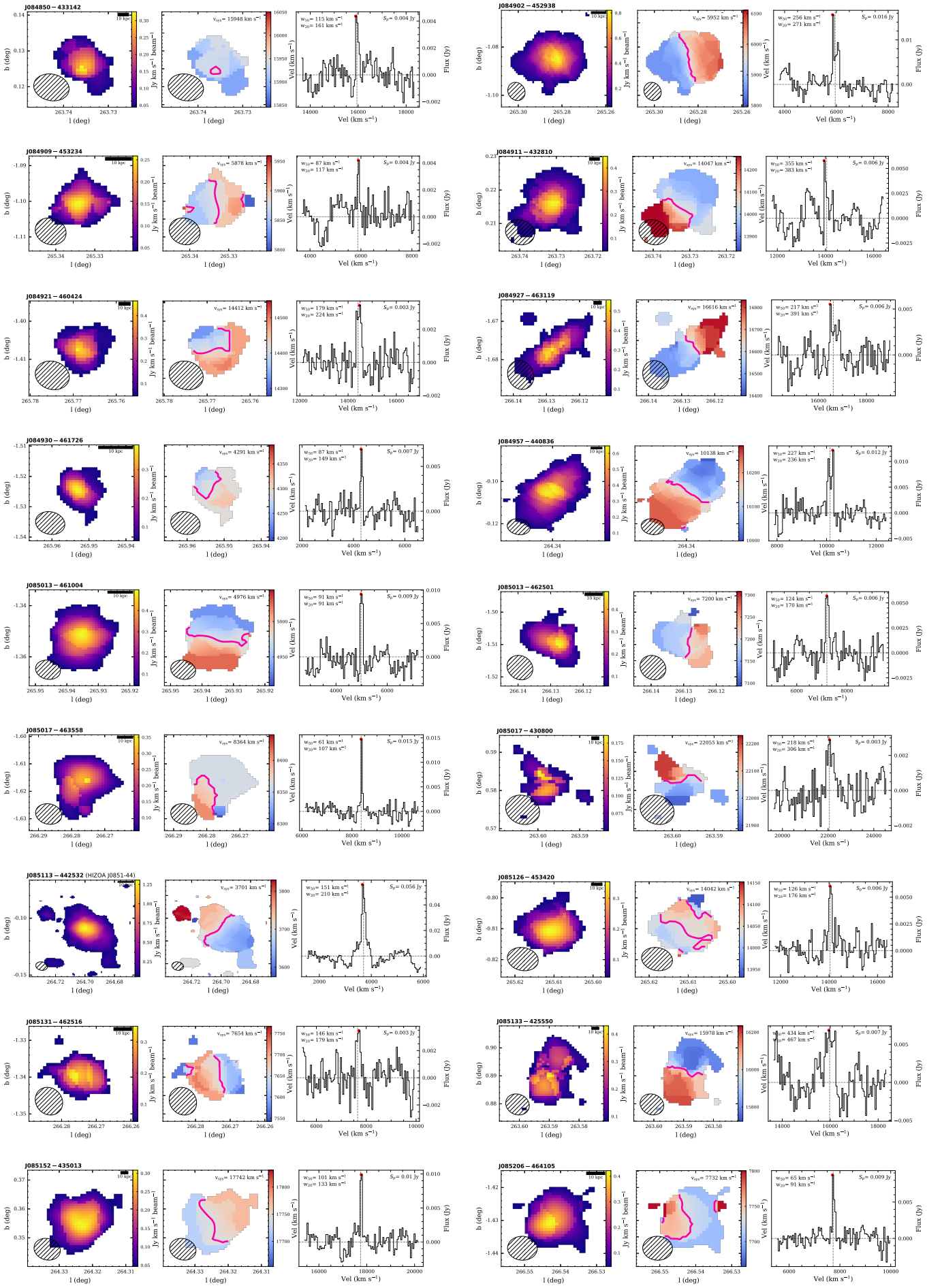
J084850 − 433142
J084902 − 452938
J084909 − 453234
J084911 − 432810
J084921 − 460424
J084927 − 463119
J084930 − 461726
J084957 − 440836
J085013 − 461004
J085013 − 462501
J085017 − 463558
J085017 − 430800
J085113 − 442532 (HIZOA J0851-44)
J085126 − 453420
J085131 − 462516
J085133 − 425550
J085152 − 435013
J085206 − 464105
b (deg)
l (deg)
Jy km s−1 beam−1
Vel (km s−1)
Flux (Jy)

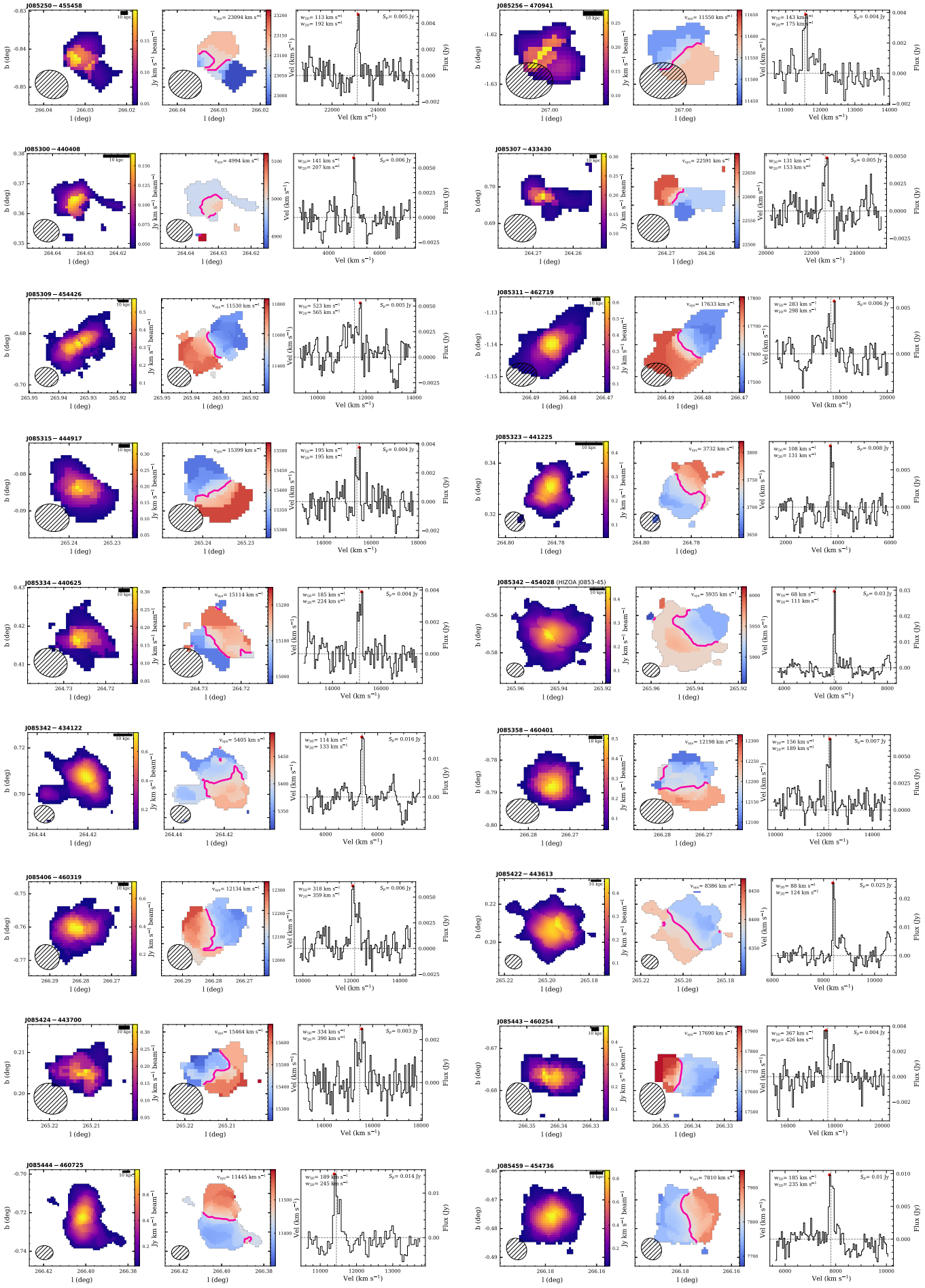
J085250 − 455458
J085256 − 470941
J085300 − 440408
J085307 − 433430
J085309 − 454426
J085311 − 462719
J085315 − 444917
J085323 − 441225
J085334 − 440625
J085342 − 460028 (HIZOA J0853-45)
J085342 − 434122
J085358 − 460401
J085406 − 460319
J085422 − 443613
J085424 − 443700
J085443 − 460254
J085444 − 460725
J085459 − 454736
l (deg)
b (deg)
Vel (km s−1)
Flux (Jy)
Jy km s−1 beam−1

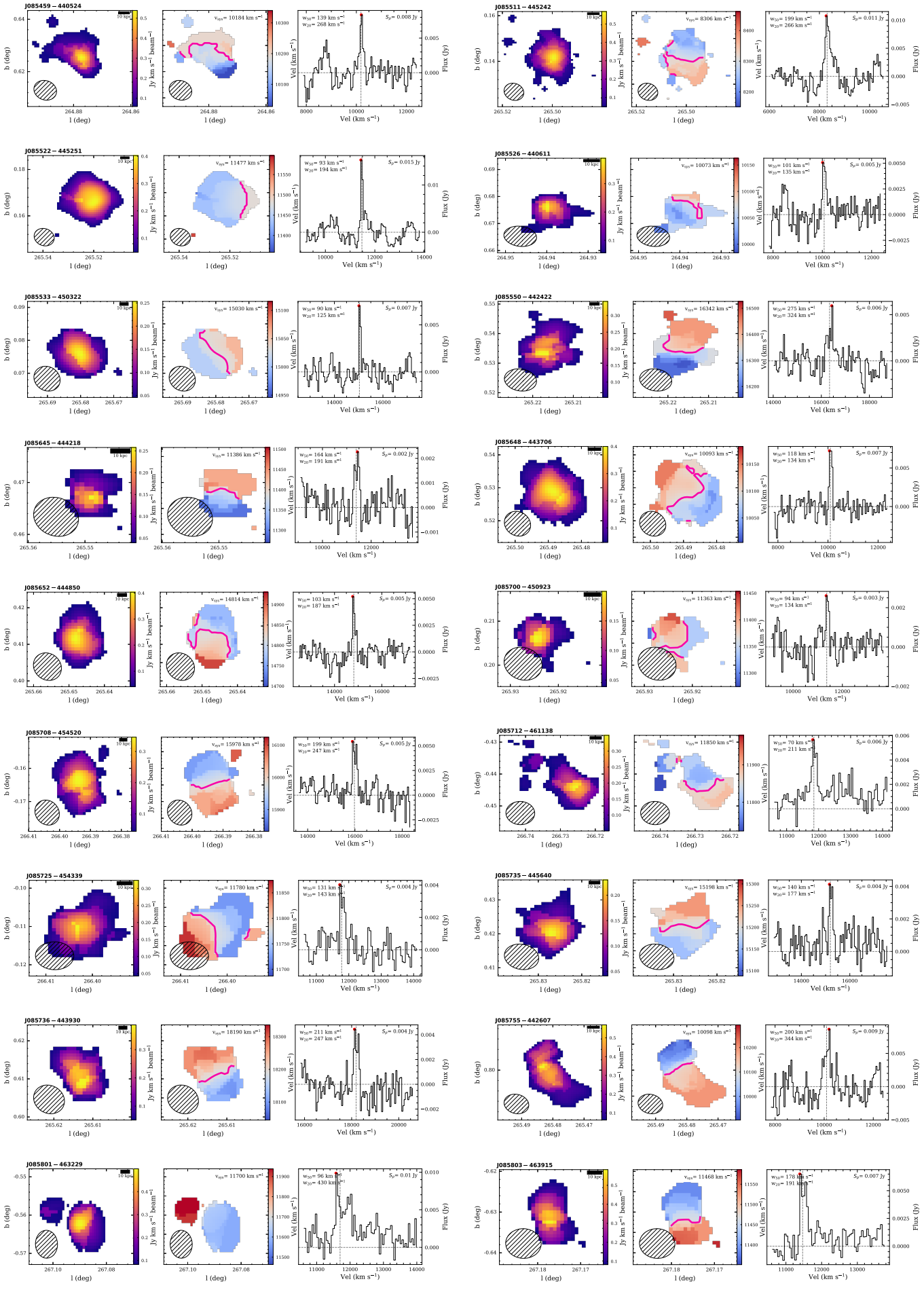
J085459 – 440524
J085511 – 445242
J085522 – 445251
J085526 – 440611
J085533 – 450322
J085550 – 442422
J085645 – 444218
J085648 – 443706
J085652 – 444850
J085700 – 450923
J085708 – 454520
J085712 – 461138
J085725 – 454339
J085735 – 445640
J085736 – 443930
J085755 – 442607
J085801 – 463229
J085803 – 463915
l (deg)
b (deg)
Vel (km s^{-1})
Flux (Jy)
Jy km s^{-1} beam^{-1}

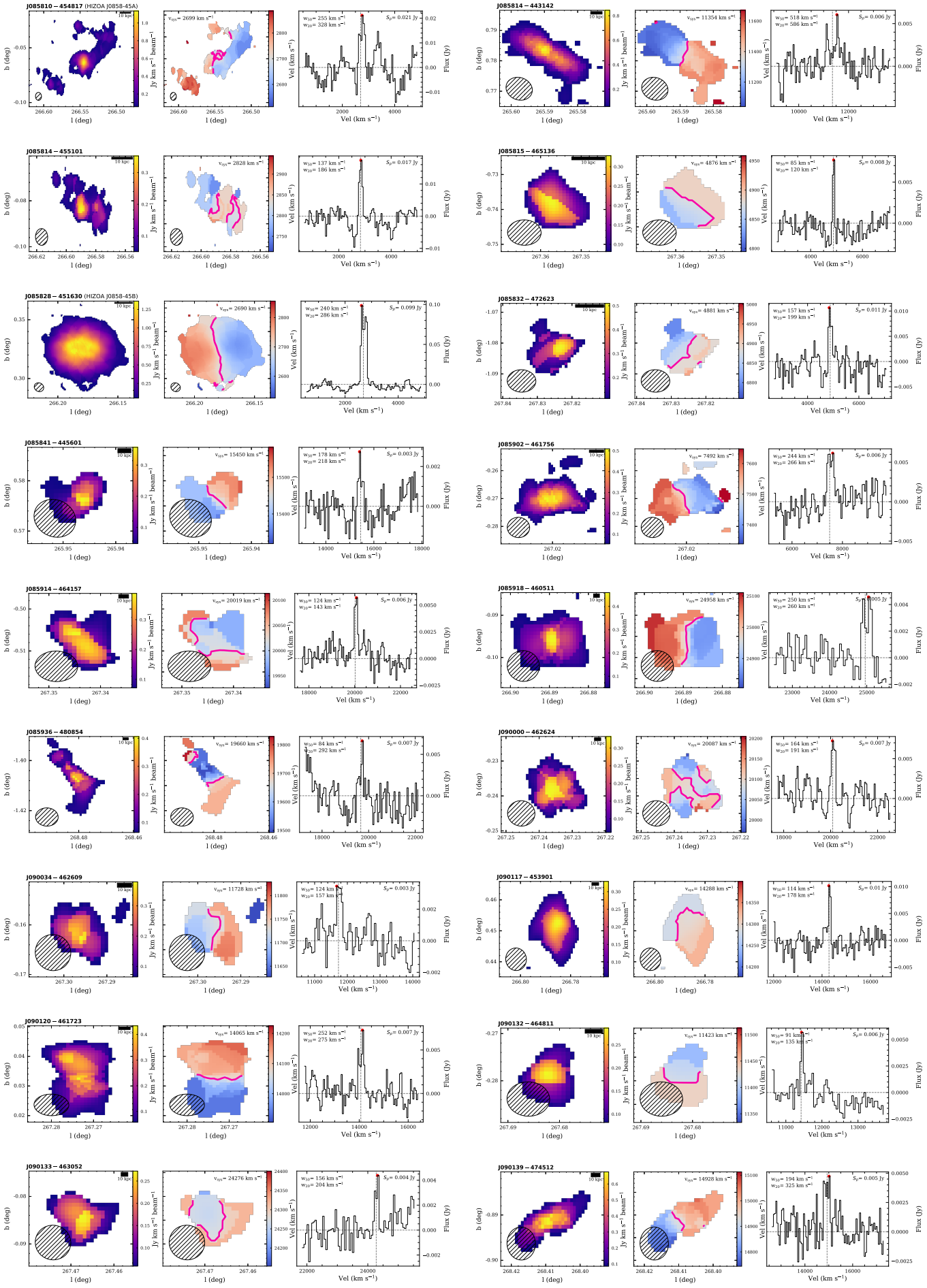
J085810 − 454817 (HIZOA J0858-45A)
J085814 − 443142
J085814 − 455101
J085815 − 465136
J085828 − 451630 (HIZOA J0858-45B)
J085832 − 472623
J085841 − 445601
J085902 − 461756
J085914 − 464157
J085918 − 460511
J085936 − 480854
J090000 − 462624
J090034 − 462609
J090117 − 453901
J090120 − 461723
J090132 − 464811
J090133 − 463052
J090139 − 474512
l (deg)
b (deg)
Vel (km s−1)
Flux (Jy)
Jy km s−1 beam−1
10 kpc

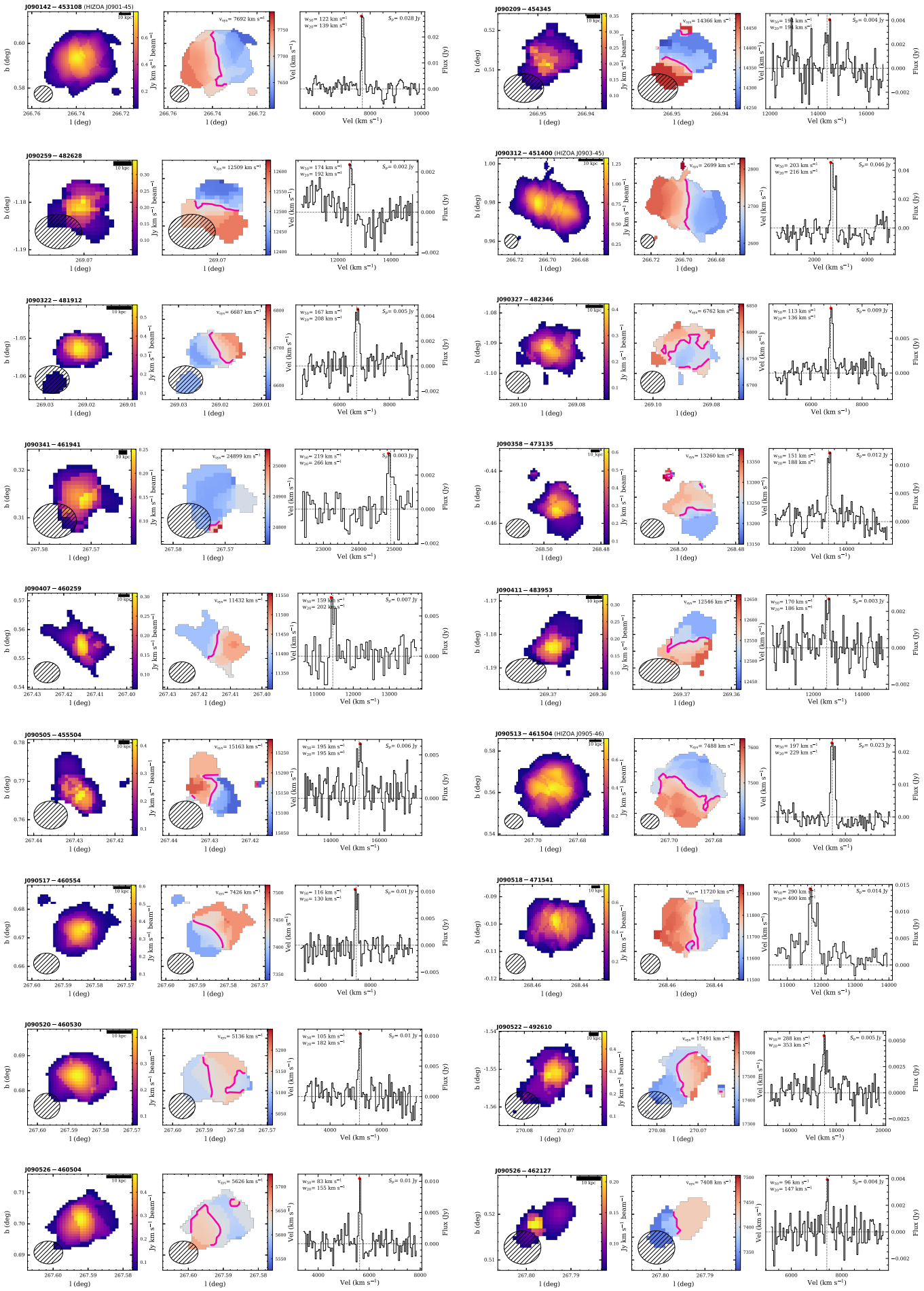
J090142 − 453108 (HIZOA J0901-45)
J090209 − 454345
J090259 − 482628
J090312 − 451400 (HIZOA J0903-45)
J090322 − 481912
J090327 − 482346
J090341 − 461941
J090358 − 473135
J090407 − 460259
J090411 − 483953
J090505 − 455504
J090513 − 461504 (HIZOA J0905-46)
J090517 − 460554
J090518 − 471541
J090520 − 460530
J090522 − 492610
J090526 − 460504
J090526 − 462127
l (deg)
b (deg)
Vel (km s−1)
Flux (Jy)
Jy km s−1 beam−1

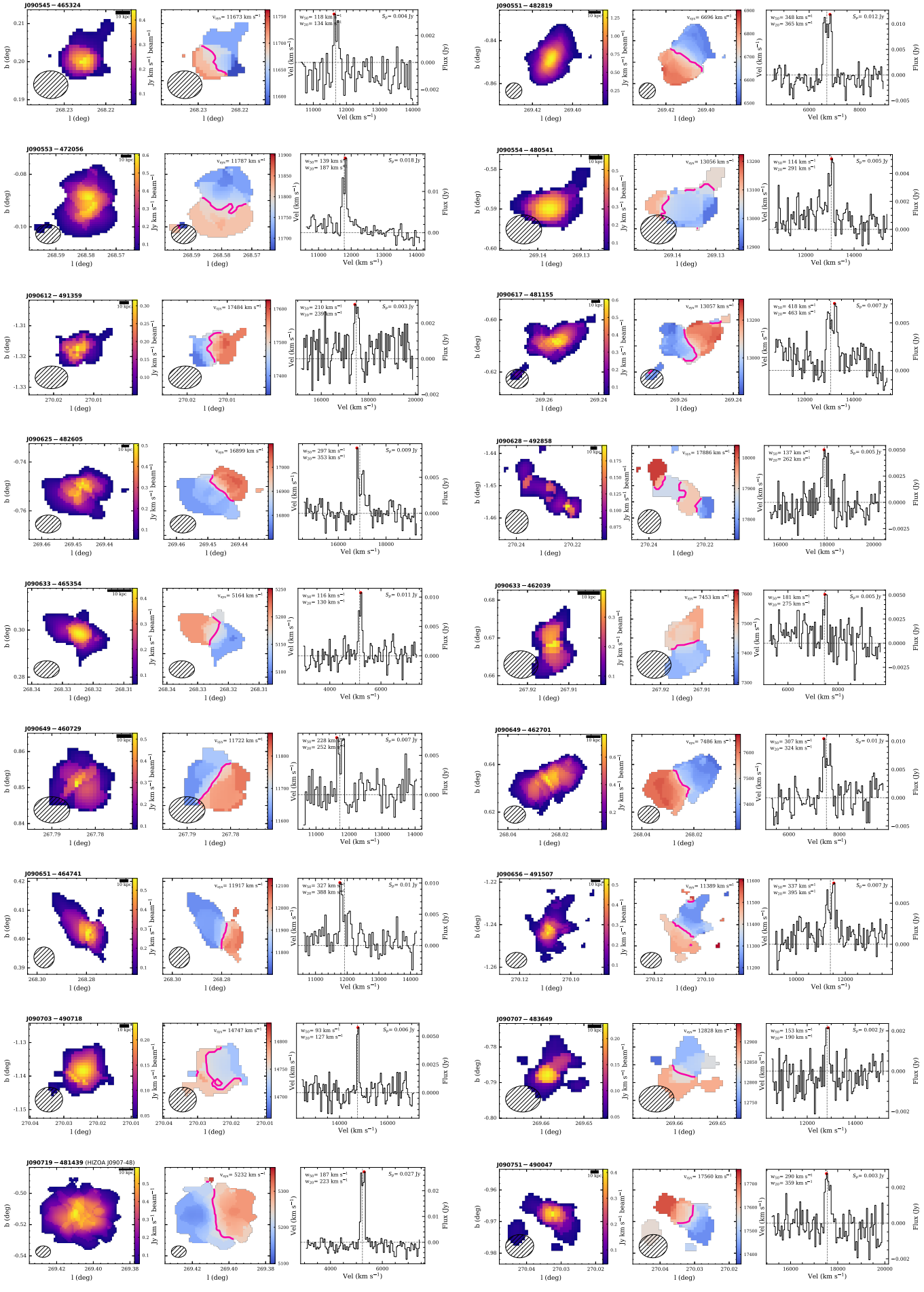
J090545 − 465324
J090551 − 482819
J090553 − 472056
J090554 − 480541
J090612 − 491359
J090617 − 481155
J090625 − 482605
J090628 − 492858
J090633 − 465354
J090633 − 462039
J090649 − 460729
J090649 − 462701
J090651 − 464741
J090656 − 491507
J090703 − 490718
J090707 − 483649
J090719 − 481439 (HIZOA J0907-48)
J090751 − 490047
l (deg)
b (deg)
Vel (km s−1)
Flux (Jy)
Jy km s−1 beam−1

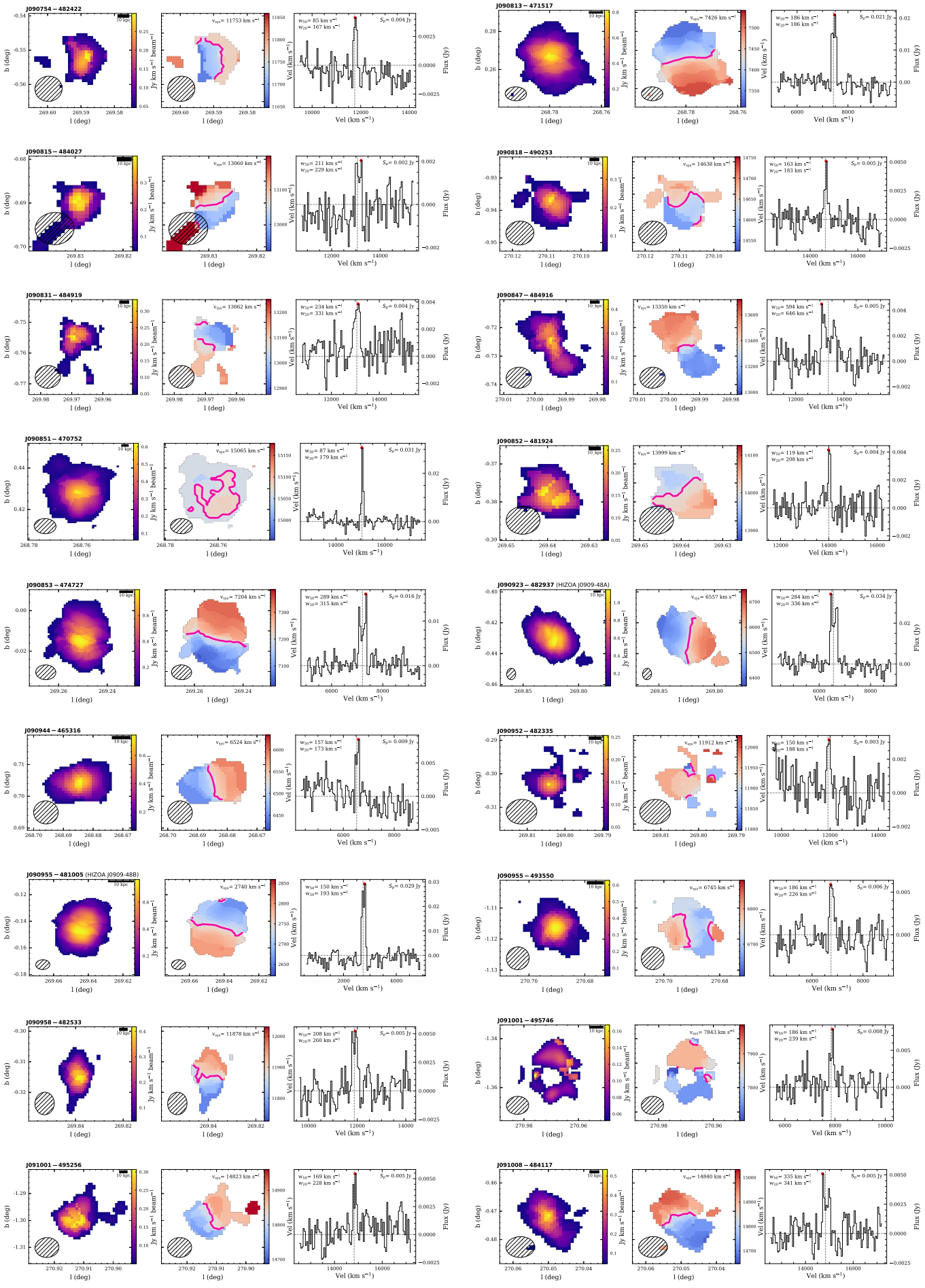
J090754 – 482422
J090813 – 471517
J090815 – 484027
J090818 – 490253
J090831 – 484919
J090847 – 484916
J090851 – 470752
J090852 – 481924
J090853 – 474727
J090923 – 482937 (HIZOA J0909-48A)
J090944 – 465316
J090952 – 482335
J090955 – 481005 (HIZOA J0909-48B)
J090955 – 493550
J090958 – 482533
J091001 – 495746
J091001 – 495256
J091008 – 484117
l (deg)
b (deg)
Vel (km s−1)
Flux (Jy)
Jy km s−1 beam−1
10 kpc

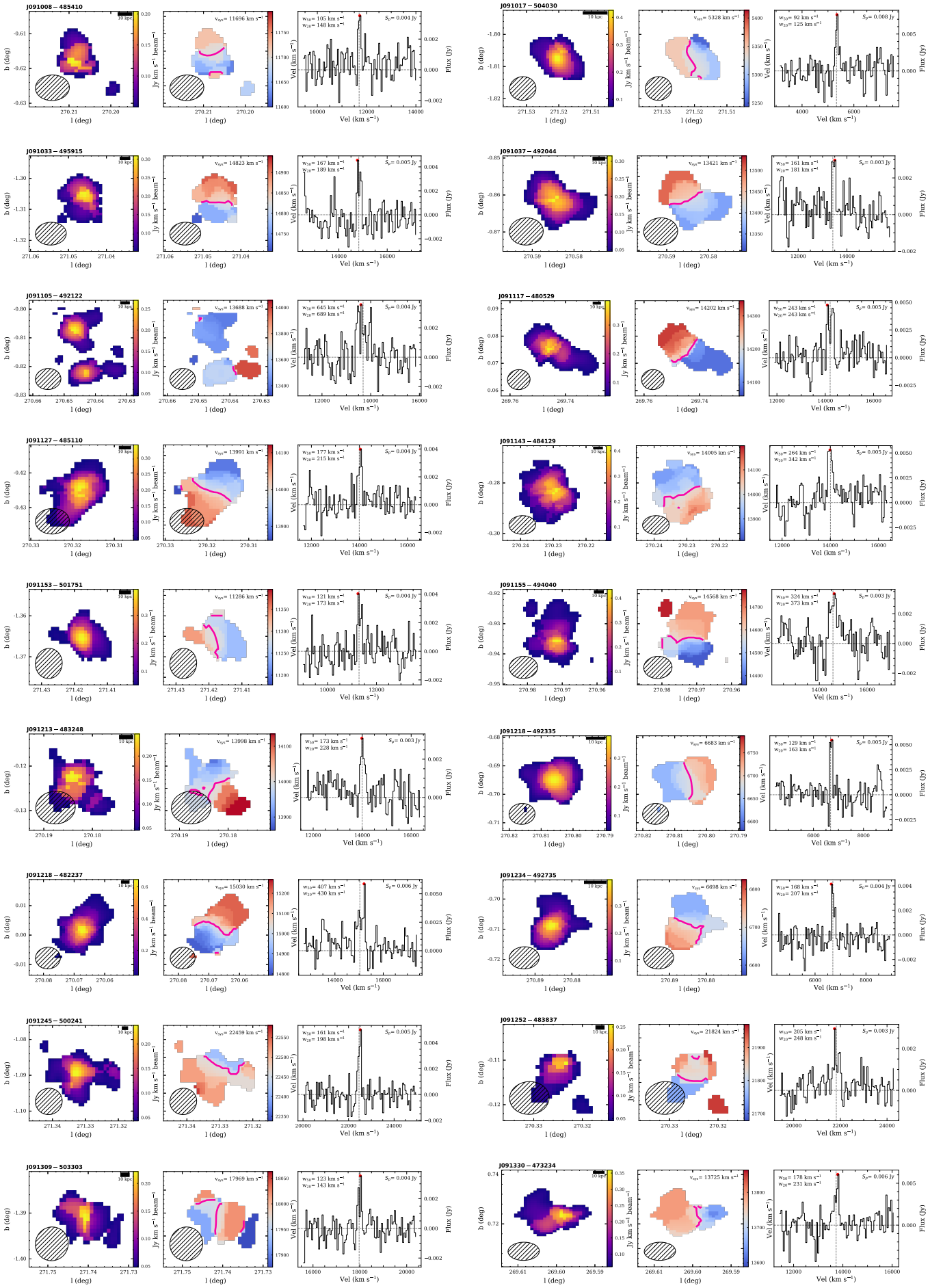
J091008 − 485410
J091017 − 504030
J091033 − 495915
J091037 − 492044
J091105 − 492122
J091117 − 480529
J091127 − 485110
J091143 − 484129
J091153 − 501751
J091155 − 494040
J091213 − 483248
J091218 − 492335
J091218 − 482237
J091234 − 492735
J091245 − 500241
J091252 − 483837
J091309 − 503303
J091330 − 473234
l (deg)
b (deg)
Vel (km s−1)
Flux (Jy)
Jy km s−1 beam−1

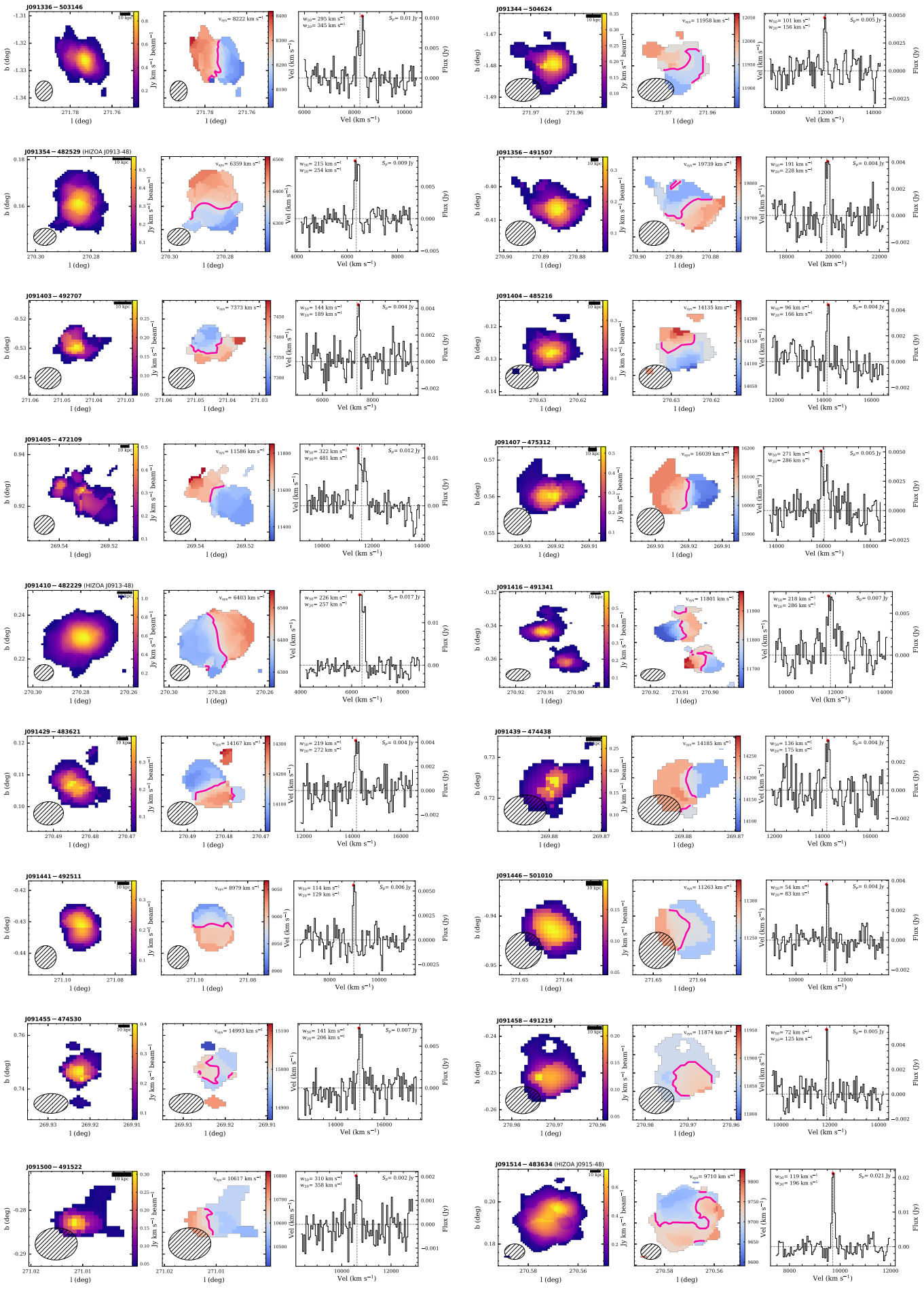
J091336 − 503146
J091344 − 504624
J091354 − 482529 (HIZOA J0913-48)
J091356 − 491507
J091403 − 492707
J091404 − 485216
J091405 − 472109
J091407 − 475312
J091410 − 482229 (HIZOA J0913-48)
J091416 − 491341
J091429 − 483621
J091439 − 474438
J091441 − 492511
J091446 − 501010
J091455 − 474530
J091458 − 491219
J091500 − 491522
J091514 − 483634 (HIZOA J0915-48)
l (deg)
b (deg)
Vel (km s−1)
Flux (Jy)
Jy km s−1 beam−1

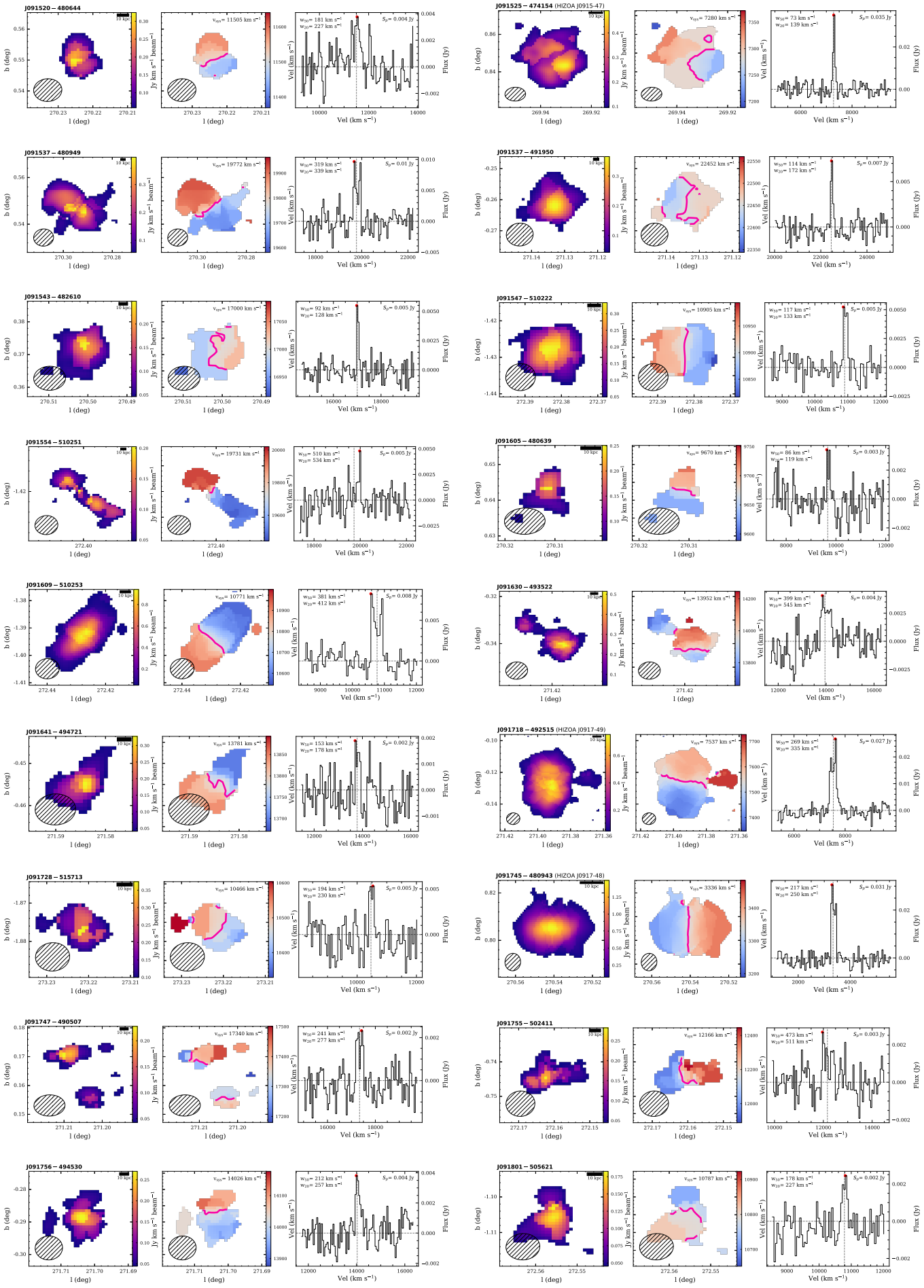
J091520 – 480644
J091525 – 474154 (HIZOA J0915-47)
J091537 – 480949
J091537 – 491950
J091543 – 482610
J091547 – 510222
J091554 – 510251
J091605 – 480639
J091609 – 510253
J091630 – 493522
J091641 – 494721
J091718 – 492515 (HIZOA J0917-49)
J091728 – 515713
J091745 – 480943 (HIZOA J0917-48)
J091747 – 490507
J091755 – 502411
J091756 – 494530
J091801 – 505621
l (deg)
b (deg)
Vel (km s−1)
Flux (Jy)
Jy km s−1 beam−1
10 kpc

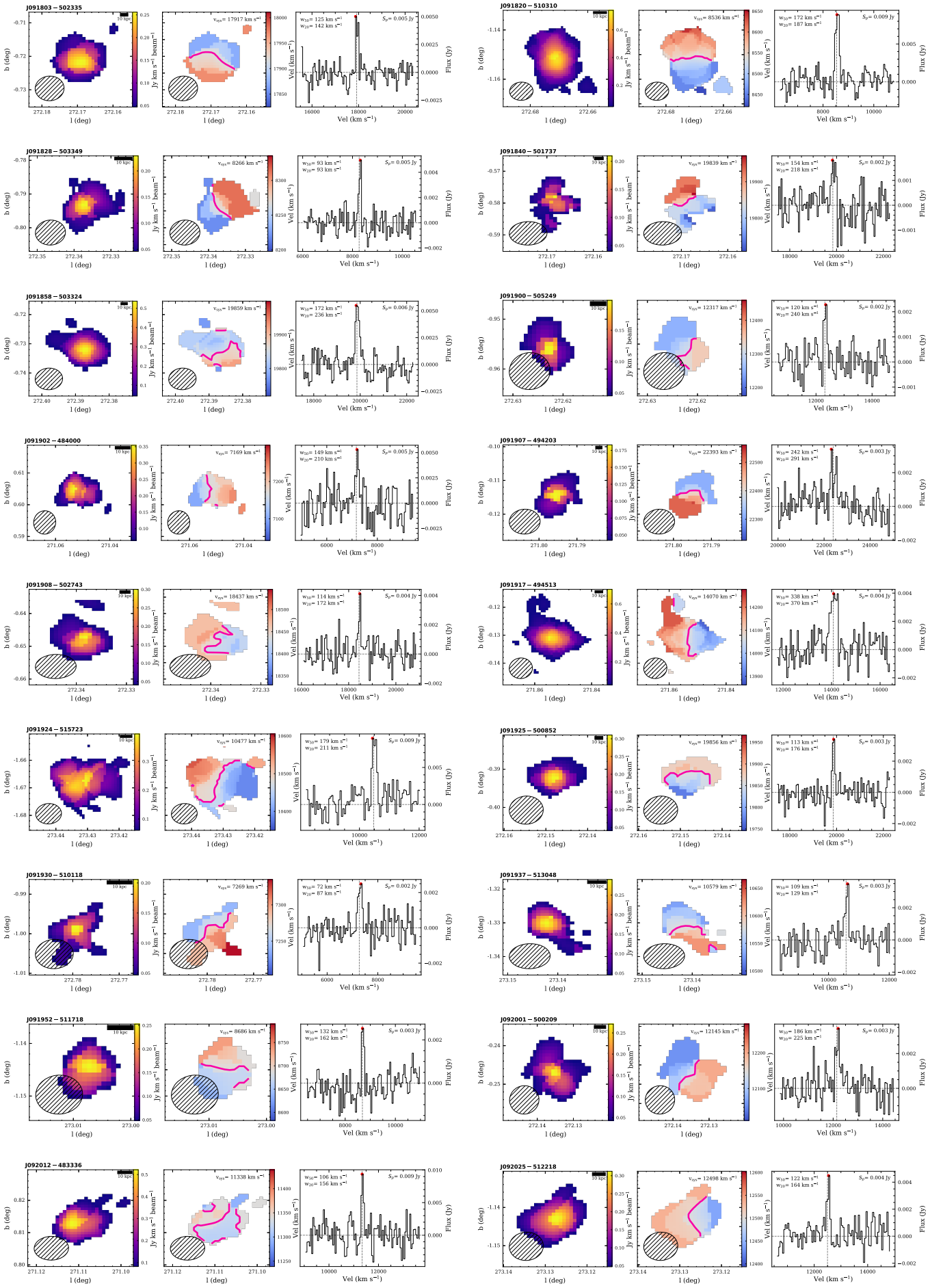
J091803 − 502335
J091820 − 510310
J091828 − 503349
J091840 − 501737
J091858 − 503324
J091900 − 505249
J091902 − 484000
J091907 − 494203
J091908 − 502743
J091917 − 494513
J091924 − 515723
J091925 − 500852
J091930 − 510118
J091937 − 513048
J091952 − 511718
J092001 − 500209
J092012 − 483336
J092025 − 512218
l (deg)
b (deg)
Vel (km s−1)
Flux (Jy)
Jy km s−1 beam−1
10 kpc

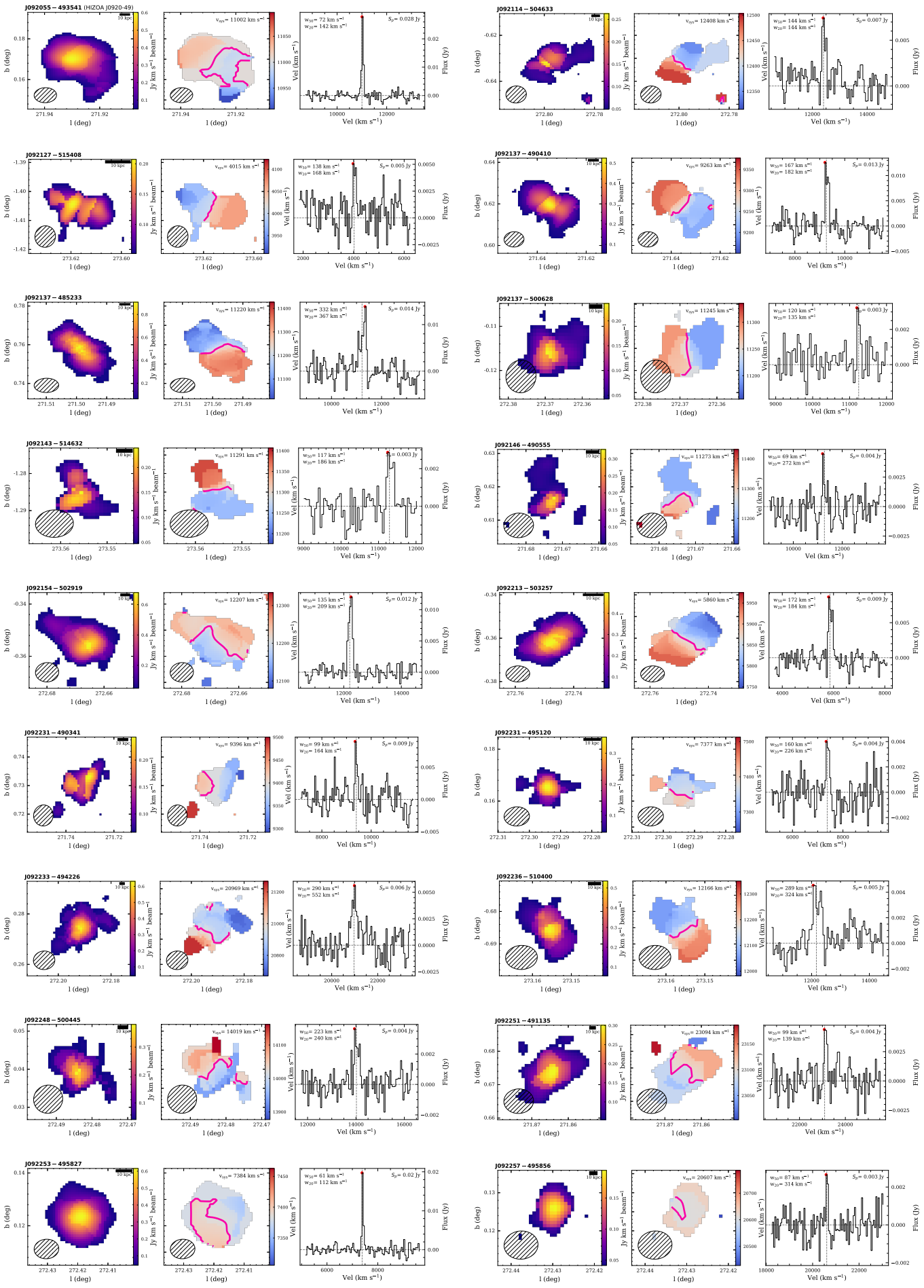
J092055 − 493541 (HIZOA J0920-49)
J092114 − 504633
J092127 − 515408
J092137 − 490410
J092137 − 485233
J092137 − 500628
J092143 − 514632
J092146 − 490555
J092154 − 502919
J092213 − 503257
J092231 − 490341
J092231 − 495120
J092233 − 494226
J092236 − 510400
J092248 − 500445
J092251 − 491135
J092253 − 495827
J092257 − 495856
l (deg)
b (deg)
Vel (km s−1)
Flux (Jy)
Jy km s−1 beam−1
10 kpc

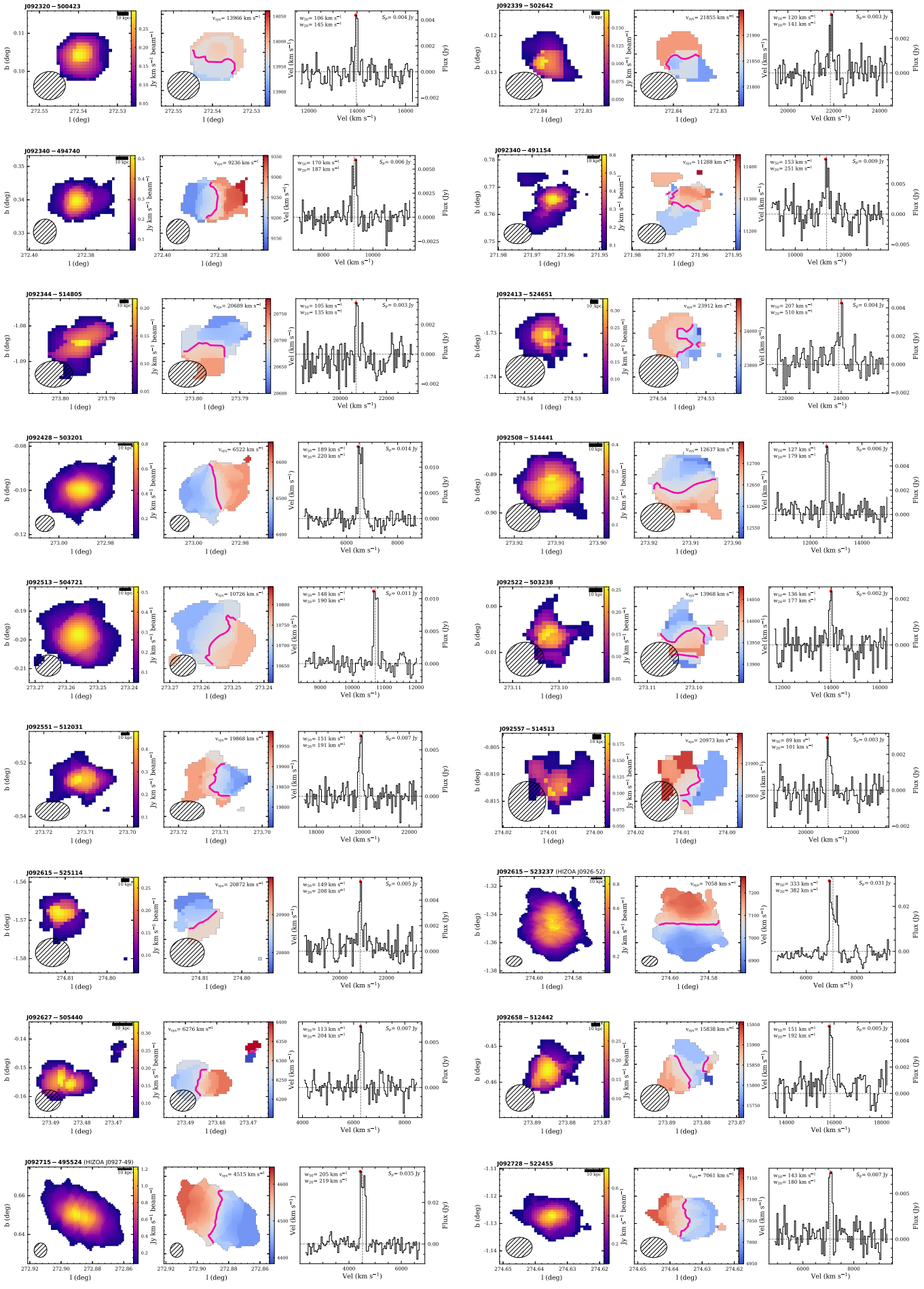
J092320 − 500423
J092339 − 502642
J092340 − 494740
J092340 − 491154
J092344 − 514805
J092413 − 524651
J092428 − 503201
J092508 − 514441
J092513 − 504721
J092522 − 503238
J092551 − 512031
J092557 − 514513
J092615 − 525114
J092615 − 523237 (HIZOA J0926-52)
J092627 − 505440
J092658 − 512442
J092715 − 495524 (HIZOA J0927-49)
J092728 − 522455
l (deg)
b (deg)
Vel (km s−1)
Flux (Jy)
Jy km s−1 beam−1

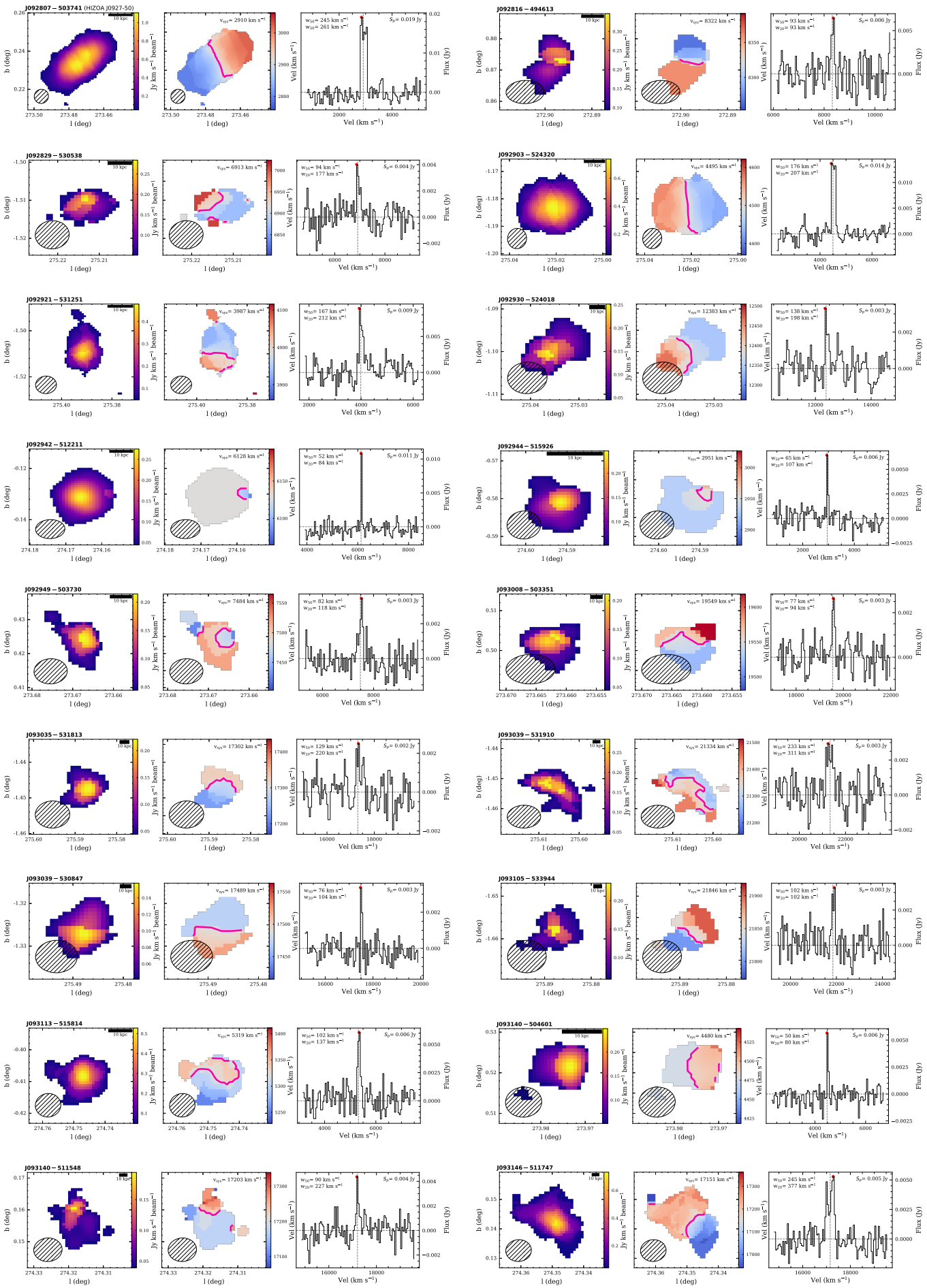
J092807 − 503741 (HIZOA J0927-50)
J092816 − 494613
J092829 − 530538
J092903 − 524320
J092921 − 531251
J092930 − 524018
J092942 − 512211
J092944 − 515926
J092949 − 503730
J093008 − 503351
J093035 − 531813
J093039 − 531910
J093039 − 530847
J093105 − 533944
J093113 − 515814
J093140 − 504601
J093140 − 511548
J093146 − 511747
l (deg)
b (deg)
Vel (km s−1)
Flux (Jy)
Jy km s−1 beam−1
10 kpc

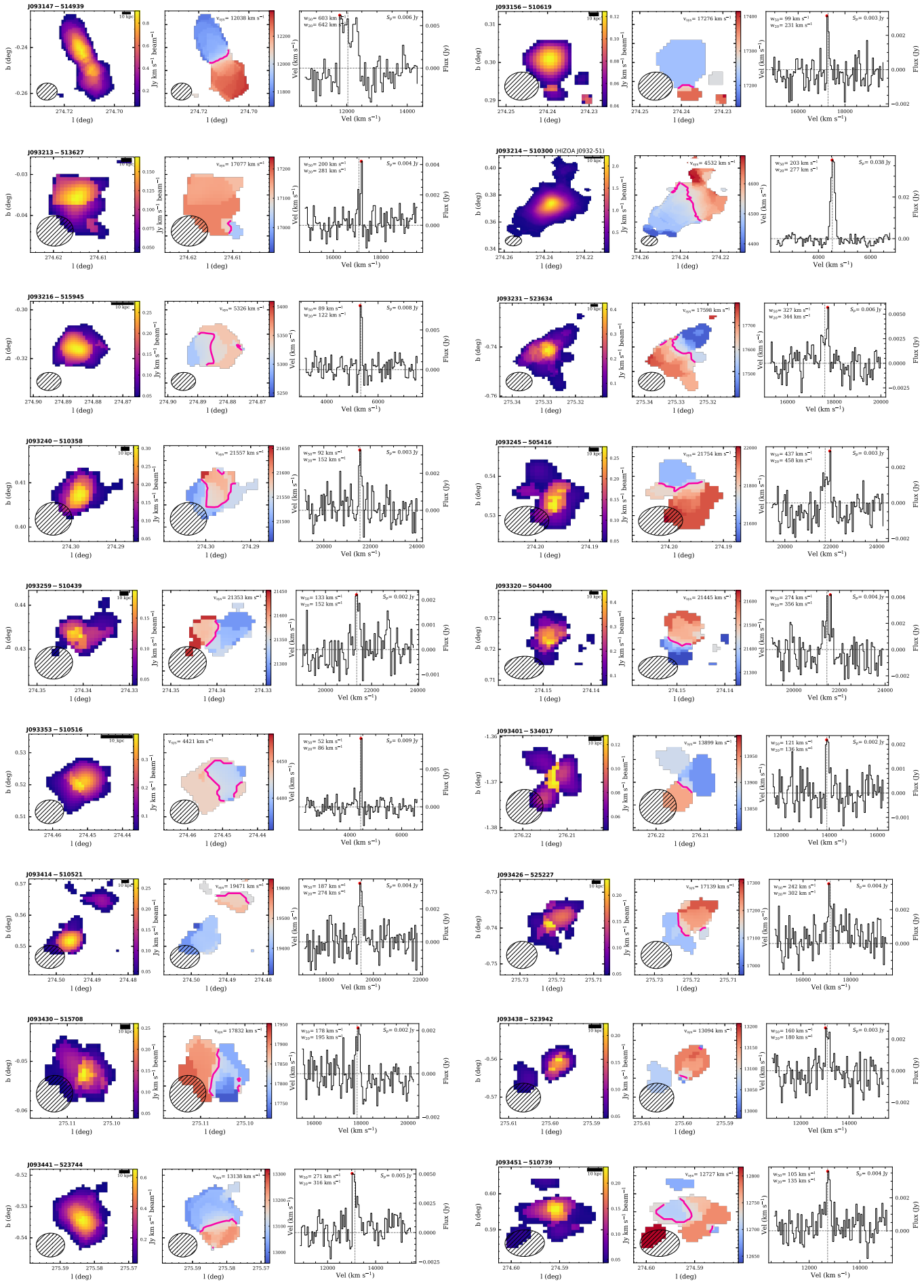
J093147 − 514939
J093156 − 510619
J093213 − 513627
J093214 − 510300 (HIZOA J0932-51)
J093216 − 515945
J093231 − 523634
J093240 − 510358
J093245 − 505416
J093259 − 510439
J093320 − 504400
J093353 − 510516
J093401 − 534017
J093414 − 510521
J093426 − 525227
J093430 − 515708
J093438 − 523942
J093441 − 523744
J093451 − 510739
l (deg)
b (deg)
Vel (km s−1)
Flux (Jy)
Jy km s−1 beam−1

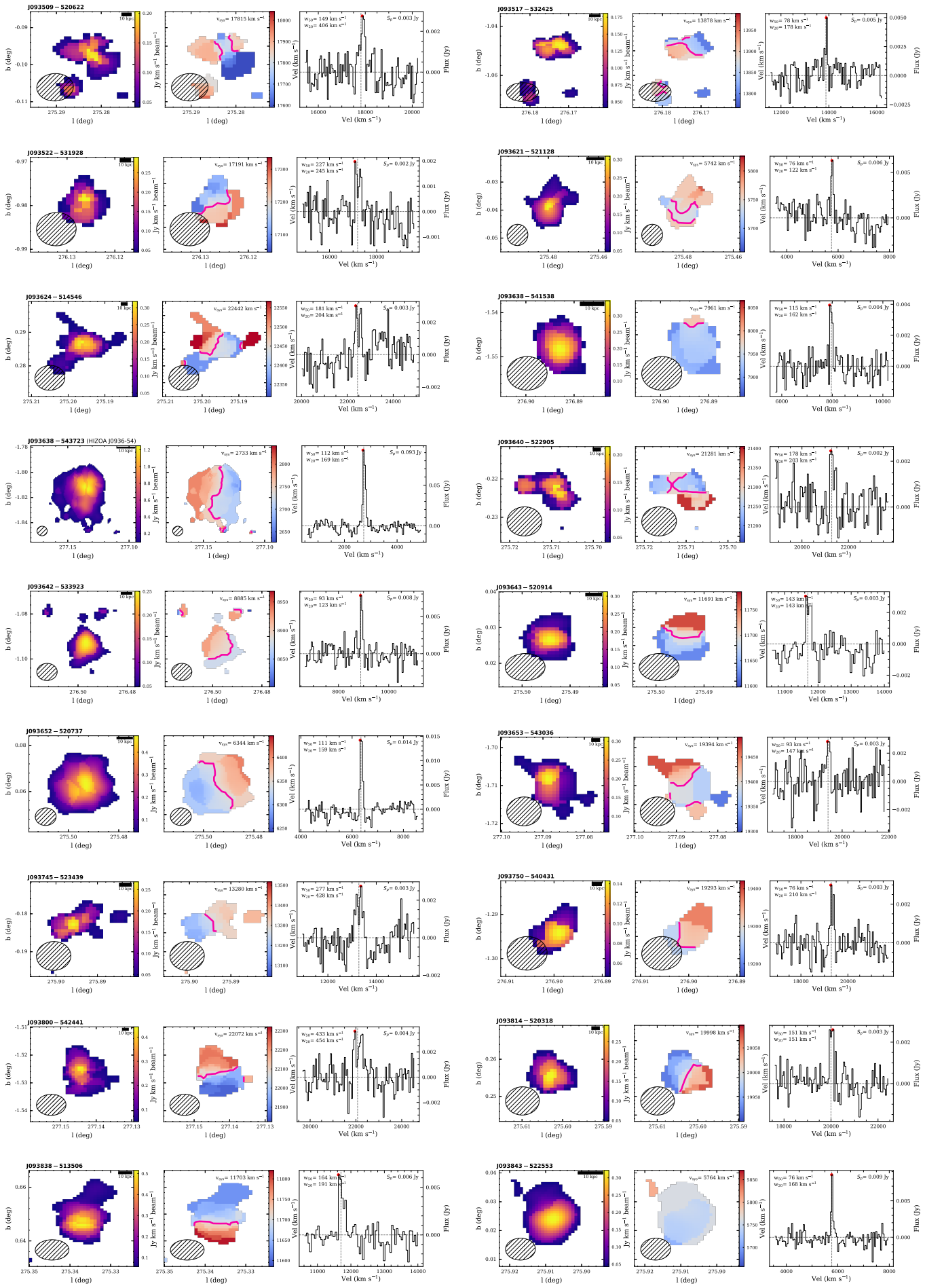
J093509 − 520622
J093517 − 532425
J093522 − 531928
J093621 − 521128
J093624 − 514546
J093638 − 541538
J093638 − 543723 (HIZOA J0936-54)
J093640 − 522905
J093642 − 533923
J093643 − 520914
J093652 − 520737
J093653 − 543036
J093745 − 523439
J093750 − 540431
J093800 − 542441
J093814 − 520318
J093838 − 513506
J093843 − 522553
l (deg)
b (deg)
Vel (km s−1)
Flux (Jy)
Jy km s−1 beam−1

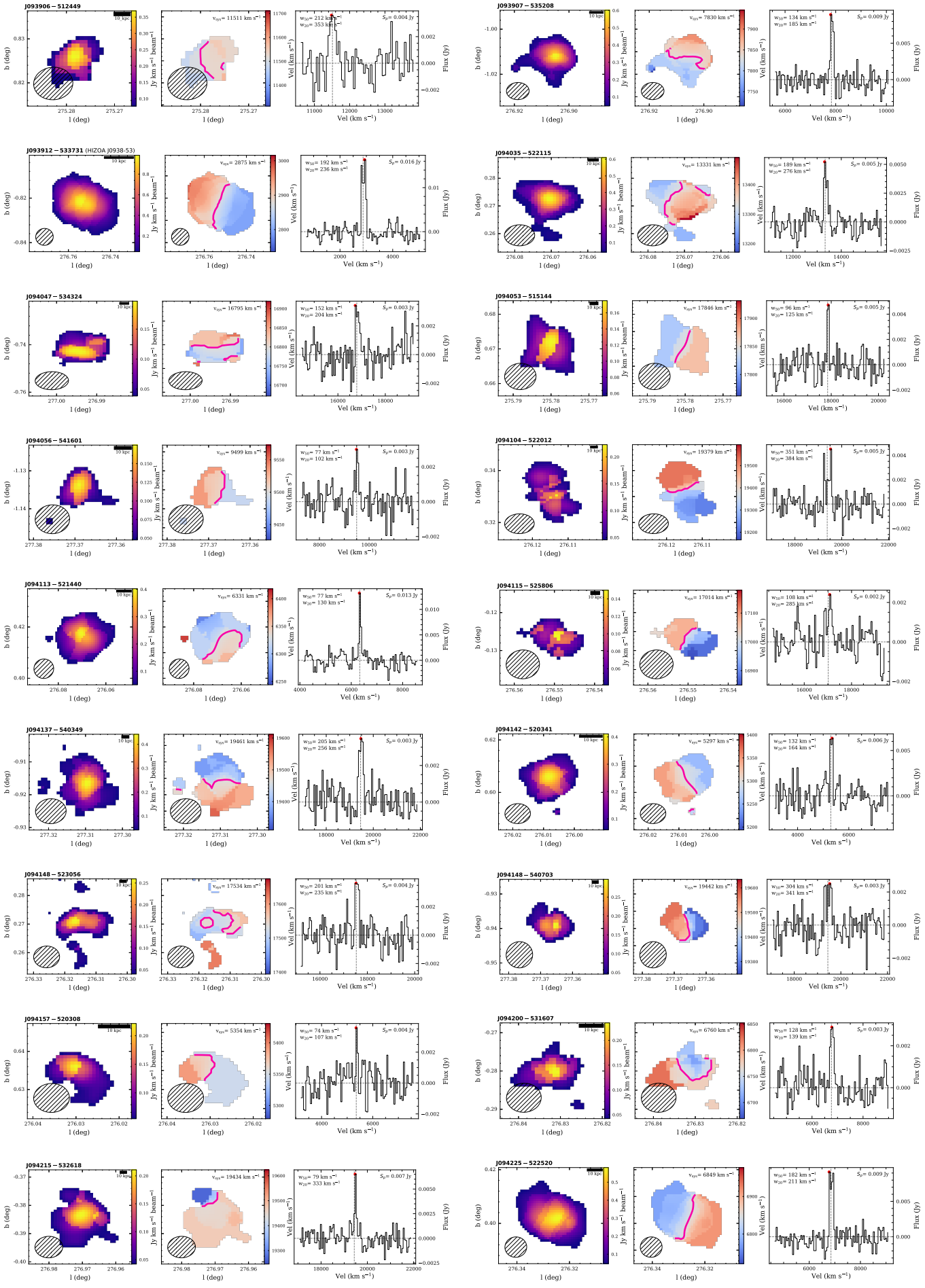
J093906 − 512449
J093907 − 535208
J093912 − 533731 (HIZOA J0938-53)
J094035 − 522115
J094047 − 534324
J094053 − 515144
J094056 − 541601
J094104 − 522012
J094113 − 521440
J094115 − 525806
J094137 − 540349
J094142 − 520341
J094148 − 523056
J094148 − 540703
J094157 − 520308
J094200 − 531607
J094215 − 532618
J094225 − 522520
l (deg)
b (deg)
Vel (km s−1)
Flux (Jy)
Jy km s−1 beam−1
10 kpc

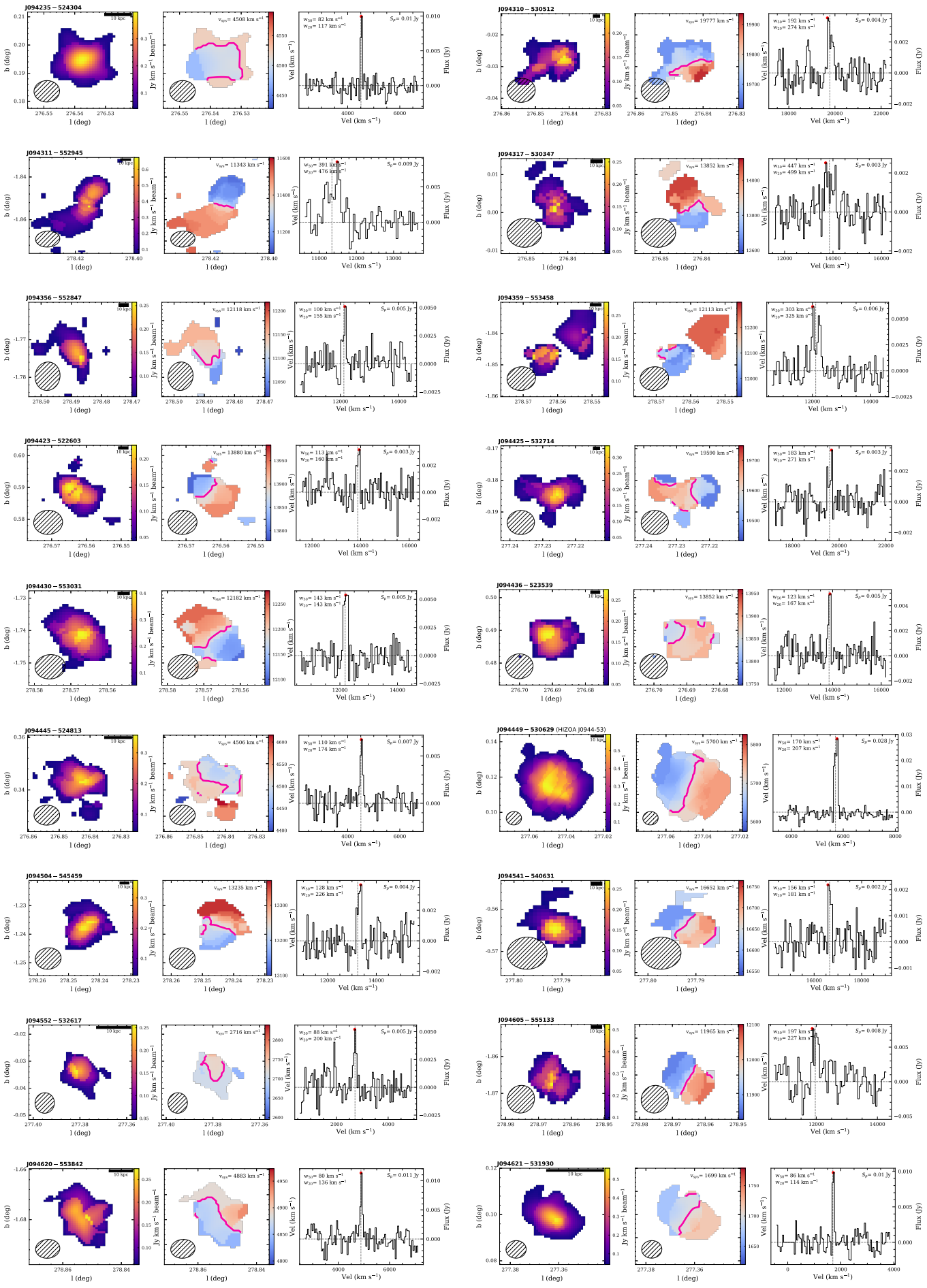
J094235 − 524304
J094310 − 530512
J094311 − 552945
J094317 − 530347
J094356 − 552847
J094359 − 553458
J094423 − 522603
J094425 − 532714
J094430 − 553031
J094436 − 523539
J094445 − 524813
J094449 − 530629 (HIZOA J0944-53)
J094504 − 545459
J094541 − 540631
J094552 − 532617
J094605 − 555133
J094620 − 553842
J094621 − 531930
l (deg)
b (deg)
Vel (km s−1)
Flux (Jy)
Jy km s−1 beam−1
10 kpc

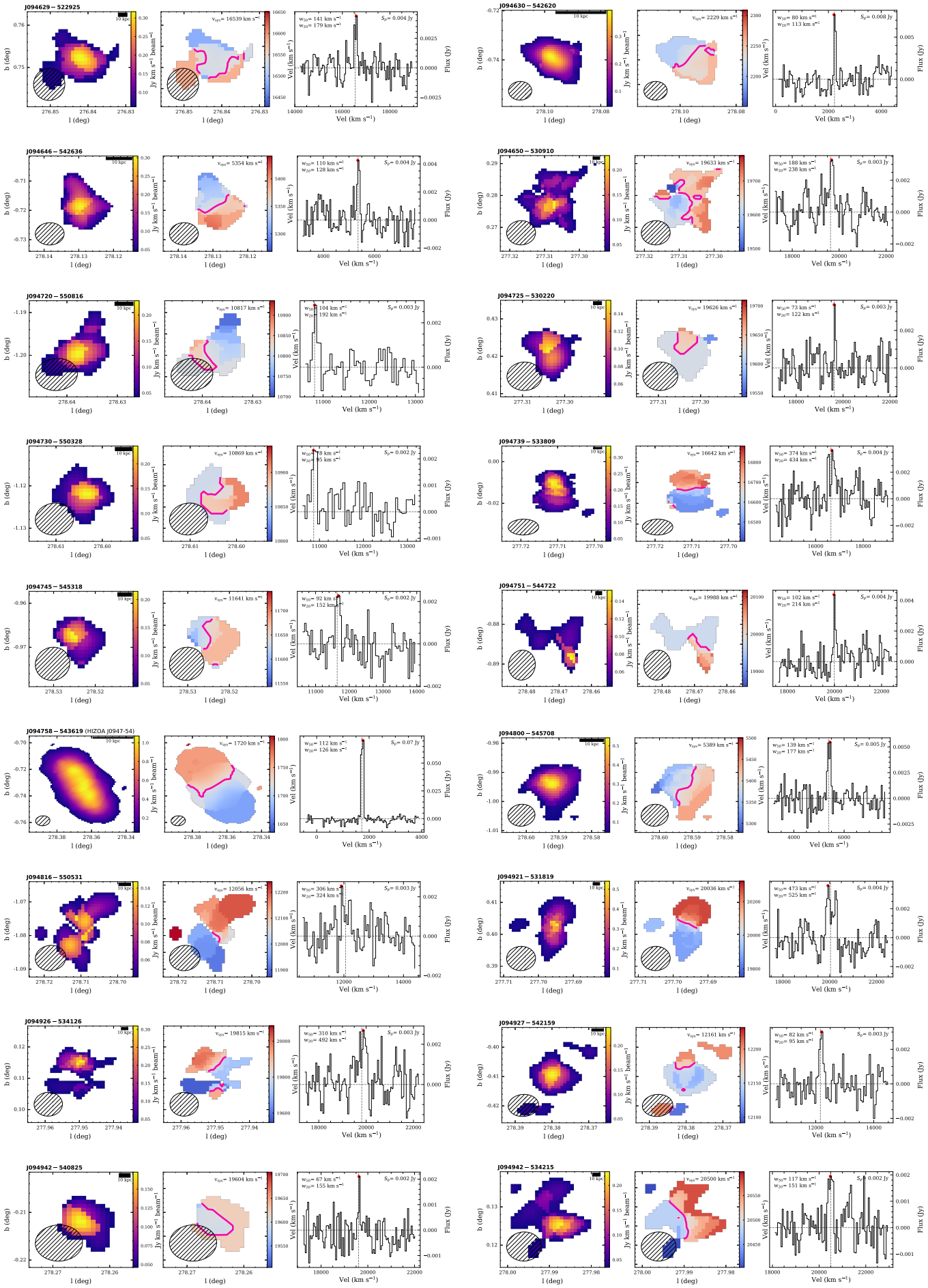
J094629−522925
J094630−542620
J094646−542636
J094650−530910
J094720−550816
J094725−530220
J094730−550328
J094739−533809
J094745−545318
J094751−544722
J094758−543619 (HIZOA J0947-54)
J094800−545708
J094816−550531
J094921−531819
J094926−534126
J094927−542159
J094942−540825
J094942−534215
l (deg)
b (deg)
Vel (km s−1)
Flux (Jy)
Jy km s−1 beam−1
10 kpc

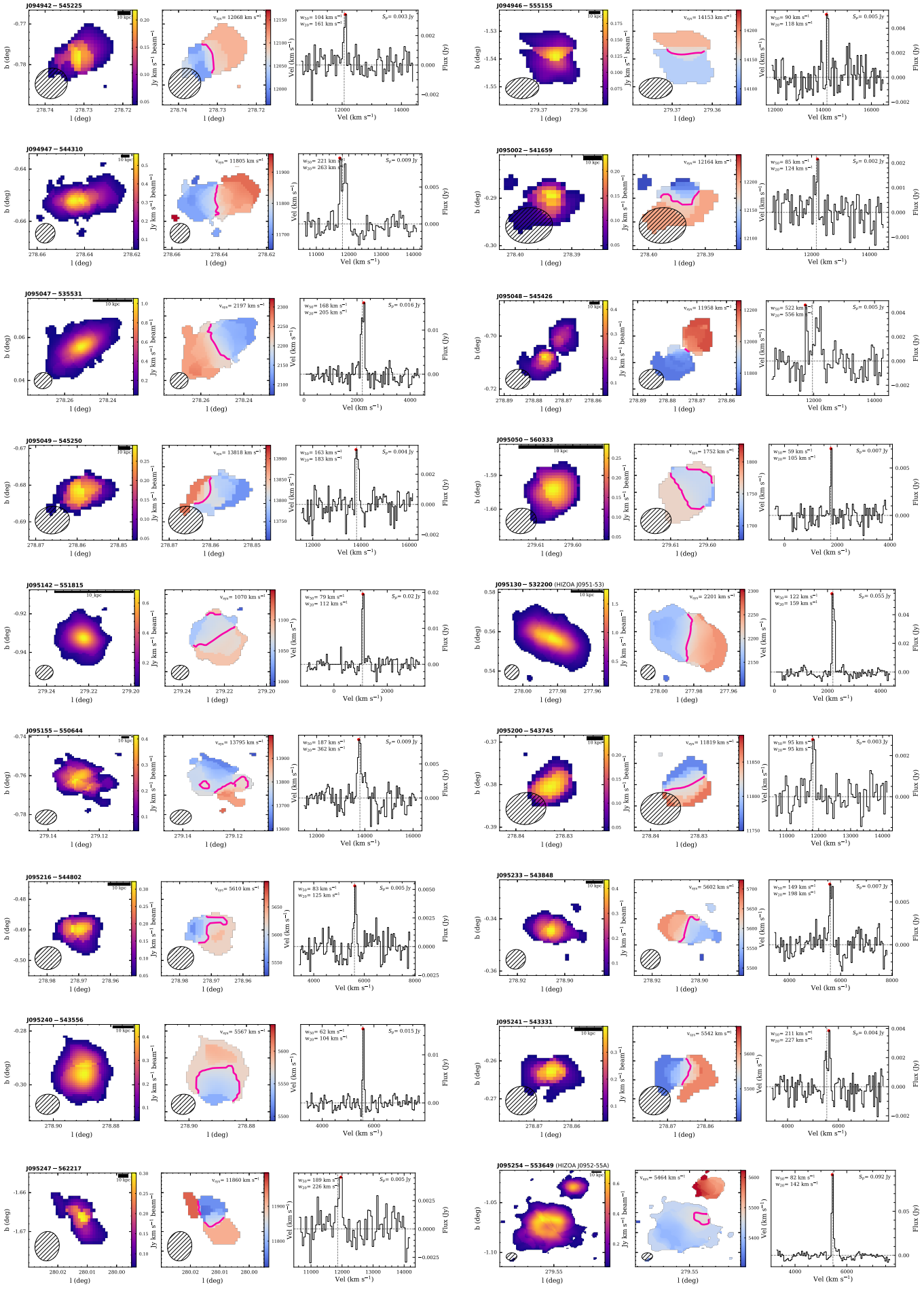
J094942 − 545225
J094946 − 555155
J094947 − 544310
J095002 − 541659
J095047 − 535531
J095048 − 545426
J095049 − 545250
J095050 − 560333
J095142 − 551815
J095130 − 532200 (HIZOA J0951-53)
J095155 − 550644
J095200 − 543745
J095216 − 544802
J095233 − 543848
J095240 − 543556
J095241 − 543331
J095247 − 562217
J095254 − 553649 (HIZOA J0952-55A)
l (deg)
b (deg)
Vel (km s−1)
Flux (Jy)
Jy km s−1 beam−1
10 kpc

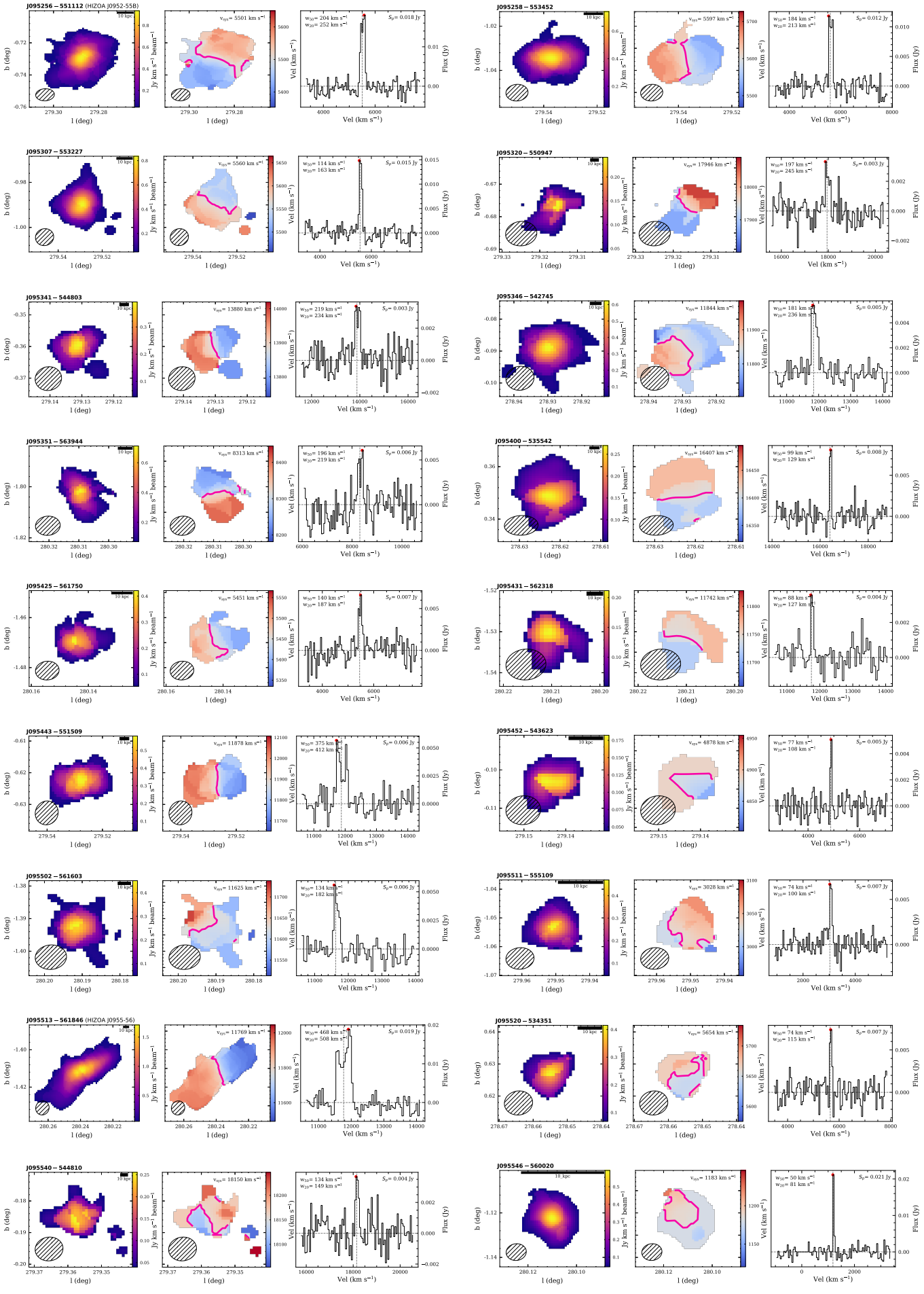
J095256 − 551112 (HIZOA J0952-55B)
J095258 − 553452
J095307 − 553227
J095320 − 550947
J095341 − 544803
J095346 − 542745
J095351 − 563944
J095400 − 535542
J095425 − 561750
J095431 − 562318
J095443 − 551509
J095452 − 543623
J095502 − 561603
J095511 − 555109
J095513 − 561846 (HIZOA J0955-56)
J095520 − 534351
J095540 − 544810
J095546 − 560020
l (deg)
b (deg)
Vel (km s−1)
Flux (Jy)
Jy km s−1 beam−1
10 kpc

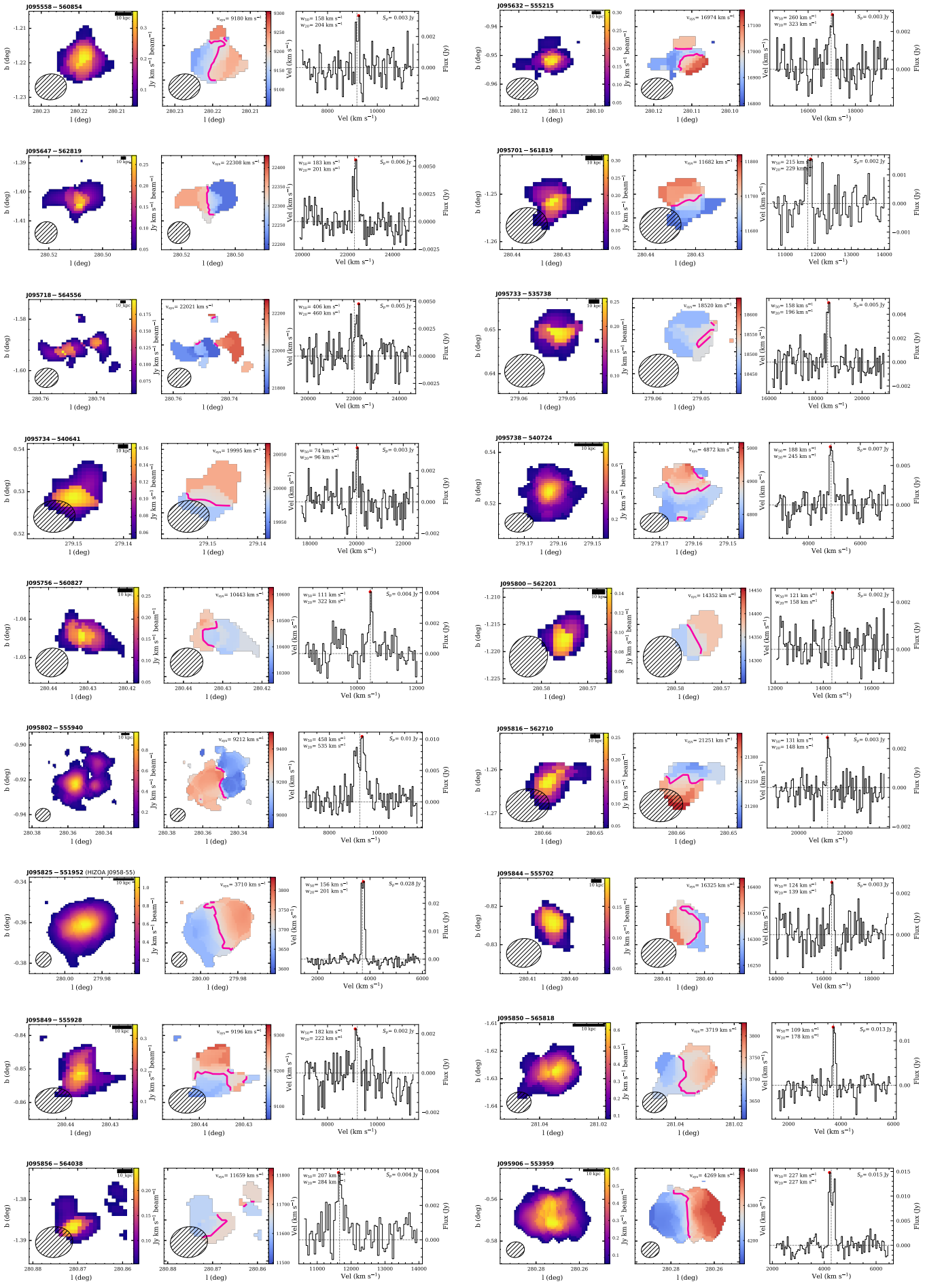
J095558 − 560854
J095632 − 555215
J095647 − 562819
J095701 − 561819
J095718 − 564556
J095733 − 535738
J095734 − 540641
J095738 − 540724
J095756 − 560827
J095800 − 562201
J095802 − 555940
J095816 − 562710
J095825 − 551952 (HIZOA J0958-55)
J095844 − 555702
J095849 − 555928
J095850 − 565818
J095856 − 564038
J095906 − 553959
l (deg)
b (deg)
Vel (km s−1)
Flux (Jy)
Jy km s−1 beam−1
10 kpc

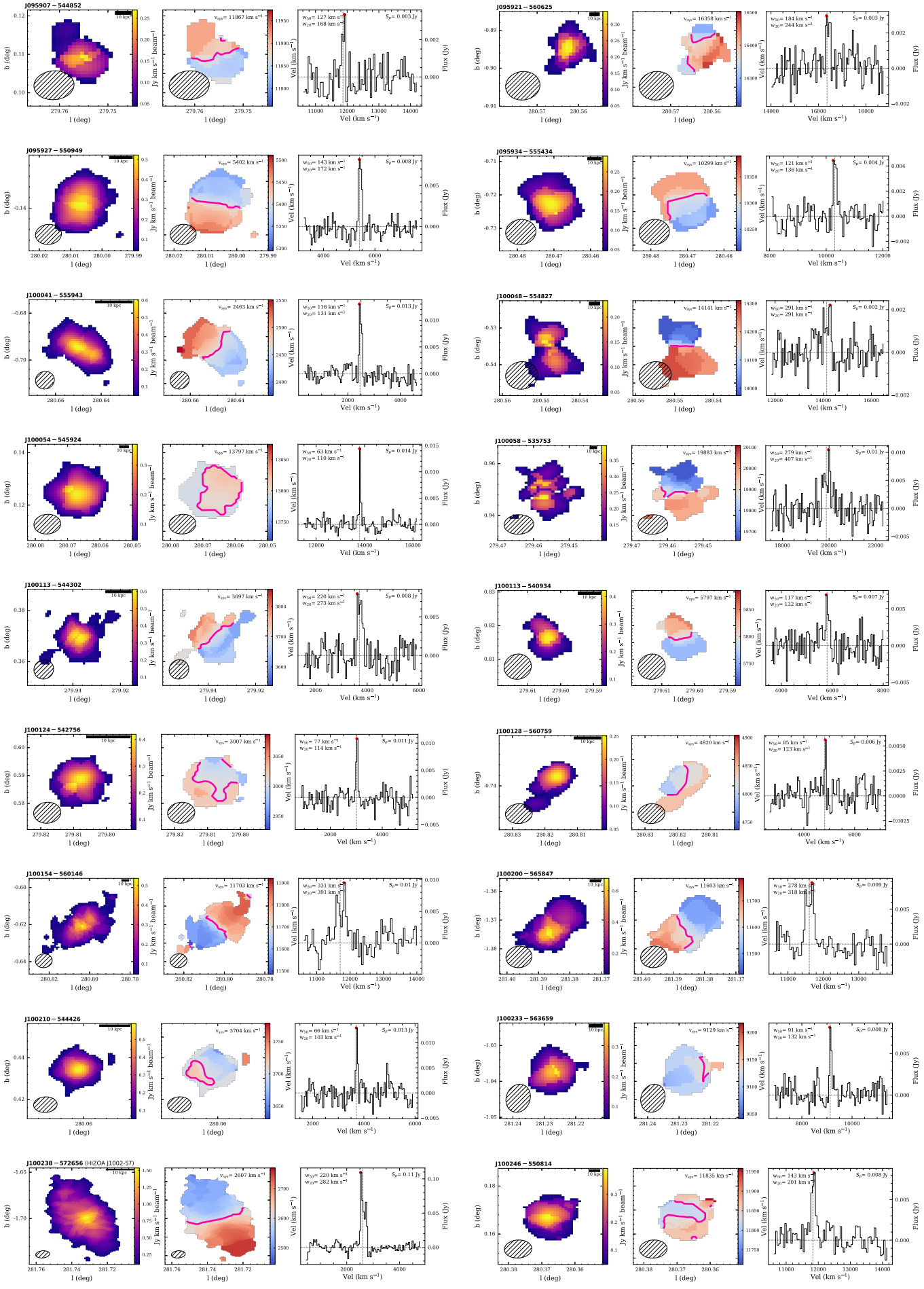
J095907 − 544852
J095921 − 560625
J095927 − 550949
J095934 − 555434
J100041 − 555943
J100048 − 554827
J100054 − 545924
J100058 − 535753
J100113 − 544302
J100113 − 540934
J100124 − 542756
J100128 − 560759
J100154 − 560146
J100200 − 565847
J100210 − 544426
J100233 − 563659
J100238 − 572656 (HIZOA J1002-57)
J100246 − 550814
l (deg)
b (deg)
Vel (km s−1)
Flux (Jy)
Jy km s−1 beam−1

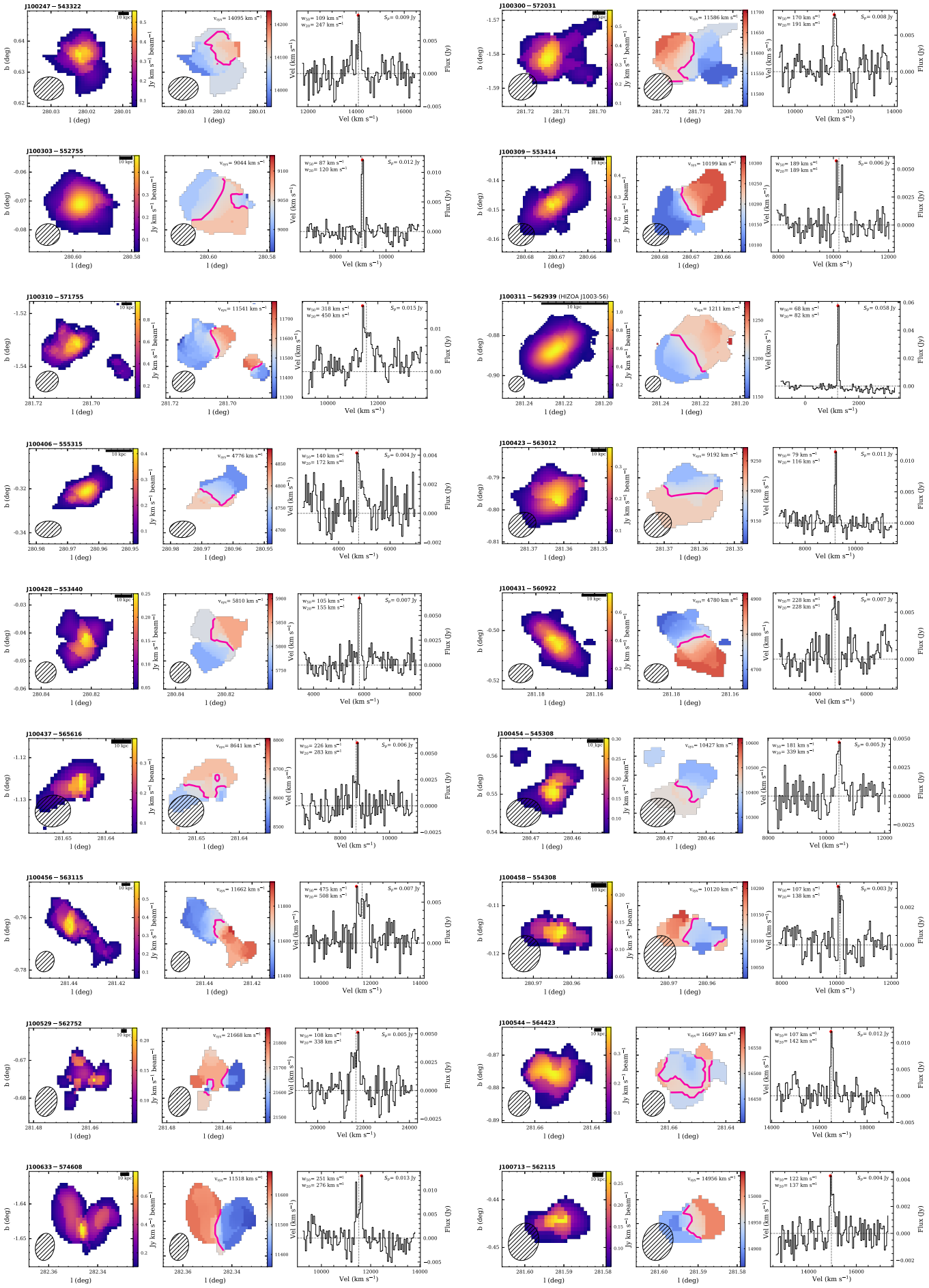
J100247 − 543322
J100300 − 572031
J100303 − 552755
J100309 − 553414
J100310 − 571755
J100311 − 562939 (HIZOA J1003-56)
J100406 − 555315
J100423 − 563012
J100428 − 553440
J100431 − 560922
J100437 − 565616
J100454 − 545308
J100456 − 563115
J100458 − 554308
J100529 − 562752
J100544 − 564423
J100633 − 574608
J100713 − 562115
l (deg)
b (deg)
Vel (km s−1)
Flux (Jy)
Jy km s−1 beam−1
10 kpc

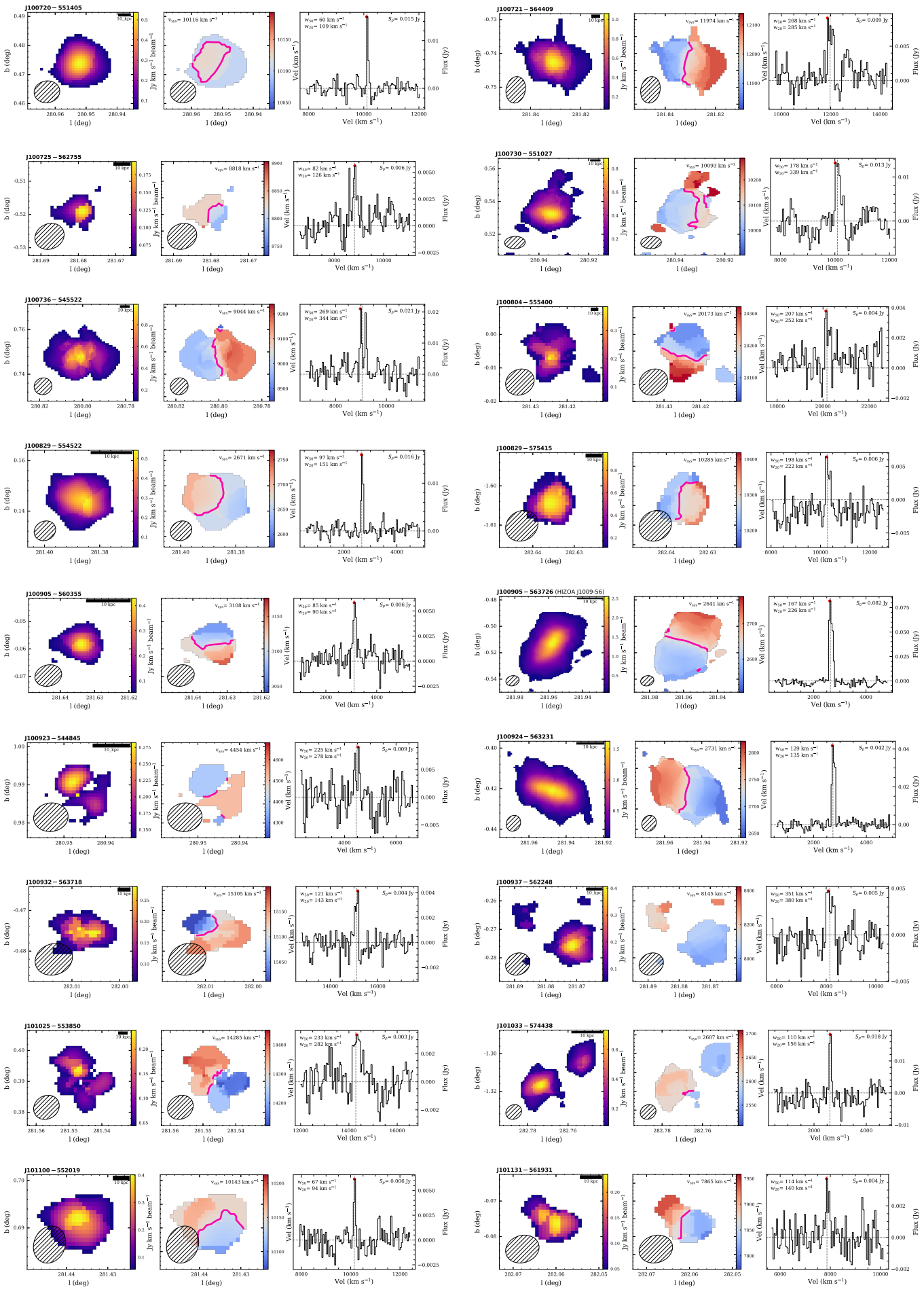
J100720 − 551405
J100721 − 564409
J100725 − 562755
J100730 − 551027
J100736 − 545522
J100804 − 555400
J100829 − 554522
J100829 − 575415
J100905 − 560355
J100905 − 563726 (HIZOA J1009-56)
J100923 − 544845
J100924 − 563231
J100932 − 563718
J100937 − 562248
J101025 − 553850
J101033 − 574438
J101100 − 552019
J101131 − 561931
l (deg)
b (deg)
Vel (km s−1)
Flux (Jy)
Jy km s−1 beam−1
10 kpc

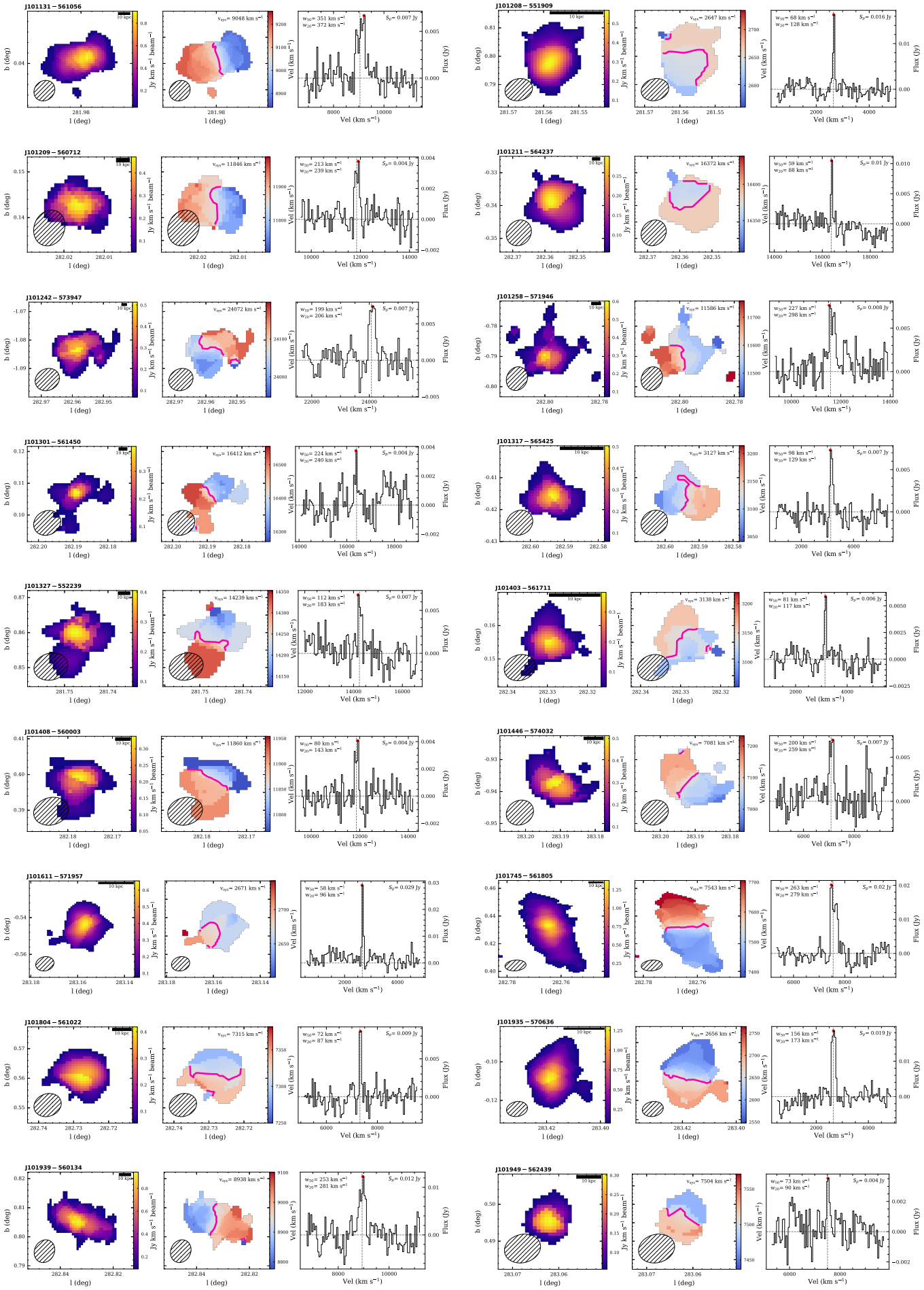
J101131 – 561056
J101208 – 551909
J101209 – 560712
J101211 – 564237
J101242 – 573947
J101258 – 571946
J101301 – 561450
J101317 – 565425
J101327 – 552239
J101403 – 561711
J101408 – 560003
J101446 – 574032
J101611 – 571957
J101745 – 561805
J101804 – 561022
J101935 – 570636
J101939 – 560134
J101949 – 562439
b (deg)
l (deg)
Jy km s^{-1} beam^{-1}
Vel (km s^{-1})
Flux (Jy)
Vel (km s^{-1})

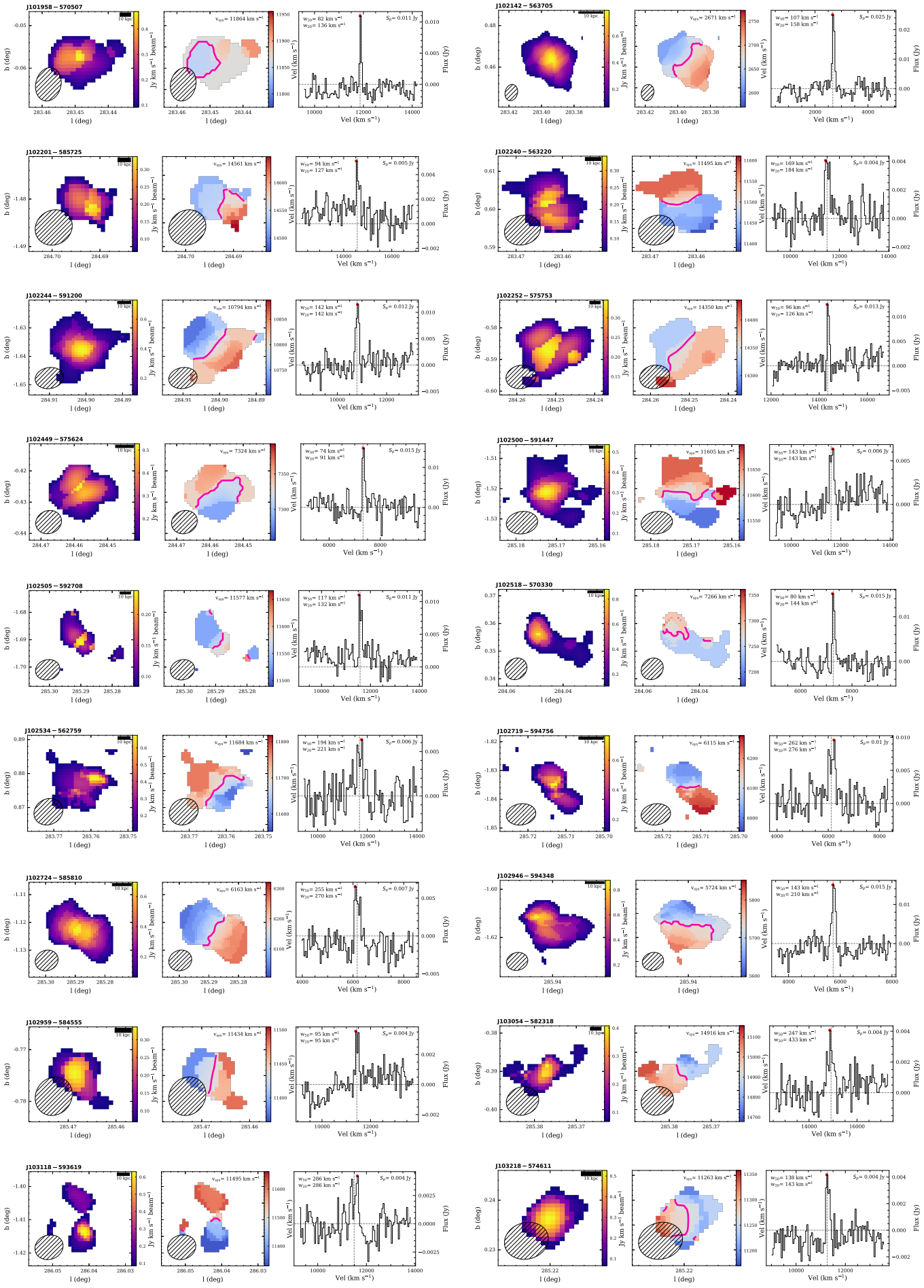
J101958−570507
J102142−563705
J102201−585725
J102240−563220
J102244−591200
J102252−575753
J102449−575624
J102500−591447
J102505−592708
J102518−570330
J102534−562759
J102719−594756
J102724−585810
J102946−594348
J102959−584555
J103054−582318
J103118−593619
J103218−574611
l (deg)
b (deg)
Vel (km s−1)
Flux (Jy)
Jy km s−1 beam−1
10 kpc

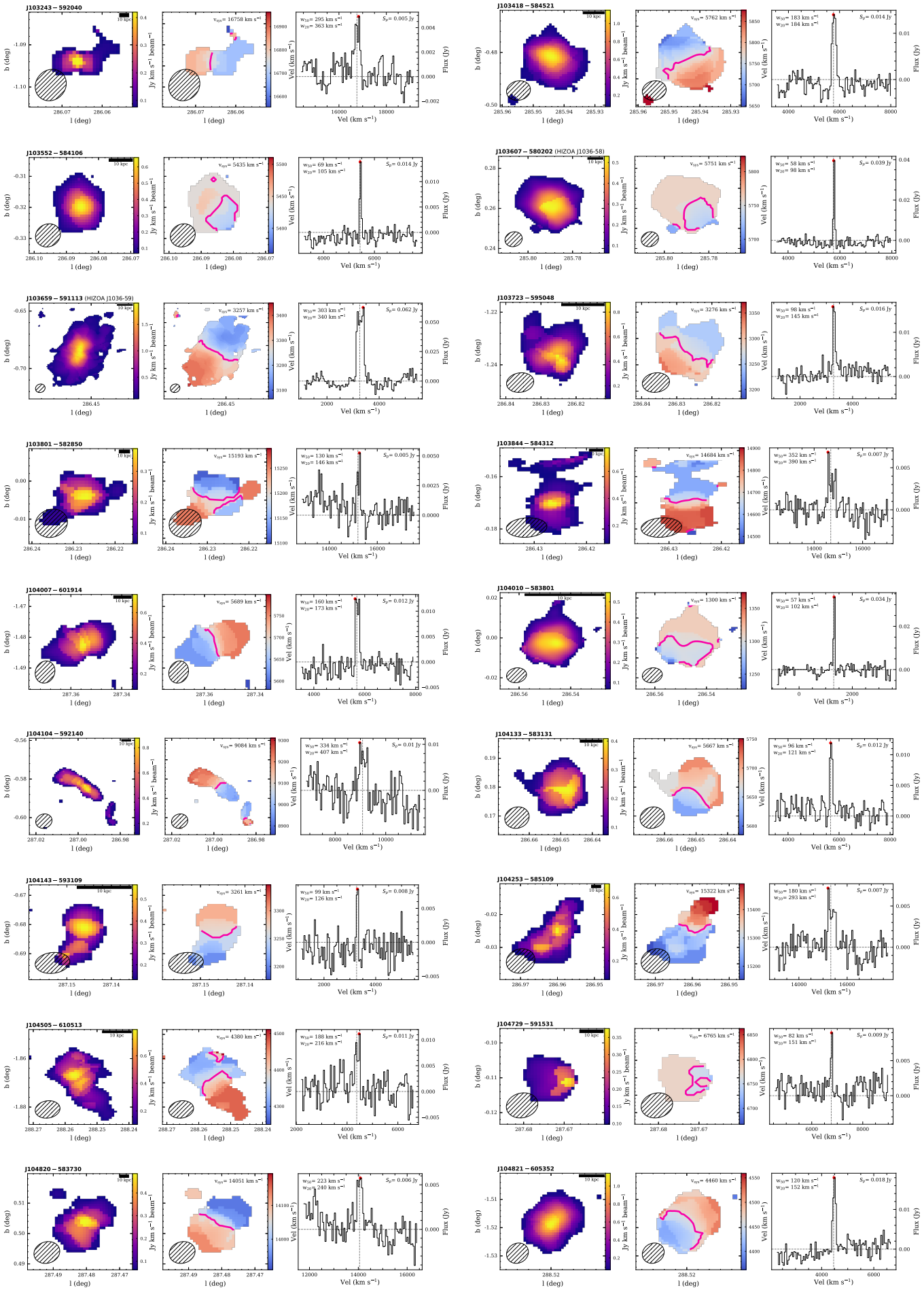
J103243 − 592040
J103418 − 584521
J103552 − 584106
J103607 − 580202 (HIZOA J1036-58)
J103659 − 591113 (HIZOA J1036-59)
J103723 − 595048
J103801 − 582850
J103844 − 584312
J104007 − 601914
J104010 − 583801
J104104 − 592140
J104133 − 583131
J104143 − 593109
J104253 − 585109
J104505 − 610513
J104729 − 591531
J104820 − 583730
J104821 − 605352
l (deg)
b (deg)
Vel (km s−1)
Flux (Jy)
Jy km s−1 beam−1
10 kpc

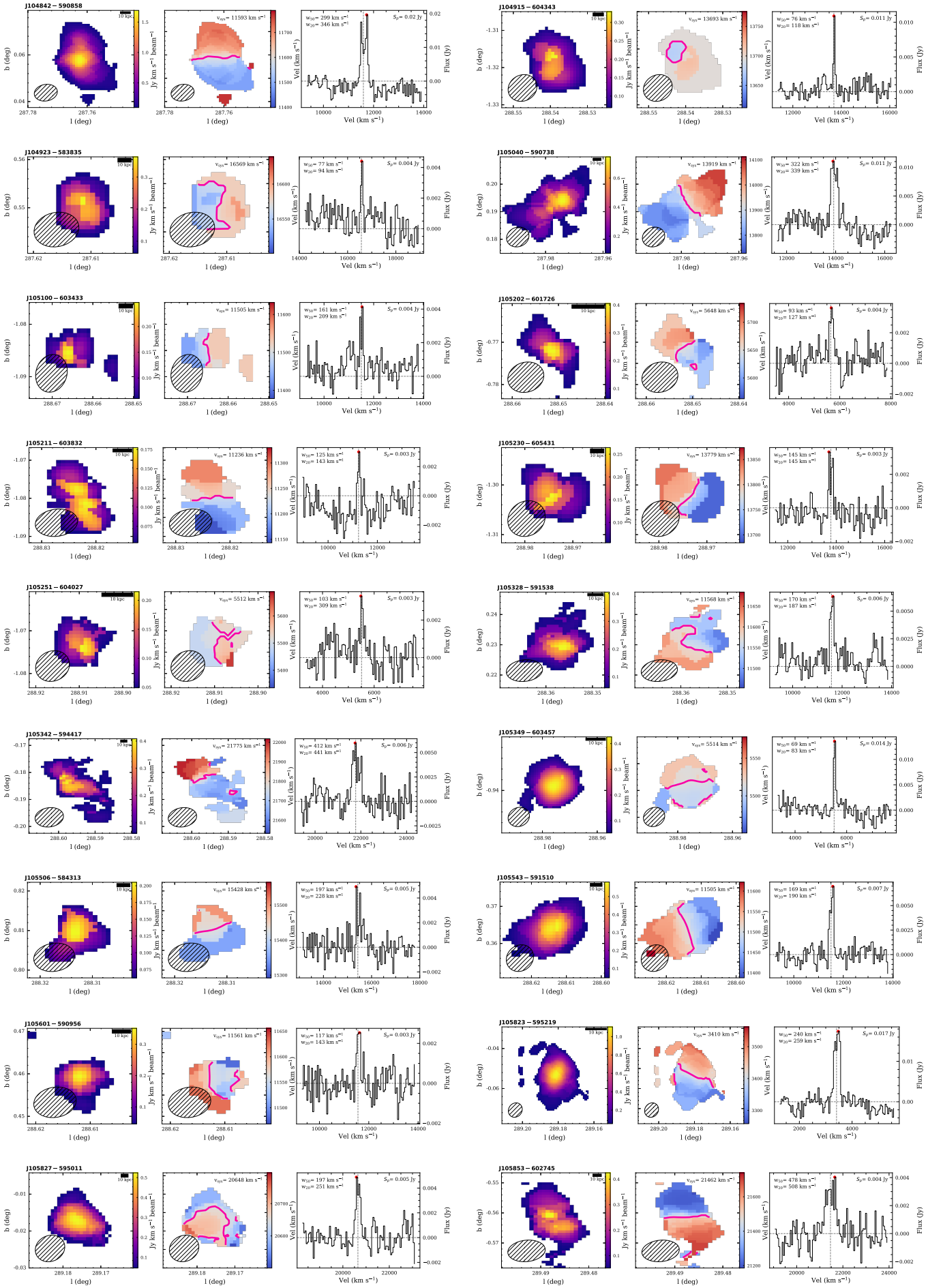
J104842 − 590858
J104915 − 604343
J104923 − 583835
J105040 − 590738
J105100 − 603433
J105202 − 601726
J105211 − 603832
J105230 − 605431
J105251 − 604027
J105328 − 591538
J105342 − 594417
J105349 − 603457
J105506 − 584313
J105543 − 591510
J105601 − 590956
J105823 − 595219
J105827 − 595011
J105853 − 602745
l (deg)
b (deg)
Vel (km s−1)
Flux (Jy)
Jy km s−1 beam−1
10 kpc

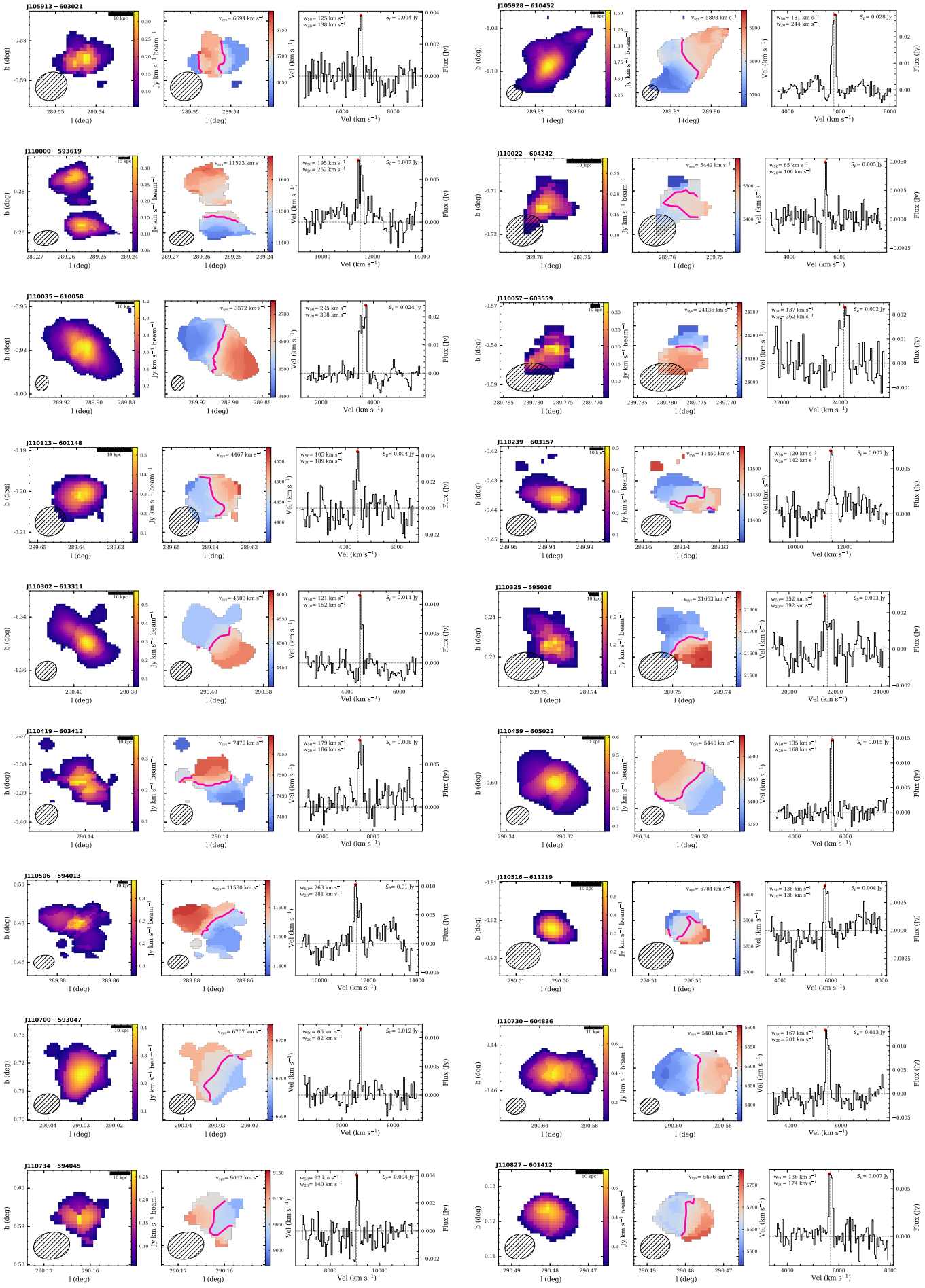
J105913 − 603021
J105928 − 610452
J110000 − 593619
J110022 − 604242
J110035 − 610058
J110057 − 603559
J110113 − 601148
J110239 − 603157
J110302 − 613311
J110325 − 595036
J110419 − 603412
J110459 − 605022
J110506 − 594013
J110516 − 611219
J110700 − 593047
J110730 − 604836
J110734 − 594045
J110827 − 601412
b (deg)
l (deg)
Jy km s⁻¹ beam⁻¹
Vel (km s⁻¹)
Flux (Jy)

B.4.2 Possible detections

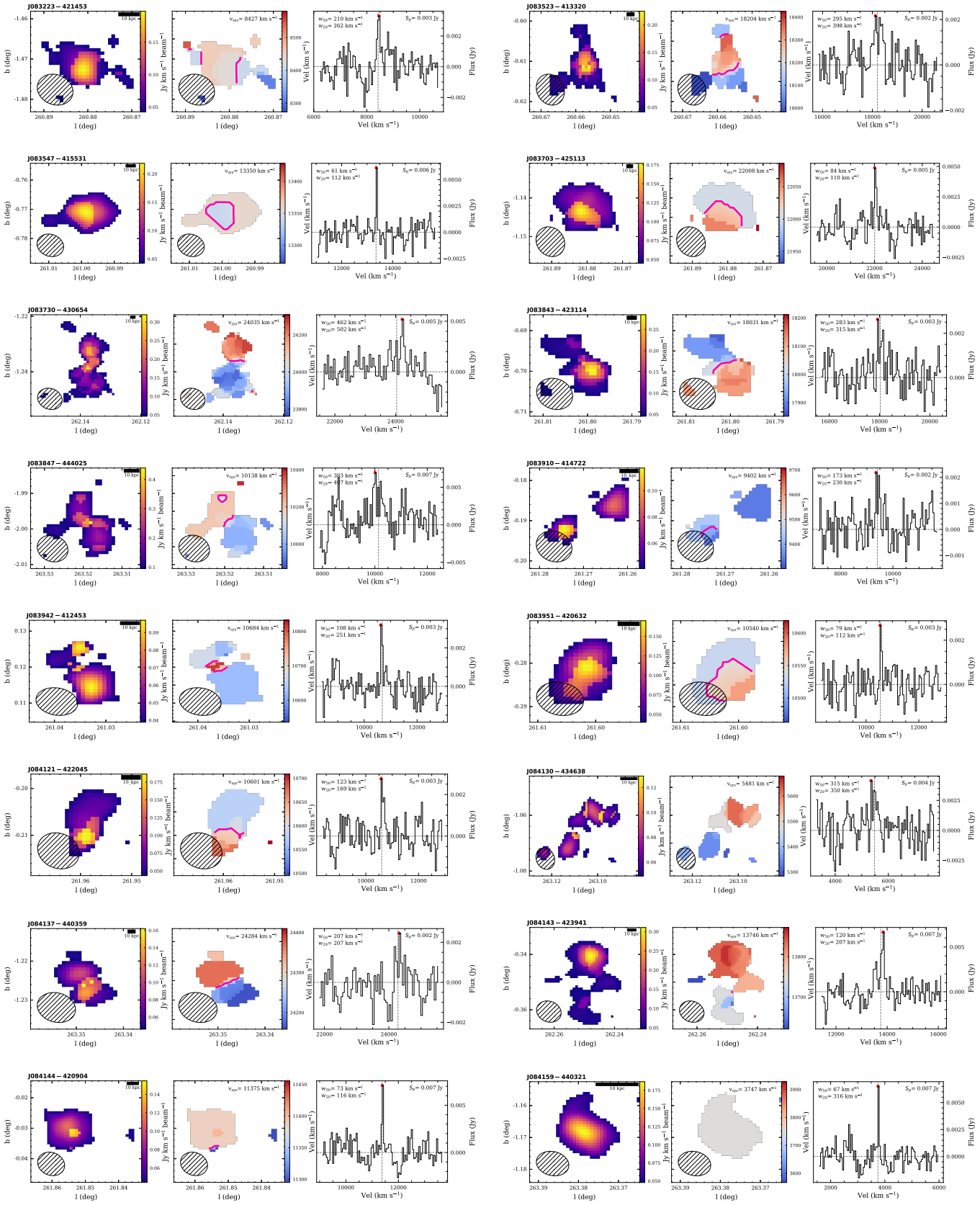

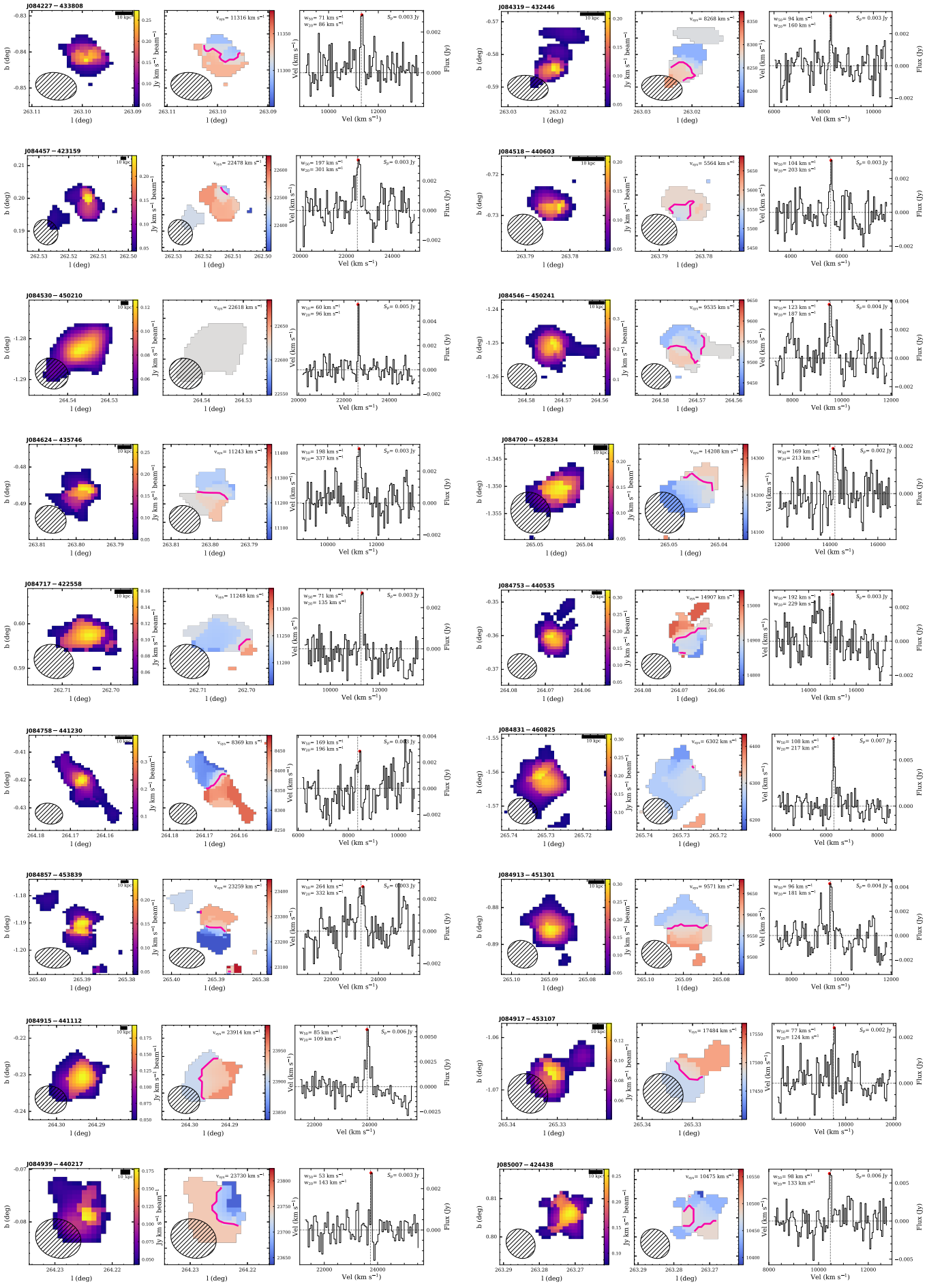
J084227 − 433808
J084319 − 432446
J084457 − 423159
J084518 − 440603
J084530 − 450210
J084546 − 450241
J084624 − 435746
J084700 − 452834
J084717 − 422558
J084753 − 440535
J084758 − 441230
J084831 − 460825
J084857 − 453839
J084913 − 451301
J084915 − 441112
J084917 − 453107
J084939 − 440217
J085007 − 424438
b (deg)
l (deg)
Vel (km s−1)
Flux (Jy)
Jy km s−1 beam−1
10 kpc

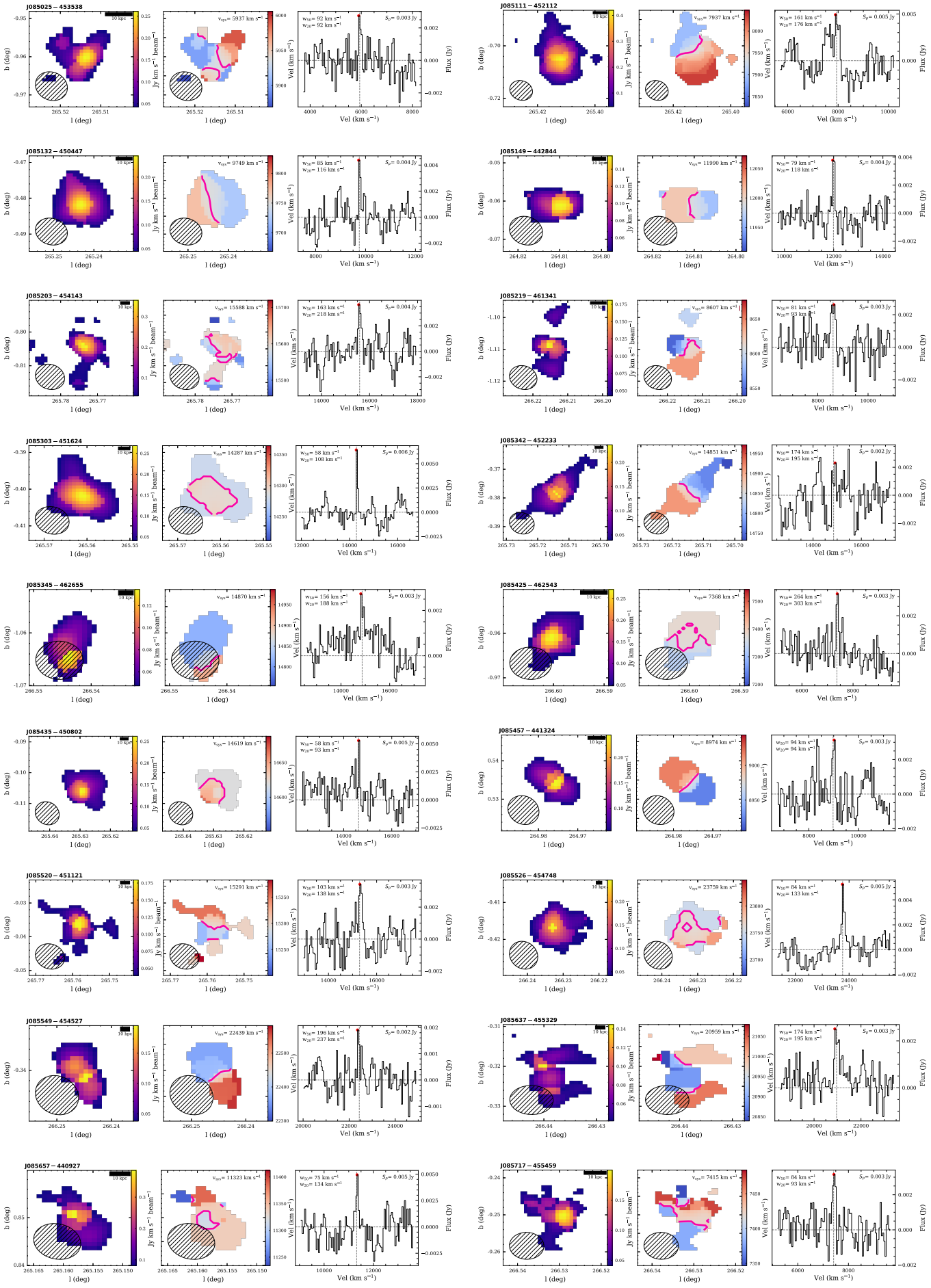
J085025 − 453538
J085111 − 452112
J085132 − 450447
J085149 − 442844
J085203 − 454143
J085219 − 461341
J085303 − 451624
J085342 − 452233
J085345 − 462655
J085425 − 462543
J085435 − 450802
J085457 − 441324
J085520 − 451121
J085526 − 454748
J085549 − 454527
J085637 − 455329
J085657 − 440927
J085717 − 455459
l (deg)
b (deg)
Vel (km s⁻¹)
Flux (Jy)
Jy km s⁻¹ beam⁻¹

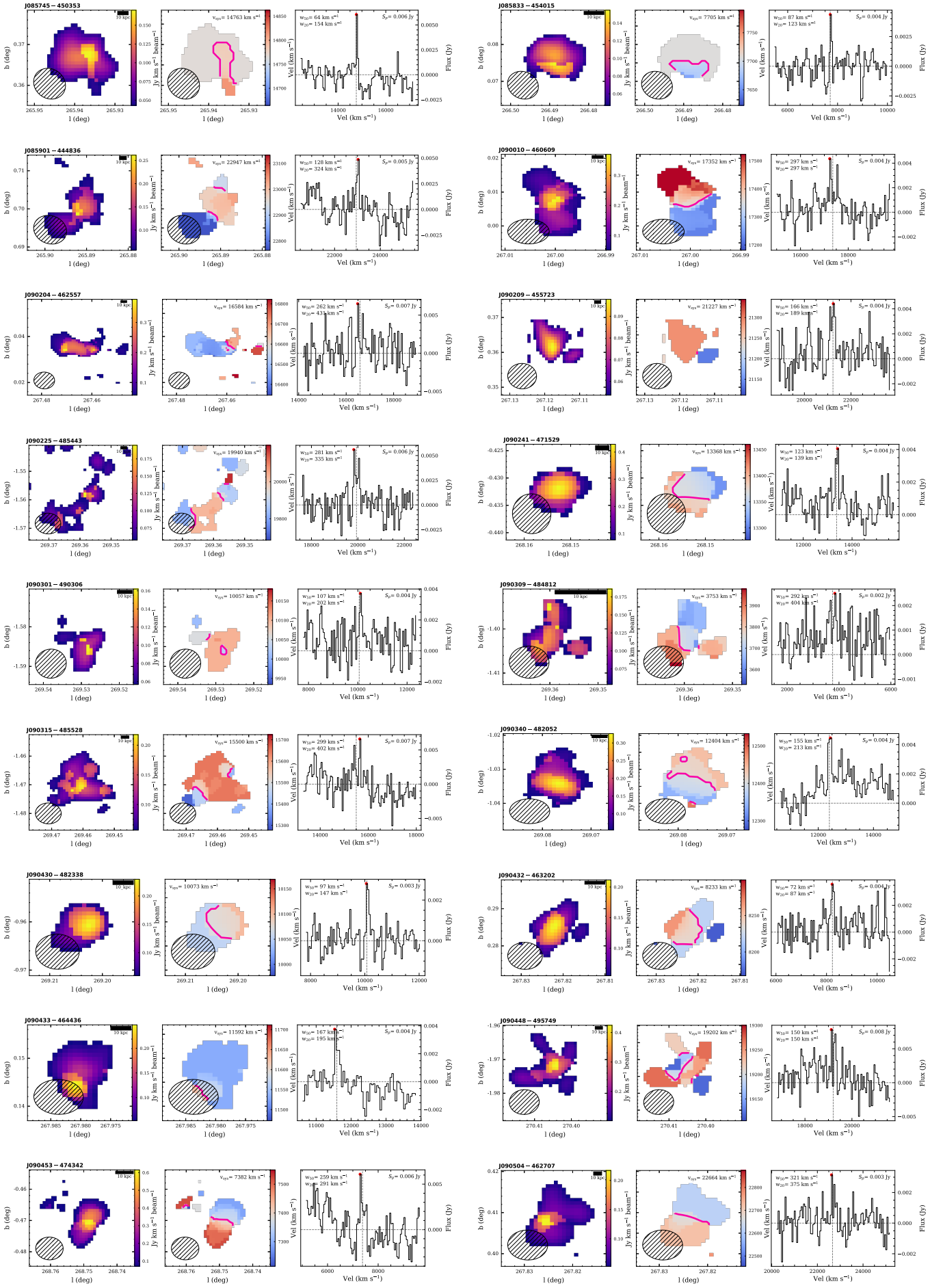
J085745 − 450353
J085833 − 454015
J085901 − 444836
J090010 − 460609
J090204 − 462557
J090209 − 455723
J090225 − 485443
J090241 − 471529
J090301 − 490306
J090309 − 484812
J090315 − 485528
J090340 − 482052
J090430 − 482338
J090432 − 463202
J090433 − 464436
J090448 − 495749
J090453 − 474342
J090504 − 462707
l (deg)
b (deg)
Vel (km s^{-1})
Flux (Jy)
Jy km s^{-1} beam^{-1}

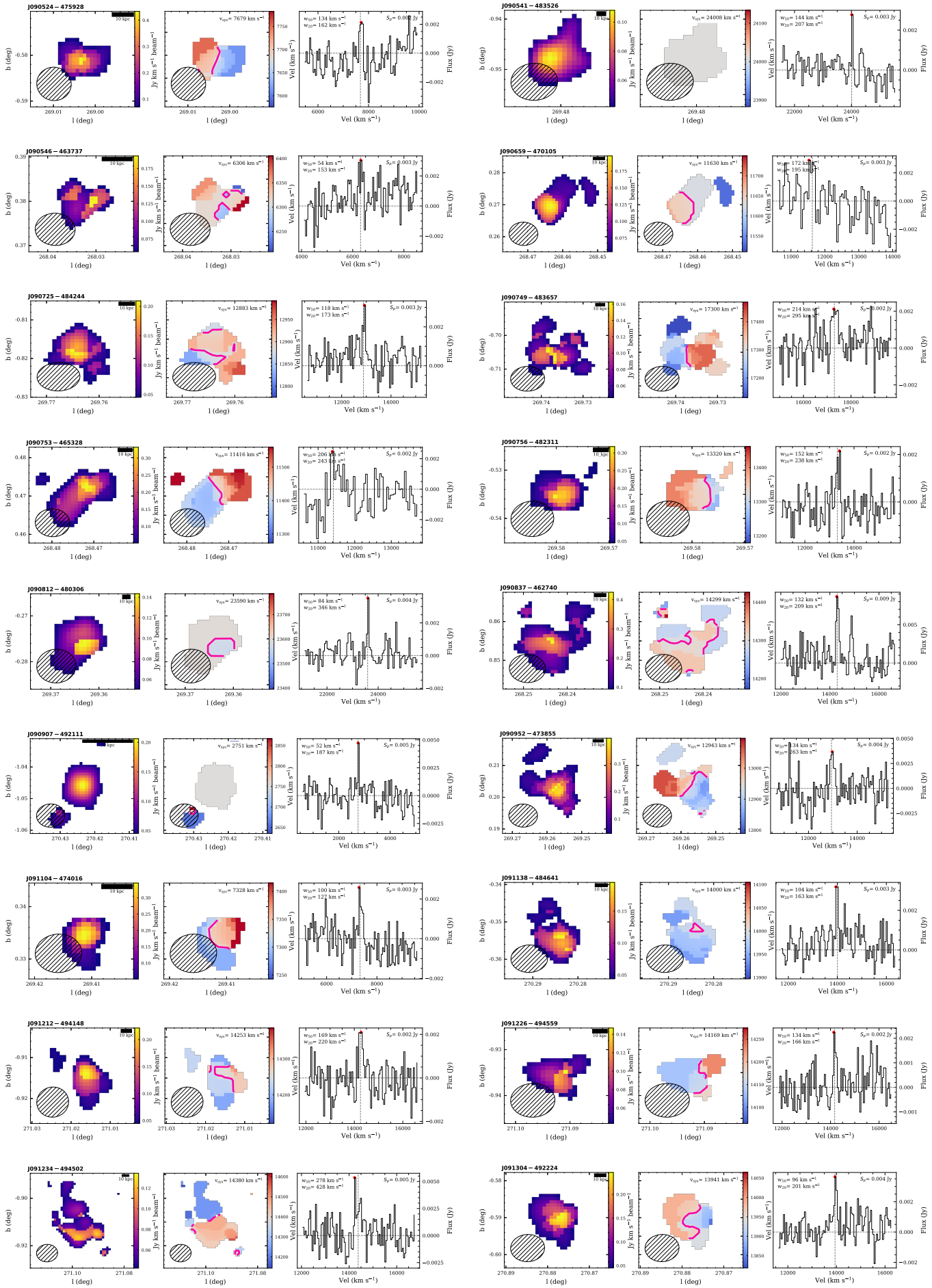
J090524 − 475928
J090541 − 483526
J090546 − 463737
J090659 − 470105
J090725 − 484244
J090749 − 483657
J090753 − 465328
J090756 − 482311
J090812 − 480306
J090837 − 462740
J090907 − 492111
J090952 − 473855
J091104 − 474016
J091138 − 484641
J091212 − 494148
J091226 − 494559
J091234 − 494502
J091304 − 492224
b (deg)
l (deg)
Jy km s⁻¹ beam⁻¹
Vel (km s⁻¹)
Flux (Jy)

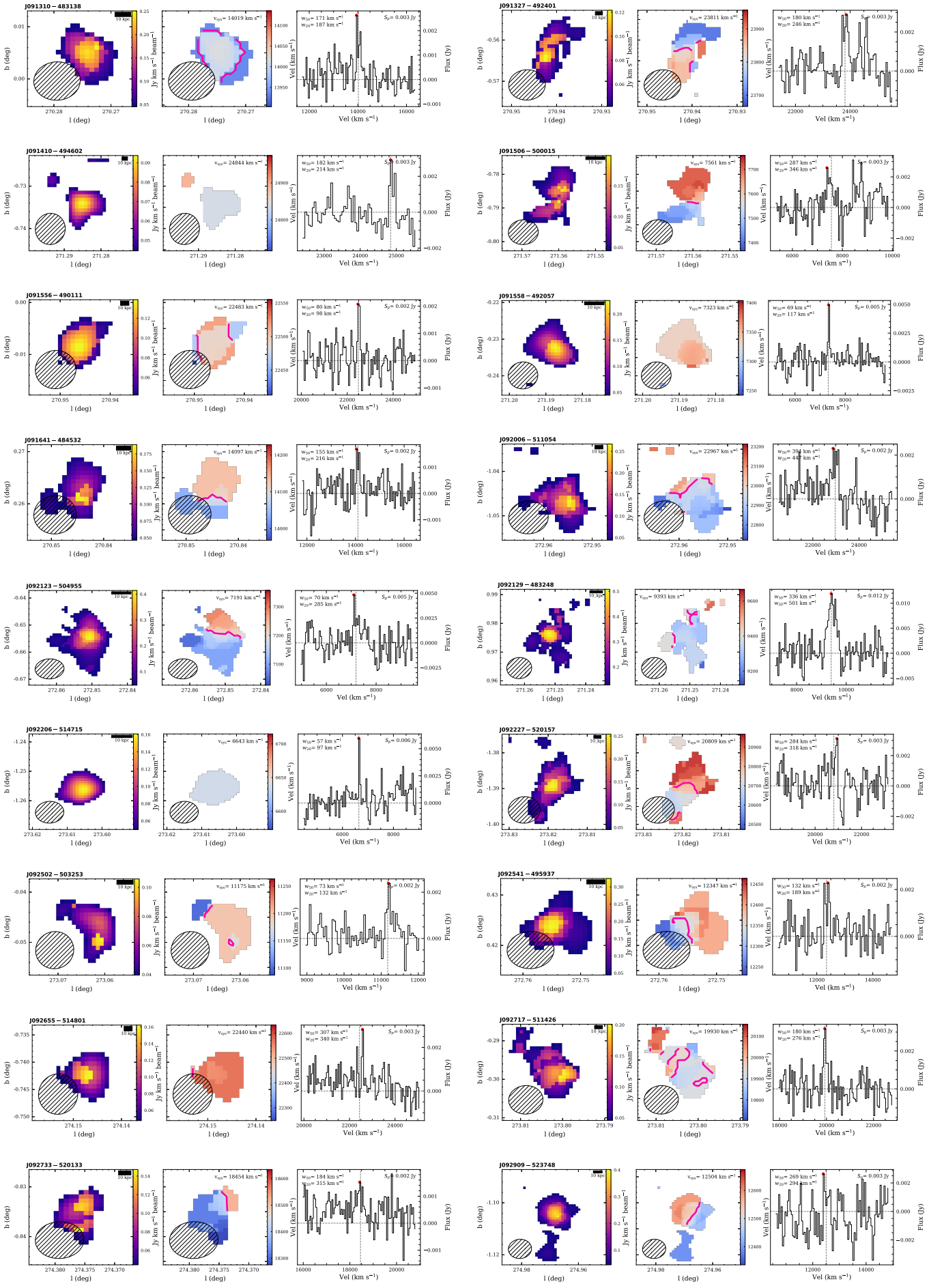
J091310 − 483138
J091327 − 492401
J091410 − 494602
J091506 − 500015
J091556 − 490111
J091558 − 492057
J091641 − 484532
J092006 − 511054
J092123 − 504955
J092129 − 483248
J092206 − 514715
J092227 − 520157
J092502 − 503253
J092541 − 495937
J092655 − 514801
J092717 − 511426
J092733 − 520133
J092909 − 523748
l (deg)
b (deg)
Vel (km s−1)
Flux (Jy)
Jy km s−1 beam−1
10 kpc

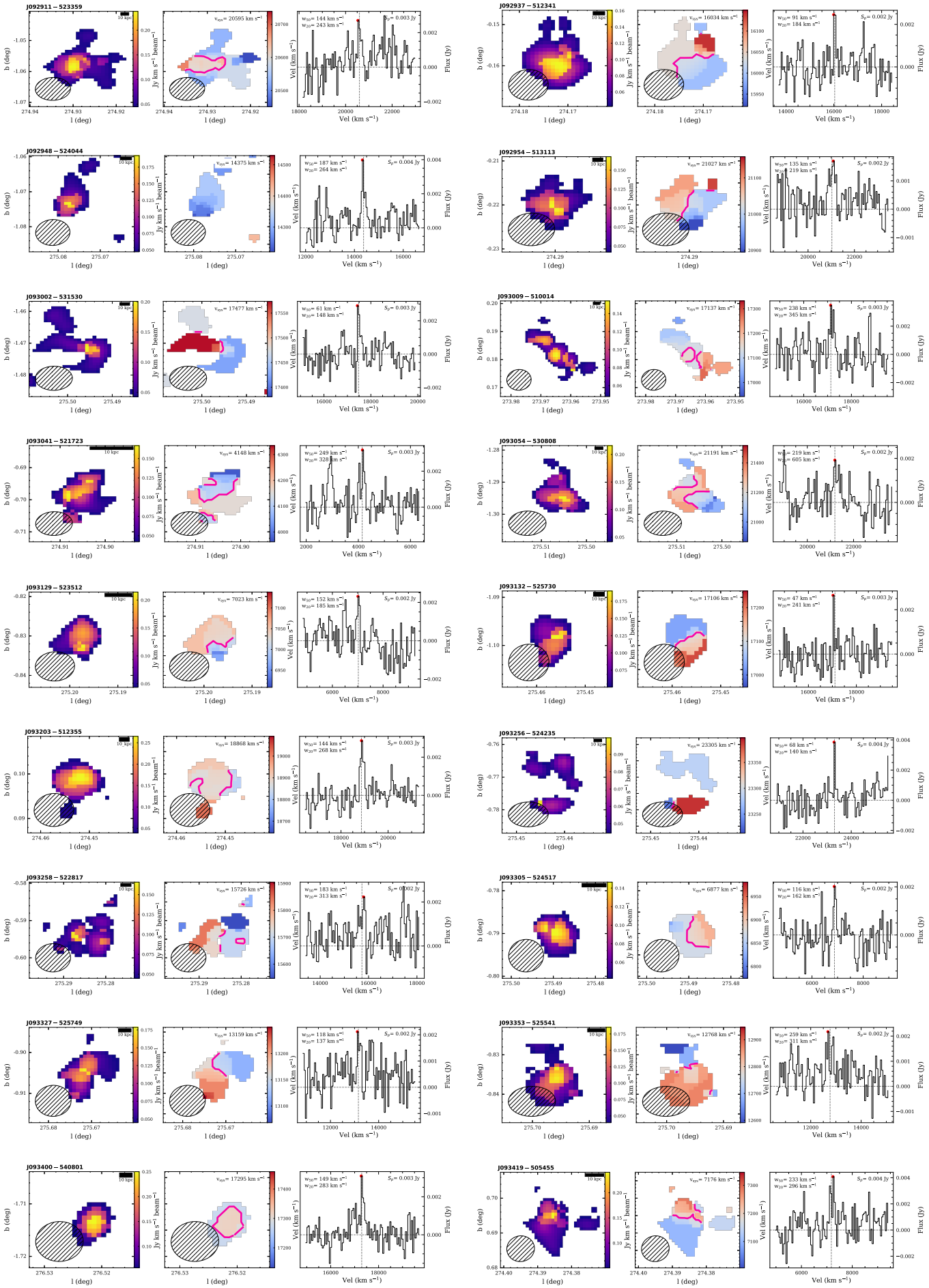
J092911 − 523359
J092937 − 512341
J092948 − 524044
J092954 − 513113
J093002 − 531530
J093009 − 510014
J093041 − 521723
J093054 − 530808
J093129 − 523512
J093132 − 525730
J093203 − 512355
J093256 − 524235
J093258 − 522817
J093305 − 524517
J093327 − 525749
J093353 − 525541
J093400 − 540801
J093419 − 505455
l (deg)
b (deg)
Vel (km s−1)
Flux (Jy)
Jy km s−1 beam−1
10 kpc

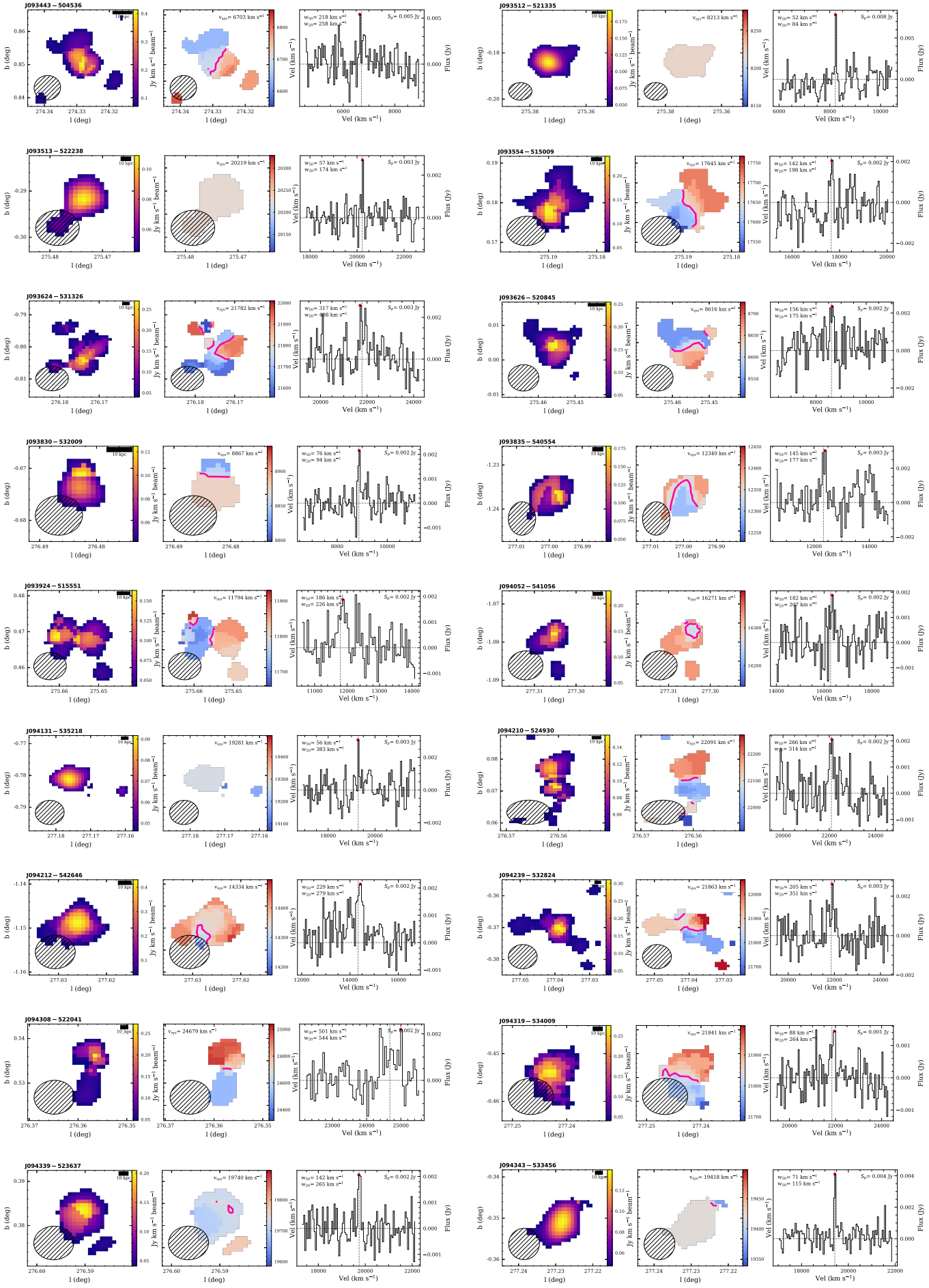
J093443 − 504536
J093512 − 521335
J093513 − 522238
J093554 − 515009
J093624 − 531326
J093626 − 520845
J093830 − 532009
J093835 − 540554
J093924 − 515551
J094052 − 541056
J094131 − 535218
J094210 − 524930
J094212 − 542646
J094239 − 532824
J094308 − 522041
J094319 − 534009
J094339 − 523637
J094343 − 533456
l (deg)
b (deg)
Vel (km s−1)
Flux (Jy)
Jy km s−1 beam−1
Vel (km s−1)
10 kpc

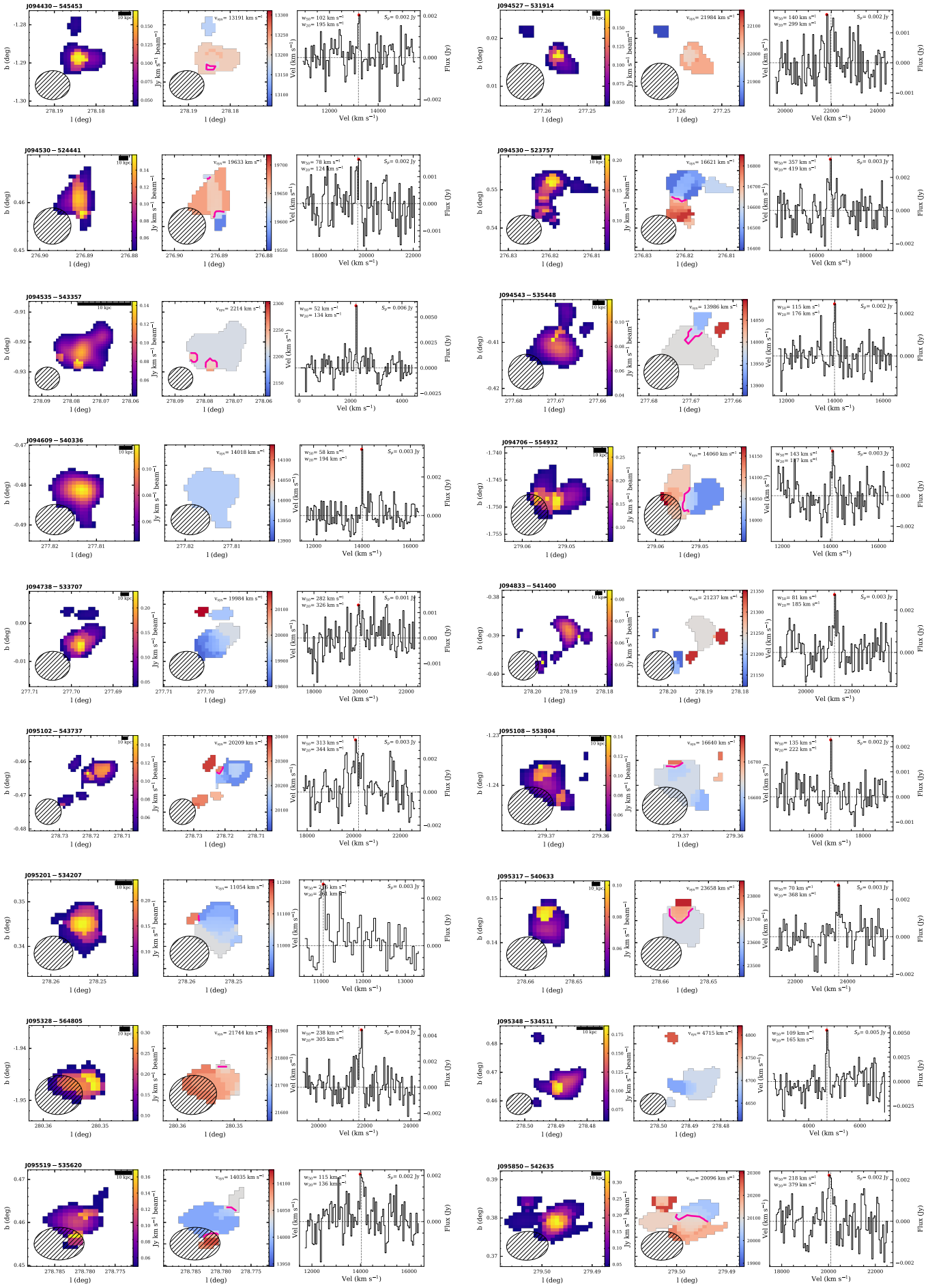
J094430 − 545453
J094527 − 531914
J094530 − 524441
J094530 − 523757
J094535 − 543357
J094543 − 535448
J094609 − 540336
J094706 − 554932
J094738 − 533707
J094833 − 541400
J095102 − 543737
J095108 − 553804
J095201 − 534207
J095317 − 540633
J095328 − 564805
J095348 − 534511
J095519 − 535620
J095850 − 542635
b (deg)
l (deg)
Jy km s⁻¹ beam⁻¹
Vel (km s⁻¹)
Flux (Jy)

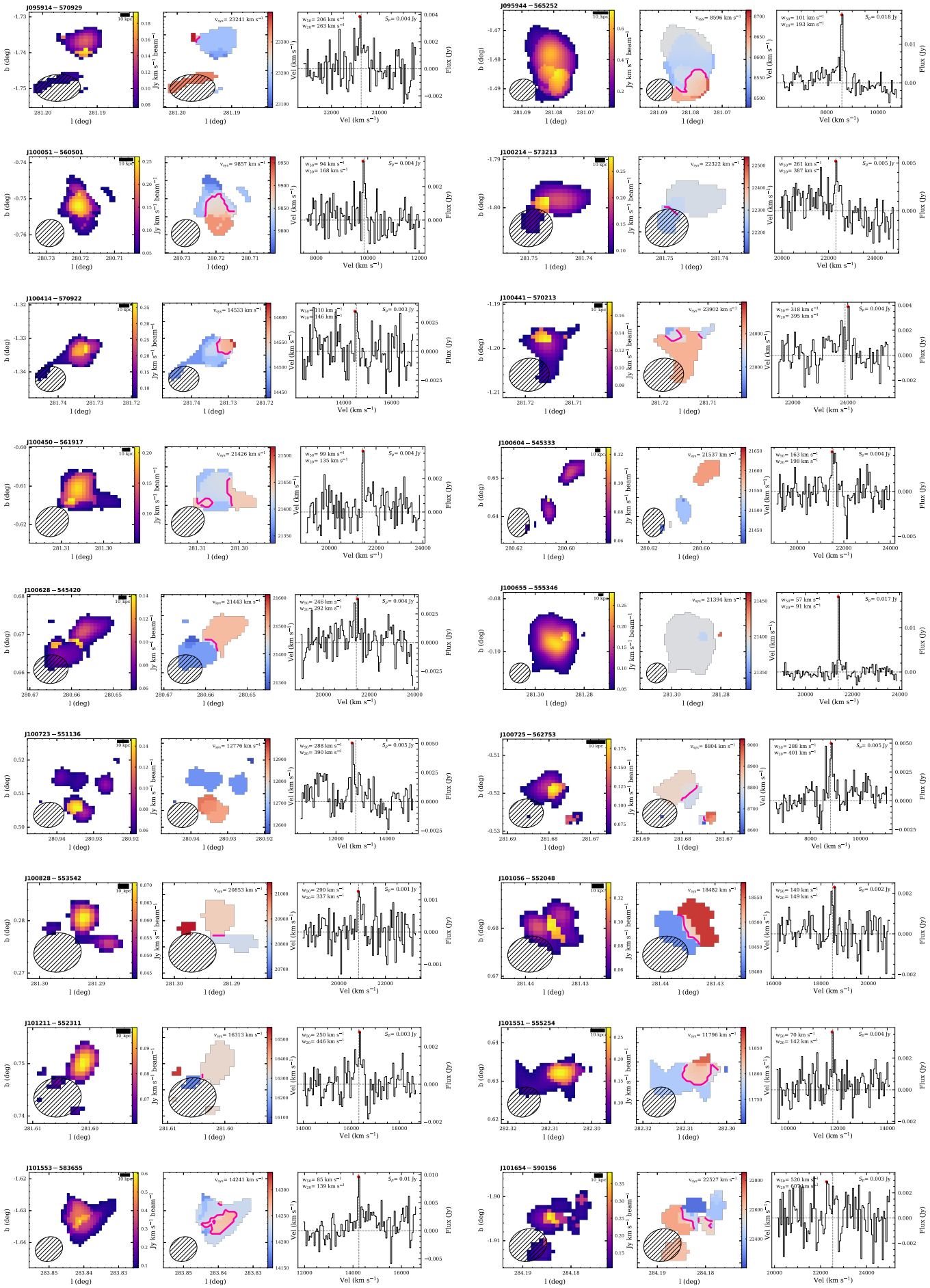
J095914 − 570929
J095944 − 565252
J100051 − 560501
J100214 − 573213
J100414 − 570922
J100441 − 570213
J100450 − 561917
J100604 − 545333
J100628 − 545420
J100655 − 555346
J100723 − 551136
J100725 − 562753
J100828 − 553542
J101056 − 552048
J101211 − 552311
J101551 − 555254
J101553 − 583655
J101654 − 590156
b (deg)
l (deg)
Jy km s⁻¹ beam⁻¹
Vel (km s⁻¹)
Flux (Jy)

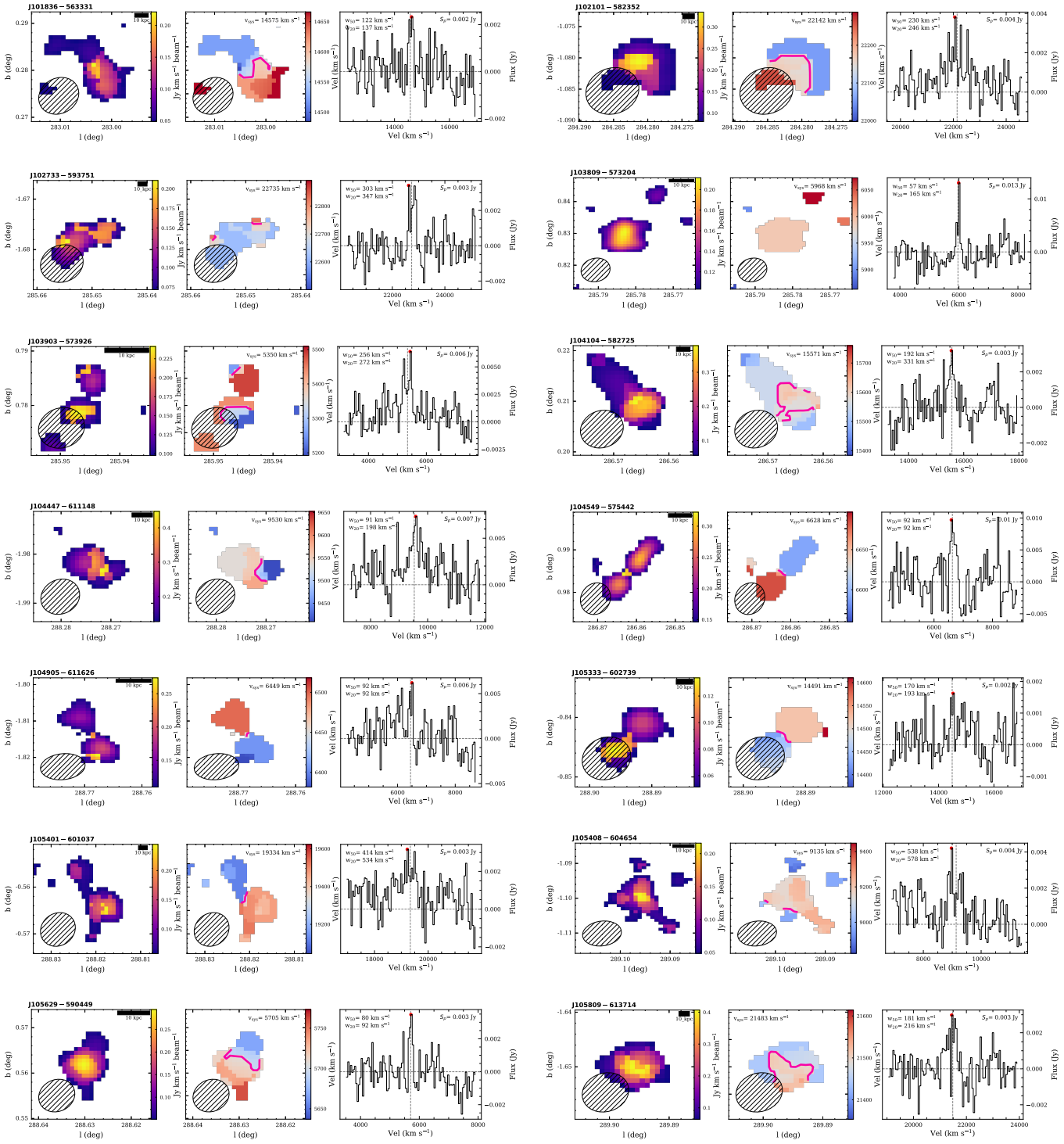
J101836 − 563331
J102101 − 582352
J102733 − 593751
J103809 − 573204
J103903 − 573926
J104104 − 582725
J104447 − 611148
J104549 − 575442
J104905 − 611626
J105333 − 602739
J105401 − 601037
J105408 − 604654
J105629 − 590449
J105809 − 613714
b (deg)
l (deg)
Jy km s−1 beam−1
Vel (km s−1)
Flux (Jy)

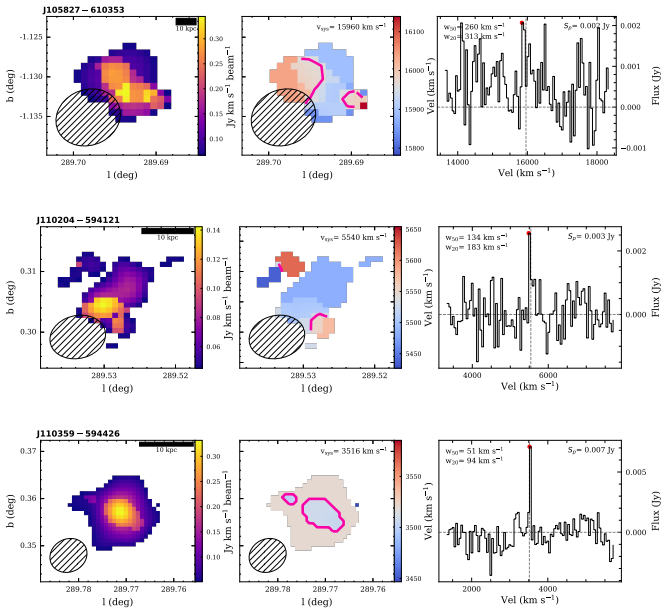
J105827 − 610353
J105940 − 593005
J110204 − 594121
J110223 − 620954
J110359 − 594426
l (deg)
b (deg)
Vel (km s^{-1})
Flux (Jy)
Jy km s^{-1} beam^{-1}

appendix C

The Vela–H I appendices

C.1 Residual RFI

This appendix explains the method employed to address short-track bugs and solar RFI observed in the Vela–H I datasets before executing the CARACal pipeline.

C.1.1 Short track bugs

The short track bug occurs during telescope slewing, where the initial two or three dumps from this motion are erroneously recorded as a track lasting six seconds or less when the telescope moves to a new field. In Fig. C.1, we have highlighted these short tracks in yellow. They are visibly shorter (see the column TIMERANGE (UTC)), containing fewer rows of data compared to an actual track. If left unflagged, the short track bug can cause emission from the previous field to erroneously appear in the subsequent field as faint 'ghost' images. While CARACal automatically identifies and flags this bug, it can also be manually addressed in CASA[1] by carefully noting the affected scans and flagging them before calibration.

```
================================================================================
           MeasurementSet Name:  /stimela_mount/msdir/1633134084_sdp_l0.ms      MS Version 2
================================================================================
   Observer: Sambatriniaina Rajohnson     Project: 20210331-0021
Observation: MeerKAT
Data records: 24791010       Total elapsed time = 29137.7 seconds
   Observed from   02-Oct-2021/00:24:34.8   to   02-Oct-2021/08:30:12.5 (UTC)

   ObservationID = 0         ArrayID = 0
  Date        Timerange (UTC)          Scan  FldId FieldName             nRows     SpwIds   Average Interval(s)     ScanIntent
  02-Oct-2021/00:24:34.8 - 00:24:42.8     1      0 J0408-6545              7320  [0]  [2] [CALIBRATE_BANDPASS,CALIBRATE_FLUX]
              00:24:42.8 - 00:27:48.7     2      0 J0408-6545            170190  [0]  [2] [CALIBRATE_BANDPASS,CALIBRATE_FLUX]
              00:28:26.7 - 00:30:24.6     3      1 J0825-5010            107970  [0]  [2] [CALIBRATE_AMPLI,CALIBRATE_PHASE]
              00:30:24.6 - 00:30:28.6     4      2 B11L16                 3660  [0]  [2] [TARGET]
              00:30:44.6 - 00:33:12.6     5      2 B11L16               135420  [0]  [2] [TARGET]
              00:33:12.6 - 00:33:16.6     6      3 B11L17                 3660  [0]  [2] [TARGET]
              00:33:24.6 - 00:35:52.5     7      3 B11L17               135420  [0]  [2] [TARGET]
              00:35:52.5 - 00:35:56.5     8      4 B11L18                 3660  [0]  [2] [TARGET]
              00:36:04.5 - 00:38:32.4     9      4 B11L18               135420  [0]  [2] [TARGET]
              00:38:32.4 - 00:38:36.4    10      5 B11L19                 3660  [0]  [2] [TARGET]
              00:38:44.4 - 00:41:12.4    11      5 B11L19               135420  [0]  [2] [TARGET]
```

Figure C.1: An example of a CASA 'listobs' file summarizing the observation information for the measurement set of block C2. Short-track bugs, which require flagging, have been highlighted in yellow.

[1] http://casa.nrao.edu

C.1.2 Solar RFI and 1380 MHz spike

Initially, our blocks of observations all started during nighttime. However, due to the extensive duration ($8 - 9$ hrs) of each session and a large number of targets, roughly 69% of our data was acquired during the daytime. This distribution is summarized in Table C.1, where blocks A1 and A2 have collected more than 80% of their data during daytime. This had significant implications, particularly for short baselines directed toward the Sun during sunrise and sunset, which were susceptible to picking up solar interference.

Upon inspecting the data, we observe a sudden fluctuation in amplitude (see left panel of Fig. C.2). The observed deviation, occurring immediately after sunrise, is attributed to solar RFI. This translates into peculiar ripples discernible in both the spatial and spectral axes when generating the H I cubes, as demonstrated in the left panels of Fig. C.3.

As shown in the middle panel of Fig. C.2, the variation of amplitude as a function of UV distance remains stable before sunrise. However, after sunrise, a significant variation is observed, particularly for UV distances below 300 m. When this occurs, it is crucial to flag affected daytime visibilities. It is important to emphasize that not all daytime data requires flagging. Specifically, flagging is necessary during the interference duration and for the affected baselines only. The baselines primarily affected are those with the shortest projected lengths when aligned with the rising or setting Sun's path. The most severely affected baselines are listed in the MeerKAT Users portal documentation[2]. Our measurements, detailed in Table 2, indicate that baseline lengths shorter than 315 m ($\sim$1.5 kλ) should be flagged for blocks A2, B2, C2, D1, and D2. For A1 and B1, this threshold is 210 m ($\sim$1 kλ). The flagged data and the total number of affected baselines together comprise less than 8.1% of the total baselines and data, resulting in a relatively low impact on sensitivity.

[2] `https://skaafrica.atlassian.net/wiki/spaces/ESDKB/pages/336232568/Known+issues` (status 30/10/2023, 08:16 UTC)

Table C.1: Overview of flagged Solar RFI in Vela–H I data, including the percentage of daytime data and the affected baseline length that requires flagging

Block ID	Daytime data (%)	Affected baseline length (m)	Flagged data (%)
A1	81.4	210	7.9
A2	89.2	315	12.0
B1	64.9	210	5.7
B2	69.1	315	6.1
C1	64.5	210	6.2
C2	40.9	315	6.1
D1	75.2	315	10.7
D2	71.9	315	10.4

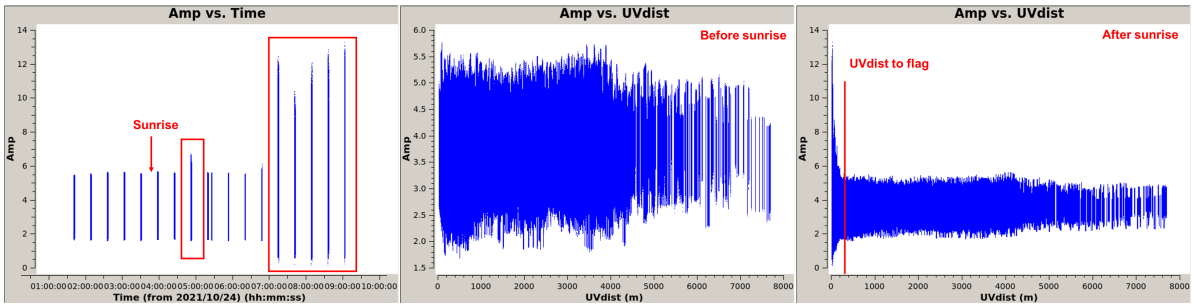

Figure C.2: Example of diagnostic plots for the phase calibrator J0825-5010 prior cross-calibration. The left panel displays the amplitude variation over time during the observations, with the sunrise (03:46 UTC) indicated by a red arrow. Scans impacted by solar RFI are marked by red boxes. The middle and right panels showcase the amplitude variation with UV distance, both pre and post-sunrise, respectively. In the right panel, the maximum UV distance for flagging (UVdist < 1.5 kλ or 315m) after sunrise, specifically for the affected baselines, is denoted by the red vertical line.

After flagging (right panel of Fig. C.3), a substantial reduction or complete elimination of the ripple effect in the position-velocity (PV) slice of the H I cubes is observed, leading to a significant improvement in sensitivity. This noise improvement in the H I cubes is further illustrated in the first two panels of Fig. C.4. The measured rms prior to solar RFI flagging ranges from 0.88 to 9.27 mJy beam^{-1}. Cubes previously highlighted in dark red (with rms > 2 mJy beam^{-1}) in the top panel, are now shaded in orange and yellow (i.e., rms $\sim$1 mJy beam^{-1}), marking a twofold increase in sensitivity after solar RFI flagging, with rms values now ranging from $0.88 - 2.57$ mJy beam^{-1}. This noise improvement continues to be remarkable after mosaicking (see Section 4.3.2), achieving an rms noise spanning 0.68 to 1.24 mJy beam^{-1} in the bottom panel of Fig. C.4.

Finally, an additional flagging step is performed after self-calibration and continuum subtraction, just before the imaging step. This step utilizes `CASA` tasks `tfcrop` and `rflag` to eliminate residual RFI sidelobes, primarily originating from Global Positioning System (GPS) satellites. While the telescope system automatically flags the strong peak at $\sim$1380 MHz, further action is required if it persists in the spectral axis of the H I cube. This scenario arises for blocks A2, B2, C1, and C2, so we applied time and frequency cutoffs of 4σ and 3σ in `tfcrop`, and 4σ in both time and frequency for `rflag`.

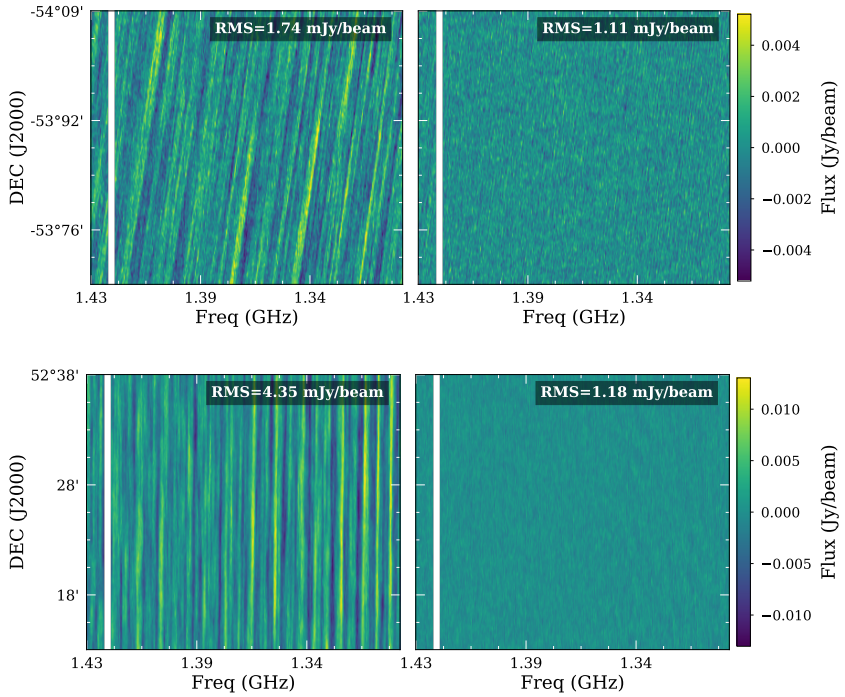

Figure C.3: Example of PV-slices of H I cubes from two target fields. The left panel demonstrates the presence of ripple artifacts, which are effectively removed in the right panel following the solar RFI flagging process.

Prior to calibration and flagging, over half of the target fields in each block (greater than 50 fields) displayed some form of stripes (classified as either strong, medium, faint, or 1380 MHz spike) in their maps, impacting our observations. After solar RFI removal and data reduction, a significant improvement in data quality is observed. Now, the majority of fields are free from RFI or exhibit medium and faint stripes, as indicated by the light purple shading in Fig. C.5. While a few instances persist, they are considered acceptable.

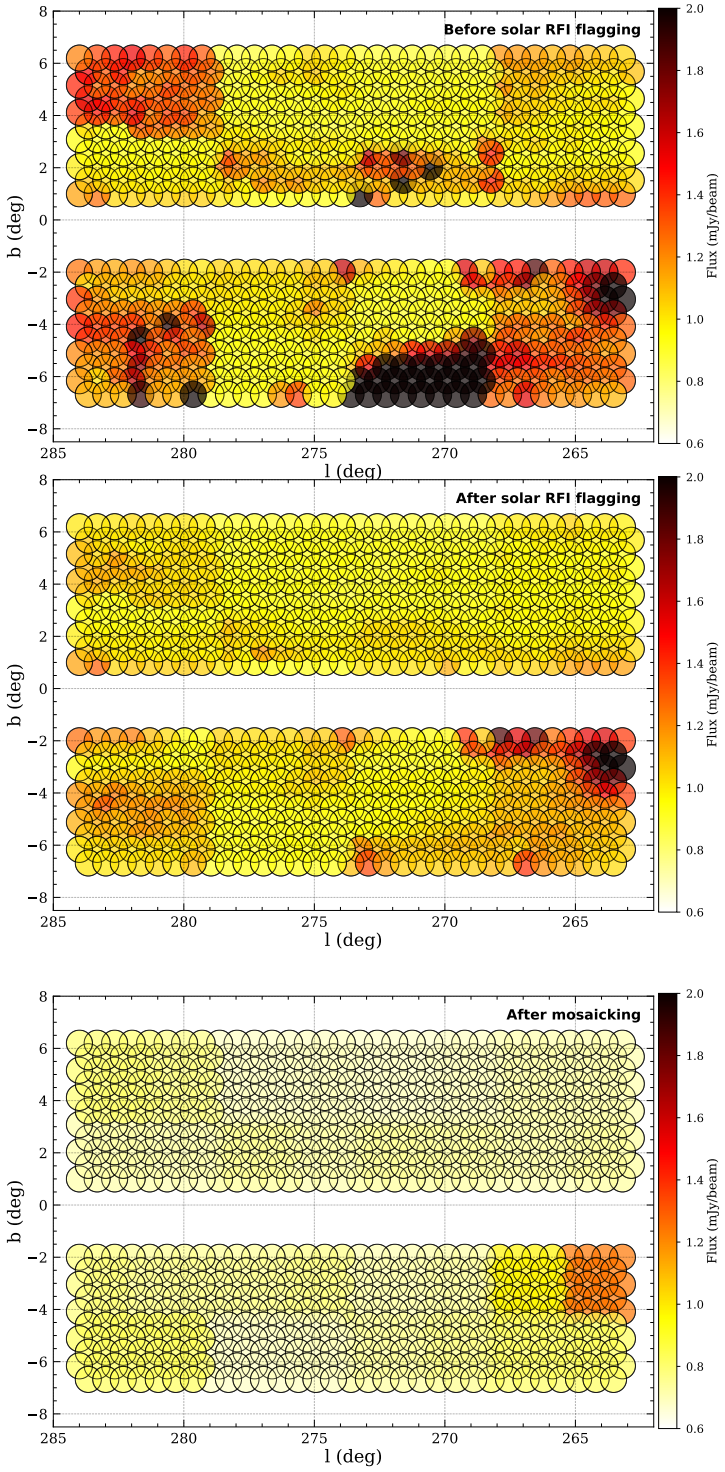

Figure C.4: RMS variations and improvements per field before and after RFI flagging and mosaicking

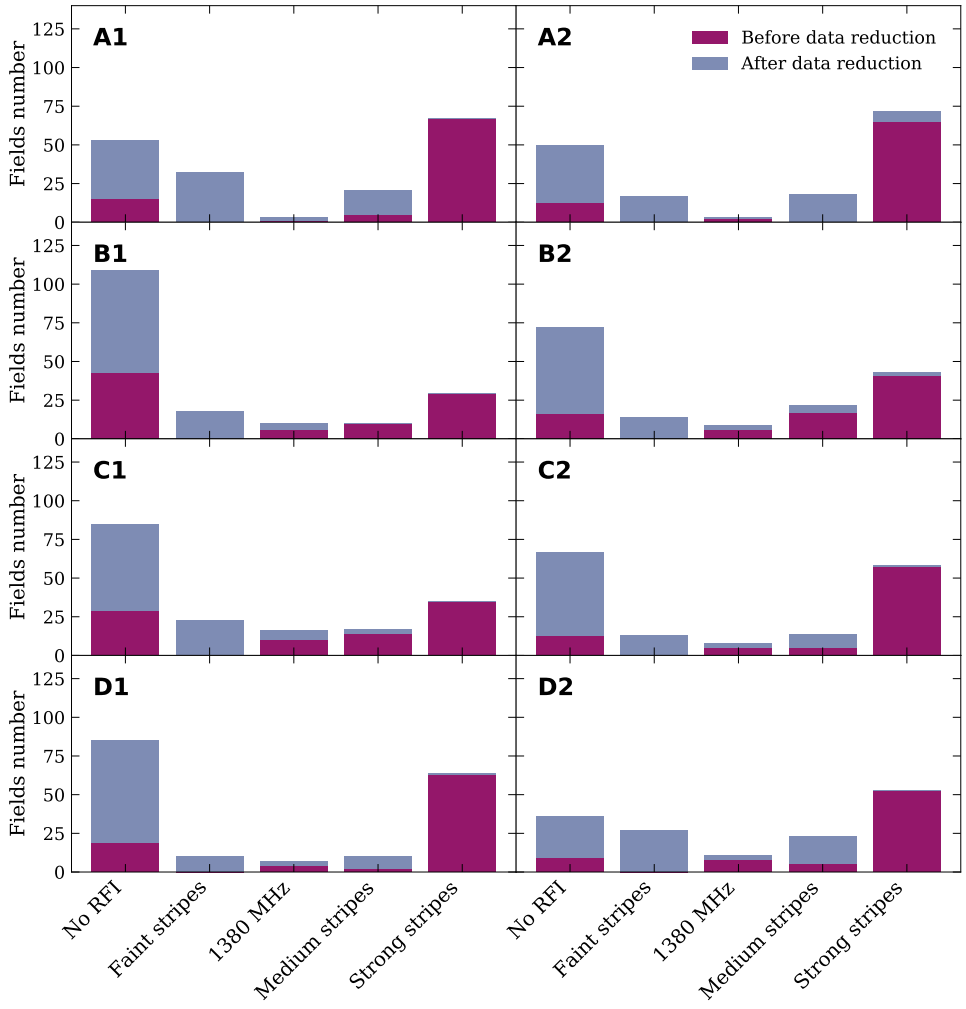

Figure C.5: Histogram displaying the transition of fields from showing strong stripes affected by solar and 1380 MHz RFI to a state of no RFI in each Vela–H I block, both before (dark purple) and after (light purple) data reduction

C.2 Vela–H I full catalog

A succinct description of the catalog parameters is presented below, sourced from SoFiA unless mentioned otherwise. The catalog columns are very similar to the Vela–SMGPS catalog presented in Appendix B.3, the only column differences are:

- (1) Galaxy identifier (VSCL–H I) Jmmhhss±ddmmss.
- (2) Mosaic name [A1A to D2D].
- (13) Flag [1 (Solid) or 2 (Possible)]. Flag+(*): detection identified in the overlapping area with the adjacent mosaic; (**): found in more than two adjacent mosaics; (!): also detected in Vela–SMGPS.
- (14) Note.
    - $B = 40''$: Angular resolution smoothed to $40''$.
    - BL: Wiggly baseline in the Global H I profile.
    - e: Detection located near the mosaic edge.
    - i: With signs of interactions.
    - r: Detection located in an area close to ripples.
    - w.comp(s): galaxy with one (or several) companion(s).
    - w_{20} unc.: w_{20} measurement unclear due to baseline behaviour.
    - I: counterpart from the IRAS Point Source Catalog (Helou & Walker, 1988).
    - H: counterpart from the southern region of the HIPASS catalog (Meyer et al., 2004).
    - M: counterpart from 2MASX (Jarrett et al., 2000).
    - W: counterpart from WISE (Cutri et al., 2021).
    - Z: counterpart from the IRSF catalogs (Williams et al., 2014; Said et al., 2016).

Table C.2: Vela–H I full galaxy catalog: H I properties.

Name	Mosaic	l	b	$S_{\rm peak}$	$S_{\rm int}$	err$_{(S_{\rm int})}$	RMS	$V_{\rm hel}$	w_{20}	w_{50}	$M_{\rm HI}$	Flag	Note
J2000	–	deg	deg	Jy	Jy km s^{-1}	Jy km s^{-1}	mJy beam^{-1}	km s^{-1}	km s^{-1}	km s^{-1}	log($M_{\rm HI}$/M$_\odot$)	1/2	
(1)	(2)	(3)	(4)	(5)	(6)	(7)	(8)	(9)	(10)	(11)	(12)	(13)	(14)
J081815-465710	A2D	263.291	-6.232	0.013	2.78	0.28	0.77	7803	261	221	9.92	1	w. comp (J081828-471025)
J081828-471025	A2D	263.497	-6.324	0.011	0.65	0.14	0.71	7821	163	117	9.29	1	B=40″, i, w.comp (J081815-465710)
J081845-473700	A2D	263.893	-6.531	0.017	4.38	0.25	0.71	7510	349	311	10.08	1	
J081859-483716	A2D	264.757	-7.055	0.013	0.60	0.11	0.98	18637	141	99	10.01	2	e
J082034-464906	A2D	263.401	-5.829	0.002	0.89	0.13	0.70	2148	81	67	8.30	1	
J082116-474921	A2D	264.305	-6.293	0.010	2.33	0.32	0.66	11823	423	380	10.20	1	i
J082148-463756	A2D	263.366	-5.549	0.011	1.23	0.20	0.72	9704	208	166	9.75	1	
J082210-473533	A2D	264.198	-6.040	0.011	1.81	0.19	0.67	7657	232	209	9.71	1	i, w.comp
J082259-493012	A2C	265.864	-7.005	0.024	1.41	0.30	1.14	7182	152	99	9.55	1*	e, i, M, W
J082307-484243	A2D	265.217	-6.542	0.010	0.39	0.08	0.64	10256	214	179	9.30	1	
J082323-483719	A2D	265.168	-6.454	0.006	0.34	0.09	0.58	19440	235	137	9.80	2	
J082328-474526	A2D	264.460	-5.951	0.011	0.87	0.15	0.65	7561	215	98	9.38	1	M, W
J082339-461117	A2D	263.180	-5.036	0.011	0.92	0.16	0.70	9605	269	127	9.62	1	BL
J082403-484045	A2D	265.279	-6.395	0.020	3.13	0.25	0.77	7950	170	118	9.98	1	w.comp, M, W
J082415-490116	A2D	265.581	-6.562	0.019	1.26	0.10	0.67	2229	113	75	8.48	1*	M, W
J082511-494217	A2C	266.234	-6.825	0.034	7.27	0.48	1.10	2218	267	225	9.24	1	e
J082525-465223	A2D	263.918	-5.177	0.010	1.70	0.24	0.65	11762	329	277	10.06	1	i?
J082600-495546	A2C	266.495	-6.845	0.016	1.09	0.18	1.27	8088	228	211	9.54	1	e, w.comp, M, W
J082640-481845	A2D	265.226	-5.831	0.012	0.80	0.23	0.66	4384	240	143	8.87	1	i
J082720-504023	A2C	267.233	-7.095	0.021	2.02	0.10	1.40	3942	124	87	9.18	1	B=40″, e
J082740-490308	A2C	265.929	-6.120	0.012	1.22	0.21	0.74	10744	224	187	9.84	1*	
J082833-475415	A2D	265.071	-5.338	0.010	0.57	0.12	0.64	8639	176	105	9.32	2	
J083055-464513	A2D	264.369	-4.341	0.011	0.33	0.07	0.75	10785	338	83	9.28	2	
J083154-485210	A2C	266.178	-5.448	0.009	0.28	0.06	0.66	18038	261	217	9.66	2	
J083216-481004	A2D	265.652	-4.986	0.011	1.21	0.22	0.64	14775	205	157	10.12	1*	i, w.comp
J083336-503002	A2C	267.674	-6.185	0.013	2.26	0.32	0.61	11486	459	430	10.17	1	M, W
J083428-445041	A2B	263.194	-2.712	0.014	1.29	0.17	1.39	18949	126	88	10.36	2	r
J083453-492218	A2C	266.885	-5.352	0.010	0.70	0.20	0.66	7745	175	104	9.31	1	
J083531-472125	A2D	265.321	-4.067	0.002	0.49	0.10	0.82	9317	256	189	9.32	2	BL
J083612-453957	A2B	264.034	-2.984	0.014	0.65	0.13	1.57	10989	193	163	9.58	2	r
J083649-521526	B2D	269.397	-6.823	0.011	1.09	0.24	0.73	7757	251	191	9.50	1	e

* Detected by the overlapping region of the adjacent mosaic.

** Detected by the overlapping region of two or more adjacent mosaics.

! Detected by the overlapping region between Vela–H I and Vela–SMGPS.

Table C.2 continued

Name	Mosaic	l	b	$S_{\rm peak}$	$S_{\rm int}$	$\mathrm{err}_{(S_{\rm int})}$	RMS	$V_{\rm hel}$	w_{20}	w_{50}	$M_{\rm HI}$	Flag	Note
J2000	–	deg	deg	Jy	Jy km s^{-1}	Jy km s^{-1}	mJy beam^{-1}	km s^{-1}	km s^{-1}	km s^{-1}	log($M_{\rm HI}$/M$_\odot$)	1/2	
(1)	(2)	(3)	(4)	(5)	(6)	(7)	(8)	(9)	(10)	(11)	(12)	(13)	(14)
J083701-495424	A2C	267.520	-5.396	0.023	3.73	0.68	0.76	7781	293	219	10.04	1	BL, i, w.comps (one is J083709-495158), I, M, W
J083709-495158	A2C	267.500	-5.352	0.015	0.69	0.22	0.66	7535	90	74	9.28	1	w.comp (J083701-495424)
J083716-514442	B2D	269.024	-6.463	0.007	0.81	0.10	0.58	10552	182	167	9.64	1	
J083721-524428	B2D	269.838	-7.046	0.007	0.52	0.16	1.03	7710	120	78	9.18	2	e
J083840-474313	A2A	265.933	-3.859	0.009	0.41	0.10	0.62	4360	134	47	8.58	1	
J083854-502036	A2C	268.052	-5.412	0.017	1.38	0.32	0.72	7659	268	131	9.60	1	BL
J083908-512046	B2D	268.879	-5.990	0.006	0.51	0.15	0.63	10344	294	212	9.43	1	
J083931-485344	A2C	266.957	-4.460	0.010	0.40	0.08	0.72	7705	298	225	9.06	2	
J084027-504926	B2D	268.587	-5.510	0.011	2.80	0.27	0.88	7100	271	239	9.84	1	M
J084045-484718	A2C	266.994	-4.234	0.023	1.78	0.16	0.69	7683	82	64	9.71	1*	
J084057-510923	B2D	268.900	-5.650	0.008	0.27	0.06	0.68	23673	292	216	9.88	2	B=40′′
J084057-482152	A2A	266.679	-3.946	0.007	0.36	0.10	0.67	7087	302	186	8.95	1	
J084059-482140	A2C	266.679	-3.942	0.006	0.43	0.08	0.81	7018	332	247	9.02	1	e
J084109-460955	A2B	264.956	-2.577	0.023	1.68	0.31	0.97	15054	181	147	10.27	1	
J084135-454530	A2B	264.674	-2.268	0.015	1.21	0.25	1.08	11629	536	505	9.91	1	i? M, W
J084141-525305	B2D	270.336	-6.612	0.006	0.26	0.05	0.72	22101	255	255	9.80	2	
J084148-512957	B2D	269.254	-5.753	0.010	1.36	0.16	0.74	10276	545	413	9.85	1	
J084206-520153	B2D	269.707	-6.043	0.009	0.38	0.08	0.71	17589	446	347	9.76	1	BL
J084219-523528	B2D	270.168	-6.354	0.008	0.20	0.04	0.70	13889	353	187	9.29	2	BL, w_{20} unc.
J084240-520214	B2D	269.765	-5.975	0.010	0.61	0.08	0.61	6075	207	79	9.04	1	
J084413-511300	B2D	269.263	-5.282	0.015	4.19	0.34	0.77	7488	417	351	10.06	1	
J084426-470831	A2A	266.073	-2.736	0.008	0.23	0.06	0.58	9205	139	109	8.97	2	
J084438-470336	A2A	266.028	-2.660	0.019	1.15	0.23	0.74	7552	192	153	9.51	1	i
J084456-484504	A2A	267.389	-3.665	0.012	1.13	0.23	0.65	7100	219	175	9.44	1	i, M, W
J084457-522946	B2D	270.346	-5.980	0.011	0.85	0.21	0.66	8954	372	222	9.52	1	i, M
J084537-530512	B2D	270.875	-6.266	0.009	0.93	0.29	0.65	7688	186	102	9.43	1*	
J084602-514431	B2D	269.853	-5.384	0.009	0.92	0.15	0.59	18883	343	317	10.21	1	
J084608-533832	B2C	271.363	-6.548	0.004	0.14	0.04	0.58	16955	266	202	9.31	2	
J084617-465948	A2A	266.156	-2.397	0.008	0.31	0.08	0.64	7550	128	97	8.93	2	
J084756-481442	A2A	267.304	-2.963	0.015	2.56	0.48	0.73	8030	278	255	9.91	1	i
J084757-482429	A2A	267.432	-3.064	0.009	0.45	0.14	0.62	7957	115	67	9.14	2	

* Detected by the overlapping region of the adjacent mosaic.

** Detected by the overlapping region of two or more adjacent mosaics.

! Detected by the overlapping region between Vela–H I and Vela–SMGPS.

Table C.2 continued

Name	Mosaic	l	b	$S_{\rm peak}$	$S_{\rm int}$	$\mathrm{err}_{(S_{\rm int})}$	RMS	$V_{\rm hel}$	w_{20}	w_{50}	$M_{\rm HI}$	Flag	Note
J2000	–	deg	deg	Jy	Jy km s^{-1}	Jy km s^{-1}	mJy beam^{-1}	km s^{-1}	km s^{-1}	km s^{-1}	log($M_{\rm HI}$/M$_\odot$)	1/2	
(1)	(2)	(3)	(4)	(5)	(6)	(7)	(8)	(9)	(10)	(11)	(12)	(13)	(14)
J084802-532009	B2C	271.298	-6.136	0.004	0.58	0.11	0.62	6659	231	221	9.10	1*	HyA0492, M
J084803-464727	A2A	266.185	-2.033	0.023	2.80	0.34	0.91	7899	278	220	9.93	1*	J0847-46
J084819-490900	A2A	268.049	-3.482	0.004	0.28	0.03	0.57	5442	309	165	8.61	2	i, w.comp
J084830-482325	A2A	267.477	-2.980	0.008	0.32	0.12	0.64	7626	178	163	8.96	1	
J084832-511634	B2D	269.730	-4.790	0.009	0.35	0.07	0.54	17404	139	102	9.73	1	
J084947-501715	B2B	269.085	-4.013	0.016	1.20	0.24	0.74	8297	218	185	9.61	1	i, w.comp? M, W
J085014-521720	B2D	270.690	-5.221	0.010	0.36	0.07	0.64	8795	143	79	9.14	1	
J085018-533452	B2C	271.702	-6.028	0.007	0.50	0.05	0.58	4026	127	108	8.59	1	
J085023-524635	B2C	271.082	-5.512	0.008	0.68	0.06	0.61	6820	135	114	9.19	1*	
J085122-491543	B2B	268.452	-3.166	0.011	0.37	0.08	0.78	19648	426	182	9.85	2	B=40″, e
J085133-425549	A1D	263.589	0.891	0.010	0.83	0.24	0.76	15957	368	313	10.02	1!	
J085154-502903	B2D	269.452	-3.877	0.008	0.78	0.21	0.79	7227	207	109	9.30	1*	i
J085235-494015	B2B	268.894	-3.274	0.029	2.66	0.09	0.66	2774	81	67	9.00	1	J0852-49
J085250-420600	A1D	263.100	1.603	0.021	3.35	0.27	0.66	3041	279	227	9.18	1	
J085342-434124	A1D	264.422	0.705	0.016	0.82	0.24	1.10	5429	119	76	9.07	1!	e
J085354-422241	A1D	263.441	1.577	0.018	1.73	0.29	0.62	5044	137	137	9.33	1	
J085411-431918	A1D	264.192	1.009	0.014	0.84	0.17	0.86	7070	367	128	9.31	1	i
J085431-544643	B2C	273.028	-6.309	0.014	1.67	0.13	0.86	2720	108	68	8.78	1	HyA0682
J085432-420511	A1D	263.292	1.853	0.009	0.45	0.08	0.55	17463	164	121	9.83	1	
J085451-420626	A1D	263.340	1.885	0.009	0.67	0.12	0.68	5033	383	136	8.91	2	B=45″
J085459-505027	B2D	270.032	-3.732	0.017	1.00	0.20	1.07	11460	138	25	9.81	2*	B=40″, e
J085457-501526	B2B	269.588	-3.359	0.004	0.18	0.04	0.52	11913	214	66	9.11	2	w.comp (J085529-501632)
J085458-545745	B2C	273.212	-6.377	0.010	1.53	0.15	0.76	3970	231	137	9.07	1	HyA0695, BL, W
J085505-423841	A1D	263.784	1.570	0.009	0.49	0.10	0.65	11475	518	316	9.50	1	
J085515-514628	B2D	270.783	-4.299	0.009	0.40	0.08	0.59	7448	83	69	9.03	1	
J085523-500345	B2B	269.484	-3.179	0.083	8.62	0.30	0.69	1605	106	73	9.03	1	J0855-50, H, Z
J085529-501632	B2B	269.658	-3.304	0.007	0.21	0.04	0.57	11999	56	31	9.17	1	w.comp (J085457-501526)
J085537-412353	A1D	262.897	2.452	0.014	2.35	0.21	0.67	5650	301	265	9.56	1	
J085537-513803	B2D	270.715	-4.161	0.008	0.32	0.09	0.72	7178	231	187	8.90	1	
J085539-415501	A1D	263.298	2.122	0.011	0.60	0.18	0.62	16126	255	199	9.88	1	i, M, W
J085546-540341	B2C	272.594	-5.712	0.008	0.48	0.10	0.64	12725	416	367	9.58	1	HyA0713, M, W

* Detected by the overlapping region of the adjacent mosaic.

** Detected by the overlapping region of two or more adjacent mosaics.

! Detected by the overlapping region between Vela–H I and Vela–SMGPS.

Table C.2 continued

Name	Mosaic	l	b	$S_{\rm peak}$	$S_{\rm int}$	$\mathrm{err}_{(S_{\rm int})}$	RMS	$V_{\rm hel}$	w_{20}	w_{50}	$M_{\rm HI}$	Flag	Note
J2000	–	deg	deg	Jy	Jy km s^{-1}	Jy km s^{-1}	mJy beam^{-1}	km s^{-1}	km s^{-1}	km s^{-1}	log($M_{\rm HI}$/M$_\odot$)	1/2	
(1)	(2)	(3)	(4)	(5)	(6)	(7)	(8)	(9)	(10)	(11)	(12)	(13)	(14)
J085557-502526	B2B	269.819	-3.345	0.016	1.85	0.39	0.64	4187	217	186	9.20	1	
J085602-493555	B2B	269.197	-2.800	0.005	0.61	0.08	0.61	17182	515	126	9.95	1	BL
J085604-550359	B2C	273.393	-6.323	0.006	0.85	0.20	0.79	6357	229	189	9.22	2	HyA0718, M
J085638-414823	A1D	263.331	2.331	0.011	0.80	0.14	0.57	15373	225	163	9.97	1	
J085638-483633	B2B	268.507	-2.083	0.024	6.32	0.32	0.86	2632	300	262	9.30	1	J0856-48, w.comp (J085659-483135), I, M, W, Z
J085648-513820	B2D	270.834	-4.029	0.019	3.03	0.56	0.79	7391	523	475	9.91	2*	i, M, W
J085649-535831	B2C	272.624	-5.537	0.008	0.63	0.07	0.53	12708	205	123	9.70	1	HyA0739, W
J085653-512553	B2D	270.684	-3.884	0.015	1.78	0.34	0.81	12450	363	319	10.13	1*	i, I
J085657-512123	B2B	270.633	-3.828	0.005	0.35	0.06	0.58	8344	168	125	9.07	1	
J085659-483135	B2B	268.488	-1.996	0.013	0.81	0.22	0.93	2880	366	108	8.51	2	i, w.comp (J085638-483633)
J085745-510936	B2B	270.564	-3.605	0.009	0.76	0.15	0.70	8465	297	247	9.42	1	w.comp (J085833-510958)
J085754-535234	B2C	272.652	-5.351	0.018	2.19	0.20	0.64	5992	184	139	9.58	1	HyA0764, M, W
J085758-432329	A1D	264.695	1.487	0.019	1.51	0.33	0.74	7881	383	307	9.66	2	BL
J085812-423228	A1D	264.078	2.074	0.008	0.31	0.07	0.54	2948	113	78	8.12	1	J0858-42, w.comp (J085838-423157), Z
J085816-443146	A1C	265.593	0.785	0.009	0.62	0.18	0.81	11152	302	186	9.58	1	e
J085826-554530	C2D	274.143	-6.512	0.005	0.15	0.08	0.56	17808	285	80	9.38	1	
J085829-554255	C2D	274.115	-6.479	0.010	0.47	0.08	0.54	10050	91	60	9.36	1	HyA0786, W
J085833-510958	B2B	270.651	-3.514	0.007	0.41	0.08	0.52	8291	234	138	9.14	1	w.comp (J085745-510936)
J085838-423157	A1D	264.124	2.141	0.014	3.42	0.33	0.66	2761	529	499	9.10	1	w.comps (one is J085812-423228), M, W
J085840-421627	A1D	263.932	2.314	0.008	0.24	0.06	0.54	2867	113	79	7.98	1	
J085840-421208	A1D	263.878	2.361	0.016	2.93	0.22	0.65	4665	261	229	9.49	1	M, W
J085842-503744	B2B	270.260	-3.145	0.008	0.55	0.11	0.59	8055	333	247	9.24	1	w.comp (J085900-503411)
J085849-552012	C2D	273.856	-6.198	0.006	0.76	0.12	0.65	6254	180	135	9.16	1	HyA0795, M, W
J085900-503411	B2B	270.247	-3.070	0.007	1.37	0.15	0.53	8206	328	272	9.65	1	w.comp (J085842-503744)
J085910-515620	B2A	271.302	-3.945	0.009	1.08	0.17	0.66	7543	360	327	9.48	1*	i, w.comp (J085925-515552), I, M, W
J085925-515552	B2A	271.320	-3.912	0.005	0.23	0.08	0.55	7315	149	105	8.78	1*	w.comp (J085910-515620)
J085929-525127	B2C	272.030	-4.509	0.012	3.12	0.22	0.61	4861	318	242	9.55	1*	J0859-52, HyA0808, w.comp (J085938-524534), I, M, W, Z
J085931-500000	B2B	269.869	-2.635	0.010	0.63	0.08	0.51	8030	280	242	9.30	1	i
J085934-422920	A1D	264.204	2.299	0.005	0.32	0.09	0.59	2733	122	78	8.06	1	
J085935-532320	B2C	272.445	-4.844	0.005	0.77	0.10	0.58	9434	264	133	9.52	1	HyA0815, w.comp (J090023-532350), M, W
J085938-524534	B2C	271.972	-4.427	0.014	1.40	0.10	0.62	4828	137	91	9.20	1*	J0859-52, w.comp (J085929-525127)

* Detected by the overlapping region of the adjacent mosaic.

** Detected by the overlapping region of two or more adjacent mosaics.

! Detected by the overlapping region between Vela–H I and Vela–SMGPS.

Table C.2 continued

Name	Mosaic	l	b	$S_{\rm peak}$	$S_{\rm int}$	$\mathrm{err}_{(S_{\rm int})}$	RMS	$V_{\rm hel}$	w_{20}	w_{50}	$M_{\rm HI}$	Flag	Note
J2000	–	deg	deg	Jy	Jy km s^{-1}	Jy km s^{-1}	mJy beam^{-1}	km s^{-1}	km s^{-1}	km s^{-1}	log($M_{\rm HI}$/M$_\odot$)	1/2	
(1)	(2)	(3)	(4)	(5)	(6)	(7)	(8)	(9)	(10)	(11)	(12)	(13)	(14)
J085959-502129	B2B	270.190	-2.818	0.013	1.10	0.36	0.58	8149	325	239	9.55	1	
J090006-515835	B2A	271.424	-3.862	0.005	0.57	0.08	0.56	12736	385	371	9.66	1	M, W
J090013-433755	A1D	265.144	1.638	0.024	2.87	0.33	0.61	4976	257	226	9.54	1*	
J090023-495526	B2B	269.908	-2.496	0.007	0.14	0.03	0.67	22840	651	505	9.56	2	
J090023-532350	B2C	272.528	-4.760	0.015	1.88	0.14	0.63	9259	134	117	9.90	1	J0900-53, w.comp (J085935-532320)
J090051-523754	B2C	271.996	-4.204	0.010	0.99	0.29	0.71	10111	548	490	9.69	1*	
J090103-444214	A1C	266.050	1.045	0.010	0.58	0.06	0.60	10071	120	84	9.46	2	e
J090120-534343	B2C	272.873	-4.870	0.005	0.77	0.14	0.54	21938	458	437	10.26	2	HyA0857
J090143-453114	A1C	266.740	0.593	0.021	1.19	0.31	1.26	7661	167	138	9.53	1!	J0901-45, e
J090143-521908	B2A	271.846	-3.899	0.007	1.55	0.10	0.62	7342	331	261	9.61	1*	
J090145-411432	A1D	263.532	3.426	0.017	3.26	0.25	0.59	5112	275	241	9.62	1*	J0901-41, M, W, Z
J090151-415637	A1D	264.070	2.975	0.006	0.24	0.04	0.50	4809	312	181	8.43	2	i
J090159-443444	A1C	266.066	1.252	0.017	1.73	0.38	0.69	5040	208	174	9.33	1	i
J090202-400719	A1B	262.720	4.206	0.107	14.53	0.46	0.97	1636	121	91	9.27	1	J0902-40, H
J090213-560020	C2D	274.680	-6.272	0.007	0.27	0.06	0.51	13030	64	34	9.36	1	
J090220-413038	A1D	263.805	3.329	0.009	0.39	0.13	0.56	4900	313	61	8.66	1	w.comp (J090239-413505)
J090239-534419	B2C	273.009	-4.731	0.008	0.90	0.17	0.61	7169	264	242	9.36	1	J0902-53, HyA0895, M, Z
J090239-413505	A1D	263.902	3.327	0.011	1.33	0.63	0.64	5221	505	453	9.25	2*	Vel2067, w.comp (J090220-413038)
J090245-532626	B2C	272.794	-4.523	0.005	1.02	0.24	0.59	12614	263	228	9.90	1	
J090247-540548	B2C	273.292	-4.952	0.009	0.74	0.09	0.55	7151	149	86	9.27	1	
J090249-411213	A1B	263.636	3.602	0.014	0.77	0.16	0.61	5234	178	159	9.01	1*	i
J090258-540842	B2C	273.345	-4.965	0.007	1.85	0.28	0.66	9546	469	452	9.92	2	
J090311-451400	A1C	266.697	0.978	0.035	6.54	0.48	0.76	2714	236	193	9.37	1!	J0903-45, Z
J090313-413541	A1D	263.974	3.400	0.010	0.52	0.14	0.66	4676	278	229	8.74	1	
J090313-411719	A1D	263.748	3.601	0.013	1.20	0.19	0.63	4578	138	120	9.08	1*	i, Part of J090323-411816 seen in the spectrum
J090314-523746	B2C	272.232	-3.932	0.018	3.62	0.39	0.84	7306	301	195	9.94	1*	J0903-52, i, M
J090318-561005	C2D	274.912	-6.268	0.006	0.46	0.09	0.62	13433	343	70	9.61	1	w_{20} unc.
J090323-411817	A1B	263.782	3.614	0.098	7.97	0.27	0.71	5459	120	91	10.06	1*	J0903-41, M, W, Z
J090346-532756	B2C	272.914	-4.426	0.011	1.11	0.08	0.56	7149	178	92	9.44	1*	J0903-53, i, w.comp (J090422-533654)
J090351-561754	C2D	275.053	-6.294	0.009	0.93	0.26	0.60	10044	331	292	9.66	1	HyA0936, M, W
J090411-425934	A1D	265.130	2.590	0.009	0.33	0.07	0.65	20808	372	173	9.85	2	w.comp?

* Detected by the overlapping region of the adjacent mosaic.

** Detected by the overlapping region of two or more adjacent mosaics.

! Detected by the overlapping region between Vela–HI and Vela–SMGPS.

Table C.2 continued

Name	Mosaic	l	b	$S_{\rm peak}$	$S_{\rm int}$	$\mathrm{err}_{(S_{\rm int})}$	RMS	$V_{\rm hel}$	w_{20}	w_{50}	$M_{\rm HI}$	Flag	Note
J2000	–	deg	deg	Jy	Jy km s^{-1}	Jy km s^{-1}	mJy beam^{-1}	km s^{-1}	km s^{-1}	km s^{-1}	log($M_{\rm HI}$/M$_\odot$)	1/2	
(1)	(2)	(3)	(4)	(5)	(6)	(7)	(8)	(9)	(10)	(11)	(12)	(13)	(14)
J090408-425648	A1D	265.102	2.625	0.010	0.59	0.11	0.58	9620	482	434	9.43	1	
J090408-521830	B2A	272.084	-3.615	0.006	0.57	0.06	0.57	7433	186	79	9.19	1	
J090422-533654	B2C	273.084	-4.459	0.009	0.64	0.07	0.54	7134	145	101	9.20	1	w.comp (J090346-532756)
J090424-451733	A1C	266.882	1.096	0.038	2.54	0.11	0.70	7207	114	71	9.81	1	J0904-45
J090437-551119	C2D	274.289	-5.478	0.009	0.27	0.06	0.52	10753	69	37	9.19	1	
J090440-550150	C2D	274.176	-5.367	0.006	0.48	0.10	0.55	9868	520	494	9.36	2	HyA0953, W
J090442-440703	A1C	266.043	1.921	0.012	0.54	0.05	0.52	5370	99	51	8.88	1	w.comp
J090447-511456	B2A	271.359	-2.835	0.012	2.54	0.46	0.61	17505	595	532	10.59	1*	
J090448-444154	A1C	266.488	1.546	0.025	4.33	0.23	0.68	7096	331	282	10.03	1	J0905-44, M, W, Z
J090451-562927	C2D	275.289	-6.319	0.009	1.43	0.29	0.62	12722	316	274	10.06	1	HyA0956, M, W
J090456-571027	C2D	275.812	-6.763	0.013	1.06	0.14	0.69	4250	165	130	8.97	1	
J090504-394956	A1B	262.891	4.831	0.014	0.94	0.17	0.69	4885	288	144	9.04	1	i
J090536-520228	B2A	272.034	-3.270	0.006	0.38	0.06	0.55	6986	175	145	8.96	2	BL
J090551-523805	B2A	272.502	-3.639	0.005	0.93	0.19	0.63	7182	360	343	9.37	1	M, W
J090551-552300	C2D	274.553	-5.472	0.008	0.63	0.13	0.60	9771	535	484	9.47	1	HyA0986, w.comp? M, W
J090555-445136	A1C	266.740	1.584	0.007	0.55	0.17	0.58	8686	185	169	9.31	1	i
J090601-445045	A1C	266.743	1.609	0.006	0.19	0.04	0.53	7129	120	86	8.68	1	
J090608-414057	A1B	264.408	3.746	0.010	0.33	0.10	0.55	8420	84	63	9.06	1	
J090615-415314	A1B	264.575	3.625	0.019	2.40	0.33	0.65	5208	198	162	9.50	1*	
J090631-504656	B2A	271.195	-2.320	0.007	0.46	0.14	0.50	17439	286	258	9.84	2*	
J090635-453313	A1C	267.334	1.206	0.006	0.35	0.04	0.56	14368	305	181	9.56	1	i
J090642-574013	C2C	276.345	-6.915	0.010	0.51	0.11	0.73	10019	137	90	9.40	2*	
J090643-394353	A1B	263.029	5.134	0.005	0.36	0.02	0.53	6157	224	137	8.82	2	
J090649-462651	A1C	268.022	0.634	0.015	1.10	0.32	1.16	7473	499	309	9.48	2!	e
J090654-414648	A1D	264.575	3.782	0.018	1.37	0.28	0.83	4706	360	288	9.17	1*	
J090703-410401	A1B	264.065	4.285	0.009	0.67	0.23	0.58	11477	405	315	9.64	1	Vel2181, i, w.comp, W
J090715-455556	A1C	267.692	1.028	0.007	0.27	0.08	0.72	18763	369	175	9.67	1	
J090725-405858	A1B	264.050	4.390	0.006	0.27	0.06	0.56	11445	250	135	9.24	1	
J090724-553647	C2D	274.872	-5.467	0.011	3.03	0.40	0.63	9931	391	338	10.17	1	BL, i, w.comp
J090732-424854	A1C	265.423	3.177	0.015	2.02	0.41	0.59	5105	228	186	9.41	1**	i
J090734-422612	A1D	265.147	3.436	0.020	1.27	0.26	0.63	2306	181	111	8.51	1**	J0907-42, BL

* Detected by the overlapping region of the adjacent mosaic.

** Detected by the overlapping region of two or more adjacent mosaics.

! Detected by the overlapping region between Vela–H I and Vela–SMGPS.

Table C.2 continued

Name	Mosaic	l	b	$S_{\rm peak}$	$S_{\rm int}$	$\mathrm{err}_{(S_{\rm int})}$	RMS	$V_{\rm hel}$	w_{20}	w_{50}	$M_{\rm HI}$	Flag	Note
J2000	–	deg	deg	Jy	Jy km s^{-1}	Jy km s^{-1}	mJy beam^{-1}	km s^{-1}	km s^{-1}	km s^{-1}	log($M_{\rm HI}$/M$_\odot$)	1/2	
(1)	(2)	(3)	(4)	(5)	(6)	(7)	(8)	(9)	(10)	(11)	(12)	(13)	(14)
J090802-514613	B2A	272.064	-2.813	0.005	0.13	0.03	0.63	13113	237	125	9.03	2	
J090802-512653	B2A	271.845	-2.591	0.004	0.18	0.05	0.51	22866	348	311	9.67	2	
J090806-512512	B2A	271.836	-2.565	0.005	2.00	0.11	0.65	1701	129	92	8.45	1	
J090817-421244	A1D	265.073	3.686	0.009	0.59	0.20	0.62	9926	117	80	9.45	1*	BL
J090901-410310	A1B	264.306	4.569	0.005	0.39	0.04	0.49	11530	147	120	9.41	2	
J090928-404835	A1B	264.185	4.798	0.014	0.99	0.22	0.62	5046	119	91	9.09	1	
J090933-555527	C2D	275.307	-5.453	0.015	1.03	0.12	0.58	9841	120	62	9.69	1	
J090942-465303	B1D	268.679	0.704	0.020	0.57	0.12	0.93	6579	77	48	9.08	2	e
J091023-440319	A1C	266.688	2.717	0.011	0.80	0.14	0.57	7019	183	139	9.28	1	i, I
J091026-534806	C2D	273.824	-3.918	0.012	0.25	0.05	0.80	23482	178	78	9.83	1	
J091034-514825	B2A	272.380	-2.547	0.002	0.97	0.19	0.61	1801	186	91	8.18	1	
J091028-462612	B1D	268.454	1.118	0.012	0.54	0.11	0.72	11803	111	54	9.57	2	
J091036-442654	A1C	267.002	2.478	0.019	1.93	0.10	0.59	1868	124	91	8.51	1	J0910-44
J091039-560311	C2D	275.507	-5.428	0.010	0.79	0.10	0.59	4139	129	96	8.81	1	HyA1086, W
J091044-425723	A1A	265.926	3.513	0.011	0.80	0.06	0.59	2899	170	148	8.51	1*	
J091105-553331	C2D	275.185	-5.046	0.008	2.42	0.24	0.60	10012	331	263	10.08	1	M
J091110-524935	B2A	273.190	-3.175	0.008	0.50	0.15	0.58	10192	290	188	9.40	1	
J091121-545043	C2D	274.684	-4.530	0.007	0.31	0.06	0.63	23924	173	138	9.95	1	
J091130-400058	A1B	263.863	5.620	0.015	0.95	0.18	0.56	16473	139	86	10.11	1	
J091129-401801	A1B	264.076	5.425	0.008	0.51	0.10	0.61	11316	294	223	9.51	1	w.comp
J091142-435457	A1C	266.746	2.984	0.016	1.09	0.11	0.59	7550	142	100	9.48	1	
J091154-530540	B2A	273.460	-3.278	0.004	0.53	0.18	0.61	5924	209	177	8.96	1	
J091156-443434	A1C	267.257	2.563	0.009	0.70	0.08	0.54	9389	208	155	9.48	1	w.comps (one is J091157-443307)
J091157-443307	A1C	267.243	2.583	0.009	0.29	0.07	0.52	9663	137	121	9.13	2	w.comp (J091156-443434)
J091209-534148	C2B	273.926	-3.663	0.032	1.54	0.14	0.76	4026	95	55	9.08	1*	J0912-53
J091230-455323	B1D	268.283	1.735	0.019	2.32	0.36	0.71	4763	178	161	9.41	1	J0912-45, i, Z
J091236-393130	A1B	263.646	6.108	0.015	1.27	0.20	0.63	6016	119	89	9.35	1	Vel2398, W
J091238-585018	C2C	277.743	-7.127	0.021	2.61	0.22	1.26	2903	237	179	9.03	1	HyA1125, I, H, M, W
J091240-404258	A1B	264.531	5.305	0.006	0.07	0.02	0.48	7994	173	72	8.35	2	
J091248-535228	C2B	274.121	-3.715	0.005	0.31	0.06	0.55	21116	436	364	9.84	2	M, W
J091314-514448	B2A	272.618	-2.206	0.027	1.98	0.36	0.73	10635	260	204	10.04	1	J0913-51, i

* Detected by the overlapping region of the adjacent mosaic.

** Detected by the overlapping region of two or more adjacent mosaics.

! Detected by the overlapping region between Vela–HI and Vela–SMGPS.

Table C.2 continued

Name	Mosaic	l	b	$S_{\rm peak}$	$S_{\rm int}$	$\mathrm{err}_{(S_{\rm int})}$	RMS	$V_{\rm hel}$	w_{20}	w_{50}	$M_{\rm HI}$	Flag	Note
J2000	–	deg	deg	Jy	Jy km s^{-1}	Jy km s^{-1}	mJy beam^{-1}	km s^{-1}	km s^{-1}	km s^{-1}	log($M_{\rm HI}$/M$_\odot$)	1/2	
(1)	(2)	(3)	(4)	(5)	(6)	(7)	(8)	(9)	(10)	(11)	(12)	(13)	(14)
J091317-560313	C2D	275.760	-5.159	0.007	0.33	0.07	0.55	10591	300	258	9.25	2	
J091330-423533	A1A	266.007	4.131	0.008	1.06	0.19	0.58	22543	534	494	10.43	1	BL, w.comp?
J091402-393736	A1B	263.911	6.240	0.009	0.94	0.09	0.65	11363	236	96	9.78	1	
J091404-412603	A1B	265.239	5.003	0.006	0.26	0.05	0.54	20682	182	99	9.74	2	
J091407-514555	B2A	272.736	-2.132	0.017	1.66	0.52	0.72	5300	378	127	9.35	1	BL, i
J091407-571425	C2D	276.706	-5.890	0.017	1.73	0.09	0.77	10104	218	175	9.94	1*	
J091413-441509	A1C	267.303	3.083	0.004	0.22	0.04	0.47	9929	292	231	9.03	2	
J091429-422550	A1A	266.014	4.373	0.014	1.27	0.10	0.60	2972	123	101	8.73	1	i, w.comp
J091437-464721	B1D	269.190	1.370	0.006	0.26	0.05	0.55	19943	251	161	9.70	2	BL
J091454-515445	B2A	272.917	-2.133	0.008	1.65	0.30	0.59	20865	357	273	10.55	1	i
J091502-410342	A1A	265.090	5.392	0.011	0.24	0.05	0.69	14044	181	144	9.38	2	BL, e
J091504-444828	A1C	267.810	2.808	0.013	0.71	0.15	0.65	3775	138	94	8.69	1	
J091505-394119	A1B	264.097	6.345	0.005	0.54	0.19	0.64	11548	402	370	9.55	2	
J091521-515120	B2A	272.922	-2.065	0.008	0.25	0.05	0.71	19171	420	96	9.65	2	w_{20} unc.
J091516-542459	C2D	274.764	-3.820	0.017	2.76	0.45	1.01	9490	523	459	10.08	1*	B=40′, e, w.comps (one is J091526-542427)
J091520-574530	C2C	277.197	-6.128	0.005	0.35	0.05	0.49	16257	214	154	9.65	2	
J091524-474200	B1D	269.935	0.845	0.009	0.49	0.09	0.91	7293	139	86	9.11	1!	J0915-47
J091526-542427	C2B	274.774	-3.804	0.006	0.58	0.06	0.61	9369	263	198	9.40	1	w.comp (J091516-542459)
J091538-533735	C2B	274.230	-3.241	0.009	1.09	0.33	0.68	19372	399	358	10.31	1	B=50′, i?
J091543-563508	C2D	276.380	-5.281	0.011	0.26	0.07	0.53	13255	85	53	9.35	1*	
J091543-520810	B2A	273.160	-2.192	0.017	2.05	0.58	0.68	10357	534	309	10.03	1	i
J091548-574007	C2C	277.175	-6.021	0.005	0.43	0.12	0.51	16278	254	198	9.75	1	
J091549-543529	C2B	274.946	-3.891	0.045	6.40	0.18	0.69	4020	148	108	9.70	1*	J0916-54A, I, M, W, Z
J091549-432929	A1A	266.952	3.817	0.010	1.45	0.21	0.59	6882	327	270	9.52	1*	M, W
J091629-563035	C2D	276.399	-5.152	0.008	0.77	0.15	0.56	12966	274	233	9.80	1*	HyA1178, i, W
J091635-420320	A1A	266.013	4.915	0.011	0.65	0.12	0.57	4968	199	150	8.89	1	w.comp
J091643-542114	C2B	274.866	-3.631	0.031	9.61	0.53	0.75	4091	347	227	9.89	1*	J0916-54B, i, I
J091649-561557	C2D	276.254	-4.950	0.007	0.28	0.09	0.54	15277	185	171	9.51	2	
J091714-465110	B1D	269.543	1.658	0.007	0.69	0.14	0.58	9710	311	276	9.50	1	i
J091717-570146	C2C	276.850	-5.435	0.006	0.48	0.09	0.56	10053	185	128	9.38	2	
J091719-513705	B2A	272.965	-1.659	0.015	0.88	0.26	0.91	19085	242	180	10.20	2	BL

* Detected by the overlapping region of the adjacent mosaic.

** Detected by the overlapping region of two or more adjacent mosaics.

! Detected by the overlapping region between Vela–H I and Vela–SMGPS.

Table C.2 continued

Name	Mosaic	l	b	$S_{\rm peak}$	$S_{\rm int}$	$\mathrm{err}_{(S_{\rm int})}$	RMS	$V_{\rm hel}$	w_{20}	w_{50}	$M_{\rm HI}$	Flag	Note
J2000	–	deg	deg	Jy	Jy km s^{-1}	Jy km s^{-1}	mJy beam^{-1}	km s^{-1}	km s^{-1}	km s^{-1}	log($M_{\rm HI}$/M$_\odot$)	1/2	
(1)	(2)	(3)	(4)	(5)	(6)	(7)	(8)	(9)	(10)	(11)	(12)	(13)	(14)
J091730-445551	B1D	268.198	3.032	0.013	1.10	0.15	0.75	5459	172	112	9.20	1	
J091730-532315	C2B	274.252	-2.875	0.093	19.60	0.50	0.80	941	208	175	8.92	1	J0917-53, I, H, M, Z
J091743-552857	C2D	275.777	-4.315	0.009	2.20	0.34	0.69	6913	355	286	9.71	1*	I, M, W
J091746-480948	B1C	270.543	0.805	0.045	5.52	0.68	0.94	3336	240	187	9.47	1*!	J0917-48
J091805-551921	C2D	275.699	-4.166	0.008	0.44	0.08	0.61	9209	141	91	9.27	1	
J091807-564421	C2C	276.721	-5.150	0.007	1.38	0.14	0.56	20799	430	384	10.47	1*	
J091810-461317	B1D	269.203	2.213	0.009	0.30	0.06	0.50	23283	250	65	9.92	1	
J091822-553341	C2D	275.894	-4.301	0.013	0.61	0.06	0.63	17455	534	446	9.97	1	i
J091827-552618	C2D	275.819	-4.209	0.009	0.23	0.05	0.55	18492	99	33	9.60	2	
J091835-445257	B1D	268.298	3.204	0.006	0.39	0.13	0.65	10145	147	101	9.30	1	w_{20} unc.
J091856-471811	B1D	270.067	1.549	0.006	0.49	0.10	0.64	14331	390	360	9.69	1	i
J091858-475712	B1C	270.536	1.098	0.007	0.43	0.31	0.74	7251	327	236	9.04	1*	w.comp
J091913-481238	B1D	270.747	0.946	0.007	0.23	0.12	0.81	18732	359	70	9.61	1*	
J091915-565617	C2C	276.972	-5.179	0.007	0.73	0.08	0.55	21121	355	324	10.21	1	
J091925-571735	C2C	277.243	-5.411	0.007	0.61	0.09	0.57	10199	265	236	9.49	1	
J091925-550307	C2B	275.640	-3.840	0.005	0.61	0.15	0.65	6891	204	177	9.15	2*	
J091931-523006	C2B	273.834	-2.036	0.009	0.94	0.19	0.92	6864	272	235	9.33	1	e
J091932-474732	B1D	270.487	1.278	0.009	0.33	0.08	0.54	4680	118	89	8.54	1	
J091944-415805	A1A	266.359	5.394	0.005	0.28	0.03	0.54	7204	130	116	8.85	1	
J092021-553757	C2D	276.147	-4.154	0.013	1.53	0.18	0.62	12750	193	126	10.09	1**	
J092032-442511	B1B	268.211	3.775	0.060	8.94	0.70	0.77	2673	213	182	9.49	1*	J0920-44, H, Z
J092038-464502	B1D	269.880	2.144	0.021	1.42	0.21	0.62	4135	120	91	9.07	1	i, w.comp?
J092041-582429	C2C	278.161	-6.073	0.004	0.21	0.04	0.46	15298	191	149	9.38	2	
J092055-443055	B1D	268.328	3.756	0.006	0.21	0.04	0.75	17499	211	160	9.51	2	
J092057-472649	B1D	270.410	1.690	0.012	1.24	0.14	0.64	9454	270	229	9.73	1	i
J092100-531131	C2B	274.481	-2.365	0.010	0.93	0.27	0.66	13940	219	162	9.95	1	
J092101-431742	A1A	267.473	4.629	0.010	1.06	0.09	0.61	5118	171	137	9.13	1	
J092112-480819	B1D	270.929	1.230	0.007	0.24	0.02	0.69	7132	99	56	8.77	2	e, w.comp (J092120-480629)
J092112-412859	A1A	266.206	5.930	0.008	0.37	0.06	0.53	7218	139	110	8.97	1	
J092120-480629	B1C	270.924	1.256	0.032	3.76	0.17	0.64	7213	197	160	9.98	1*	J0921-48, i, w.comps (one is J092112-480819)
J092125-451625	B1D	268.928	3.282	0.016	0.93	0.09	0.57	9683	130	79	9.63	1*	i, w.comp

* Detected by the overlapping region of the adjacent mosaic.

** Detected by the overlapping region of two or more adjacent mosaics.

! Detected by the overlapping region between Vela–H I and Vela–SMGPS.

Table C.2 continued

Name	Mosaic	l	b	$S_{\rm peak}$	$S_{\rm int}$	$\mathrm{err}_{(S_{\rm int})}$	RMS	$V_{\rm hel}$	w_{20}	w_{50}	$M_{\rm HI}$	Flag	Note
J2000	–	deg	deg	Jy	Jy km s^{-1}	Jy km s^{-1}	mJy beam^{-1}	km s^{-1}	km s^{-1}	km s^{-1}	log($M_{\rm HI}$/M$_\odot$)	1/2	
(1)	(2)	(3)	(4)	(5)	(6)	(7)	(8)	(9)	(10)	(11)	(12)	(13)	(14)
J092128-483240	B1C	271.248	0.975	0.007	0.37	0.04	0.58	9353	152	94	9.20	1	
J092136-485240	B1C	271.499	0.755	0.011	1.42	0.33	0.87	11236	327	287	9.94	1!	e, i
J092151-542733	C2B	275.465	-3.174	0.015	1.03	0.08	0.58	12676	172	129	9.91	1	M, W
J092151-474557	B1D	270.744	1.572	0.008	0.66	0.17	0.63	7187	189	116	9.22	1*	
J092156-535248	C2B	275.065	-2.755	0.010	0.82	0.21	0.66	14387	490	285	9.92	1	
J092216-443510	B1B	268.549	3.877	0.006	0.48	0.12	0.53	10964	270	245	9.45	2	
J092224-551619	C2B	276.096	-3.694	0.005	0.32	0.05	0.57	12753	222	189	9.41	1	
J092229-415719	A1A	266.712	5.766	0.011	0.76	0.08	0.67	7377	84	60	9.31	1	
J092232-592017	C2C	278.994	-6.558	0.006	0.94	0.13	0.73	6612	254	91	9.30	1	
J092237-474722	B1D	270.851	1.645	0.007	0.18	0.05	0.60	8177	265	186	8.76	1	e, M
J092238-412110	A1A	266.304	6.213	0.015	3.09	0.70	0.74	4881	205	173	9.55	1	Vel2604, BL, M, W
J092251-473644	B1C	270.755	1.800	0.008	1.17	0.22	0.65	7497	272	251	9.51	1*	
J092256-570838	C2C	277.473	-4.969	0.011	3.00	0.16	0.64	6769	357	321	9.83	1	HyA1272, w.comp (J092313-570116), I, M, W
J092306-454420	B1D	269.466	3.161	0.006	0.35	0.08	0.47	23415	279	220	9.98	1	Face-on galaxy with hole at the centre?
J092313-570116	C2C	277.414	-4.854	0.006	0.78	0.09	0.58	6736	221	115	9.24	1	w.comp (J092256-570838), I
J092323-555250	C2A	276.625	-4.028	0.005	0.25	0.08	0.61	9183	201	146	9.02	2	w.comp (J092329-555401)
J092329-555401	C2B	276.649	-4.034	0.009	0.51	0.09	0.67	9416	158	90	9.34	1*	i, w.comp (J092323-555250)
J092334-424542	A1A	267.426	5.336	0.022	5.60	0.34	0.70	2989	198	151	9.38	1	J0923-42, Vel2630, H, M, W, Z
J092335-442426	B1B	268.588	4.168	0.007	0.67	0.10	0.56	11036	221	182	9.60	2	
J092342-421629	A1A	267.100	5.699	0.005	0.36	0.08	0.55	10057	395	264	9.25	1	
J092344-415236	A1A	266.821	5.982	0.008	0.42	0.09	0.60	9805	226	173	9.30	2	Vel2637, i, M, W
J092434-585501	C2C	278.882	-6.075	0.005	0.41	0.07	0.64	6672	181	117	8.95	2	
J092438-475217	B1C	271.149	1.824	0.008	0.54	0.04	0.57	7118	130	93	9.12	1	
J092441-411533	A1A	266.512	6.551	0.013	2.15	0.15	0.91	4678	224	180	9.36	2	Vel2667, BL, e
J092443-542654	C2B	275.755	-2.873	0.007	0.34	0.08	0.54	4078	125	94	8.43	1	
J092455-582741	C2C	278.593	-5.719	0.006	0.50	0.14	0.57	15186	188	113	9.76	2	
J092459-452538	B1B	269.483	3.615	0.011	0.55	0.04	0.57	9726	181	143	9.40	1	
J092514-583640	C2C	278.728	-5.796	0.010	0.57	0.05	0.57	9886	123	91	9.43	1	
J092516-462723	B1D	270.239	2.914	0.013	0.84	0.20	0.61	21984	211	121	10.31	1	BL
J092517-593015	D2D	279.362	-6.429	0.004	2.02	0.24	0.83	2989	245	205	8.94	2	HyA1312, M, W
J092524-475223	B1C	271.244	1.913	0.005	0.60	0.12	0.60	11402	294	264	9.58	1	

* Detected by the overlapping region of the adjacent mosaic.

** Detected by the overlapping region of two or more adjacent mosaics.

! Detected by the overlapping region between Vela–H I and Vela–SMGPS.

Table C.2 continued

Name	Mosaic	l	b	$S_{\rm peak}$	$S_{\rm int}$	err$_{(S_{\rm int})}$	RMS	$V_{\rm hel}$	w_{20}	w_{50}	$M_{\rm HI}$	Flag	Note
J2000	–	deg	deg	Jy	Jy km s^{-1}	Jy km s^{-1}	mJy beam^{-1}	km s^{-1}	km s^{-1}	km s^{-1}	log($M_{\rm HI}$/M$_\odot$)	1/2	
(1)	(2)	(3)	(4)	(5)	(6)	(7)	(8)	(9)	(10)	(11)	(12)	(13)	(14)
J092525-455124	B1D	269.830	3.366	0.007	0.39	0.08	0.60	15240	179	93	9.65	1	
J092540-580342	C2C	278.383	-5.364	0.009	0.92	0.13	0.59	10427	187	149	9.69	1	w.comp (J092622-580706)
J092542-464455	B1D	270.496	2.755	0.012	0.50	0.19	0.63	6423	195	139	9.00	1	i
J092548-432724	B1B	268.207	5.126	0.010	1.13	0.25	0.77	5059	196	110	9.15	1	i
J092555-413108	A1A	266.861	6.527	0.017	2.57	0.83	1.07	5035	241	195	9.50	1	Vel2695, BL, e, M, W
J092605-415016	A1A	267.106	6.320	0.028	4.78	0.58	0.81	4687	169	145	9.71	1	H, M, W
J092607-572454	C2C	277.973	-4.859	0.012	1.17	0.14	0.59	6802	218	188	9.42	1	
J092624-603627	D2D	280.240	-7.130	0.014	6.66	0.27	1.54	2108	144	95	9.15	2	e
J092622-580706	C2C	278.488	-5.341	0.013	3.31	0.20	0.65	10217	645	513	10.23	1	HyA1326, Edge-on Sp, w.comp (J092540-580342), M, W
J092629-454533	B1B	269.900	3.556	0.009	0.47	0.10	0.59	15193	185	46	9.73	2	B=40″
J092628-570548	C2C	277.783	-4.599	0.007	0.32	0.07	0.51	12303	175	135	9.38	1	w.comp
J092638-552538	C2A	276.637	-3.382	0.008	0.70	0.19	0.61	9369	166	106	9.48	1*	i, w.comp
J092711-414646	A1A	267.214	6.506	0.011	1.94	0.34	0.89	2624	171	142	8.81	1	BL, e
J092715-495527	B1C	272.887	0.649	0.029	4.75	0.48	1.14	4537	236	204	9.68	1!	J0927-49, e, i
J092730-542319	C2B	276.004	-2.549	0.007	0.20	0.04	0.53	20850	99	81	9.63	1	
J092731-604613	D2D	280.453	-7.140	0.020	3.45	0.19	1.41	2138	466	392	8.88	1	HyA1353, e, I, M, W
J092736-433200	B1B	268.500	5.300	0.009	0.39	0.08	0.62	16410	297	172	9.72	1	w.comp
J092739-424854	A1A	268.001	5.822	0.012	1.55	0.20	0.81	5000	170	152	9.27	1	e
J092742-490255	B1C	272.335	1.332	0.004	0.25	0.05	0.59	11277	122	89	9.19	2	
J092746-555840	C2A	277.134	-3.669	0.156	32.64	0.19	0.67	1147	185	134	9.32	1*	J0927-55, H
J092751-474934	B1C	271.508	2.233	0.010	0.67	0.09	0.57	7070	175	158	9.21	1	
J092757-450531	B1B	269.625	4.219	0.006	0.30	0.03	0.47	19457	506	398	9.76	2	
J092759-565922	C2C	277.858	-4.378	0.010	2.88	0.14	0.58	12196	385	277	10.32	1*	i
J092805-563236	C2A	277.559	-4.046	0.024	4.48	0.22	0.68	4587	202	172	9.66	1*	J0928-56, M, W, Z
J092804-482518	B1C	271.960	1.832	0.028	1.53	0.11	0.63	7151	87	23	9.58	1	J0927-48, i, w.comp?
J092826-562601	C2A	277.518	-3.933	0.005	0.43	0.11	0.59	10669	190	190	9.38	2	
J092851-422821	A1A	267.923	6.222	0.009	0.63	0.13	0.67	16656	221	179	9.93	1	Vel2728, e, i, M
J092902-421808	A1A	267.828	6.368	0.017	5.42	0.99	0.98	6557	527	449	10.05	1	Vel2731, M, W
J092924-422309	A1A	267.937	6.355	0.019	4.41	1.32	0.97	6738	324	309	9.99	1	Vel2736, M, W
J092938-481954	B1C	272.072	2.071	0.016	3.07	0.45	0.68	7348	337	310	9.91	1	J0929-48, I, M, W, Z
J092953-440308	B1B	269.154	5.208	0.006	0.78	0.09	0.54	5306	271	232	9.03	1	

* Detected by the overlapping region of the adjacent mosaic.

** Detected by the overlapping region of two or more adjacent mosaics.

! Detected by the overlapping region between Vela–HI and Vela–SMGPS.

Table C.2 continued

Name	Mosaic	l	b	$S_{\rm peak}$	$S_{\rm int}$	$\mathrm{err}_{(S_{\rm int})}$	RMS	$V_{\rm hel}$	w_{20}	w_{50}	$M_{\rm HI}$	Flag	Note
J2000	–	deg	deg	Jy	Jy km s^{-1}	Jy km s^{-1}	mJy beam^{-1}	km s^{-1}	km s^{-1}	km s^{-1}	log($M_{\rm HI}$/M$_\odot$)	1/2	
(1)	(2)	(3)	(4)	(5)	(6)	(7)	(8)	(9)	(10)	(11)	(12)	(13)	(14)
J093006-454649	B1D	270.374	3.979	0.012	0.39	0.08	0.90	8351	131	117	9.12	2	e
J093007-432510	B1B	268.747	5.696	0.019	3.27	0.67	0.61	5088	324	282	9.61	1	Vel2740, M, W
J093019-545215	C2A	276.633	-2.617	0.012	1.61	0.05	0.61	3903	213	166	9.08	1*	
J093029-453759	B1B	270.323	4.134	0.011	1.96	0.23	0.60	11915	440	372	10.14	1	i
J093048-555515	C2A	277.403	-3.335	0.023	2.27	0.21	0.63	2740	147	91	8.90	1	J0930-55
J093052-580322	C2C	278.876	-4.885	0.013	1.68	0.30	0.72	10283	557	355	9.94	1	w.comp
J093059-423217	B1B	268.254	6.450	0.010	0.51	0.10	0.98	17120	424	260	9.87	2	e, i, w.comp
J093109-594757	D2D	280.105	-6.128	0.002	2.74	0.22	0.73	2957	233	180	9.06	1	HyA1419, w. comp (J093235-595336), M
J093111-435653	B1B	269.253	5.445	0.013	0.67	0.15	0.57	5099	138	87	8.93	1	J0931-43? i
J093116-590703	D2D	279.645	-5.622	0.007	0.78	0.14	0.64	2278	162	117	8.29	1	
J093116-434633	B1B	269.147	5.581	0.019	1.03	0.15	0.55	5134	112	73	9.12	1	J0931-43?
J093119-424539	B1B	268.458	6.333	0.006	0.35	0.07	0.68	14769	180	131	9.58	1	
J093131-542115	C2B	276.406	-2.122	0.008	0.36	0.09	0.63	9008	166	127	9.16	1	
J093202-473740	B1C	271.884	2.860	0.006	0.66	0.14	0.54	14419	223	179	9.83	1	HyA1426, I, M, W
J093211-432432	B1B	269.018	5.961	0.008	0.56	0.11	0.55	14819	289	248	9.78	2	
J093219-435317	B1B	269.362	5.628	0.014	1.18	0.13	0.55	4981	125	108	9.15	1	
J093234-572803	C2C	278.639	-4.299	0.009	0.85	0.09	0.65	9441	219	176	9.57	1*	
J093235-595336	D2D	280.301	-6.073	0.003	1.89	0.11	0.74	2991	238	193	8.91	2	w.comp (J093109-594757)
J093246-434859	B1B	269.372	5.736	0.011	1.08	0.16	0.52	5225	220	164	9.15	1	Vel2765, i, M, W
J093255-545229	C2A	276.910	-2.364	0.019	0.66	0.07	0.63	1005	63	19	7.50	2	
J093259-551456	C2A	277.171	-2.628	0.007	0.42	0.12	0.61	13804	227	179	9.60	1	
J093308-484539	B1C	272.789	2.153	0.013	1.47	0.35	0.65	7368	196	130	9.59	1	
J093313-435642	B1B	269.519	5.696	0.013	1.94	0.53	0.62	5407	289	242	9.44	1	i
J093316-491337	B1C	273.122	1.822	0.007	0.42	0.09	0.80	7351	265	208	9.05	1	
J093322-434524	B1B	269.410	5.853	0.006	0.20	0.04	0.47	16351	157	125	9.41	1	
J093324-501758	C1D	273.862	1.049	0.010	1.29	0.27	0.69	7357	260	205	9.53	1	
J093346-441248	B1B	269.776	5.567	0.004	0.53	0.05	0.47	14635	315	269	9.75	1	
J093348-434324	B1B	269.446	5.931	0.012	0.56	0.11	0.55	5225	87	71	8.87	1	w.comp?
J093356-462724	B1A	271.326	3.935	0.009	1.00	0.32	0.61	11489	409	363	9.81	1	
J093356-552033	C2A	277.334	-2.610	0.012	1.28	0.09	0.62	11209	233	211	9.90	1	
J093413-611653	D2D	281.402	-6.952	0.007	2.93	0.51	1.18	2628	211	154	8.99	1*	HyA1464, e, w. comp, HI LSB with a hole at the centre? I, H, M

* Detected by the overlapping region of the adjacent mosaic.

** Detected by the overlapping region of two or more adjacent mosaics.

! Detected by the overlapping region between Vela–HI and Vela–SMGPS.

Table C.2 continued

Name	Mosaic	l	b	$S_{\rm peak}$	$S_{\rm int}$	$\mathrm{err}_{(S_{\rm int})}$	RMS	$V_{\rm hel}$	w_{20}	w_{50}	$M_{\rm HI}$	Flag	Note
J2000	–	deg	deg	Jy	Jy km s^{-1}	Jy km s^{-1}	mJy beam^{-1}	km s^{-1}	km s^{-1}	km s^{-1}	log($M_{\rm HI}$/M$_\odot$)	1/2	
(1)	(2)	(3)	(4)	(5)	(6)	(7)	(8)	(9)	(10)	(11)	(12)	(13)	(14)
J093417-541300	C2A	276.620	-1.746	0.011	0.22	0.04	0.94	16316	149	39	9.46	2	
J093424-481552	B1C	272.608	2.661	0.006	0.41	0.08	0.53	7322	139	89	9.03	1	i
J093428-442842	B1B	270.049	5.457	0.014	0.82	0.13	0.53	14631	148	81	9.94	1	i, w.comp
J093454-555439	C2A	277.819	-2.937	0.017	4.64	0.14	0.59	4020	239	209	9.56	1	J0934-55
J093458-564632	C2A	278.409	-3.571	0.016	3.12	0.15	0.65	9342	309	262	10.12	1	I, M, W
J093507-471453	B1A	272.010	3.493	0.006	0.41	0.09	0.59	11378	136	108	9.42	2*	e
J093516-483019	B1C	272.877	2.580	0.008	0.94	0.10	0.56	17676	236	178	10.16	1	BL, i
J093519-492903	C1D	273.541	1.860	0.009	0.56	0.15	0.79	7067	148	100	9.14	1	
J093523-434628	B1B	269.688	6.088	0.010	0.58	0.12	0.62	11616	402	253	9.59	1	i, w.comp
J093529-434939	B1B	269.743	6.061	0.010	0.79	0.16	0.53	19916	394	342	10.19	1	i, I
J093533-444840	B1B	270.418	5.343	0.008	0.38	0.08	0.49	13693	108	63	9.55	1	i
J093548-470259	B1A	271.962	3.717	0.006	0.26	0.05	0.52	14888	190	95	9.46	2	
J093606-453530	B1A	271.018	4.831	0.012	1.24	0.37	0.61	17529	322	280	10.27	1*	i
J093617-433619	B1B	269.698	6.321	0.012	0.77	0.15	0.60	11666	184	169	9.71	1	M, W
J093635-463105	B1A	271.704	4.201	0.008	0.38	0.08	0.50	6860	158	117	8.94	1	
J093639-543719	C2A	277.137	-1.815	0.080	9.34	0.38	0.94	2746	169	102	9.48	1!	J0936-54, i, I, M, W, Z
J093639-495935	C1D	274.042	1.627	0.011	0.41	0.06	0.59	6955	168	28	8.98	1	
J093659-605552	D2D	281.411	-6.468	-0.000	3.35	0.14	0.76	2811	303	284	9.11	1*	HyA1492, I, H, M, W
J093659-493752	C1D	273.844	1.932	0.007	0.31	0.06	0.57	20667	236	195	9.82	1	
J093701-455420	B1A	271.348	4.705	0.009	1.65	0.21	0.63	6776	277	234	9.57	1	i? w.comp?
J093708-480214	B1C	272.792	3.134	0.009	0.57	0.06	0.58	3275	160	104	8.47	1	
J093708-452247	B1A	271.010	5.110	0.007	0.24	0.04	0.50	8019	92	75	8.88	1	
J093723-465844	B1A	272.115	3.949	0.008	0.23	0.07	0.54	3942	170	44	8.24	2	
J093730-601851	D2D	281.041	-5.969	0.009	2.76	0.14	0.65	3088	207	178	9.10	1	HyA1499, M, W
J093730-462729	B1A	271.782	4.350	0.006	0.41	0.08	0.55	18532	378	339	9.85	1	i, w.comps, M, W
J093730-563016	C2A	278.487	-3.135	0.007	0.38	0.08	0.61	2257	104	67	7.98	1	
J093732-452834	B1A	271.126	5.085	0.005	0.22	0.02	0.51	17605	116	69	9.53	2	
J093732-560516	C2A	278.211	-2.821	0.009	1.81	0.22	0.66	9180	241	218	9.87	1	
J093733-465720	B1A	272.121	3.986	0.009	0.71	0.20	0.53	17867	229	187	10.05	1	i, w.comp
J093739-503052	C1D	274.508	1.345	0.012	0.83	0.05	0.53	8366	177	143	9.45	1	
J093756-444955	B1B	270.740	5.610	0.005	0.12	0.03	0.63	11507	254	207	8.89	1	

* Detected by the overlapping region of the adjacent mosaic.

** Detected by the overlapping region of two or more adjacent mosaics.

! Detected by the overlapping region between Vela–H I and Vela–SMGPS.

Table C.2 continued

Name	Mosaic	l	b	$S_{\rm peak}$	$S_{\rm int}$	$\mathrm{err}_{(S_{\rm int})}$	RMS	$V_{\rm hel}$	w_{20}	w_{50}	$M_{\rm HI}$	Flag	Note
J2000	–	deg	deg	Jy	Jy km s^{-1}	Jy km s^{-1}	mJy beam^{-1}	km s^{-1}	km s^{-1}	km s^{-1}	log($M_{\rm HI}$/M$_\odot$)	1/2	
(1)	(2)	(3)	(4)	(5)	(6)	(7)	(8)	(9)	(10)	(11)	(12)	(13)	(14)
J093827-614914	D2D	282.142	-7.011	0.018	1.53	0.14	1.96	2869	316	290	8.78	2	e
J093828-614951	D2C	282.151	-7.016	0.015	4.59	0.21	1.19	2920	314	273	9.28	1	HyA1517, e, I, M, W
J093838-453650	B1A	271.363	5.111	0.007	0.18	0.05	0.47	17347	86	61	9.42	1	
J093908-584728	D2D	280.176	-4.695	0.009	0.86	0.07	0.63	4263	247	76	8.88	1	
J093916-465115	B1A	272.272	4.257	0.009	0.36	0.07	0.53	19458	142	125	9.83	2	BL
J093923-504125	C1D	274.832	1.397	0.010	1.14	0.26	0.61	8395	257	217	9.59	1	w.comp (J093928-504343)
J093923-564747	C2A	278.874	-3.178	0.008	0.71	0.14	0.79	12152	572	512	9.71	1	M, W
J093928-504343	C1D	274.867	1.377	0.012	0.53	0.16	0.60	8297	113	60	9.25	1	w.comp (J093923-504125)
J093945-442406	B1A	270.701	6.148	0.007	0.25	0.04	0.55	17304	84	62	9.57	1	e
J093949-564551	C2A	278.896	-3.119	0.019	1.00	0.08	0.72	2963	124	69	8.63	1	J0939-56
J093956-451201	B1A	271.260	5.571	0.005	0.33	0.06	0.45	17903	231	187	9.72	1	
J094037-443253	B1A	270.912	6.144	0.007	0.40	0.08	0.57	21598	325	294	9.97	1	
J094040-593844	D2D	280.891	-5.206	0.018	1.02	0.15	0.68	2353	97	50	8.44	1	J0940-59, H, Z
J094044-493138	C1D	274.226	2.413	0.009	0.89	0.10	0.54	12072	188	136	9.80	1	
J094059-603026	D2D	281.486	-5.826	0.011	2.82	0.11	0.75	3108	129	59	9.12	1*	B=40″
J094055-473105	B1A	272.922	3.964	0.006	0.21	0.04	0.62	11234	495	452	9.11	2	
J094111-580103	D2D	279.864	-3.938	0.009	0.40	0.08	0.73	10226	124	87	9.32	2*	
J094123-485552	C1D	273.913	2.931	0.006	0.30	0.08	0.56	7859	140	121	8.96	1	i
J094124-612541	D2C	282.144	-6.484	0.005	0.83	0.11	0.62	11198	323	306	9.71	1	HyA1557, M, W
J094141-493309	C1D	274.358	2.494	0.011	0.54	0.11	0.55	11894	122	85	9.58	1	HyA1554, M, W
J094143-604756	D2C	281.754	-5.987	0.004	3.45	0.30	0.75	3127	271	267	9.21	1*	HyA1561, I, M, W
J094150-552932	C2A	278.274	-1.975	0.009	0.51	0.10	0.75	7828	283	125	9.18	2	B=40″, i, w.comp
J094202-560800	C2A	278.713	-2.441	0.006	0.15	0.05	0.55	2705	89	54	7.72	2	BL
J094211-603558	D2C	281.665	-5.799	0.006	1.66	0.05	0.64	3172	172	158	8.91	1*	HyA1568, W
J094233-480734	C1D	273.531	3.666	0.015	0.78	0.14	0.66	17770	224	172	10.09	2	
J094235-470412	B1A	272.841	4.467	0.016	1.47	0.40	0.62	16951	228	186	10.32	1	M, W
J094239-485410	C1D	274.050	3.088	0.011	1.24	0.41	0.62	7879	299	209	9.57	1	
J094252-601728	D2C	281.526	-5.511	0.011	0.58	0.18	0.65	4569	178	81	8.77	2*	Face-on?
J094300-601953	D2C	281.565	-5.530	0.011	2.46	0.18	0.75	2832	135	125	8.98	1*	
J094303-570732	D2B	279.467	-3.101	0.006	0.32	0.04	0.54	10708	94	63	9.25	1	
J094308-520147	C1C	276.165	0.775	0.009	0.29	0.06	0.84	13812	532	469	9.44	2	

* Detected by the overlapping region of the adjacent mosaic.

** Detected by the overlapping region of two or more adjacent mosaics.

! Detected by the overlapping region between Vela–H I and Vela–SMGPS.

Table C.2 continued

Name	Mosaic	l	b	$S_{\rm peak}$	$S_{\rm int}$	$\mathrm{err}_{(S_{\rm int})}$	RMS	$V_{\rm hel}$	w_{20}	w_{50}	$M_{\rm HI}$	Flag	Note
J2000	–	deg	deg	Jy	Jy km s^{-1}	Jy km s^{-1}	mJy beam^{-1}	km s^{-1}	km s^{-1}	km s^{-1}	log($M_{\rm HI}$/M$_\odot$)	1/2	
(1)	(2)	(3)	(4)	(5)	(6)	(7)	(8)	(9)	(10)	(11)	(12)	(13)	(14)
J094317-452103	B1A	271.803	5.846	0.013	2.16	0.12	0.54	5348	255	224	9.48	1	Vel2962
J094326-453013	B1A	271.923	5.748	0.008	0.68	0.20	0.56	12072	261	193	9.69	1	Vel2966
J094333-452150	B1A	271.847	5.867	0.006	0.65	0.12	0.57	18078	528	487	10.02	1	Vel2969, B=40″, w.comp, M
J094339-583333	D2D	280.461	-4.133	0.012	0.88	0.16	0.75	20082	212	140	10.25	2	B=40″
J094357-490251	C1D	274.310	3.120	0.009	0.37	0.12	0.52	7839	91	74	9.04	1	
J094407-593134	D2D	281.143	-4.830	0.016	6.51	0.46	0.84	2413	203	158	9.26	1	J0944-59, H, Z
J094407-573532	D2B	279.882	-3.360	0.005	0.47	0.09	0.60	10852	210	172	9.43	1	
J094427-600410	D2D	281.531	-5.214	0.012	0.33	0.09	0.73	5779	145	95	8.72	2	
J094428-491944	C1D	274.558	2.962	0.007	0.35	0.07	0.54	12180	326	230	9.40	2	
J094435-510826	C1D	275.746	1.593	0.008	0.34	0.09	0.56	4624	86	71	8.55	1	
J094440-453801	B1A	272.174	5.791	0.005	0.24	0.06	0.47	11459	127	93	9.18	1	
J094449-513036	C1D	276.013	1.335	0.011	0.54	0.13	0.63	2751	104	56	8.30	1*	
J094450-463222	B1A	272.787	5.121	0.012	1.20	0.15	0.57	11414	243	161	9.88	1	w.comp
J094451-484728	C1B	274.254	3.409	0.025	1.03	0.13	0.73	2156	54	30	8.37	1*	
J094503-611942	D2C	282.410	-6.122	0.007	0.96	0.10	0.63	11202	354	307	9.77	1	
J094511-484803	C1D	274.303	3.438	0.006	0.51	0.13	0.50	7797	186	186	9.18	1	
J094516-604149	D2C	282.017	-5.625	0.011	1.31	0.17	0.70	3103	146	108	8.79	1*	
J094523-455452	B1A	272.452	5.658	0.005	0.53	0.05	0.49	21024	298	210	10.07	1	Vel3013
J094524-480829	C1B	273.903	3.964	0.099	8.56	0.12	0.57	862	109	59	8.54	1*	J0945-48, HyA1610, H
J094531-515720	C1C	276.384	1.065	0.014	2.54	0.48	0.74	5348	262	228	9.55	1*	i, M, W
J094534-462153	B1A	272.770	5.336	0.007	0.30	0.06	0.55	7477	111	81	8.92	2	i
J094541-494647	C1D	275.000	2.742	0.008	0.33	0.07	0.60	21135	361	215	9.87	2	i?
J094605-492115	C1D	274.774	3.112	0.006	0.73	0.18	0.56	21172	293	276	10.21	1	HyA1621, w.comp? M, W
J094622-463854	B1A	273.060	5.209	0.057	14.90	0.70	0.68	2697	339	304	9.72	1	J0946-46, Vel3035, H, M, W, Z
J094630-511251	C1D	276.024	1.731	0.008	0.66	0.07	0.67	1782	163	140	8.00	1*	
J094754-462958	B1A	273.165	5.492	0.010	0.69	0.19	0.68	2744	284	229	8.40	1	
J094801-572258	D2B	280.148	-2.863	0.018	1.64	0.27	0.61	9411	174	154	9.85	1	
J094814-464417	B1A	273.363	5.345	0.022	1.39	0.25	0.78	17458	276	228	10.32	1	Vel3072, e, i
J094823-562731	D2B	279.595	-2.120	0.044	9.19	0.88	0.70	1677	260	225	9.10	1	w.comp (J094953-563235), M
J094839-452958	B1A	272.623	6.344	0.012	1.23	0.32	0.70	13437	417	371	10.04	1	Vel3084
J094843-494107	C1D	275.316	3.132	0.017	1.20	0.20	0.57	7076	123	88	9.60	1	J0948-49

* Detected by the overlapping region of the adjacent mosaic.

** Detected by the overlapping region of two or more adjacent mosaics.

! Detected by the overlapping region between Vela–HI and Vela–SMGPS.

Table C.2 continued

Name	Mosaic	l	b	$S_{\rm peak}$	$S_{\rm int}$	$\mathrm{err}_{(S_{\rm int})}$	RMS	$V_{\rm hel}$	w_{20}	w_{50}	$M_{\rm HI}$	Flag	Note
J2000	–	deg	deg	Jy	Jy km s^{-1}	Jy km s^{-1}	mJy beam^{-1}	km s^{-1}	km s^{-1}	km s^{-1}	log($M_{\rm HI}$/M$_\odot$)	1/2	
(1)	(2)	(3)	(4)	(5)	(6)	(7)	(8)	(9)	(10)	(11)	(12)	(13)	(14)
J094851-514331	C1C	276.631	1.571	0.008	0.64	0.19	0.72	6959	176	134	9.18	1	M
J094901-500310	C1D	275.587	2.879	0.015	1.36	0.06	0.57	11746	183	106	9.96	1	
J094906-492208	C1D	275.161	3.415	0.023	2.80	0.36	0.64	2686	193	145	8.99	1*	J0949-49
J094916-475535	C1B	274.261	4.544	0.057	8.90	0.27	0.66	1870	189	134	9.18	1	J0949-47A, HyA1664, i, w.comp (J094924-480028), I, H, M, W, Z
J094924-480028	C1B	274.330	4.495	0.066	7.97	0.29	0.71	1979	154	105	9.18	1	J0949-47A, HyA1666, H I bridge, i, w.comp (J094916-475535), H, M, W, Z
J094924-454232	B1A	272.858	6.266	0.033	2.65	0.18	0.66	5319	151	85	9.56	1	Vel3106, M, W
J094925-490810	C1B	275.058	3.625	0.011	0.68	0.14	0.64	16967	303	217	9.98	1*	HyA1669, BL, M, W
J094930-570707	D2B	280.134	-2.532	0.006	0.56	0.11	0.57	10326	379	276	9.47	1	
J094932-513903	C1C	276.665	1.696	0.009	1.63	0.29	0.67	7045	269	242	9.60	1	J0949-51
J094940-454319	B1A	272.901	6.286	0.008	0.36	0.12	0.60	16409	432	393	9.68	1	Vel3118, I, H, M
J094944-471104	C1B	273.847	5.166	0.029	5.50	0.32	0.71	5365	222	185	9.89	1	J0949-47B, Vel3119, H, M, W, Z
J094953-563235	D2B	279.808	-2.054	0.140	39.29	6.35	0.78	1761	263	231	9.77	1	J0949-56, B=45′,i, w.comps (J095106, J094823), I, H, M, W, Z
J094955-571545	D2B	280.269	-2.611	0.010	0.56	0.13	0.53	16751	263	84	9.89	1	
J094954-504421	C1D	276.133	2.439	0.010	0.61	0.14	0.60	6974	165	80	9.16	1*	i
J094958-481700	C1B	274.583	4.342	0.008	1.01	0.20	0.68	5148	381	227	9.11	1	
J095002-522411	C1C	277.203	1.165	0.031	3.07	0.14	0.78	2225	142	88	8.87	1	J0950-52, i
J095019-452602	B1A	272.805	6.580	0.010	0.63	0.16	0.80	12164	201	145	9.66	1	Vel3139, e, M, W
J095034-494246	C1D	275.563	3.300	0.020	3.47	0.24	0.61	3775	243	196	9.38	1*	J0950-49, I, Z
J095035-500912	C1D	275.845	2.960	0.007	0.38	0.06	0.52	6946	176	162	8.95	1	
J095049-522540	C1C	277.320	1.219	0.007	0.50	0.10	0.78	8672	409	297	9.27	2	i
J095059-580933	D2B	280.950	-3.216	0.005	0.15	0.03	0.61	19190	514	197	9.44	2	
J095106-564841	D2B	280.107	-2.156	0.015	0.73	0.28	0.68	1654	109	78	7.98	1	w.comp (J094953-563235)
J095113-614527	D2C	283.254	-5.980	0.007	0.56	0.09	0.56	10208	266	130	9.46	1	
J095115-491531	C1B	275.362	3.722	0.008	0.58	0.19	0.57	12143	313	271	9.62	1	
J095123-524422	C1C	277.574	1.032	0.016	0.83	0.14	0.67	6692	116	72	9.26	1	
J095131-532201	C1C	277.984	0.557	0.049	5.76	0.65	1.45	2203	158	126	9.13	1!	J0951-53, H
J095144-591607	D2D	281.724	-4.011	0.013	4.35	0.32	0.89	4397	390	358	9.61	1**	J0951-59, M, W, Z
J095146-520334	C1C	277.192	1.598	0.023	2.57	0.22	0.70	4009	161	119	9.30	1	J0951-52, Z
J095207-485929	C1B	275.303	4.018	0.007	0.49	0.14	0.55	12216	214	169	9.56	1	HyA1713
J095207-570714	D2B	280.411	-2.309	0.013	0.96	0.16	0.60	4526	129	92	8.98	1	
J095211-464300	C1B	273.874	5.792	0.010	1.66	0.19	0.58	13582	273	246	10.18	1	Vel3189

* Detected by the overlapping region of the adjacent mosaic.

** Detected by the overlapping region of two or more adjacent mosaics.

! Detected by the overlapping region between Vela–H I and Vela–SMGPS.

Table C.2 continued

Name	Mosaic	l	b	$S_{\rm peak}$	$S_{\rm int}$	err$_{(S_{\rm int})}$	RMS	$V_{\rm hel}$	w_{20}	w_{50}	$M_{\rm HI}$	Flag	Note
J2000	–	deg	deg	Jy	Jy km s^{-1}	Jy km s^{-1}	mJy beam^{-1}	km s^{-1}	km s^{-1}	km s^{-1}	log($M_{\rm HI}$/M$_\odot$)	1/2	
(1)	(2)	(3)	(4)	(5)	(6)	(7)	(8)	(9)	(10)	(11)	(12)	(13)	(14)
J095240-470640	C1B	274.189	5.539	0.014	1.68	0.10	0.56	1808	181	67	8.42	1	w.comp
J095244-474729	C1B	274.626	5.016	0.008	0.44	0.15	0.55	5381	116	72	8.79	1	
J095254-491618	C1B	275.580	3.881	0.011	0.81	0.17	0.61	7781	174	155	9.38	1*	w.comp (J095310-491957)
J095258-491949	C1B	275.624	3.841	0.031	3.16	0.46	0.68	2258	137	99	8.89	1*	J0953-49, H
J095300-613136	D2C	283.272	-5.667	0.025	2.94	0.24	0.76	4454	107	75	9.45	1	J0952-61, I, H, Z
J095310-491957	C1B	275.653	3.861	0.009	1.50	0.19	0.60	7794	291	218	9.65	1*	w.comp (J095254-491618)
J095321-522850	C1C	277.644	1.421	0.008	0.56	0.14	0.61	11862	259	119	9.59	1	
J095321-515411	C1C	277.284	1.872	0.022	1.33	0.11	0.67	2735	71	44	8.68	1	J0953-51
J095341-495053	C1D	276.040	3.510	0.009	0.29	0.09	0.56	4013	127	95	8.35	2	
J095347-455758	C1B	273.618	6.550	0.014	1.46	0.30	1.48	7105	360	327	9.55	2	Vel3231, M, W
J095400-520930	C1C	277.521	1.735	0.010	0.64	0.08	0.59	14023	181	154	9.79	1	
J095417-512919	C1C	277.140	2.288	0.010	0.41	0.04	0.57	2682	116	87	8.15	1	J0954-51, w.comp (J095427-513059), Z
J095418-495236	C1B	276.136	3.550	0.005	0.14	0.15	0.70	7235	205	162	8.57	2	w.comp (J095420-495422)
J095420-495422	C1B	276.158	3.530	0.007	0.37	0.15	0.70	7204	144	80	8.97	1*	HyA1744, w.comp (J095418-495236)
J095427-513059	C1C	277.176	2.281	0.006	0.49	0.09	0.60	2735	144	97	8.25	2	J0954-51, w.comp (J095417-512919)
J095435-492233	C1B	275.861	3.971	0.010	0.46	0.07	0.53	3734	110	66	8.50	1*	
J095446-494549	C1B	276.125	3.686	0.014	2.20	0.42	0.67	7107	307	266	9.73	1**	HyA1749, M, W
J095456-480421	C1B	275.093	5.028	0.007	1.32	0.24	0.57	11548	401	265	9.94	1	M
J095503-483436	C1B	275.422	4.644	0.012	1.03	0.16	0.56	17116	207	159	10.17	1	HyA1754, i, w.comp, M
J095504-573107	D2B	280.971	-2.368	0.011	0.71	0.14	0.64	10479	265	221	9.58	1	
J095510-604012	D2C	282.940	-4.835	0.011	5.98	0.36	0.76	3280	265	210	9.49	2	J0955-60, HyA1766, BL, r, H, M, W, Z
J095600-593612	D2A	282.358	-3.934	0.006	1.12	0.16	0.78	14656	269	150	10.07	2	B=40″
J095619-514119	C1C	277.511	2.326	0.009	0.55	0.08	0.53	11454	127	97	9.55	1	
J095622-584631	D2A	281.883	-3.253	0.010	0.47	0.16	0.61	2540	116	85	8.16	1*	
J095630-593234	D2A	282.371	-3.847	0.005	4.17	0.10	0.76	3436	272	249	9.38	2**	J0956-59, BL, r, M, W, Z
J095632-495045	C1B	276.401	3.797	0.010	1.11	0.19	0.75	6696	239	152	9.39	1**	HyA1792, W
J095642-513436	C1C	277.489	2.450	0.010	0.35	0.08	0.56	2686	78	60	8.09	1	
J095704-512912	C1C	277.479	2.556	0.017	1.73	0.32	0.68	11378	439	320	10.04	1	i
J095710-485625	C1B	275.923	4.575	0.074	6.64	0.83	0.68	3730	106	77	9.64	1*	J0957-48, H, Z
J095750-581159	D2A	281.681	-2.681	0.044	5.66	0.60	0.70	3304	208	175	9.48	1*	J0957-58
J095757-511233	C1C	277.418	2.861	0.008	0.35	0.09	0.57	14167	187	83	9.55	2	i, w.comp

* Detected by the overlapping region of the adjacent mosaic.

** Detected by the overlapping region of two or more adjacent mosaics.

! Detected by the overlapping region between Vela–HI and Vela–SMGPS.

295

Table C.2 continued

Name	Mosaic	l	b	$S_{\rm peak}$	$S_{\rm int}$	$\mathrm{err}_{(S_{\rm int})}$	RMS	$V_{\rm hel}$	w_{20}	w_{50}	$M_{\rm HI}$	Flag	Note
J2000	–	deg	deg	Jy	Jy km s^{-1}	Jy km s^{-1}	mJy beam^{-1}	km s^{-1}	km s^{-1}	km s^{-1}	log($M_{\rm HI}$/M$_\odot$)	1/2	
(1)	(2)	(3)	(4)	(5)	(6)	(7)	(8)	(9)	(10)	(11)	(12)	(13)	(14)
J095809-472102	C1B	275.072	5.930	0.019	2.33	0.07	0.64	3639	126	96	9.18	1	
J095837-470458	C1B	274.969	6.189	0.012	1.02	0.10	0.63	3613	165	111	8.81	1	Vel3418, I, M
J095859-501154	C1A	276.929	3.760	0.008	0.97	0.21	0.58	6648	309	265	9.32	1	HyA1835, i, w.comp, M
J095901-480721	C1B	275.661	5.408	0.006	0.36	0.06	0.52	12548	240	77	9.45	2	
J095903-490321	C1B	276.239	4.673	0.012	1.44	0.34	0.68	14155	326	293	10.15	1*	M, W
J095922-503240	C1A	277.187	3.522	0.007	0.30	0.06	0.60	8547	217	146	9.03	1	HyA1841, W
J095926-480950	C1B	275.743	5.418	0.011	0.67	0.14	0.60	6613	312	80	9.16	2	Face-on?
J095936-501102	C1A	276.998	3.832	0.015	1.65	0.25	0.62	7127	193	136	9.61	1*	HyA1849, M
J095956-512026	C1C	277.743	2.944	0.006	0.63	0.14	0.58	14075	538	493	9.79	1	
J100019-583828	D2A	282.209	-2.833	0.115	10.82	1.14	0.75	2682	186	89	9.58	1*	J1000-58A, w.comp (J100130-584224), H
J100032-495839	C1A	276.976	4.073	0.005	0.28	0.06	0.65	19050	381	290	9.70	2	
J100036-465941	C1B	275.184	6.465	0.027	1.85	0.11	0.89	3684	103	48	9.08	1	
J100038-482637	C1A	276.073	5.317	0.006	0.44	0.11	0.56	13878	281	163	9.62	1	
J100058-535750	D1D	279.455	0.949	0.008	0.91	0.18	0.68	19844	388	367	10.25	1!	e
J100103-481251	C1B	275.989	5.542	0.006	0.38	0.08	0.53	12686	183	147	9.47	2	
J100110-573755	D2B	281.687	-1.961	0.007	0.33	0.11	0.75	12904	140	92	9.43	1	i, w.comp
J100116-534553	D1D	279.371	1.135	0.012	0.47	0.10	0.65	11931	116	72	9.51	1	
J100130-584224	D2A	282.370	-2.793	0.038	5.20	0.53	0.70	2594	214	139	9.23	1*	J1000-58B, w.comp (J100019-583828), H
J100130-601021	D2A	283.255	-3.963	0.010	0.46	0.13	0.68	17652	185	97	9.85	1	
J100152-511724	C1C	277.954	3.167	0.013	1.77	0.12	0.66	6829	253	184	9.60	1	
J100159-581829	D2A	282.180	-2.437	0.011	0.83	0.05	0.60	2594	140	103	8.43	2	
J100203-575509	D2A	281.955	-2.120	0.024	3.94	0.63	0.87	11495	302	254	10.41	1*	w.comp
J100216-510243	C1A	277.856	3.400	0.009	0.39	0.06	0.65	2701	83	52	8.14	1*	
J100219-580122	D2A	282.044	-2.182	0.011	0.47	0.10	0.65	5540	122	92	8.84	2	
J100235-572714	D2A	281.734	-1.704	0.084	11.45	1.03	1.25	2647	290	253	9.59	1*!	J1002-57, M, W, Z
J100246-500355	C1A	277.332	4.232	0.005	0.36	0.08	0.50	19014	180	140	9.81	1	
J100300-492855	C1A	277.012	4.722	0.067	7.88	0.76	0.67	2401	156	110	9.34	1	J1003-49, H, Z
J100307-493721	C1A	277.110	4.622	0.006	0.22	0.04	0.49	19267	273	139	9.60	2	
J100354-590436	D2A	282.841	-2.904	0.018	1.50	0.38	0.61	2407	166	123	8.62	1	
J100356-583904	D2A	282.591	-2.559	0.081	20.70	0.89	0.75	3717	341	287	10.14	1	w.comp (J100437-583134), M, W, Z
J100414-500640	C1A	277.549	4.336	0.012	1.32	0.14	0.56	5282	213	181	9.25	1	

* Detected by the overlapping region of the adjacent mosaic.

** Detected by the overlapping region of two or more adjacent mosaics.

! Detected by the overlapping region between Vela–H I and Vela–SMGPS.

Table C.2 continued

Name	Mosaic	l	b	$S_{\rm peak}$	$S_{\rm int}$	$\mathrm{err}_{(S_{\rm int})}$	RMS	$V_{\rm hel}$	w_{20}	w_{50}	$M_{\rm HI}$	Flag	Note
J2000	–	deg	deg	Jy	Jy km s^{-1}	Jy km s^{-1}	mJy beam^{-1}	km s^{-1}	km s^{-1}	km s^{-1}	log($M_{\rm HI}$/M$_\odot$)	1/2	
(1)	(2)	(3)	(4)	(5)	(6)	(7)	(8)	(9)	(10)	(11)	(12)	(13)	(14)
J100426-490323	C1A	276.946	5.204	0.007	0.23	0.10	0.56	5788	173	150	8.58	1	HyA1911
J100433-585949	D2A	282.861	-2.790	0.028	1.01	0.18	0.64	3654	75	47	8.82	2	Face-on? w.comp (J100505-590811)
J100436-490335	C1A	276.970	5.217	0.026	4.76	0.16	0.66	3392	234	186	9.42	1	HyA1916, w.comp (J100446-485936), W
J100437-583134	D2A	282.589	-2.405	0.088	21.90	1.14	0.80	3712	344	294	10.16	1	J1004-58, w.comps (one is J100356-583904), H
J100446-485936	C1A	276.953	5.287	0.012	0.35	0.04	0.53	3438	43	27	8.31	2	w.comp (J100436-490335)
J100447-484426	C1A	276.803	5.491	0.006	1.19	0.17	0.67	6725	244	190	9.42	1	HyA1919, M, W
J100452-501212	C1A	277.686	4.323	0.012	1.16	0.10	0.58	6815	139	119	9.42	1	
J100502-533052	D1D	279.670	1.669	0.012	0.93	0.14	0.56	12218	157	105	9.83	1	Face-on? i
J100505-590811	D2A	282.999	-2.855	0.008	0.31	0.09	0.59	3650	213	55	8.31	2	w.comp (J100433-585949)
J100454-583828	D2A	282.712	-2.454	0.018	0.97	0.20	0.76	11673	161	108	9.81	1	
J100526-514220	C1C	278.649	3.164	0.010	0.83	0.17	0.71	7311	245	199	9.33	2	
J100527-581826	D2A	282.546	-2.165	0.016	1.01	0.22	0.73	2671	120	84	8.54	1	
J100528-525125	D1D	279.333	2.238	0.010	0.85	0.16	0.59	7506	216	166	9.37	1	i
J100542-480255	C1A	276.514	6.139	0.011	2.45	0.15	0.66	4018	298	270	9.28	1	
J100557-504532	C1A	278.152	3.977	0.009	0.56	0.11	0.67	8532	358	314	9.30	1	w.comp
J100606-503647	C1A	278.088	4.108	0.020	5.89	0.44	0.67	5319	349	308	9.91	1	J1006-50B, HyA1939, M, W, Z
J100616-492835	C1A	277.437	5.042	0.070	10.11	0.42	0.70	2396	170	139	9.45	1	J1006-49, H, Z
J100621-525428	D1D	279.471	2.275	0.008	0.32	0.07	0.61	15838	295	191	9.60	1	i, M, W
J100621-510431	C1A	278.392	3.758	0.006	0.61	0.19	0.65	14721	173	101	9.82	2	
J100629-501436	C1A	277.919	4.443	0.017	4.05	0.45	0.62	5282	304	271	9.74	1	J1006-50A, HyA1945, M, W, Z
J100645-500002	C1A	277.805	4.660	0.002	2.89	0.60	0.65	6740	308	159	9.81	1	J1006-50C
J100644-494416	C1A	277.655	4.870	0.010	0.76	0.14	0.59	21183	330	153	10.23	1	HyA1950, M, W
J100644-500822	C1A	277.889	4.550	0.011	0.71	0.20	0.57	6833	122	80	9.21	1	HyA1951, M, W
J100646-474148	C1A	276.449	6.528	0.010	1.45	0.15	0.93	4022	346	312	9.06	1	Vel3666, M
J100647-520619	D1D	279.053	2.964	0.041	2.06	0.12	0.67	6727	80	50	9.66	1	J1006-52, face-on
J100714-532653	D1D	279.895	1.915	0.008	0.42	0.09	0.55	14102	262	74	9.62	1	
J100725-494107	C1A	277.713	4.983	0.017	0.66	0.07	0.53	7003	75	47	9.20	1	
J100734-591147	D2A	283.294	-2.720	0.010	0.44	0.12	0.62	6265	154	110	8.93	1	w.comp (J100803-591855)
J100737-545527	D1D	280.803	0.750	0.015	0.89	0.31	0.97	9044	397	250	9.55	1!	e, M, W
J100803-591855	D2A	283.412	-2.783	0.065	7.54	0.62	0.74	6251	199	152	10.16	1	J1007-59, w.comp (J100734-591147)
J100809-513236	D1B	278.895	3.543	0.010	0.79	0.14	0.76	8648	225	209	9.46	1*	

* Detected by the overlapping region of the adjacent mosaic.

** Detected by the overlapping region of two or more adjacent mosaics.

! Detected by the overlapping region between Vela–H I and Vela–SMGPS.

Table C.2 continued

Name	Mosaic	l	b	$S_{\rm peak}$	$S_{\rm int}$	$\mathrm{err}_{(S_{\rm int})}$	RMS	$V_{\rm hel}$	w_{20}	w_{50}	$M_{\rm HI}$	Flag	Note
J2000	–	deg	deg	Jy	Jy km s^{-1}	Jy km s^{-1}	mJy beam^{-1}	km s^{-1}	km s^{-1}	km s^{-1}	log($M_{\rm HI}$/M$_\odot$)	1/2	
(1)	(2)	(3)	(4)	(5)	(6)	(7)	(8)	(9)	(10)	(11)	(12)	(13)	(14)
J100809-491307	C1A	277.545	5.445	0.007	0.61	0.11	0.64	18671	455	421	10.02	2	HyA1977, I, M, W
J100821-483759	C1A	277.217	5.925	0.012	1.39	0.09	0.57	2751	164	118	8.70	1	HyA1978, W
J100858-540840	D1D	280.504	1.499	0.022	1.74	0.35	0.72	4919	227	162	9.31	1	i
J100915-494323	C1A	277.975	5.125	0.012	1.28	0.40	0.60	6791	275	175	9.46	1	
J100920-500309	C1A	278.178	4.864	0.007	0.50	0.11	0.51	18987	161	84	9.95	1	HyA1998, W
J100925-485900	C1A	277.566	5.743	0.011	0.34	0.09	0.57	5659	88	53	8.73	2	
J100938-505610	C1A	278.732	4.173	0.009	1.10	0.25	0.73	11814	330	273	9.88	1	HyA2007, M, W
J100940-510431	D1B	278.817	4.062	0.024	3.73	0.23	0.98	2837	190	139	9.16	1	J1009-51, e
J101007-524211	D1D	279.810	2.773	0.026	3.11	0.88	0.69	7388	328	276	9.92	1	HyA2014, M, W
J101012-602256	D2A	284.250	-3.497	0.015	0.56	0.11	1.00	15824	216	150	9.84	1	e
J101026-544128	D1D	281.000	1.175	0.015	1.02	0.14	0.63	3595	130	115	8.81	1	
J101027-521222	D1D	279.570	3.209	0.006	0.45	0.10	0.53	12266	326	223	9.52	1	i
J101028-601135	D2A	284.170	-3.322	0.010	0.98	0.26	0.91	6278	277	261	9.27	2	e, i, M, W
J101031-490436	C1A	277.768	5.771	0.019	1.37	0.10	0.57	5367	120	92	9.28	1	
J101049-592041	D2A	283.716	-2.604	0.029	1.20	0.14	0.71	3280	102	41	8.80	2	Face-on? w.comp (J101136-591511)
J101106-490807	C1A	277.882	5.776	0.010	0.95	0.26	0.59	5781	228	171	9.19	1	i
J101122-492600	C1A	278.090	5.560	0.006	0.56	0.17	0.54	14097	236	211	9.74	2	
J101135-492742	C1A	278.132	5.552	0.011	0.50	0.13	0.53	5339	187	127	8.84	1	HyA2041
J101136-591511	D2A	283.746	-2.471	0.013	0.53	0.18	0.68	3293	126	67	8.44	1	w.comp (J101049-592041)
J101147-530008	D1D	280.188	2.675	0.011	0.57	0.22	0.61	2768	141	100	8.33	1	
J101155-514244	D1B	279.472	3.743	0.012	0.76	0.07	0.61	21700	99	45	10.25	2	Face-on?
J101207-512803	D1B	279.356	3.961	0.014	1.39	0.16	0.65	5271	152	117	9.27	1*	J1012-51, w.comp (J101231-513221)
J101208-551907	D1C	281.559	0.801	0.011	0.45	0.08	0.73	2662	120	87	8.19	1!	e
J101210-540416	D1D	280.852	1.828	0.017	1.09	0.12	0.61	7346	153	98	9.46	1	
J101231-513221	D1B	279.450	3.939	0.008	0.34	0.08	0.59	5252	104	61	8.65	1	w.comp (J101207-512803)
J101231-513717	D1B	279.497	3.871	0.005	0.44	0.04	0.58	8554	242	194	9.20	1	HyA2064, M
J101249-544917	D1D	281.356	1.265	0.011	1.73	0.35	0.67	8858	390	336	9.82	1*	i, M
J101250-591844	D2A	283.909	-2.431	0.021	2.84	0.41	0.91	5529	224	208	9.63	1	
J101300-531541	D1D	280.490	2.563	0.010	1.71	0.39	0.58	12191	453	408	10.10	1	
J101321-522704	D1D	280.075	3.261	0.028	1.76	0.22	0.66	8654	125	84	9.81	1*	J1013-52A, HyA2091, w.comp (J101324-523120)
J101324-523120	D1D	280.121	3.207	0.013	3.11	0.60	0.67	8584	350	337	9.90	1	HyA2095, w.comp (J101321-522704), I, M, W, Z

* Detected by the overlapping region of the adjacent mosaic.

** Detected by the overlapping region of two or more adjacent mosaics.

! Detected by the overlapping region between Vela–H I and Vela–SMGPS.

Table C.2 continued

Name	Mosaic	l	b	$S_{\rm peak}$	$S_{\rm int}$	$\mathrm{err}_{(S_{\rm int})}$	RMS	$V_{\rm hel}$	w_{20}	w_{50}	$M_{\rm HI}$	Flag	Note
J2000	–	deg	deg	Jy	Jy km s^{-1}	Jy km s^{-1}	mJy beam^{-1}	km s^{-1}	km s^{-1}	km s^{-1}	log($M_{\rm HI}$/M$_\odot$)	1/2	
(1)	(2)	(3)	(4)	(5)	(6)	(7)	(8)	(9)	(10)	(11)	(12)	(13)	(14)
J101325-523117	D1B	280.122	3.208	0.012	1.06	0.17	1.08	8545	299	215	9.58	1	J0913-52A? HyA2095, e, i, w.comp (J101321-522704), I, M, W, Z
J101329-495259	C1A	278.630	5.387	0.010	0.66	0.11	0.66	2817	130	55	8.40	1	
J101331-523959	D1D	280.218	3.098	0.008	0.45	0.09	0.54	12081	212	98	9.51	1	w.comp (J101407-524456)
J101334-533408	D1D	280.740	2.346	0.008	0.44	0.09	0.66	19805	148	97	9.93	1	Face-on?
J101342-500318	C1A	278.756	5.265	0.010	0.97	0.21	0.67	6734	209	157	9.33	1	HyA2103, M, W
J101346-521708	D1D	280.032	3.433	0.046	14.69	1.05	0.76	2731	277	256	9.72	1*	J1013-52B, HyA2109, I, H, M, W, Z
J101347-504608	D1B	279.174	4.685	0.007	0.49	0.12	0.63	8759	256	59	9.26	1	
J101352-493913	C1A	278.557	5.594	0.016	0.63	0.13	0.77	5740	233	152	9.01	1	HyA2111, M, W
J101359-514544	D1B	279.764	3.884	0.011	2.09	0.12	0.60	2963	246	198	8.95	1*	HyA2114, M, W
J101407-524456	D1D	280.332	3.081	0.008	0.48	0.10	0.64	12070	145	118	9.53	1	w.comp (J101331-523959)
J101407-494026	C1A	278.594	5.616	0.013	0.66	0.17	0.64	7364	83	69	9.24	1	HyA2119, W
J101422-490800	C1A	278.330	6.080	0.017	3.32	0.56	0.72	2729	337	154	9.08	2	B=90″, BL
J101427-510415	D1B	279.430	4.495	0.010	0.80	0.15	0.62	11675	365	59	9.73	1	HyA2127, M, W
J101436-530539	D1D	280.595	2.838	0.011	1.72	0.21	0.59	12228	268	236	10.10	1	i
J101453-545418	D1C	281.648	1.363	0.033	2.50	0.31	0.70	1230	143	94	8.26	1*	J1014-54
J101502-531031	D1D	280.694	2.807	0.012	0.55	0.09	0.51	18818	126	62	9.98	1	Face-on?
J101548-523934	D1D	280.504	3.296	0.008	0.33	0.07	0.65	18753	340	261	9.76	1	BL
J101604-521014	D1D	280.265	3.727	0.007	0.37	0.07	0.75	14086	184	136	9.55	1*	
J101645-533057	D1D	281.098	2.668	0.007	0.78	0.22	0.57	10017	319	274	9.58	2	HyA2198, M, W
J101646-523459	D1D	280.579	3.444	0.006	0.38	0.07	0.58	19406	474	347	9.85	2	M, W
J101650-545827	D1C	281.919	1.462	0.010	0.26	0.08	0.60	6460	188	131	8.71	2	i
J101655-485241	C1A	278.524	6.532	0.034	27.68	0.66	1.19	2738	420	371	10.00	1	HyA2200, B=60″, I, H, M, W, Z
J101706-552227	D1C	282.174	1.152	0.013	1.49	0.32	0.69	14489	360	298	10.19	1	
J101714-493903	D1B	279.001	5.920	0.009	0.69	0.12	0.65	12809	219	117	9.74	1	e
J101720-525719	D1D	280.858	3.188	0.011	0.57	0.12	0.62	6324	116	64	9.05	1	
J101753-521505	D1B	280.536	3.814	0.009	1.44	0.11	0.63	2996	219	186	8.80	1*	
J101756-534932	D1D	281.415	2.507	0.006	0.26	0.06	0.52	18356	226	187	9.64	2	
J101810-524517	D1D	280.851	3.419	0.007	0.39	0.06	0.61	12150	175	140	9.45	2	
J101822-515505	D1B	280.413	4.133	0.010	1.60	0.17	0.62	8288	493	430	9.73	2	
J101831-510332	D1B	279.957	4.862	0.022	5.06	0.29	0.75	4067	252	221	9.61	1	J1018-51, H, Z
J101848-500949	D1B	279.497	5.633	0.010	0.60	0.06	0.55	6826	92	91	9.13	1	

* Detected by the overlapping region of the adjacent mosaic.

** Detected by the overlapping region of two or more adjacent mosaics.

! Detected by the overlapping region between Vela–HI and Vela–SMGPS.

299

Table C.2 continued

Name	Mosaic	l	b	$S_{\rm peak}$	$S_{\rm int}$	$\mathrm{err}_{(S_{\rm int})}$	RMS	$V_{\rm hel}$	w_{20}	w_{50}	$M_{\rm HI}$	Flag	Note
J2000	–	deg	deg	Jy	Jy km s^{-1}	Jy km s^{-1}	mJy beam^{-1}	km s^{-1}	km s^{-1}	km s^{-1}	log($M_{\rm HI}$/M$_\odot$)	1/2	
(1)	(2)	(3)	(4)	(5)	(6)	(7)	(8)	(9)	(10)	(11)	(12)	(13)	(14)
J101856-495401	D1B	279.372	5.865	0.009	0.53	0.15	0.54	22369	389	339	10.12	1	HyA2277, M, W
J101857-531016	D1D	281.181	3.137	0.007	0.38	0.08	0.52	20019	223	177	9.88	2	
J101917-531033	D1D	281.226	3.156	0.007	0.40	0.11	0.63	4096	136	114	8.51	1*	
J101924-545130	D1C	282.163	1.763	0.008	0.25	0.07	0.54	10077	85	71	9.09	1	
J101938-560123	D1C	282.832	0.806	0.014	0.82	0.17	0.93	8910	299	232	9.50	1!	e, i
J101939-513339	D1B	280.383	4.541	0.004	0.35	0.11	0.59	17702	320	243	9.73	2	HyA2308, M, W
J101941-540331	D1C	281.759	2.454	0.028	2.47	0.40	0.63	6207	141	98	9.67	1*	J1019-54, M, W, Z
J101949-495554	D1B	279.506	5.916	0.007	0.85	0.20	0.57	12559	266	118	9.82	1	HyA2316, M, W
J101956-501318	D1B	279.679	5.685	0.011	0.48	0.10	0.65	8546	419	279	9.24	1	HyA2320, i, w.comp, M, W
J102032-533149	D1C	281.575	2.965	0.008	0.58	0.11	0.54	10172	174	152	9.47	1	
J102052-495218	D1B	279.616	6.060	0.007	1.17	0.32	0.65	19842	396	373	10.36	1	
J102132-534039	D1C	281.780	2.923	0.014	0.70	0.14	0.60	6511	116	76	9.16	1	
J102209-541413	D1C	282.159	2.501	0.011	0.50	0.17	0.58	10439	115	66	9.42	1	i
J102232-533111	D1C	281.819	3.135	0.006	0.26	0.04	0.48	22398	154	73	9.81	2	w_{20} unc.
J102250-503849	D1B	280.305	5.580	0.011	0.60	0.08	0.56	21184	137	99	10.13	1	
J102311-533051	D1C	281.898	3.192	0.005	0.30	0.04	0.57	6001	271	93	8.71	2	HyA2431, M, W
J102321-495927	D1B	280.017	6.176	0.005	0.47	0.16	0.55	12720	232	208	9.58	1	HyA2433
J102325-501118	D1B	280.133	6.015	0.012	1.06	0.14	0.69	7362	171	131	9.45	1	HyA2435
J102344-513156	D1B	280.901	4.909	0.010	1.12	0.15	0.65	7966	344	52	9.54	2	HyA2443, M, W
J102347-535523	D1C	282.193	2.895	0.026	5.86	1.33	0.67	6174	447	406	10.04	1	J1023-53, M, W, Z
J102410-515910	D1B	281.204	4.563	0.017	2.80	0.51	0.78	9232	296	236	10.07	1*	J1024-52
J102415-543922	D1C	282.643	2.312	0.009	0.31	0.06	0.57	1111	117	88	7.26	1	w.comp (J102445-544757)
J102424-533526	D1C	282.091	3.224	0.006	0.35	0.02	0.56	6598	266	159	8.87	1	M, W
J102425-502700	D1B	280.409	5.884	0.004	0.18	0.04	0.62	20935	236	181	9.59	2	B=35″
J102445-544757	D1C	282.779	2.228	0.110	14.60	0.27	0.74	1083	157	127	8.99	1	J1024-54, HyA2469, w.comp (J102415-543922), H, W, Z
J102450-502301	D1B	280.432	5.973	0.007	0.56	0.11	0.67	7526	110	73	9.19	2	B=40″
J102454-535204	D1C	282.303	3.030	0.006	0.30	0.11	0.52	5626	92	73	8.66	1	
J102510-533120	D1C	282.152	3.343	0.007	0.91	0.18	0.63	6421	245	216	9.26	2	i, I, M, W
J102525-550555	D1C	283.020	2.026	0.033	6.48	0.46	0.66	6983	394	355	10.19	1	
J102540-535121	D1C	282.391	3.099	0.015	1.30	0.27	0.58	7034	178	102	9.50	1	i
J102552-513243	D1B	281.190	5.075	0.011	1.65	0.17	0.68	7750	223	208	9.68	1*	HyA2502, i, H, M, W

* Detected by the overlapping region of the adjacent mosaic.

** Detected by the overlapping region of two or more adjacent mosaics.

! Detected by the overlapping region between Vela–H I and Vela–SMGPS.

Table C.2 continued

Name	Mosaic	l	b	$S_{\rm peak}$	$S_{\rm int}$	$\mathrm{err}_{(S_{\rm int})}$	RMS	$V_{\rm hel}$	w_{20}	w_{50}	$M_{\rm HI}$	Flag	Note
J2000	–	deg	deg	Jy	Jy km s^{-1}	Jy km s^{-1}	mJy beam^{-1}	km s^{-1}	km s^{-1}	km s^{-1}	log($M_{\rm HI}$/M$_\odot$)	1/2	
(1)	(2)	(3)	(4)	(5)	(6)	(7)	(8)	(9)	(10)	(11)	(12)	(13)	(14)
J102559-535202	D1C	282.437	3.114	0.062	5.56	0.36	0.65	6791	139	88	10.10	1	J1026-53, face-on, H
J102605-543425	D1C	282.824	2.525	0.007	0.37	0.05	0.48	11812	200	151	9.40	1	
J102609-543532	D1C	282.841	2.511	0.015	2.00	0.40	0.63	6361	279	226	9.60	1	i
J102611-534650	D1C	282.416	3.203	0.014	1.08	0.25	0.61	7207	147	118	9.44	1	HyA2512, M, W, Z
J102630-523510	D1A	281.825	4.243	0.004	0.49	0.13	0.67	6339	126	92	8.98	1	
J102631-503508	D1B	280.750	5.975	0.017	0.70	0.14	0.82	7183	194	21	9.24	2	Face-on?
J102638-512334	D1A	281.212	5.268	0.010	0.73	0.07	0.72	7811	139	86	9.34	1*	
J102640-510355	D1B	281.042	5.548	0.015	2.20	0.11	0.64	3000	210	175	8.98	1	HyA2521, W
J102705-512239	D1A	281.265	5.316	0.006	0.30	0.10	0.70	14388	402	365	9.48	1	B=40″, i
J102721-542945	D1C	282.939	2.685	0.014	1.44	0.27	0.60	12157	259	205	10.02	1	i
J102727-502831	D1B	280.826	6.108	0.008	0.37	0.08	0.72	15978	232	166	9.67	2	HyA2549, B=35″, M, W
J102815-503103	D1B	280.967	6.146	0.016	2.40	0.30	0.72	6018	347	292	9.63	1	HyA2579, i, M, W
J102820-512220	D1B	281.426	5.424	0.012	0.60	0.15	0.61	7603	93	81	9.23	1	
J102825-504757	D1B	281.137	5.920	0.017	1.79	0.14	0.64	7120	141	97	9.64	1	w.comp (J102825-504127)
J102825-533634	D1A	282.609	3.523	0.050	4.90	0.40	0.69	2725	132	90	9.26	1*	J1028-53, Z
J102825-504127	D1B	281.080	6.014	0.010	1.28	0.28	0.62	6979	416	356	9.48	1	HyA2585, w.comp (J102825-504757), I, M, W
J102840-552911	D1C	283.618	1.939	0.007	0.38	0.11	0.55	15105	144	104	9.64	1	
J102844-505816	D1B	281.270	5.799	0.013	5.12	0.25	0.66	6082	464	416	9.96	1*	HyA2595, I, M, W
J102859-502533	D1B	281.018	6.285	0.015	3.23	0.16	0.83	6751	373	348	9.85	1	HyA2602, M
J103030-532937	D1C	282.817	3.782	0.007	0.55	0.10	0.65	6549	174	127	9.06	1	B=42″, e
J103042-524148	D1A	282.430	4.481	0.004	0.36	0.06	0.58	12784	240	175	9.46	2	HyA2641, M, W
J103124-512240	D1A	281.841	5.667	0.009	2.30	0.30	0.69	6370	299	258	9.66	1	HyA2659, BL, i, M, W
J103219-504230	D1A	281.622	6.317	0.007	0.77	0.12	0.68	6251	170	147	9.16	1*	HyA2687, e, M, W
J103313-523535	D1A	282.724	4.776	0.007	0.23	0.05	0.81	9841	121	78	9.04	1	BL
J103329-524545	D1A	282.826	4.639	0.005	0.38	0.11	0.58	13294	193	140	9.52	2	i
J103403-534306	D1A	283.384	3.857	0.021	1.29	0.22	0.71	6474	124	86	9.42	1*	e
J103423-542810	D1C	283.804	3.231	0.006	0.29	0.05	0.54	12936	267	218	9.38	1	
J103444-535837	D1C	283.601	3.684	0.010	0.71	0.19	0.69	6366	124	102	9.14	1*	e, i, w.comp
J103520-535641	D1C	283.662	3.756	0.014	1.37	0.22	0.79	8264	179	146	9.66	1*	e, i
J103550-540601	D1C	283.810	3.657	0.015	1.95	0.40	0.88	6282	461	421	9.57	1*	J1035-54, HyA2740, e, i, w.comp? I, M, W, Z
J103704-530112	D1A	283.423	4.686	0.009	0.72	0.15	0.68	15193	424	211	9.92	1	

* Detected by the overlapping region of the adjacent mosaic.

** Detected by the overlapping region of two or more adjacent mosaics.

! Detected by the overlapping region between Vela–HI and Vela–SMGPS.

Table C.2 continued

Name	Mosaic	l	b	$S_{\rm peak}$	$S_{\rm int}$	$\mathrm{err}_{(S_{\rm int})}$	RMS	$V_{\rm hel}$	w_{20}	w_{50}	$M_{\rm HI}$	Flag	Note
J2000	–	deg	deg	Jy	Jy km s^{-1}	Jy km s^{-1}	mJy beam^{-1}	km s^{-1}	km s^{-1}	km s^{-1}	log($M_{\rm HI}$/M$_\odot$)	1/2	
(1)	(2)	(3)	(4)	(5)	(6)	(7)	(8)	(9)	(10)	(11)	(12)	(13)	(14)
J103844-524728	D1A	283.531	5.009	0.008	0.39	0.10	0.61	6084	175	73	8.85	2	
J103925-525456	D1A	283.683	4.952	0.015	0.99	0.09	0.64	17630	227	22	10.18	1	
J103932-520528	D1A	283.294	5.679	0.008	0.64	0.17	0.63	12333	336	294	9.68	1	i, w.comp
J104004-524010	D1A	283.649	5.213	0.006	0.37	0.06	0.58	9848	141	138	9.25	1	
J104109-521004	D1A	283.550	5.732	0.010	0.51	0.10	0.61	15087	219	185	9.76	2	BL, i?
J104131-513246	D1A	283.302	6.304	0.005	0.47	0.05	0.62	14900	261	196	9.71	2	

C.3 Vela–H I atlas

This Atlas presents a similar configuration to that of the Vela–SMGPS Atlas. Solid detections are shown in Section C.3.1, while possibles are in Section C.3.2.

C.3.1 Solid detections

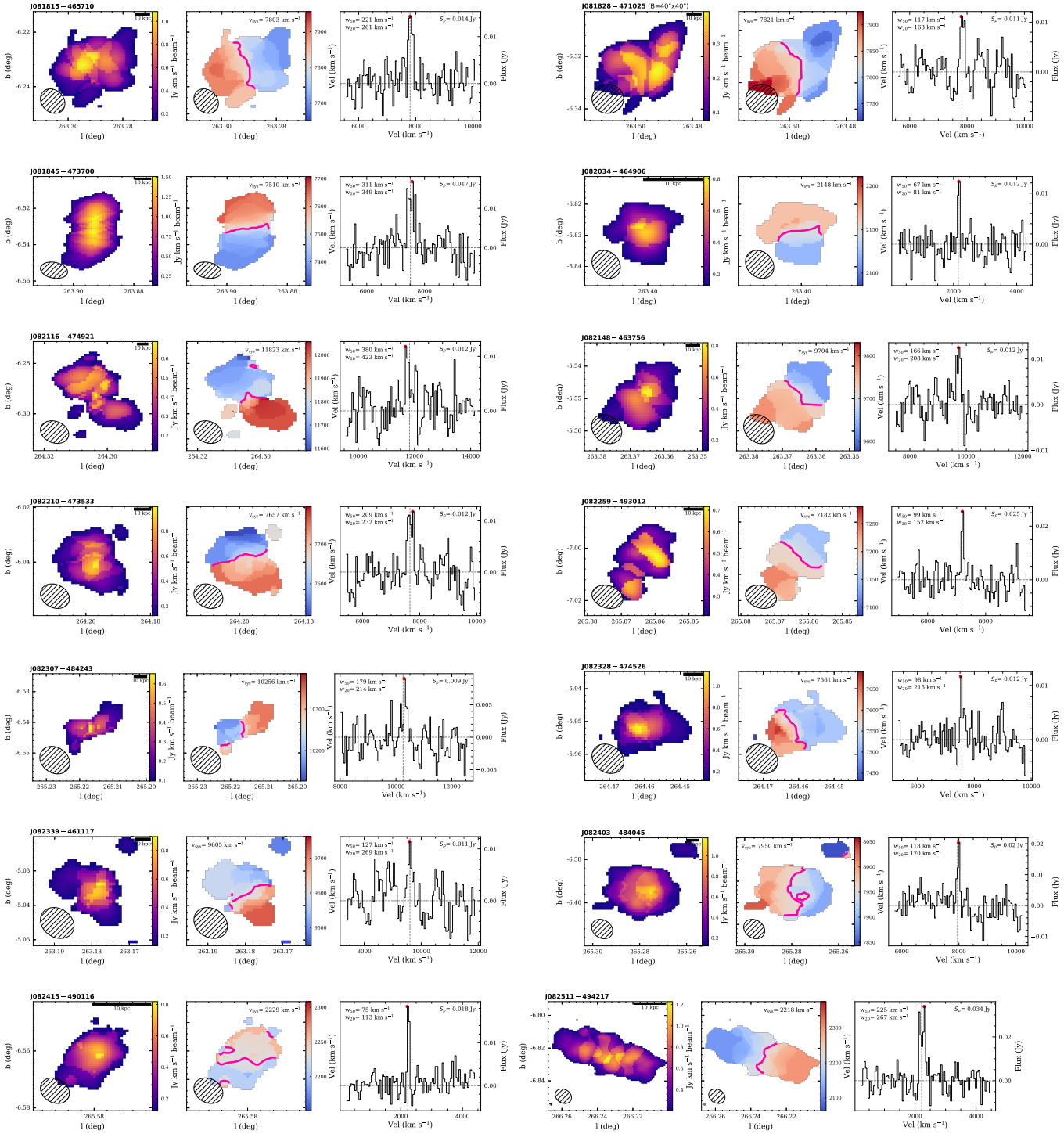

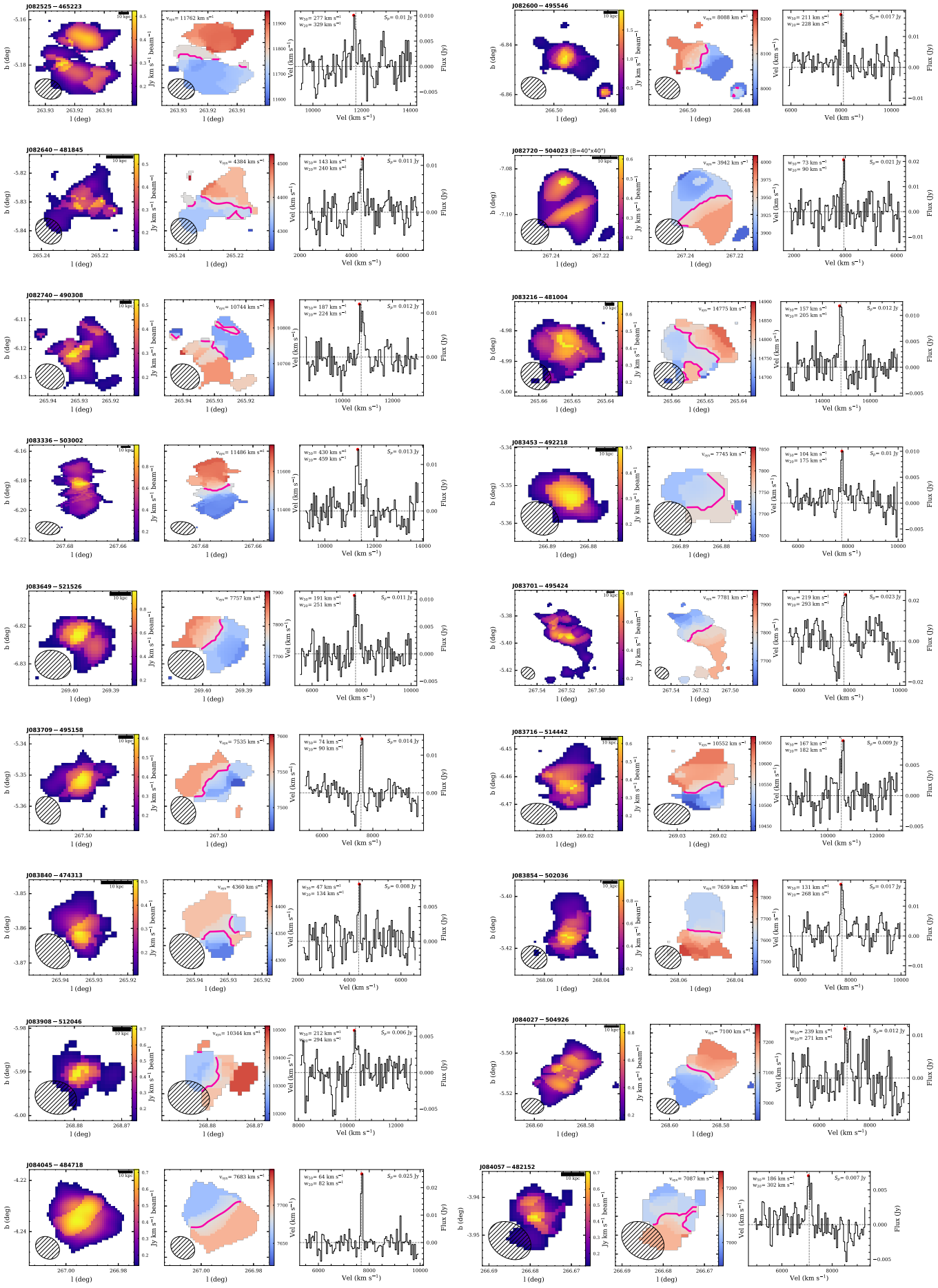
J082525−465223
J082600−495546
J082640−481845
J082720−504023 (B=40"x40")
J082740−490308
J083216−481004
J083336−503002
J083453−492218
J083649−521526
J083701−495424
J083709−495158
J083716−514442
J083840−474313
J083854−502036
J083908−512046
J084027−504926
J084045−484718
J084057−482152
b (deg)
l (deg)
Vel (km s−1)
Flux (Jy)
Jy km s−1 beam−1
10 kpc

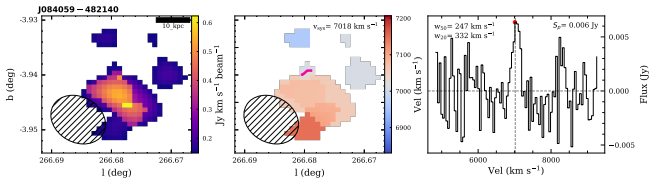
J084059 − 482140
J084109 − 460955

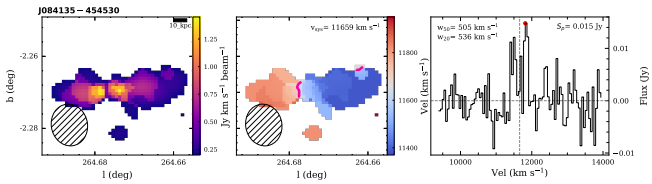
J084135 − 454530
J084148 − 512957

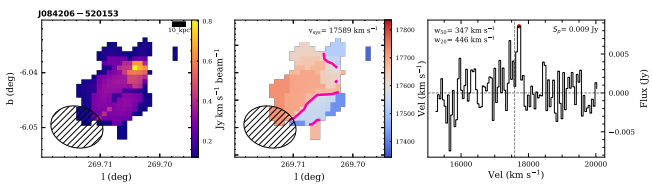
J084206 − 520153
J084240 − 520214

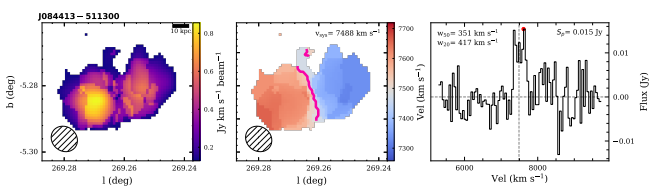
J084413 − 511300
J084438 − 470336

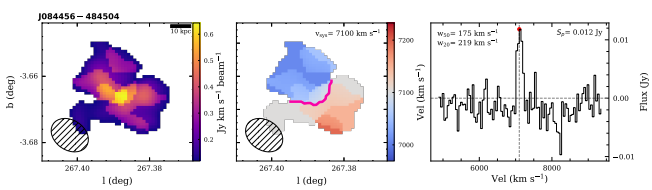
J084456 − 484504
J084457 − 522946

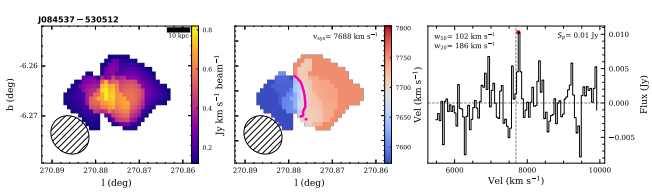
J084537 − 530512
J084602 − 514431

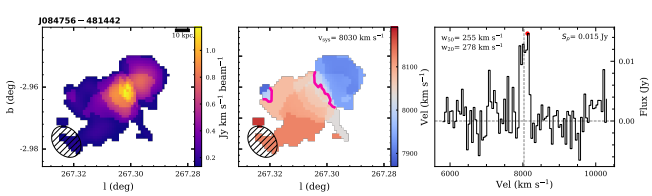
J084756 − 481442
J084802 − 532009

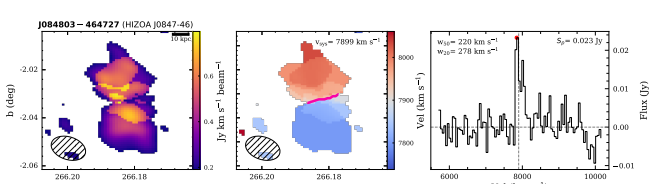
J084803 − 464727 (HIZOA J0847-46)
J084830 − 482325

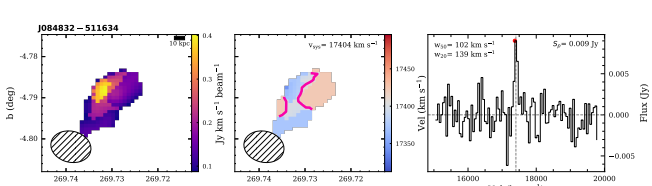
J084832 − 511634
J084947 − 501715

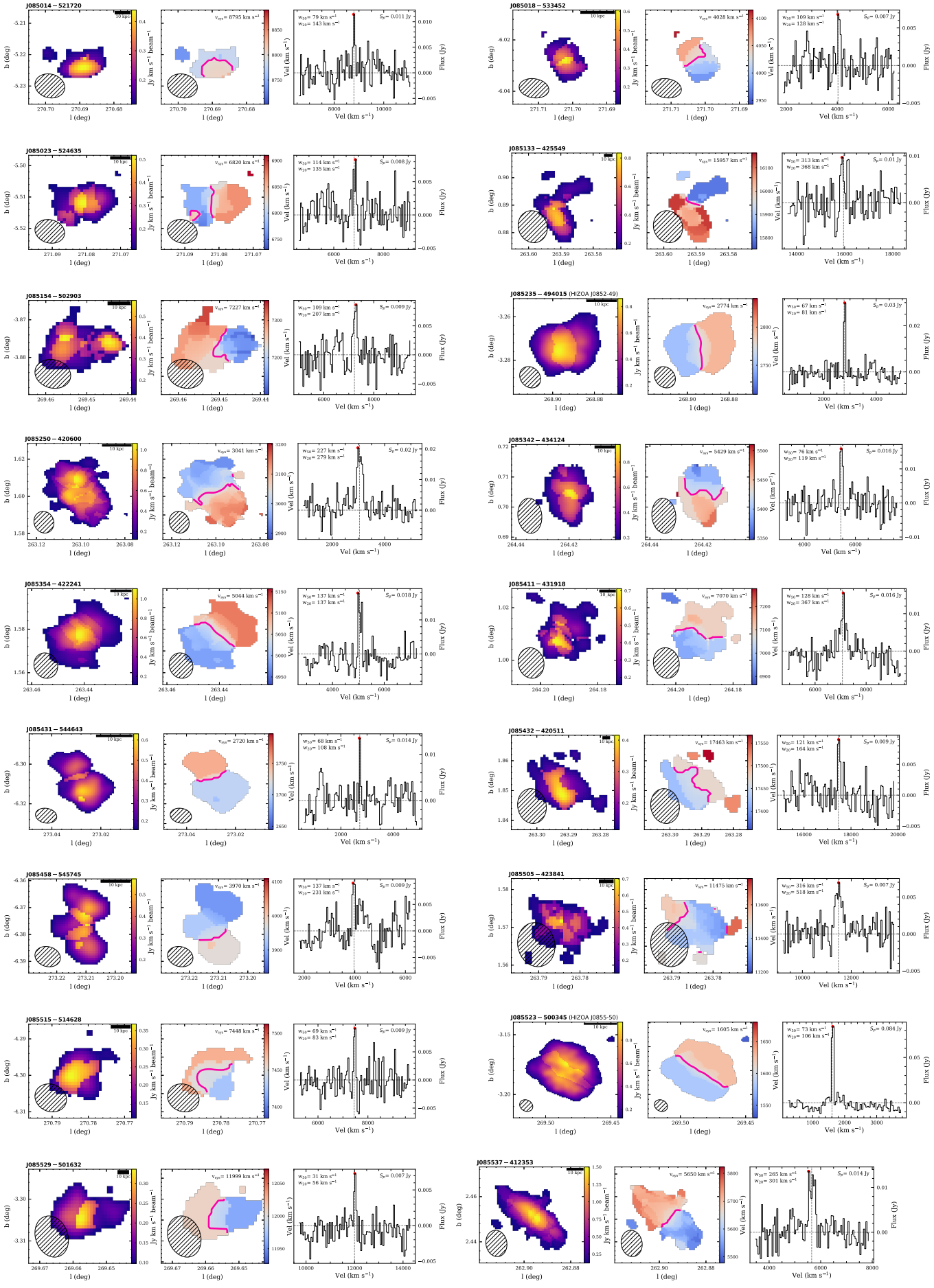
J085014 – 521720
J085018 – 533452
J085023 – 524635
J085133 – 425549
J085154 – 502903
J085235 – 494015 (HIZOA J0852-49)
J085250 – 420600
J085342 – 434124
J085354 – 422241
J085411 – 431918
J085431 – 544643
J085432 – 420511
J085458 – 545745
J085505 – 423841
J085515 – 514628
J085523 – 500345 (HIZOA J0855-50)
J085529 – 501632
J085537 – 412353
l (deg)
b (deg)
Vel (km s⁻¹)
Flux (Jy)
Jy km s⁻¹ beam⁻¹
10 kpc

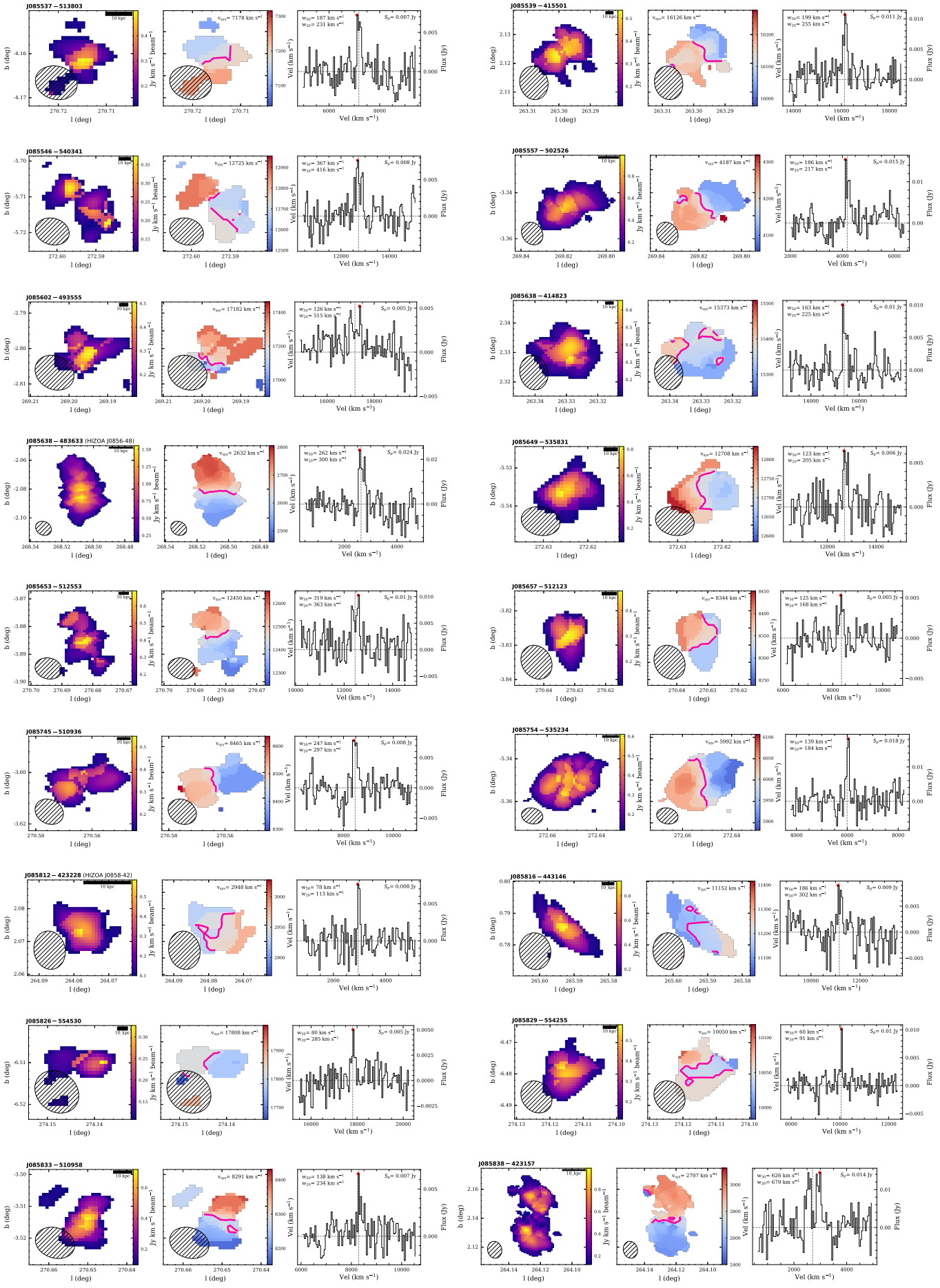
J085537 − 513803
J085539 − 415501
J085546 − 540341
J085557 − 502526
J085602 − 493555
J085638 − 414823
J085638 − 483633 (HIZOA J0856-48)
J085649 − 535831
J085653 − 512553
J085657 − 512123
J085745 − 510936
J085754 − 535234
J085812 − 423228 (HIZOA J0858-42)
J085816 − 443146
J085826 − 554530
J085829 − 554255
J085833 − 510958
J085838 − 423157
l (deg)
b (deg)
Vel (km s−1)
Flux (Jy)
Jy km s−1 beam−1

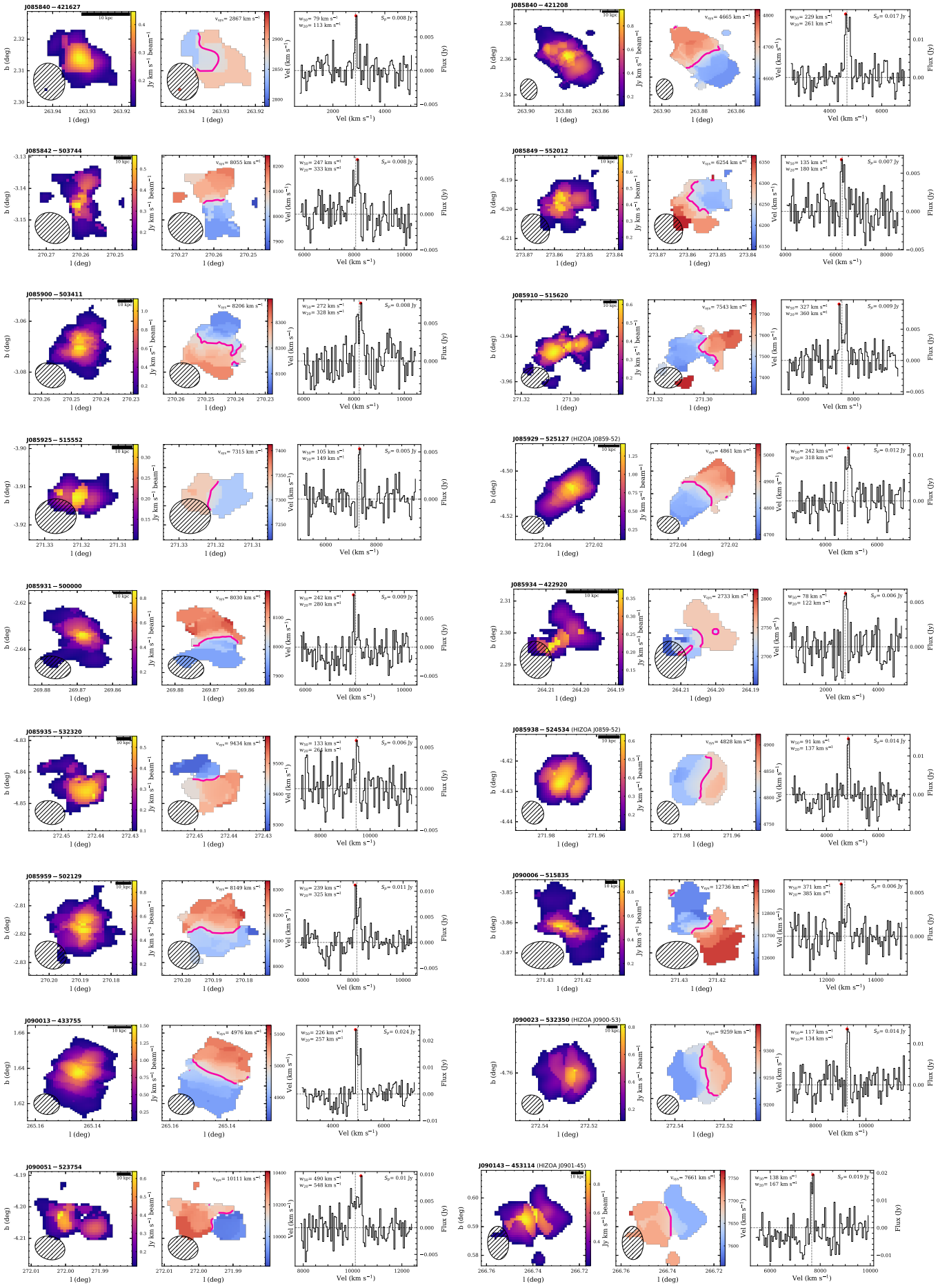
J085840 − 421627
J085840 − 421208
J085842 − 503744
J085849 − 552012
J085900 − 503411
J085910 − 515620
J085925 − 515552
J085929 − 525127 (HIZOA J0859-52)
J085931 − 500000
J085934 − 422920
J085935 − 532320
J085938 − 524534 (HIZOA J0859-52)
J085959 − 502129
J090006 − 515835
J090013 − 433755
J090023 − 532350 (HIZOA J0900-53)
J090051 − 523754
J090143 − 453114 (HIZOA J0901-45)
l (deg)
b (deg)
Vel (km s−1)
Flux (Jy)
Jy km s−1 beam−1
10 kpc

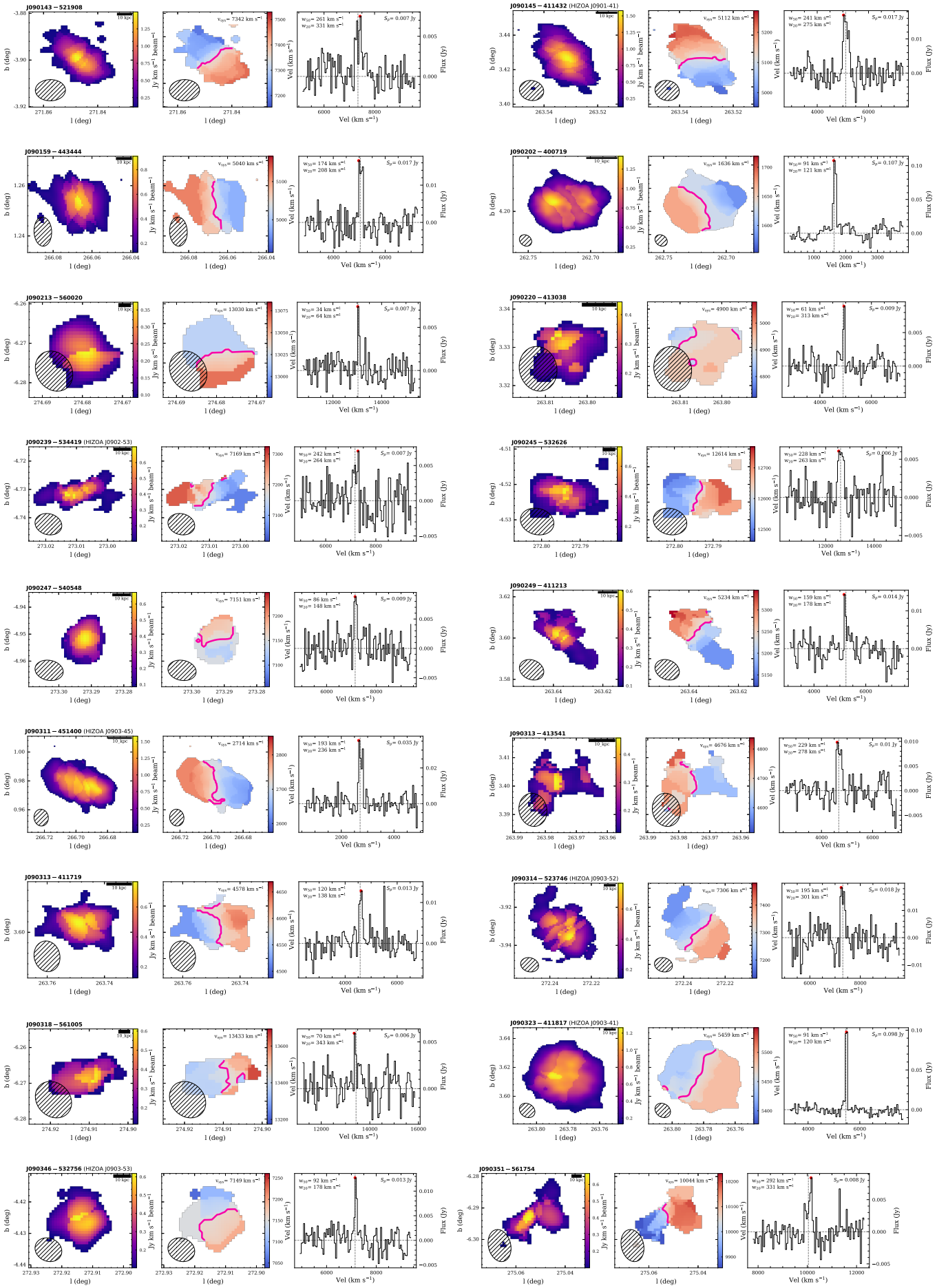
J090143 − 521908
J090145 − 411432 (HIZOA J0901-41)
J090159 − 443444
J090202 − 400719
J090213 − 560020
J090220 − 413038
J090239 − 534419 (HIZOA J0902-53)
J090245 − 532626
J090247 − 540548
J090249 − 411213
J090311 − 451400 (HIZOA J0903-45)
J090313 − 413541
J090313 − 411719
J090314 − 523746 (HIZOA J0903-52)
J090318 − 561005
J090323 − 411817 (HIZOA J0903-41)
J090346 − 532756 (HIZOA J0903-53)
J090351 − 561754
l (deg)
b (deg)
Vel (km s−1)
Flux (Jy)
Jy km s−1 beam−1

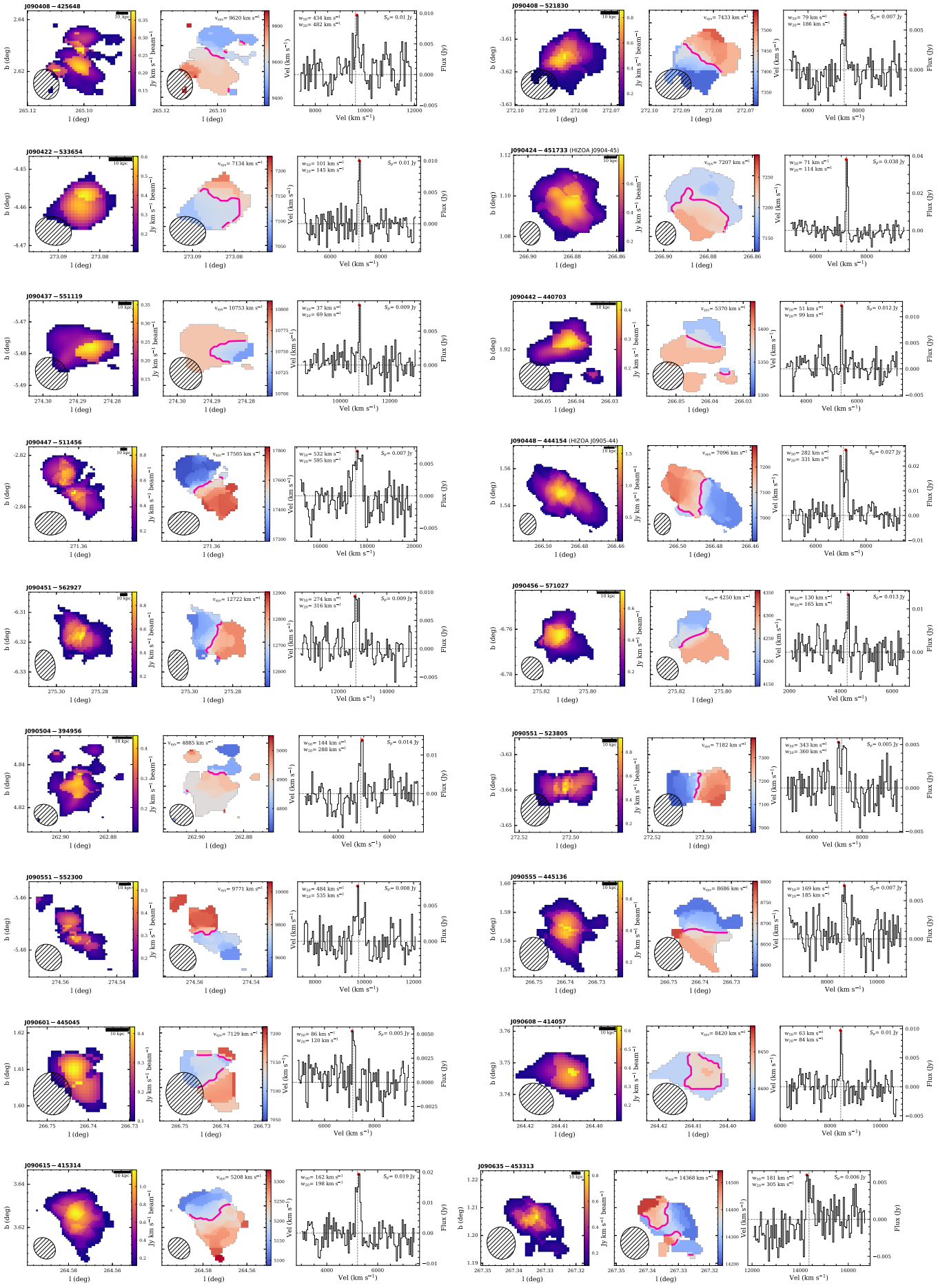
J090408−425648
J090408−521830
J090422−533654
J090424−451733 (HIZOA J0904-45)
J090437−551119
J090442−440703
J090447−511456
J090448−444154 (HIZOA J0905-44)
J090451−562927
J090456−571027
J090504−394956
J090551−523805
J090551−552300
J090555−445136
J090601−445045
J090608−414057
J090615−415314
J090635−453313
l (deg)
b (deg)
Vel (km s−1)
Flux (Jy)
Jy km s−1 beam−1

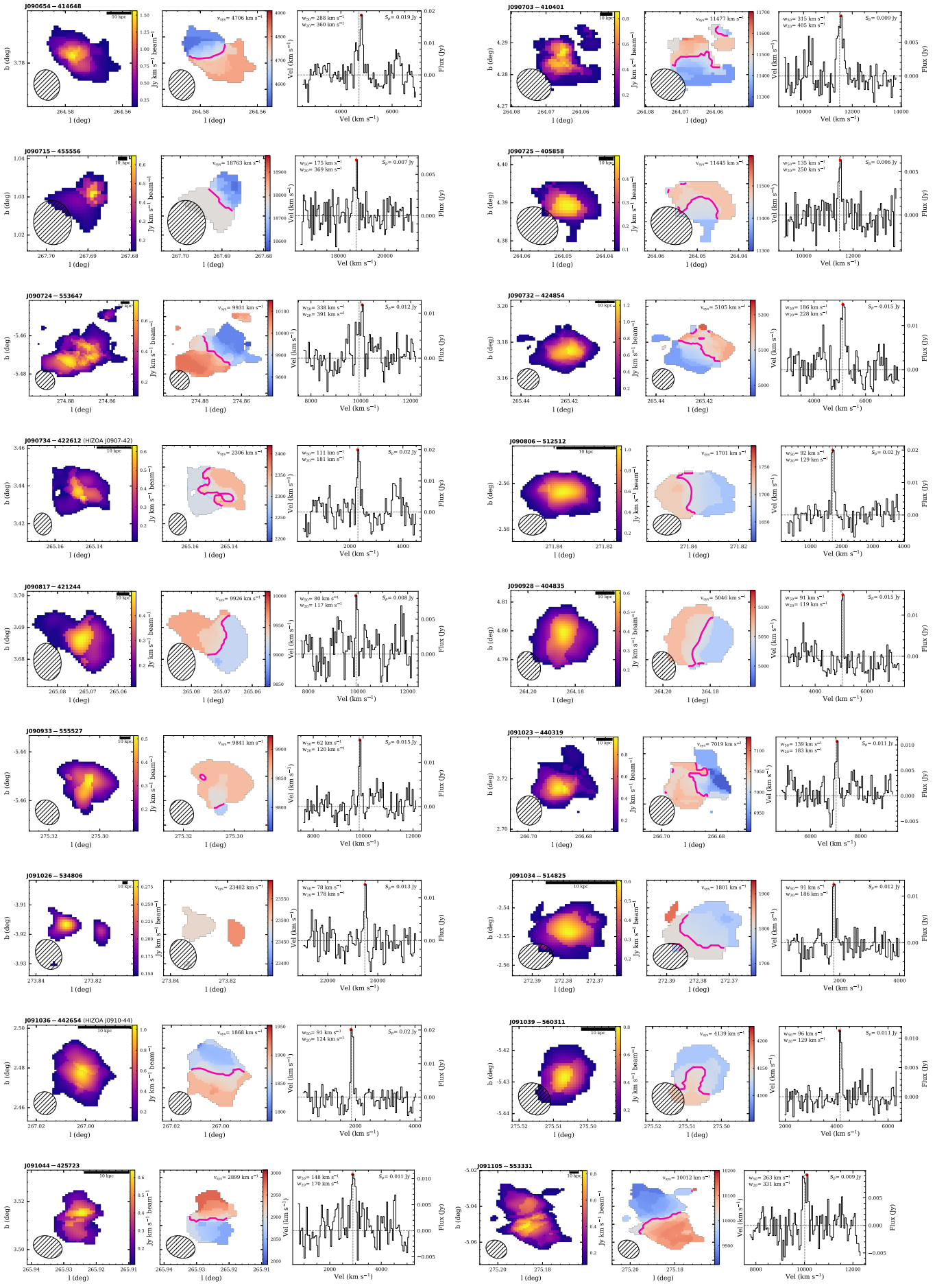
J090654 − 414648
J090703 − 410401
J090715 − 455556
J090725 − 405858
J090724 − 553647
J090732 − 424854
J090734 − 422612 (HIZOA J0907-42)
J090806 − 512512
J090817 − 421244
J090928 − 404835
J090933 − 555527
J091023 − 440319
J091026 − 534806
J091034 − 514825
J091036 − 442654 (HIZOA J0910-44)
J091039 − 560311
J091044 − 425723
J091105 − 553331
l (deg)
b (deg)
Vel (km s−1)
Flux (Jy)
Jy km s−1 beam−1
10 kpc

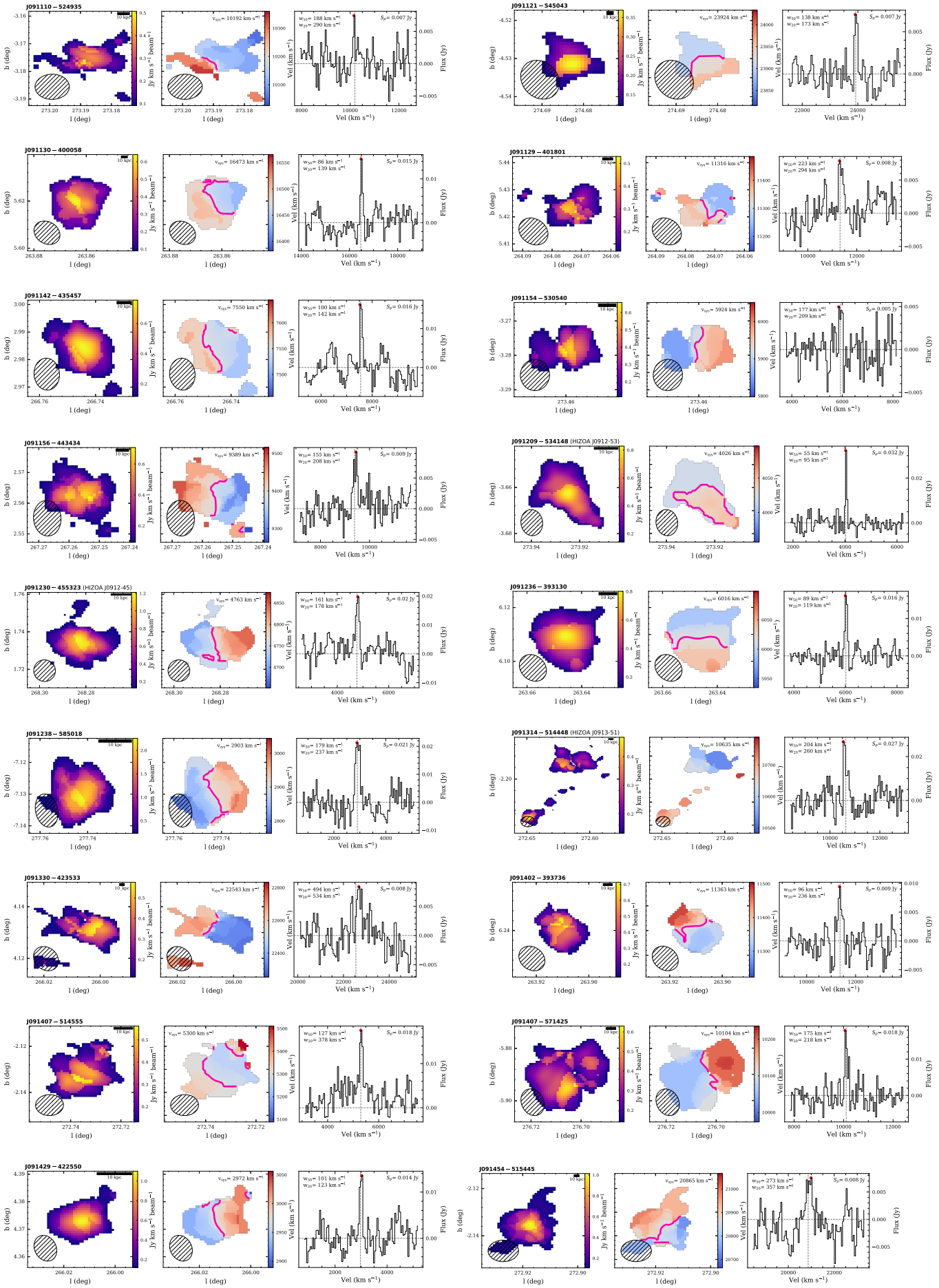
J091110 − 524935
J091121 − 545043
J091130 − 400058
J091129 − 401801
J091142 − 435457
J091154 − 530540
J091156 − 443434
J091209 − 534148 (HIZOA J0912-53)
J091230 − 455323 (HIZOA J0912-45)
J091236 − 393130
J091238 − 585018
J091314 − 514448 (HIZOA J0913-51)
J091330 − 423533
J091402 − 393736
J091407 − 514555
J091407 − 571425
J091429 − 422550
J091454 − 515445
l (deg)
b (deg)
Vel (km s−1)
Flux (Jy)
Jy km s−1 beam−1
10 kpc

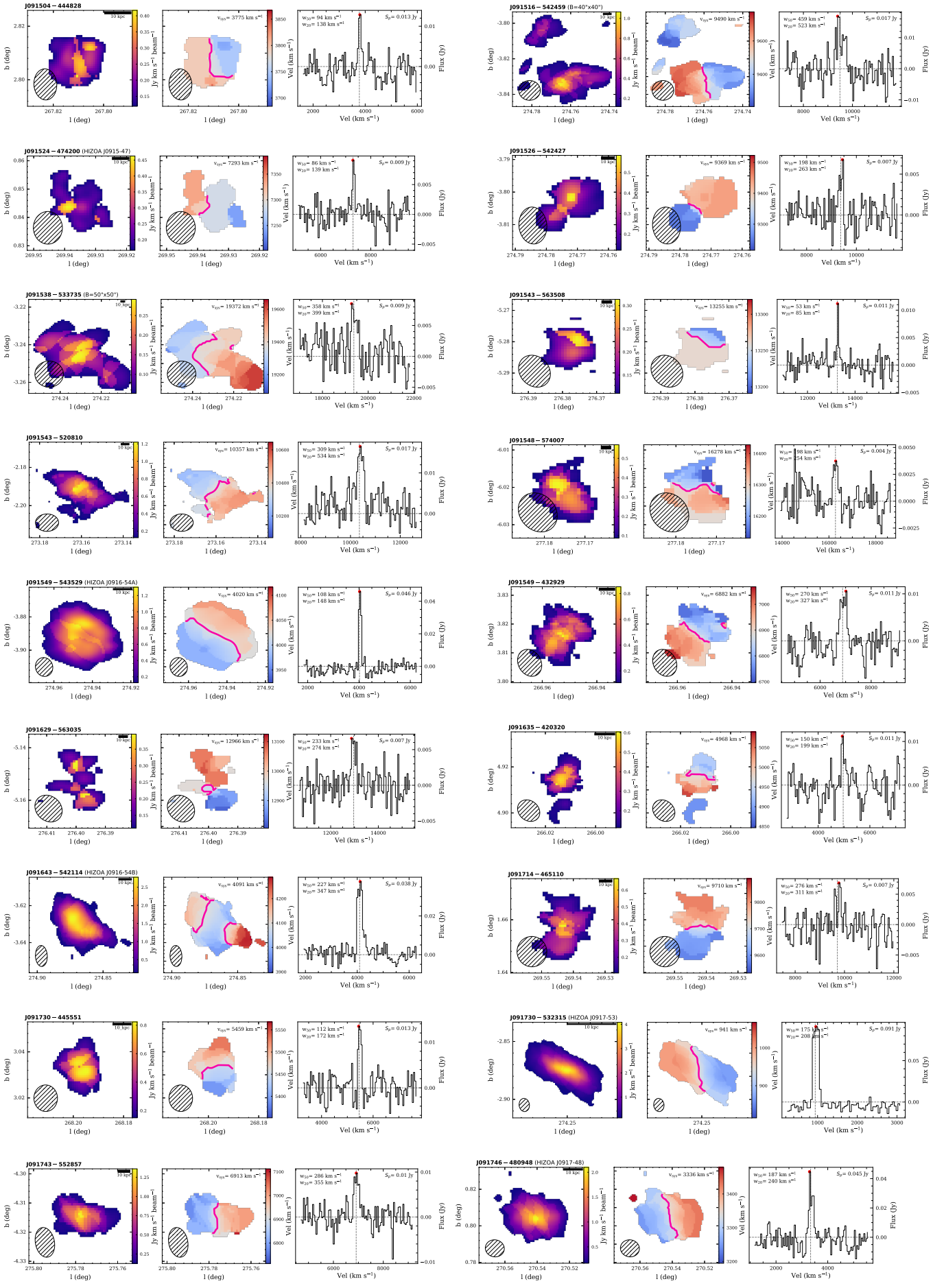
J091504−444828
J091516−542459 (B=40"x40")
J091524−474200 (HIZOA J0915-47)
J091526−542427
J091538−533735 (B=50"x50")
J091543−563508
J091543−520810
J091548−574007
J091549−543529 (HIZOA J0916-54A)
J091549−432929
J091629−563035
J091635−420320
J091643−542114 (HIZOA J0916-54B)
J091714−465110
J091730−445551
J091730−532315 (HIZOA J0917-53)
J091743−552857
J091746−480948 (HIZOA J0917-48)
l (deg)
b (deg)
Vel (km s−1)
Flux (Jy)
Jy km s−1 beam−1

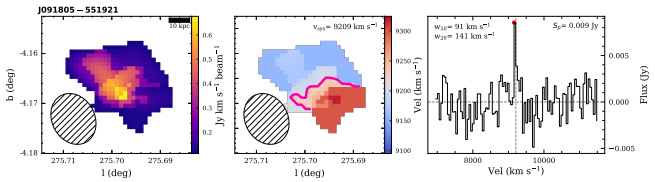
J091805 − 551921
10 kpc
b (deg)
l (deg)
Jy km s⁻¹ beam⁻¹
v_sys = 9209 km s⁻¹
Vel (km s⁻¹)
w50 = 91 km s⁻¹
w20 = 141 km s⁻¹
Sp = 0.009 Jy
Flux (Jy)

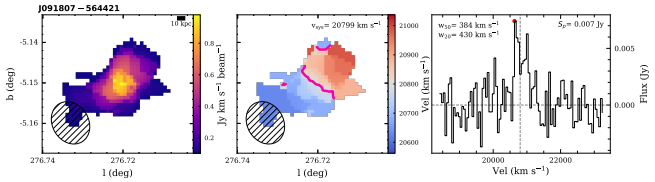
J091807 − 564421
10 kpc
b (deg)
l (deg)
Jy km s⁻¹ beam⁻¹
v_sys = 20799 km s⁻¹
Vel (km s⁻¹)
w50 = 384 km s⁻¹
w20 = 430 km s⁻¹
Sp = 0.007 Jy
Flux (Jy)

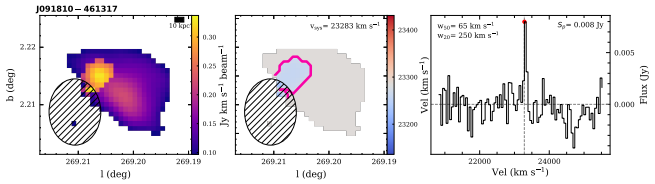
J091810 − 461317
10 kpc
b (deg)
l (deg)
Jy km s⁻¹ beam⁻¹
v_sys = 23283 km s⁻¹
Vel (km s⁻¹)
w50 = 65 km s⁻¹
w20 = 250 km s⁻¹
Sp = 0.008 Jy
Flux (Jy)

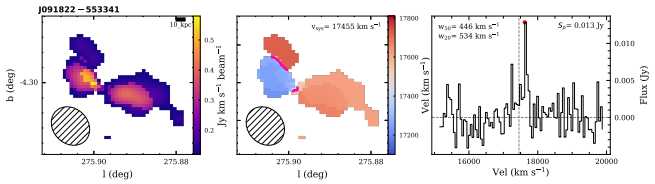
J091822 − 553341
10 kpc
b (deg)
l (deg)
Jy km s⁻¹ beam⁻¹
v_sys = 17455 km s⁻¹
Vel (km s⁻¹)
w50 = 446 km s⁻¹
w20 = 534 km s⁻¹
Sp = 0.013 Jy
Flux (Jy)

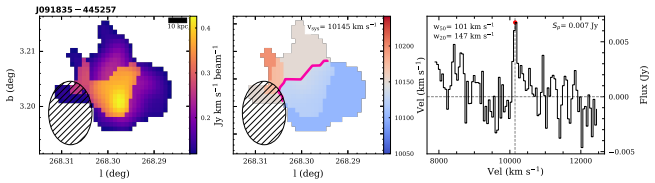
J091835 − 445257
10 kpc
b (deg)
l (deg)
Jy km s⁻¹ beam⁻¹
v_sys = 10145 km s⁻¹
Vel (km s⁻¹)
w50 = 101 km s⁻¹
w20 = 147 km s⁻¹
Sp = 0.007 Jy
Flux (Jy)

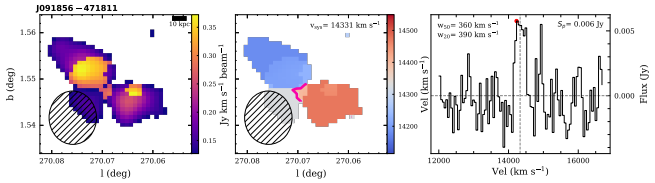
J091856 − 471811
10 kpc
b (deg)
l (deg)
Jy km s⁻¹ beam⁻¹
v_sys = 14331 km s⁻¹
Vel (km s⁻¹)
w50 = 360 km s⁻¹
w20 = 390 km s⁻¹
Sp = 0.006 Jy
Flux (Jy)

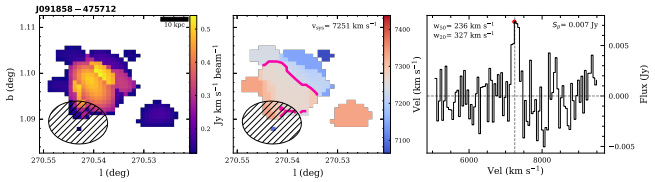
J091858 − 475712
10 kpc
b (deg)
l (deg)
Jy km s⁻¹ beam⁻¹
v_sys = 7251 km s⁻¹
Vel (km s⁻¹)
w50 = 236 km s⁻¹
w20 = 327 km s⁻¹
Sp = 0.007 Jy
Flux (Jy)

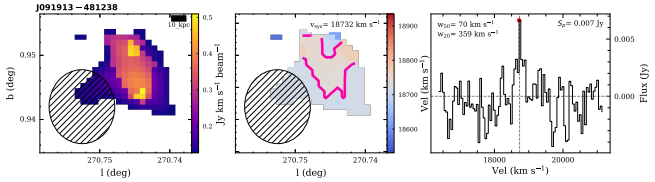
J091913 − 481238
10 kpc
b (deg)
l (deg)
Jy km s⁻¹ beam⁻¹
v_sys = 18732 km s⁻¹
Vel (km s⁻¹)
w50 = 70 km s⁻¹
w20 = 359 km s⁻¹
Sp = 0.007 Jy
Flux (Jy)

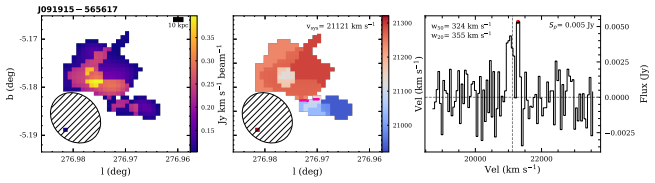
J091915 − 565617
10 kpc
b (deg)
l (deg)
Jy km s⁻¹ beam⁻¹
v_sys = 21121 km s⁻¹
Vel (km s⁻¹)
w50 = 324 km s⁻¹
w20 = 355 km s⁻¹
Sp = 0.005 Jy
Flux (Jy)

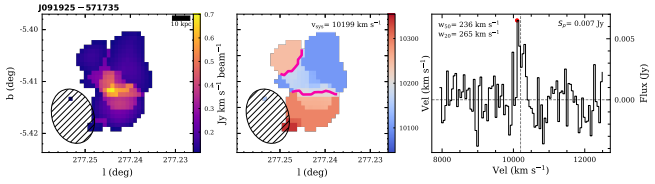
J091925 − 571735
10 kpc
b (deg)
l (deg)
Jy km s⁻¹ beam⁻¹
v_sys = 10199 km s⁻¹
Vel (km s⁻¹)
w50 = 236 km s⁻¹
w20 = 265 km s⁻¹
Sp = 0.007 Jy
Flux (Jy)

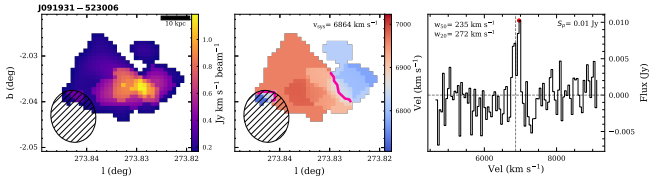
J091931 − 523006
10 kpc
b (deg)
l (deg)
Jy km s⁻¹ beam⁻¹
v_sys = 6864 km s⁻¹
Vel (km s⁻¹)
w50 = 235 km s⁻¹
w20 = 272 km s⁻¹
Sp = 0.01 Jy
Flux (Jy)

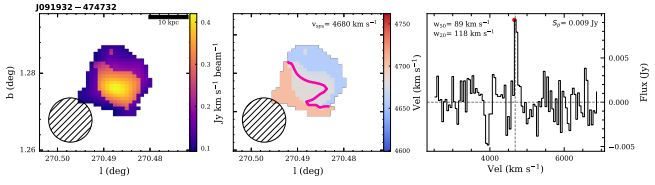
J091932 − 474732
10 kpc
b (deg)
l (deg)
Jy km s⁻¹ beam⁻¹
v_sys = 4680 km s⁻¹
Vel (km s⁻¹)
w50 = 89 km s⁻¹
w20 = 118 km s⁻¹
Sp = 0.009 Jy
Flux (Jy)

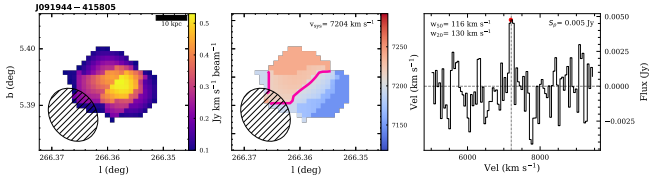
J091944 − 415805
10 kpc
b (deg)
l (deg)
Jy km s⁻¹ beam⁻¹
v_sys = 7204 km s⁻¹
Vel (km s⁻¹)
w50 = 116 km s⁻¹
w20 = 130 km s⁻¹
Sp = 0.005 Jy
Flux (Jy)

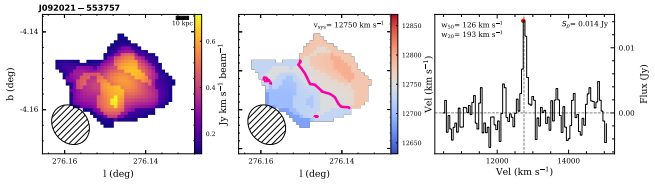
J092021 − 553757
10 kpc
b (deg)
l (deg)
Jy km s⁻¹ beam⁻¹
v_sys = 12750 km s⁻¹
Vel (km s⁻¹)
w50 = 126 km s⁻¹
w20 = 193 km s⁻¹
Sp = 0.014 Jy
Flux (Jy)

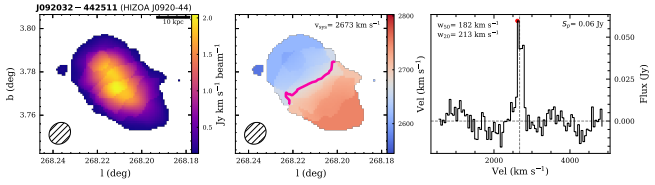
J092032 − 442511 (HIZOA J0920-44)
10 kpc
b (deg)
l (deg)
Jy km s⁻¹ beam⁻¹
v_sys = 2673 km s⁻¹
Vel (km s⁻¹)
w50 = 182 km s⁻¹
w20 = 213 km s⁻¹
Sp = 0.06 Jy
Flux (Jy)

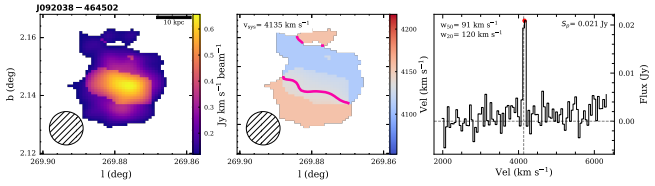
J092038 − 464502
10 kpc
b (deg)
l (deg)
Jy km s⁻¹ beam⁻¹
v_sys = 4135 km s⁻¹
Vel (km s⁻¹)
w50 = 91 km s⁻¹
w20 = 120 km s⁻¹
Sp = 0.021 Jy
Flux (Jy)

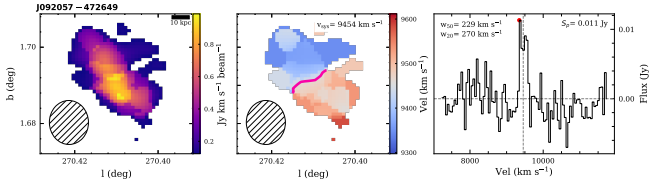
J092057 − 472649
10 kpc
b (deg)
l (deg)
Jy km s⁻¹ beam⁻¹
v_sys = 9454 km s⁻¹
Vel (km s⁻¹)
w50 = 229 km s⁻¹
w20 = 270 km s⁻¹
Sp = 0.011 Jy
Flux (Jy)

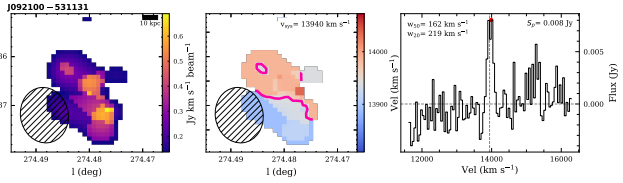
J092100 − 531131
10 kpc
b (deg)
l (deg)
Jy km s⁻¹ beam⁻¹
v_sys = 13940 km s⁻¹
Vel (km s⁻¹)
w50 = 162 km s⁻¹
w20 = 219 km s⁻¹
Sp = 0.008 Jy
Flux (Jy)

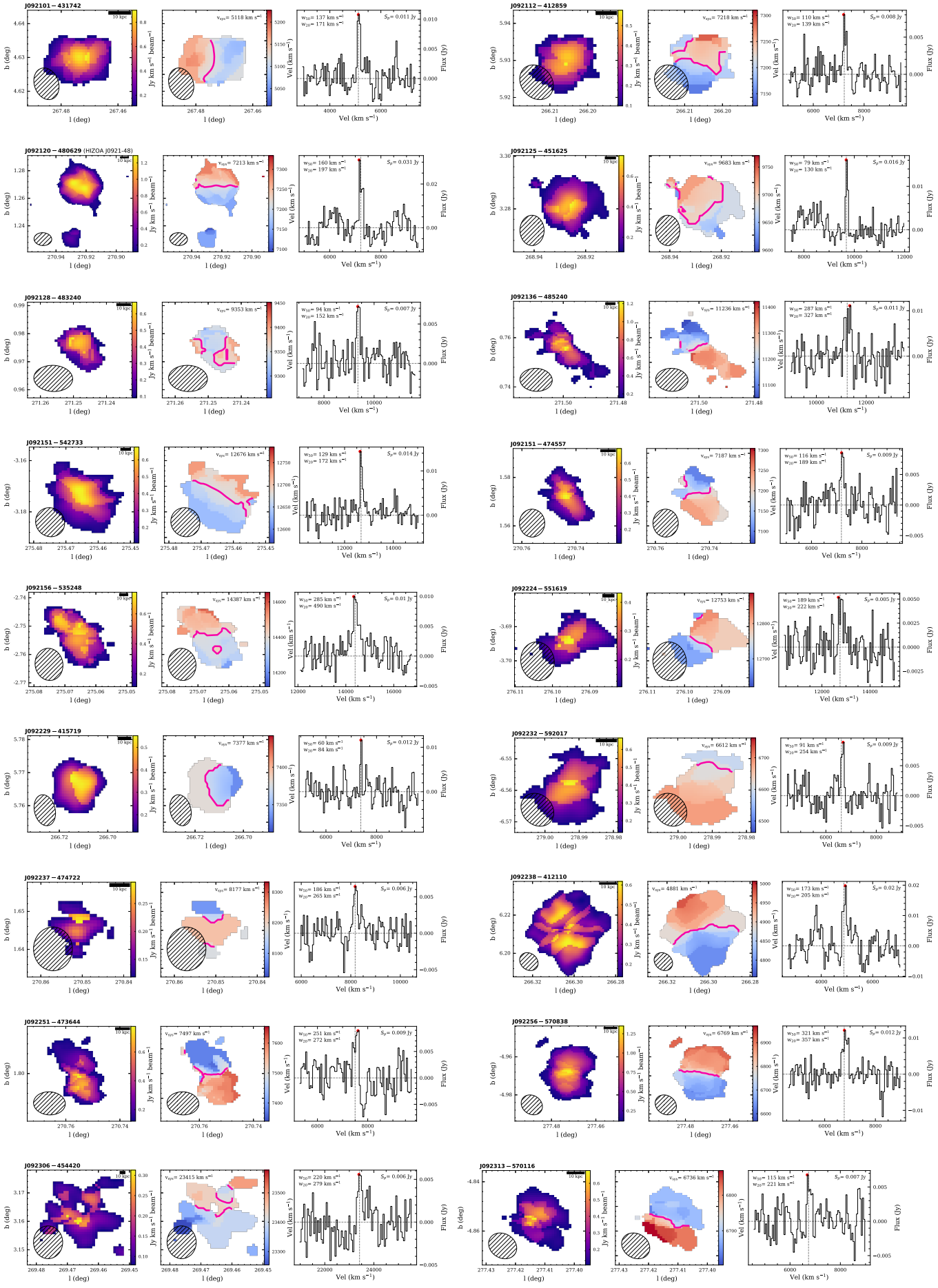
J092101 − 431742
J092112 − 412859
J092120 − 480629 (HIZOA J0921-48)
J092125 − 451625
J092128 − 483240
J092136 − 485240
J092151 − 542733
J092151 − 474557
J092156 − 535248
J092224 − 551619
J092229 − 415719
J092232 − 592017
J092237 − 474722
J092238 − 412110
J092251 − 473644
J092256 − 570838
J092306 − 454420
J092313 − 570116
l (deg)
b (deg)
Vel (km s−1)
Flux (Jy)
Jy km s−1 beam−1
10 kpc

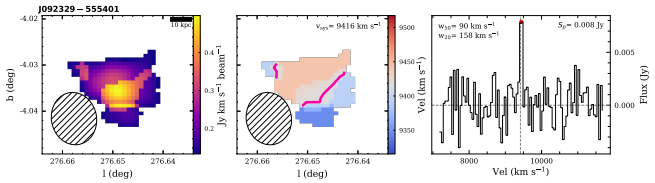
J092329 − 555401
b (deg)
l (deg)
Jy km s⁻¹ beam⁻¹
Vel (km s⁻¹)
Vel (km s⁻¹)
Flux (Jy)
w50= 90 km s⁻¹
w20= 158 km s⁻¹
Sp= 0.008 Jy

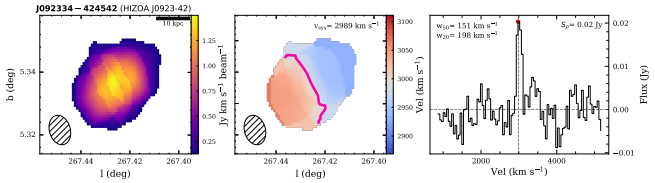
J092334 − 424542 (HIZOA J0923-42)
b (deg)
l (deg)
Jy km s⁻¹ beam⁻¹
Vel (km s⁻¹)
Vel (km s⁻¹)
Flux (Jy)
w50= 151 km s⁻¹
w20= 198 km s⁻¹
Sp= 0.02 Jy

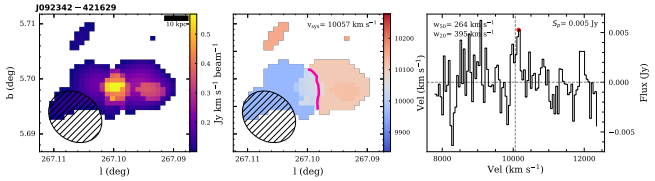
J092342 − 421629
b (deg)
l (deg)
Jy km s⁻¹ beam⁻¹
Vel (km s⁻¹)
Vel (km s⁻¹)
Flux (Jy)
w50= 264 km s⁻¹
w20= 395 km s⁻¹
Sp= 0.005 Jy

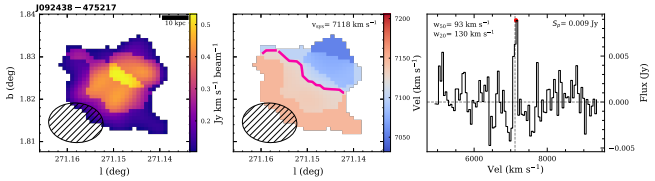
J092438 − 475217
b (deg)
l (deg)
Jy km s⁻¹ beam⁻¹
Vel (km s⁻¹)
Vel (km s⁻¹)
Flux (Jy)
w50= 93 km s⁻¹
w20= 130 km s⁻¹
Sp= 0.009 Jy

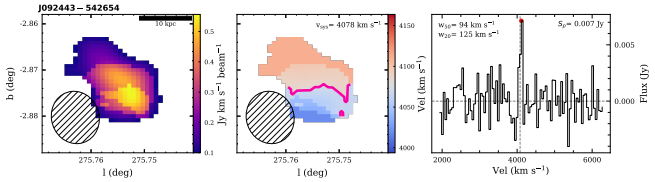
J092443 − 542654
b (deg)
l (deg)
Jy km s⁻¹ beam⁻¹
Vel (km s⁻¹)
Vel (km s⁻¹)
Flux (Jy)
w50= 94 km s⁻¹
w20= 125 km s⁻¹
Sp= 0.007 Jy

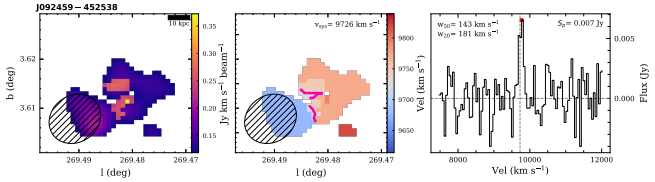
J092459 − 452538
b (deg)
l (deg)
Jy km s⁻¹ beam⁻¹
Vel (km s⁻¹)
Vel (km s⁻¹)
Flux (Jy)
w50= 143 km s⁻¹
w20= 181 km s⁻¹
Sp= 0.007 Jy

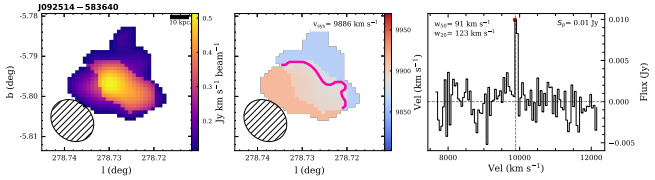
J092514 − 583640
b (deg)
l (deg)
Jy km s⁻¹ beam⁻¹
Vel (km s⁻¹)
Vel (km s⁻¹)
Flux (Jy)
w50= 91 km s⁻¹
w20= 123 km s⁻¹
Sp= 0.01 Jy

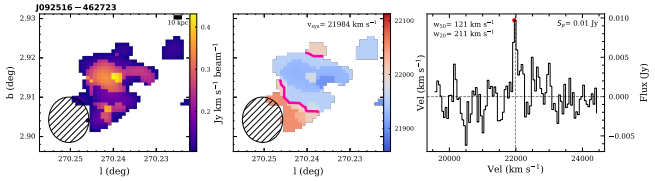
J092516 − 462723
b (deg)
l (deg)
Jy km s⁻¹ beam⁻¹
Vel (km s⁻¹)
Vel (km s⁻¹)
Flux (Jy)
w50= 121 km s⁻¹
w20= 211 km s⁻¹
Sp= 0.01 Jy

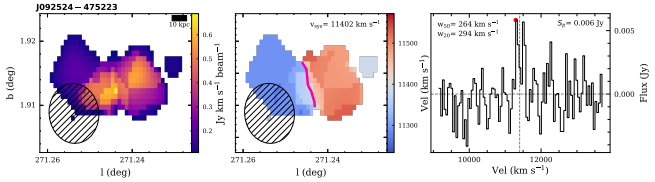
J092524 − 475223
b (deg)
l (deg)
Jy km s⁻¹ beam⁻¹
Vel (km s⁻¹)
Vel (km s⁻¹)
Flux (Jy)
w50= 264 km s⁻¹
w20= 294 km s⁻¹
Sp= 0.006 Jy

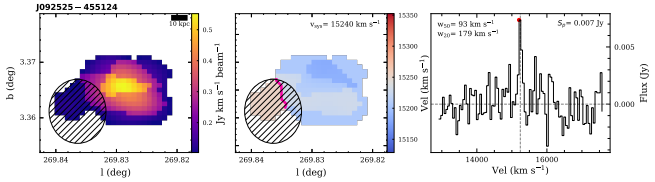
J092525 − 455124
b (deg)
l (deg)
Jy km s⁻¹ beam⁻¹
Vel (km s⁻¹)
Vel (km s⁻¹)
Flux (Jy)
w50= 93 km s⁻¹
w20= 179 km s⁻¹
Sp= 0.007 Jy

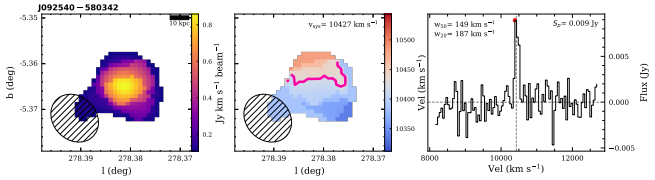
J092540 − 580342
b (deg)
l (deg)
Jy km s⁻¹ beam⁻¹
Vel (km s⁻¹)
Vel (km s⁻¹)
Flux (Jy)
w50= 149 km s⁻¹
w20= 187 km s⁻¹
Sp= 0.009 Jy

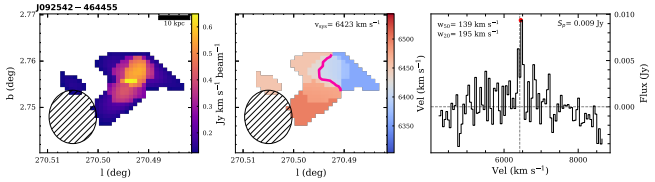
J092542 − 464455
b (deg)
l (deg)
Jy km s⁻¹ beam⁻¹
Vel (km s⁻¹)
Vel (km s⁻¹)
Flux (Jy)
w50= 139 km s⁻¹
w20= 195 km s⁻¹
Sp= 0.009 Jy

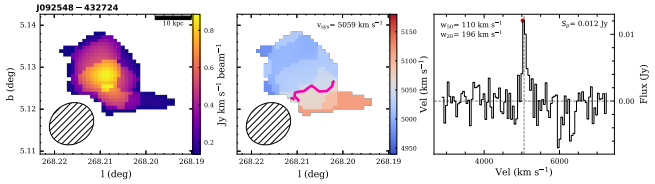
J092548 − 432724
b (deg)
l (deg)
Jy km s⁻¹ beam⁻¹
Vel (km s⁻¹)
Vel (km s⁻¹)
Flux (Jy)
w50= 110 km s⁻¹
w20= 196 km s⁻¹
Sp= 0.012 Jy

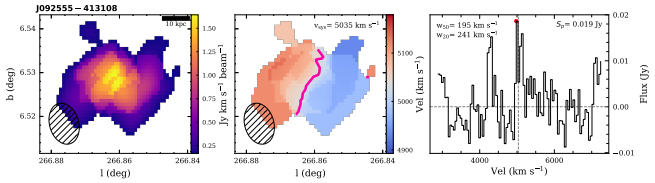
J092555 − 413108
b (deg)
l (deg)
Jy km s⁻¹ beam⁻¹
Vel (km s⁻¹)
Vel (km s⁻¹)
Flux (Jy)
w50= 195 km s⁻¹
w20= 241 km s⁻¹
Sp= 0.019 Jy

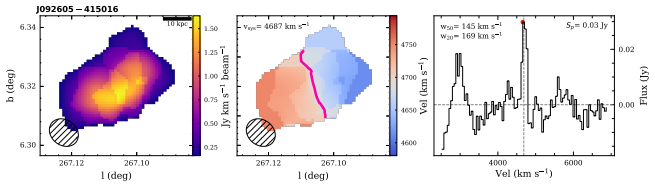
J092605 − 415016
b (deg)
l (deg)
Jy km s⁻¹ beam⁻¹
Vel (km s⁻¹)
Vel (km s⁻¹)
Flux (Jy)
w50= 145 km s⁻¹
w20= 169 km s⁻¹
Sp= 0.03 Jy

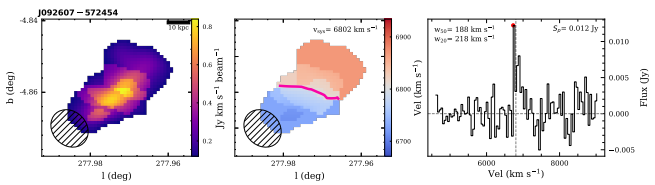
J092607 − 572454
b (deg)
l (deg)
Jy km s⁻¹ beam⁻¹
Vel (km s⁻¹)
Vel (km s⁻¹)
Flux (Jy)
w50= 188 km s⁻¹
w20= 218 km s⁻¹
Sp= 0.012 Jy

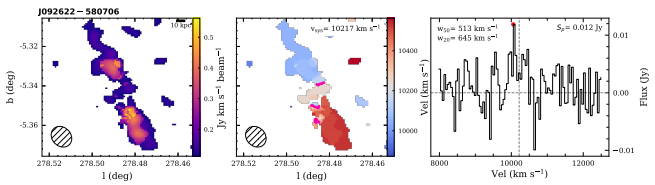
J092622 − 580706
b (deg)
l (deg)
Jy km s⁻¹ beam⁻¹
Vel (km s⁻¹)
Vel (km s⁻¹)
Flux (Jy)
w50= 513 km s⁻¹
w20= 645 km s⁻¹
Sp= 0.012 Jy

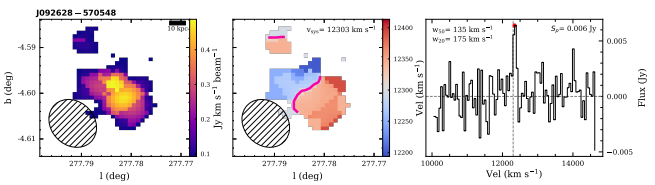
J092628 − 570548
b (deg)
l (deg)
Jy km s⁻¹ beam⁻¹
Vel (km s⁻¹)
Vel (km s⁻¹)
Flux (Jy)
w50= 135 km s⁻¹
w20= 175 km s⁻¹
Sp= 0.006 Jy

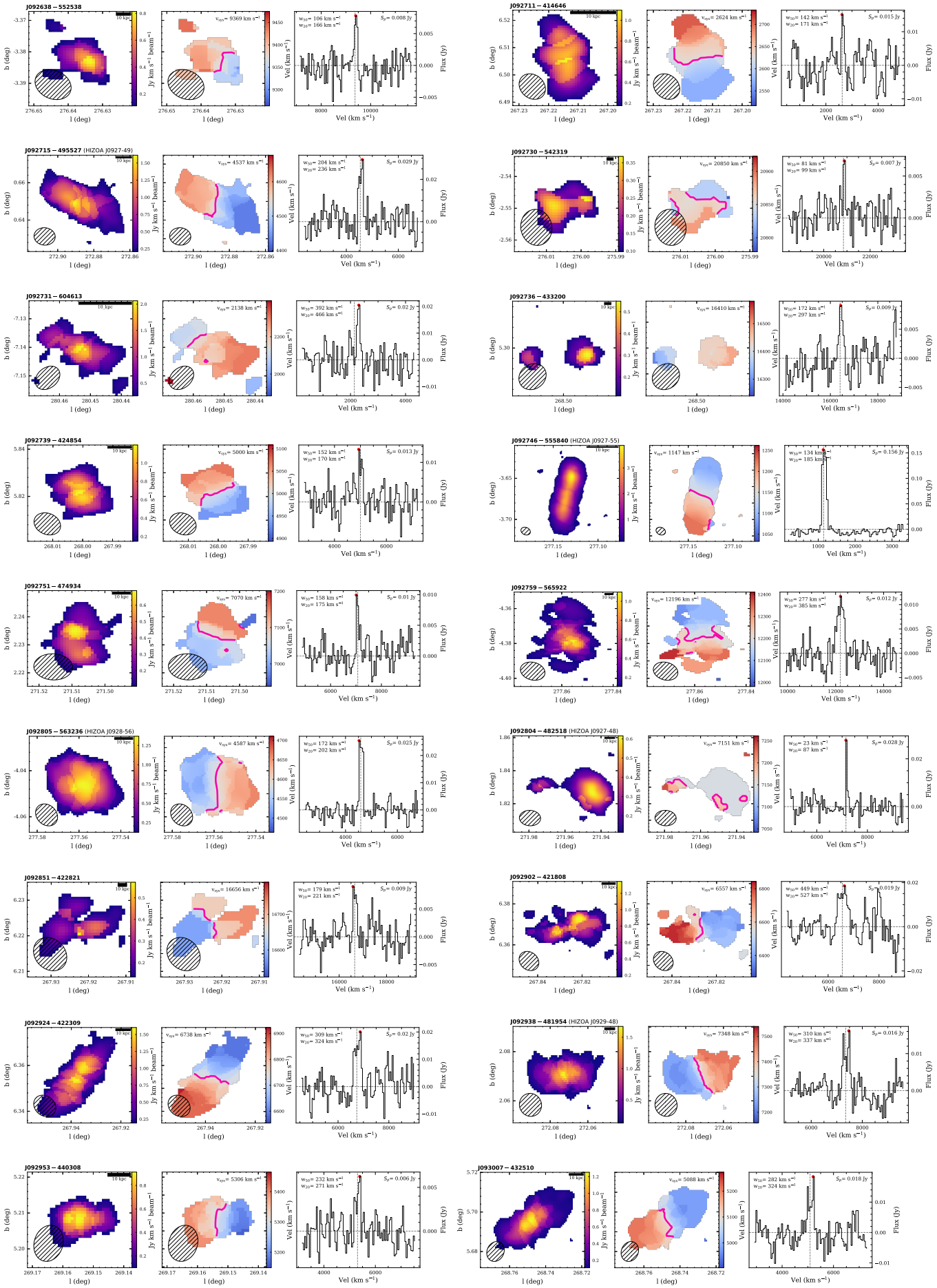
J092638 − 552538
J092711 − 414646
J092715 − 495527 (HIZOA J0927-49)
J092730 − 542319
J092731 − 604613
J092736 − 433200
J092739 − 424854
J092746 − 555840 (HIZOA J0927-55)
J092751 − 474934
J092759 − 565922
J092805 − 563236 (HIZOA J0928-56)
J092804 − 482518 (HIZOA J0927-48)
J092851 − 422821
J092902 − 421808
J092924 − 422309
J092938 − 481954 (HIZOA J0929-48)
J092953 − 440308
J093007 − 432510
l (deg)
b (deg)
Vel (km s−1)
Flux (Jy)
Jy km s−1 beam−1
10 kpc

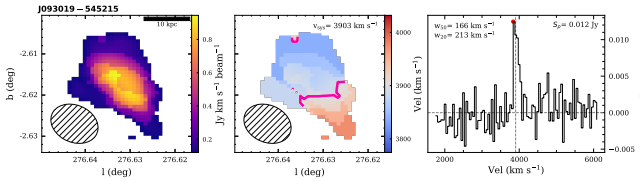
J093019−545215
10 kpc
b (deg)
l (deg)
Jy km s⁻¹ beam⁻¹
Vel (km s⁻¹)
Flux (Jy)
Vel (km s⁻¹)
v_sys= 3903 km s⁻¹
w_50= 166 km s⁻¹
w_20= 213 km s⁻¹
S_p= 0.012 Jy

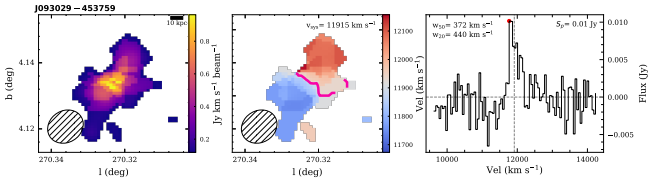
J093029−453759
10 kpc
b (deg)
l (deg)
Jy km s⁻¹ beam⁻¹
Vel (km s⁻¹)
Flux (Jy)
Vel (km s⁻¹)
v_sys= 11915 km s⁻¹
w_50= 372 km s⁻¹
w_20= 440 km s⁻¹
S_p= 0.01 Jy

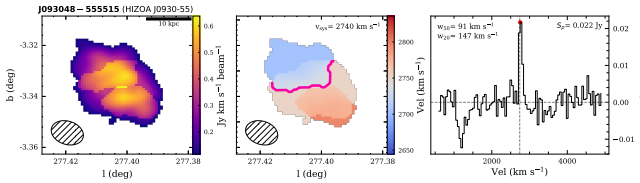
J093048−555515 (HIZOA J0930-55)
10 kpc
b (deg)
l (deg)
Jy km s⁻¹ beam⁻¹
Vel (km s⁻¹)
Flux (Jy)
Vel (km s⁻¹)
v_sys= 2740 km s⁻¹
w_50= 91 km s⁻¹
w_20= 147 km s⁻¹
S_p= 0.022 Jy

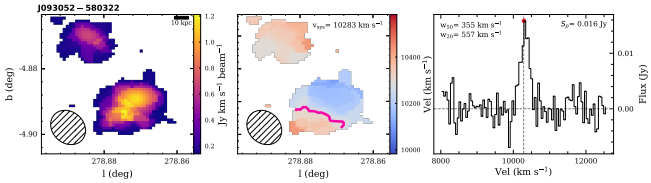
J093052−580322
10 kpc
b (deg)
l (deg)
Jy km s⁻¹ beam⁻¹
Vel (km s⁻¹)
Flux (Jy)
Vel (km s⁻¹)
v_sys= 10283 km s⁻¹
w_50= 355 km s⁻¹
w_20= 557 km s⁻¹
S_p= 0.016 Jy

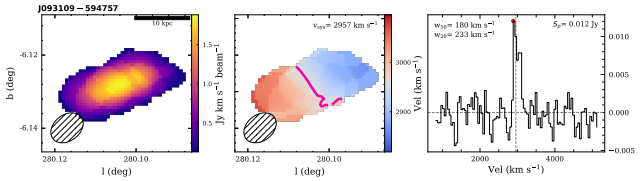
J093109−594757
10 kpc
b (deg)
l (deg)
Jy km s⁻¹ beam⁻¹
Vel (km s⁻¹)
Flux (Jy)
Vel (km s⁻¹)
v_sys= 2957 km s⁻¹
w_50= 180 km s⁻¹
w_20= 233 km s⁻¹
S_p= 0.012 Jy

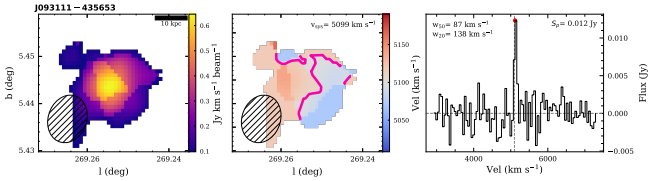
J093111−435653
10 kpc
b (deg)
l (deg)
Jy km s⁻¹ beam⁻¹
Vel (km s⁻¹)
Flux (Jy)
Vel (km s⁻¹)
v_sys= 5099 km s⁻¹
w_50= 87 km s⁻¹
w_20= 138 km s⁻¹
S_p= 0.012 Jy

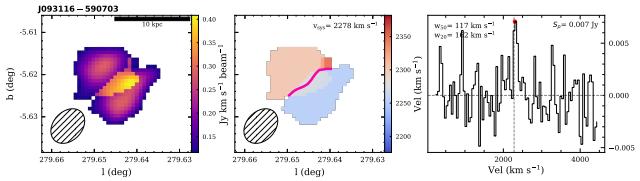
J093116−590703
10 kpc
b (deg)
l (deg)
Jy km s⁻¹ beam⁻¹
Vel (km s⁻¹)
Flux (Jy)
Vel (km s⁻¹)
v_sys= 2278 km s⁻¹
w_50= 117 km s⁻¹
w_20= 162 km s⁻¹
S_p= 0.007 Jy

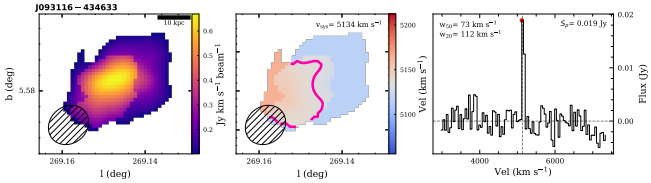
J093116−434633
10 kpc
b (deg)
l (deg)
Jy km s⁻¹ beam⁻¹
Vel (km s⁻¹)
Flux (Jy)
Vel (km s⁻¹)
v_sys= 5134 km s⁻¹
w_50= 73 km s⁻¹
w_20= 112 km s⁻¹
S_p= 0.019 Jy

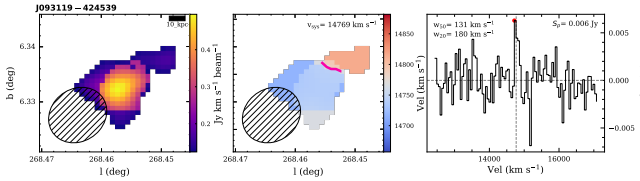
J093119−424539
10 kpc
b (deg)
l (deg)
Jy km s⁻¹ beam⁻¹
Vel (km s⁻¹)
Flux (Jy)
Vel (km s⁻¹)
v_sys= 14769 km s⁻¹
w_50= 131 km s⁻¹
w_20= 180 km s⁻¹
S_p= 0.006 Jy

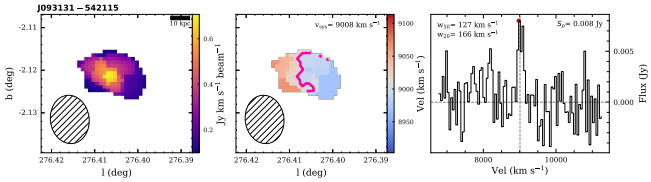
J093131−542115
10 kpc
b (deg)
l (deg)
Jy km s⁻¹ beam⁻¹
Vel (km s⁻¹)
Flux (Jy)
Vel (km s⁻¹)
v_sys= 9008 km s⁻¹
w_50= 127 km s⁻¹
w_20= 166 km s⁻¹
S_p= 0.008 Jy

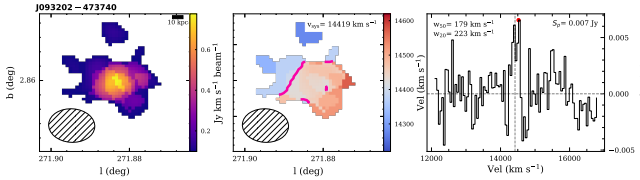
J093202−473740
10 kpc
b (deg)
l (deg)
Jy km s⁻¹ beam⁻¹
Vel (km s⁻¹)
Flux (Jy)
Vel (km s⁻¹)
v_sys= 14419 km s⁻¹
w_50= 179 km s⁻¹
w_20= 223 km s⁻¹
S_p= 0.007 Jy

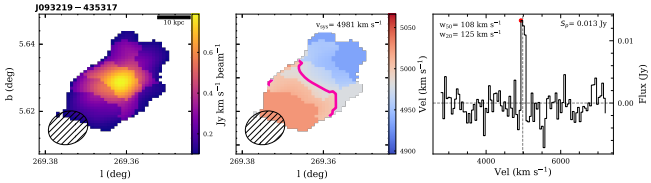
J093219−435317
10 kpc
b (deg)
l (deg)
Jy km s⁻¹ beam⁻¹
Vel (km s⁻¹)
Flux (Jy)
Vel (km s⁻¹)
v_sys= 4981 km s⁻¹
w_50= 108 km s⁻¹
w_20= 125 km s⁻¹
S_p= 0.013 Jy

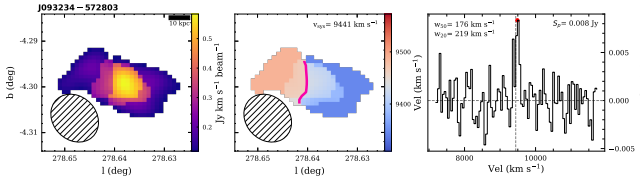
J093234−572803
10 kpc
b (deg)
l (deg)
Jy km s⁻¹ beam⁻¹
Vel (km s⁻¹)
Flux (Jy)
Vel (km s⁻¹)
v_sys= 9441 km s⁻¹
w_50= 176 km s⁻¹
w_20= 219 km s⁻¹
S_p= 0.008 Jy

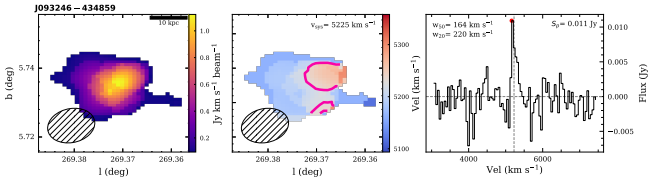
J093246−434859
10 kpc
b (deg)
l (deg)
Jy km s⁻¹ beam⁻¹
Vel (km s⁻¹)
Flux (Jy)
Vel (km s⁻¹)
v_sys= 5225 km s⁻¹
w_50= 164 km s⁻¹
w_20= 220 km s⁻¹
S_p= 0.011 Jy

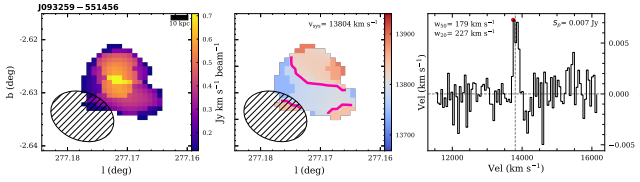
J093259−551456
10 kpc
b (deg)
l (deg)
Jy km s⁻¹ beam⁻¹
Vel (km s⁻¹)
Flux (Jy)
Vel (km s⁻¹)
v_sys= 13804 km s⁻¹
w_50= 179 km s⁻¹
w_20= 227 km s⁻¹
S_p= 0.007 Jy

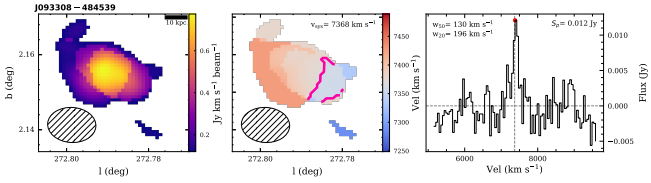
J093308−484539
10 kpc
b (deg)
l (deg)
Jy km s⁻¹ beam⁻¹
Vel (km s⁻¹)
Flux (Jy)
Vel (km s⁻¹)
v_sys= 7368 km s⁻¹
w_50= 130 km s⁻¹
w_20= 196 km s⁻¹
S_p= 0.012 Jy

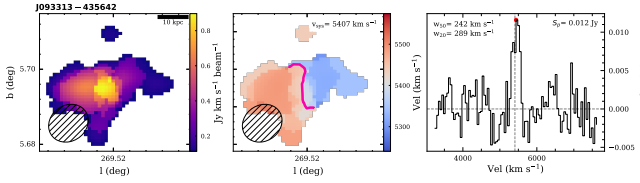
J093313−435642
10 kpc
b (deg)
l (deg)
Jy km s⁻¹ beam⁻¹
Vel (km s⁻¹)
Flux (Jy)
Vel (km s⁻¹)
v_sys= 5407 km s⁻¹
w_50= 242 km s⁻¹
w_20= 289 km s⁻¹
S_p= 0.012 Jy

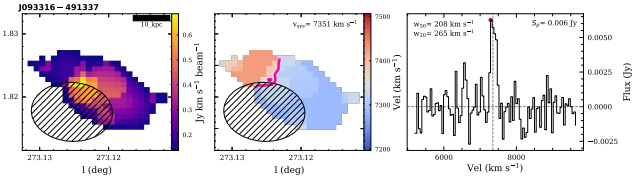
J093316−491337
10 kpc
b (deg)
l (deg)
Jy km s⁻¹ beam⁻¹
Vel (km s⁻¹)
Flux (Jy)
Vel (km s⁻¹)
v_sys= 7351 km s⁻¹
w_50= 208 km s⁻¹
w_20= 265 km s⁻¹
S_p= 0.006 Jy

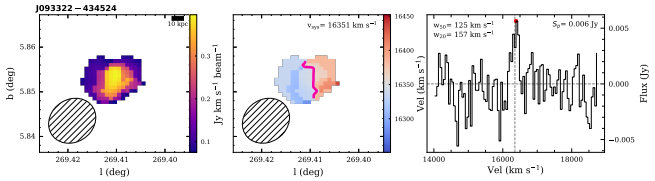
J093322 – 434524
J093324 – 501758

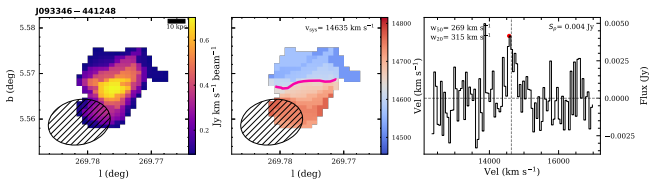
J093346 – 441248
J093348 – 434324

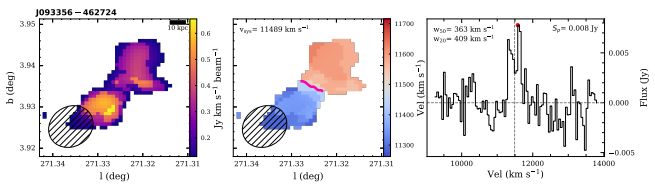
J093356 – 462724
J093356 – 552033

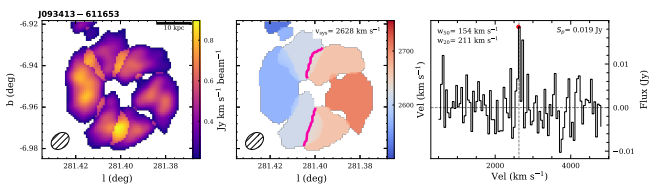
J093413 – 611653
J093424 – 481552

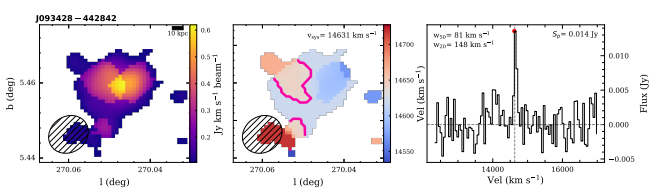
J093428 – 442842
J093454 – 555439 (HIZOA J0934-55)

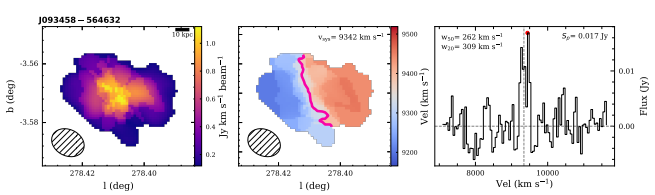
J093458 – 564632
J093516 – 483019

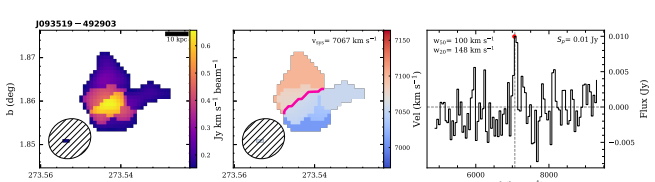
J093519 – 492903
J093523 – 434628

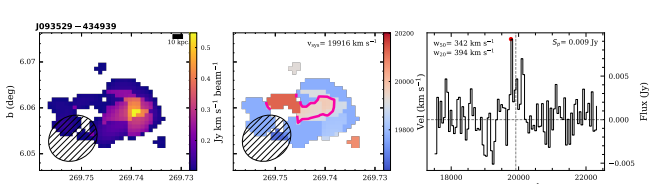
J093529 – 434939
J093533 – 444840

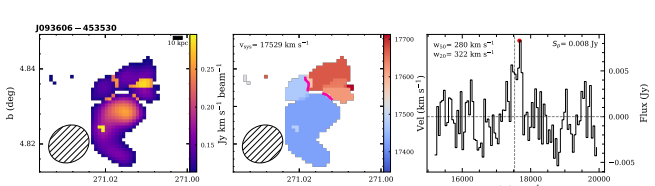
J093606 – 453530
J093617 – 433619

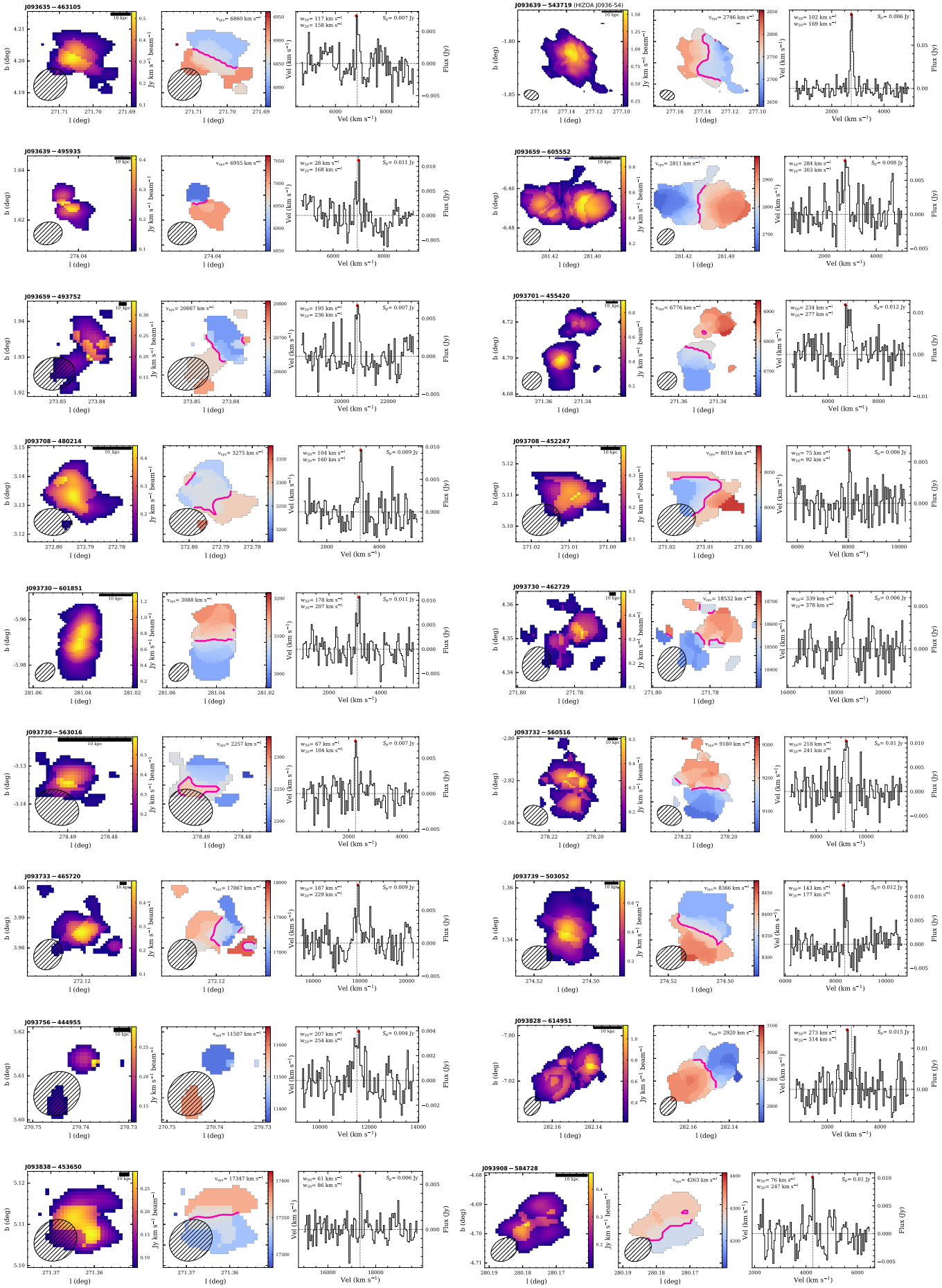
J093635 − 463105
J093639 − 543719 (HIZOA J0936-54)
J093639 − 495935
J093659 − 605552
J093659 − 493752
J093701 − 455420
J093708 − 480214
J093708 − 452247
J093730 − 601851
J093730 − 462729
J093730 − 563016
J093732 − 560516
J093733 − 465720
J093739 − 503052
J093756 − 444955
J093828 − 614951
J093838 − 453650
J093908 − 584728
l (deg)
b (deg)
Vel (km s⁻¹)
Flux (Jy)
Jy km s⁻¹ beam⁻¹

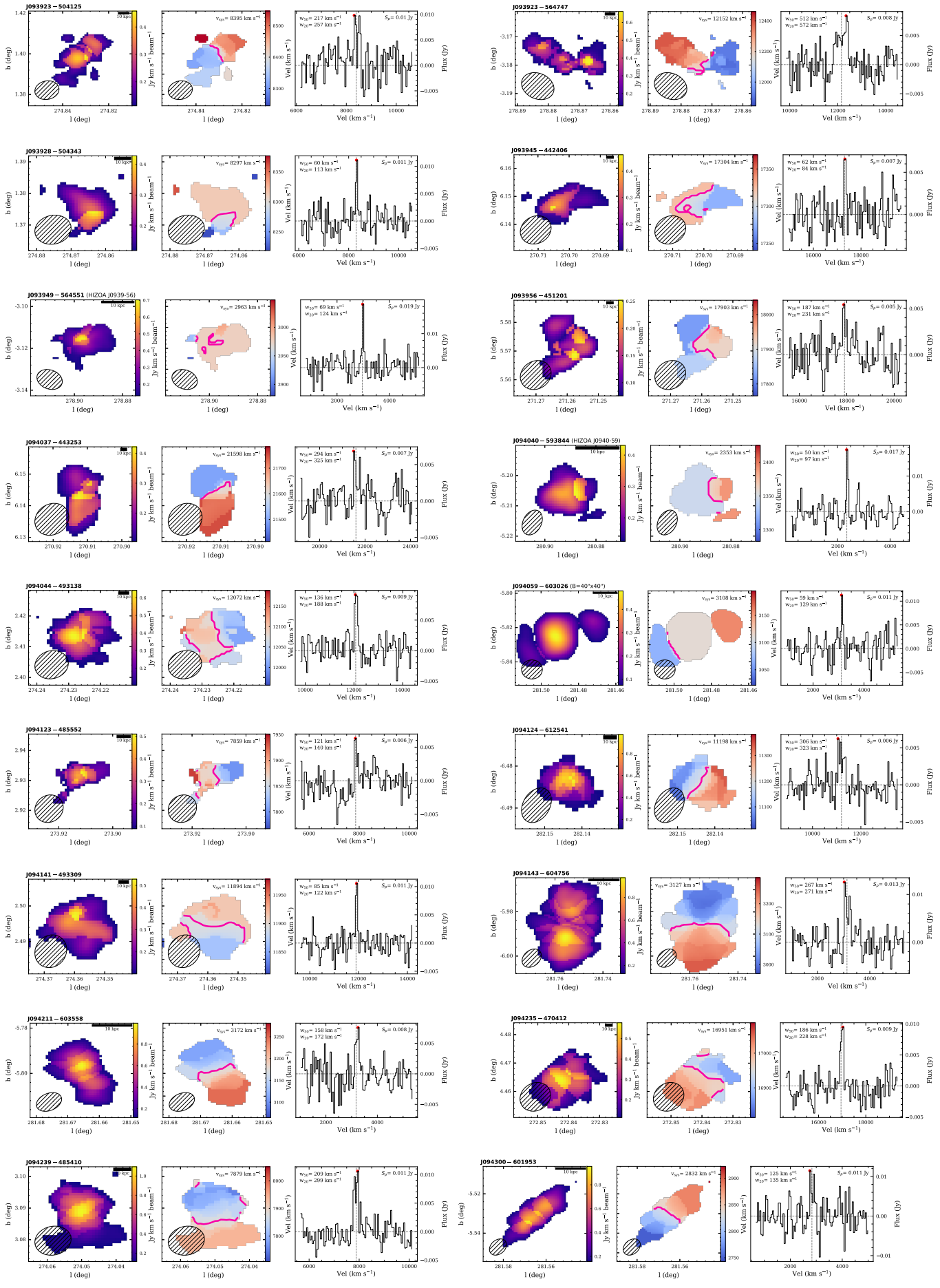
J093923 − 504125
J093923 − 564747
J093928 − 504343
J093945 − 442406
J093949 − 564551 (HIZOA J0939-56)
J093956 − 451201
J094037 − 443253
J094040 − 593844 (HIZOA J0940-59)
J094044 − 493138
J094059 − 603026 (B=40°x40°)
J094123 − 485552
J094124 − 612541
J094141 − 493309
J094143 − 604756
J094211 − 603558
J094235 − 470412
J094239 − 485410
J094300 − 601953
l (deg)
b (deg)
Vel (km s⁻¹)
Flux (Jy)
Jy km s⁻¹ beam⁻¹

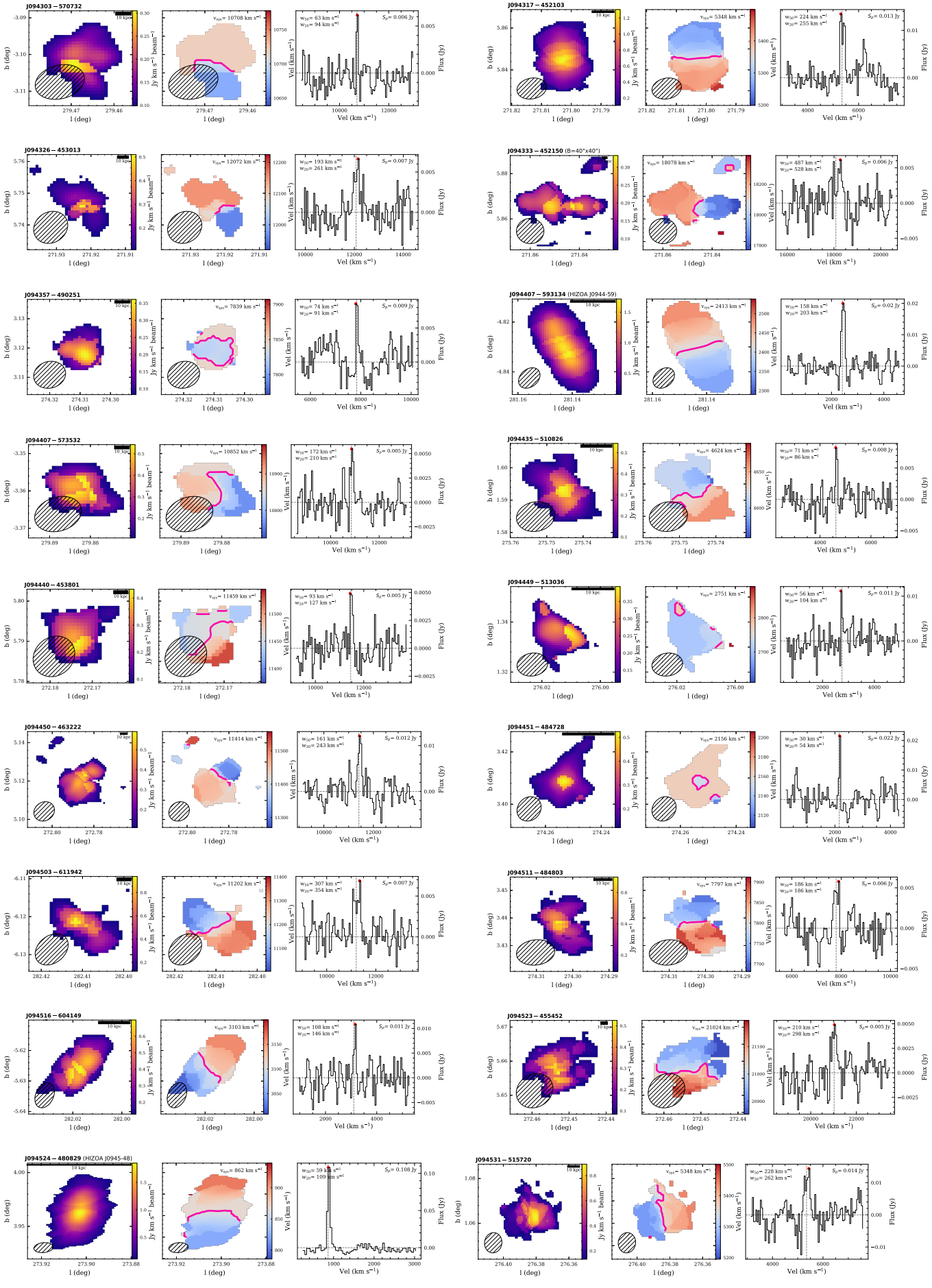
J094303 − 570732
J094317 − 452103
J094326 − 453013
J094333 − 452150 (B=40"x40")
J094357 − 490251
J094407 − 593134 (HIZOA J0944-59)
J094407 − 573532
J094435 − 510826
J094440 − 453801
J094449 − 513036
J094450 − 463222
J094451 − 484728
J094503 − 611942
J094511 − 484803
J094516 − 604149
J094523 − 455452
J094524 − 480829 (HIZOA J0945-48)
J094531 − 515720
l (deg)
b (deg)
Vel (km s−1)
Flux (Jy)
Jy km s−1 beam−1
10 kpc

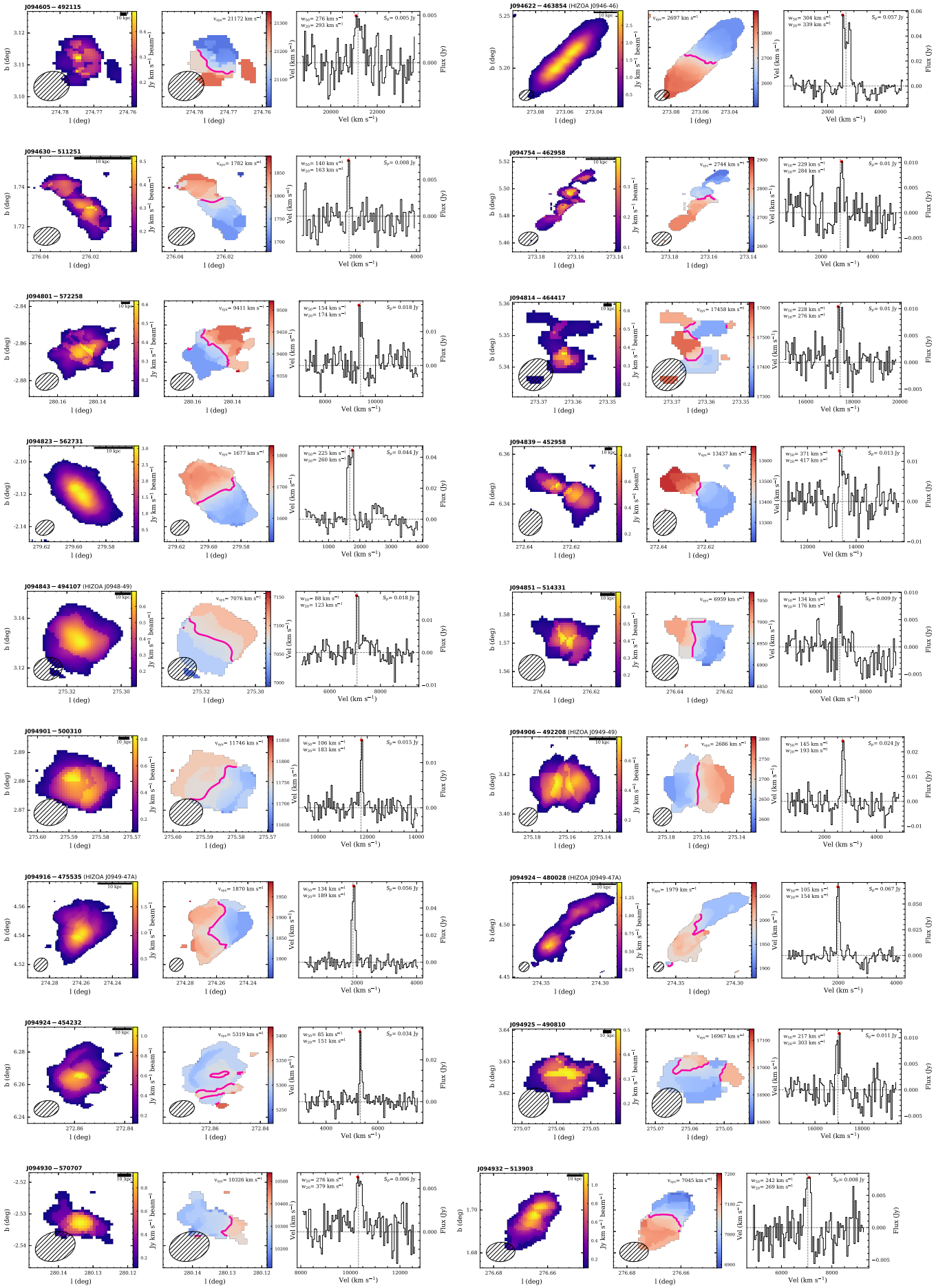
J094605 − 492115
J094622 − 463854 (HIZOA J0946-46)
J094630 − 511251
J094754 − 462958
J094801 − 572258
J094814 − 464417
J094823 − 562731
J094839 − 452958
J094843 − 494107 (HIZOA J0948-49)
J094851 − 514331
J094901 − 500310
J094906 − 492208 (HIZOA J0949-49)
J094916 − 475535 (HIZOA J0949-47A)
J094924 − 480028 (HIZOA J0949-47A)
J094924 − 454232
J094925 − 490810
J094930 − 570707
J094932 − 513903
l (deg)
b (deg)
Vel (km s−1)
Flux (Jy)
Jy km s−1 beam−1
10 kpc

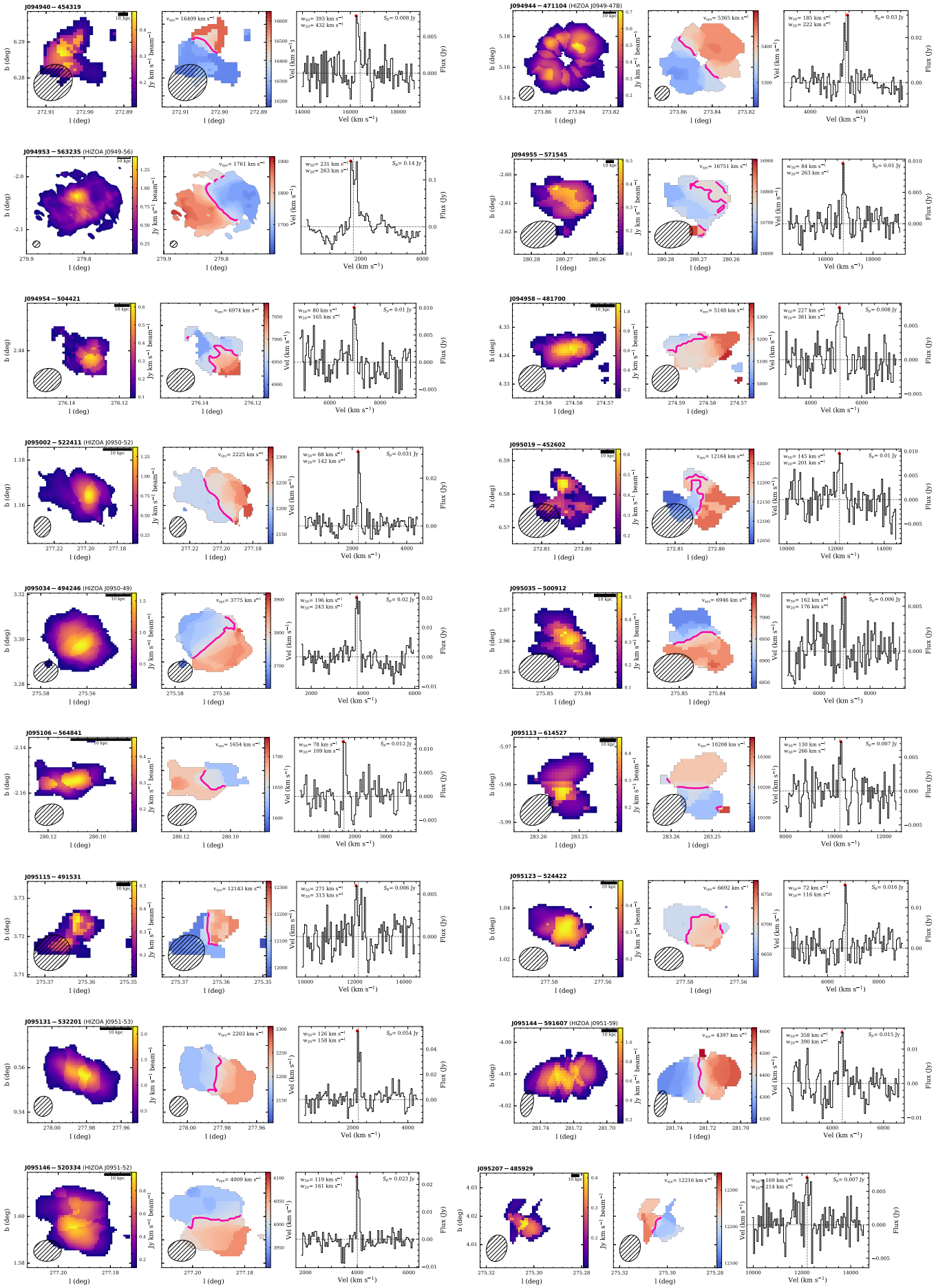
J094940 – 454319
J094944 – 471104 (HIZOA J0949-47B)
J094953 – 563235 (HIZOA J0949-56)
J094955 – 571545
J094954 – 504421
J094958 – 481700
J095002 – 522411 (HIZOA J0950-52)
J095019 – 452602
J095034 – 494246 (HIZOA J0950-49)
J095035 – 500912
J095106 – 564841
J095113 – 614527
J095115 – 491531
J095123 – 524422
J095131 – 532201 (HIZOA J0951-53)
J095144 – 591607 (HIZOA J0951-59)
J095146 – 520334 (HIZOA J0951-52)
J095207 – 485929
b (deg)
l (deg)
Jy km s−1 beam−1
Vel (km s−1)
Flux (Jy)

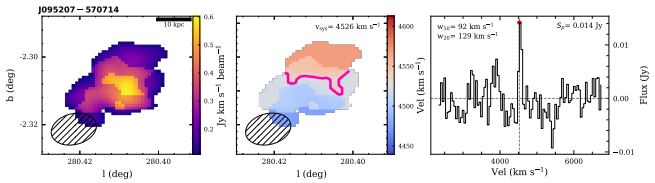
J095207 − 570714
J095211 − 464300

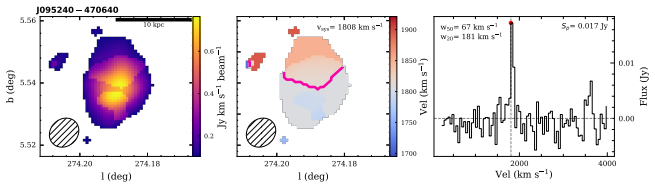
J095240 − 470640
J095244 − 474729

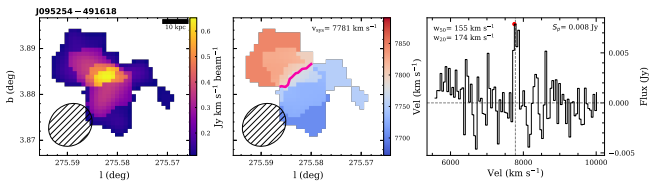
J095254 − 491618
J095258 − 491949

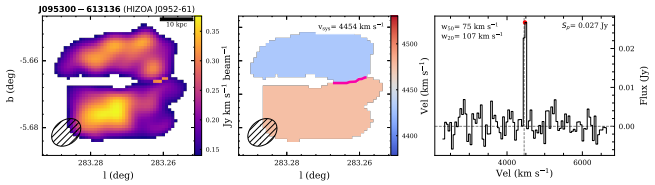
J095300 − 613136 (HIZOA J0952-61)
J095310 − 491957

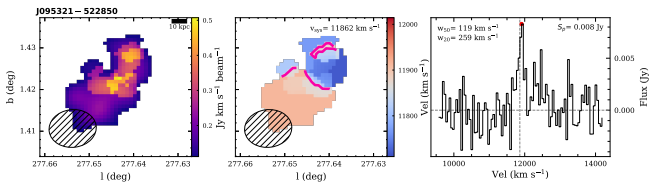
J095321 − 522850
J095321 − 515411 (HIZOA J0953-51)

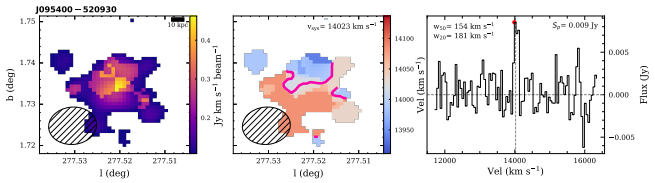
J095400 − 520930
J095417 − 512919 (HIZOA J0954-51)

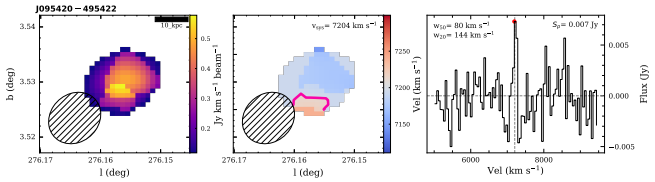
J095420 − 495422
J095435 − 492233

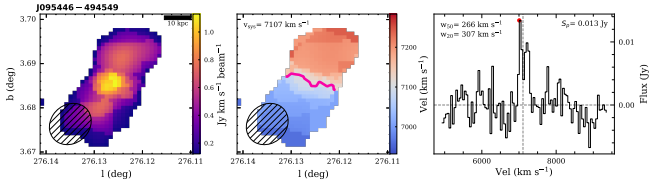
J095446 − 494549
J095456 − 480421

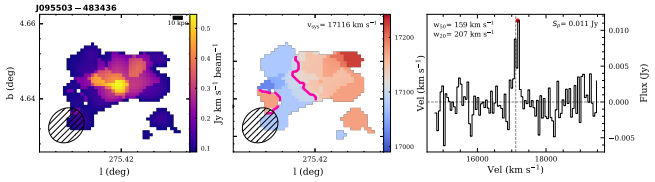
J095503 − 483436
J095504 − 573107

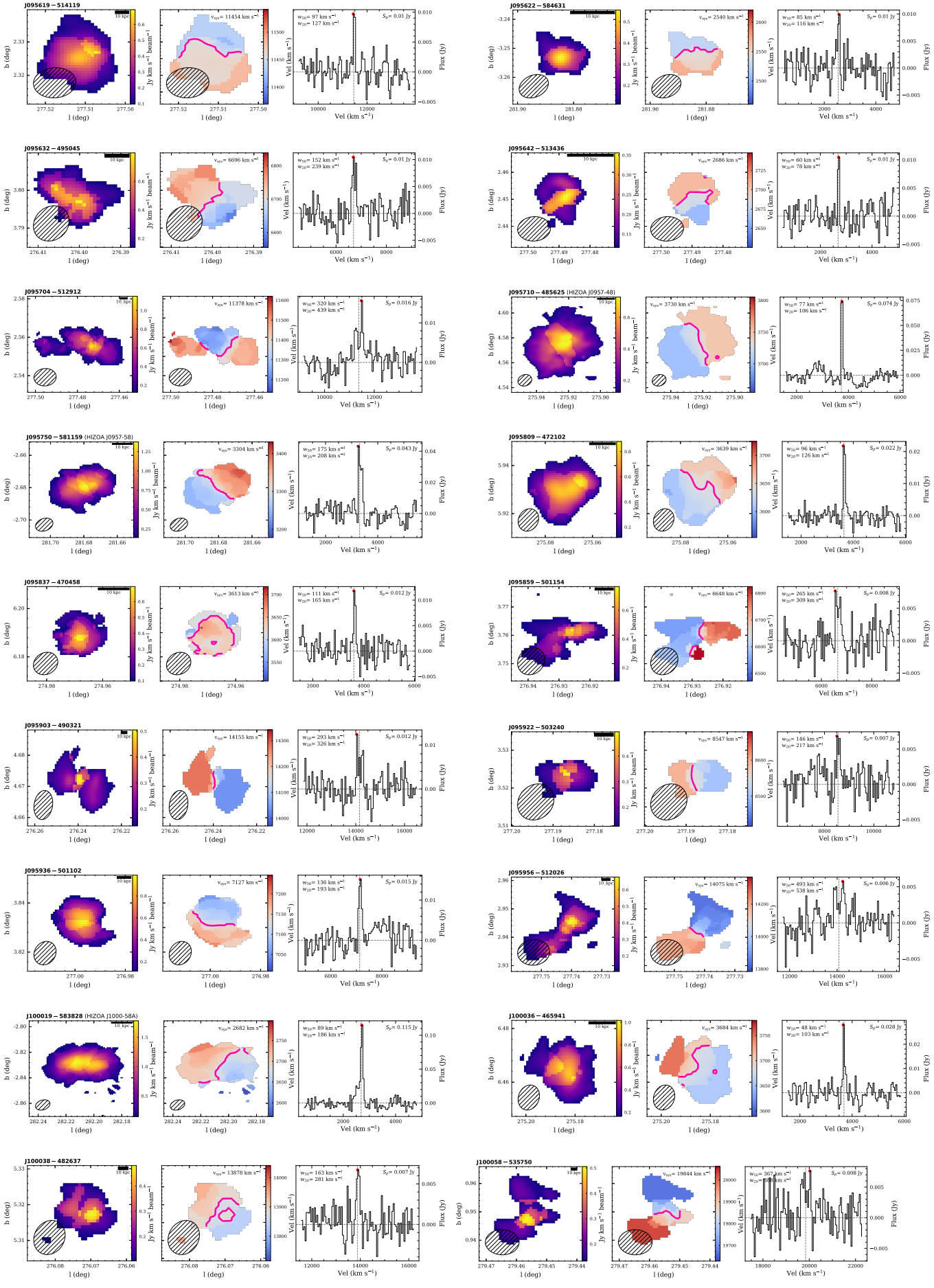
J095619 − 514119
J095622 − 584631
J095632 − 495045
J095642 − 513436
J095704 − 512912
J095710 − 485625 (HIZOA J0957-48)
J095750 − 581159 (HIZOA J0957-58)
J095809 − 472102
J095837 − 470458
J095859 − 501154
J095903 − 490321
J095922 − 503240
J095936 − 501102
J095956 − 512026
J100019 − 583828 (HIZOA J1000-58A)
J100036 − 465941
J100038 − 482637
J100058 − 535750
l (deg)
b (deg)
Vel (km s−1)
Flux (Jy)
Jy km s−1 beam−1
10 kpc

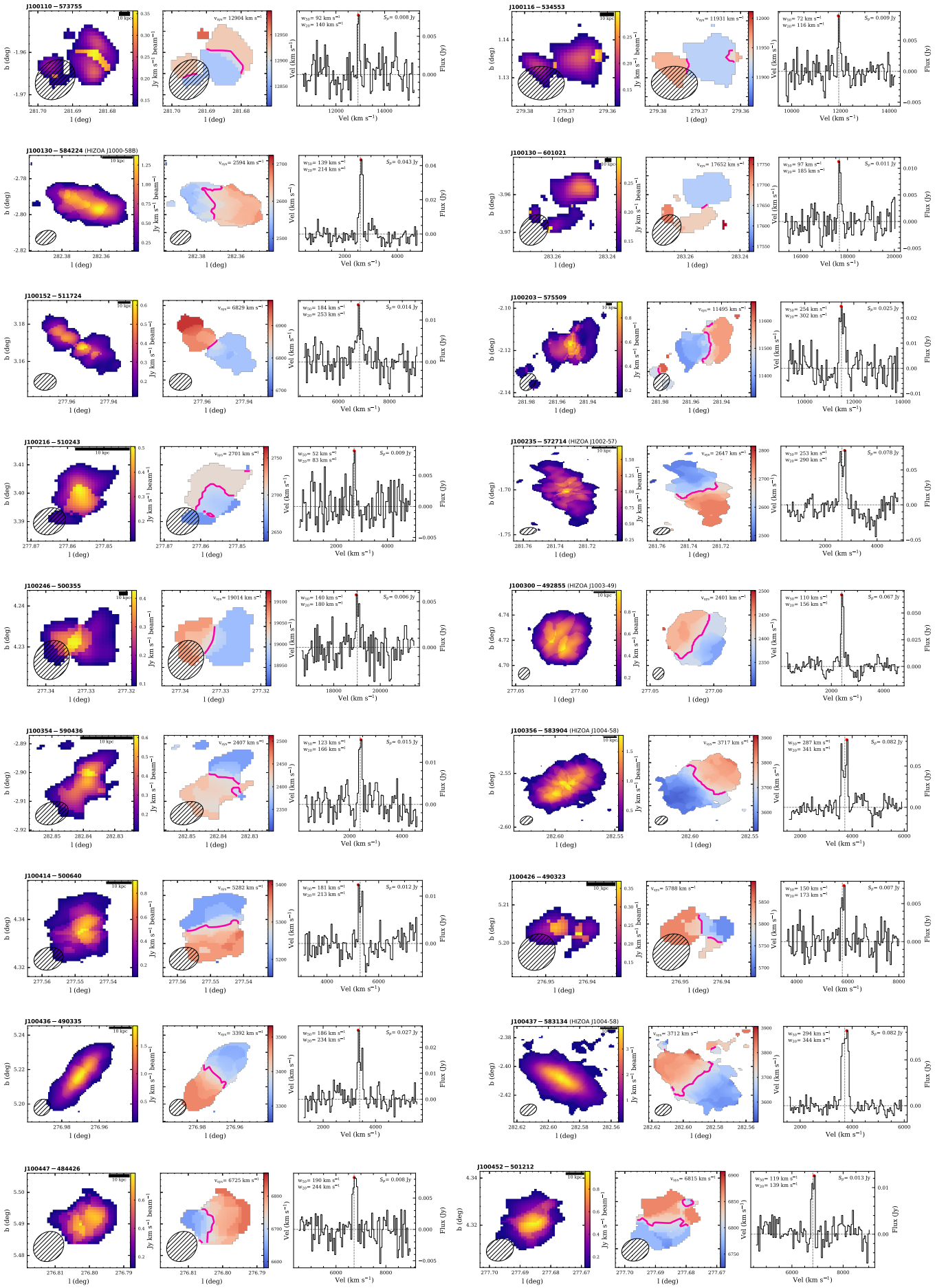
J100110 − 573755
J100116 − 534553
J100130 − 584224 (HIZOA J1000-58B)
J100130 − 601021
J100152 − 511724
J100203 − 575509
J100216 − 510243
J100235 − 572714 (HIZOA J1002-57)
J100246 − 500355
J100300 − 492855 (HIZOA J1003-49)
J100354 − 590436
J100356 − 583904 (HIZOA J1004-58)
J100414 − 500640
J100426 − 490323
J100436 − 490335
J100437 − 583134 (HIZOA J1004-58)
J100447 − 484426
J100452 − 501212
l (deg)
b (deg)
Vel (km s−1)
Flux (Jy)
Jy km s−1 beam−1
10 kpc

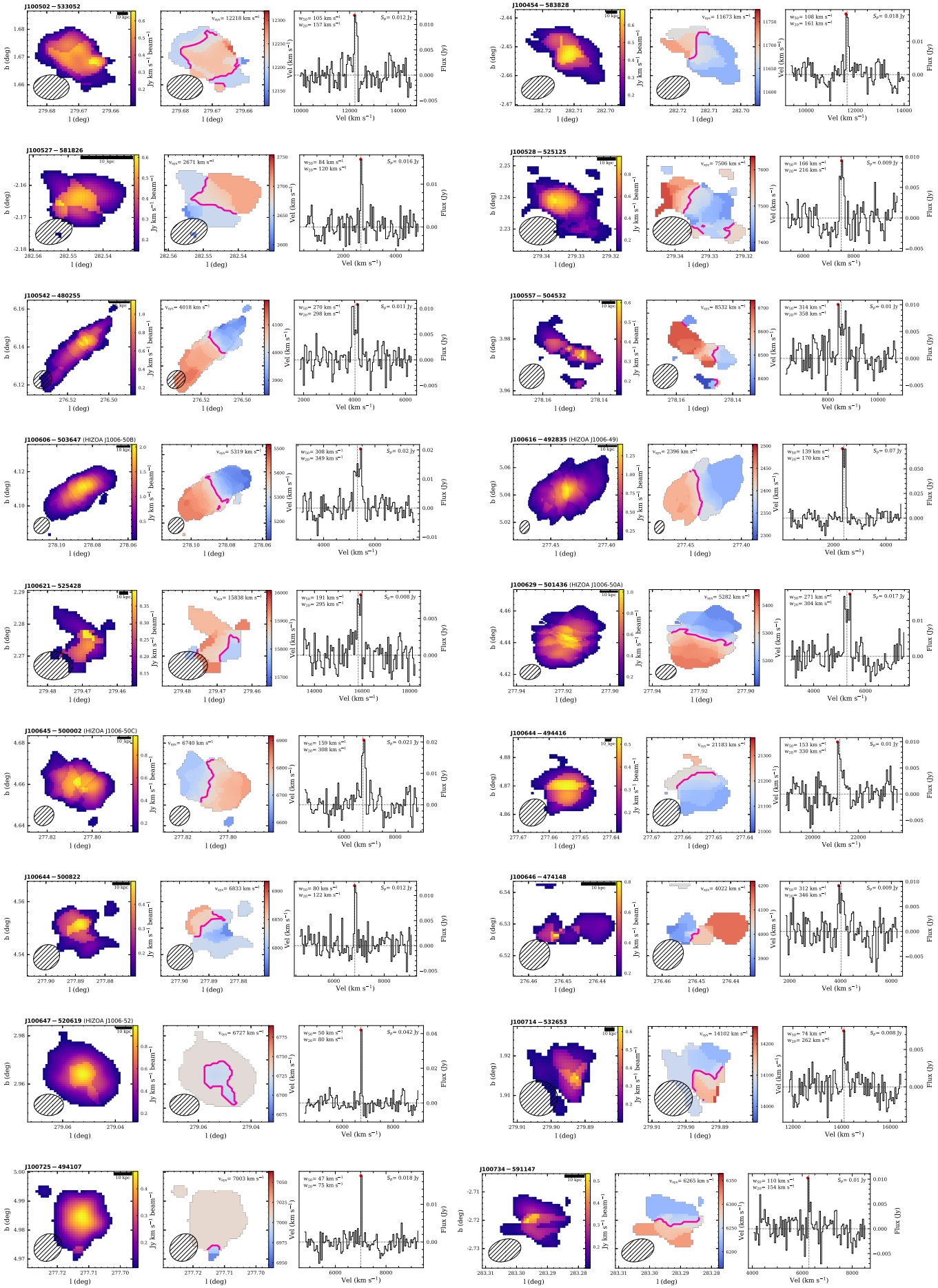
J100502 − 533052
J100454 − 583828
J100527 − 581826
J100528 − 525125
J100542 − 480255
J100557 − 504532
J100606 − 503647 (HIZOA J1006-50B)
J100616 − 492835 (HIZOA J1006-49)
J100621 − 525428
J100629 − 501436 (HIZOA J1006-50A)
J100645 − 500002 (HIZOA J1006-50C)
J100644 − 494416
J100644 − 500822
J100646 − 474148
J100647 − 520619 (HIZOA J1006-52)
J100714 − 532653
J100725 − 494107
J100734 − 591147
l (deg)
b (deg)
Vel (km s−1)
Flux (Jy)
Jy km s−1 beam−1
10 kpc

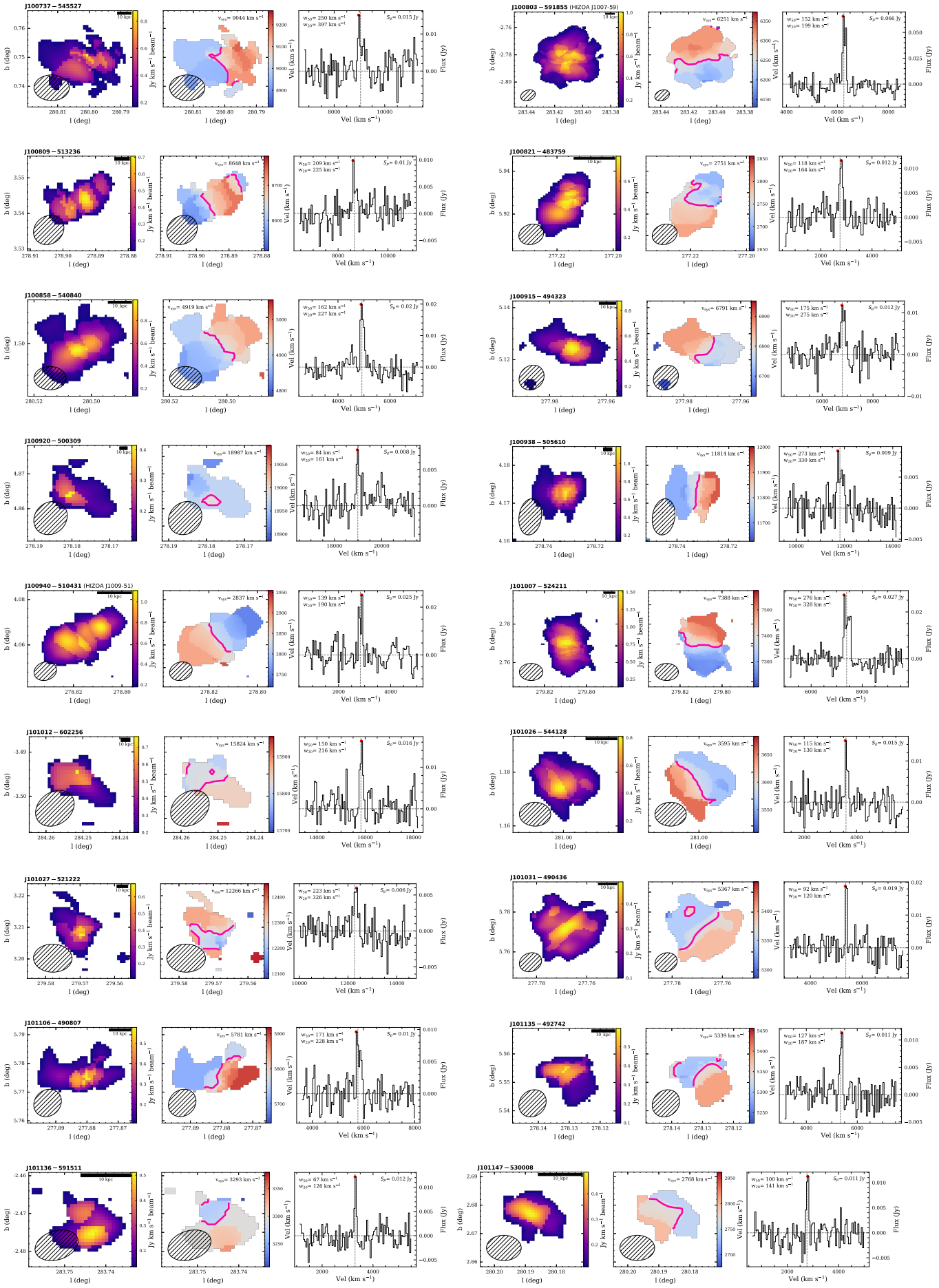
J100737−545527
J100803−591855 (HIZOA J1007-59)
J100809−513236
J100821−483759
J100858−540840
J100915−494323
J100920−500309
J100938−505610
J100940−510431 (HIZOA J1009-51)
J101007−524211
J101012−602256
J101026−544128
J101027−521222
J101031−490436
J101106−490807
J101135−492742
J101136−591511
J101147−530008
l (deg)
b (deg)
Vel (km s−1)
Flux (Jy)
Jy km s−1 beam−1
Vel (km s−1)

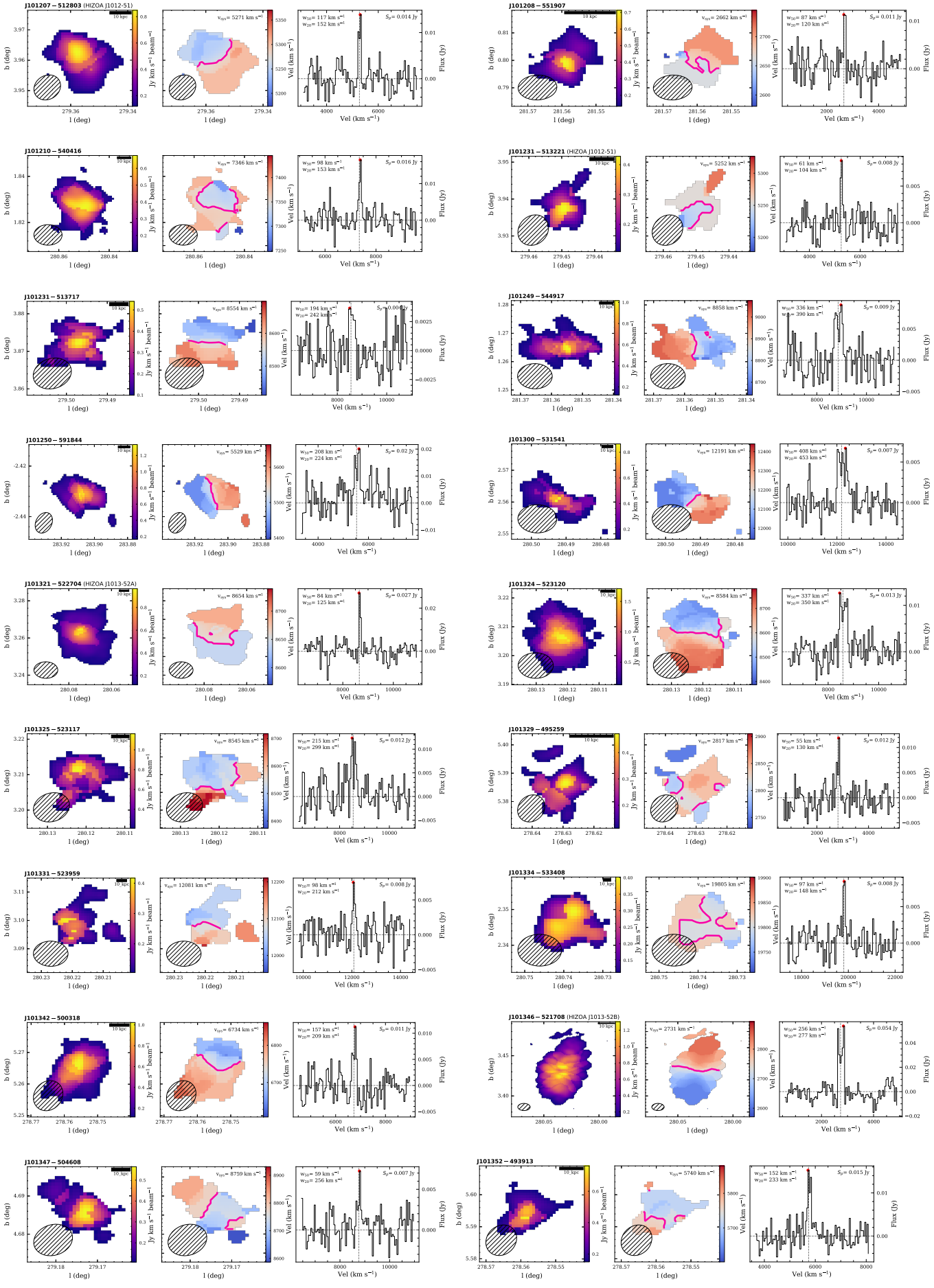
J101207 − 512803 (HIZOA J1012-51)
J101208 − 551907
J101210 − 540416
J101231 − 513221 (HIZOA J1012-51)
J101231 − 513717
J101249 − 544917
J101250 − 591844
J101300 − 531541
J101321 − 522704 (HIZOA J1013-52A)
J101324 − 523120
J101325 − 523117
J101329 − 495259
J101331 − 523959
J101334 − 533408
J101342 − 500318
J101346 − 521708 (HIZOA J1013-52B)
J101347 − 504608
J101352 − 493913
l (deg)
b (deg)
Vel (km s−1)
Flux (Jy)
Jy km s−1 beam−1
10 kpc

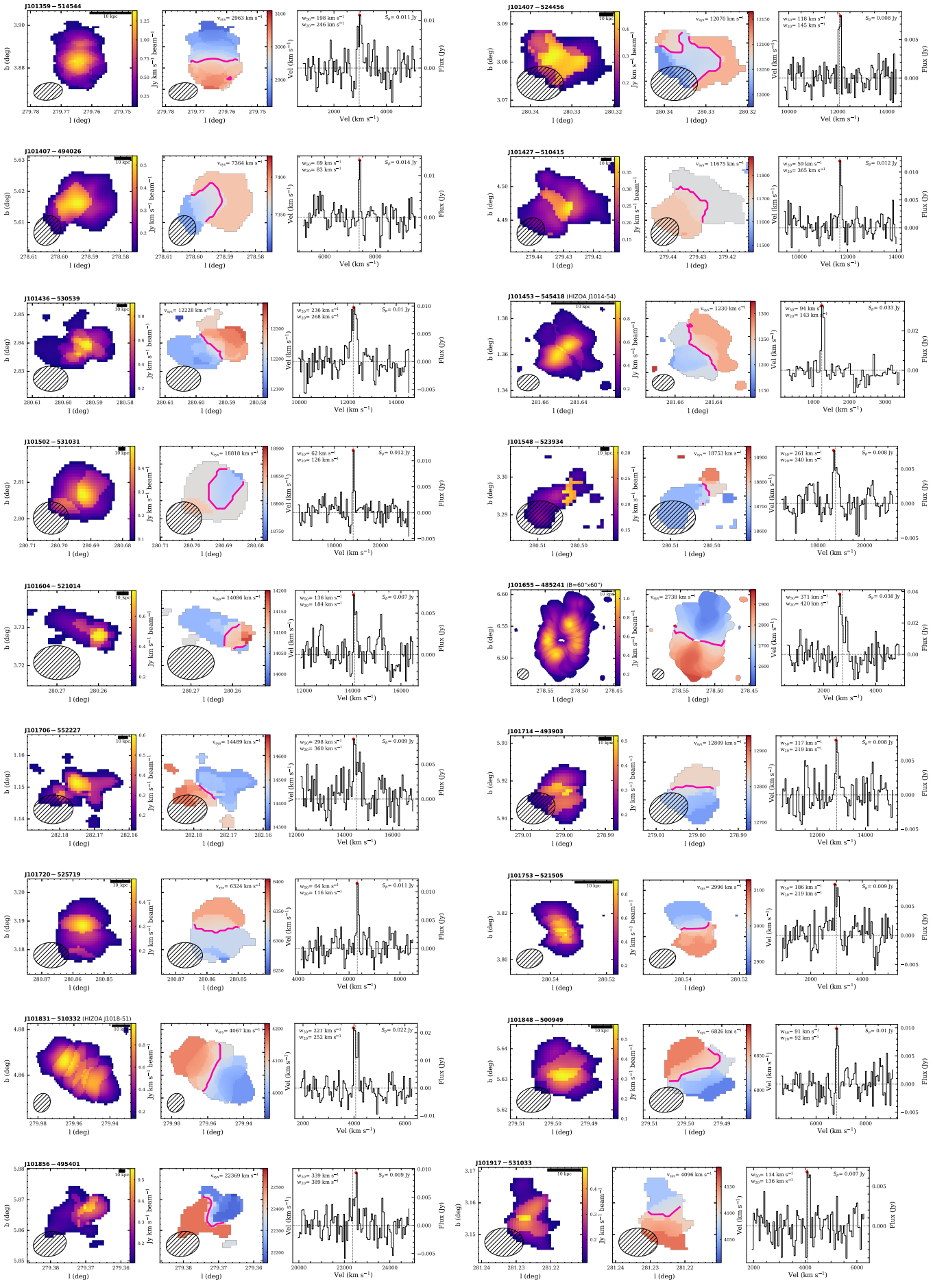
J101359 – 514544
J101407 – 524456
J101407 – 494026
J101427 – 510415
J101436 – 530539
J101453 – 545418 (HIZOA J1014-54)
J101502 – 531031
J101548 – 523934
J101604 – 521014
J101655 – 485241 (B=60"x60")
J101706 – 552227
J101714 – 493903
J101720 – 525719
J101753 – 521505
J101831 – 510332 (HIZOA J1018-51)
J101848 – 500949
J101856 – 495401
J101917 – 531033
l (deg)
b (deg)
Vel (km s−1)
Flux (Jy)
Jy km s−1 beam−1
10 kpc

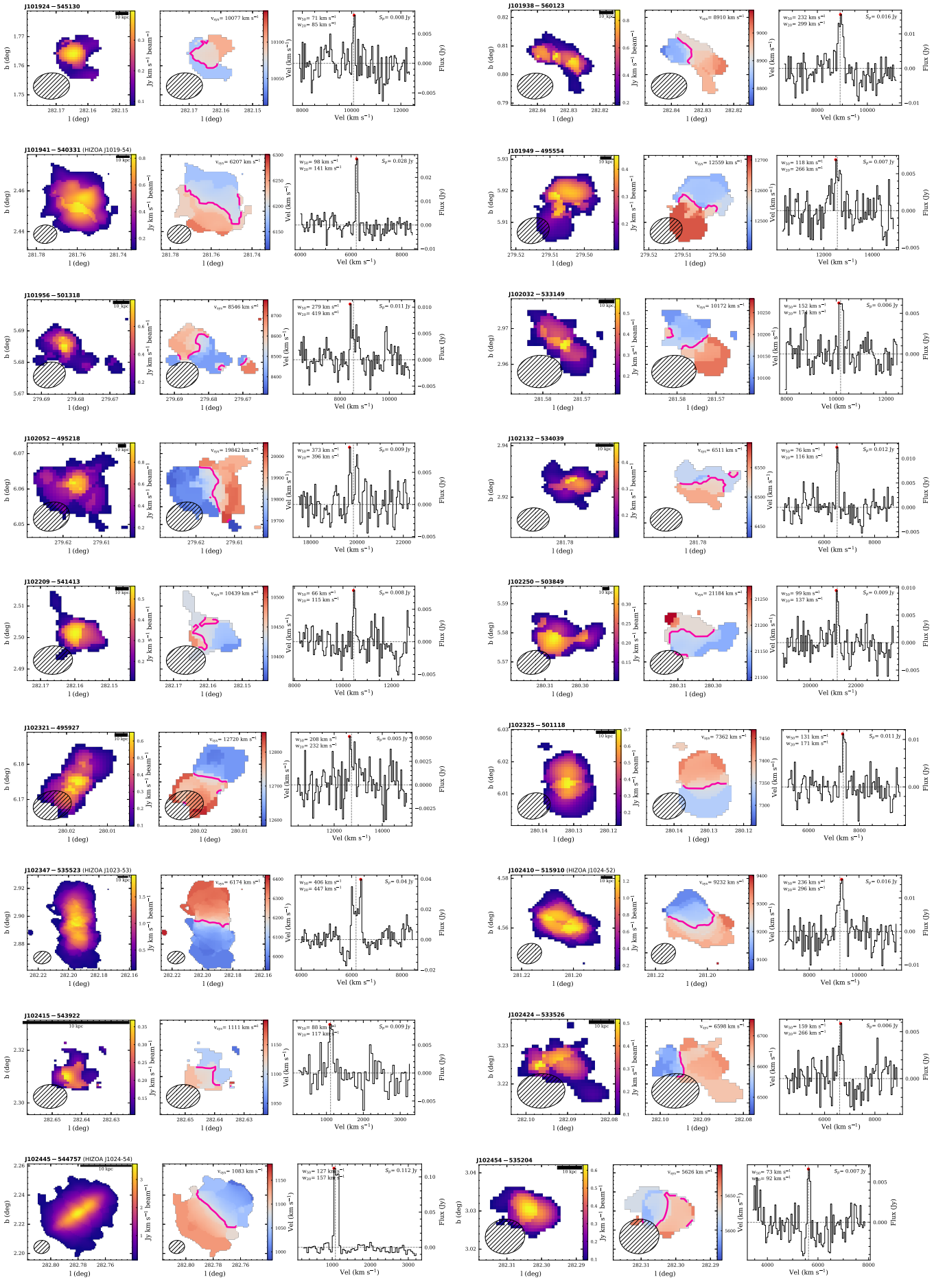
J101924−545130
J101938−560123
J101941−540331 (HIZOA J1019-54)
J101949−495554
J101956−501318
J102032−533149
J102052−495218
J102132−534039
J102209−541413
J102250−503849
J102321−495927
J102325−501118
J102347−535523 (HIZOA J1023-53)
J102410−515910 (HIZOA J1024-52)
J102415−543922
J102424−533526
J102445−544757 (HIZOA J1024-54)
J102454−535204
l (deg)
b (deg)
Vel (km s−1)
Flux (Jy)
Jy km s−1 beam−1
10 kpc

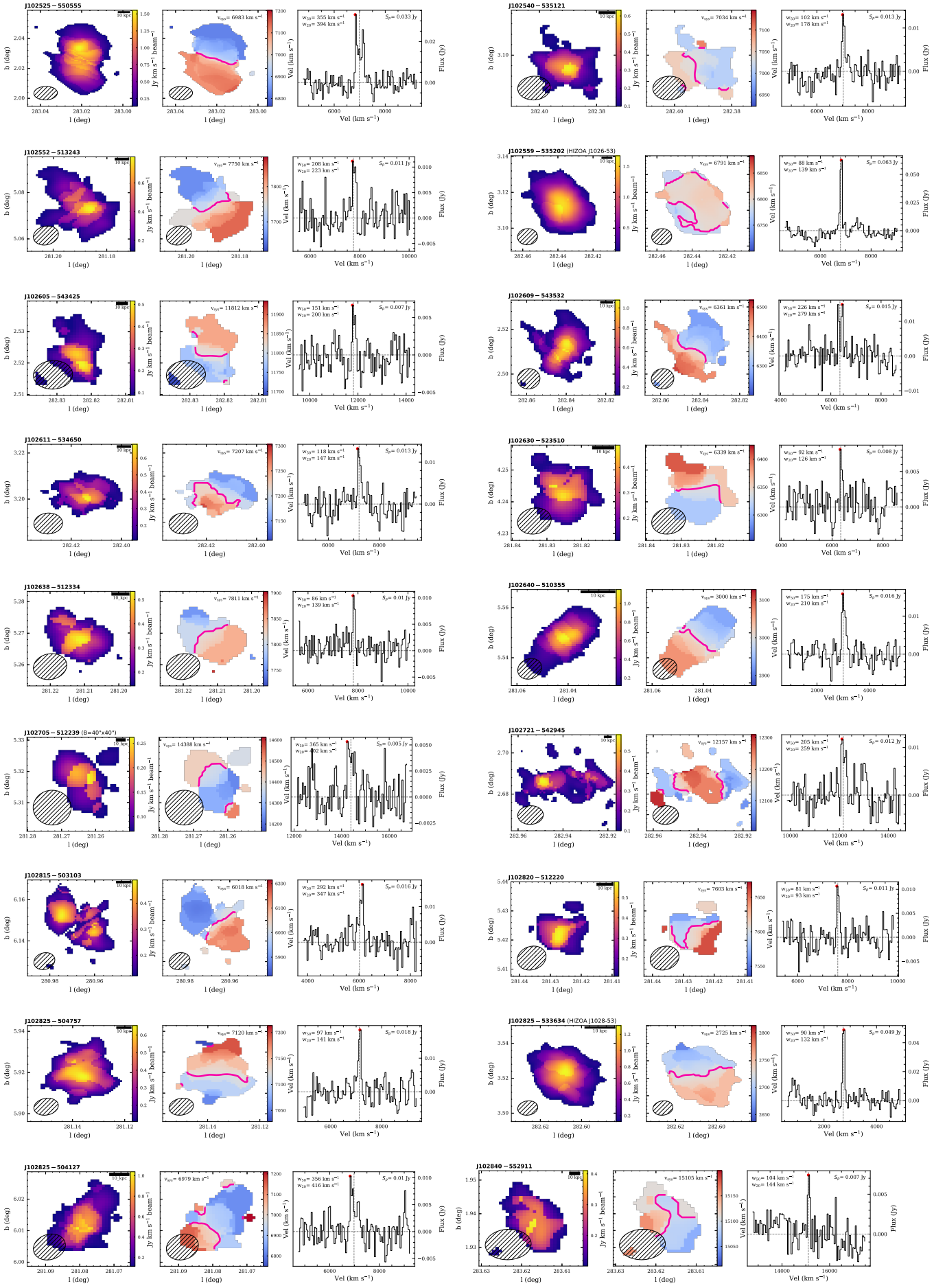
J102525 − 550555
J102540 − 535121
J102552 − 513243
J102559 − 535202 (HIZOA J1026-53)
J102605 − 543425
J102609 − 543532
J102611 − 534650
J102630 − 523510
J102638 − 512334
J102640 − 510355
J102705 − 512239 (B=40"x40")
J102721 − 542945
J102815 − 503103
J102820 − 512220
J102825 − 504757
J102825 − 533634 (HIZOA J1028-53)
J102825 − 504127
J102840 − 552911
l (deg)
b (deg)
Vel (km s−1)
Flux (Jy)
Jy km s−1 beam−1
10 kpc

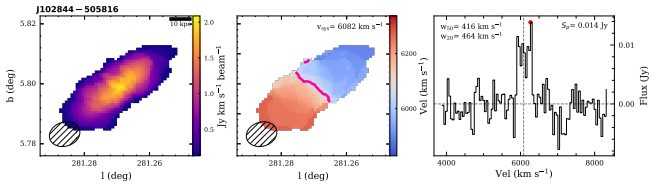
J102844 − 505816
10 kpc
v_{sys}= 6082 km s^{-1}
w_{50}= 416 km s^{-1}
w_{20}= 464 km s^{-1}
S_p= 0.014 Jy
b (deg)
l (deg)
Jy km s^{-1} beam^{-1}
Vel (km s^{-1})
Flux (Jy)

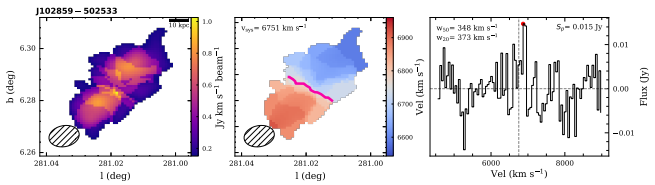
J102859 − 502533
10 kpc
v_{sys}= 6751 km s^{-1}
w_{50}= 348 km s^{-1}
w_{20}= 373 km s^{-1}
S_p= 0.015 Jy
b (deg)
l (deg)
Jy km s^{-1} beam^{-1}
Vel (km s^{-1})
Flux (Jy)

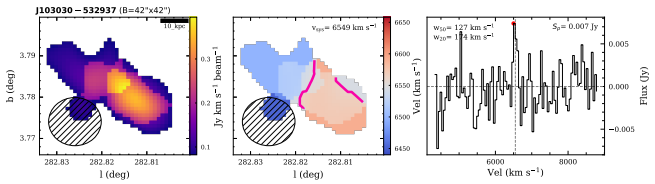
J103030 − 532937 (B=42"x42")
10 kpc
v_{sys}= 6549 km s^{-1}
w_{50}= 127 km s^{-1}
w_{20}= 174 km s^{-1}
S_p= 0.007 Jy
b (deg)
l (deg)
Jy km s^{-1} beam^{-1}
Vel (km s^{-1})
Flux (Jy)

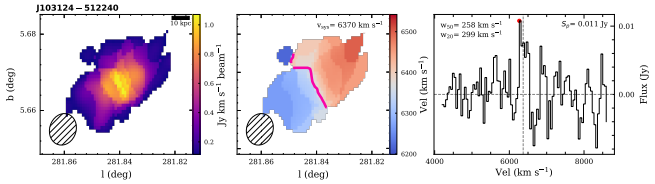
J103124 − 512240
10 kpc
v_{sys}= 6370 km s^{-1}
w_{50}= 258 km s^{-1}
w_{20}= 299 km s^{-1}
S_p= 0.011 Jy
b (deg)
l (deg)
Jy km s^{-1} beam^{-1}
Vel (km s^{-1})
Flux (Jy)

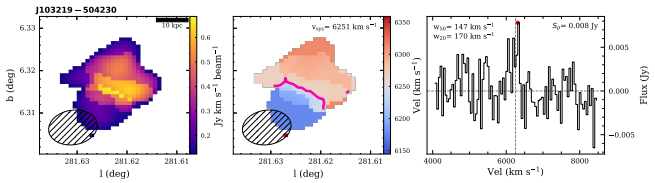
J103219 − 504230
10 kpc
v_{sys}= 6251 km s^{-1}
w_{50}= 147 km s^{-1}
w_{20}= 170 km s^{-1}
S_p= 0.008 Jy
b (deg)
l (deg)
Jy km s^{-1} beam^{-1}
Vel (km s^{-1})
Flux (Jy)

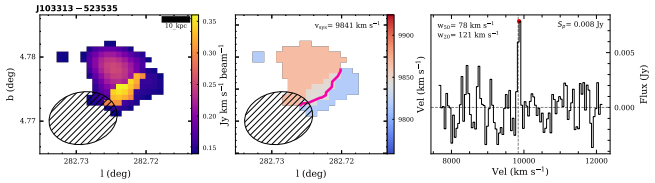
J103313 − 523535
10 kpc
v_{sys}= 9841 km s^{-1}
w_{50}= 78 km s^{-1}
w_{20}= 121 km s^{-1}
S_p= 0.008 Jy
b (deg)
l (deg)
Jy km s^{-1} beam^{-1}
Vel (km s^{-1})
Flux (Jy)

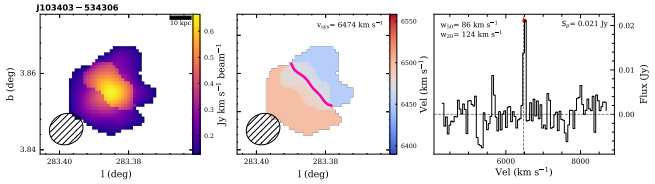
J103403 − 534306
10 kpc
v_{sys}= 6474 km s^{-1}
w_{50}= 86 km s^{-1}
w_{20}= 124 km s^{-1}
S_p= 0.021 Jy
b (deg)
l (deg)
Jy km s^{-1} beam^{-1}
Vel (km s^{-1})
Flux (Jy)

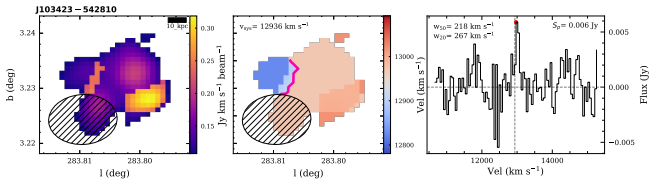
J103423 − 542810
10 kpc
v_{sys}= 12936 km s^{-1}
w_{50}= 218 km s^{-1}
w_{20}= 267 km s^{-1}
S_p= 0.006 Jy
b (deg)
l (deg)
Jy km s^{-1} beam^{-1}
Vel (km s^{-1})
Flux (Jy)

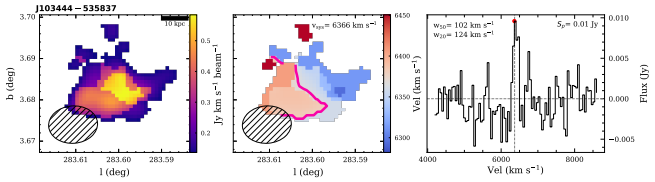
J103444 − 535837
10 kpc
v_{sys}= 6366 km s^{-1}
w_{50}= 102 km s^{-1}
w_{20}= 124 km s^{-1}
S_p= 0.01 Jy
b (deg)
l (deg)
Jy km s^{-1} beam^{-1}
Vel (km s^{-1})
Flux (Jy)

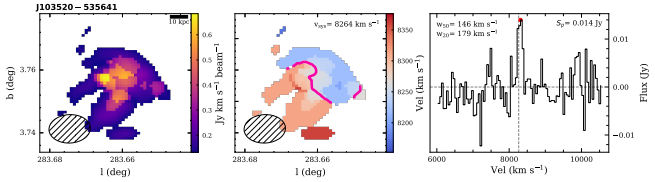
J103520 − 535641
10 kpc
v_{sys}= 8264 km s^{-1}
w_{50}= 146 km s^{-1}
w_{20}= 179 km s^{-1}
S_p= 0.014 Jy
b (deg)
l (deg)
Jy km s^{-1} beam^{-1}
Vel (km s^{-1})
Flux (Jy)

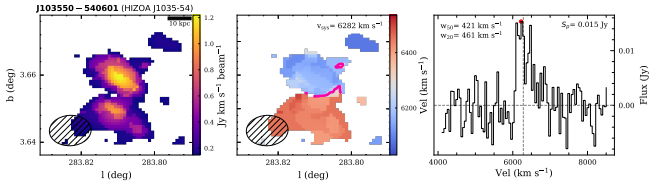
J103550 − 540601 (HIZOA J1035-54)
10 kpc
v_{sys}= 6282 km s^{-1}
w_{50}= 421 km s^{-1}
w_{20}= 461 km s^{-1}
S_p= 0.015 Jy
b (deg)
l (deg)
Jy km s^{-1} beam^{-1}
Vel (km s^{-1})
Flux (Jy)

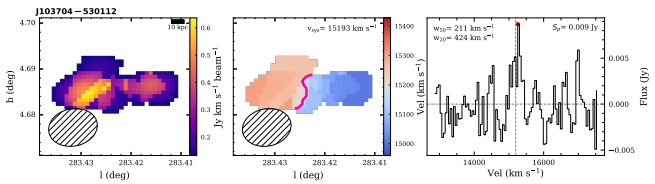
J103704 − 530112
10 kpc
v_{sys}= 15193 km s^{-1}
w_{50}= 211 km s^{-1}
w_{20}= 424 km s^{-1}
S_p= 0.009 Jy
b (deg)
l (deg)
Jy km s^{-1} beam^{-1}
Vel (km s^{-1})
Flux (Jy)

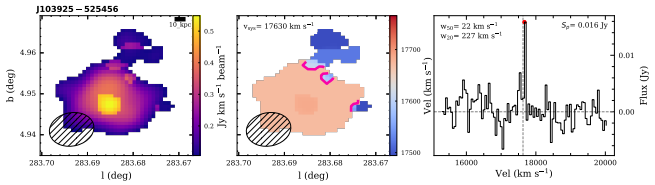
J103925 − 525456
10 kpc
v_{sys}= 17630 km s^{-1}
w_{50}= 22 km s^{-1}
w_{20}= 227 km s^{-1}
S_p= 0.016 Jy
b (deg)
l (deg)
Jy km s^{-1} beam^{-1}
Vel (km s^{-1})
Flux (Jy)

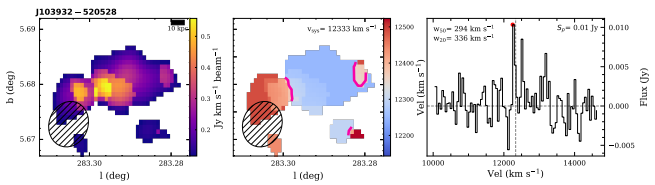
J103932 − 520528
10 kpc
v_{sys}= 12333 km s^{-1}
w_{50}= 294 km s^{-1}
w_{20}= 336 km s^{-1}
S_p= 0.01 Jy
b (deg)
l (deg)
Jy km s^{-1} beam^{-1}
Vel (km s^{-1})
Flux (Jy)

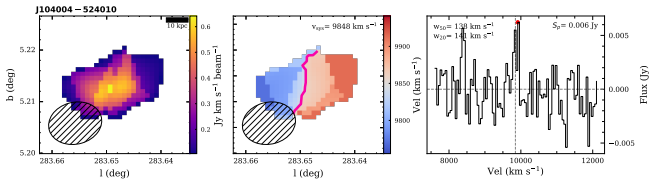
J104004 − 524010
10 kpc
v_{sys}= 9848 km s^{-1}
w_{50}= 130 km s^{-1}
w_{20}= 140 km s^{-1}
S_p= 0.006 Jy
b (deg)
l (deg)
Jy km s^{-1} beam^{-1}
Vel (km s^{-1})
Flux (Jy)

C.3.2 Possible detections

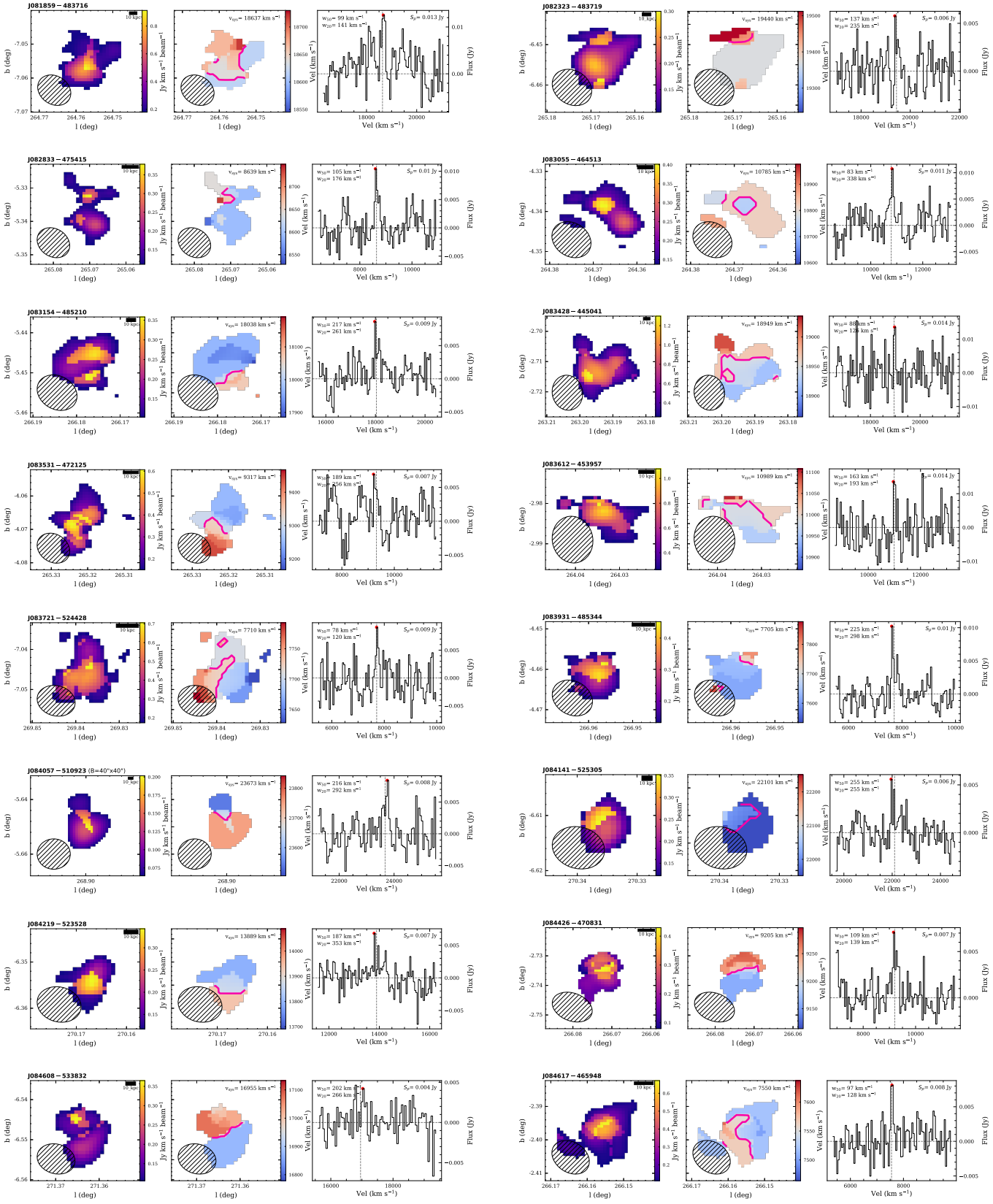

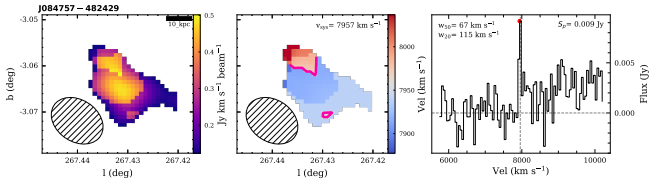
J084757 − 482429
b (deg)
l (deg)
Jy km s⁻¹ beam⁻¹
Vel (km s⁻¹)
Vel (km s⁻¹)
Flux (Jy)

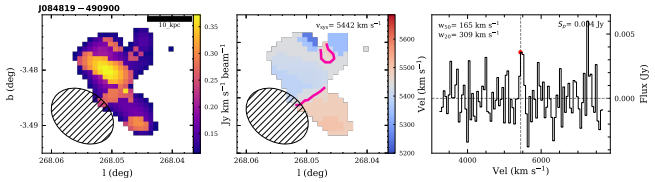
J084819 − 490900
b (deg)
l (deg)
Jy km s⁻¹ beam⁻¹
Vel (km s⁻¹)
Vel (km s⁻¹)
Flux (Jy)

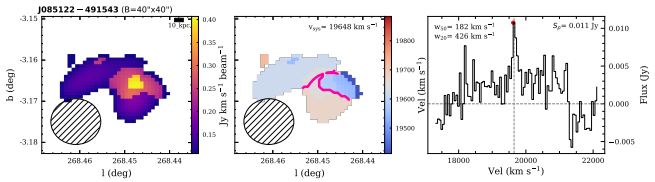
J085122 − 491543 (B=40"x40")
b (deg)
l (deg)
Jy km s⁻¹ beam⁻¹
Vel (km s⁻¹)
Vel (km s⁻¹)
Flux (Jy)

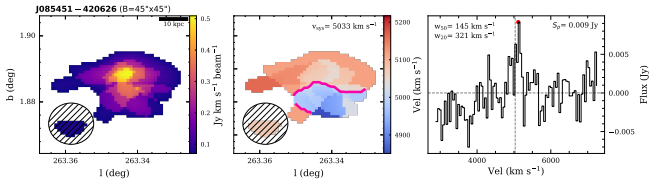
J085451 − 420626 (B=45"x45")
b (deg)
l (deg)
Jy km s⁻¹ beam⁻¹
Vel (km s⁻¹)
Vel (km s⁻¹)
Flux (Jy)

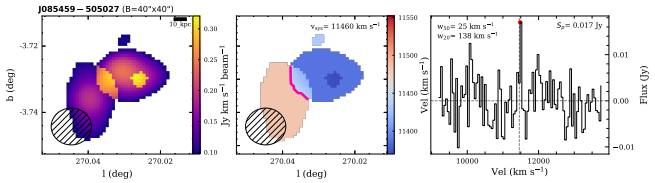
J085459 − 505027 (B=40"x40")
b (deg)
l (deg)
Jy km s⁻¹ beam⁻¹
Vel (km s⁻¹)
Vel (km s⁻¹)
Flux (Jy)

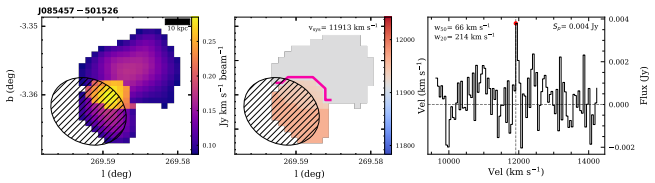
J085457 − 501526
b (deg)
l (deg)
Jy km s⁻¹ beam⁻¹
Vel (km s⁻¹)
Vel (km s⁻¹)
Flux (Jy)

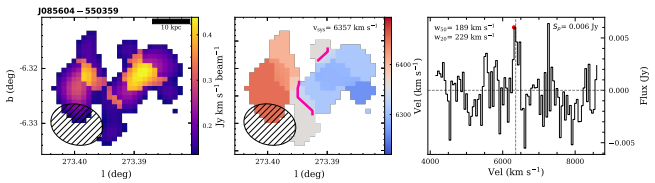
J085604 − 550359
b (deg)
l (deg)
Jy km s⁻¹ beam⁻¹
Vel (km s⁻¹)
Vel (km s⁻¹)
Flux (Jy)

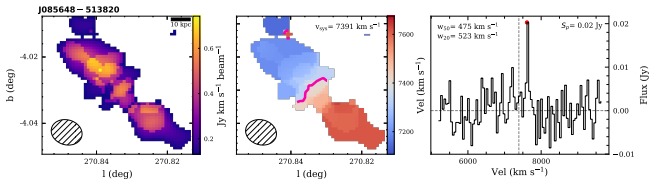
J085648 − 513820
b (deg)
l (deg)
Jy km s⁻¹ beam⁻¹
Vel (km s⁻¹)
Vel (km s⁻¹)
Flux (Jy)

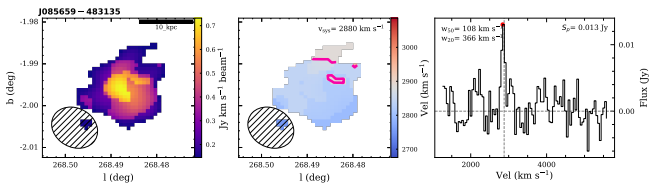
J085659 − 483135
b (deg)
l (deg)
Jy km s⁻¹ beam⁻¹
Vel (km s⁻¹)
Vel (km s⁻¹)
Flux (Jy)

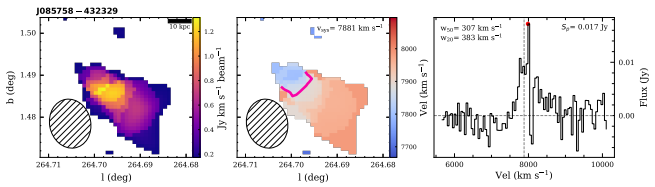
J085758 − 432329
b (deg)
l (deg)
Jy km s⁻¹ beam⁻¹
Vel (km s⁻¹)
Vel (km s⁻¹)
Flux (Jy)

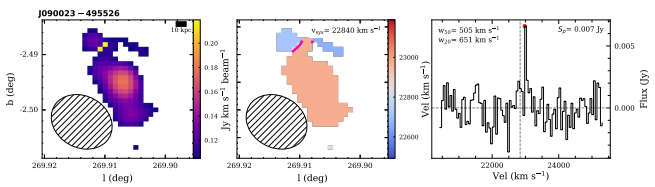
J090023 − 495526
b (deg)
l (deg)
Jy km s⁻¹ beam⁻¹
Vel (km s⁻¹)
Vel (km s⁻¹)
Flux (Jy)

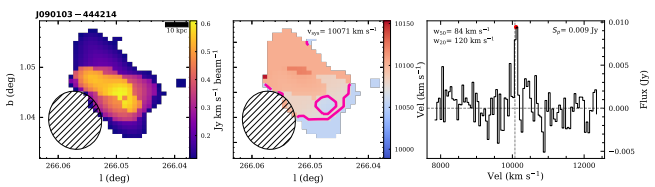
J090103 − 444214
b (deg)
l (deg)
Jy km s⁻¹ beam⁻¹
Vel (km s⁻¹)
Vel (km s⁻¹)
Flux (Jy)

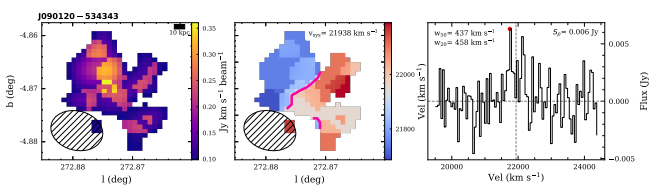
J090120 − 534343
b (deg)
l (deg)
Jy km s⁻¹ beam⁻¹
Vel (km s⁻¹)
Vel (km s⁻¹)
Flux (Jy)

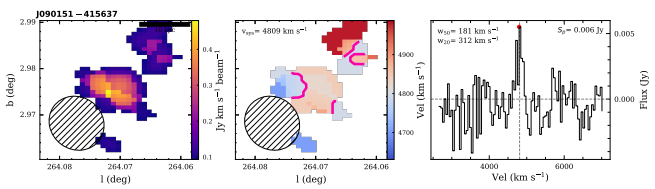
J090151 − 415637
b (deg)
l (deg)
Jy km s⁻¹ beam⁻¹
Vel (km s⁻¹)
Vel (km s⁻¹)
Flux (Jy)

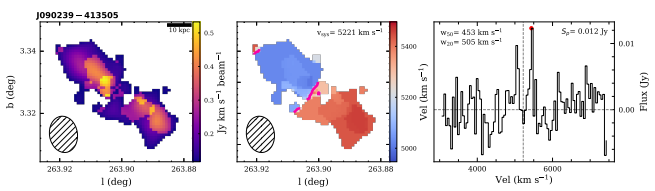
J090239 − 413505
b (deg)
l (deg)
Jy km s⁻¹ beam⁻¹
Vel (km s⁻¹)
Vel (km s⁻¹)
Flux (Jy)

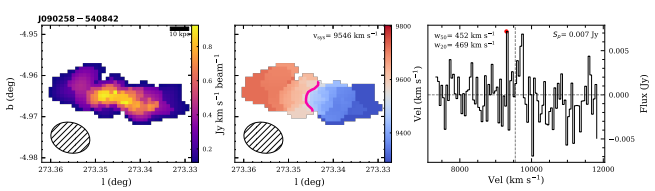
J090258 − 540842
b (deg)
l (deg)
Jy km s⁻¹ beam⁻¹
Vel (km s⁻¹)
Vel (km s⁻¹)
Flux (Jy)

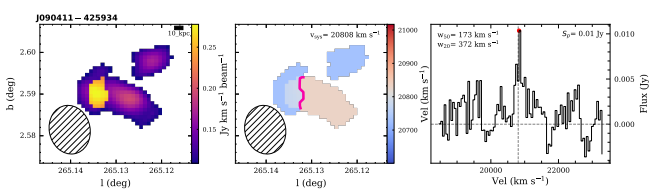
J090411 − 425934
b (deg)
l (deg)
Jy km s⁻¹ beam⁻¹
Vel (km s⁻¹)
Vel (km s⁻¹)
Flux (Jy)

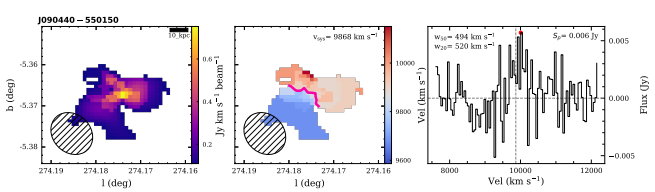
J090440 − 550150
b (deg)
l (deg)
Jy km s⁻¹ beam⁻¹
Vel (km s⁻¹)
Vel (km s⁻¹)
Flux (Jy)

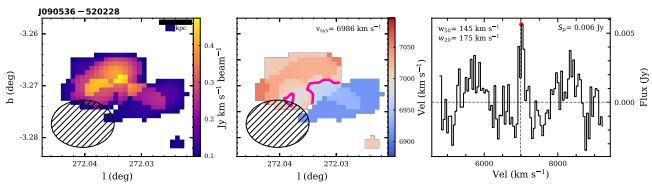
J090536 − 520228
J090631 − 504656

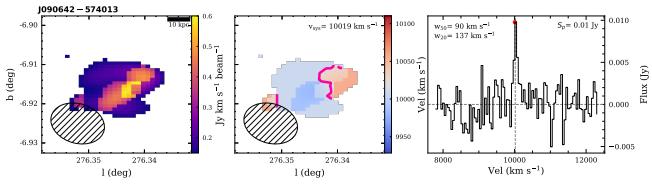
J090642 − 574013
J090643 − 394353

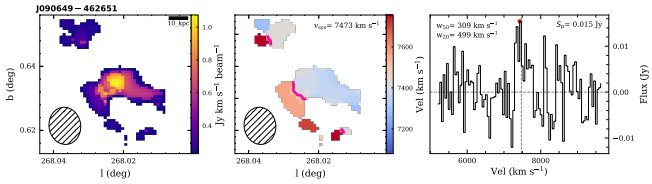
J090649 − 462651
J090802 − 514613

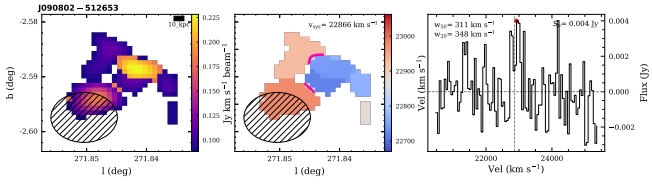
J090802 − 512653
J090901 − 410310

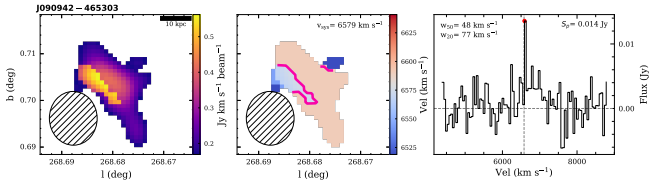
J090942 − 465303
J091028 − 462612

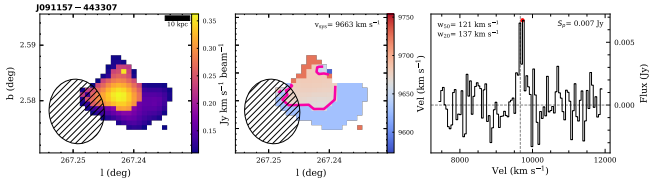
J091157 − 443307
J091240 − 404258

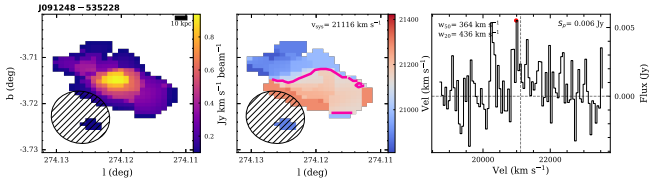
J091248 − 535228
J091317 − 560313

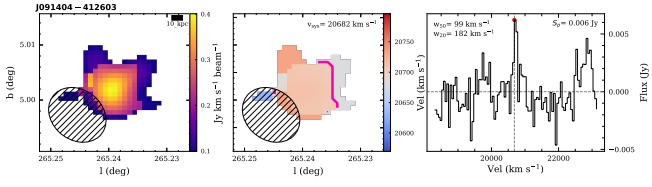
J091404 − 412603
J091413 − 441509

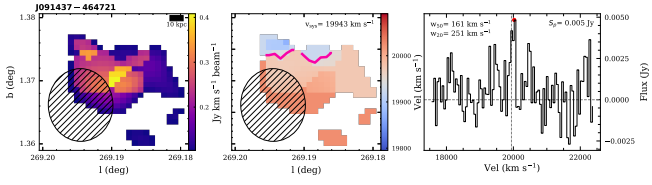
J091437 − 464721
J091502 − 410342

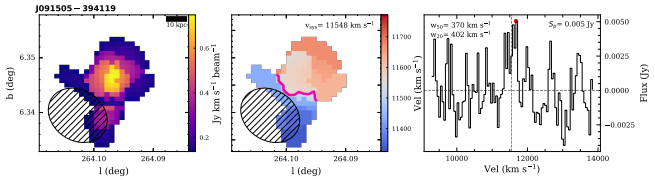
J091505−394119
J091521−515120

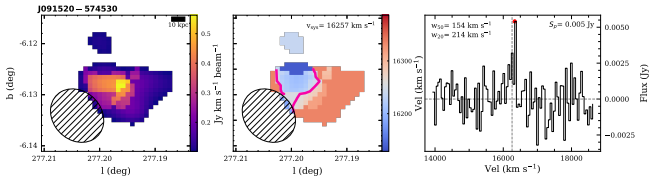
J091520−574530
J091649−561557

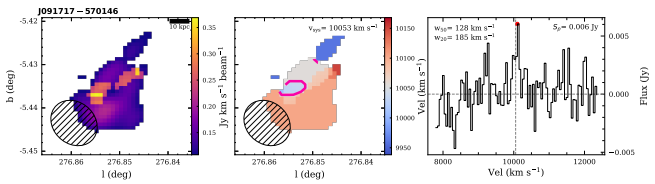
J091717−570146
J091719−513705

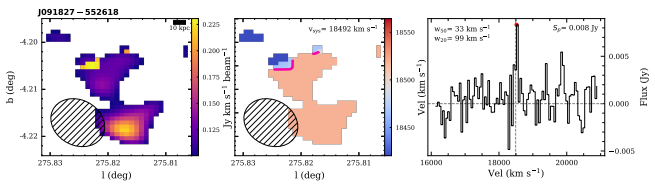
J091827−552618
J091925−550307

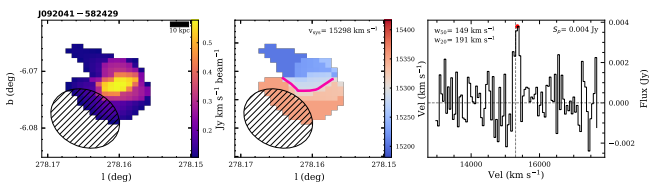
J092041−582429
J092055−443055

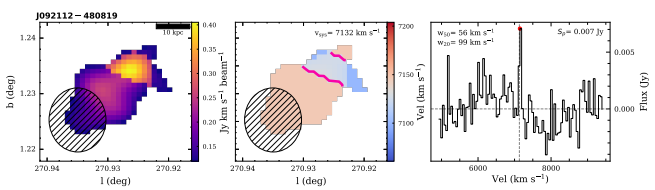
J092112−480819
J092216−443510

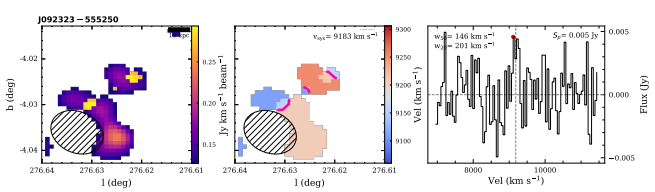
J092323−555250
J092335−442426

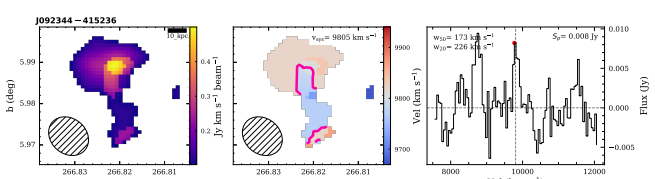
J092344−415236
J092434−585501

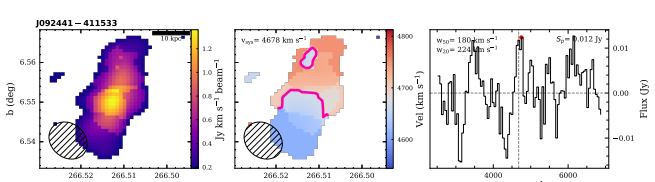
J092441−411533
J092455−582741

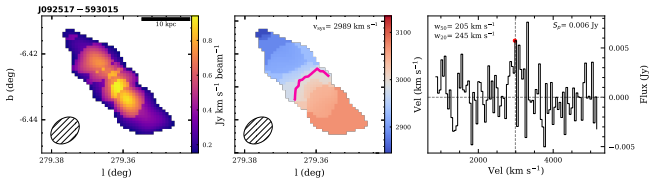
J092517 − 593015
10 kpc
b (deg)
l (deg)
Jy km s⁻¹ beam⁻¹
Vel (km s⁻¹)
Flux (Jy)
v_sys = 2989 km s⁻¹
w50 = 205 km s⁻¹
w20 = 245 km s⁻¹
S_p = 0.006 Jy

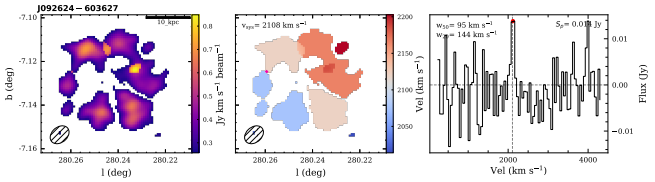
J092624 − 603627
10 kpc
b (deg)
l (deg)
Jy km s⁻¹ beam⁻¹
Vel (km s⁻¹)
Flux (Jy)
v_sys = 2108 km s⁻¹
w50 = 95 km s⁻¹
w20 = 144 km s⁻¹
S_p = 0.011 Jy

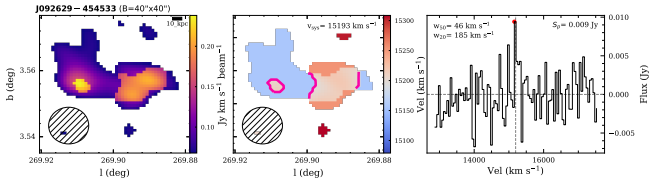
J092629 − 454533 (B=40"×40")
10 kpc
b (deg)
l (deg)
Jy km s⁻¹ beam⁻¹
Vel (km s⁻¹)
Flux (Jy)
v_sys = 15193 km s⁻¹
w50 = 46 km s⁻¹
w20 = 185 km s⁻¹
S_p = 0.009 Jy

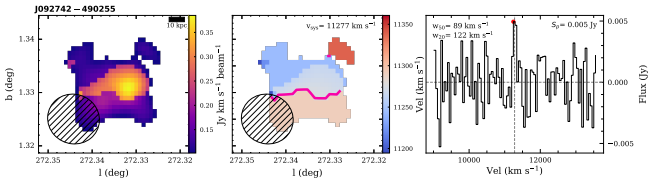
J092742 − 490255
10 kpc
b (deg)
l (deg)
Jy km s⁻¹ beam⁻¹
Vel (km s⁻¹)
Flux (Jy)
v_sys = 11277 km s⁻¹
w50 = 89 km s⁻¹
w20 = 122 km s⁻¹
S_p = 0.005 Jy

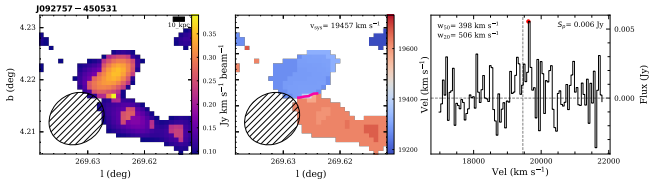
J092757 − 450531
10 kpc
b (deg)
l (deg)
Jy km s⁻¹ beam⁻¹
Vel (km s⁻¹)
Flux (Jy)
v_sys = 19457 km s⁻¹
w50 = 398 km s⁻¹
w20 = 506 km s⁻¹
S_p = 0.006 Jy

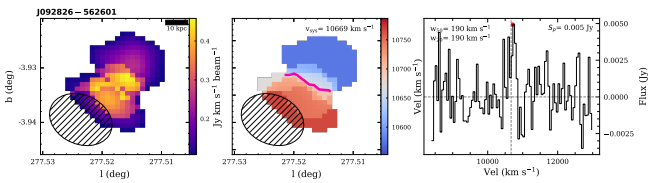
J092826 − 562601
10 kpc
b (deg)
l (deg)
Jy km s⁻¹ beam⁻¹
Vel (km s⁻¹)
Flux (Jy)
v_sys = 10669 km s⁻¹
w50 = 190 km s⁻¹
w20 = 190 km s⁻¹
S_p = 0.005 Jy

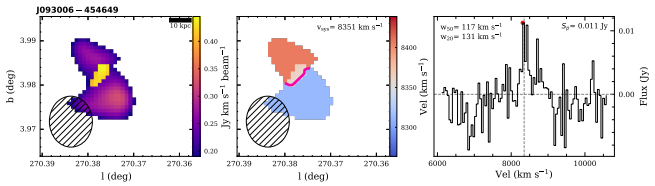
J093006 − 454649
10 kpc
b (deg)
l (deg)
Jy km s⁻¹ beam⁻¹
Vel (km s⁻¹)
Flux (Jy)
v_sys = 8351 km s⁻¹
w50 = 117 km s⁻¹
w20 = 131 km s⁻¹
S_p = 0.011 Jy

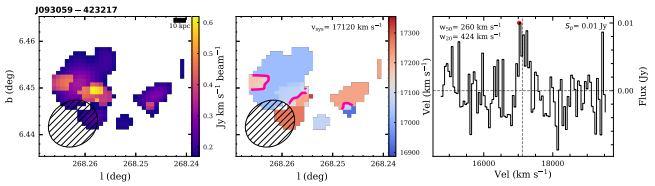
J093059 − 423217
10 kpc
b (deg)
l (deg)
Jy km s⁻¹ beam⁻¹
Vel (km s⁻¹)
Flux (Jy)
v_sys = 17120 km s⁻¹
w50 = 260 km s⁻¹
w20 = 424 km s⁻¹
S_p = 0.01 Jy

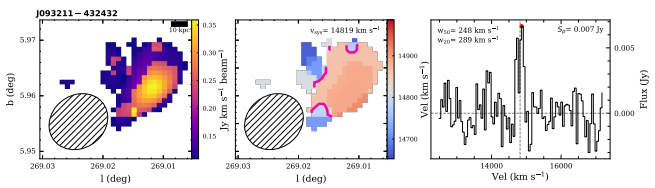
J093211 − 432432
10 kpc
b (deg)
l (deg)
Jy km s⁻¹ beam⁻¹
Vel (km s⁻¹)
Flux (Jy)
v_sys = 14819 km s⁻¹
w50 = 248 km s⁻¹
w20 = 289 km s⁻¹
S_p = 0.007 Jy

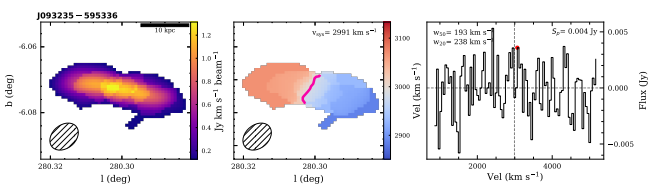
J093235 − 595336
10 kpc
b (deg)
l (deg)
Jy km s⁻¹ beam⁻¹
Vel (km s⁻¹)
Flux (Jy)
v_sys = 2991 km s⁻¹
w50 = 193 km s⁻¹
w20 = 238 km s⁻¹
S_p = 0.004 Jy

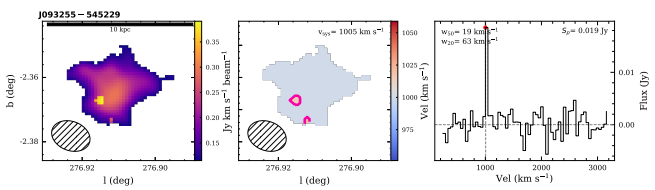
J093255 − 545229
10 kpc
b (deg)
l (deg)
Jy km s⁻¹ beam⁻¹
Vel (km s⁻¹)
Flux (Jy)
v_sys = 1005 km s⁻¹
w50 = 19 km s⁻¹
w20 = 63 km s⁻¹
S_p = 0.019 Jy

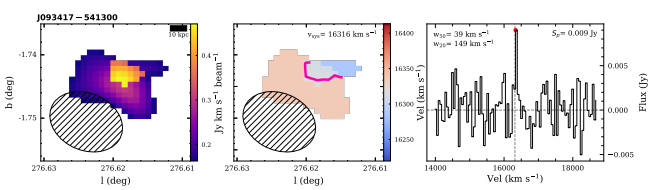
J093417 − 541300
10 kpc
b (deg)
l (deg)
Jy km s⁻¹ beam⁻¹
Vel (km s⁻¹)
Flux (Jy)
v_sys = 16316 km s⁻¹
w50 = 39 km s⁻¹
w20 = 149 km s⁻¹
S_p = 0.009 Jy

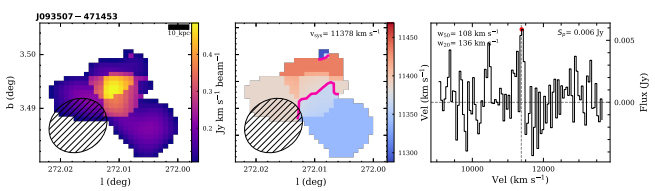
J093507 − 471453
10 kpc
b (deg)
l (deg)
Jy km s⁻¹ beam⁻¹
Vel (km s⁻¹)
Flux (Jy)
v_sys = 11378 km s⁻¹
w50 = 108 km s⁻¹
w20 = 136 km s⁻¹
S_p = 0.006 Jy

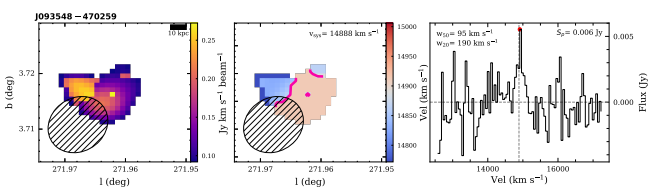
J093548 − 470259
10 kpc
b (deg)
l (deg)
Jy km s⁻¹ beam⁻¹
Vel (km s⁻¹)
Flux (Jy)
v_sys = 14888 km s⁻¹
w50 = 95 km s⁻¹
w20 = 190 km s⁻¹
S_p = 0.006 Jy

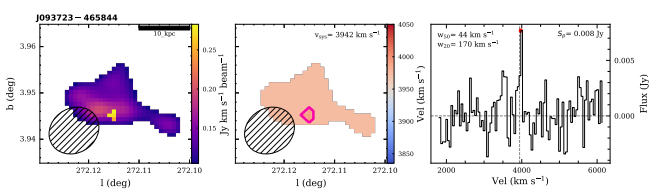
J093723 − 465844
10 kpc
b (deg)
l (deg)
Jy km s⁻¹ beam⁻¹
Vel (km s⁻¹)
Flux (Jy)
v_sys = 3942 km s⁻¹
w50 = 44 km s⁻¹
w20 = 170 km s⁻¹
S_p = 0.008 Jy

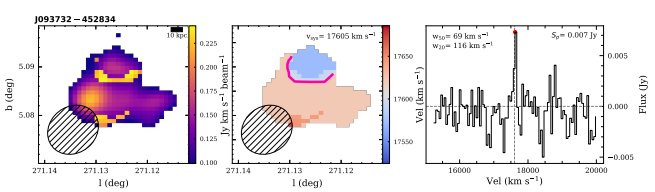
J093732 − 452834
10 kpc
b (deg)
l (deg)
Jy km s⁻¹ beam⁻¹
Vel (km s⁻¹)
Flux (Jy)
v_sys = 17605 km s⁻¹
w50 = 69 km s⁻¹
w20 = 116 km s⁻¹
S_p = 0.007 Jy

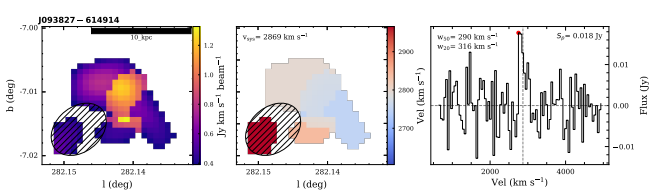
J093827 − 614914
10 kpc
b (deg)
l (deg)
Jy km s⁻¹ beam⁻¹
Vel (km s⁻¹)
Flux (Jy)
v_sys = 2869 km s⁻¹
w50 = 290 km s⁻¹
w20 = 316 km s⁻¹
S_p = 0.018 Jy

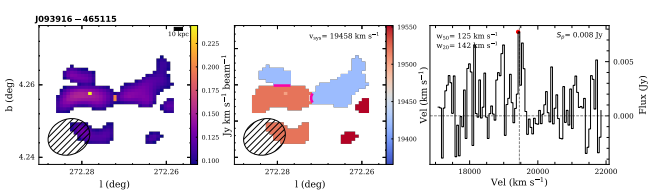
J093916 − 465115
10 kpc
b (deg)
l (deg)
Jy km s⁻¹ beam⁻¹
Vel (km s⁻¹)
Flux (Jy)
v_sys = 19458 km s⁻¹
w50 = 125 km s⁻¹
w20 = 142 km s⁻¹
S_p = 0.008 Jy

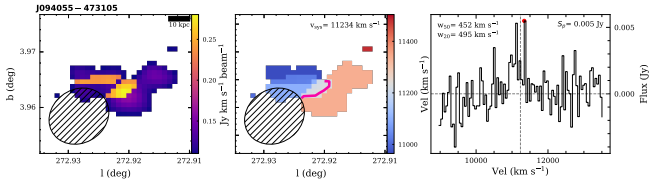
J094055−473105
J094111−580103

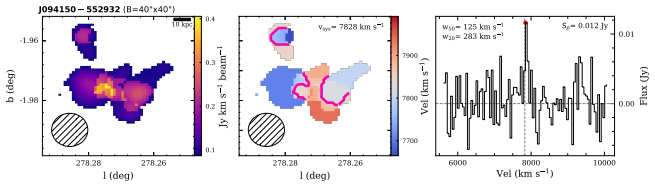
J094150−552932 (B=40"x40")
J094202−560800

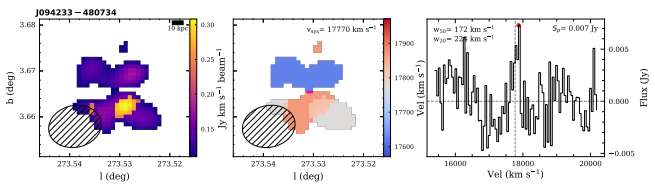
J094233−480734
J094252−601728

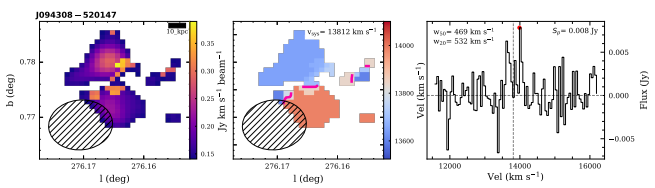
J094308−520147
J094339−583333 (B=40"x40")

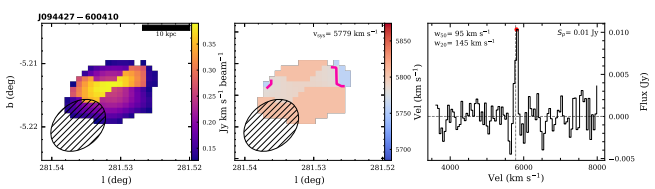
J094427−600410
J094428−491944

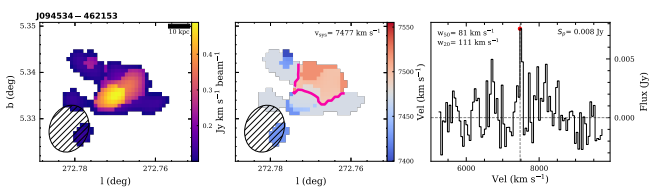
J094534−462153
J094541−494647

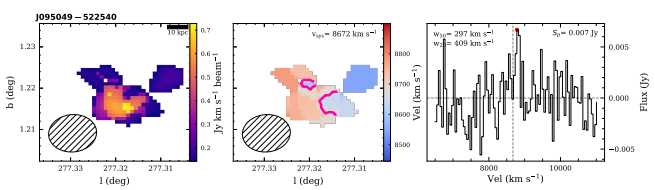
J095049−522540
J095059−580933

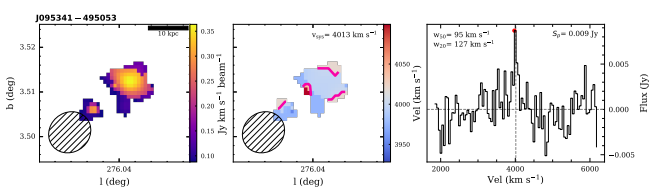
J095341−495053
J095347−455758

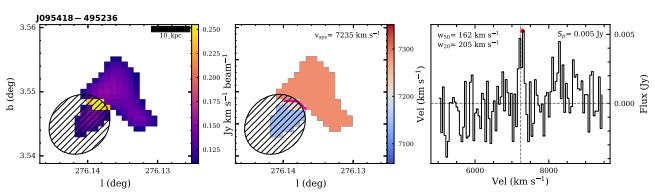
J095418−495236
J095427−513059 (HIZOA J0954-51)

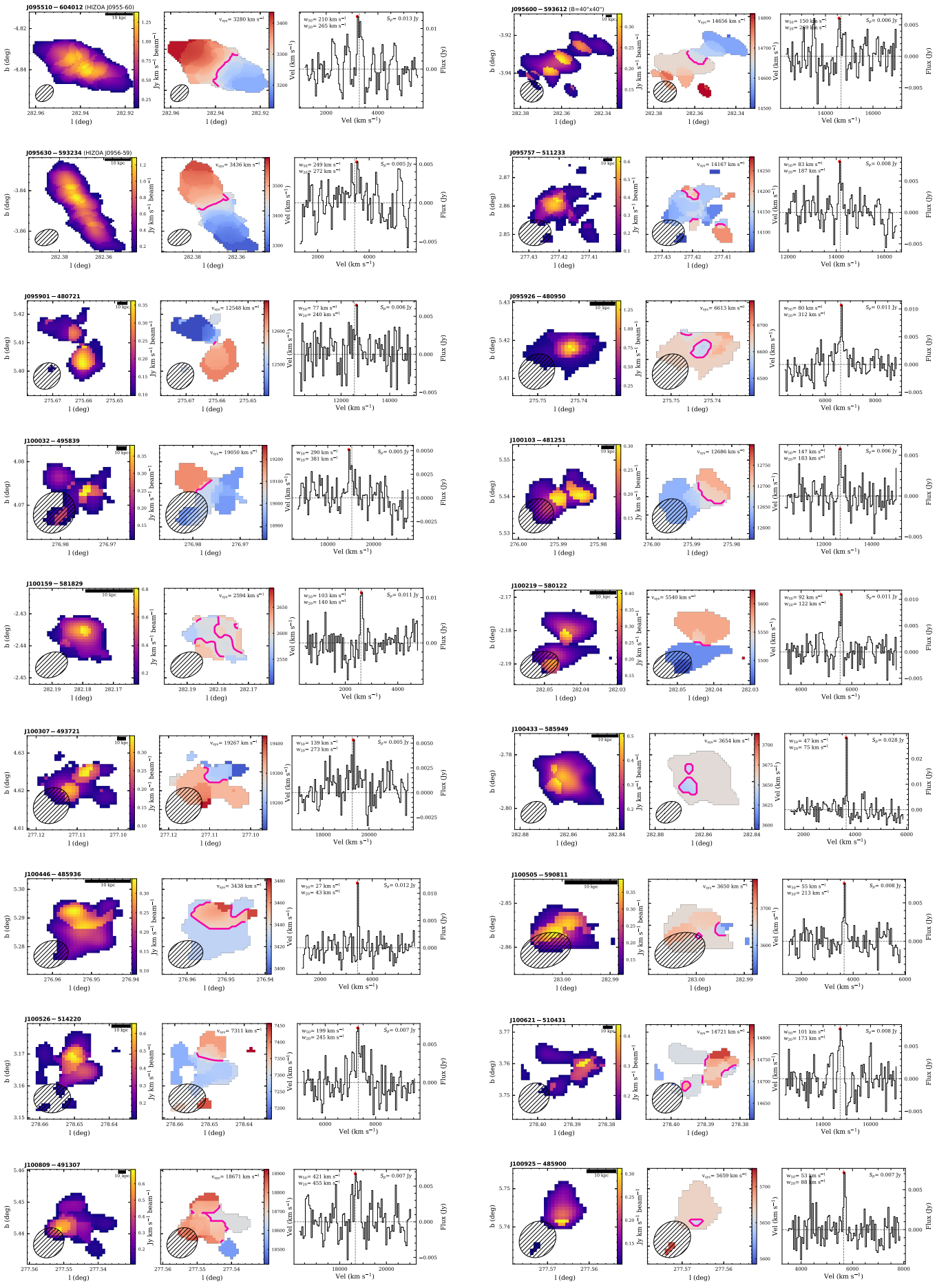
J095510−604012 (HIZOA J0955-60)
J095600−593612 (B=40"×40")
J095630−593234 (HIZOA J0956-59)
J095757−511233
J095901−480721
J095926−480950
J100032−495839
J100103−481251
J100159−581829
J100219−580122
J100307−493721
J100433−585949
J100446−485936
J100505−590811
J100526−514220
J100621−510431
J100809−491307
J100925−485900
l (deg)
b (deg)
Vel (km s−1)
Flux (Jy)
Jy km s−1 beam−1
10 kpc

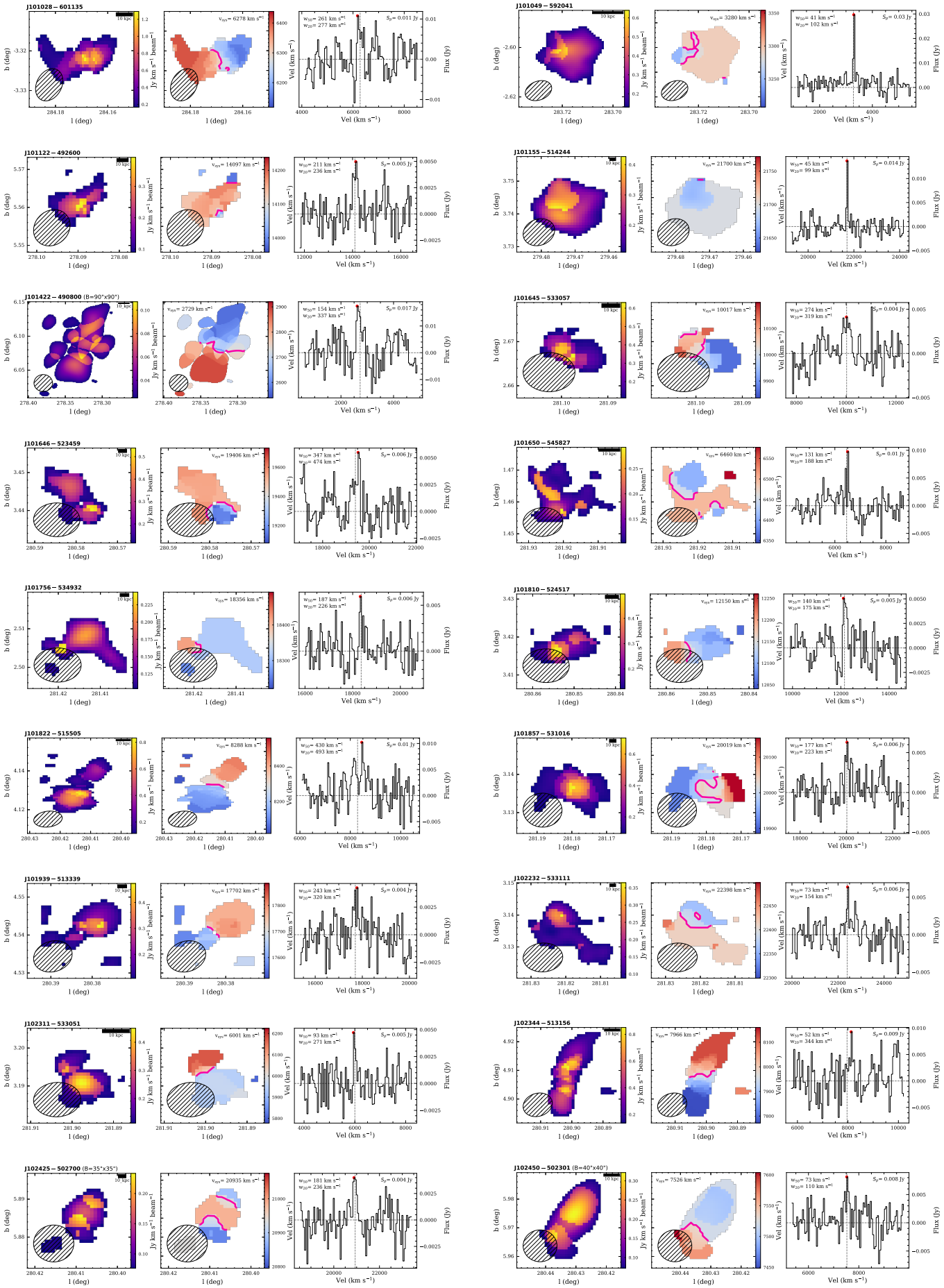
J101028−601135
J101049−592041
J101122−492600
J101155−514244
J101422−490800 (B=90"x90")
J101645−533057
J101646−523459
J101650−545827
J101756−534932
J101810−524517
J101822−515505
J101857−531016
J101939−513339
J102232−533111
J102311−533051
J102344−513156
J102425−502700 (B=35"x35")
J102450−502301 (B=40"x40")
l (deg)
b (deg)
Vel (km s−1)
Flux (Jy)
Jy km s−1 beam−1

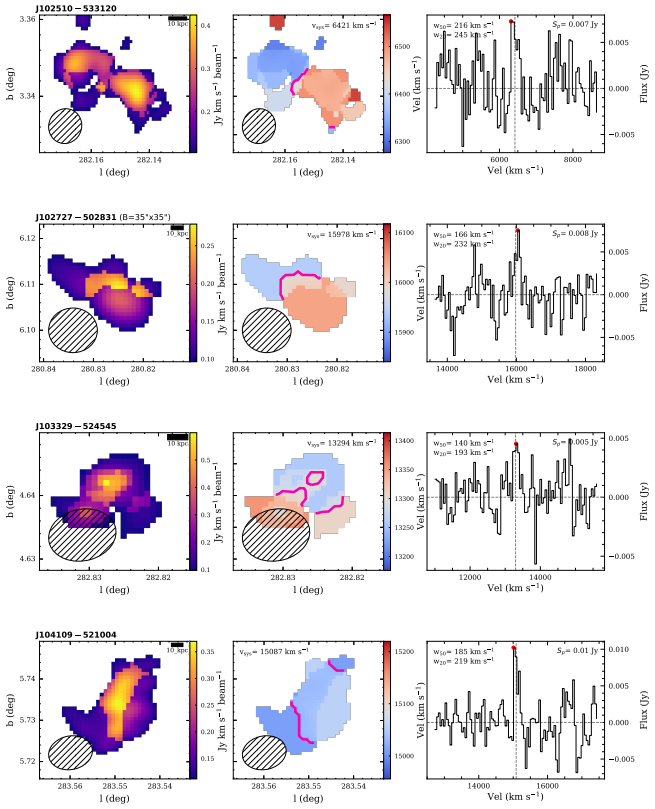
J102510 – 533120
J102631 – 503508
J102727 – 502831 (B=35"x35")
J103042 – 524148
J103329 – 524545
J103844 – 524728
J104109 – 521004
J104131 – 513246
l (deg)
b (deg)
Vel (km s^{-1})
Flux (Jy)
Jy km s^{-1} beam^{-1}